# International Journal of Modern Engineering Research (IJMER)

# International Journal of Modern Engineering Research (IJMER)

## Contents :

# Analysis of Glass Epoxy Reinforced Monolithic Leaf Spring

Mohammed Mathenulla Shariff[1], N. Sreenivasa Babu[2], Dr. Jaithirtha Rao[3]

*#Engineering Department, Shinas College of Technology, Sultanate of Oman*
*#3 IDST consultant, RCI, DRDO, Hyderabad, India*

***Abstract:*** *The automobile industry has been showing an interest in the replacement of steel spring with fiberglass composite leaf spring because of its high strength to weight ratio. Therefore the aim of this paper is to design and analyze composite mono leaf spring of constant width and thickness having the same bending stiffness of semi-elliptical laminated leaf spring. Stress analysis was done by using analytical method and results obtained by analytical methods are compared with ansys. The results obtained by analytical methods showed good agreement with ansys results. A Tsai-Hill failure criterion was used to check whether stresses are within reasonable levels for each ply. The stresses induced in the composite leaf springs were found to be 33.79% less compared to steel leaf spring. When steel leaf spring is replaced by composite leaf spring a weight reduction of 77.29% is obtained , 2.23 times higher natural frequency, 1.371 times more strain energy storage capacity, 33.79 % lesser stress and lesser value of spring rate is obtained in the composite leaf spring compared to steel leaf spring.*

***Keywords:*** *Monolithic, Stress Analysis, Natural Frequency, Strain Energy, Glass Epoxy.*

## I. Introduction

The newest innovation in leaf-spring technology is the composite design, or what some would call a fiberglass leaf, although there are other materials involved in the construction of these products. Composite leaf springs are a new concept.
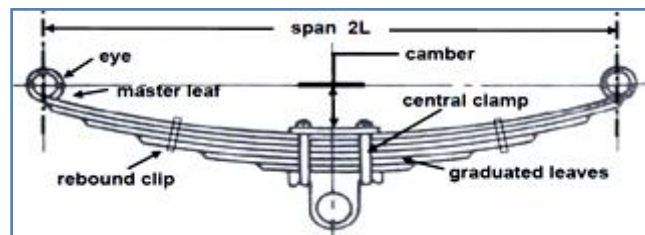

Fig: 1 A laminated semi- elliptic leaf spring.

The primary advantages of using a composite leaf spring are a 60-70 percent weight savings over steel springs and the tendency of the composite spring to maintain its shape, it doesn't sag. The composite leaf springs, just like the steel, come in various rates from 35 to 250 pounds. They can be used as a "single" leaf in low rates or as a "stack" leaf, still a mono-design but thicker (like a stacked steel spring). Even a small amount in weight reduction of the vehicle, may have a wider economic impact. Composite materials are proved as suitable substitutes for steel in connection with weight reduction of the vehicle. Hence, the composite materials have been selected for leaf spring design.

## II. Problem Description & Formulation

A semi-elliptical leaf spring is chosen for analysis Using FEA by considering a simple supported beam with a concentrated load at the center. Composite beam material Fiber is Glass (Reinforcement Phase) and Matrix is Epoxy. Consider laminate of ten layers each of 2.9528 mm thick. Then thickness of the laminate is 29.9528 mm. Initially consider ten laminas of Zero degree orientations for ease of manufacturing for hand layup process. A Flow Chart for design Calculation is formulated as follows.

---
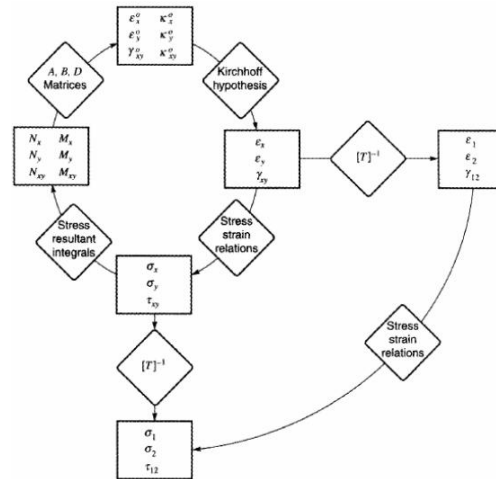
Fig: 2 Calculation Spiral flow chart
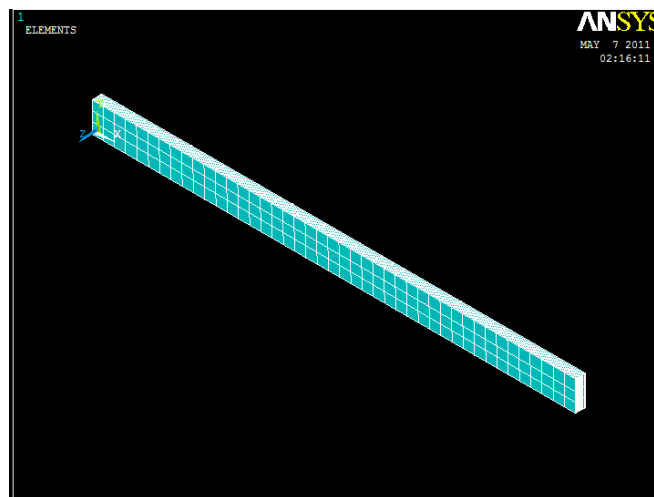


Fig: 3 Isometric view of model

## III. Result Analysis And Validation

Stress Analysis of composite leaf spring was done using Ansys for composite leaf spring of constant width and constant thickness so as to compare the results of stress analysis obtained analytically.
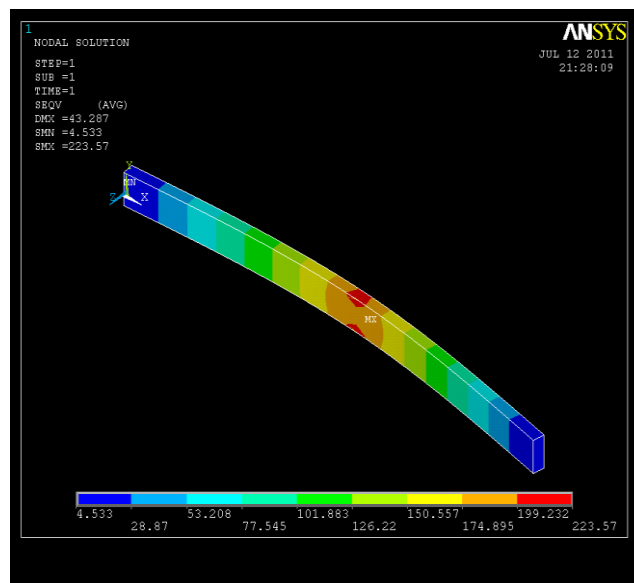


Fig: 4 Isometric view of model

The value of Spring Rate for a steel leaf spring found analytically (K) = 187.4507 N/mm. The following is the comparison table of load, max stress and deflection of composite leaf spring calculated analytically and using Ansys for 0.6 fiber volume fraction.

| Load (N) | Deflection (mm) | | Stress (MPa) | |
|---|---|---|---|---|
| | Analytical | Ansys | Analytical | Ansys |
| 0.0 | 0.000 | 0.0000 | 0.000 | 0 |
| 1000.0 | 5.093 | 5.2090 | 27.955 | 28.364 |
| 2000.0 | 10.186 | 10.4170 | 55.911 | 56.728 |
| 3000.0 | 15.279 | 15.6260 | 83.866 | 85.092 |
| 4000.0 | 20.372 | 20.8350 | 111.822 | 113.456 |
| 5000.0 | 25.465 | 26.0440 | 139.777 | 141.82 |
| 6000.0 | 30.558 | 31.2520 | 167.733 | 170.183 |
| 7000.0 | 35.651 | 36.4610 | 195.688 | 198.547 |
| 7500.0 | 38.196 | 43.287 | 209.665 | 223.57 |

Table: 1 Load, Deflection and Stress for 0.6 Fiber Volume Fraction

| Load (N) | Deflection (mm) | | Stress (MPa) | |
|---|---|---|---|---|
| | Analytical | Ansys | Analytical | Ansys |
| 0.0 | 0.000 | 0.0 | 0.000 | 0.0 |
| 1000.0 | 4.725 | 4.7 | 27.955 | 28.4 |
| 2000.0 | 9.448 | 9.5 | 55.911 | 56.7 |
| 3000.0 | 14.172 | 14.2 | 83.866 | 85.1 |
| 4000.0 | 18.896 | 18.9 | 111.822 | 113.4 |
| 5000.0 | 23.620 | 23.7 | 139.777 | 141.8 |
| 6000.0 | 28.344 | 28.4 | 167.733 | 170.1 |
| 7000.0 | 33.068 | 33.1 | 195.688 | 198.5 |
| 7500.0 | 35.435 | 35.5 | 209.665 | 212.6 |

Table: 2 Load, Deflection and Stress for 0.65 Fiber Volume Fraction

| Load (N) | Deflection (mm) | | Stress (MPa) | |
|---|---|---|---|---|
| | Analytical | Ansys | Analytical | Ansys |
| 0.0 | 0.000 | 0.0000 | 0.000 | 0 |
| 1000.0 | 4.406 | 4.4120 | 27.955 | 28.364 |
| 2000.0 | 8.812 | 8.9120 | 55.911 | 56.728 |
| 3000.0 | 13.218 | 13.5670 | 83.866 | 85.092 |
| 4000.0 | 17.624 | 17.7340 | 111.822 | 113.456 |
| 5000.0 | 22.030 | 22.2010 | 139.777 | 141.82 |
| 6000.0 | 26.436 | 26.6750 | 167.733 | 170.183 |
| 7000.0 | 30.842 | 30.8490 | 195.688 | 198.547 |
| 7500.0 | 33.046 | 33.2160 | 209.665 | 212.723 |

Table: 3 Load, Deflection and Stress for 0.7 Fiber Volume Fraction

| Material | Weight( Kg) | Strain energy (N- mm) Analytical | Spring Rate (N- mm) Analytical |
|---|---|---|---|
| Steel | 28.1856 | 872146.6551 | 187.4507 |
| Composite $V_f$=0.6 | 6.399 | 1289126.397 | 196.3556 |
| Composite $V_f$=0.65 | 6.399 | 1195936.527 | 211.655 |
| Composite $V_f$=0.7 | 6.399 | 1115311.593 | 226.956 |

Table: 4 Comparison of Steel and Composite Leaf Spring
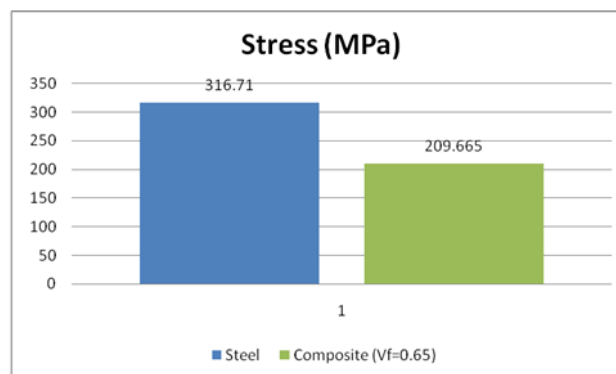


Fig: 4 Comparison of stress for Steel and composite

## IV. CONCLUSIONS

➢ The analytical results were compared with FEA and the results show good agreement.
➢ From the results, it is observed that the composite leaf spring is lighter and more economical than the conventional steel spring with similar design specifications.
➢ When steel leaf spring is replaced by composite leaf spring, weight reduction of 77.29% is obtained, 2.23 times higher natural frequency, 1.371 times more strain energy storage capacity, 33.79 % lesser stress and lesser value of strain rate is obtained in the composite leaf spring compared to steel leaf spring is obtained.

## Acknowledgment

## REFERENCES

[1]    W.G.Gottenberg and K.H.Lo. Glasss fiber reinforced epoxy leaf spring design. Int.J.of Vehicle Design, vol.4,no.3,1983.
[2]    W.J.Yu and H.C.Kim. Double Tapered FRP beam for Automotive Suspension Leaf spring Int.J.of composite structures, vol.9 ,279-300,1988.
[3]    Erol Sancaktar and Mathieu Gratton. Design, Analysis and optimization of Composite Leaf Springs for Light Vehicle Applications. Int.J.of composite structures, vol.44 ,195-204, 1999.
[4]    Onur Sayman and Mesut Uyaner. Elastic-Plastic analysis of Composite Beams Loaded by Bending Moment. Journal of Reinforced plastics and composites, vol.21, N0.1/2002.
[5]    Gulur Siddramanna and Shivshankar. Mono composite leaf spring for light weight vehicles –Design and Testing. ISSN 1392–1320 MATERIALS SCIENCE (MEDŽIAGOTYRA). Vol. 12, No. 3. 2006.
[6]    Daugherty, R. L. Composite Leaf Springs in Heavy Truck Applications. K. Kawata, T.Akasaka (Eds). Composite Materials Proceedings of Japan-US Conference Tokyo, 1981: pp. 529 – 538.
[7]    Rajendran, I., Vijayarangan, S. Optimal Design of a Composite Leaf Spring using Genetic Algorithms Int. Jr. of Computer and Structures 79 2001: pp. 1121 – 1129.
[8]    Madhujit Mukhopadhyay, "Mechanics of composite materials and structures" Universities Press, 1st edition , 2004
[9]    Design data handbook (Si and metric units) for mechanical engineering. K-Mahadevan and Dr K Balaveera Reddy

# A Novel Multi Port Dc/Dc Converter Topology Using Zero Voltage Switching For Renewable Energy Applications

Vinay Kumar V.[1]**,** Senthil S.[2]**,** Rama Raju K.[3]
*(Department of Electrical and Electronics Engineering, SVCET, JNTU Anantapur, A.P, India)*

**ABSTRACT:** *This paper proposes a novel dc/dc converter topology that interfaces the non-conventional energy sources. It consists of four power ports: two sources (namely solar and wind), one bidirectional storage port, and one isolated load port. The proposed four-port dc/dc converter is derived by simply adding two switches and two diodes to the traditional half-bridge topology. Zero-voltage switching is realized for all four main switches. This paper proposes a new four-port-integrated dc/dc topology, which is suitable for various renewable energy harvesting applications. An application interfacing hybrid photovoltaic (PV) and wind sources, one bidirectional battery port, and an isolated output port is given as a design example. It can achieve maximum power-point tracking (MPPT) for both PV and wind power simultaneously or individually, while maintaining a regulated output voltage.*

**Index Terms:** *DC–DC converter, half-bridge, multiple-input single-output (MISO), multiport, zero-voltage switching (ZVS).*

## I.   Introduction

As interest in renewable energy systems with various sources becomes greater than before, there is a supreme need for integrated power converters that are capable of interfacing, and concurrently, controlling several power terminals with low cost and compact structure. This paper proposes a new four-port-integrated dc/dc topology, which is suitable for various renewable energy harvesting applications. Three of the four ports can be tightly regulated by adjusting their independent duty-cycle values, while the fourth port is left unregulated to maintain the power balance for the system. Compared to the effort spent on the traditional two-port converter, less work has been done on the multiport converterCircuit analysis and design considerations are presented. Four-port dc/dc converter has bidirectional capability.

## II.   Topology and Circuit Analysis

The four-port topology is derived based on the traditional two port half-bridge converter, which consists of two main switches $S_1$ and $S_2$ . As shown in Fig. 1, one more input power port can be obtained by adding a diode$D_3$ and an active switch $S_3$ . Another bidirectional power path can be formed by adding a freewheeling branch across the transformer primary side, consisting of a diode $D_4$ and an active switch $S_4$ . As a result, the topology ends up with four active switches and two diodes, plus the transformer and the rectification circuit. The proposed converter topology is suitable for a number of power-harvesting applications, and this paper will target the hybrid PV wind application. It should be noted that since the wind turbine normally generates a three phase ac power, an ac/dc rectifier needs to be installed before this four-port dc/dc interface and after the wind turbine output. However, the ac/dc solution is beyond the scope of this paper.
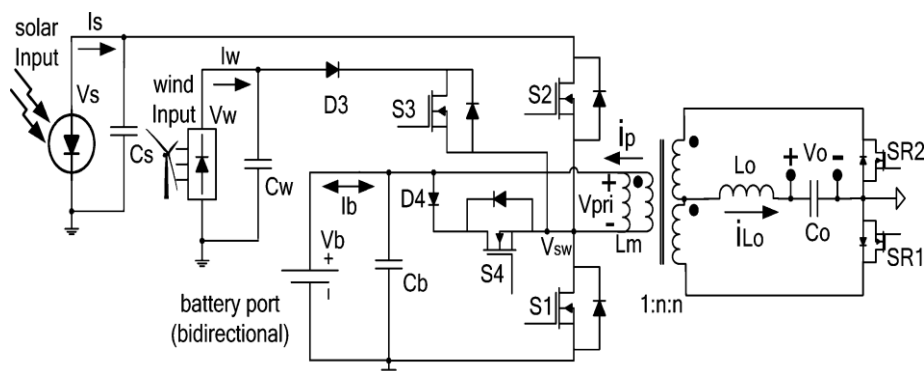


Fig. 1. Four-port half-bridge converter topology, which can achieve ZVS for all four main switches ($S_1$ , $S_2$ , $S_3$, and $S_4$ )

### 2.1 Principle of Circuit Operation

The steady-state waveforms of the four-port converter are shown in Fig. 3, and the various operation stages in one switching cycle can be explained by using their respective circuits. To simplify the analysis of operation, components are considered ideal. The main operation stages are described as follows shown in fig. 2:.
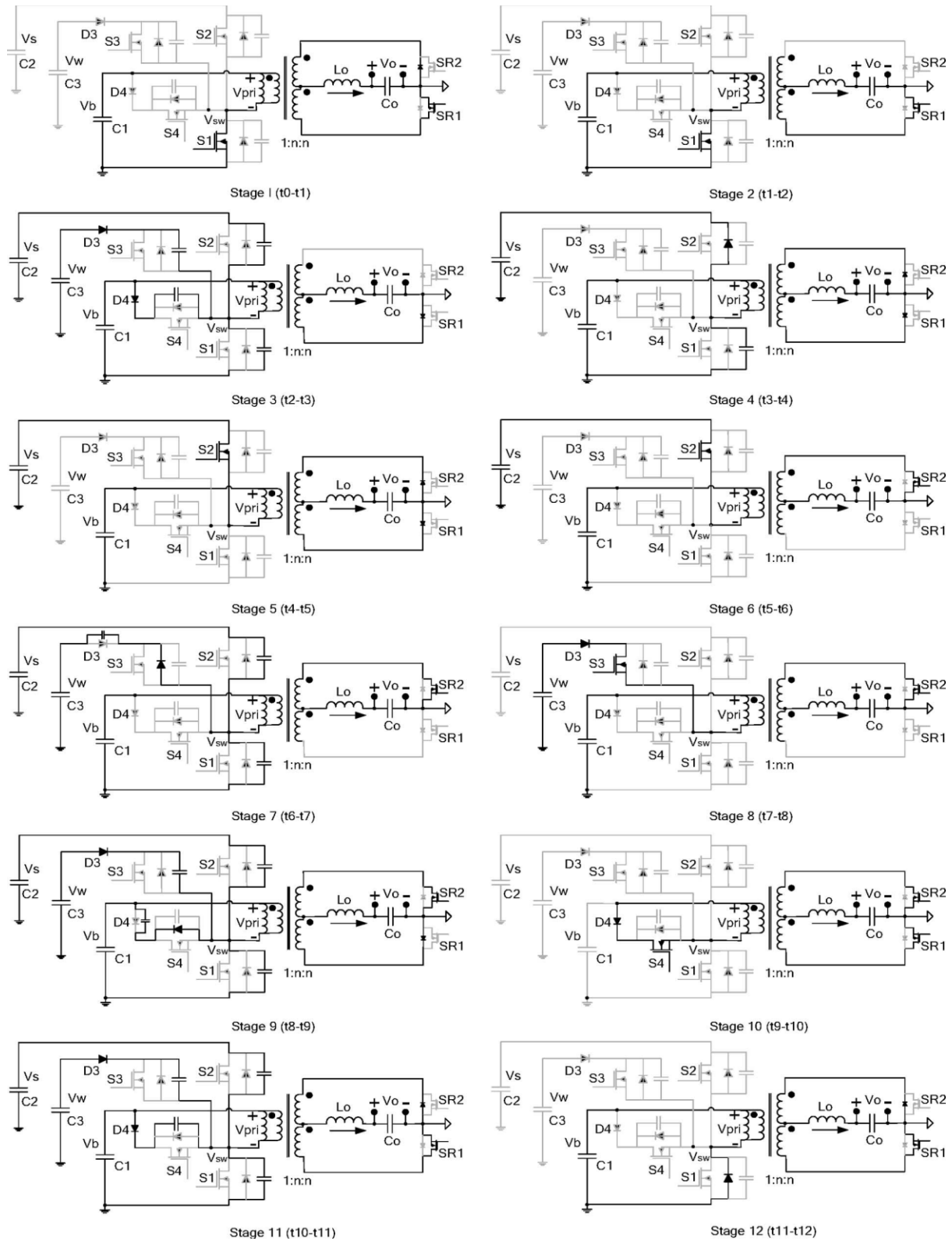


Fig.2: Operation stages of the four-port half-bridge converter.

2.2 Steady-State Analysis
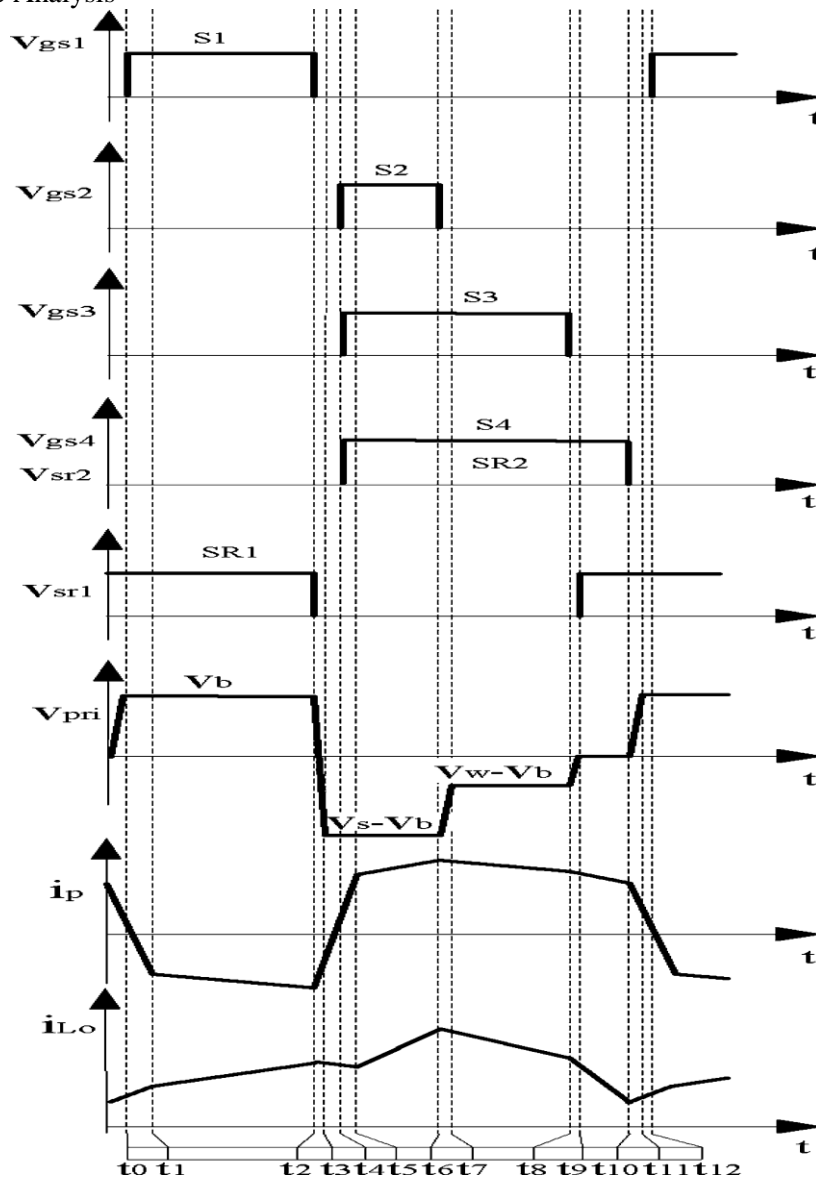


Fig. 3. Steady-state waveforms of the four-port half-bridge converter

The steady-state voltage governing relations between different port voltages can be determined by equating the voltage–second product across the converter's two main inductors to zero. First, using volt–second balance across the primary transformer magnetizing inductance LM in time continuous conduction mode(CCM), we have

$$VbD1 = (Vs - Vb)D2 + (Vw - Vb)D3 \qquad . (1)$$

Assuming CCM operation, the voltage-second balance across the load filter inductor *Lo* then yields

$$VbD1 + (Vs - Vb)D2 + (Vw - Vb)D3 = Von \qquad . (2)$$

The following equation is based on the power balance principle, by assuming a lossless converter, steady-state port currents can be related as follows:

$$VsIs + Vw\,Iw = VbIb + VoIo \qquad . (3)$$

The battery current *Ib* is positive during charging and negative during discharging.

## 2.3 ZVS Analysis

ZVS of the switches S1 and S2 can be realized through the energy stored in the transformer leakage inductor, while ZVS of S3 and S4 is always maintained, because the proposed driving scheme ensures that paralleling diodes of S3 and S4 will be forced on before the two switches turn ON. To sum up, ZVS of all main

switches can be achieved to maintain higher efficiency when the converter is operated at higher switching frequency, because of the potential savings in switching losses.

## 2.4 Circuit Design Considerations

The major difference is that the transformer design of this four-port converter needs to allow for a dc current flow, and therefore, becomes similar to an inductor or a flyback transformer design. The dc biasing current rating is dictated by average transformer magnetizing current $I_M$, which determines the amount of the air gap to be inserted. Other than the transformer, the circuit design and optimization technique used for the traditional half-bridge topology can be used here for this four-port topology, which provides great convenience for the practicing engineers to implement the power stage design.

**TABLE I** Values of Circuit Parameters

| Output inductor | $L_0$ | 45μH | Solar port filter capacitor | $C_s$ | 100 μF |
|---|---|---|---|---|---|
| Magnetizing inductor | $L_m$ | 45μH | Battery port filter capacitor | $C_b$ | 330 μF |
| Output filter capacitor | $C_0$ | 330 μF | Wind port filter capacitor | $C_w$ | 100 μF |

## III.   Control Structure and Dynamic Modelling

The proposed converter has three freedoms to control the power flow of three power ports, while the fourth port is to maintain the power balance. That means the operating point of up to three ports can be tightly regulated, while the fourth port should be left "flexible" and would operate at any point that satisfies the power balance constraints. The choice of the flexible power port dictates the feedback control layout, which is based on different control objectives. For instance, if the battery is chosen to be left "flexible," the maximal power from the solar and wind sources can be tracked by their port voltages or currents independently, and the load voltage can be regulated by a voltage feedback as well.

### 3.1 Control Structure

Fig. 3 shows the control structure for the hybrid PV wind system. Three feedback controllers are as follows: a solar voltage regulator (SVR), a wind voltage regulator (WVR), and an output voltage regulator (OVR). In this system, the battery storage plays the significant role of balancing the system energy by injecting power at heavy loads and absorbing excess power when available PV and wind power exceeds the load demand.
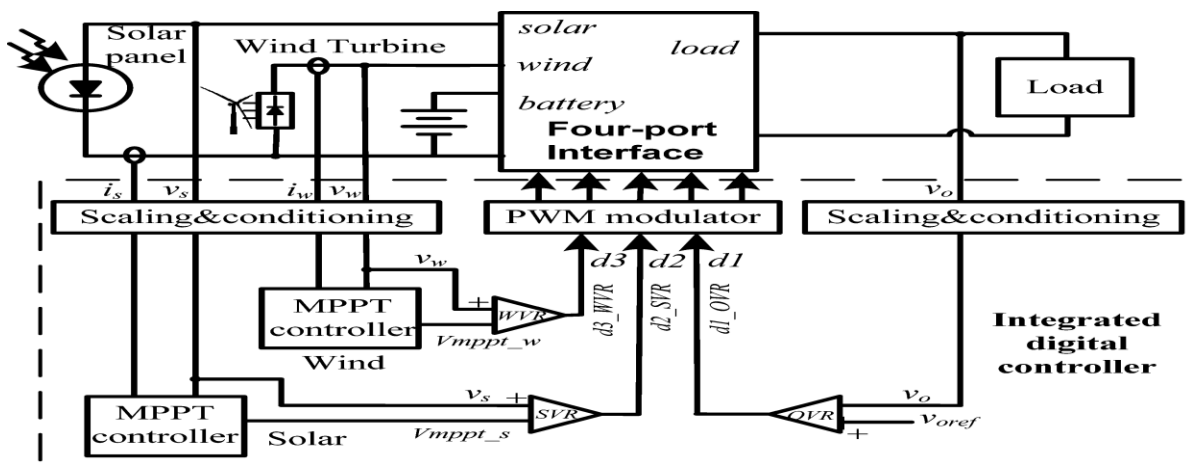


Fig.4. Possible control structure to achieve MPPT for the PV panel and the wind turbine,

### 3.2 Dynamic Modelling

In order to design the SVR, WVR, and OVR controllers, a small signal model of the four-port converter is desired.  First, state-space equations for five energy storage elements during the four main circuit stages are developed. For the aforementioned mode of operation, these include the solar side capacitor $Cs$ , the wind-side capacitor $Cw$ , the transformer magnetizing inductor $LM$ , the output inductor $Lo$ , and the output capacitor $Co$ . In the next step, state-space equations in the four main circuit stages (corresponding to the turn ON of four main switches) will be averaged, and then applied with the small signal perturbation. Finally, the first-order small-signal perturbation components will be collected to form the matrices A and B, which actually represent the converter power stage model. Alternatively, the dynamics of the plant can be calculated by computer software like MATLAB. The resultant state-space averaging model takes the following form:

$$d\hat{}x(t)/dt = A\hat{}x(t) + B\hat{}u(t), \ \hat{}y(t) = I\,\hat{}x(t) \qquad (8)$$

$\hat{}iLo\ (t),$ and $\hat{}vo\ (t),$ $\hat{}u(t)$ is a matrix containing the control inputs $\hat{}d1\ (t),$ $\hat{}d2\ (t),$ and $\hat{}d3\ (t),$ $\hat{}y(t)$ is a matrix containing the system outputs, and $I$ is the identity matrix.

## IV. MATLAB Design and Experimental Results

A four-port dc/dc converter prototype is built to verify the circuit operation. The switching frequency is 100 kHz, and it is implemented by the digital control to achieve the close-loop regulation. The conclusion is that all four main switches can achieve ZVS, because they all turn ON after their *V*ds go to zero.
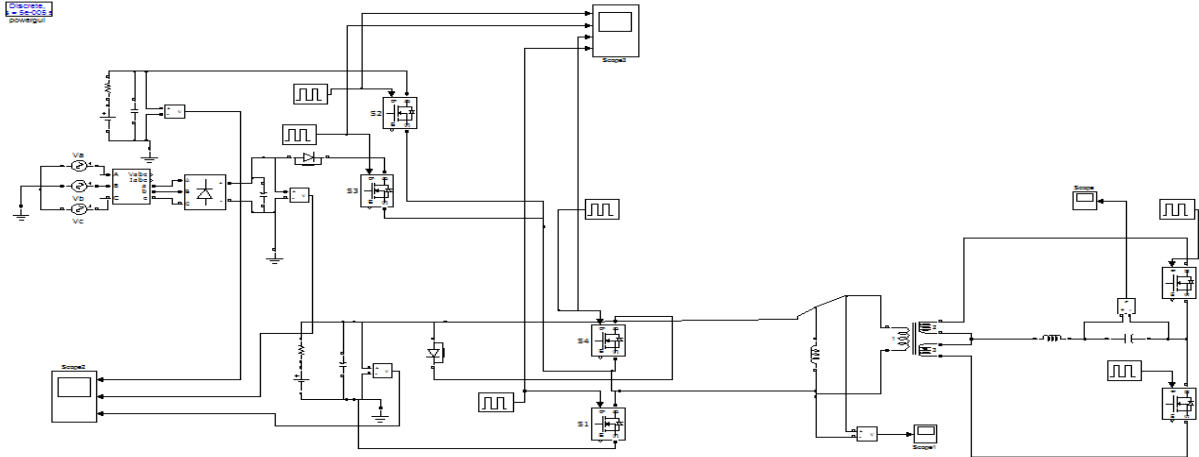


Fig. 4. MATLAB Design of the proposed four port dc/dc converter
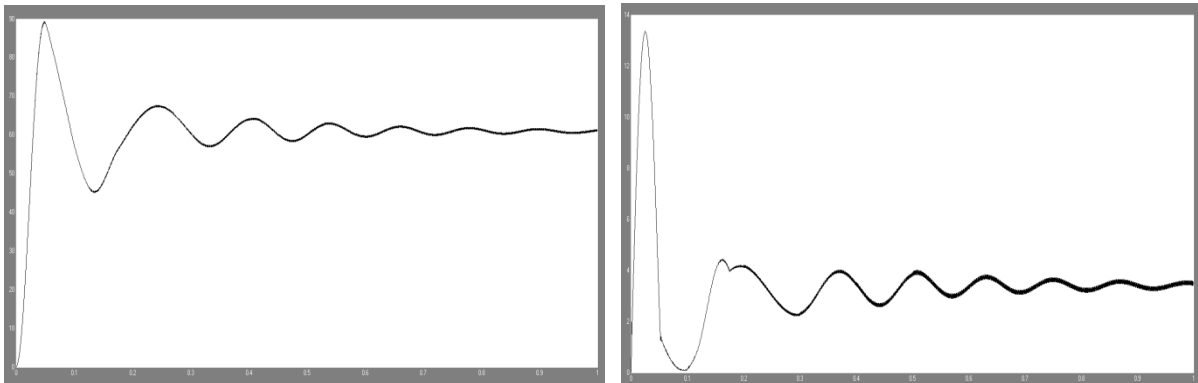


Fig. 5. Transient responses of the MPPT controller
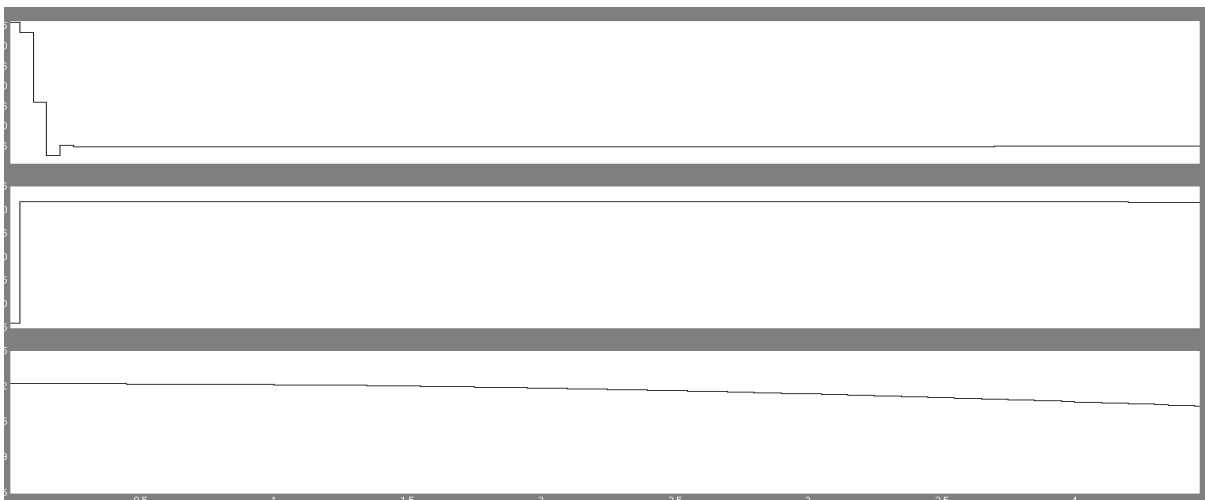


Fig. 6: Steady state waveforms: Solar, Wind, and battery output voltage responses under different load and source conditions

---

(a) Vo                                                           (b) Io
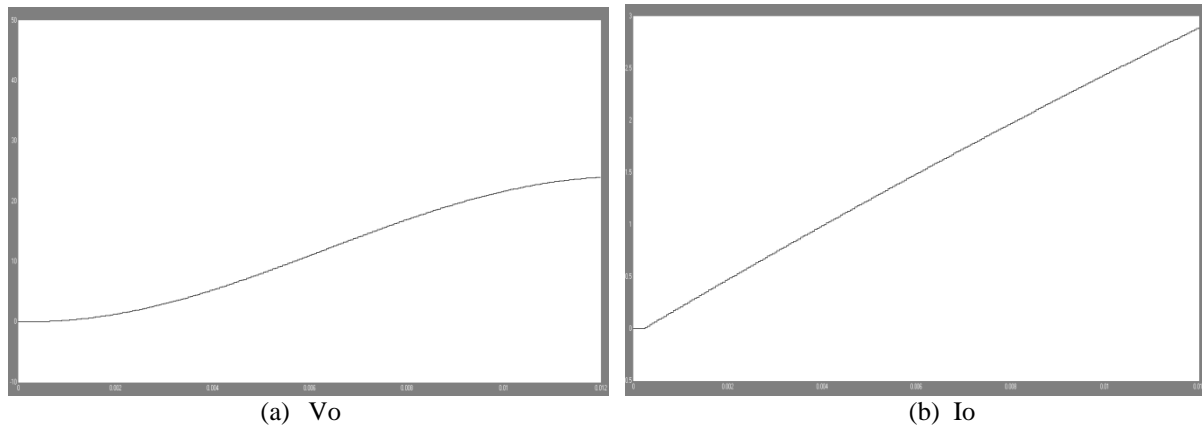
Fig. 7. (a) Output voltage and (b) Output current waveforms

## V.  Extension Of The Topology

In the proposed four-port dc/dc converter, there are two input switch branches, which enable two sources. However, the number of the unidirectional switch branches is not limited. Addition of a half-bridge upper switch plus a diode will provide one more input port to interface another renewable energy source which is one of the extension of the proposed. In order to use the same for high power applications, a full bridge multiport converter can be designed which is also considered as the extension for the proposed.

## VI.  Conclusion

This paper has presented a novel dc/dc converter topology in which, the converter features low component count and ZVS operation for all primary switches. Modification based on the traditional half-bridge topology makes it convenient for the practicing engineers to follow the power stage design. Three degrees of freedom necessary to control power flow in the system are provided by a four-stage constant-frequency switching sequence. This four-port converter is suitable for renewable energy systems, where the energy storage is required while allowing tight load regulation. It is suitable for low-power applications since based on the half-bridge topology, while the multiport converter based on the full-bridge topology maybe suitable for high-power applications. For the hybrid PV wind system, the proposed control structure is able to achieve maximum power harvesting for PV and/or wind power sources, meanwhile maintaining a regulated output voltage. The circuit operation of this converter and its control system is experimentally verified.

## REFERENCES

[1]     Y. Liu and Y. M. Chen, "A systematic approach to synthesizing multi input DC–DC converters," Power Electroics., vol. 24, no. 2, pp. 116–127, Jan. 2009.
[2]     D. Liu; H. Li, "A ZVS bi-directional DC-DC converter for multiple energy storage elements,". Power Electronics, pp.1513-1517, Sept. 2006.
[3]     F. A. Farret and M. G. Simes, Integration of Alternative Sources of Energy, New York: Wiley, 2006.
[4]     S. Jain; V. Agarwal, "An integrated hybrid power supply for distributed generation applications fed by nonconventional energy sources,"Trans. Energy Conversion, vol.23, no.2, pp.622-631, June 2008.
[5]     A. D. Napoli; F. Crescimbini; S. Rodo; L. Solero, "Multiple input dc-dc power converter for fuel-cell powered hybrid vehicles," Power Electronics Specialist Conf., vol.4, pp.1685-1690, 2002.
[6]     Y.M. Chen; Y.C. Liu; F.Y. Wu "Multi-input dc/dc converter based on the multi-winding transformer for renewable energy application," Ind. Appl., pp.1096-1104, 2002.
[7]     R. D. Doncker; D. M. Divan; M. H. Kheraluwala, "A three-phase soft-switched high-power-density DC/DC converter for high-power applications," Industry Applications, on, vol.27, no.1, pp.63-73, Jan/Feb 1991.
[8]     F. Z. Peng; H. Li; G-J Su; J. S. Lawler, "A new ZVS bidirectional DC-DC converter for fuel cell and battery application," Industry Applications, on, vol.27, no.1, pp.63-73, Jan/Feb 1991.
[9]     O. D. Patterson; D. M. Divan, "Pseudo-resonant full bridge DC/DC converter," Power Electronics,on, vol.6, no.4, pp.671-678, Oct 1991.
[10]    H. Tao; A. Kotsopoulos; J. L. Duarte; M.A.M. Hendrix, "Design of a soft switched three-port converter with DSP control for power flow management in hybrid fuel cell systems," presented at the 2005 European Conf. on Power Electronics and Applications, Dresden, Germany.
[11]    D. Xu; C. Zhao; H. Fan, "A PWM plus phase-shift control bidirectional DC-DC converter," Power Electronics on , vol.19, no.3, pp. 666-675, May 2004.

# Three-dimensional Streamline Design of the Pump Flow Passage of Hydrodynamic Torque Converter

Shiping Liu[1], Shujuan Zheng[2]

[1]*(School of Mechanical Engineering, North China University of Water Resources and Electric Power, China)*
[2]*(School of Mechanical Engineering, North China University of Water Resources and Electric Power, China)*

**ABSTRACT:** *The design methods of three-element, centripetal turbine hydrodynamic torque converters were investigated. A new design method, three-dimensional streamline design method, was proposed. Firstly, the three-dimensional central streamline of the flow passage was designed and the streamline consists of a circular arc and a short straight line segment. After that, the central streamline equation was obtained and the design path equation was derived. Next, any other meridional flow path can numerically be obtained. Finally, the three-dimensional streamline corresponding to any meridional flow path was computed numerically. Investigation results show that the proposed method is feasible and possesses obvious advantages. First, the curvature radius of the three-dimensional central streamline remains unchanged, while any other three-dimensional streamline is close to a circular arc as well. Therefore, the energy losses caused by streamline bending can be reduced. Second, because the fluid particle near the flow passage outlet flows in a straight line law and the energy losses due to flow deviation can be reduced. Third, all the three-dimensional streamlines are theoretically located in an identical plane. Thereby energy losses caused by the turbulence can be reduced. Fourth, because of the flat blades, the manufacture cost of a torque converter can be reduced.*

***Keywords:*** *hydrodynamic torque converter, three-dimensional streamline, curvature radius of streamline, flat blade.*

## I. Introduction

A hydrodynamic torque converter is an important device used to transmit power and to improve the traction performance of a vehicle. However, an obvious disadvantage of a hydrodynamic torque converter is that its efficiency is not high enough, which will affect the economy of the vehicle.

As the flow field of a hydrodynamic torque converter is extraordinarily complex, the working mechanism of torque converters has not been understood very well. It is necessary to investigate the design theories and methods of hydrodynamic torque converters. Traditionally, one-dimensional design theory is used for the design of torque converters [1-2]. However, the flow field described by using one-dimensional theory does not entirely agree with the actual flow field of a torque converter because of too many assumptions and simplifications. Therefore, it is inevitable to introduce modeling error. After this situation taken into account, two-dimensional design theory was developed [3]. It is feasible for the two-dimensional theory to be used to describe the flow field of a centrifugal or axial-flow turbine torque converter, but the large modeling error still exists if the two-dimensional theory is used to describe the flow field of a commonly used centripetal-turbine torque converters. Actually, the flow field of a torque converter is three-dimensional, but the three-dimensional design theory is still at a exploratory stage [3-8]. Currently, one-dimensional theory is still predominant theory, and widely used methods are still the circulation distributing method and the conformal mapping method, which are based on empirical and statistical data [9]. Ref. [10] established a analytical system of research and design, Ref. [11] proposed torus streamline design method, Ref. [12] studied the streamline bending impact on energy loss, and Ref. [13] put forward a plane streamline design method. These results promote the research of design theories and design methods of torque converters.

The purpose for the investigation is to improve the efficiency of a hydrodynamic torque converter. Therefore, a new design method, three-dimensional streamline design method, is proposed in this paper.

## II. Determination of 3-Dimensional Central Streamline

According to [11], construct a tangent vector at the passage inlet of the pump, as shown in Fig. 1.
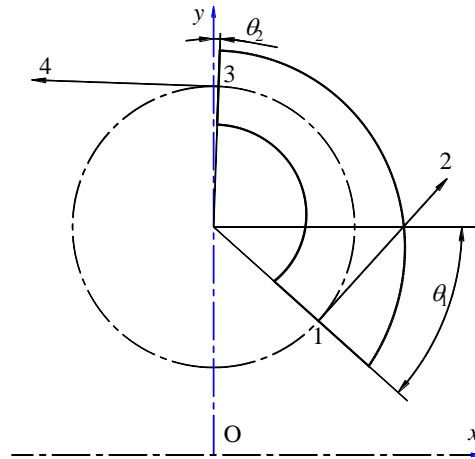
Figure 1: Tangent vectors at the pump blade inlet and outlet

The tangent vector at the passage inlet of the pump can be expressed as:

$$\mathbf{V}_{12} = (a_{12}, b_{12}, c_{12}) = (x_2 - x_1, y_2 - y_1, z_2 - z_1) \tag{1}$$

The length of the vector is:

$$L_{12} = \sqrt{a_{12}^2 + b_{12}^2 + c_{12}^2} \tag{2}$$

The tangent vector at the passage outlet is:

$$\mathbf{V}_{34} = (a_{34}, b_{34}, c_{34}) = (x_4 - x_3, y_4 - y_3, z_4 - z_3) \tag{3}$$

The length of the vector takes on $L_{12}$ too.

Rotate tangent vector $\mathbf{V}_{34}$ an angle around x-axis to the position $3'4'$, just located in an identical plane with the vector $\mathbf{V}_{12}$. The expression of the rotation angle is:

$$\alpha = \arcsin \frac{C_2}{\sqrt{1 + C_1^2}} - \arcsin \frac{C_1}{\sqrt{1 + C_1^2}} \tag{4}$$

where

$$C_1 = \frac{(x_3 - x_2)y_1 z_4 + (x_1 - x_4)y_3 z_2 + (x_1 - x_3)(y_2 z_4 - y_4 z_2)}{(x_3 - x_2)y_1 y_4 + (x_4 - x_1)y_2 y_3 + (x_1 - x_3)(y_2 y_4 + z_2 z_4) + (x_2 - x_4)y_1 y_3} \tag{5}$$

$$C_2 = \frac{(x_3 - x_4)y_1 z_2 + (x_1 - x_2)y_3 z_4}{(x_3 - x_2)y_1 y_4 + (x_4 - x_1)y_2 y_3 + (x_1 - x_3)(y_2 y_4 + z_2 z_4) + (x_2 - x_4)y_1 y_3} \tag{6}$$

The plane determined by vector $\mathbf{V}_{12}$ and $\mathbf{V}_{3'4'}$ equation is:

$$Ax + By + Cz = 1 \tag{7}$$

where

$$A = \frac{y_1 z_2 + (y_2 y_3 - y_1 y_3)\sin \alpha - y_3 z_2 \cos \alpha}{x_3 y_1 z_2 + (x_1 y_2 y_3 - x_2 y_1 y_3)\sin \alpha - x_1 y_3 z_2 \cos \alpha} \tag{8}$$

$$B = \frac{(x_3 z_2 - x_1 z_2) + (x_1 y_3 - x_2 y_3)\sin \alpha}{x_3 y_1 z_2 + (x_1 y_2 y_3 - x_2 y_1 y_3)\sin \alpha - x_1 y_3 z_2 \cos \alpha} \tag{9}$$

$$C = \frac{(x_3 y_1 - x_2 y_1 + x_1 y_2 - x_3 y_2) + (x_2 y_3 - x_1 y_3)\cos \alpha}{x_3 y_1 z_2 + (x_1 y_2 y_3 - x_2 y_1 y_3)\sin \alpha - x_1 y_3 z_2 \cos \alpha} \tag{10}$$

With the plane, it is convenient to design three-dimensional streamlines.
After rotation, the tangent vector at the passage outlet of the pump becomes:

$$\mathbf{V}_{3'4'} = (a_{3'4'}, b_{3'4'}, c_{3'4'}) = (x_{4'} - x_{3'}, y_{4'} - y_{3'}, z_{4'} - z_{3'}) \tag{11}$$

Construct the third vector from point 1 to point $3'$. The vector can be expressed as:

$$\mathbf{V}_{13'} = (a_{13'}, b_{13'}, c_{13'}) = (x_{3'} - x_1, y_{3'} - y_1, z_{3'} - z_1) \tag{12}$$

The length of the vector is:

$$L_{13'} = \sqrt{(x_{3'} - x_1)^2 + (y_{3'} - y_1)^2 + (z_{3'} - z_1)^2} \tag{13}$$

By using the dot product of two vectors and their lengths, the angle between vector $\mathbf{V}_{12}$ and vector $\mathbf{V}_{13'}$ can be obtained:

$$\alpha_1 = \arccos \frac{a_{12}a_{13'} + b_{12}b_{13'} + c_{12}c_{13'}}{L_{12}L_{13'}} \tag{14}$$

Similarly, the angle between vector $\mathbf{V}_{3'4'}$ and $\mathbf{V}_{13'}$ is:

$$\alpha_2 = \arccos \frac{a_{3'4'}(-a_{13'}) + b_{3'4'}(-b_{13'}) + c_{3'4'}(-c_{13'})}{L_{12}L_{13'}} \tag{15}$$

With $\alpha_1, \alpha_2$ and $L_{13'}$, a triangle $\Delta 13'5$ determined by the three parameters can be drawn, as shown in Fig. 2.
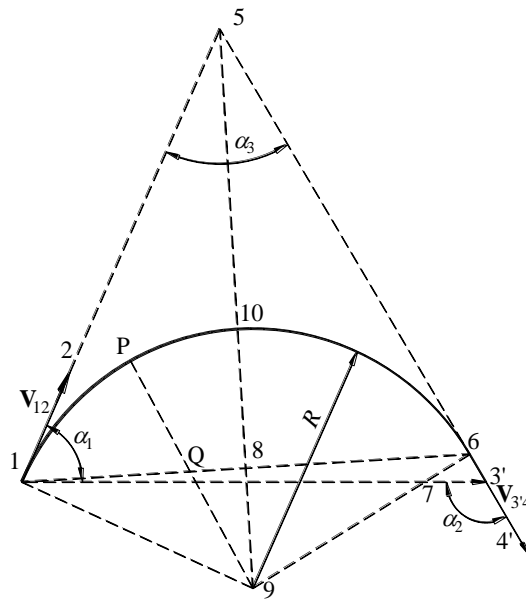


Figure 2: Triangle determined by $\alpha_1, \alpha_2$ and $L_{13'}$

From Fig. 2, it can be seen that point 5 is the intersection point of extended lines of vector $\mathbf{V}_{12}$ and $\mathbf{V}_{3'4'}$, while the angle between vector $\mathbf{V}_{12}$ and $\mathbf{V}_{3'4'}$ is $\alpha_3 = \alpha_2 - \alpha_1$. On the other hand, it can be noted that the length of straight line segment $\overline{15}$ is not equal to the length of straight line segment $\overline{3'5}$ generally.

In order to make the curvature radius of the three-dimensional central streamline reach its maximum, the three-dimensional streamline should consist of a circular arc and a straight line segment.

According to sine theorem, the length of straight line segment $\overline{15}$ is:

$$L_{15} = \frac{\sin(\pi - \alpha_2)}{\sin \alpha_3} L_{13'} \tag{16}$$

The length of straight line segment $\overline{3'5}$ is

$$L_{3'5} = \frac{\sin \alpha_1}{\sin \alpha_3} L_{13'} \tag{17}$$

The length of straight line segment $\overline{3'6}$ is

$$L_{3'6} = L_{3'5} - L_{15} \tag{18}$$

Construct auxiliary line segment $\overline{19}$ which is perpendicular to $\overline{15}$. In addition, construct auxiliary line segment $\overline{69}$ perpendicular to $\overline{65}$. Point 9 is the circular arc center of three-dimensional central streamline. The circular arc radius of the three-dimensional central streamline is:

$$R = L_{15} \tan \frac{\alpha_3}{2} \tag{19}$$

The coordinates of point 5 are:

$$\begin{cases} x_5 = x_1 + (L_{15} / L_{12})(x_2 - x_1) \\ y_5 = y_1 + (L_{15} / L_{12})(y_2 - y_1) \\ z_5 = z_1 + (L_{15} / L_{12})(z_2 - z_1) \end{cases} \tag{20}$$

The coordinates of point 6 are:

$$\begin{cases} x_6 = x_{3'} + (L_{3'6} / L_{3'5})(x_5 - x_{3'}) \\ y_6 = y_{3'} + (L_{3'6} / L_{3'5})(y_5 - y_{3'}) \\ z_6 = z_{3'} + (L_{3'6} / L_{3'5})(z_5 - z_{3'}) \end{cases} \tag{21}$$

Construct auxiliary line segment $\overline{16}$. The middle point coordinates of the auxiliary segment line $\overline{16}$ are:

$$\begin{cases} x_8 = (x_1 + x_6) / 2 \\ y_8 = (y_1 + y_6) / 2 \\ z_8 = (z_1 + z_6) / 2 \end{cases} \tag{22}$$

Construct auxiliary line $\overline{59}$. Its length is:

$$\left| \overline{59} \right| = \left| \overline{15} \right| / \cos(\alpha_3 / 2) = \left| \overline{58} \right| / \cos^2(\alpha_3 / 2) \tag{23}$$

Consequently, the circular arc center coordinates of thee-dimensional central streamline arc are:

$$\begin{cases} a = x_5 + (x_8 - x_5) / \cos^2(\alpha_3 / 2) \\ b = y_5 + (y_8 - y_5) / \cos^2(\alpha_3 / 2) \\ c = z_5 + (z_8 - z_5) / \cos^2(\alpha_3 / 2) \end{cases} \tag{24}$$

The three-dimensional circular arc can be regarded as the intersection line of a sphere and a plane. Thus, the arc equation of three-dimensional central streamline can be expressed as:

$$\begin{cases} (x-a)^2 + (y-b)^2 + (z-c)^2 = R^2 \\ Ax + By + Cz = 1 \end{cases} \tag{25}$$

For the short straight line segment $\overline{3'6}$ near the passage outlet, the equation of three-dimensional central streamline takes the form of:

$$\frac{x - x_{3'}}{x_6 - x_{3'}} = \frac{y - y_{3'}}{y_6 - y_{3'}} = \frac{z - z_{3'}}{z_6 - z_{3'}} \tag{26}$$

## III. Equation of Design Path

The design path reflects the correlation between revolution radius $r$ and $x$-coordinate. The three-dimensional central streamline equation can be used to derive design path equation.

### 3.1 Rectangular coordinate equation of design path

Expanding the first formula of (25), we can obtain:

$$\begin{cases} 2by + 2cz = (x-a)^2 + r^2 + e \\ By + Cz = 1 - Ax \end{cases} \tag{27}$$

where $e = b^2 + c^2 - R^2$

The above Simultaneous equations solved by using Cramer's rule, determinants are:

$$\Delta = 2(Cb - Bc) \tag{28}$$

$$\Delta_1 = C[(x-a)^2 + r^2 + e] - 2c(1 - Ax) \tag{29}$$

$$\Delta_2 = 2b(1 - Ax) - B[(x-a)^2 + r^2 + e] \tag{30}$$

Therefore, the solution of (27) is:

$$\begin{cases} y = \dfrac{C[(x-a)^2 + r^2 + e] - 2c(1 - Ax)}{2(Cb - Bc)} \\ z = \dfrac{2b(1 - Ax) - B[(x-a)^2 + r^2 + e]}{2(Cb - Bc)} \end{cases} \tag{31}$$

The revolution radius squared is:

$$r^2 = y^2 + z^2 = [(x-a)^2 + r^2 + e]^2 / w - u(1 - Ax)[(x-a)^2 + r^2 + e] / w + v(1 - Ax)^2 / w \tag{32}$$

where $u = 4(Bb + Cc)/(B^2 + C^2)$, $v = 4(b^2 + c^2)(B^2 + C^2)$, $w = 4(Cb - Bc)^2/(B^2 + C^2)$

Thus, the rectangular coordinate equation of design path is:

$$[(x-a)^2 + r^2 + e]^2 + v(1-Ax)^2 = u(1-Ax)[(x-a)^2 + r^2 + e] + wr^2 \qquad (33)$$

From the above equation, it can be found that the design path equation is a fourth degree equation expressed with an implicit function.

For the straight line segment of the three-dimensional central streamline, according to (26), we have:

$$\begin{cases} y = px + (y_{3'} - px_{3'}) \\ z = qx + (z_{3'} - qx_{3'}) \end{cases} \qquad (34)$$

where $p = (y_6 - y_{3'})/(x_6 - x_{3'})$, $q = (z_6 - z_{3'})/(x_6 - x_{3'})$.

The revolution radius expression is:

$$r = \sqrt{[px + (y_{3'} - px_{3'})]^2 + [qx + (z_{3'} - qx_{3'})]^2} \qquad (35)$$

From (35), it can be seen that the meridional flow path is a hyperbola if the three-dimensional streamline is a straight line segment.

### 3.2 Parametric equation of design path

From (33), it can be noted that the rectangular coordinate equation of the design path is substantially complex. It is inconvenient for the expression to be used for design calculation. Therefore, it is necessary to create the parametric equation of design path. Construct a straight line segment from the circle center point 9 to point P which is located on the three-dimensional circular arc. The straight line segment $\overline{9P}$ intersects with straight line segment $\overline{16}$. The coordinates of intersection point $Q(x', y', z')$ are:

$$\begin{cases} x' = x_1 + \lambda(x_6 - x_1) \\ y' = y_1 + \lambda(y_6 - y_1) \\ z' = z_1 + \lambda(z_6 - z_1) \end{cases} \qquad (36)$$

where $\lambda$ is a parameter, $0 \leq \lambda \leq 1$.

The distance from point 9 to point Q is:

$$L_{Q9} = \sqrt{(x'-a)^2 + (y'-b)^2 + (z'-c)^2} \qquad (37)$$

The coordinates of point P are:

$$\begin{cases} x = a + (R/L_{Q9})(x'-a) \\ y = b + (R/L_{Q9})(y'-b) \\ z = c + (R/L_{Q9})(z'-c) \end{cases} \qquad (38)$$

Thus, we have:

$$r = \sqrt{\left[b + (R/L_{Q9})(y'-b)\right]^2 + \left[c + (R/L_{Q9})(z'-c)\right]^2} \qquad (39)$$

For the straight line segment of the three- dimensional streamline, let:

$$\frac{x - x_{3'}}{x_6 - x_{3'}} = \frac{y - y_{3'}}{y_6 - y_{3'}} = \frac{z - z_{3'}}{z_6 - z_{3'}} = \lambda \qquad (40)$$

Rewrite the above expression, there resulting:

$$\begin{cases} x = x_{3'} + \lambda(x_6 - x_{3'}) \\ r = \sqrt{[y_{3'} + \lambda(y_6 - y_{3'})]^2 + [z_{3'} + \lambda(z_6 - z_{3'})]^2} \end{cases} \qquad (41)$$

## IV. Calculation of Other Meridional Flow Paths

With the equation of design path, it is possible to calculate the coordinates of other meridional flow paths.

### 4.1 Numerical calculation of outer wall contour line Let:

$$F(x,r) = [(x-a)^2 + r^2 + e]^2 + v(1-Ax)^2 - u(1-Ax)[(x-a)^2 + r^2 + e] - wr^2 = 0 \qquad (42)$$

Then, the two partial derivatives are:

$$F_x = [4(x-a)+Au][(x-a)^2+r^2+e] - 2[u(x-a)+Av](1-Ax) \tag{43}$$

$$F_r = \{4[(x-a)^2+r^2+e] - 2u(1-Ax) - 2w\}r \tag{44}$$

The derivative of revolution radius with respect to *x*-coordinate is:

$$r' = -F_x / F_r \tag{45}$$

For the straight line segment of the three-dimensional central streamline, differentiating (35), we have:

$$r' = [(p^2+q^2)(x-x_{3'}) + py_{3'} + qz_{3'}] / r \tag{46}$$

With the derivative $r'$, the normal line slope of design path is:

$$k = -1 / r' \tag{47}$$

The angle between the normal line and *x* axis is:

$$\gamma = \arctan k \tag{48}$$

The correlation between outer wall contour line and design path is shown in Fig. 3.
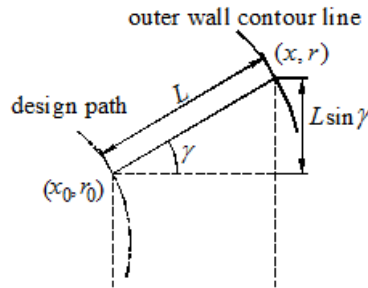


Figure 3: Correlation between design path and outer wall contour line

The spacing between design path and outer wall contour line is the a half of the flow passage. Let *L* denote the spacing. By using the lateral area formula of a right truncated cone, the correlation between design path and out wall contour line can be established:

$$\pi(2r_0 + L\sin\gamma)L = A/2 \tag{49}$$

Simplifying the above expression, we can obtain a quadric equation:

$$(\sin\gamma)L^2 + 2r_0 L - A/(2\pi) = 0 \tag{50}$$

Solving the equation, we can obtain the spacing:

$$L = \frac{-2r_0 + \sqrt{(2r_0)^2 + 4(\sin\gamma)A/(2\pi)}}{2\sin\gamma} = \frac{A/(2\pi)}{r_0 + \sqrt{r_0^2 + (\sin\gamma)A/(2\pi)}} \tag{51}$$

With a given point $(x_0, r_0)$ located on the design path, normal direction angle $\gamma$ through the point, and the flow passage spacing *L*, the coordinates of the point located on the outer contour line can be obtained:

$$\begin{cases} x = x_0 + L\cos\gamma \\ r = r_0 + L\sin\gamma \end{cases} \tag{52}$$

*4.2 Numerical calculation of inner wall contour line*
Similarly reasoning, the *x* and *r*-coordinate of inner wall contour line can be obtained:

$$\begin{cases} x = x_0 - L\cos\gamma \\ r = r_0 - L\sin\gamma \end{cases} \tag{53}$$

*4.3 General formula of meridional flow paths*
Equation (52) compared with (53), it can be found that the two equations are similar. If a parameter $\xi$ is introduced, a universal expression can be obtained:

$$\begin{cases} x = x_0 + \xi L\cos\gamma \\ r = r_0 + \xi L\sin\gamma \end{cases} \tag{54}$$

**From (54), the follows can be found:**
If $\xi = 0$, point $(x, r)$ represents the point located on the design path; if $\xi = -1$, point $(x, r)$ denotes the point located on the inner wall; if $\xi = 1$, point $(x, r)$ is the point located on the outer wall.

Obviously, parameter $\xi$ can take on any real number ranging from -1 to 1. That is to say, Equation (54) can be used to express any meridional flow path. Fig. 4 illustrates the meridional flow path drawn according to (54).
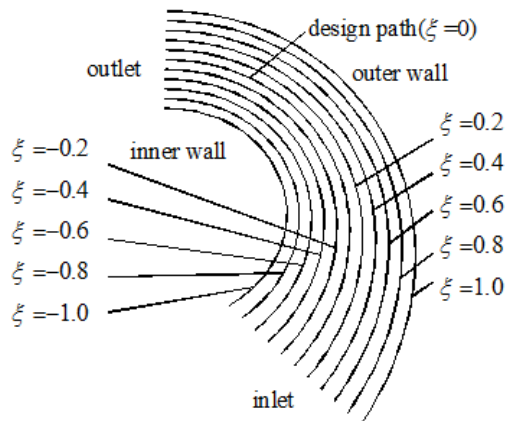


Figure 4: Meridional flow path of pump flow passage

## V.  Computation of Three-Dimensional Streamline Coordinates From Given Meridional Flow Path Coordinates

For a given point $(x, r)$ located on a meridional flow path, according to the plane equation as well as the correlation between revolution radius and coordinates, there results:

$$\begin{cases} By + Cz = 1 - Ax \\ y^2 + z^2 = r^2 \end{cases} \tag{55}$$

The second expression of (55) is equivalent to:

$$\begin{cases} y = r\cos\phi \\ z = r\sin\phi \end{cases} \tag{56}$$

Equation (56) substituted into the first expression of (55), a transcendental equation can be obtained:

$$\sin\phi + (B/C)\cos\phi = (1 - Ax)/(Cr) \tag{57}$$

The solution of the equation is:

$$\phi = \arcsin\frac{(1 - Ax)/r}{\sqrt{B^2 + C^2}} - \arcsin\frac{B}{\sqrt{B^2 + C^2}} \tag{58}$$

With angle $\phi$, the $y$ and $z$-coordinate of three-dimensional streamline can be obtained. In a numerical manner, the three-dimensional streamlines of the pump flow passage can be drawn, as shown in Fig. 5.
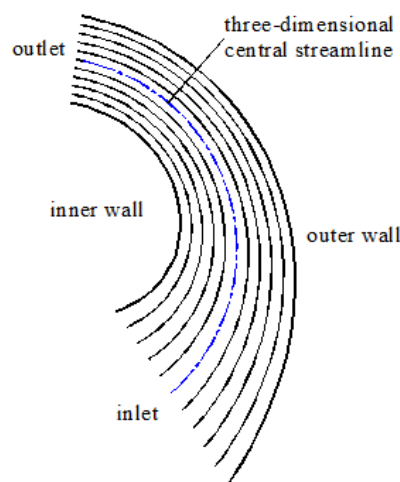


Figure 5: Three-dimensional streamlines of pump flow passage

From Fig. 5, it can be clearly seen that each three-dimensional central streamline consists of a circular arc and a short straight line segment, while any other three-dimensional streamline consists of a curved line and a short straight line segment. Each curved line is close to a circular arc. The streamlines of entire flow passage conform to

boundaries and the curvature radii of streamlines change gradually. Therefore, this design is more reasonable and will greatly reduce the energy loss caused by streamline bending.

## VI. Conclusion

The design methods of hydrodynamic torque converters were investigated, the main results are as follows:

(1) A three-dimensional streamline design method is proposed.

(2) A Fourth degree implicit function curved line and a hyperbola are used as the curved line type of design path.

(3) By using design path equation and its normal equation, on the other hand, with the help of numerical methods, the coordinates of the point located on any other meridional flow path can be obtained.

(4) According to each meridional flow path, the three-dimensional streamline is numerically calculated. The three-dimensional central streamline consists of a circular arc and a short straight line segment, while any other three-dimensional streamline consists of a curve and a short straight line segment.

Theoretical derivation and program calculation results show that three-dimensional streamline design method is feasible. The method possesses many advantages.

(1) The curvature radius of the three-dimensional central streamline reaches a maximum and remains unchanged (constant curvature). As a result, the energy loss caused by streamline bending can greatly be reduced.

(2) At the flow passage outlet, each three-dimensional streamline is a straight line segment. It is helpful to reduce the flow deviation angle. That is to say, the method can reduce the energy loss caused by flow deviation.

(3) As the fluid flows in a plane, theoretically, the flow field of a torque converter pump becomes quasi-two-dimensional flow field. Obviously, the method can reduce the strength of the turbulence. Therefore, it is beneficial to reduce the turbulence energy loss.

(4) All blades are flat, which can greatly reduce the manufacturing cost Of course, the disadvantage of the three-dimensional streamline design method is that the axial dimension of the torque converter increases slightly.

To sum up, advantages of the three-dimensional streamline design method are very outstanding. Therefore, the method is of engineering application value.

## ACKNOWLEDGMENTS

## REFERENCES

[1]     P J Strachan, F P Reynaud, et al. The hydrodynamic modeling of torque converter. *N&O Joernaal,4,* 1992,21-28.
[2]     J V Dingenen. Development of a hydraulic torque converter design method. master diss. *GHENT University Academic Thesis*, Belguim, 2008.
[3]     Wentong Liu. A method about drawing 2-dimension flow to design the blade-type of torque converter. *Journal of Jilin University (Engineering and Technology Edition), (2),* 1990,76-84 (in Chinese).
[4]     H Schuliz, R Greim, and  W Volgmann. Calculation of three dimensional viscous flow in hydrodynamic torque converters. *Journal of Turbomachinery, 118(6),* 1996, 578-589.
[5]     Wenxing Ma, Bangjie Luo and Shurong Wu. The research on quasi-three-dimensional flow design of hydrodynamic torque converter blades. *SAE Paper 912701,* 1991.
[6]     S Kämmerer, J F Mayer, H Stetter, M Paffrath, et al. Development of a three-dimensional geometry optimization method for turbomachinery applications. *International Journal of Rotating Machinery, 10(5),* 2004, 373-385.
[7]     Jian Wang, Anlin Ge, Yulong Lei, et al. Three-dimensional design for hydraulic torque converter blades and its performance analysis. *Journal of Jilin University (Engineering and Technology Edition), 37(1),* 2007, 43-47 (in Chinese).
[8]     Wei Wei and Dongqing Yan. Optimized design of visualization of blades and forecast of performance based on genetic algorithm. *Fluid Power Transmission and Control, 17(4),* 2006, 41-44, 48 (in Chinese).
[9]     Wenxing Ma. *Hydrodynamic Transmission Theory and Design*(Chemical Industry Press, Peking, China,2004).
[10]    Shiping Liu and Long Quan. Mathematical model of hydrodynamic torque converter and analytic description of streamline. *Chinese Journal of Mechanical Engineering, 22(1),* 2009, 70-77.
[11]    Shiping Liu and Long Quan. Torus streamline method design of 3-element centripetal-turbine hydraulic torque converters. *Transactions of the Chinese Society for Agricultural Machinery, 40(7),* 2009, 20-24, 44 (in Chinese).
[12]    Shiping Liu and Long Quan. Minimum curvature design of three-element centripetal-turbine hydrodynamic torque converters. *Journal of China Ordnance, 5(2),* 2009, 119-125.
[13]    Shiping Liu and Xiaoshen Zhao. Plane streamline method design of hydrodynamic torque converter. *Third International Conference on Theoretical and Mathematical Foundations of Computer Science,* Bali, Indonesia. 2012.

# Evaluation of Total Productive Maintenance Implementation in a Selected Semi-Automated Manufacturing Industry

Chowdury M. L. Rahman[1], M. A. Hoque[2]

[1]*Assistant Professor, Department of IPE, ShahJalal University of Science and Technology, Sylhet, Bangladesh.*
[2]*4th Yr B.Sc.Engg. student, Dept of IPE, ShahJalal University of Science and Technology, Sylhet, Bangladesh.*

**ABSTRACT:** *Manufacturing industries around the world spend a lot of money on buying new equipment to increase production but a little is done to get hundred percent output from the machine. However, because of increased competency levels and demand of quality products at lower costs, buying latest equipment is not a solution unless it is fully utilized. Therefore machine maintenance and in general, implementing an appropriate maintenance strategy has become increasingly important for manufacturing companies to accomplish these requirements. Total productive maintenance (TPM) has become one of the most popular maintenance strategies to ensure high machine reliability since it is regarded as an integral part of Lean Manufacturing. Performance evaluation is the most important aspects in the field of continuous improving of the production process and overall equipment effectiveness (OEE) is one of the justified performance evaluation methods that is popular in the manufacturing industries to assess the machine's effectiveness and performance. In this concern, this research work has been conducted in a selected semi-automated manufacturing industry to study and evaluate the implementation of autonomous maintenance and planned maintenance pillars of TPM. After the OEE measurement, it has been benchmarked with the world class OEE. Pareto and statistical analysis of downtimes were performed to show the most affecting downtime factors hierarchically. Based on the obtained results, maintenance management and production planning have been suggested to improve their maintenance procedures and the productivity as well.*

*Keywords: Maintenance management, Maintenance strategy, Overall Equipment Effectiveness, Pareto analysis, Total Productive Maintenance.*

## I. Introduction

Total productive maintenance (TPM) is a holistic approach to equipment maintenance that strives to achieve perfect production:
- No breakdowns
- No small stops or slow running
- No defects

In addition it values a safe working environment:
- No accidents

TPM emphasizes proactive and preventative maintenance to maximize the operational efficiency of equipment. It blurs the distinction between the roles of production and maintenance by placing a strong emphasis on empowering operators to help maintain their equipment. The TPM system addresses production operation with a solid, team-based program, i.e. - proactive instead of reactive. It helps to eliminate losses, whether from breakdowns, defects or accidents [1].

### 1.1 TPM Pillars

The implementation of a TPM program creates a shared responsibility for equipment that encourages greater involvement by plant floor workers. In the right environment this can be very effective in improving productivity.

Total productive maintenance (TPM) which is one of the key concepts of lean manufacturing provides a comprehensive, life cycle approach, to equipment management that minimizes equipment failures, production defects, and accidents. It involves everyone in the organization, from top level management to production mechanics, and production support groups to outside suppliers. TPM developed as a spin-off that focused more on equipment efficiency. Total Productive Maintenance has eight pillars.
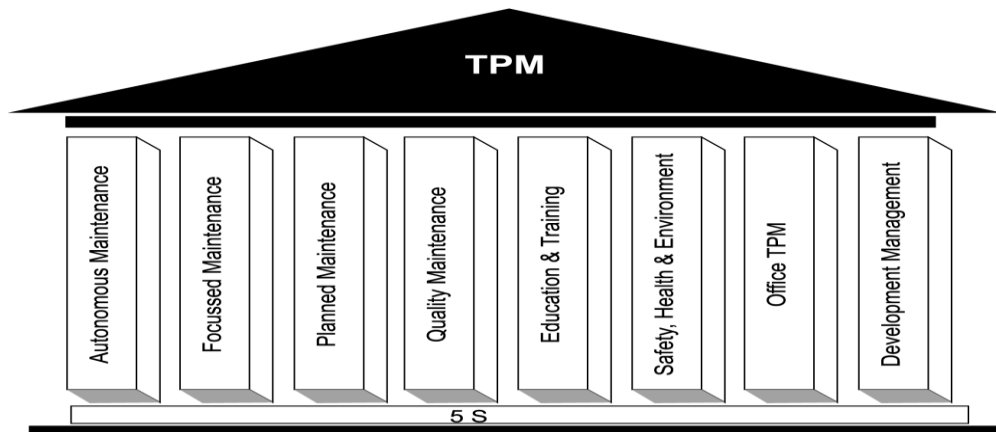
Figure 1: Eight pillars approach for TPM implementation

### 1.1.1 Autonomous Maintenance

The term autonomous doesn't mean performing maintenance in a vacuum or solely by the traditional maintenance department. Rather, it means that operators perform certain equipment maintenance activities and that maintenance crafts get closely involved in the daily operation of equipment. There are two types of tags used, namely- red tag and yellow tag. Red tag is used to represent the scenario that requires highly technical knowledge while yellow tag is used for simple condition which does not require highly technical knowledge.
Patra et.al. stated that employees have the ability to "detect abnormality" with regard to services and equipment, based on a feeling that "there is something wrong" on work [2]. This pillar is geared towards developing operators to be able to take care of small maintenance tasks, thus freeing up the skilled maintenance people to spend time on more value added activity and technical repairs. The operators are responsible for upkeep of their equipment to prevent it from deteriorating.

### 1.1.2 Planned Maintenance

Planned preventive maintenance (PPM) or more usual just planned maintenance (PM) or scheduled maintenance is any variety of scheduled maintenance to an object or item of equipment. Specifically, planned maintenance is a scheduled service visit carried out by a competent and suitable agent, to ensure that an item of equipment is operating correctly and to therefore avoid any unscheduled breakdown and downtime. It is aimed to have trouble free machines and equipment producing defect free products for total customer satisfaction. This breaks maintenance down into four families or groups which are noted below.

- preventive maintenance
- breakdown maintenance
- corrective maintenance
- maintenance prevention

### 1.2 Pareto Chart

In 1906, Italian economist V. Pareto created a mathematical formula to describe the unequal distribution of wealth in his country, observing that twenty percent of the people owned eighty percent of the wealth. In the late 1940s, Dr. Joseph M. Juran inaccurately attributed the 80/20 Rule to Pareto, calling it Pareto's Principle [3]. This technique helps identify the top portion of causes that need to be addressed to resolve the majority of problems. While this neither is common to refer to Pareto as "80/20" rule, under the assumption that, in all situations, 20% of causes determine 80% of problems, this ratio is merely a convenient rule of thumb and is not nor should it be considered immutable law of nature.

### 1.3 Paired Samples t-test

The paired samples *t-test* compares the means of two variables. It computes the difference between the two variables for each case, and tests to see if the average difference is significantly different from zero.

**Assumption**
-  Both variables should be normally distributed.
**Hypothesis**
Null: There is no significant difference between the means of the two variables.
Alternate: There is a significant difference between the means of the two variables.

If the significance value is less than .05, there is a significant difference. If the significance value is greater than .05, there is no significant difference [4]. The paired sample *t-test*, Pearson correlation, partial correlation and other analysis can be performed by different computer programs. These programs are Microsoft Excel, SPSS, Stata, SAS and R.

### 1.4 Review of the Past Works

A paper was published on "Implementation of Total Productive Maintenance and Overall Equipment Effectiveness Evaluation" by - Islam H. Afefy, Industrial Engineering Department, Faculty of Engineering, Fayoum University, Al Fayoum, Egypt, in the year January 2013. This paper focused on a study of total productive maintenance and evaluating overall equipment effectiveness. A study was conducteded on "Total Productive Maintenance Review and Overall Equipment Effectiveness Measurement" by - Osama Taisir R.Almeanazel, Department Of Industrial Engineering, Hashemite University, Zarqa, 13115 Jordan, in September 2010. This paper emphasized the goals and benefits of implementing Total Productive Maintenance and also focused on calculating the overall equipment effectiveness in one of Steel Company in Jordan. Another paper was published on "Implementation of Total Productive Maintenance on Haldex Assembly Line" by - Zahid Habib and Kang Wang, Department of Production Engineering, Royal Institute of Technology, Sweden, in March, 2008. The core of this thesis was doing a study on assembly line of automatic brake adjusters at Haldex Brake Products and autonomous maintenance were described with a list of daily and weekly checks of the equipment's and whole assembly line to implement total productive maintenance. A research work was accomplished on "The initiation of Total Productive Maintenance to a pilot production line in the German Automobile industry" by – Daniel Ottoson, Luleå University of Technology, Sweden, in October 2009. In this research, a task force had been introduced called TPM-commando, specialized in eliminating the major losses and rendered a continuous improvement process to be applied.

## II. Methodology

### 2.1 Overall Equipment Effectiveness

OEE is an abbreviation for the manufacturing metric overall equipment effectiveness (OEE). OEE takes into account the various sub components of the manufacturing process – availability, performance and quality. This percentage can be viewed as a snapshot of the current production efficiency for a machine, line or cell.

OEE= Availability x Performance Rate x Quality Rate

### 2.1.1 Availability

Availability takes into account down time loss, and is calculated as: Availability = $\frac{Operating\ time}{Planned\ run\ time}*100\%$.

Here, planned production time is defined as the total time that equipment is expected to produce [5].
So, planned production time or run time = Available time – (Breakdown + Set up).

During the available time, equipment may be not operating for a number of reasons: planned breaks in production schedule, planned maintenance, precautionary resting time, lack of work and others. So, if there is any planned downtime, this should be subtracted from the available time and what is left is the active time.

Active time is the time during which an equipment is actually scheduled to operate and available for production.
So, active time = available time – planned downtime
During the Active time, however:
- Equipment may be subject to Break-downs and/or
- Equipment may need to be Set-up

If breakdown and/or set-up occur, their corresponding duration in time must be subtracted from the active time, and what is left is the operating time.

Operating time is the time during which equipment actually operates [6].
Operating time = active time – (breakdown + Set up)
 = available time – (planned downtime + breakdown + set up)
 = actual Capacity time – total Downtime
Now, considering the above mentioned formula for planned run time and operating time:
Operating time = available time – (breakdown + set up) –planned downtime
 = planned run time – planned Downtime
So, Availability is calculated using the given formula below.

$$\text{Availability} = \frac{\text{Planned run time} - \text{Planned Down time}}{\text{Planned run time}} *100\%$$

When downtime losses are zero, the availability is 1 or 100%, the gross operating time equals the available time for production. In other words, the installation throughput equals zero at no point of time, during the available time for production [7].

### 2.1.2 Performance Rate

The performance only concerns the gross operating time. A property of the gross operating time is that the speed exceeds zero at any time. There are no down time losses in the gross operational time. The performance factor is a measure for the speed losses.

$$\text{Performance Rate} = \frac{\text{Planned run time} - \text{Planned Down time}}{\text{Planned run time}} *100\% = \text{ideal cycle time} / (\text{operating time} / \text{total pieces})$$

Ideal cycle time is the minimum cycle time that the process can be expected to achieve in optimal circumstances.

$$\text{Design cycle time} = \frac{\text{Daily average planned run time}}{\text{Daily average target of production}}.$$

It is sometimes called design cycle time, theoretical cycle time or nameplate capacity [8].

### 2.1.3 Quality Rate

During the net operational time, no down time or speed losses occur. It is not certain that the total produced output is conform quality specifications. To gain insight into this, the quality factor is defined:

$$\text{Quality Rate} = \frac{\text{Total output} - \text{Average reject}}{\text{Total output}} *100\%$$

$$= \frac{\text{Good pieces}}{\text{Total pieces}} *100\%$$

The individual value of the three effectiveness factors lies between 0 and 1. Measuring these effectiveness factors independently, a satisfactory value would be 0.9 or 90%. The value of the OEE is in this specific case = 0.9 x 0.9 x 0.9 = 0.73.

Rate of expected OEE=availability (100 %)*performance rate*quality rate

The practice of maximizing Overall equipment effectiveness (OEE) involves taking a structured approach to minimizing the six major losses that impact upon these three factors [9].

### 2.2 World Class OEE

OEE is essentially the ratio of fully productive time to planned production time (refer to the OEE factors section for a graphic representation). In practice, however, OEE is calculated as the product of its three contributing factors:

OEE = availability*performance*quality

This type of calculation makes OEE a severe test. For example, if all three contributing factors are 90.0%, the OEE would be 72.9%. In practice, the generally accepted world-class goals for each factor are quite different from each other, as is shown in the Table 1 below.

*Table 1: World class OEE rate*

| OEE Factor | World Class Rate |
|---|---|
| Availability rate | >90.0% |
| Performance rate | >95.0% |
| Quality rate | >99% |
| OEE | 85.0% |

Every manufacturing plant is different. Worldwide studies indicate that the average OEE rate in manufacturing plants is 60%. From the above TABLE 1, a world class OEE is considered to be 85% or better.

*Table 2: Comparative world class OEE rate for various industries*

| Industry | OEE set from top-level | Total OEE |
|---|---|---|
| Manufacturing | 85% | 60% |
| Process | > 90% | > 68% |
| Metallurgy | 75% | 55% |
| Paper | 95% | > 70% |
| Cement | > 80% | 60% |

The above Table 2 shows top-level OEE and total OEE values for different types of industries [10].

## III. Analysis and Discussion

Avery Dennison Bangladesh Ltd. is a printing and packaging industry. From the very beginning of 2012, this company had started the practicing of autonomous maintenance and planned maintenance in the Offset sections' machines. Necessary data were collected from questionnaire, production data and factory complaint sheet to evaluate the impact of TPM practising.

### 3.1 Overall Equipment Effectiveness Calculation
Here OEE has been used to determine the effectiveness of the offset section machines.

### 3.1.1 Daily Availability Calculation
Firstly, daily average availability has been calculated for the existing machines in the floor. As for example, for a particular machine (Name: L-1) of type GTO, the following information regarding operations of the machine on day Jan 6th, 2013 have been collected.

Actual capacity time = 600 min.

Total downtime (sum of loss time) = 130 min. In this offset printing section set up time is zero.

Planned downtime = Total downtime − (breakdown time + set up) = 130-60 = 70 min.

Planned run time = 540 min.

Operating time = Planned run time − Planned downtime = 470-200 = 270 min.

Therefore- Availability $= \frac{\text{Operating time}}{\text{Planned run time}} *100\% = \frac{470}{540} *100\% = 87.037\%$

= 87.04% (approx.) of machine L-1 on day Jan 6$^{th}$, 2013.

Calculating operating time and planned run time, daily average availability for every machines existing on that floor has been measured. Daily availability has been calculated by taking the average of equipment availability for 6$^{th}$ Jan, 2013.After calculating the equipment daily availability average daily availability for that month has been calculated similarly. Availability for every month, in the years 2012 and 2013, has also been measured in this way.

### 3.1.2 Daily Target of Production
As for example, for a particular machine (Name: L-3) of type GTO, the following information regarding operations of the machine on day Jan 6$^{th}$, 2013 have been collected.

Number of impression sheet produced (per hour), according to machine type = 3000.

Number of label produced (per sheet) = 20

Quantity of label produced = No. of impression sheet produced (per hour)* Label quantity (per sheet)

=3000*20 = 60000 units

Operating time (hour) $= \frac{480}{60} = 8$ hours

Daily target of production = Operating time (hour)* Label quantity produced

= 8*60000 = 480000

### 3.1.3 Daily Performance Rate Calculation
For a particular machine (Name: L-3) of type GTO, the following information regarding operations of the machine on day Jan 6$^{th}$, 2013 have been collected.

Design cycle time $= \frac{\text{Daily average planned run time}}{\text{Daily average target of production}}$ $= \frac{480}{480000} = 0.001$

Actual run time = Operating time = 480 minutes

So performance rate $= \frac{\text{Design cycle time} *\text{Quantity produced}}{\text{Actual run time}} *100\%$.

$= \frac{0.001*60000}{480} *100\% = 19.016\%$ (approx.) for L-3 machine in Jan 6$^{th}$, 2013.

### 3.1.4 Monthly Quality Rate Calculation
Quality rate is defined as the ratio of accepted output over total output.

Quality Rate $= \frac{\text{Total output} - \text{Rejected quantity}}{\text{Total output}} *100\%$.

As for example, for every machine in the selected Offset printing section, the following information regarding operations of the machines on month January, 2013 have been collected.

Total output = 37620606 units.

Rejected quantity = 74491 units

Quality rate $= \frac{37620606 - 74491}{37620606} *100 = 99.80199$

= 99.80% (approximate)

Similarly quality rate of these years 2012 and 2013 has been measured.

### 3.1.5 OEE Measurement for Two Years

Calculating the three factors of OEE such as availability, performance rate and quality rate monthly, OEE for two years have been measured. As for example, availability, performance rate and quality rate of the machines in offset printing section have been measured for January, 2013.

Availability rate = 79.7%

Performance rate = 32.1% and

Quality rate = 99.8%

So OEE = availability*performance rate*quality rate   = (79.7*32.1*99.8) %   = 25.5%

Taking the availability as one hundred percent, rate of expected OEE has been measured. As for example, expected OEE rate of the selected Offset printing section have been measured on month January, 2013.

Availability rate = 100%. So rate of expected OEE = (100*32.1*99.8) % = 29.6%

Expected OEE rate was 29.6% in January, 2013. Here, monthly OEE measurement for 2012 is shown in Table 3.

*Table 3: OEE measurement in 2013*

| Months' Name | Availability (%) | Performance rate (%) | Quality (%) | OEE (%) |
|---|---|---|---|---|
| January | 79.7 | 32.1 | 99.8 | 25.5 |
| February | 78.1 | 30.5 | 100 | 23.8 |
| March | 78.0 | 30.4 | 99.9 | 23.7 |
| April | 80.8 | 28.6 | 99.4 | 22.9 |
| May | 81.8 | 22.0 | 99.9 | 18.0 |
| June | 78.5 | 23.3 | 99.8 | 18.3 |
| July | 77.1 | 42.4 | 99.9 | 32.7 |
| August | 82.0 | 28.0 | 99.9 | 23.0 |
| September | 81.9 | 27.8 | 99.9 | 22.8 |
| October | 80.5 | 40.5 | 99.9 | 32.6 |
| November | 82.0 | 24.1 | 99.9 | 19.7 |
| December | 75.7 | 25.6 | 99.9 | 19.3 |

In 2013, average OEE was 23.5% and expected OEE could be 29.5% if the equipment were cent percent available.

Plotting the avg. monthly availability in 2012, following graph is drawn below.
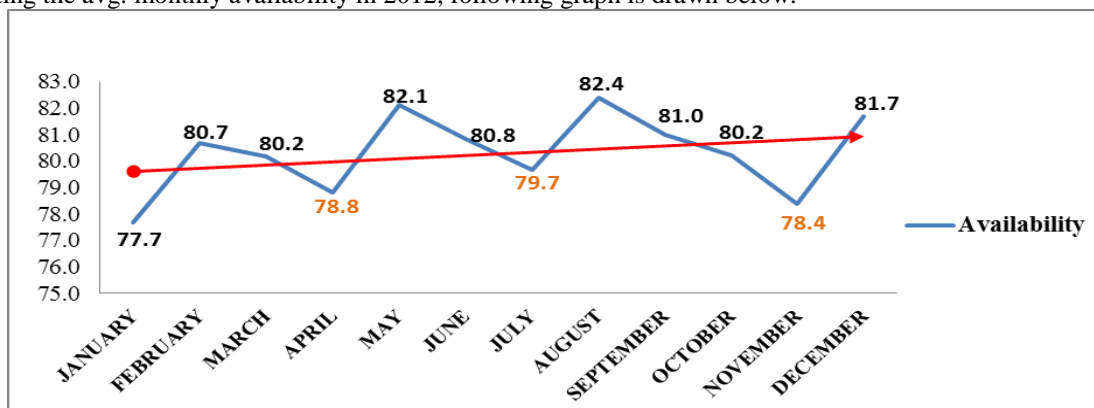


**Figure 2: Average monthly availability in 2012**

It has been identified from the Figure 2 that the availability in January was the lowest as the TPM program has just been launched. Afterwards, availability was increasing which implied the effect of TPM launching but comparatively lower availability rate have been found in April, July and November which required detailed analysis of downtimes for corresponding months. Plotting the avg. monthly availability in 2013, following graph is drawn.
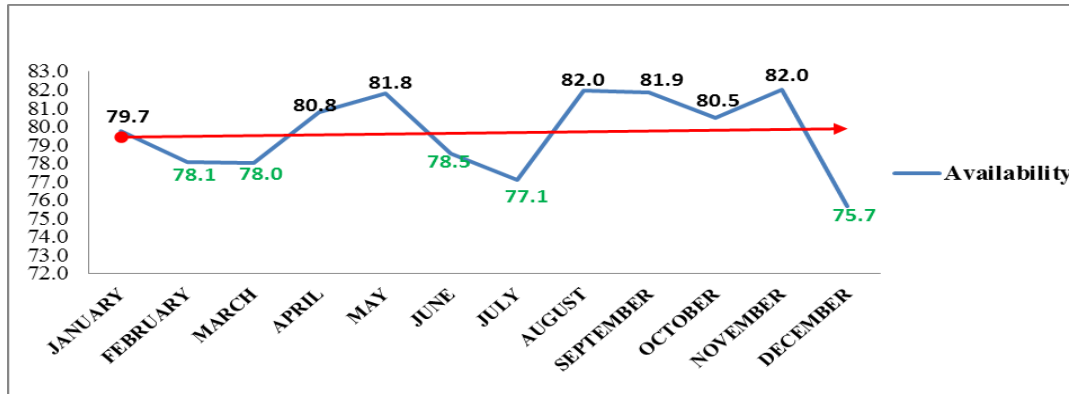
**Figure 3: Average monthly availability in 2013**

The following facts have been revealed from Fig. 3 regarding the monthly availability values. The availability figures in February, March, June and July have been found comparatively lower than the average availability. In order to identify the causes behind these findings it is required detailed downtime analysis of those months. The lowest availability in December showed the TPM program was not maintained properly. The trend line of 2012 was just reaching 80% whereas trend line of 2013 had exceeded 81%. Trend lines of two years reflect the inadequate practice of autonomous maintenance and planned maintenance.

The comparative scenario of monthly OEE values for the years of 2012 and 2013 is exhibited in Figure 4.
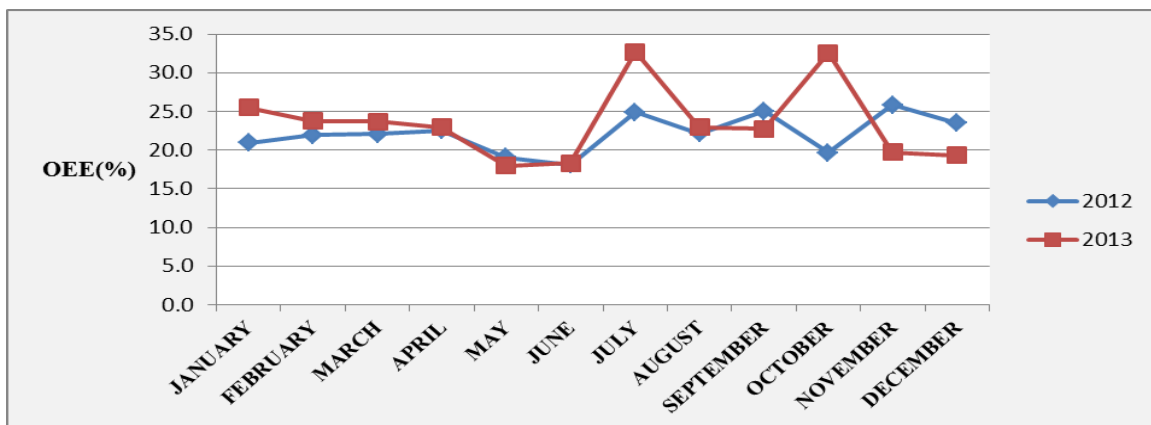


**Figure 4: Comparison between monthly OEE values for 2012 and 2013**

### 3.1.6 Discussion on OEE analysis
It has been found that from the OEE measurement and comparative analyses of OEE monthly OEE of 2013 was slightly upper than of 2012 because it was the impact of TPM's implementation of two pillars, autonomous maintenance and planned maintenance implementation. Consistent OEE has been achieved for both years at first quartile which showed the co-ordination of planning and production. Significant lower OEE rate for May, June months for both years because of lacking in the coordination among planning, production and maintenance which resulted in lower performance rate though the availability rate was higher. Downward direction of OEE rate, at the end of year 2013 (November and December), shows that irregular AM and PM practicing.

### 3.2 Downtime Analysis with Pareto Chart
Pareto Analysis has been used in downtime analysis. According to Pareto analysis, around 20% of the downtime factors cause 80% of total downtime. To identify the downtimes that have caused around 80% of total downtime, Pareto chart was drawn. It has been found that comparative lower availability rate was in April, July and November which was shown in Fig. 1. Availability is reversely proportional to downtime. Therefore, Pareto analysis has been performed on the downtimes data for those corresponding months.

Cumulative percentage of downtime has been measured and shown in TABLE 4 below.

*Table 4: Cumulative percentage calculation (April, 2012)*

| Downtime name | Downtime (min.) | Cumulative Percentage |
|---|---|---|
| Scheduled maintenance | 22331 | 43.61 |
| Machine Breakdown | 13370 | 69.72 |
| Ink preparation | 4354 | 73.46 |
| Changing job | 3539 | 81.96 |
| Waiting for Material | 2970 | 87.76 |
| Meeting/ Training | 1915 | 94.67 |
| Power failure | 1531 | 96.59 |
| Waiting for instruction | 981 | 97.01 |
| Plate error | 215 | 100.00 |
| Proof reading (quality checking) | 0 | 100.00 |

Using the data from the above table, a Pareto chart has been drawn and shown in Figure 5 below.
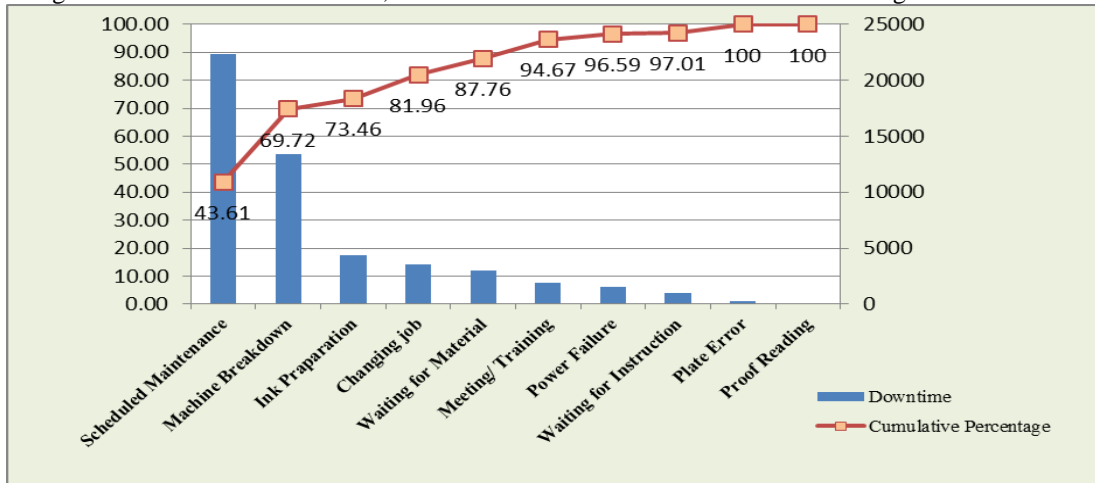


**Figure 5: Pareto Chart of April, 2012**

From the Pareto chart it has been obtained that scheduled maintenance and machine breakdown have caused around 75% of the total downtime. Whereas scheduled maintenance was unavoidable and machine breakdown could be reduced.

It has been found that comparative lower availability rate was in February, March, June and July which was shown in Fig. 2. Pareto chart on downtime in March, 2013 is drawn among these months.

Using the data from the above table, a Pareto chart has been drawn and shown in Figure 6 accordingly.
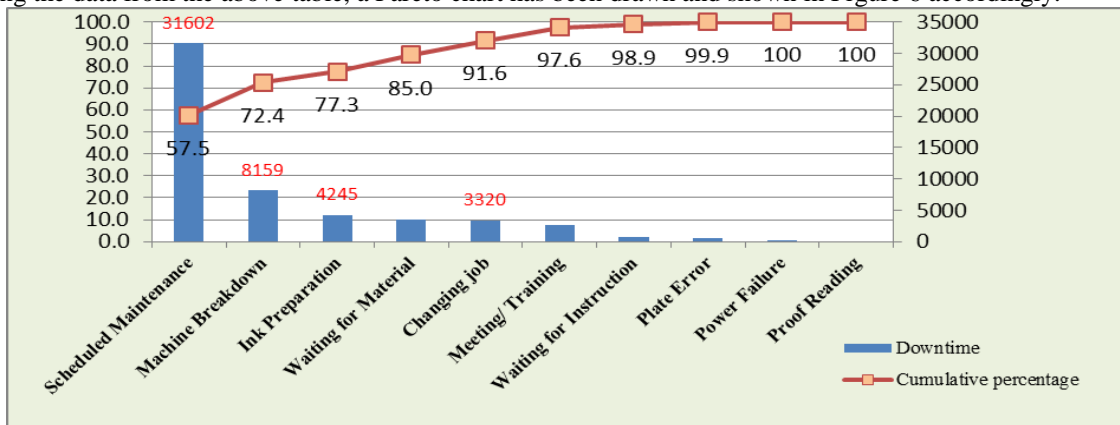


**Figure 6: Pareto Chart of March, 2013**

From the Pareto chart, it has been obtained that scheduled maintenance and machine breakdown have caused more than 70% of the total downtime. Whereas scheduled maintenance was unavoidable and machine breakdown could be reduced. Individual percentage contribution of machine breakdown was around 20%.

### 3.2.1 Discussion on Pareto Analysis

It has been found from the Pareto chart analysis of downtimes that scheduled maintenance and machine breakdown have caused around 75% to 80% of total downtime. As scheduled maintenance is part of planned maintenance, it is not avoidable in large extent. Machine breakdown, ink preparation and waiting for material were next prioritizing downtime factors those should be focused for further reduction of total downtime. Machine breakdown was comparative lower for particular months and other downtime factors should be analyzed for downtime reduction.

### 3.3 Comparative Downtime Analysis for Two Years

The downtimes can be classified into four types considering the causes of downtimes. These types are noted below including relevant downtimes.
1. Planned downtimes that contain scheduled maintenance, meeting/training and proof reading (quality checking).
2. Unplanned downtimes that contain machine breakdown, plate error and power failure.
3. Process downtimes – downtimes due to process deficiencies that include ink preparation and waiting for materials.
4. Personnel downtimes – downtimes due to operator or maintenance personnel deficiencies that include changing job and waiting for instructions.
Considering these four types of downtime for two years, comparative downtime analysis has been performed and given here.

### 3.3.1 Comparative Downtime Analysis in July

The various downtimes for the month of July for two consecutive years has been calculated and tabulated in Table 6 below and is shown in Figure 7 accordingly.

*Table 6: Comparative downtime calculation in July*

| *Downtime type* | *Downtime in 2012 (min.)* | *Downtime in 2013 (min.)* |
|---|---|---|
| Planned downtimes | 20824 | 19904 |
| Unplanned downtimes | 16165 | 2431 |
| Process downtimes | 5894 | 3625 |
| Personnel downtimes | 2090 | 1260 |

Percentage of every downtime in total downtime is plotted in the graph below.
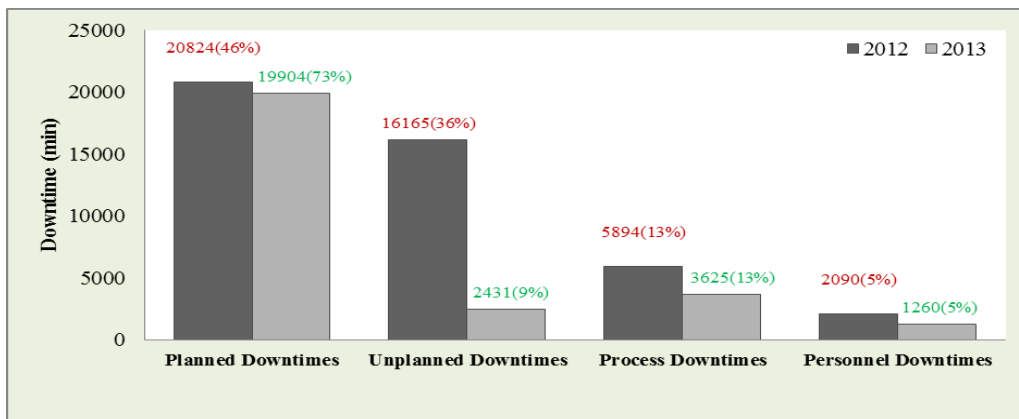


**Figure 7: Downtime comparison in July (2012 versus 2013)**

From the above Figure 6, the facts being identified are that every downtime has been reduced in 2013. Unplanned downtimes, process downtimes and personnel downtimes were reduced significantly. As scheduled maintenance was being practiced, maintenance checklist maintained effectively, unplanned downtimes were reduced significantly.

### 3.3.2 Overall Comparative Analysis of Downtimes in Year 2013

Scheduled Maintenance from planned downtimes, machine breakdown from unplanned downtimes, ink preparation from process downtimes and changing job from personnel downtimes in February, March, June, July and November with the position in corresponding Pareto chart has been  tabulated in Table 7 below from the analysis of corresponding Pareto charts.

*Table 7: Overall Analysis of Pareto Charts in 2013*

| Downtime (min.) | February | March | June | July | November |
|---|---|---|---|---|---|
| Scheduled Maintenance | 24382 | 31602 | 21618 | 17835 | 19315 |
| Machine Breakdown | 6155 | 8159 | 5440 | 2151 | 7362 |
| Position in the Pareto chart | Second | second | second | third | Second |
| Ink preparation | 3015 | 4245 | 1475 | 2160 | 4080 |
| Position in the Pareto chart | third | third | fourth | second | Third |
| Changing job | 2660 | 3320 | 1445 | 1110 | 2585 |
| Position in the Pareto chart | Sixth | fifth | sixth | Sixth | Fifth |

### 3.4 Ranking of the different Downtimes based on Individual Percentage Contribution and Paired t- test Analysis

To identify the most affecting and contributing downtime in total downtime, ranking of the downtime has been done. Ranking has been performed in two ways- based on percentage contribution and *t-test* data interpretation.

### 3.4.1 Individual Percentage of Contribution Calculation

To measure the individual contribution of every downtime this formula is used. Individual percentage of contribution $= \frac{X_i}{\sum_i^n X_i}$ $*100\%$ $= \frac{\text{Individual Downtime}}{\text{Total Downtime}}*100\%$.

As for example, percentage contribution of meeting/training in total downtime has been measured, by collecting the following in 2012.  Meeting/training = 32633 min.  Total downtime = 580957 min.

So, percentage contribution of meeting/training $= \frac{32633}{580957}*100\%$ $= 5.6\%$ of total downtime. Similarly percentage contribution for every downtime for both years has been measured.

### 3.4.2 Ranking of Downtimes Based on Percentage of Individual Contribution

According to hierarchical sequence of individual contribution, different downtimes have been ranked. To establish a chronological order of all downtimes according to their contribution and inter-dependability, ranking of all downtime was needed. As Scheduled maintenance contributed the most, this was ranked as First.

*Table 8:  Ranking on Contribution (Year: 2012)*

| Downtime type | Downtime | Percentage | Rank |
|---|---|---|---|
| Scheduled maintenance | 272966 | 47.0 | 1 |
| Breakdown | 146169 | 25.2 | 2 |
| Waiting for material | 41125 | 7.1 | 3 |
| Ink preparation | 39535 | 6.8 | 4 |
| Meeting/training | 32633 | 5.6 | 5 |
| Changing job | 30809 | 5.3 | 6 |
| Waiting for instruction | 7256 | 1.2 | 7 |
| Power failure | 5497 | 0.9 | 8 |
| Plate error | 4617 | 0.8 | 9 |
| Proof reading | 350 | 0.1 | 10 |

### 3.4.3 Paired Comparison t-test Analysis of Downtimes (2012)

Comparing all variable (downtime) with each other using SPSS software, a two-tailed alternative hypothesis test has been performed.

*Table 9: t-test Data Interpretation (Year: 2012)*

| Downtime type | Highest value of "*t*" | Lowest value of "*t*" | Level of significance for highest "*t*" value | Valid value within confidence level (< .05) | Rank |
|---|---|---|---|---|---|
| Scheduled Maintenance | 17.614 | 5.189 | .0000000021 | 9 | 1 |
| Machine breakdown | 12.776 | 7.876 | .0000000609 | 8 | 2 |
| Waiting for material | 13.560 | .395 | .0000000328 | 5 | 3 |
| Ink preparation | 8.458 | 1.155 | .0000038314 | 4 | 4 |
| Meeting /training | 7.327 | .381 | .0000149037 | 4 | 4 |
| Changing Job | 12.002 | 8.497 | .0000001161 | 4 | 4 |
| Waiting for Instruction | 5.193 | .728 | .0002978488 | 1 | 5 |
| Plate error | 3.226 | -.329 | .0080738508 | 1 | 5 |
| Power Failure | 2.602 | | .0245870693 | 1 | 5 |

Different t-value with the level of significance for 2012 downtimes pair was calculated using SPSS. According to the null and alternate hypothesis, level of significance means the significant changes in mean values.

*Table 10: Comparison between t-test ranking and Percentage Contribution ranking (2012)*

| According to percentage of contribution | | According to *t-test* | |
|---|---|---|---|
| **Downtime** | **Rank** | **Downtime** | **Rank** |
| Scheduled maintenance | 1 | Scheduled maintenance | 1 |
| Machine breakdown | 2 | Machine breakdown | 2 |
| Waiting for material | 3 | Waiting for material | 3 |
| Ink preparation | 4 | Ink preparation | 4 |
| Meeting/training | 5 | Meeting/training | 4 |
| Changing job | 6 | Changing job | 4 |
| Waiting for instruction | 7 | Waiting for instruction | 5 |
| Power failure | 8 | Plate error | 5 |
| Plate error | 9 | Power failure | 5 |

If the significance value is less than .05, there is a significant difference. If the significance value is greater than .05, there is no significant difference. Counting the existing pair below the standard level of significance (<.05), most affecting factor (downtime) has been found. Thus, paired t-test analysis has been accomplished for both year downtimes data. Comparing the mean values of every pair the t-value has been obtained, this value showed the dependence factor of all variables. Comparison of the downtime ranking from two ways has been presented in Table 10 below. Similarly performing the individual percentage of contribution calculation and paired *t-test* analysis of every downtime in 2013, ranking of the downtimes based on their comparative inter-dependence has been performed and presented in Table 11 below.

*Table 11: Comparison between t-test Ranking and Percentage Contribution ranking (2013)*

| According to percentage of contribution | | According to *t-test* | |
|---|---|---|---|
| **Downtime** | **Rank** | **Downtime** | **Rank** |
| Scheduled maintenance | 1 | Scheduled maintenance | 1 |
| Machine breakdown | 2 | Machine breakdown | 2 |
| Waiting for material | 3 | Waiting for material | 4 |
| Ink preparation | 4 | Ink preparation | 3 |
| Meeting/Training | 5 | Meeting/Training | 4 |
| Changing job | 6 | Changing job | 4 |
| Waiting for instruction | 7 | Waiting for instruction | 5 |
| Power failure | 8 | Plate error | 6 |
| Plate error | 9 | Power failure | 6 |

From Table 11, it has been identified that scheduled maintenance was the most affecting factor among the downtime factors, which was unavoidable. Machine breakdown was ranked as the second factor which requires rigorous maintenance practices to reduce this. Waiting for materials and ink preparation were the next prioritize factors to be marked according to t-test analysis.

### *3.4.4 Discussion on Paired t-test*

From the Table 10, it has been revealed that ink preparation, meeting/training and changing job factors have been ranked as fourth combined according to t-test that refers to these downtimes have similar dependence over other downtimes. So, kobetsu kaizen (continuous focused improvement) can be used to reduce these downtimes simultaneously. Similar interpretation can be drawn from form Table 11. Percentage of contribution showed the effect of every downtime over total downtime whereas paired t-test interpretation indicated the downtimes to focus at certain priority.

## IV. Results And Findings

In this research work different types of analyses have been performed to evaluate the impact of TPM implementation. Corresponding results of these analyses are given below.

### *4.1 Results of OEE Analysis*

Monthly OEE rate for every month in 2012 and 2013 is measured. Following points have been found from the analysis-
- In 2012, Avg. OEE was 22.4% whereas it had changed to 23.5% in 2013.
- In 2012, Avg. of expected OEE was 27.6% whereas it had changed to 29.6% in 2013.
- Highest monthly OEE rate was in July, 2013.
- Lowest monthly OEE rate was in May, 2013.

### *4.2 Results of Downtime Analysis*

Pareto chart for comparatively lower availability rate indicating months' are drawn. Following facts have been found from the analysis-
- Scheduled maintenance and machine breakdown have caused around 80% of total downtime.
- Ink preparation, meeting/training and waiting for material were the next level of affecting downtimes in most of the months.
- According to *t-test*, fourth level of downtimes' was ink preparation, meeting/training and changing job in 2012.
- According to *t-test*, fourth level of downtimes' was waiting for material, meeting/training and changing Job in 2013.

## V. Conclusions

Performance evaluation is the most important aspects in the field of continuous improving of the production process and accordingly overall equipment effectiveness (OEE) is one of the justified performance evaluation methods that is popular in the manufacturing industries to assess the machine's effectiveness and performance. In this concern, this research work has been conducted in a selected semi-automated manufacturing industry to study and evaluate the implementation of autonomous maintenance and planned maintenance pillars of TPM. This case-study research has extracted an overall scenario of machine effectiveness, key downtime causes during the total productive maintenance (TPM) practice in the selected industry. In order to gain a reasonable market share as well as to sustain in the present competitive market, it is necessary to improve the productivity level of any manufacturing industry. Overall equipment effectiveness (OEE) has been measured because it helps to take subjective decision in strategic level of any manufacturing organization. It has been found from the study that OEE rate was 22.4% in 2012 and 23.5% in 2013 whereas world class OEE for similar type industry is 68%.

Availability was quite satisfactory comparing world class rate and quality rate resemble the world class rate. Average OEE rate increment was 4.6% from 2012 to 2013. But average availability was reduced in 2013 from 80.3% to 79.9% which shows the deterioration of maintenance practices.

Different downtimes of machines are non-value adding activity. This non-value added time is the scope of improvement for a company. Pareto chart of all downtimes has been analyzed monthly. Some downtimes were unavoidable, inter-dependent and partially avoidable. Statistical analysis of downtimes focuses on the prioritized downtime factors to consider for reduction of downtime. Applying modern maintenance practices and production improvement techniques the downtime of machines can be reduced to some extent.

## REFERENCES

[1]  K. Venkataraman, March, *Maintenance Engineering and Management,* PHI Learning Private Limited, 2009.
[2]  Patra, N. K., Tripathy, J. K. and Choudhary B. K., *"Implementing the Office Total Productive Maintenance ("Office TPM") Program: A Library Case Study,"* Vol. 54 No. 7, page 415-424, 2005.
[3]  (9 June, 2014) The Management About website. [Online]. Available: http://management.about.com/
[4]  Md. Omar Faruk, Saiful Islam and Raj Narayan Acharjee, *"Identification of the causes of downtime and its impact on production time in RMG sector of Bangladesh,"* thesis paper, Dept. of IPE, SUST, March, 2012.
[5]  (15-June, 2013) The OEE Glossary website. [Online]. Available: http://www.oee.com/
[7]  Kaplan, Robert S., *"Cost & effect: Using integrated cost systems to drive profitability and performance,"* Harvard Business Press, 1998.
[8]  (03Oct, 2013) The OEE calculating website. [Online]. Available: http://www.oee.com/
[9]  Willmott, Peter; and Dennis McCarthy, *"TPM-A Route to World Class Performance: A Route to World Class Performance,"* Newnes, 2000.
[10] (20-May, 2014) The e-book website. [Online]. Available:http://www.e-bookspdf.org/
[11] Karim, Rubayet; Rahman, Chowdury M L; *"Application of Lean Manufacturing Tools for Performance Analysis: A Case Study"*, Proceedings of the 2012 International Conference on Industrial Engineering and Operations Management (IEOM), Istanbul, Turkey, July 3 - 6, 2012; Paper ID. 403.
[12] Karim, Rubayet; Rahman, Chowdury M L; *"A performance analysis of OEE and improvement potentials at a selected apparel Industry"*, Proceedings of the 6th International Mechanical Engineering Conference and 14th Annual Paper Meet (6IMEC&14APM), 28 - 29 September, 2012, Dhaka, Bangladesh; Paper No. IMEC&APM-IE-17.

# Effectiveness of Internal Audits in Public Educational Institutions in Kenya: Rethinking Value

Owalla Wilfred[1], Luanga Salome A[2], Museve Elijah[3]

[1]*Kisumu Polytechnic, Business Studies Department, P.O. Box 143- 40100 Kisumu, Kenya*
[2]*Siaya Institute, Business Education Department, P.O. Box 1087 – 40600 Siaya, Kenya*
[3]*JaramogiOgingaOdinga University, School of Business and Economics, P.O. Box 210 Bondo, Kenya*

**ABSTRACT:** *Internal auditing has become a factor of the new accountability and control era. The manner in which public sector entities maintain internal control and how they are held accountable has evolved to require more transparency and more accountability from these organizations that spend investor or taxpayer funds. This trend has significantly impacted how management implements, monitors, and reports on internal control. Although internal auditors can be a valuable advisory resource on internal control, the internal auditor should not be a substitute for a strong internal control system. A system of internal control is the primary response to risks. The role of internal auditing has evolved from an administrative procedure with a focus on compliance, to an important element of good governance. In many cases the existence of internal auditing is mandatory (intosaigov 9140).*

Governments have continued reducing the cost of education to households through the provision of teachers, teaching and learning materials and grants to schools to cover operational and maintenance expenses under the Free Primary education (FPE) and Free Day Secondary Education (FDSE) policy; capitation grants be allocated to learners in ECDE, primary, secondary, special needs education, adult education and not-for-profit non-formal schools that meet set criteria; that technical education be brought into mainstream education so that the students can benefit from mainstream financing and enhanced skills development. There is need for the diversification and institutionalization of university education funding sources to include government (grants, education bond and loans), private sector, development partners, scholarships, bursaries, financial institutions, income generating activities and philanthropy; encouragement of local, regional and international public private partnerships in financing education and for investment in teacher professional development.

As part of the strategy to modernize internal audit methodologies, the Internal Audit Department has been undertaking reforms within the context of Public Financial Management Reform (PFMR) programme. These reform initiatives aim at moving away from regularity and compliance audits and adapting more value adding audit techniques and include; shift from pre-auditing/transactions audit to systems audit, adoption of risk based audit approach and spearheading development of institutional risk management policy framework in the public sector, adoption of internal audit standards and best practices as promulgated by the Institute of Internal Auditors (IIA), enhancement of governance through establishment of audit & risk management committees, introduction of IT supported audits and roll out of audit management system, adoption of value for money audits.

The aim of the study was to investigate whether internal audits as currently carried out in public educational institutions added value to the institutions with the objectives being to understand the internal audit function as carried out in public financial institutions, analyze effectiveness of internal audit function, and finally determine whether the internal audit function is adding any value to public educational institutions.

The study adopted a hypothetico-deductive approach with triangulation of a survey and a case study as a research. Management, accountants and auditors of public primary schools, public secondary schools, public tertiary and vocational institutions and public universities in Kenya were sampled.

The study found that the majority of auditors were still using the traditional approach probably caused by their lack of full accountancy qualification and absence of membership in professional associations.

The study therefore concluded that the internal audit function as it is currently carried out in public educational institutions did not add value to the said institutions.

It was therefore recommended among others to institute a more formal and systemic training of internal auditors in order to enhance their proficiency and skills, have the relevant professional bodies compelled to regulate and institute quality measures in audit work of public educational institutions, management training courses to involve the function of internal audit and boardroom diversity enhanced not only to improve on the management function but also on the audit function.

**Key words:** *Internal Audit, Public Educational Institutions, Public Financial Management Reform, Value for Money Audit.*

# I. Definition of Operating Terms

**Access:** The opportunity availed for one to attain education and training

**Equity:** Being fair and impartial in providing access to education and training to all

**Free Primary Education:** Refers to the waiver of all forms of contributions to education by the parents in the primary school level. The government shoulders the financing of education. This applies to the public schools only.

**Free Secondary Education:** Refers to the waiver of tuition fees by the government for secondary school level. The parents are expected to meet other requirements like lunch, transport and boarding fees for those in boarding schools, besides development projects.

# II. Background of the Study

An educational institution is classified as public if it is controlled and managed directly by a public education authority or agency or it is controlled and managed either by a government agency directly or by a governing body, most whose members are appointed or elected by public franchise (OECD 2001). Public educational institutions normally receive funding from various sources like school fees paid by parents and other grants, either from the government or other donors. Such funds are aimed at improving educational standards in educational institutions; therefore their proper utilization is paramount. Public education expenditure includes government spending on educational institutions, educational administration and subsidies for private entities i.e. students, households, and other private entities.

# III. Problem Statement

Kenya spends about 6.5 % of GDP or 20 percent of total central government spending on the education sector; which sums to Kes136.89 billion in 2008/9. Adding in education spending financed by development partners, CDF and LATF funds, and the total amount of spending was Kes 142.22 billion in 2008/9. Of this 4.1 % is financed by development partners (largely flowing through government systems) and 3.7 % is financed by devolved funds, the remainder is from central government sources. Half of central government education spending is on primary schooling, and a further 25 % is on secondary. About 12 % is transferred from the central budget to tertiary education to supplement the fee income raised at university level. The biggest rise in education spending in recent years has been at the secondary level. Public spending on education is predominantly on teachers and administrative staff salaries (66 % of all spending). Only 3.4 % of central government spending is on goods and services and 2.6 % on capital from 2006/7 to 2008/9. CDF and LATF funds supplement the resources for capital and operations and maintenance expenditures

In line these funding in public schools some government officials are corrupt and hence they mismanage or misallocation of funds that are allocated to them, (UNESCO, 2005). For instance, the sponsor's funds; this makes some children who are poor miss the opportune moments of schooling. Senior officials in the Ministry of Education, in Kenya have been accused of protecting corrupt headmasters and members of PTA (Parents Teacher Association) suspected of embezzling funds because they are also indirectly benefiting from incentives that are being paid by parents, disgruntled senior education officials have revealed, (UNESCO, 2005).

They allege that several internal audit reports as well as complaints by parents and teachers to the ministry against certain school heads and PTAs have been swept under the carpet. Many officials say the payment of incentives to teachers had resulted in an upsurge of fraud by school heads who are now exposed to huge amounts of money which they were not used to handling

Given the prevailing unfavorable economic conditions in developing countries, governments are unable to adequately finance the provision of education services (Riech, 2012). It is as a result of these that most arguments point at unethical auditors who end up not giving value to finances channeled to the education sector. In Kenya, public spending on education and training increased from Kes 92.6 billion in 2005/6 to Kes 160 billion in 2009/10 accounting for 28% of aggregate public expenditure in 2005/06 and 26% in 2009/10. These costs exclude off-budget expectations such as household spending on education and off budget financing by development parties and Non-Governmental Organizations.

(Odongo 1998) in his study realized that accounting control systems in education institutions was generally very weak implying poor financial management in schools. (Oduor, A 2012) in the East African Standard informed of a major audit of free education cash in all the public schools as it emerged that some head teachers could be involved in a syndicate to siphon funds meant for textbooks.

Finance and resource mobilization of education should be guided by the principles of affordability, needs-based resource allocation including capitation grants, efficiency in resource utilization, partnerships, strong decentralized financing and accountability systems and effective coordination.

The Minister of Education and Finance both confirmed fears that the Government may be funding ghost learners in public schools.

Omanga B, in The East African Standard of Wednesday August 2012 reported that auditing of government financial institutions in some parts of the country had been halted and a couple of senior auditors suspended.

It is against this backdrop that the study aims to investigate whether the internal audit function is performing its work well as well as adding any value to the educational institutions.

## IV. AIM of the Study

The aim of the study was to investigate whether internal audit function as currently carried out in public educational institutions add value to these institutions.

## V. Objectives of the Study

The objectives of the study was to
- understand the internal audit function as carried out in public educational institutions in Kenya
- analyze effectiveness of internal audit function and
- determine whether the internal audit function is adding any value to the public educational institutions

## VI. Hypothesis of the Study

Internal Audit Function as currently practiced in public educational institutions in Kenya is not effective

## VII. Justification of the Study

Several CEO's of educational institutions have been caught in the snare of embezzlement of funds. Periodic audits have been done on the schools' financial status, but this has not stopped the ever increasing cases of embezzlement. Funds coming into the schools as fee payment and grants are expected to be properly utilized for the intended purpose of improving standards in the educational institutions.

## VIII. Literature Review

**Funding In the Kenyan Education Sector**

This presents an analysis on the funding of education in Kenya, covering early childhood development (ECD), primary, secondary, technical and vocational schooling and university education and adult education.

The provision of widely spread education and training opportunities has been a long-standing objective of the Government of Kenya (GoK). Since Independence, the Government has sought to address the challenges facing the education sector through a range of policy initiatives. A major focus has been the attainment of Universal Primary Education (UPE) and the key concerns of achieving greater access, participation, equity, quality and relevance. Over the last 30 years, the education sector has undergone major transformations with more than ten reviews by special commissions and working parties established by the Government. The increased public demand for education and training has stretched the Government budget, and in response partnerships have been intensified with parents and communities, individual investors, civil society and donors. Financing of education has been a partnership between the government, parents, communities and the international community. The government has always been responsible for financing teacher salaries and offering limited development finance for specific projects in public schools. However, at university level government has continued to fund both the recurrent and development budgets of the public universities. Donors have been instrumental in funding capital projects. An analysis of government funding reveals that the education sector has over the years taken the largest proportion of the government budget.

Kenya spends about 6.5 % of GDP or 20 percent of total central government spending on the education sector; which sums to Ksh. 136.89 billion in 2008/9. Adding in education spending financed by development partners, CDF and LATF funds, and thetotal amount of spending was Kes 142.22 billion in 2008/9. Of this 4.1 % is financed by development partners (largely flowing through government systems) and 3.7 %t is financed by devolved funds, the remainder is from central government sources. Half of central government education spending is on primary schooling, and a further 25 % is on secondary. About 12 % is transferred from the central budget to tertiary education to supplement the fee income raised at university level. The biggest rise in education spending in recent years has been at the secondary level. Public spending on education is predominantly on teachers and administrative staff salaries (66 % of all spending). Only 3.4 % of central

government spending is on goods and services and 2.6 % on capital from 2006/7 to 2008/9. CDF and LATF funds supplement the resources for capital and operations and maintenance expenditures.

The share of total government expenditure taken up by education for the years since 1990 has averaged 17.0 percent, although with considerable growth to more than one quarter during the present decade. Moreover, since the turn of the century, recurrent expenditure on education has accounted for about 35 percent of the overall annual government recurrent budget. This partly reflects the fact that Kenya's spending on education, both as a proportion of GDP and of total public spending, is well above both the global average and those of her immediate neighbors.

Focusing on the post 2003-period reveals the changing pattern of government expenditure on education associated with the recent changes in policy in the sector. Over these years, the SWAp's was established, the FPE policy was adopted in 2003, basic education was redefined as the first 12 years of schooling and tuition fee-waivers were introduced at secondary level. Higher education expanded significantly, and a dual track system of admission to public universities was adopted.

The share of education development funds in the total government development budget has varied, though not significantly. A notable aspect is the high proportion of the MoE development vote in the years 2000/01 to 2005/06. This followed from the introduction of FPE and spending to meet the MDGs by increasing system capacity. The FPE programme resulted in the highest development spending on education over the 16-year period, through the introduction of school improvement grants (SIGs). These entailed direct transfers to schools of a sum of Kes 200,000 for improving school buildings, furniture, and water and sanitation services.
The distribution of development expenditure among the different components of education has varied over the years. On average, university education has taken the largest share, but since the overall development vote has been low, this has not implied high allocations in absolute terms. The impact of FPE on the realignment of development funding is visible from the higher proportions of development spending allocated to primary education from 2003. As with recurrent funding, ECD, special education and technical education have received the least attention. The small share of special education arises from the fewer number of institutions, but that for ECD implies low priority, given that the number of ECD institutions in the country is larger than the number of primary schools.

The Kenyan government began providing textbooks in schools immediately after independence as one of the measures to support children from poor families. Under the Kenya School Equipment Scheme (KSES), Kes 20 per child were provided at the primary school level for the provision of learning materials. Increased enrolment in subsequent years, however, constrained the government's ability to fully meet the needs of schools and pupils. Subsequently, the cost-sharing programme shifted the entire burden of book provision to the parents, and KSES was abolished in 1989. However, the procurement and supply of textbooks to poor schools under an adjustment credit was re-introduced in the 1990/91 financial year. The importance of textbooks in the FPE programme is underscored by the fact that out of the FPE funds of Kes 1,020 per pupil, about two thirds (Kes 650 or 64%) is earmarked for the purchase of textbooks, supplementary readers and reference materials, among other items. But some background information is necessary to facilitate an understanding of the current policy context.

Following the policy realignment, in 1998, the government, with support from the Netherlands embassy, initiated the Direct Budget Support for Textbook Project (short-lived though it turned out to be). In the meantime, the government, with the support of DFID, initiated a programme under SPRED III project that had a textbook component. Under this project, some 1.6 million pupils in 5,387 schools spread over 28 districts and municipalities benefited at a cost of approximately Kes 1.2 billion. The Kenya government spent a similar amount in a matched funding arrangement. During the financial year 2000/1, MoE released Kes 260 million to schools to buy books.
According to the Free Secondary Education policy, the government was expected to meet the tuition fees of Kes 10,265 per student, while the parents were required to meet other requirements like lunch, transport and boarding fees for those in boarding schools, besides development projects. This was in line with the government commitment to ensure that regional special needs and gender disparities were addressed (Ohba, 2009). These efforts were a positive move towards the realization of the Millennium Development Goals (MDGs) and Education for All.

It is worth noting that this expansion in university education has happened without donor support. The largest programme for university education in Kenya was the Universities Investment Project (UIP), ending in 1993-94. Yet at that time, enrolments actually stagnated, mainly because universities were restricted to enrolling a maximum of 10,000 new students per year. This condition was part of the education sector adjustment credit (EdSAC) conditionalities attached by the World Bank to the UIP grant. Universities compensated for the lack of donor support by pursuing private income-generating programs that have proved useful in stabilizing the financial health of the institutions, facilitating completion of stalled projects, clearing pending bills and

generally allowing investment in infrastructure and other projects that enhance the quality of teaching and learning.

**Technical and Vocational Education**

Technical and vocational education in Kenya is currently under the Ministry of Science and Technology. Like ECD, this has received far less government funding than other levels. As a result, most institutions have out-of-date equipment, a fact that has played a great role in the varying enrolment pattern. While there was an increase in enrolment between 2002/03 and 2003/04, there was a sharp contraction between 2004 and 2005 and, whilst picking up in 2006, still remaining below the 2003 enrolments. This sharp drop may be attributable to the expensive nature of TIVET especially in the national polytechnics, or to the abolishing of production courses in these institutions.

However, the inclusion of this sector as one of the investment programmes in the SWAp (Kenya Education Sector Support Project (KESSP), and therefore being in principle eligible for donor funding) may have played a role in rekindling interest - as did the diversification of courses offered in the institutions and the improved relevance of the same to the labor market, made possible by the reform program in 2003. The expansion of technical education in 2005/6 came with its inclusion in the SWAp, with donors becoming willing to fund TIVET. In this regard, the Italian government aided the expansion and upgrading of two of the national polytechnics - Mombasa and Kenya polytechnics - to offer degree programs as campuses of existing national universities. This initiative raised the profile of these institutions and enhanced their ability to attract students. The Italian government funding provided an example of the positive impact of donor funding on access expansion. Lack of enough qualified teachers/instructors, however, remains an impediment to expansion. Female student enrolment in TIVET comprises 41.1 % of total student enrolment. This is much higher than in public universities, where women constitute just about one-third of total enrolments. However, underlying this ostensibly better enrolment for women is their concentration in courses like secretarial studies, home economics, textile design and related subjects, where gender-stereotyping has strong influence.

The highest level of external support for university education was in 1991/1992, since when it declined. The diminished external support for higher education in the period after 2003 was associated with two principal factors. First, the increased revenues from Module II programmes, discussed above, meant that even with constant funding from the state and donors, their share would reduce. Second, the country adopted a sector wide approach (SWAp) approach, which initially excluded university education as a sub-sector for external support. The SWAp - Kenya Education Sector Support Programme (KESSP) – was established in 2005 following a major education conference in 2003 and the publication of a new sector policy paper (Sessional Paper No. 1 of 2005). The KESSP consists of 23 thematic areas in education, termed investment programs (IPs), which have to meet specific requirements before being eligible for donor funding from the pooled account. University education has remained one of the ineligible expenditure items for pooled funds (along with seven others) owing to there being no strategy for university development. A strategy has since been developed and it is expected that, following ratification by stakeholders, university education will be included in the eligible expenditure list from FY 2008/09.

**International Aid to Kenyan Education**

Kenya has had a long history of receiving international assistance for its education sector. At independence, the World Bank loaned the country a sum of Kenya Pounds (K£) 2.5 million (US$ 649,350) in order to implement one of the recommendations of the first Kenya Education Commission for the expansion of secondary schools over the 1965-76 period (Abagi, 1999). This was the genesis of donor assistance to Kenyan education which has continued to date.

These projects illustrate the importance of donor assistance to the Kenyan education sector. Donor programs have traditionally funded either special programs (such as those listed above) or capital projects. The impact of donor funding can therefore be judged from the perspective of the specific changes resulting from their implementation. As an example, the PRISM project funded by DFID has been lauded by some observers for the successful institution of school development planning in Kenyan primary schools. By the mid-2000s, all schools in the country developed these plans, which form the basis of funding from communities and, where applicable, from government sources, such as FPE funds. A second program that is believed to have resulted in significant change is the School-based Teacher Development (SbTD) programme, which was again funded by the British Government through DFID. This programme instituted school mentorship through the training of key resource teachers (KRTs) who in turn have provided continuous support to other teachers at the school level (OWN and Associates, 2002).

Whilst many donor-funded projects in the county have had notable impact, these two programmes are amongst the most recent, having had a direct impact on school administration and on teaching and learning processes. On the other hand, there have also been cases where funds for special programmes have been

misused and the programmes have been suspended or scaled down. One notable such project is the Direct Budget Support for Textbook Project funded by the Dutch government. Aid was suspended by the donor agency because of glaring malpractices in its implementation. Substantial amounts of funding were thus held back, reducing the overall inflow of international assistance. The experience pointed to the dangers of depending on donor aid for specific projects, even though in this case, the concern was well-founded. Not only can aid be withdrawn at will, but it is also unpredictable as the recipient countries do not have total control on its disbursement. The universities investment project (UIP) was also attended by controversy, when it was discovered that the suppliers delivered reconditioned Tata buses from India, after colluding with some government officials, instead of the Isuzu brand that was specified in the tender. The situation was rectified when one senior university officer advised the other universities not to accept the buses. It can be simplistic therefore, to blame donor agencies for systemic ills when their best efforts in assisting countries are frustrated by graft. The suspension of aid arising from such concerns was not confined to the education sector. In the transport sector, the Kenya Urban Transport Infrastructure Project (KUTIP), heavily funded by the World Bank, was also terminated at about the same time due to similar, if not more grave, concerns.

**The Free Primary Education (FPE) Programme and Resumption of Aid, 2003**
        The launching of the free primary education (FPE) programme, in January 2003 was a landmark policy decision by the new government. Seen by donors as a key step towards school fee abolition, it opened the door to new levels of donor support, and it has subsequently taken the bulk of government and donor development funding for education. The World Bank gave a grant of Kes 3.7 billion in June 2003 while the British government through DFID had earlier given a grant of Kes 1.6 billion to boost the programme (Aduda, 2003). Other donors include the Organisation of Oil Petroleum Exporting Countries (OPEC)
        (Kes 1.2 billion), the government of Sweden (Kes 430 million) and UNICEF (Kes 250 million) (Daily Nation July 10 2003, p.5). Over time, the number of projects increased from nine in 2003/04 to 15 in 2006/07. External support to education in 2006/07 alone was equivalent to more than one third (35.3percent) of total external support to education for the entire period under review, totaling KES 5,053.05. The adoption of the SWAp in 2005 resulted in setting clearer priorities and the design of a framework for joint financing, including annual sector reviews and budget workshops, which set the stage for this huge increase in external support. An important change in the way funding was allocated was made under FPE, whereby the government decided to transfer funds to schools directly. This included donor funds for such programmes as the Instructional Materials (IM) and school-building grants. The process appears to have worked well: an audit of funds-utilization under the free primary education program (MoE, 2005) concluded that overall, the resources earmarked for this purpose - both from government and donors - do reach the schools.
        Another area that has received little government funding is early childhood development. It has recently accounted for less than one percent of the total public budget for education. Donor support to the extent of Kes 300 million is much higher than total public budgetary provision to ECCE over the last two decades. External support to education has therefore played a very significant role in meeting the expenditure needs especially of the neglected sectors and sub-sectors. It may not account for a high proportion of the overall sector budget, but aid has often provided the only significant source of funding for specialized programs, such as NFE and ECCD, that receive little government attention. Although there are more than 20 agencies involved in supporting the sector, only DFID, World Bank, UNICEF and CIDA, have signed up to the JFA and, consequently, contribute to the pooled resources. Some of the non-pooling partners, including the United States Agency for International Development (USAID), are constrained by accountability requirements of their home governments which prevent them joining the JFA.
        The bulk of aid funds are committed to the basic education sector, with only three projects targeting higher education consistently over the three years. The project with the heaviest funding in 2006/7 was SPRED at Kes 1,885 million. Instructional materials programmes building heavily on SPRED received generous funding, accounting for 51 percent of the entire grants to the sector in 2006/07 and more than one third (37.3%) of the total external support in the same year. Most of the other projects targeted infrastructure (with the exception of WFP projects, which focus on school health), thereby providing a good mix of external support to major items which underpin learning.

**Embezzlement of Funds**
        Some government officials are corrupt and hence they mismanage or misallocation of funds that are allocated to them, (UNESCO, 2005). For instance, the sponsor's funds; this makes some children who are poor miss the opportune moments of schooling.
        Senior officials in the Ministry of Education, in Kenya have been accused of protecting corrupt headmasters and members of PTA (Parents Teacher Association) suspected of embezzling funds because they

are also indirectly benefiting from incentives that are being paid by parents, disgruntled senior education officials have revealed, (UNESCO, 2005).

They allege that several internal audit reports as well as complaints by parents and teachers to the ministry against certain school heads and PTAs have been swept under the carpet. Many officials say the payment of incentives to teachers had resulted in an upsurge of fraud by school heads who are now exposed to huge amounts of money which they were not used to handling

## THE INTERNAL AUDIT FUNCTION

The traditional view of internal audit department is that it is numbers based retrospective and always looking back and emphasizes on finding faults. The present view is that the modern internal auditor is process oriented with systemic concerns i.e. "why are we doing this?" and "what is the standard?" His perspective is on the future i.e., "how can we do this better?" and he will evaluate, advice and assist i.e. "we are here to help" Definition of internal auditing that was issued in 1999 says (Glenn 2001)

*"An independent objective assurance and consulting activity designed to add value and improve organizations operations. It helps an organization to accomplish its objectives by bringing a systematic, disciplined approach to evaluate and improve the effectiveness of risk management, control and governance processes"*

IIA definition of internal audit therefore places emphasis on the value adding role of internal audit as an assurance and consulting activity. The key words here therefore are independence, objectivity, risk management activities, control and governance. Independence and objectivity are important for assurance activities whereas consulting activities are necessary for risk management, control and governance processes.

## IX. Independence and Objectivity
### Internal Audit and Independence and Objectivity

Auditor independence and objectivity are the cornerstones of the profession. The assurance services provided by the auditors derive their value and credibility from the fundamental assumptions of independence of mind and independence of appearance. Prior research on auditor independence and objectivity has been undertaken predominantly in the context of external audit. However, in more recent years there has been a heightened interest in issues associated with independence and objectivity of internal audit (Stewart J and Subramanian N 2009).

The Institute of Internal Auditors (IIA) has issued a number of professional standards and guidelines with respect to independence and objectivity. The IIA has published "Independence and Objectivity: A Framework for Internal Auditors (IIA 2001) as a guide to managing threats to objectivity. The framework identifies seven key threats i.e., self-review, social pressure, economic interest, personal relationship, familiarity, cultural and cognitive biases. It also identifies a number of safeguards against these threats.

Today's internal auditors are much more than financial analysts. They provide assurance and consulting activities. They add value by helping to improve organizations operations and meet objectives. As the internal auditor's responsibilities grow, so does the demand for greater accountability, independence and objectivity (Mutchler et al, 2001).

The internal auditor is an employee of the organization but at the same time expected to review the activity of management and report any significant issues to the audit committee. Independence and objectivity are vital in ensuring that stake holders views audit work performed and the results are credible and unbiased which is the committee of the board. This may severely affect the auditors' independence and objectivity. Independence means freedom from conditions that threaten objectivity or the appearance of objectivity. Such threats of objectivity must be managed at the individual auditor engagement functional and organizational levels (IIA)

Objectivity is an impartial, unbiased mental attitude and avoidance of conflict of interest, allowing internal auditors to perform engagements in such a manner that they have a honest belief in their work product and that no significant quality are made (IIA)

INTOSAI Govt, 9140, acknowledges that auditors operating in the public sectors operate in complex organizational structures. They contend that the manner in which public sector entities maintain internal control and how they are held accountable has evolved to require more transparency and more accountability from these organizations that spend investors or tax payers' funds.

Various models can be used to resource the internal audit activity which would then enhance objectivity and independence. The internal audit department can be performed in-house by employees who understand the operations and activities being undertaken. This function can also be co-sourced with the services being provided by in-house employees and service providers usually other audit firms. It could still further be provided by these external service providers but managed by in-house employees and finally and especially when funds have been provided by other un-regularsources could lead to full outsourcings.

## X.  Proficiency and Due Professional Care

**Internal Audit and Proficiency**

Modern auditing operates in a very dynamic and complex environment.  Professional proficiency implies having up to date knowledge and abilities that are related to higher education, financial management, and government policies as well as accounting and auditing issues.  Professional proficiency is achieved and enhanced throughformal education, on the job training, continuing education programs, professional certification and service to the profession.  Professional proficiency can only be demonstrated through job performance (http://www.unc.edu/depts/intaudit/AuditMan/Professional%20Proficiency.htm).

Internal auditors should possess the knowledge, skills, and other competencies needed to perform their individual responsibilities. The internal audit activity collectively should possess or obtain the knowledge, skills, and other competencies needed to perform its responsibilities. The internal auditor should have sufficient knowledge to identify the indicators of fraud but is not expected to have the expertise of a person whose primary responsibility is detecting and investigating fraud. (IIA, 2007). The rationale is that internal auditors' experiences, knowledge and education are most valuable to management (http://www.ukessays.com/essays/accounting/internal-audit-proficiency-internal-controls.php).

**Internal Audit and Due Professional Care**

Internal auditors must apply the care and skill expected of a reasonably prudent and competent internal auditor. Due professional care does not imply infallibility.Internal auditors must exercise due professional care by considering the extent of work needed to achieve the engagement's objectives, relative complexity, materiality, or significance of matters to which assurance procedures are applied, adequacy and effectiveness of governance, risk management and control processes, probability of significant errors, fraud, or non-compliance; and cost of assurance in relation to potential benefits (IIA 1220).

**Quality Assurance and Improvement Programme**

A Quality Assurance and Improvement Program assesseswhetherinternal audit function conforms with international auditing standards and guidelines and whether the internal auditors also apply professional code of ethics.  The program also assesses the efficiency and effectiveness of the internal audit activity and identifies opportunities for improvement.

Every internal audit function needs a quality assurance programme to enable it provide the best possible services.  The benefits associated with having quality assurance include consistent application of institution processes, standardization and completeness of documentation and reporting reliability.  Quality assurance ensures that value added services are delivered to customers.

Quality assurance if well designed increases effectiveness of the audit work as well as enhancing reliability of internal audit reporting.  Consistently used, internal audit is able to face new challenges arising from increasing audit work demands caused by for example globalization, information technology, preferential free trade areas, mergers, etc.  Quality assurance will help the internal audit function to achieve these new roles by improving on their work output through continuous process improvement.

## XI.  Managing the Internal Audit Activity

**Internal Audit and Control**

INTOSAI Govt. 9100 defines internal control as an integral process that is effected by an entity's management and redesigned to address risks and provide reasonable assurance that the organization is executing orderly, ethical, economical, efficient and effective operations, it is fulfilling its accountability obligations and complying with applicable laws and regulations and eventually safeguard resources against loss, misuse and damage. It is a dynamic and integral process that is continually adapting to the changes that an organization is facing.

Effective internal control, no matter how well conceived and operated, can only provide reasonable but not absolute assurance. Effective internal control reduces the probability of not achieving objectives, but there will always be the risk that internal control will be poorly designed or fail to operate as intended.

**Internal Audit and Risk Management**

Recent corporate governance developments have raised the profile of risk management within organizations.  While the prime responsibility for risk management lies with governors, directors and senior staff, internal auditors are also seen as key contributors as consultants and assurance providers on risk management and systems.  In particular, the internal audit profession has become a key driver of the concept of Enterprise Risk Management defined by COSO (2004) as the "process affected by the entity's board of

directors, management and other persons applied in strategy setting across the enterprise defined to identify potential events that may affect the entity, and manage risk to be within its risk appetite, to provide reasonable assurance regarding achievement of the entity's objectives".

The IIA's international standard defines risk as "The possibility of an event occurring that will have an impact on the achievement of objectives". Risk is measured in terms of impact and likelihood. Risk management therefore is a structured, consistent and continuous process for identifying, assessing and mitigating on risk. Risk managers involve the evaluation of both opportunities and threats.

The IIA has also published "Risk Management Process: The Fundamentals" that summarizes the risk management process. Though as mentioned earlier the primary responsibility of the operation of a risk management process and establishment of procedures rests with the body charged with governance, every person within the organization has a role to play.

The Institute of Internal Auditors – Wales and Ireland in 2002 issued a position paper on "The Role of Internal Auditor in Risk Management" to provide guidance to members on the roles are permissible and the safeguards needed to protect the internal auditors independence and objectivity.

The internal auditor's core role identified with regard to risk management is to provide objective assurance that the major business risks are being managed appropriately. Research has shown that the two most important ways that internal audit provides value to the organization are providing objective assurance that the major business risks are being managed appropriately and providing assurance that the risk management and internal control framework is operating effectively (IIA and Delloitte and Touche 2003).

In summary the role of the internal audit will normally be to provide assurance in the design and how well the risk management processes are working, management of risks and reliable and appropriate assessment of risks and the subsequent risk reporting.

The internal auditor could also offer a consultancy role including providing advice, facilitating training programmes on risk management, development of common terms in a risk framework, supporting management on the best way to identify, analyze, and mitigate risk in so far as these consulting roles do not compromise the auditor's objectivity and independence.

**Charter and Structure**

The internal audit charter is a formal document that defines the internal auditor's activity, purpose, authority and responsibility. The purpose of this charter as mentioned is to set out the nature, role, responsibility, status and authority of the internal audit department and to outline the scope of their work. The charter also establishes the internal audit function's position within the organization, authorizes access to records, personnel, and physical properties relevant to the performance of engagements in addition to defining the scope of the audit work.

Apart from defining the scope of the audit work, the internal audit charter also defines the authority of the internal audit function, the responsibility of the department plus the standards of audit practice that will be applicable in the conduct of the audit work.

# XII.  Governance

**Internal Audit and Governance**

Governance is the domain of internal audit. The internal audit activity must assess and make appropriate recommendations for improving the governance process by coordinating the activities of and communicating information among the board, external and internal audit and management, ensuring effective organization performance management and accountability, communicating risk and control information to appropriate areas of the organization and promoting appropriate ethics and values within the organization (East African Standard 2010).

In assessing if the internal audit function would add value to an organization, it is important to check if the internal auditor is strategically positioned to contribute to business performance especially in terms of its missions and objectives, structure and funding. Do they use the appropriate processes which are proactive and not reactive? This would involve use of IT, planning methodology, etc. The internal auditor must also have professionally qualified staff

Recent events have highlighted the critical role of board of directors in promoting good cooperate governance. Boards are being charged with ultimate responsibility for effectiveness of their organizations internal control systems. They further highlight that an effective internal audit function plays a key role in assisting the governing body to discharge its governance responsibilities (KPMG, 2003).

Internal audit through the audit committee are now also expected to address the following key areas i.e. fair, balanced and understandable annual reports, greater disclosure of audit committee activities- internal audit being among them and board room diversity (KPMG 2012).

They further assert that fair balanced and understandable means giving appropriate weight to good news as well as bad news, describing strategy and risk according to the auditors understanding, whether the disclosed risks are genuinely the principal risks, a report on the link between the business model strategy, risk and performance and important messages on policies and transactions. In assessing board room diversity, there should be published the boardroom policy on board room diversity and report prepared annually. There also should be full disclosure of the audit committee activities of which internal audit is part.

## XIII.   Research Methodology

The study adopted a hypothetico-deductive approach with triangulation of a survey and a case study. Qualitative datawas collected in this study in order to provide both descriptive and interactive forms of empirical evidence.

Our first studies were explanatory in nature and found and confirmed that there was a relationship between internal audit and value addition.

For the purpose of our study we adopted a multiple case design with a single unit of analysis per case. This involved the management of the institutions, the accountants in charge of finance in the institutions, and the auditors of the institutions. The multiple cases allowed the researchers to collect more factors that could contribute to effectiveness of internal audit. It also gave a wider variety of factors. In any case evidence from multiple case studies shows higher data reliability than evidence from one study and this makes the study to be more robust and reliable than the case of a single case design. Interviews were also used as a source of evidence. This study also utilized ex post facto analysis which involved examination of relevant documents to the study.
The study sampling frame was from public educational institutions registered under the relevant Acts of Parliament under the GOK. Samples were from 3 public primary schools, 3 public secondary schools, 3 tertiary and vocational institutions and 1public university.

## XIV.   Findings

This study was to look at whether the internal audit function in public educational institutions added any value to those institutions. Value addition was presumed to include independence and objectivity in performance of work, proficiency of the auditor and due professional care, quality assurance and improvement programs, how the internal audit activity was managed, whether the internal audit had a charter and structure, governance issues of internal audit and finally how they themselves rated their own performance.
The internal audit function in the public educational institutions in Kenya is mainly carried out by auditors from the ministry in charge of education and in special cases auditors from other government ministries, regulatory bodies and the donor community. The larger institutions were able to in addition to using ministry auditors were also able to employ their own internal auditors.

The study found out that majority of auditors was(8 out of 10) partially qualified and were not members of a professional organization. The institutions audited on average were large, most of them having budgeted revenue above 10 million. All the auditors sampled reported to the CEO on behalf of the governing body. The internal audit function was understaffed in all institutions sampled.

All the auditors interviewed expressed lack of independence as their main link to the governing bodies was the CEO. There was also the aspect of the accounts being sent to the ministry headquarters for approval which took a lot of time before being sent back to the institution, mostly well into the next financial year thereby affecting the implementation of the audit recommendations. Transfers of auditors to other stations also affected the work being done in these institutions.

There were also instances where the schools CEOs were promoted to be senior officials in the ministry concerned with the running of the public institutions thereby becoming superior officers to the auditors. Auditors had a phobia for this and tended to deal with such senior CEOs cautiously thereby affecting the objectivity and independence of their work.

It was noted that the internal auditors tended to concentrate on financial statements and did very little if any of consulting engagements. Some of these internal auditors were even part of the management decision making process as evidenced by their presence on various institution management committees. This was ostensibly to enable then to clean the financial statements before the year ended.

Most of the auditors personally thought they had the knowledge and skills requisite to perform their work effectively and efficiently. However majority of them neither did not have full professional qualifications nor were members of a professional body. There also existed no formal process for enhancement of their knowledge or skills and those who upgraded their skills did it through personal initiative.

On the important aspect of quality assurance and improvement programs, the internal auditors seemed not to receive any useful feedback from management of the institutions concerning their work as they mostly looked at financial statements. The emphasis was on whether the financial statements were balancing. The work of the internal auditor was not adequately supervised as the management function of the institution had no clear

idea of what work they do. Therefore the auditors were more or less self-regulating. It was also noted that none of the auditors sampled had auditing standards and guidelines in their offices.

On managing the internal audit activity, very few of the internal auditors adopted a risk based approach. They also all had resource limitations especially in the area of information systems. It is also important to note that all internal auditors interviewed had adequate understanding of the institutions business, risk environment, and control framework as opposes to strong understanding or weak understanding.

Though the internal auditors had documented roles and responsibilities, there was no existence of an audit charter. The expectations of management of the internal audit function was not clear as was the scope of work which was basically limited to financial statements audit and in some cases involvement in the preparation of the financial statements. In the larger, tertiary institutions, there were challenges faced in accessing information.

The internal auditor's terms of reference seemed to be constant despite the changing environment. The documented terms of reference did not also address the institutions future needs. The internal audit department was therefore not strong in enhancing its objectivity and understanding of the institutions issues and the ability to respond to changing needs.

In relation to governance, financial statements were not always presented to the main stakeholders. The auditors were strong on fair, balanced and understandable annual reports and adequate disclosure and weak on boardroom diversity.

On their opinion on how they possibly added value, there was a consensus on reduction of incidences of fraud and errors, improvement of control procedures and enhancement of accountability and responsibility.

## XV. Conclusions

As was noted earlier, internal audit is moving away from the traditional view of being retrospective, always looking back and finding faults to a more modern approach which is process oriented with systemic concerns i.e. 'why are we doing this?', 'what is the standard?' and 'how can we do this better?'

It was noted that due to the governance structure of schools, most of the auditors reported to CEO as there did not exist a specific committee detailed to look at audit issues. This had an effect on objectivity and independence.

As a number of auditors still practiced the traditional approach to internal audit, they had no idea as to what consulting engagements were. This affected the objectivity of their work. Due to this approach, their work was not understood hence finding them sitting on management committees which then actually compromise their own independence and objectivity.

The aspect of sending the accounts to the ministry headquarters for approval is also a serious impairment to the objectivity and independence of the internal audit function. The auditors especially in the secondary and primary schools sat on governing committees that discussed the accounts which had not been approved and where they had been approved, it was well into the following financial year, in some instances years later meaning that then they served no useful purpose and no follow up was possible.

There was the issue of CEOs being promoted to the ministry headquarters thereby turning to be superior officers to the auditor i.e. a classical case of the 'hunter becoming the hunted.' This had a twofold effect in affecting the independence and objectivity of the internal auditor. On the one hand, the auditors in institutions that had CEOs ranked highly in the governments structures and who stand a high chance of being promoted to the ministry headquarters were treated differently thus affecting the independence and objectivity of the auditor and secondly, in instances where the CEO turned to be superior officers, not only was this a discouragement to the auditor but also affected future performance of his work.

On the issue of the internal audit function sitting in the various management committees within the institution is definitely impairment to the independence and objectivity of the internal audit function.

Though the auditors personally thought they had the requisite knowledge and skills to perform their responsibilities, their being partially qualified and absence of membership to a professional organization hindered their ability to effectively carry out their work. Evidence of auditors sitting on operational committees was evidence of lack of understanding of the internal audit function. Though a number of auditors made a personal initiative to improve on their proficiency, in order to enhance this, there is need to have a formal institutional or systemic approach to the improvement of the proficiency of the auditor.

Due to lack of the understanding of the role and function of the internal audit by both the internal audit and management, there was therefore no documented quality assurance and documented programme in place in the educational institutions. The internal audit work plans were financial statement centered. The lack of internal audit function coupled with the absence of committees specifically dealing with audit work, meant that there were no quality procedures in place.

The absence of audit standards and guidelines coupled with absence of best practice procedures resulted in the compromise of the audit work.

The internal audit activity was not well managed in these institutions.  There were resource limitations affecting the work of the auditor.  The internal audit function by adopting the traditional approach, just had a working knowledge of the business of the institution, and in most tertiary institutions operations were quite complex, meant that working knowledge was not enough. It was necessary to have thorough knowledge of the institutions operations.

The internal audit function also displayed working knowledge of the institutions risk environment and control framework.  These areas also require a high level of knowledge for there to be value addition.

The absence of a charter meant the absence of a strategic audit plan.  As a result the documented roles and responsibilities were not dynamic and hence could nod address affectively the independence and objectivity of the auditor, long term proficiency plans, quality plans and hence the effectiveness of the work being carried out.  The absence of the charter reduced the internal audit function to a 'fire-fighting role.'

It is also important to note that the absence of a reporting structure that includes major stakeholders, compromises the work of the internal auditor.  Organizations exist to serve stakeholders needs.  The internal audit functions must likewise address the stakeholders' expectations. This can be achieved by providing the stakeholders with not only reports of the internal audit function activities, but also reports on significant activities of the institution.

Board room diversity is also an area that needs to be addressed as the governing body must have requisite knowledge of the internal audit function.  It was not mandatory for all the board members to have this knowledge.

In conclusion therefore, though the internal audit function reduced instances of fraud and error, improved control procedures, and enhanced accountability and responsibility, there was no significant improvement in value to the institutions in which they were placed.  Shrewd management activities could still have achieved the same result.

## XVI.  Recommendations

Due to the fact that the study has concluded that the internal audit function has not added any significant value to the institutions in which they are placed, the following recommendations were made:

The institutions should put in place formal training programs that not only will enhance the proficiency of the internal auditors but will also equip them with specialized skills necessary to enable them to perform their work effectively.

The government, being the provider of the funds should introduce systemic approaches to enable the internal audit function to improve on their proficiency and due professional care.

The relevant professional bodies should also be compelled by the government, even possibly through an act of parliament to regulate and institute quality measures given the significance and the amount of public funds passing through these public educational institutions.

The institution should also include in its management training courses, functions of the internal audit functions and expectations of management in relation to internal audit function.

Boardroom diversity should be enhanced in order to manage and control the internal audit function. The governing body should also find ways in which more stakeholder participation could be enhanced thereby increasing the value of internal audit reporting.

It will also be necessary to delink the internal audit function from the ministry function to prevent instances where the auditee becomes a superior officer of the auditor via promotion.

## REFERENCES

[1]     2001, Data Collection on Education System: Definitions, explanations and Instructions,  UNESCO, OECD. Eurostat, pg. 49
[2]     Abagi, O. (1999). Education for the Next Decade: A Demarcation of Imperatives. In Kimuyu, P.,
[3]     Wagacha, M. and Abagi, O. (Eds).Kenya's Strategic Policies for the 21st Century:Macroeconomic and Sectoral Choices. Nairobi: IPAR.
[4]     Aduda, D. (2003). "Record Sh 71 billion Allocated to Boost Free Learning". Daily Nation 13 June 2003, 3.
[5]     Committee of Sponsoring Organizations (COSO) (2004) Internal Control – Integrated Framework executive summaryhttp://www.coso.org/publications/executive summary_integrated_framework.htm
[6]     Glenn I. 2001, CIA review; Part 1, Internal Audit Process.  Institute of Internal Auditors
[7]     INTOSAI GOVERNMENT 9100: Guidelines for Internal Control Standards for the Public Sector
[8]     http://www.unc.edu/depts/intaudit/AuditMan/Professional%20Proficiency.htm accessed on 18/03/2013
[9]     http://www.ukessays.com/essays/accounting/internal-audit-proficiency-internal-controls.php accessed on 18/03/2013
[10]    Karani, F. A. et. al. (1995).Cost and Financing of Education in Kenya: Access, Quality and Equity in Secondary Education. Nairobi: World Bank and MoE
[11]    Khasiani, S.A. (1997), "Situational Analysis of Women in Kenya: Literature Survey". Nairobi:
[12]    Family Support Institute.

[13] KPMG Internal Audit's Role in Modern Corporate Governance.Thought Leadership Services. Australia September 2003

[14] Mitha, N. J. et. al. (1995), "Cost and Financing of Education in Kenya: Access, Quality and Equity in Primary Education". Nairobi: World Bank/MoE.

[15] Mutchler J., Chang S., Prawitt D., 2001 Independence and Objectivity: A Framework for Internal Auditors. The IIA Research Foundation

[16] National Council of NGOs. (1997). "Position Paper of the Voluntary Sector on the Education and Training Master Plan, 1997 – 2010". Nairobi: Action Aid.

[17] Ngome, C.K. 2002.The Impact of School Feeding Programme on the School Participation Rates of Primary School Pupils in Kajiado District, Kenya.Unpublished PhD Thesis, Kenyatta University, Nairobi, Kenya.

[18] Ohba, A. (2009). Does Free Secondary Education Enable the Poor to Gain Access? A Study from Rural Kenya, CREATE Pathways to Access, Research Monograph No 21

[19] Olembo, J. and Waudo, J. (1999), "Parental Attitude and the Cost of Schooling", Baseline Survey

[20] Riechi A. 2012 Revenue Diversification in Kenya's Public Universities and Implications for Efficiency and Equity. An Analysis of Education Finance in the African Context

[21] Stewart J, Subremania N (2009), Internal Audit Independence and Objectivity: A Review of Current Literature and Opportunities for Further Research Griffith Business School: Discussion Papers - Accounting

[22] The Value Agenda: Institute of Internal Auditors – UK and Ireland Delloitte and Touche 2003

[23] UNESCO (2005).Challenges of implementing free primary education in Kenya: assessment report. Kenya. Nairobi: Ministry of Education, Science & Technology.

## ACRONYMS

| | |
|---|---|
| ASE | Affordable Secondary Education |
| ASAL | Arid and Semi-Arid Lands |
| CDF | Constituency Development Fund |
| CEO | County Education Officer |
| CHE | Commission for Higher Education |
| CIDA | Canadian International Development Agency |
| COSO | Committee of Sponsoring Organizations |
| DFID | Department for International Development |
| ECD | Early Childhood Development |
| ERM | Enterprise Risk Management |
| FPE | Free Primary Education |
| GDP | Gross Domestic Product |
| GOK | Government of Kenya |
| IIA | Institute of Internal Auditors |
| INTOSAI | International Organization of Supreme Audit Institutions |
| JICA | Japan International Cooperation Agency |
| Kes | Kenya Shillings |
| KSES | Kenya School Equipment Scheme |
| KIE | Kenya Institute of Education |
| LATF | Local Authority Transfer Fund |
| MDGs | Millennium Development Goals |
| MoE | Ministry of Education |
| MoEST | Ministry of Education, Science and Technology |
| NGO | Non-Governmental Organization |
| ODA | Official Development Assistance |
| OECD | Organization for Economic Co-operation and Development |
| PTA | Parents Teachers Association |
| SbTD | School-based Teacher Development |
| SWAp | Sector Wide Approach |
| TIVET | Technical, Industrial and Vocational Education and Training |
| UNICEF | United Nations' Children's Fund |
| UoN | University of Nairobi |
| UPE | Universal Primary Education |

# An Experimental Analysis of Performance, Combustion and Emission Characteristics of Rice bran Biodiesel and Its Blends on CI Engine

Syed Shakeer[1],  M. C. Navindgi[2]

*([1]PG Student, Thermal Power Engineering PDACE Gulbarga, Karnataka, India)*
*([2]Associate professor, Dept of Mechanical Engineering PDACE Gulbarga, Karnataka, India)*

**Abstract:** *The use of biodiesel, the methyl esters of vegetable oils are becoming popular due to their low environmental impact and potential as a green alternative fuel for diesel engine. With this objective, the present work has focused on the performance and emission characteristics of diesel engine using rice bran oil and its blends with diesel. In this investigation, the blends of varying proportions of rice bran biodiesel with diesel (RB20, RB40, RB60, RB80 & RB100) were prepared, analyzed, and compared the performance and exhaust emission with diesel using 5.2 kW Single cylinder, 4stroke diesel engine. The performance and emission characteristics of blends are evaluated at variable loads and constant rated speed of 1500 rpm and found that the performance of RB20 blend of rice bran oil gives result, that is near to the diesel and also found that the emission CO, CO2, HC, smoke & $NO_X$ of this blend is less than the diesel.*
**Keywords:**  *Biodiesel, Rice bran, Alternate fuel, CI Engine.*

## I.  Introduction

According to the present scenario diesel engines are commonly used as prime movers in the transportation, industrial and agricultural sectors because of their high brake thermal efficiency and reliability. Energy conservation and efficiency have always been the quest of engineers concerned with internal combustion engines. In this work, we have adopted Rice bran oil. Rice bran belongs to family Oryza sativa linn.

## II.  Materials and Methods

The extraction of biodiesel is carried out by base catalyzed transesterification method.

### 2.1. Process of Extracting
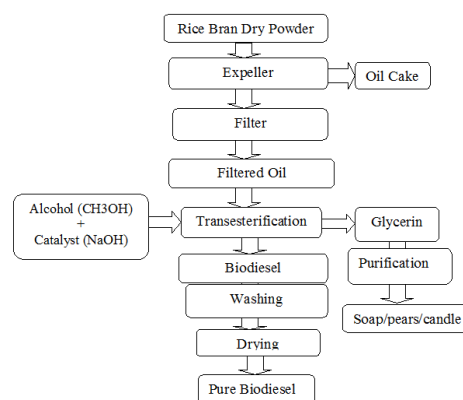


Fig 2.1: The flow chart for biodiesel production

To a one liter of raw Rice bran oil is heated up to $70^0$C. 300 ml of methanol & 5-7gms of NaoH (catalyst) is added and the mixture is maintained at 65-$70^0$C is about 1½ hours and stirred continuously. The mixture is allowed to settle for 20-30 min until the formation of biodiesel and glycerin layers. The glycerin is removed from the bio-diesel in a separating funnel. The bio diesel produced from Rice bran oil is ready to use.

### 2.2. Transesterification

It is most commonly used and important method to reduce the viscosity of vegetable oils. In this process triglyceride reacts with three molecules of alcohol in the presence of a catalyst producing a mixture of fatty acids, alkyl ester and glycerol. The process of removal of all the glycerol and the fatty acids from the vegetable oil in the presence of a catalyst is called esterification.

```
CH2COOR1                                      CH2OH         R1COOR
|                                             |             |
CHCOOR2                                       CHOH          R1COOR
|              +    3ROH    ⟷                 |        +    |
CH2COOR3                                       CH2OH         R1COOR
                          Catalyst
                          (NaOH)

Rice bran Glyceride      Alcohol            Glycerin       Biodiesel
```

Chemical reaction

Physical and chemical properties are more improved in esterified vegetable oil because esterified vegetable oil contains more cetane number than diesel fuel. These parameters induce good combustion characteristics in vegetable oil esters. So unburnt hydrocarbon level is decreased in the exhaust. It results in lower generation of hydrocarbon and carbon monoxide in the exhaust than diesel fuel. The vegetable oil esters contain more oxygen and lower calorific value than diesel. So, it enhances the combustion process and generates lower nitric oxide formation in the exhaust than diesel fuel.

## III. Properties of Diesel and Some Blends

After transesterification the properties of Rice bran oil blends was determined. It was found that the properties of Rice bran oil blends were similar to diesel. Rice bran oil blends were similar to diesel.

Table 3.1: Properties of Rice bran oil blends

| Properties | Diesel | RB20 | RB40 | RB100 |
|---|---|---|---|---|
| Kinematic viscosity at $40_0$C (Cst) | 2.54 | 3.024 | 3.617 | 5.4 |
| Calorific value (kJ/Kg) | 42500 | 42270 | 41976 | 37933 |
| Density (kg/m$_3$) | 840 | 838 | 846 | 875 |
| Flash Point ($^0$C) | 54 | 79 | 98 | 165 |
| Fire Point ($^0$C) | 64 | 89 | 110 | 185 |

## IV. Experimental Setup

The experimental setup enables study performance, combustion and emission characteristics. The experiments have been carried out on a DI compression ignition engine for various blends of rice bran oil with diesel (RB20, RB40, RB60, RB80, and RB100) with varying brake power. The experiment is carried out at constant compression ratio of 17.5:1 and constant injection pressure of 200 bar by varying brake power.

Table 4.1: Engine specifications



| Manufacturer | Kirloskar oil engines Ltd, India |
|---|---|
| Model | TV-SR, naturally aspirated |
| Engine | Single cylinder, DI |
| Bore/stroke | 87.5mm/110mm |
| Compression Ratio | 17.5:1 |
| speed | 1500r/min, constant |
| Rated power | 5.2kw |
| Working cycle | 4 stroke |
| Injection pressure | 200bar/23 def TDC |
| Type of sensor | Piezo electric |
| Response time | 4 micro seconds |

Fig 4.1: Photograph of engine setup

<center>

## V.    Result and Discussion
</center>

### 5.1    Performance characteristics

5.1.1    Specific fuel consumption
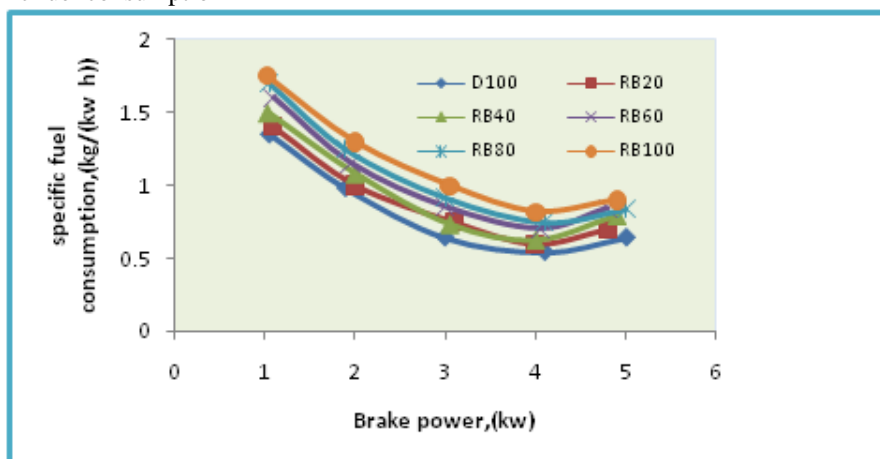


Fig 5.1 Variation of the specific fuel consumption with brake power for diesel and rice bran blends

The variation of  specific fuel consumption with Brake power for diesel, and rice bran biodiesel oil and it's blends  are shown in figure 5.1. The specific fuel consumption for rice bran biodiesel blends are higher than diesel for certain lower loads, but for higher loads, consumption rate remains  almost constant as evident from the graph. This may be due to fuel density, viscosity and heating value of the fuels. The main reason for this could be that percent increase in fuel required to operate the engine is less than the percent increase in brake power due to relatively less portion of the heat losses at higher loads.
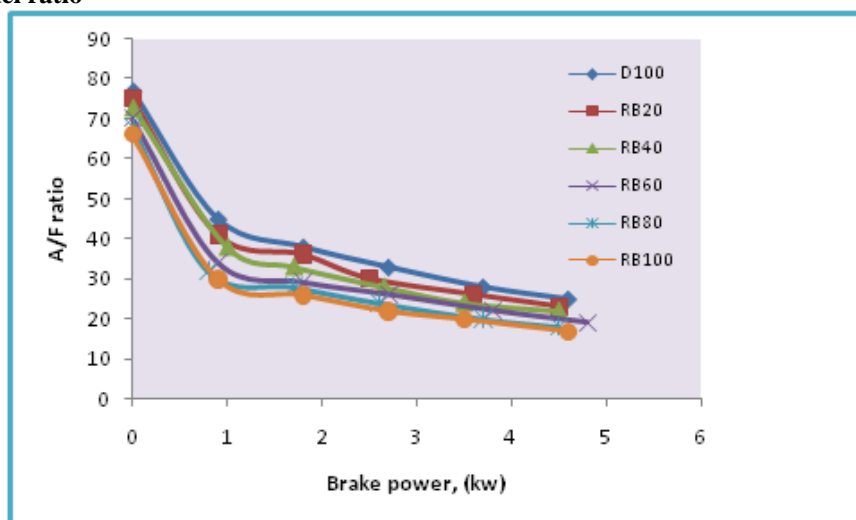
### 5.1.2    Air fuel ratio



Fig 5.2 Variation of the specific fuel consumption with brake power for diesel and rice bran blends

The variation of air fuel ratio with brake power for diesel and rice bran biodiesel blends are shown in figure 5.2. It can be observed that air fuel ratio of pure diesel is higher than other rice bran biodiesel and its blends, and we can also see that the air fuel ratio decreases as the load increases. Because the reason is air fuel ratio decreases due to increase in load because of the compensation of load can only be done with increasing the quantity of fuel injection to develop the power required to bare the load.

### 5.1.3    Brake thermal efficiency
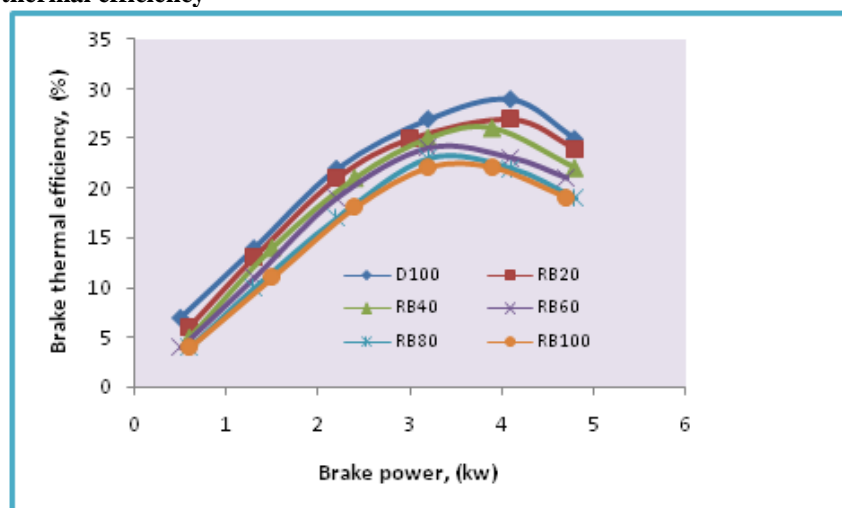


Fig 5. 3  The variation of the brake thermal efficiency  with brake power for diesel and rice bran blends

The variation of  brake thermal efficiency with brake power for diesel, and rice bran biodiesel and its blend are shown in figure 5.3. shows the break thermal efficiency of rice bran biodiesel and its blends with respect to brake power. The Increase in thermal efficiency due to high percentage of oxygen presence in the biodiesel, the extra oxygen leads to causes better combustion inside the combustion chamber. The thermal efficiency of the engine is improved by increasing the concentration of the biodiesel in the blends and also the additional lubricant provided by biodiesel. The decrease in brake thermal efficiency with increase in rice bran biodiesel concentration is due to the poor atomization of the blends due to their high viscosity and reduction in heat loss and increase in power with increase in load.

### 5.1.4    Exhaust gas emission
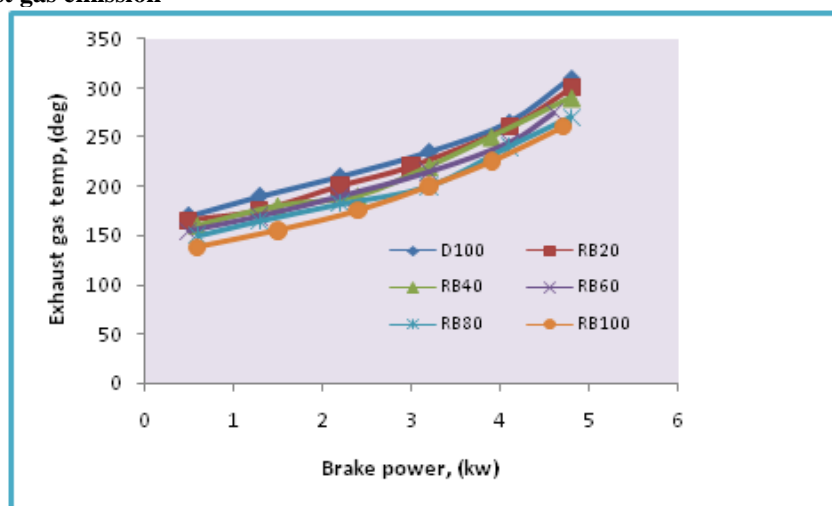


Fig 5.4  The variation of the exhaust gas temperature  with brake power for diesel and rice bran blends

Figure 5.4 shows the Exhaust gas temperature the variation of exhaust emission temperature with brake power for diesel, and other blends of rice bran biodiesel is shown. the exhaust emission temperature of all the biodiesel are higher than the diesel as it is evident from the graph. The exhaust gas temperature of all the blends and 100% diesel increase as the load increases. It is observed that, at full load the exhaust gas temperature is maximum, this is because; at full load the chemically correct ratio of air and fuel is used, due to chemically correct ratio of air and fuel, high heat is generated inside the cylinder.

### 5.2      Emission characteristics

### 5.2.1      Carbon  monoxide



Fig 5.5 The variation of the carbon monoxide  with brake power for diesel and rice bran blends

The plots of carbon monoxide CO emissions of rice bran and diesel fuel operation at different load conditions are shown in figure 5.5 The plots show reducing CO emissions at higher loads. The decrease in carbon monoxide emission for biodiesel is due to more oxygen molecule present in the fuel and more atomization of fuel as compared to that of diesel. The decrease in CO emission may be due to better vaporization biodiesel fuel and more oxygen present in the biodiesel, resulting in complete combustion.

### 5.2.2      Hydro carbon
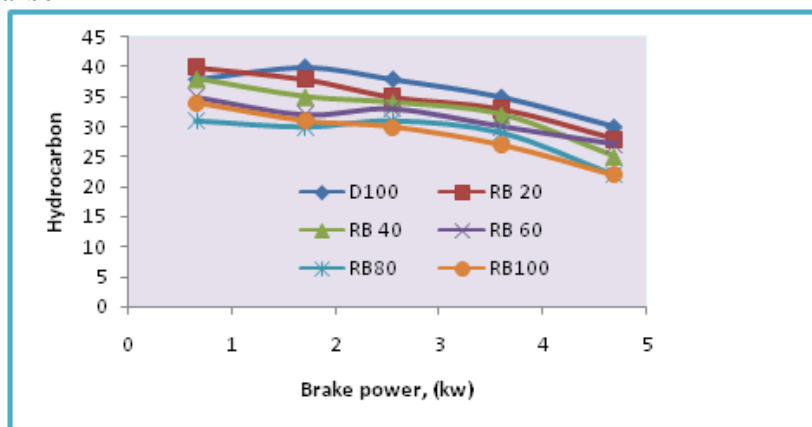


Fig 5.6 The variation of the hydro carbon  with brake power for diesel and rice bran blends

The variations of HC emission for diesel and biodiesel are shown in the figure 5.6 it has been observed that HC emissions are nominal for RB80, RB100, and more at RB20, RB40 and RB60. The reason for this may be incomplete combustion. The higher cetane number of biodiesel results decrease in HC emission due to shorter ignition delay. Lower HC emissions in the exhaust gas of the engine may be attributed to the efficient combustion of rice bran  biodiesel and blends due to the presence of fuel bound oxygen and warmed-up conditions at higher loads. This is due to the reason that at lower loads the lower cylinder pressure and temperatures were experienced that was caused by lower rate of burning. This feature results in higher HC emissions.

**5.2.3 Nitrogen oxide**
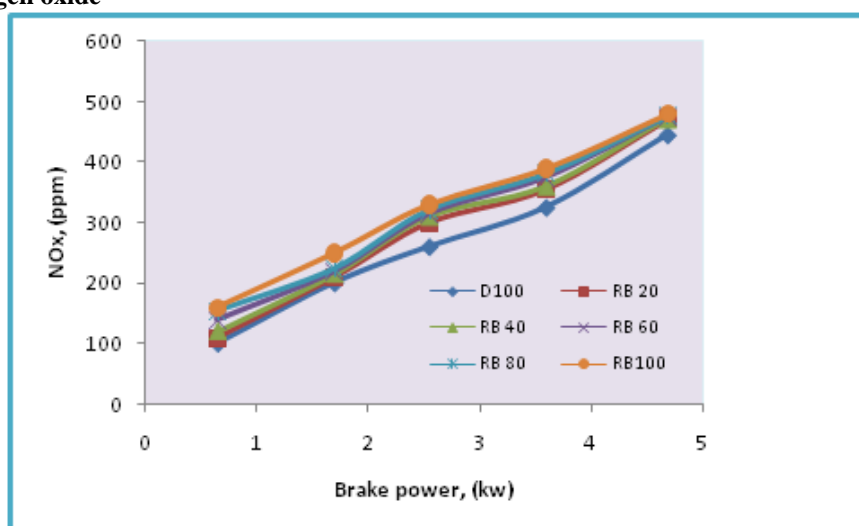


Fig 5.7  The variation of the nitrogen oxide  with brake power for diesel and rice bran blends

The average percentage of change in $NO_x$ emission for RB20, RB40, RB60, RB80, and RB100 are shown in the graph. This shows that the $NO_x$ emission increased with the increase of percentage ratio of biodiesel. $NO_x$ emission is primarily a function of total oxygen inside the combustion chamber, temperature, pressure, compressibility, and velocity of sound. Invariably biodiesel has high level of oxygen bound to its chemical structures. Thus, oxygen concentration in biodiesel blends fuel might have caused the formation of $NO_x$ . Furthermore, the increase of $NO_x$ emission is due to the higher cetane number of biodiesel which will reduce the ignition delay. The increase of $NO_x$ emission is a result of the reduced ignition delay. However, the $NO_x$ emissions can be reduced through engine tuning or using exhaust catalytic converter. At any rate, the $NO_x$ still can be reduced with the advanced technologies such as catalytic converter, EGR and engine tuning.

**5.3 Combustion Characteristics**
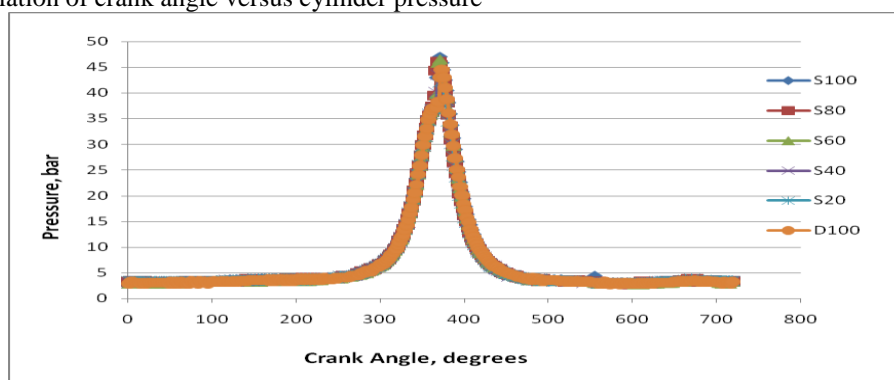
5.3.1     Variation of crank angle versus cylinder pressure



Fig 5.8  Variation of crank angle versus cylinder pressure

In a CI engine the cylinder pressure is depends on the fuel-burning rate during the premixed burning phase, which in turn leads better combusion and heat release. The variation of cylinder pressure with respective crange angle for diesel and different blends of simarouba biodiesel are presented in fig 5.8 peak pressure of 44.54bar and 43.69bar are found for puer diesel and RB40 respectively. From the test results it is observed that the peak presure variations are less since the properties such as calorific value, viscosity and density are brought closer to diesel after transestirification of vagitable oil, no magare variation in the pressure are found.

**5.3.2    Variation of crank angle versus heat release rate**
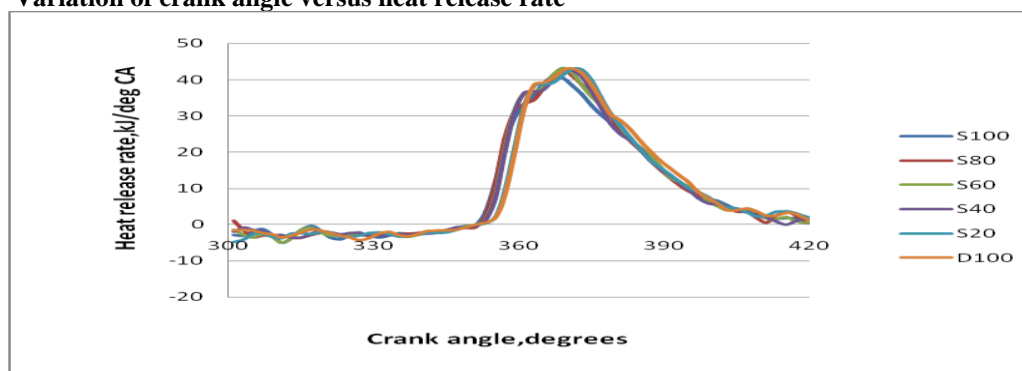


Fig 5.9 Variation of crank angle versus heat release rate

The fig-5.9 shows that the variation of the heat release rate with crank angle.It is observed that all the blends of rice bran oil traces the path of pure diesel and RB60 are 43,11044kj and 43,2087kj at 3710.

5.3.3     Variation of crank angle versus cumulative heat release rate
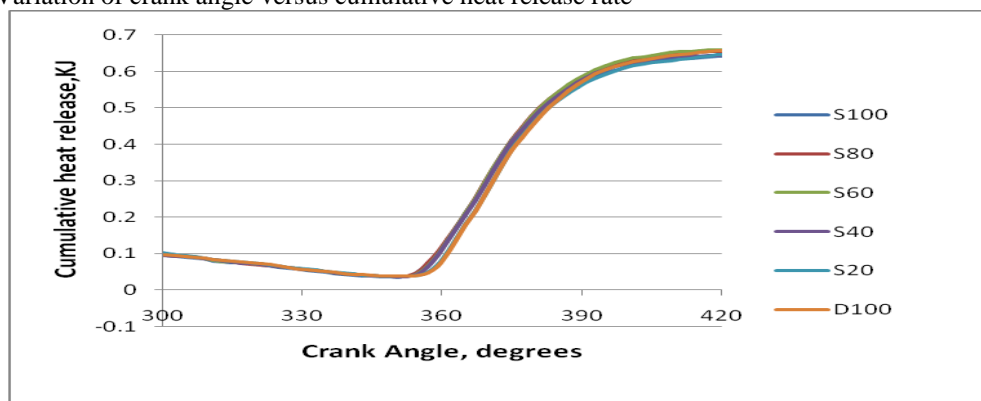


Fig 5.10  Variation of crank angle versus cumulative heat release rate

The fig-5.10 shows the variation of comulative heat transfer with crank angle. It is observed that from the fig-5.10 that all blends of rice bran biodiesl traces the same path as that of the diesel.initially the cumulative heat transfer decreases at first cycle and then increases in the second cycle as shown in the fig-5.3.3.

## VI.  Conclusion

- Specific fuel consumption increases as the concentration of rice bran biodiesel increases so we can observe that with 20% rice bran biodiesel blend almost matches with diesel fuel.
- Air fuel ratio for diesel is lower than rice bran biodiesel and its blends which is evident from the graph.
- The mechanical efficiency of diesel is slightly higher than the rice bran biodiesel blends and D100 and RB20 are seen to be almost nearer to each other also from the graph.
- Brake thermal efficiency of rice bran biodiesel at 20% blend has slightly higher efficiency than diesel.
- The exhaust emission temperature of all the biodiesel are higher than the diesel and It is observed that, at full load the exhaust gas temperature is maximum, due to chemically correct ratio of air and fuel.
- The RB20 has lower average percentage of change in CO, and HC compared to Diesel. Yet, S20 is producing higher NOx emission. Nevertheless, the RB20 is still the suitable biodiesel blend amongst all as the NOx emission can be reduced with the advanced technologies.

## REFERENCES
[1]    Bryan R. Moser, *"Biodiesel production, properties, and feedstock", In Vitro Cell.Dev.Biol.—Plant (2009) 45:229–266.*
[2]    Kalligeros S, Zannikos F, Stournas S, Lois E, Anastopoulos G, Teas CH and Sakellaropoulos F(2003) *An investigation of using biodiesel/marine diesel blends on the performance of stationary diesel engine. Biomass Bioenergy.24, 141-149.*
[3]    K.M. Shereena, T.Thangaraj, *"Biodiesel: an Alternative fuel Produced From Vegetable Oils by Transesterification", Electronic Journal of Biology, 2009, Vol.5 (3): 67-74.*

[4]     Sanjaykumar DALVI, Swati SONAWANE, and Raghunath POKHARKAR, *"Preparation of Biodiesel of Undi seed with In-situ Transesterification", Leonardo Electronic Journal of Practices and Technologies ISSN 1583-1078 Issue 20, January-June 2012.*

[5]     Mohammed Chakrabarti, Mehmood Ali, *"performance of compression ignition engine with indigenous castor oil bio diesel", Ned University Journal of Research, Vol VI, No. 1, 2009.*

[6]     Bello E.I and Makanju A, *"Production, Characterization and Evaluation of Castor oil Biodiesel as Alternative Fuel for Diesel Engines", Journal of Emerging Trends in Engineering and Applied Sciences (JETEAS), 2011 (ISSN: 2141-7016).*

[7]     G.Durga Devi, Mahesh.C, "*Performance evaluation of a diesel engine fueled with methyl ester of castor seed oil", International Journal of Engineering Science and Technology (IJEST) Vol. 4 No.07 July 2012.*

[8]     Sergio C. Capareda, Jacob Powell, *"Engine Performance and Exhaust Emissions Of Cottonseed Oil Biodiesel", 2008 Beltwide Cotton Conferences, Nashville, Tennessee, January 8-11, 2008.*

# An Investigative Review on Thermal Characterization of Hybrid Metal Matrix Composites

S. A. Mohan Krishna[1], Dr. T N Shridhar[2], Dr. L Krishnamurthy[2]

[1]*Department of Mechanical Engineering, Vidyavardhaka College of Engineering, Mysore, India*
[2]*Dept. of Mechanical Engineering, The National Institute of Engineering, Mysore-570 008, India*

**Abstract:** *Composite materials have become cynosure among all materials that have applications in profusion. The applications of these materials are absolutely appreciative and applicable in almost all areas of mechanical engineering. The mechanical characterization of these materials has become common nowadays. But the thermal characterization of hybrid metal matrix composites is increasingly important in a wide range of applications. Aluminium Silicon alloys in particular finds extensive and increased applications in industries due to their properties viz., high fluidity, low melting point, high strength, corrosion resistance, good casting characteristics and lower coefficient of thermal expansion. In the present scenario, research work is accomplished on hybrid composites based on mechanical properties but very limited research has been carried out on hybrid composite based on thermal properties and characterization. The thermal analysis of hybrid metal matrix composites is required to clearly examine the thermal properties viz., Thermal Conductivity, Temperature Difference, Thermal Capacity or Heat Difference, Coefficient of Thermal Expansion and Rate of Heat Transfer. Thermal Analysis is also often used as a term for the study of Heat Transfer to measure Heat capacity and Thermal Conductivity. The behaviour of hybrid composite materials is often sensitive to changes in temperature. This is mainly because, the response of the matrix to an applied load is temperature-dependent and changes in temperature can cause internal stresses to be set up as a result of differential thermal contraction and expansion of the constituents. The flash method is a well-established unsteady-state measurement technique for measuring the thermal diffusivity, α, of solid homogeneous isotropic opaque materials. This technique is regarded to be the most polished and sophisticated technique for the determination of thermal parameters of composites. On the basis of the present review, it is obvious and pragmatic that the thermal properties on hybrid composites have not been adequately experimented and investigated. The thermal analysis of hybrid composites is beneficial in automotive, aeronautical and many other engineering applications. This review summarizes illustratively about the experimental and analytical investigations and corroborations about the thermal analysis of hybrid metal matrix composites also provide convincing and conclusive recommendations for emerging trends in composite materials.*
**Key words:** *Metal Matrix Composites, Thermal Analysis, Thermal Conductivity, Heat Capacity, Temperature Potential, Heat Capacity.*

## I. Introduction

A composite material is a macroscopic combination of two or more distinct materials having a recognizable interface between them. Composites are used not only for their structural properties, but also for electrical, thermal, tribological and environmental applications [1]. The term Metal Matrix Composites (MMCs) covers a very wide range of materials to simple reinforcements of castings with low cost refractory wool, to complex continuous fires lay-ups in foreign alloys. The properties of MMCs are controlled by the matrix, the reinforcement and the interface. In particular many of the considerations arising due to fabrication, processing and service performance of composites are related of processes that take place in the interfacial region between matrix and reinforcement.

Among modern composite materials, particle reinforced Aluminium Matrix Composites (AMCs) are finding increased application due to their favorable mechanical properties and good wear resistance [2]. Aluminium-Silicon Carbide and Aluminium-Graphite are used as reinforced composites to study its unique characteristics and behaviour. Aluminium Matrix Composites (AMC) consists of Aluminium or its alloys as the continuous matrix and a reinforcement that can be particle, short fiber or whisker or continuous fiber. Research

and development activities of the last decade have resulted in the evolution of a class of MMCs termed as Discontinuously Reinforced Aluminium (DRA) composites. Particle or discontinuously reinforced AMCs have become very important because they are economical when compared to continuous fiber reinforced composites and they have relatively good isotropic properties compared to fiber-reinforced composites. These materials have captivated the attention of producers and researchers all over the world because of their outstanding properties such as high-strength-to-weight ratio, improved wear and elevated temperature resistance and low density. In addition these materials are comparatively easier to manufacture than the continuously reinforced composites and have a great potential to be available at low cost [3]. Though initially aimed only at aerospace and defense products, AMCs have progressively moved into higher volume applications. These materials employ a metallic matrix such as Aluminium to which is added reinforcement materials such as Alumina or Silicon Carbide (SiC). The net result is a composite material with enhanced mechanical properties particularly with regard to density and stiffness.

The development of metal matrix composites has been catalyzed by the need for structural materials with high specific strength and stiffness. The composites mainly with Aluminium matrix are fabricated either by molten metal infiltration or by powder metallurgical routes. The mechanical and fracture properties of Al-SiC composites are of primary importance in design and thermal considerations when they are to be used as structural materials. Metal Matrix Composites are a diverse class of materials that consist of a metallic alloy matrix typically reinforced with a ceramic phase in the form of particles, platelets, whiskers, short fibers and continuously aligned fibers. These composites are used in structural applications, and in applications requiring wear resistance, thermal management and weight savings. By far the most common commercial metal matrix composites are based on aluminium, magnesium and titanium alloys reinforced with either Silicon Carbide, Alumina, Carbon or Graphite [4].

## II. Thermo physical Properties of Metal Matrix Composites

The thermophysical properties of metal matrix composites are required to characterize the composites comfortably. Some of the important thermophysical properties considered are Density, Coefficient of Thermal Expansion, Thermal Conductivity and Diffusivity, Specific Heat and Thermal Stresses. The measurement and characterisation of thermophysical properties such as density, CTE (Coefficient of Thermal Expansion), Specific Heat and Thermal conductivity or resistivity plays an important role. Additionally requirements to this material class are given through their use under varying temperature conditions. So investigations and observations of thermophysical properties are not only performed at room temperature but also at higher temperatures or under cycling conditions.

The determination of Thermal Conductivity and Diffusivity can be accomplished by Laser Flash Technique. On the contrary, the evaluation of Specific Heat can be carried out using Differential Scanning Calorimetry or using Thermal Conductivity tester. Measurement of thermal cycling is necessary in order to simulate the behaviour and the performance of a material during its operation. Therefore the measurement of CTE or thermal conductivity of a material during several temperature cycles can be useful. Temperature ranges can be between room temperature and the proposed temperature of operation. Measuring of CTE during several cycling leads to the information about the deformation per cycle or the total resulting deformation during all cycles. The behaviour of CTE and Thermal conductivity during thermal cycling also allows a practical approach to understand about the interface properties in the material [5].

## III. Thermal Analysis of Composites

The need for the thermal analysis of hybrid metal matrix composites must be comprehensively discussed. The behaviour of composite materials is often sensitive to changes in temperature. This is mainly because, the response of the matrix to an applied load is temperature-dependent and changes in temperature can cause internal stresses to be set up as a result of differential thermal contraction and expansion of the constituents. Thermal analysis of hybrid composites is a pragmatic approach to clearly study its thermal characteristics. Most of the thermal studies are mainly concerned with AMCs but less information is available on hybrid composites [6].

The development, specification, and quality control of materials often require the measurement of thermo physical properties. This data can be critical to a successful design, especially with the rapidly increasing cooling requirements that result from the packaging of higher performance devices. A variety of methods, involving both steady state and transient techniques, are available for measuring thermal diffusivity, specific heat, thermal conductivity and thermal resistance. Information of the thermo physical properties of materials and heat transfer optimization of final products is becoming more and more vital for industrial applications. Over the past few decades, the flash method has developed into the most commonly used technique for the measurement of the thermal diffusivity and thermal conductivity of various kinds of solids,

powders and liquids. Application areas are electronic packaging, heat sinks, brackets, reactor cooling, heat exchangers, thermal insulators and many others. Trouble-free sample preparation, small required sample dimensions, fast measurement times and high accuracy are only a few of the advantages of this non-contact and non-destructive measurement technique.

Metal matrix composites with high thermal conductivity and coefficient of thermal expansion are found widespread applications in electronic package and thermal management. The increasing requirement imposed on thermal management materials in microelectronics and semiconductors drives the development of advanced metal matrix composites (MMC) with high thermal conductivity (TC) to effectively dissipate heat and coefficient of thermal expansion (CTE) to minimize thermal stresses. This is of vital importance to enhance the performance, life cycle and reliability of electronic devices. Metal matrix composites with high volume fraction of reinforcement are attractive in view of the possibility to further enhance TC by the use of high TC components and the flexibility to adjust the CTE by controlling the content of reinforcement. Al and Cu were usually used as metal matrix due to their high TCs, and the reinforcements involved SiC, carbon and diamond. On the consideration that the composites produced from the same reinforcement have similar difficulties during fabrication, the composites with high TC were divided into three main categories: SiC/metal, C/metal and diamond/metal composites. Owing to the fact that specific thermal conductivity (thermal conductivity divided by density) of Al-based composites was higher than that of Cu-based composites, Al-based composites are more desirable in avionic applications where light weight is demanded [7].

Thermal studies on composite materials are getting greater importance in the present scenario. Thermal analysis will help to understand the properties of materials as they change with temperature. It is often used as a term for the study of heat transfer through structures. The assessment of thermal parameters of composites will benefit to analyze heat capacity, variation in the intensity of heat, heat diffusion and heat release rate. The main parameter considered in thermal analysis of composites is thermal conductivity. The increase in thermal conductivity of composites will depend on strength and porosity, which finds this property in aerospace and automobile applications extensively. Thermal diffusivity is an important property for materials being used to determine the optimal work temperature in design applications referred under transient heat flow. It is the thermophysical property that determines the speed of heat propagation by conduction during changes in temperature with time. The heat propagation is faster is faster for materials with high thermal diffusivity. Metal Matrix Composites can be customized to provide good CTE matching for thermal management and thermal conductivity applications. It is essential to evaluate new materials for the thermal stability and to measure properties including CTE and thermal conductivity for specialty products [16].

## IV.  Measurement Techniques

Laser Flash technique is highly resourceful for the evaluation of Thermal Conductivity and Diffusivity The sample is positioned on an electronically controlled and programmable robot located in a furnace. The furnace is then held at a predetermined temperature. At this temperature the sample surface is then irradiated with a programmed energy pulse (laser or xenon flash). This energy pulse results in a homogeneous temperature rise at the sample surface. The resulting temperature rise of the rear surface of the sample is measured by a high speed infrared detector and thermal diffusivity values are computed from the temperature rise versus time data. The resulting measuring signal computes the thermal diffusivity, and in most cases the specific heat ($C_p$) data. The Laser Flash technique covers the widest measuring range of all techniques, 0.1 up to 2000 W/mK for Thermal Conductivity and 0.01 up to 1000 $mm^2$/s for Thermal Diffusivity. The used Nd: YAG Laser will have a power output of 25 J/pulse. Both the power and the pulse length can be easily adjusted by the Software. Application areas are electronic packaging, heat sinks, brackets, reactor cooling, heat exchangers, thermal insulators and many others. Trouble-free sample preparation, small required sample dimensions, fast measurement times and high accuracy are only a few of the advantages of this non-contact and non-destructive measurement technique.

The thermal conductivity of metals, alloys or composites with 0,2 ... 100 W/mK can be measured by comparative method with steady state longitudinal heat flow in a temperature range room temperature up to about 1000°C. The comparative instrument measures heat flow based upon the known thermal properties of standard reference materials. The test specimen is sandwiched between two identical reference samples. This stack is placed between two heating elements controlled at different temperatures. A guard heater is placed around the test stack to ensure a constant heat flux through the stack and no lateral heat flow losses.  As heat flows from the hot element to the cold element the temperature gradient across the stack is measured with thermocouples. In a laser flash method, laser fires a pulse at the sample's front surface and the infrared detector measures the temperature rise of the sample's back surface. The software uses literature-based analysis routines to match a theoretical curve to the experimental temperature rise curve. The thermal diffusivity value is the diffusivity value associated with the selected theoretical curve. To determine specific heat, the infrared detector

measures the actual temperature rise of the sample. The response of the infrared detector is calibrated with a reference sample of known specific heat.

Coefficient of Thermal Expansion is one of the most important properties of MMCs. Since nearly all Metal Matrix Composites are used in various temperature ranges, measurement of CTE as a function of temperature is necessary in order to know the behaviour of the material. Several different systems for measurement of CTE can be used depending on the temperature conditions. One of the most common used system is a dilatometer. A dilatometer measures the length or the volume changes of the sample, when the sample follows a temperature program and submits a small force. In a push rod dilatometer the change in length of the sample is detected by an inductive displacement transducer. Calibration and corrections of measurements are done by using various standards and comparison with materials of known expansion. The measurement of the coefficient of thermal expansion (CTE) can be carried out in the temperature range from approximately – 150°C to 1500°C.

## V.  Investigative Review on Hybrid MMC

The investigations of thermal characterization of hybrid metal matrix composites have become a challenging task for the researchers. The thermal characterization on few hybrid composites have been carried out with convincing experimentations and evidences, but unable to emphasize on mainly Al-Gr-SiC composites. Some of the important research works carried out in MMC are mentioned:

L Z Zhao, M J Zhao, X M Cao et al [8] in their research on thermal expansion of hybrid SiC foam-SiC and Al composites have focussed on a new type of hybrid SiC foam–SiC particles–Al composites to be used as an electronic packaging substrate material were fabricated by squeeze casting technique, and their thermal expansion behaviour was evaluated. It was investigated that the measured CTEs are much lower than those of SiC particle-reinforced aluminium (SiC-Al) composites with the same content of SiC because of the characteristic interpenetrating structure of the hybrid composites. A material of such a low CTE is ideal for electronic packaging because of the low thermal mismatch and therefore low thermal stresses between the electronic component and the substrate

S Cem Okumus, Sardar Aslam et al [9] carried out an investigative study on Thermal Expansion and Thermal Conductivity behaviours of Al/Si/SiC hybrid composites clearly highlights that  Aluminium-silicon based hybrid composites reinforced with silicon carbide and graphite particles were prepared by liquid phase particle mixing and squeeze casting. The thermal expansion and thermal conductivity behaviours of hybrid composites with various graphite contents (5.0; 7.5; 10 wt.%) and different silicon carbide particle sizes (45 μm and 53 μm) were investigated. Results indicated that increasing the graphite content improved the dimensional stability, and there was no obvious variation between the thermal expansion behaviours of the 45 μm and the 53 μm silicon carbide reinforced composites. The thermal conductivity of hybrid composites was reduced due to the enrichment of the graphite component Figures 1,2and 3 below depict CTE V/s Temperature which are based on the above observations.
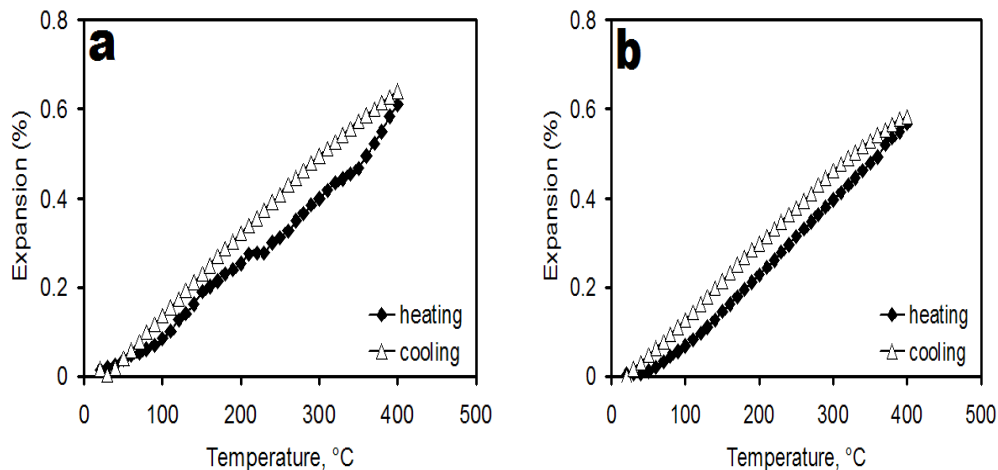


Fig. 1.  Thermal strain response curves recorded during the heating and cooling between 20°C and 400 °C for
  (a) the hybrid Al-Si-20 vol.% SiC (53 μm)/graphite composites, (b)7.5 wt.% graphite and 10 wt.% graphite
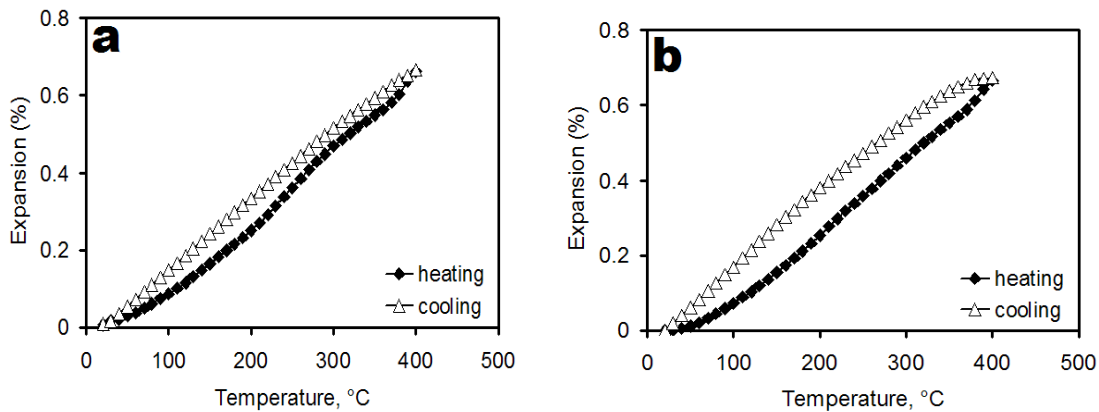
Fig. 2 Thermal strain response curves recorded during the heating and cooling between 20 °C and 400 °C for (a) the hybrid Al-Si-20 vol.% SiC (45 μm)/graphite composites (b)7.5 wt.% graphite and 10 wt.% graphite
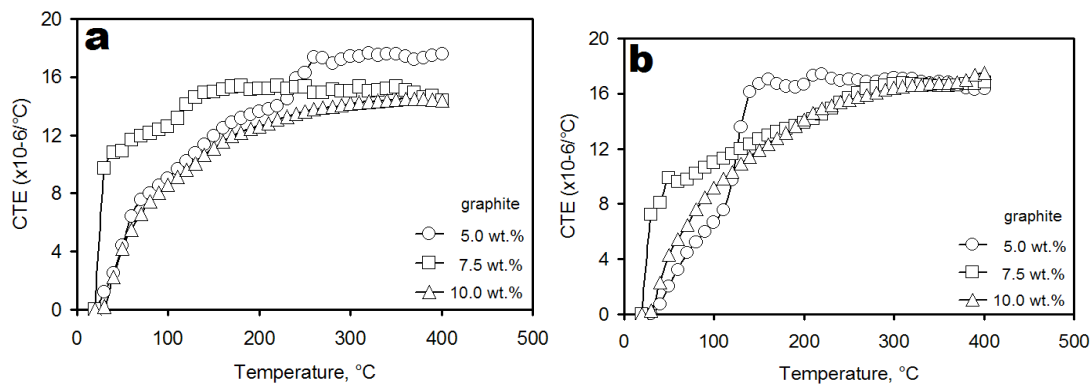


Fig. 3 Coefficient of Thermal Expansion as a function of temperature for (a) Al-Si-20 Vol % SiC (53 μm)/graphite composites (b) Al-Si-20 Vol % SiC (45 μm)/graphite composites

The table 1 shows the thermal conductivity results obtained at different temperatures for SiC reinforced Al-Si based hybrid MMC with various graphite contents. Thermal Conductivity decreases with increasing graphite content. The percentage volume fraction is maintained constant at 20% with variation in weight by considering grain size to be 45 μm and 53 μm.

Table I: Thermal Conductivity values (W/mK) of the Al-Si hybrid composites between 50 °C and 300 °C

| Composite | 50 °C | 100 °C | 150 °C | 200 °C | 250 °C | 300 °C |
|---|---|---|---|---|---|---|
| Al-Si 20 vol.% SiC at 5.0 wt.% graphite (45 μm) | 186.4 | 178.8 | 171.1 | 165.4 | 161.2 | 158.1 |
| Al-Si 20 vol.% SiC at 7.5 wt.% graphite (45 μm) | 181.2 | 173.5` | 157.6 | 148.2` | 138.8 | 130.5 |
| Al-Si 20 vol.% SiC at 10 wt.% graphite (45 μm) | 176.4 | 165.5 | 152.4 | 136.3 | 128.8 | 118.4 |
| Al-Si 20 vol.% SiC at 5.0 wt.% graphite (53 μm) | 202.2 | 195.5 | 188.4 | 171.5 | 168.3 | 158.6 |
| Al-Si 20 vol.% SiC at 7.5 wt.% graphite (53 μm) | 194.8 | 190.4 | 181.1 | 170.5 | 162.1 | 150.8 |
| Al-Si 20 vol.% SiC at 10 wt.% graphite (53 μm) | 185.6 | 175.5 | 166.2 | 155.3 | 146.21 | 136.7 |

Davis L C [10] described that thermal conductivity of metal matrix composites describes the thermal conductivity of metal-matrix composites, which are potential electronic packaging materials, is calculated using

effective medium theory and finite-element techniques. The thermal boundary resistance, which occurs at the interface between the metal and the included phase (typically ceramic particles), has a large effect for small particle sizes. It is found that SiC particles in Al must have radii in excess of 10 μm to obtain the full benefit of the ceramic phase on the thermal conductivity. Bimodal distributions of particle size are considered, since these are often used to fabricate high-volume fraction composites. It is found that if the small particles (in a bimodal distribution) have a radius less than 2.5 μm in SiC/Al their addition reduces the thermal conductivity of the composite.

J M Molina, J Narciso, E Louis et al [11] studied on thermal conductivity of Al-SiC composites demonstrates that the thermal conductivity of aluminium matrix composites having a high volume fraction of SiC particles is investigated by comparing data for composites fabricated by infiltrating liquid aluminium into preforms made either from a single particle size, or by mixing and packing SiC particles of two largely different average sizes (170 and 16 μm). For composites based on powders with a monomodal size distribution, the thermal conductivity increases steadily from 151 W/m K for particles of average diameter 8 μm to 216 W/m K for 170 μm particles. For the bimodal particle mixtures the thermal conductivity increases with increasing volume fraction of coarse particles and reaches a roughly constant value of 220 W/m K for mixtures with 40 or more percentage volume of coarse particles. It is shown that all present data can be accounted for by the differential effective medium (DEM) scheme taking into account a finite interfacial thermal resistance.

J M Molina, M Rheme et al [12] reviewed on thermal conductivity of aluminium matrix composites reinforced with mixtures of diamond and SiC particles is carried out that illustrates that aluminium matrix composites reinforced with mixtures of diamond and SiC particles of equal size were produced by gas pressure-assisted liquid metal infiltration. Replacing SiC gradually by diamond particles results in a steady increase of thermal conductivity from 220 to 580 W m K. Electrical conductivity measurements indicate that the silicon content in the matrix decreases with increasing diamond volume fraction. Predictions of the differential effective medium scheme generalized for multiple types of inclusions agree well with experimental results.

R Arpon, E Louis et al [13] carried out a detailed analysis is also carried out on thermal expansion behaviour of aluminium/SiC composites with bimodal particle distributions where it summarizes that The thermal response and the coefficient of thermal expansion (CTE) of aluminium matrix composites having high volume fractions of SiC particulate have been investigated. The composites were produced by infiltrating liquid aluminium into preforms made either from a single particle size, or by mixing and packing SiC particulate of two largely different average diameters (170 and 16 μm, respectively). The experimental results for composites with a single particle size indicate that the hysteresis in the thermal strain response curves is proportional to the square root of the particle surface area per unit volume of metal matrix, in agreement with current theories. Instead, no simple relationship is found between the hysteresis and any of the system parameters for composites with bimodal particle distributions. On the other hand, the overall CTE is shown to be mainly determined by the composite compactness or total particle volume fraction; neither the particle average size nor the particle size distribution seems to affect the overall CTE. This result is in full agreement with published numerical results obtained from finite element analyses of the effective CTE of aluminium matrix composites. The results also indicate that the CTE varies with particle volume fraction at a pace higher than predicted by theory.

R A Saravanan, J Narciso et al [14] in their investigative approach on thermal expansion behaviour of particulate metal matrix composites explains that Aluminium-matrix composites containing thermally oxidized SiC particles of controlled diameter ranging from 3 to 40 μm have been produced successfully by vacuum assisted high-pressure infiltration. Their thermal-expansion coefficients (CTEs) were measured between 25°C and 500°C with a high-precision thermal mechanical analyser (TMA), and compared with the predictions of various theoretical models. The thermal-expansion behavior of the three-phase Al/SiC/SiO2 composite shows no significant deviation from the predictions of elastic analysis, since the measured CTEs lie within the elastic bounds derived by Schapery's analysis. The effect of particle size is quite evident in the pressure-infiltrated composites: the larger the particles, the greater the thermal expansion of the composite. The observed behavior of these composites is discussed in terms of particle size, silica layer formed during oxidation, and thermal stresses developed as a result of the CTE mismatch between the reinforcement and the matrix.

Parker W J, Jenkins R J, Abbott G L et al [15] carried out a comprehensive study on Flash method of determining Thermal Diffusivity, Heat Capacity and Thermal Conductivity is carried out that lucidly narrates that a flash method of measuring the thermal diffusivity, heat capacity and thermal conductivity is described for the first time. A high-intensity short-duration light pulse is absorbed in the front surface of a thermally insulated specimen a few millimeters thick coated with camphor black, and the resulting temperature history of the rear surface is measured by a thermocouple and recorded with an oscilloscope and camera. The thermal diffusivity is determined by the shape of the temperature versus time curve at the rear surface, the heat capacity by the maximum temperature indicated by the thermocouple, and the thermal conductivity by the product of the heat

capacity, thermal diffusivity and the density. These three thermal properties are determined for copper, silver, iron, nickel, aluminium, tin, zinc, and some alloys at 22°C and 135°C and compared with previously reported values. In another review on metal matrix composites with high thermal conductivity for thermal management applications, it emphasizes that the latest advances in manufacturing process, thermal properties and brazing technology of SiC/metal, carbon/metal and diamond/metal composites were presented. Key factors controlling the thermo-physical properties were discussed in detail. The problems involved in the fabrication and the brazing of these composites were elucidated and the main focus was put on the discussion of the methods to overcome these difficulties. This review shows that the combination of pressure-less infiltration and powder injection molding offers the benefits to produce near-net shape composites [7]

Na Chen, Zhang et al [16] examined the effect of thermal cycling on the expansion behaviour Al/SiC composites is carried out where the coefficient of thermal expansion (CTE) and accumulated plastic strain of the pure aluminium matrix composite containing 50% SiC particles (Al/SiCp) during thermal cycling (within temperature range 298–573 K) were investigated. The composite was produced by infiltrating liquid aluminum into a preform made by SiC particles with an average diameter of 14 microns. Experiment results showed that the relationship between the CTE of Al/SiCp and temperature is nonlinear; CTE could reach a maximum value at about 530 K. The theoretical accumulated plastic strain of Al/SiC composites during thermal cycling has also been calculated and compared with the experimental results.

Tran Nam, Requena et al [17] have emphasized on thermal expansion behaviour of aluminium matrix composites with densely packed SiC particles where The coefficient of thermal expansion (CTE) of Al-based metal matrix composites containing 70 vol.% SiC particles (Al/SiC) has been measured based on the length change from room temperature to 500 °C. In the present work, the instantaneous CTE of Al/SiC is studied by thermo-elastic models and micromechanical simulation using finite element analysis in order to explain abnormalities observed experimentally. The CTE is predicted according to analytical thermo-elastic models of Kerner, Schapery and Turner. The CTE is modelled for heating and cooling cycles from 20 deg C to 500 deg C considering the effects of microscopic voids and phase connectivity. The finite element analysis is based on a two-dimensional unit cell model comparing between generalized plane strain and plane stress formulations. The thermal expansion behaviour is strongly influenced by the presence of voids and confirms qualitatively that they cause the experimentally observed decrease of the Coefficeint of Thermal Expansion above 250 deg C.

The graphical analysis on CTE versus temperature is shown below. The CTE results using GPE formulation during the 2nd heating shows good agreement with the experimental results for the whole temperature range for C1 and up to about 350°C for C2, respectively. The CTE curves of both unit cell models with voids using genaralized plane strain during cooling fall between lower and upper Schapery bound in the whole temperature range and fit to the experiment below 250°C.
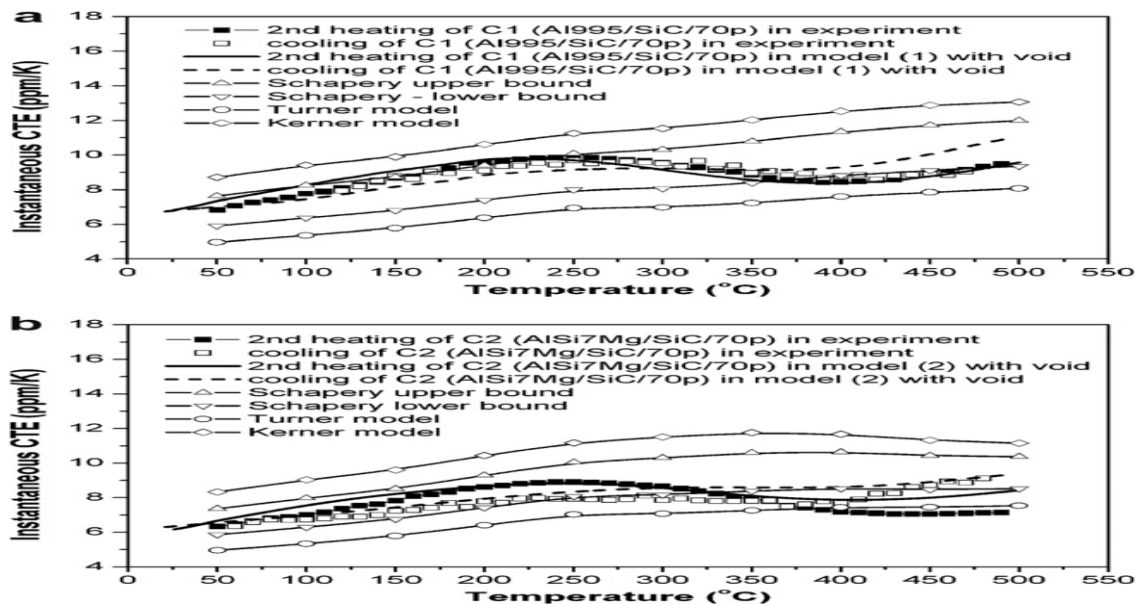


Fig 4: CTE results obtained from thermo-elastic models and unit cell models with voids during heating compared with experimental results of composite C1 and composite C2.

N Chawla, X Deng et al [18] has carried out research on thermal expansion anisotropy in extruded SiC particle reinforced 2080 aluminium alloy matrix composites where Thermal expansion behavior is an important

physical property of metal matrix composites (MMCs). For extruded Al/SiC composites, both the particle volume percent and the orientation relative to the extrusion direction have significant effects on the coefficient of thermal expansion (CTE) of a composite. In this study, the coefficient of thermal expansion of extruded, SiC particle reinforced 2080 Al composites were measured using a thermal mechanical analyzer (TMA). It was found that the anisotropic distribution of SiC particles determines the anisotropic thermal behaviour of Al/SiCp composites. For the same SiC content, the CTE in the short transverse direction (normal to the extrusion axis) is higher than that in the transverse direction, with the longitudinal direction (parallel to the extrusion axis) having the lowest CTE. Finite element modeling (FEM), based on the actual microstructure of Al/SiCp composites, was employed to simulate the thermal behavior. The experimental results for the CTE of the composite correlated very well with those predicted by two-dimensional (2D) numerical models. The FEM results showed that orientation of SiC particles changes the internal stress in the composite, which yields anisotropic thermal behavior. A comparison was made between the experimental results and the FEM model, and these were related to several analytical models.

The graphical analyses are shown that emphasises CTE comparison between experimental results and microstructure based FEM simulation for longitudinal, transverse and short transverse orientations. The FEM results of the current study, as shown in Fig. 5, show the anisotropy of CTE, which is quite similar to the experimental data. At a particular SiC content, the short transverse direction has the largest CTE followed by transverse and then the longitudinal direction.
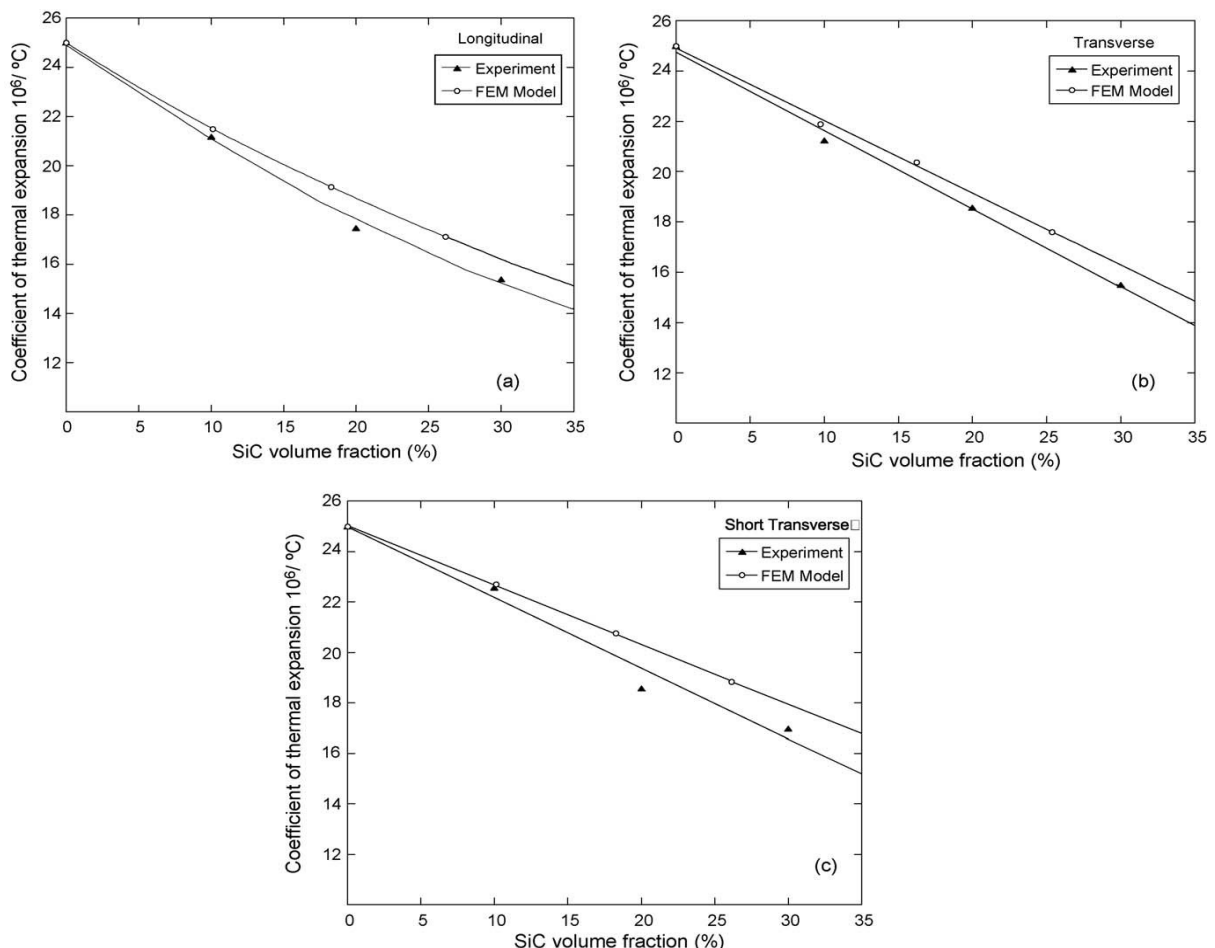


Fig 5: CTE comparison between experimental results and microstructure-based FEM simulation for: (a) longitudinal, (b) transverse, and (c) short transverse orientation. The FEM results are consistent with the experiment, although the predictions are slightly higher.

Zhang, Wu et al [19] scrutinized a study on microstructure and thermal conduction properties of an Al-12 Si matrix composite reinforced with dual sized SiC particles is carried out where it deal with the microstructural characterization and thermal conduction properties of an Al-12Si matrix composite reinforced with 70 vol% SiC particles of two sizes, with an emphasis on the effect of dual sized particles on thermal conductivity. In this work, the SiC particles were a mixture of 20 μm and 60 μm with a weight ratio of 4:1. This gives a particle size

of 23 μm. The SiC particles had a thermal conductivity of 160–180 W/(m·K). The calculated value agrees well with the experimental value, suggesting that the modified EMA with an equivalent particle size was valid in the case of a dual sized particle reinforced composite.
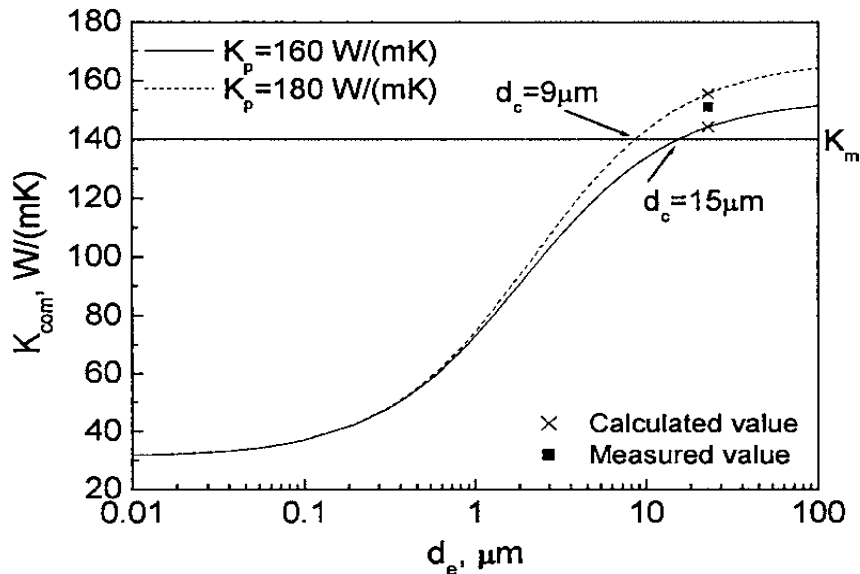


Fig 6: Variation of K of SiC/Al composite with particle size

Weidenfeller, Hofer et al [20] summarized an analysis on thermal conductivity, thermal diffusivity and specific heat capacity of particle filled polypropylene is carried out where Composites samples of polypropylene (PP) with various fillers in different fractions (up to 50 vol%) were prepared with an injection moulding process to study the evolution of the properties as a function of filler content. Standard filler materials like magnetite, barite, talc, copper, strontium ferrite and glass fibres were used. Thermal diffusivities, specific heat capacities and densities of the prepared composite samples were measured, and thermal conductivities were derived. Thermal conductivity of the polypropylene is increased from 0.27 up to 2.5 W/(m K) with 30 vol% talc in the polypropylene matrix. Thermal conductivities of the filled polypropylene samples are compared with the modelled values according to Hashin and Shtrikman. The interconnectivity of the particles in the polypropylene matrix is derived from a comparison between modelled and measured thermal conductivity values.

Hohenauer et al [21] studied on flash methods to examine diffusivity and thermal conductivity of metal foams is conducted where The analysis of the standard uncertainty of thermal conductivity results obtained by a comparative set-up motivated the use of a laser flash device to determine the thermal conductivity of metallic foam materials. In particular a Magnesium alloy is investigated. To meet the requirements of flash techniques coplanar samples are prepared. Therefore the surface near open porosity is filled with a ceramic paste (e.g. SiC). A finite element model is generated to study the influences of the preparation method to the measurement results. This enables to separate the conductivity behaviour of the foam structure from the inhomogeneity effects of the prepared sample.

## VI. Summary

From the above research reviews, it can be noticed that the thermal characterization on hybrid MMC is carried out to limited extent. Expansive studies are to be carried out on different hybrid composites with proper experimentation and validation. In the future investigation, it is proposed to use Aluminium-Silicon Carbide-Graphite Hybrid Composite standard test specimens using thermal analyzer namely Dilatometer, Thermal Conductivity tester or Laser Flash apparatus, Differential Scanning Calorimeter, Modulated Differential Scanning Calorimeter. These specimens have different proportions of reinforcements and while conducting the experiments the parameters are varied to analyze their thermal characterization. The results obtained can be analyzed using Analysis of Variance. Then the significant factors affecting thermal parameters are determined and the thermal parameters are optimized. A mathematical model could be developed involving thermal parameters and the response. The theoretical results can be compared with the experimental results to establish an effective transient thermal analysis. Maximum emphasis is given to the experimentation to carry out thermal analysis for the metal matrix composites. A CFD tool can also be used to carry out the thermal analysis.

In the present scenario, it is pertinent to carry out research work on hybrid composites for their mechanical and thermal characteristics. Limited research has been carried out on Aluminium-Silicon Carbide-

Graphite hybrid composite based on its thermal properties. The Aluminium-Silicon Carbide-Graphite hybrid composites are expected to have excellent thermal property and possess unique behaviour. Thermal analysis of Aluminium-Silicon Carbide-Graphite hybrid composites may help to know its hidden properties and also benefits to clearly comprehend its applications in the fields of Manufacturing, Automotive applications and Thermal Engineering. The investigation may be beneficial for the industries to know about the developments and advanced techniques in the field of composite materials.

The structured reinforced metal matrix composites selected are Silicon Carbide (SiC) and Graphite (Gr) with aluminum as matrix material. This combination is unique and is capable of exhibiting substantial transient characterization behaviour. These reinforced composites possess unique thermal properties and help in exhibiting transient characterization behaviour. The effect of Silicon Carbide and Graphite particulates on the resultant thermal behavior can be expansively investigated and studied The Aluminium-Silicon Carbide-Graphite hybrid composites are expected to have excellent thermal property and possess unique behaviour. Thermal analysis of Aluminium-Silicon Carbide-Graphite hybrid composites may help to know its hidden properties and also benefits to clearly comprehend its applications in the fields of Manufacturing and Thermal Engineering. The present investigation may be beneficial for the industries to know about the developments and advanced techniques in the field of composite materials. They can also acquire complete information about the thermal characterization of hybrid metal matrix composites. The evaluation of thermal parameters requires extensive experimentation, which is both expensive and time consuming. Experimentation should be carried out in a systematic way so as to get reliable results with minimum, cost and time.

## REFERENCES

[1]     "Introduction to composites", Composites ASM Hand Book, Vol 21, May 2002.
[2]     N. R. Habbu "Use of Aluminium Silicon Alloys in Automobile Application" proceedings of one day Industry Institute Interactive Meet on Al-Si alloys, Development and Application for transport sector, IISC Bangalore, September 2000.
[3]     S.S. Joshi, N. Ramakrishnan & P. Ramakrishnan, "Micro Structural Analysis of Chip Formation during Orthogonal Machining of Al/ SiCp Composites" Journal of Engg. Metals Technology, July 2001, Volume 123, pp 315 – 321.
[4]     David E Alman, "Properties of Metal Matrix Composites", Composites-ASM International, May 2002, ASM Hand Book.
[5]     G Korb, E Neubauer, Thermophysical Properties of Metal Matrix Composites, MMC- Assess Thematic Network.
[6]     J. Zhang, R.J. Perez, E.J. Lavernia, "Effect of SiC and graphite particulates on the damping behavior of metal matrix composites", Volume 42, Issue 2, pp 395-409, February 1994.
[7]     Xuan-hui Qu, Lin Zhang, Mao Wu, Shu-bin Ren, "Review of metal matrix composites with high thermal conductivity for thermal management applications", State Key Laboratory for Advanced Metals and Materials, Beijing Key Laboratory for Powder Metallurgy and Particulate Materials, University of Science and Technology Beijing, Beijing 100083, China
[8]     L Z Zhao, M J Zhao, X M Cao et al, "Thermal Expansion of a novel hybrid SiC foam-SiC particles-Al composites", Volume 67, Issues 15-16, December 2007, Pages 3404-3408.
[9]     S Cem Okumus, Sardar Aslam et al, "Thermal Expansion and Thermal Conductivity Behaviors of Al-Si/SiC/graphite Hybrid Metal Matrix Composites (MMCs)", Volume 18, No 4 (2012).
[10]    Davis L C, "Thermal Conductivity of Metal Matrix Composites", Journal of Applied Physics, Volume 77, Issue 10.
[11]    J M Molina, J Narciso, E Louis et al, "Thermal conductivity of Al–SiC composites with monomodal and bimodal particle size distribution", Volume 480, Issues 1-2, 15 May 2008, Pages 483-499.
[12]    J M Molina, M Rheme et al, "Thermal conductivity of aluminum matrix composites reinforced with mixtures of diamond and SiC particles", Volume 58, Issue 5, March 2008, Pages 393-398.
[13]    R Arpon, E Louis et al, "Thermal expansion behaviour of aluminium/SiC composites with bimodal particle distributions", Volume 51, Issue 11, 27 June 2003, Pages 3145-3156.
[14]    R A Saravanan, J Narciso et al, "Thermal expansion studies on aluminium-matrix composites with different reinforcement architecture of SiC particles" Volume 51, Issue 11, 27 June 2003, Pages 3145-3156.
[15]    Parker W J, Jenkins R J, Abbott G L et al, "Flash method of determining Thermal Diffusivity, Heat Capacity and Thermal Conductivity", Journal of Applied Physics, Volume 31, Issue 9.
[16]    Na Chen, Zhang et al, "Effect of Thermal cycling on the expansion behaviour of Al/SiC composites", Journal of Materials Processing Technology 2009, 1471-1476,
[17]    Tran Nam, Requena et al, "Thermal expansion behaviour of aluminium matrix composites with densely packed SiC particles", Applied Science and manufacturing, Part A 39 (2009) 856-865.
[18]    N Chawla, X Deng et al, "Thermal expansion anisotropy in extruded SiC particle reinforced 2080 aluminium alloy matrix composites", Material Science and Engineering, A 426 (2006) 314-322.
[19]    Zhang, Wu et al, "Microstructure and thermal conduction properties of an Al-12 Si matrix composite reinforced with dual sized SiC particles", Journal of Materials Science, 2004, 303-305, Volume 39.
[20]    Weidenfeller, Hofer et al, "Thermal conductivity, thermal diffusivity and specific heat capacity of particle filled polypropylene", Applied Science and Manufacturing, Part A 35 (2004), 423-429.
[21]    Hohenauer et al, "Flash methods to examine diffusivity and thermal conductivity of metal foams", Pittsburg, 2009.

# Experimental Investigation of Performance and Emission Characteristics of Simarouba Biodiesel and Its Blends on LHR Engine

Vishwanath Kasturi[1],  M. C. Navindgi[2]

(*[1]PG Student, Thermal Power Engineering PDACE Gulbarga, Karnataka, India*)
(*[2]Associate professor, Dept of Mechanical Engineering PDACE Gulbarga, Karnataka, India*)

**Abstract:** *Diesel is a fossil fuel that is getting depleted at a fast rate. So an alternative fuel is necessary and a need of the hour. simarouba oil, which is cultivated in India at large scales, has a high potential to become an alternative fuel to replace diesel fuel. Direct use of simarouba oil cannot be done, as its viscosity is more than the diesel fuel, and hence affects the combustion characteristics. The simarouba oil is esterified to reduce the viscosity and it is blended with diesel on volume basis in different proportions. The use of thermal barrier coatings (TBCs) to increase the combustion temperature in diesel engines has been pursued for over 20 years. Increased combustion temperature can increase the efficiency of the engine, decrease. However, TBCs have not yet met with wide success in diesel engine applications because of various problems associated with the thermo-mechanical properties of the coating materials. Although, the in-cylinder temperatures that can be achieved by the application of ceramic coatings can be as high as 850-9000C compared to current temperatures of 650-7000C. The increase in the in-cylinder temperatures helped in better release of energy in the case of biodiesel fuels thereby reducing emissions at, almost the same performance as the diesel fuel. Here the effort has been made to determine the performance and emission characteristics of SOME blend with diesel in conventional engine and LHR engine.*

**Keywords*:** *LHR Engine, normal engine Biodiesel, Simarouba oil, SOME, Performance and Emission Characteristics. Thermal barrier coating.*

## I.  Introduction

Petroleum based fuels play a vital role in rapid depletion of conventional energy sources along with increasing demand and also major contributors of air pollutants. Major portion of today's energy demand in India is being met with fossil fuels. Hence it is high time that alternate fuels for engines should be derived from indigenous sources. As India is an agricultural country, there is a wide scope for the production of vegetable oils (both edible and non-edible) from different oil seeds. The present work focused only on non-edible oils as fuel for engines, as the edible oils are in great demand and far too expensive. The past work revealed that uses of vegetable oils for engines in place of diesel were investigated. Though the concerned researchers recommended the use of vegetable oils in diesel engines, there was no evidence of any practical vegetable oil source engines.

It is known that the efficiency of internal combustion diesel engines changes 38-42%. It is about 60% of the fuel energy dismissed from combustion chamber. To save energy, combustion chamber component are coated with low thermal conduction materials. The effect of thermal barrier coating on the cylinder components like piston crown top, cylinder liner, cylinder head inside and valves. The thermal barrier coated engines are otherwise known as low heat rejection (LHR) engines. Due to the insulation of the cylinder wall the heat transfer through the cylinder walls to the cooling system is reduced which change the combustion characteristics of the diesel engine. To know the changes during combustion the steady-state LHR engines operation have been studied by applying either the first or second law of thermodynamics. The state of the art of the thermal barrier coating is the yattria stabilized zirconia. In addition, other material systems have been investigated for the next generation of TBC. The study also focuses on coating method for Yattria Stabilized Zirconia (YSZ) to improve coating under high load and temperature cyclical conditions encountered in the real engine. The effect of insulation on engine performance, heat transfer characteristics, combustion and emission characteristics are studied and compared with standard (STD) diesel engine

## II.  Materials and Methods

The extraction of biodiesel is carried out by base catalyzed transesterification method.

**2.1. Process of Extracting**



Fig 2.1: The flow chart for biodiesel production

To a one liter of raw Simaroauba oil is heated up to $70^0$C. 300 ml of methanol & 5-7gms of NaOH (catalyst) is added and the mixture is maintained at 65-70$^0$C is about 1½ hours and stirred continuously. The mixture is allowed to settle for 20-30 min until the formation of biodiesel and glycerin layers. The glycerin is removed from the bio-diesel in a separating funnel. The bio diesel produced from Simarouba oil is ready to use.

**2.2. Transesterification**

It is most commonly used and important method to reduce the viscosity of vegetable oils. In this process triglyceride reacts with three molecules of alcohol in the presence of a catalyst producing a mixture of fatty acids, alkyl ester and glycerol. The process of removal of all the glycerol and the fatty acids from the vegetable oil in the presence of a catalyst is called esterification.

```
CH2COOR1                                    CH2OH          R1COOR
|                                           |              |
CHCOOR2                                     CHOH           R1COOR
|            +    3ROH    ⟷                 |        +     |
CH2COOR3                 Catalyst           CH2OH          R1COOR
                         (NaOH)

Cottonseed Glyceride     Alcohol            Glycerin       Biodiesel
```

Chemical reaction

Physical and chemical properties are more improved in esterified vegetable oil because esterified vegetable oil contains more cetane number than diesel fuel. These parameters induce good combustion characteristics in vegetable oil esters. So unburnt hydrocarbon level is decreased in the exhaust. It results in lower generation of hydrocarbon and carbon monoxide in the exhaust than diesel fuel. The vegetable oil esters contain more oxygen and lower calorific value than diesel. So, it enhances the combustion process and generates lower nitric oxide formation in the exhaust than diesel fuel.

### III.   Properties of Diesel and Some Blends

After transesterification the properties of Simarouba oil blends was determined. It was found that the properties of Simarouba oil blends were similar to diesel. Simarouba oil blends were similar to diesel.

Table 3.1: Properties of Simarouba oil blends

| Properties | Diesel | S20 | S40 | S100 |
|---|---|---|---|---|
| Kinematic viscosity at 40$_0$C (Cst) | 2.54 | 3.104 | 3.891 | 5.6 |
| Calorific value (kJ/Kg) | 42500 | 42270 | 41949 | 37933 |
| Density (kg/m$_3$) | 840 | 838 | 846 | 875 |
| Flash Point ($^o$C) | 54 | 79 | 98 | 165 |
| Fire Point ($^o$C) | 64 | 89 | 110 | 185 |

## IV.   Experimental Setup

The experimental setup enables study performance, combustion and emission characteristics. The experiments have been carried out on a DI compression ignition engine for various blends of simarouba oil with diesel (S20, S40, S60, S80, and S100) with varying brake power. The experiment is carried out at constant compression ratio of 17.5:1 and constant injection pressure of 200 bar by varying brake power.



Fig 4.1: Photograph of engine setup

Table 4.1: Engine specifications

| Manufacturer | Kirloskar oil engines Ltd, India |
|---|---|
| Model | TV-SR, naturally aspirated |
| Engine | Single cylinder, DI |
| Bore/stroke | 87.5mm/110mm |
| Compression Ratio | 17.5:1 |
| speed | 1500r/min, constant |
| Rated power | 5.2kw |
| Working cycle | 4 stroke |
| Injection pressure | 200bar/23 def TDC |
| Type of sensor | Piezo electric |
| Response time | 4 micro seconds |

## V.   Result and Discussion

After detail study of performance and emission characteristics of simarouba biodiesel and its blends in normal engine and low heat rejection engine it can be seen that 20% simarouba biodiesel blend and diesel are having same almost same characteristics so here the comparative analysis is carried out between normal engine and LHR engine.

### 5.1  Performance characteristics
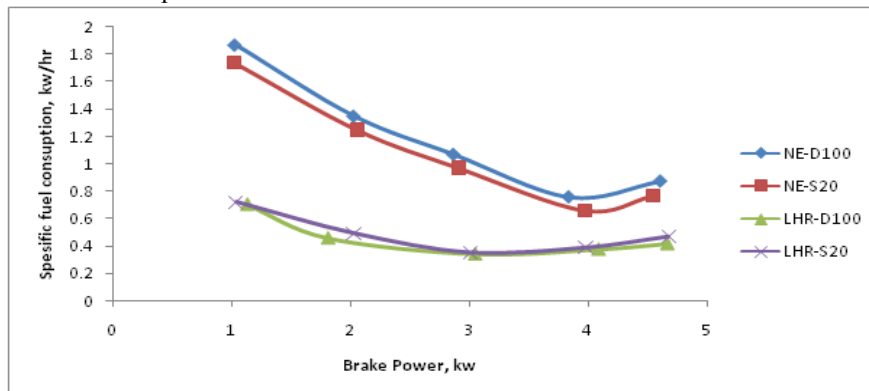
5.1.1     Specific fuel consumption



Fig 5.1  The variation of the specific fuel consumption with brake power for diesel and simarouba blends

Fig 5.1 shows the specific fuel consumption for simarouba biodiesel and its blends with respect to brake power for both normal engine and LHR engine. At maximum load the specific fuel consumption of LHR engine fuelled with biodiesel is higher than LHR engine fuelled with diesel and lower than normal engine fuelled with diesel and biodiesel. This higher fuel consumption was due to the combined effect of lower calorific value and high density of biodiesel. The test engine consumed additional biodiesel fuel in order to retain the same power output. Because the reason is heat leakage in engine cylinder is developed therefore the amount of fuel required to generate 1kw of  power compare to without LHR.

### 5.1.2 Air fuel ratio
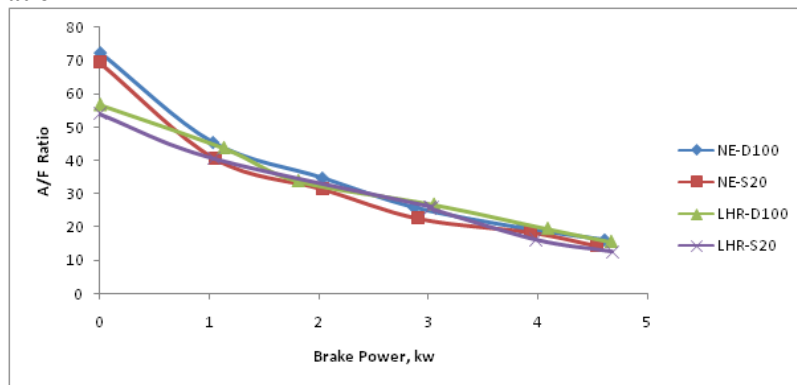


Fig 5.2  The variation of the air fuel ratio with brake power for diesel and simarouba blends

The variation of air fuel ratio for diesel and 20% SOME blend is shown in fig 5. 2 for both normal engine and LHR engine. Fuel consumption is higher in case of LHR engine due to increased temperature and completes combustion. Air fuel ratio decreases with increase in load because air fuel mixing process is affected by the difficulty in atomization of biodiesel due to its higher viscosity.

### 5.1.3 Brake thermal efficiency
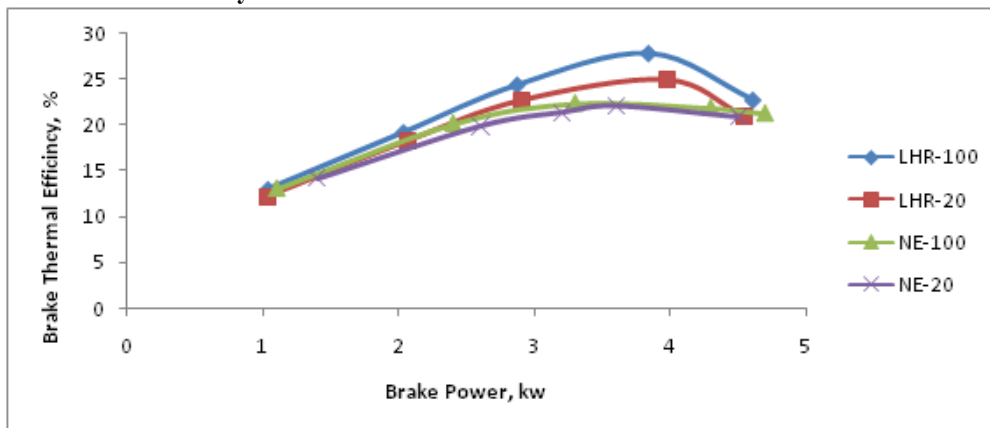


Fig 5.3  The variation of the brake thermal efficiency  with brake power for diesel and simarouba blends

The variation of the brake thermal efficiency with load for diesel and SOME blends are shown in figure 5.3. We can observe that S20 with LHR has higher brake thermal efficiency than normal engine D100 this is because of increased combustion rate which provides complete burning of fuel and due to low heat rejection. The thermal efficiency of S20 is lower than diesel because the reason is large difference in viscosity, specific gravity and volatility.

### 5.1.4 Exhaust gas emission
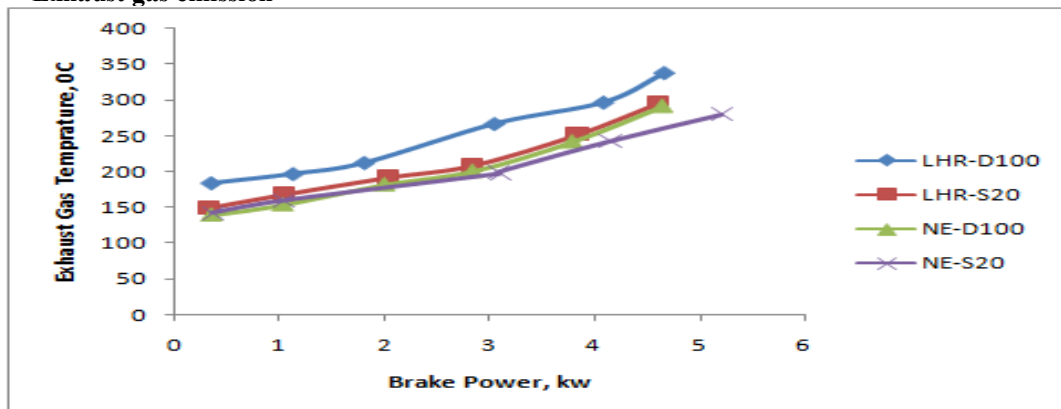


Fig 5.4  The variation of the exhaust gas temperature  with brake power for diesel and simarouba blends

The variation of the exhaust gas temperature with load for diesel and SOME blends are shown in figure 5.4. When bio fuel concentration increases the exhaust temperature increase. The same also when load increases the exhaust temperature increases. Because the reason is the heat release rate by the biodiesel during the expansion is comparatively lower than diesel.

## 5.2    Emission characteristics
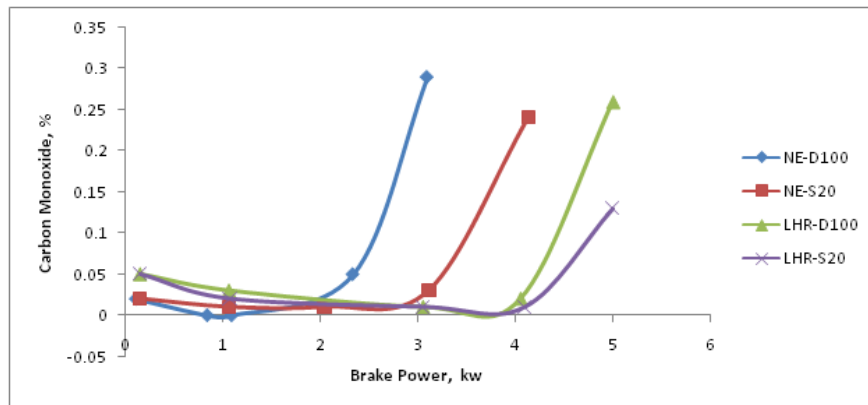
### 5.2.1  Carbon  monoxide



Fig 5.5 The variation of the carbon monoxide  with brake power for diesel and simarouba blends

The variation of carbon monoxide (CO) with engine power output is presented in figure 5.5. The fuels are producing higher amount of carbon monoxide emission at low power outputs and giving lower values at higher power conditions. Carbon monoxide emission decreases with increasing power output. With increasing biodiesel the 20% CO emission level decreases. Biodiesel itself has about 11 % oxygen content in it and it may helps for the complete combustion. Hence, CO emission level decreases with increasing biodiesel percentage in the fuel.

### 5.2.2  Hydro carbon
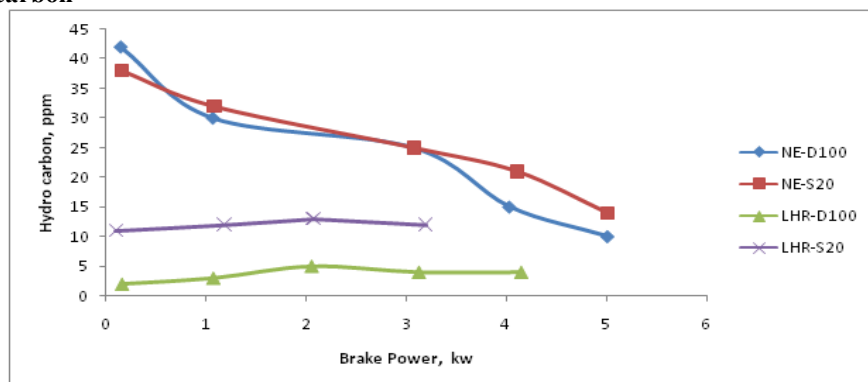


Fig 5.6  The variation of the hydro carbon  with brake power for diesel and semarouba blends

The variation of hydrocarbon (HC) with respect to engine power output for different fuels are shown in figure 5.6. The high operating temperature in LHR engine makes the combustion nearly complete than the limited operating temperature condition as in the case of diesel engine. All full load hydrocarbon emission levels are decreases for LHR engine fueled with biodiesel than LHR engine fueled with diesel and diesel engine fueled with diesel. The air fuel mixture, which was accumulated in the crevice volume, was reduced due to the high temperature and availability of oxygen, which in turn leads to reduction in unburned hydrocarbon emissions.

**5.2.3 Nitrogen oxide**
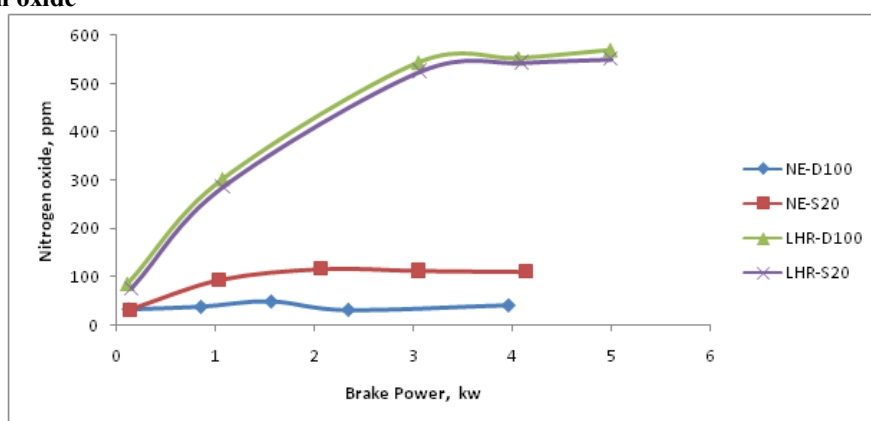


Fig 5.7 The variation of the nitrogen oxide with brake power for diesel and semarouba blends

Figure 5.7 shows the variation of oxides of nitrogen with engine power output. The main reason for the formation of oxides of nitrogen in an IC engines are high temperature and availability of oxygen. At maximum load, NOx emission for LHR engine with biodiesel fuel is higher. In LHR engine, the operating conditions are in favor of NO species and such as the availability of oxygen in the fuel itself other than the oxygen available in the air and high temperature due to insulation coating, which enhance the NO species formation.

## VI. Conclusion

- As detail study of performance characteristics of simarouba biodiesel and its blends on normal engine we can observe that 20% blend of simarouba biodiesel in diesel fuel has almost same mechanical efficiency, same specific fuel consumption.
- We can also see that there is slight increase in brake thermal efficiency which is a positive sign with this blend.. So we can conclude that without any modification in engine we can save diesel fuel for certain extent without any compromise with standard performance characteristics and in future semarouba biodiesel can be a best alternative fuel which can replace the diesel.
- As same parameters studied with engine modification, here we observed that there is increase in performance parameters than normal engine. There is increase in parameters like brake thermal efficiency, mechanical efficiency and there is decrease in specific fuel consumption and fuel consumption which can be observed in comparative graph.
- By studying performance characteristics on normal engine and low heat rejection engine, it can concluded that with 20% blend we can achieve same characteristics as that of diesel fuel so S20 is the best blend and in future simarouba methyl ester can be a best and most suitable alternative fuel which can replace diesel fuel for years to come and with thermal barrier coating we can meet needy requirements.
- Simarouba biodiesel shows lower heat release rate during premixed burning phase compared to diesel. The high viscosity and poor volatility of NE-D100 result in poor atomization and fuel air mixing rates. Heat release rate is more in LHR-S20 compared to LHR-D100 and heat release rate in NE-D100 and NE-S20 are almost similar.
- We can conclude that the S20 with LHR shows same graphs as compared to D100 this blend is best suitable for an engine.
- It was found that, CO and HC emissions for LHR engine with biodiesel was considerably lower than LHR engine fueled with diesel. This reduction of emissions due to excess oxygen availability along with higher operating temperature.
- NO emission for LHR engine with biodiesel fuel was higher than LHR engine fueled with diesel. The operating conditions of LHR engine were favorable to NO formation. However this increase in emission level was within the acceptable limits.

## REFERENCES

[1]     Murthy P.V.K , Murali Krishna M.V.S , Sitarama Raju A, Vara Prasad C.M. Srinivasulu N.V.  *Performance evaluation of low heat rejection diesel engine with pure diesel. international journal of applied engineering research, dindigul volume 1, No 3, 2010*

[2]     Sivanathan Sivalaxmi and Thangavel Baluswamy. *Experimental investigation on a diesel engine fueled with neem oil and its methyl ester, thermal science, year 2011, Vol. 15, No. 4, Pp. 1193-1204.*

[3]     Lovekush Prasad1, Dr. Alka Agrawal, *Experimental investigation of performance of diesel engine working on diesel and neem oil blends, iosr journal of mechanical and civil engineering (IOSRJMCE) ISSN : 2278-1684 Volume 1, Issue 4 (July-August 2012), PP 48-51.*

[4]     K.Dilip Kumar1 P.Ravindra Kumar. *Experimental investigation of cotton seed oil and neem methyl esters as biodiesel on CI engine. international journal of modern engineering research (IJMER) Vol.2, Issue.4, July-Aug 2012 pp-1741-1746 ISSN: 2249-6645*

[5]     K. Arun Balasubramanian, *Dual Biodiesel Blends in Diesel Engine - Performance and Emission Analysis, European Journal of Scientific ResearchISSN 1450-216X Vol.75 No.3 (2012), pp. 400-408.*

[6]     Ashish Jawalkar1 et.al.  *Performance and emission characteristics of mahua and linseed biodiesel operated at varying injection pressures on ci engine, international journal of modern engineering research (IJMER) www.ijmer.com Vol.2, Issue.3, May-June 2012 pp-1142-1149 ISSN: 2249-6645.*

[7]     B.K.Venkanna, C.Venkataramana Reddy. *Performance, emission and combustion characteristics of direct injection diesel engine running on calophyllum inophyllum linn oil (honne oil) Int J Agric & Biol Eng Vol. 4 March, 2011.*

[8]     M. C. Navindgi et.al.  *Influence of injection pressure, injection timing and compression ratio on performance, combustion and emission of diesel engine using castor methyl ester blends. International Journal of Engineering Science and Technology (IJEST).*

[9]     Elango T et.al. *Effect of methyl esters of neem and diesel oil blends on the combustion and emission characteristics of a CI engine. Vol. 5, No. 10, October 2010 ISSN 1819-6608 Arpn Journal Of Engineering And Applied Sciences.*

# Heavy Mineral Studies of Beach Sands of Vagathor, North Goa, India

A. Sreenivasa[1], H. M. Jayasheela[2], P. Bejugam[3], A. R. Gujar (NIO)[4]

[1,2,3,4,] *Department of Geology, Karnatak University, Dharwad 580 003, India*

**Abstract:** *Vagator beach is situated 22 km away from panjim on the northern side Bardez taluk approachable via Candolim are Mapusa by road. The beach is projected on both the sides by promontories. The beach is in arcuate shape, the area included with survey of India toposheet No 48/E/14 which is bounded by latitudes 15º35'N 15º38'N and longitude 78º43'E. The Chapora river and its tributaries drain the entire region that is the Vagator beach. It flows from North-East to South-West direction. The drainage pattern is structurally controlled; the Chapora River has its source in the Ramghat hills of Belgaum district in Karnataka then it flows through the Thilari ghat and enters Goa. Its length in Goa is about 31 km and the mouth of the river bank, mud bank and mangroves swamps are common.*

*In laboratory techniques heavy mineral separation are based mass separation in a liquid with specific gravity and magnetic separation using hand magnet and Frantz isodynamic separator at different volts. X-ray analysis was carried out by using RIGAKU ALTIMA IV copper target on the basis of Bragg's law. The non magnetic sand grains was observed under optical microscope to identify diagnostic properties of minerals.*

*The heavy mineral shoot comprises of opaque (magnetite and illmenite) and transparent heavy minerals like hornblende, epidote, garnet, rutile, zircon, enstatite and minor amounts of tourmaline. The light minerals are mainly quartz and feldspars. The magnetite concentration ranges between 2.01 to 56.86% and Ilmenite between 2.83 to 41.04% and non mangnetics between 1.18 to 44.81%. X ray diffraction studies and SEM (Scanning electron microscope) studies were employed to study the mineralogical composition of beach sands of Vagator and detailed investigations are dealt in the paper.*

## I. Introduction

Throughout the human history, oceans have serve as a source of food and valuable minerals helps in trade and commerce. Beaches are interfaces of oceans and land, dynamic landforms altered continuously by wind and waves undergo creation and erosion. Beach formation begins with the accumulation of eroded continental material like sand, gravel and cobble fragments. River and stream action process result the deposition. Most of the sediments is suspended in sea water and transported along the coast by the long shore current. A stream of water flowing parallel to the beach that is created by the action of waves breaking at an angle to shore

A beach is a geological land form along the shoreline of an ocean usually consists of loose particle often composed of rock such as sand, gravel, shingle, pebbles, cobblestones among them are economically important heavy mineral placers. Most of the placers are exploited as commercial use and these deposits have been formed by mechanical concentration of detrital mineral particles in subaqueous environments. The term beach may refer to small system the rock material moves onshore, offshore or along the shore by forces of waves and currents or geological units of considerable size. These geomorphic features composed of beach profile, it can changes in wave energy experienced during seasonal variations. The drift line is one of the potential demarcations which significant wind movement of sand occur and move inland under assault by storm waves. The shape of the beach depends on whether constructive or destructive may be sand or shingle. The present study of Vagator beach situated along southern part of Chapora river mouth contains appreciable quantities of heavy mineral sand with high specific gravity.

## II.   The Aim Of The Study Is To Investigate

1. To determine the grain size characters, Mineralogy and grain morphology to understand the environment of deposition and the nature of sediments in the area.
2. To quantify the various mineral components with special emphasis on heavy mineral content.
3. To estimate the heavy mineral resources of the area.
4. To decipher the source of these minerals through mineralogy and transportation history of surficial textures.

The Chapora river and its tributaries drain the entire region of the Vagator beach. It flows east to south direction. The drainage is well developed and structurally controlled and the length of the river in about  in Goa is 31 km running  through Pernem and Bardez talukas of North Goa, at the estuary of Vagator beach in the Morjim village. At the mouth of the river bank mud banks and mangroves swamps are common (Iyer and Wagle, 1987).

Goa is dominantly covered by the rocks of the Goa group belongs to the Dharwar super group of Archean – proterozoic age, except a narrow strip along the north eastern  corner occupied by the Deccan traps of Upper cretaceous  to lower Eocene age. The Goa group consisting of green schist facies of metamorphic rocks and divided into the Barcem formation, Sanvordem formation, Bicholim – Rivona formation comprises basic and acid metavolcanics associated with Meta – tuffs of Meta sediments. The Sanvordem formation made up of meta-greywacke, tilloids and argillites, the Bicholim – Rivona formation representing metapyroclasts and tuffs with calcareous, manganiferrous and ferruginous chemical precipitates. The Vageri formations consist of meta greywacke and meta basalts. The early Proterozoic included acid and basic intrusive, the Goa group of rocks have been intruded by granite, felpathic gneiss, hornblende granite and basic intrusive and over laid by Deccan traps represented by massive and vesicular metabasalt in the north eastern corner of the area.
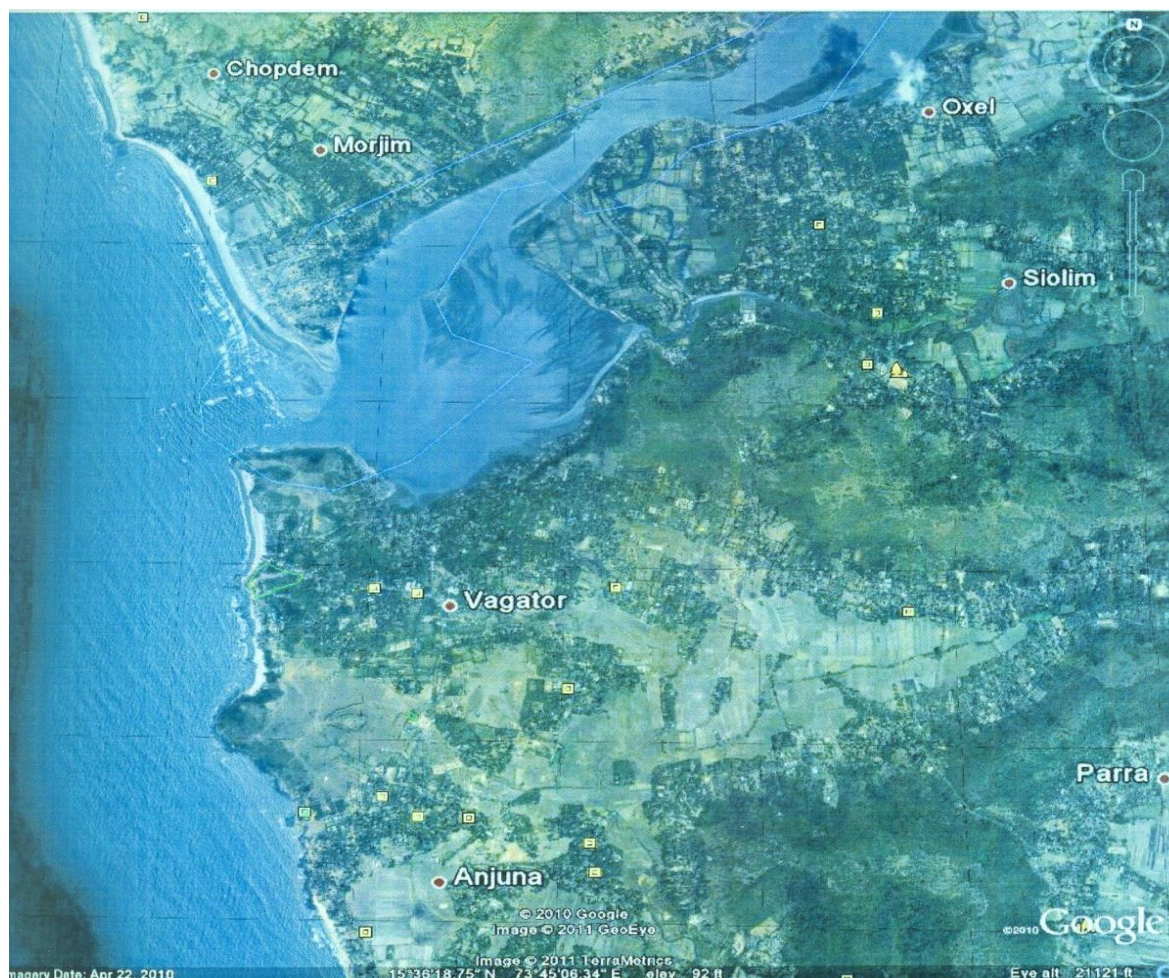


Fig.1 Satellite imagery of study area, Chapora-Vagator, Goa

| | | | |
|---|---|---|---|
| Sub-recent to recent | | | Sea sand, alluvium, laterite |
| Sub cretaceous to lower Eocene | | Deccan Trap | Basalt |
| Proterozoic | | Basic Intrusive | Dolerite, Gabbro |
| | | Acidic Intrusive | Pegmatite vein, Quartz, Porphyritic Granite, Hornblende Granite, Felspathic Granite, Granite Gneiss |
| ARCHEAN TO PROTEROZOIC | DHARWAR SUPER GROUP | GOA GROUP | Vageri Formation | Metabasalt, Metagreywacke. |
| | | | Bicholim Formation | Banded ferruginous Quartzite, Manganiferous Chert, Breccias with Pink ferruginous Phyllite, Limestone, Pink ferruginous phyllite, Quartz-Chlorite-Amphibolite schist |
| | | | Sanvordem Formation | Argillite, Quartzite, Tilloid Metagreywacke. |
| | | | Barcem Formation | Metagabbro, Peridotite, Talc – chlorite schist, Variegated phyllite, Quartz – chlorite schist, Red phyllite, Quartz porphyry, Massive Schistose and Vesicular & Metabasalt. |
| (>3000 Ma) | Basement Trondhjemite Gneiss | | |

**Table.No.2. Chronostratigraphic sequence of Goa**

## III.   Heavy Mineral Studies

Heavy minerals or placers are mineral deposits have been formed by the mechanical concentration of detrital mineral particles in subaqueous environments, occurs at river banks, lakes and ocean floor. They usually originate from primary igneous or vein minerals which are liberated from the breakdown of their parent rocks. Most of the placers are high specific gravity grater then 2.85 and are resistant to chemical breakdown otherwise they would not have survived the erosion, transportation and depositional processes that took place prior to their concentration. Important placer minerals include elements in their native state such as gold, platinum, and diamond and resistant minerals are cassiterite, ilmenite, rutile, zircon, monazite, garnet, magnetite and corundum (Dunham, 1969).
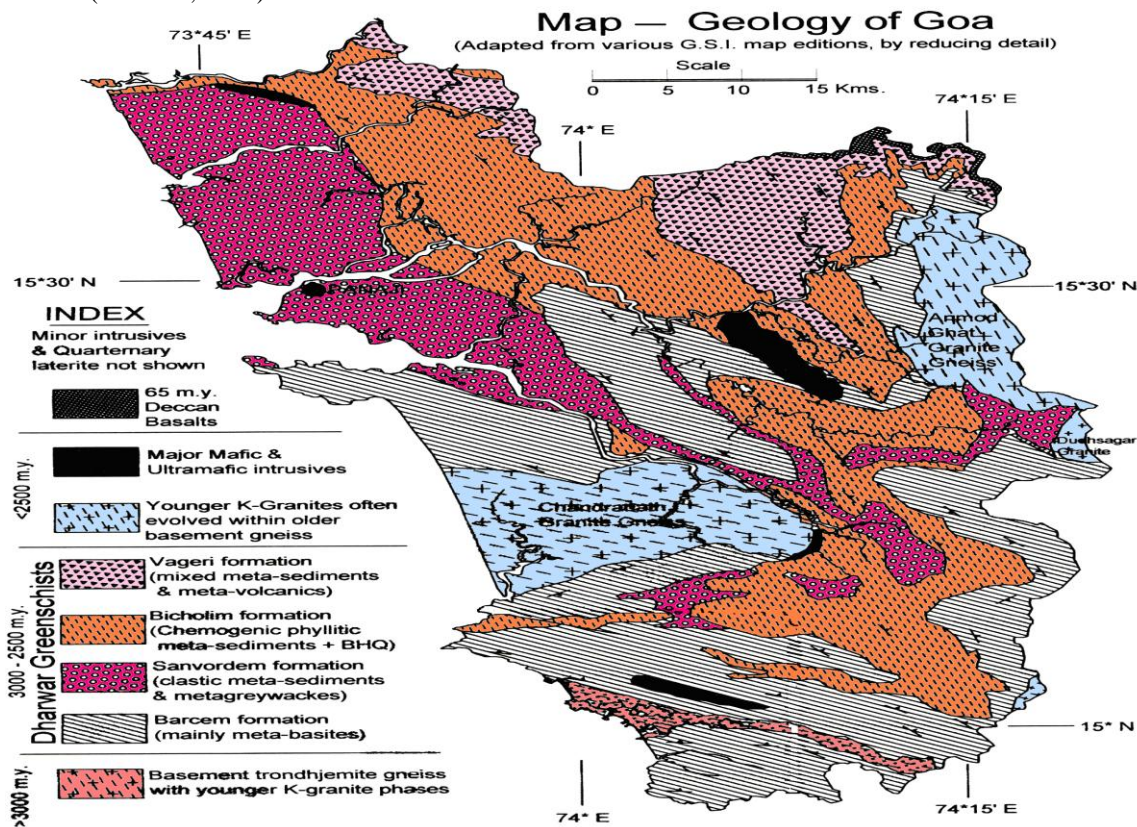
Despite their small amount of great value in studying provenance, transportation and weathering history of a sediment in correlation with paleosediment studies. They represent the accessory and varietal minerals of igneous and metamorphic rocks which are reduced in quantity as they passed into sediments because they are chemically unstable, considerably softer than quartz. The heavy minerals as a sediment is function of various factors like lithology of the region, stability of minerals during movement from the source rock. The Movement of heavy minerals from one place to another place along its course is dependent hydraulic factor, specific gravity, the amount of distance travelled from the source rock. During its movement the distribution of heavy mineral may lead to change in mineral ratio of the deposition is depending on the velocity of the water.

The concentration of heavy mineral occurs in river banks, beaches, offshore areas and river draining areas, the energy level in the river drops to allow the placers to settle. The formation of placer mineral deposits on beaches results essentially form the selective sorting of the intertidal zone by wave current action with the velocity of the backwash is sufficient to remove the light mineral and leave the heavy minerals. According to (Emery and Noakes 1968) modern beaches probably represent the optimum conditions of light and heavy minerals.

In the present studies using laboratory techniques for heavy mineral separation are based on mass separation in a liquid with specific gravity between the specific gravity of the light and heavy minerals. It is based on the principal of gravity settling and bromoform is used with a specific gravity of 2.89. The other heavy liquids are tetrabromoethane, methylene iodide and clerici solution. The sample is washed, treated with HCL and sieved accurately into three size fractions. Each sample is poured into a separating funnel which contains bromoform. The heavy minerals settle to the bottom while the lighter ones float, they collected separately on a filter paper, (Rubbey 1933) showed that the grains of heavy minerals are hydraulically equivalent to light mineral grains of some larger size depending upon the specific gravity of the heavy minerals and heavy mineral suits therefore vary in composition with grain size of the sample.

## IV. Methodology

- The heavy minerals were separated using bromoform at Sp.Gr 2.89 using procedure (Milner 1962) each fraction of sample along with bromoform was pored in to a separating funnel. After the heavy and light mineral separated the sediment was released by opening the cock of the funnel in to filter paper (Whatman .1).
- The sample was washed with methanol and kept for air drying, weighed and the percentage were tabulated.
- Separated heavy minerals were subjected to magnetic separation using hand magnet and Frantz isodynamic separator.
- Magnetite was first separated with a hand magnet and the strongly magnetic minerals were separated first, later the remaining magnetite was separated by isodynamic separator at 0.05 volts.
- The ilmenite is later separated at 0.22 volts. The amperage as given by Rosenblum (1958) and (1959). The separated ilmenite and magnetite weighed their percentage were calculated.
- The separated fractions of ilmenite and magnetite were confirmed by X-Ray diffraction method.

## V. X-Ray Analysis

X-ray analysis of the samples was carried out by using RIGAKU ALTIMA IV by copper target (Fig.1), the X-ray diffraction is based on the elastic scattering of X-rays from the electron clouds of the individual atoms in the system. The most comprehensive description of scattering from crystals is given by the dynamical theory of diffraction. In this study the powder diffraction is a scientific technique by X-ray, neutron or electron diffraction on powder or microcrystalline samples for structural characterization of materials. RIGAKU a machine used to carry out the procedure which is based the Bragg's law the formula $n\lambda = (hkl) \sin \emptyset$ where

$\lambda$ = the true lattice spacing for planes (hkl)
$\emptyset$ = glancing angle of reflection
$\lambda$ = wavelength of X-ray
n = order of reflection

A reflection on a given set of planes only occurs when a certain glancing angle $\emptyset$ results for fixed wavelengths, a variation of $\emptyset$ is obtained in the powder method by exposing a very fine grained powder whose crystals have random orientation. A crystal plane (hkl) then reflects at the angle $\emptyset$ according to above relationship Anon (1980). Analysis of sample is powdered on agate mortar to the size of -230 mesh i.e. 64 microns, the powder was mounted on a X-ray machine holder and the machine operated for specific degrees of light fraction - 20° - 60°, Ilmenite - 20° - 71°, magnetite 17° - 65°, non- magnetite - 3° - 70° to obtain the required X-ray diffractograms. The data is subjected to RIGAKU software programme to obtain desired X-ray diffractograms. Interpretation for identifying the different minerals was done according to Anon (1981).

The X-ray diffractograms of ilmenite, magnetite and light minerals show various peaks which are identified using JCPDS data, Anon (1981). The X-ray diffractograms of limonite shows the intergrowth of other minerals along with limonite. The minerals include ilmenorutile and titanite shows major peaks. The non-magnetic sand grains were mounted in Canada balsam and observed under optical microscope to identify diagnostic properties of the minerals.
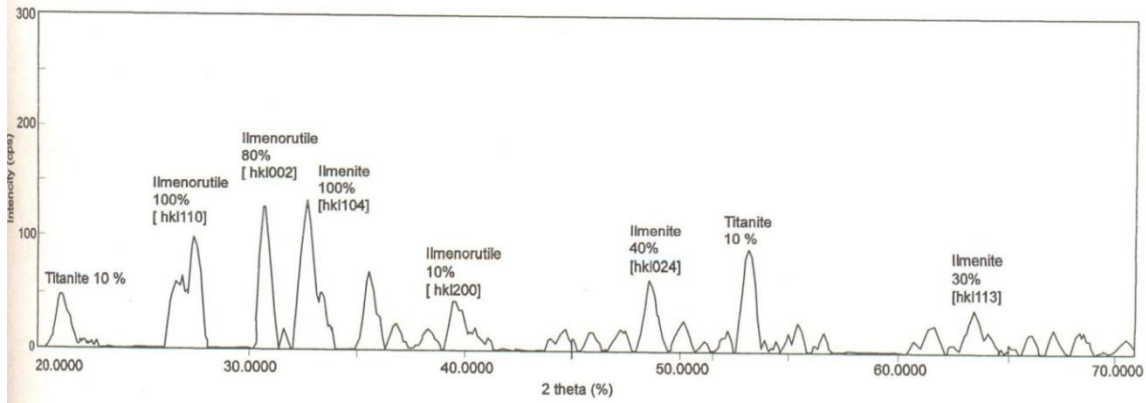
Fig . 1 X-ray diffractogram of ilmenite, Vagator, Goa
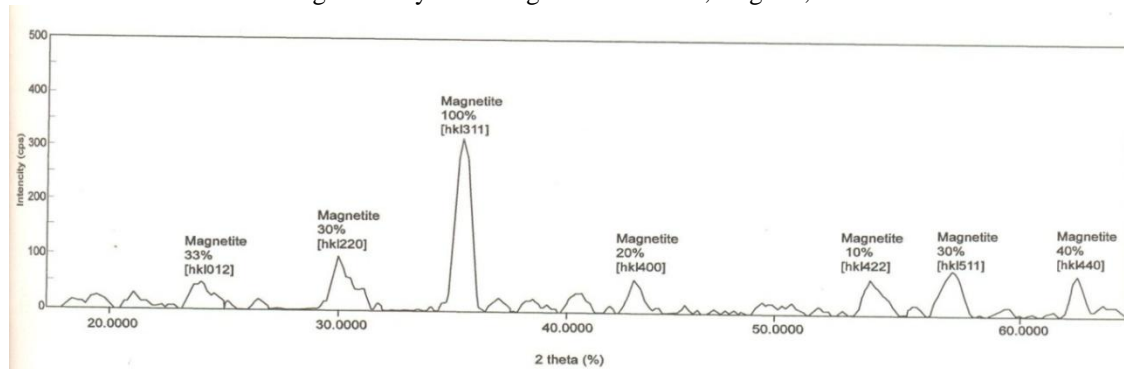
Fig. 2. X-ray diffractogram of Magnetite, Vagator, Goa
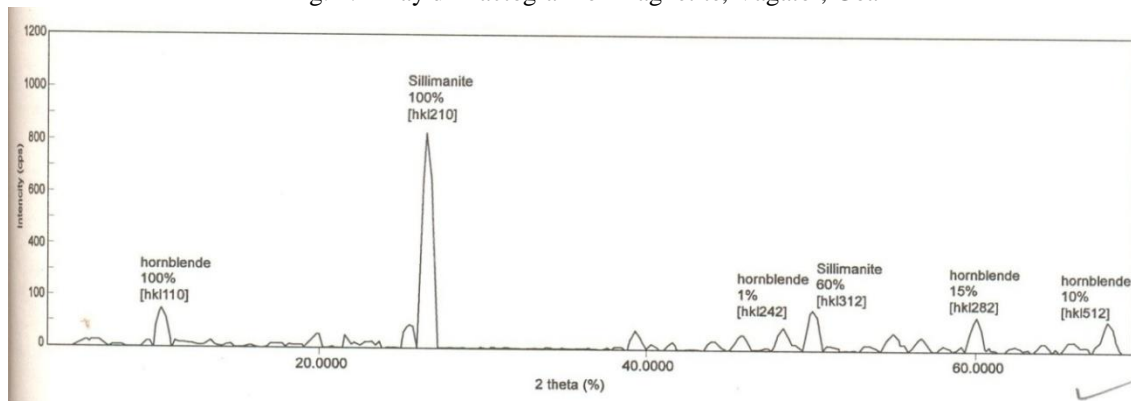
Fig.3. X-ray diffractograms of Non-magnetite, Vagator, Goa

## VI.  Scanning Electron Microscopy (SEM)

Krinsley and Doornkamp (1973) used the surface textures of quartz grains in order to achieve an understanding the post depositional history of the sediments. During the process of transportation and deposition the sand grains are exposed to continuous mechanical and chemical action. As a result various micro features are developed on the surface of the grains, This study of the magnetite, ilmenite and quartz grains under the scanning electron microscope, observed the micro textures developed on quartz grains and its significance in understanding the action of transportation and depositional environments. In this study the methodology is used the sediment sample from different locations were selected, washed and treated with 10%HCL. Dried samples were separated for light and heavy minerals by using bromoform (Sp.Gr. 2.89) following standard procedures (Hutchinson 1974). A few grains of magnetite, ilmenite and quartz grains were taken in to SEM study. The

grains were mounted on SEM brass stub, and coated with gold in a vacuum evaporator and slowly rotated. The grains were studies in detail and typical micrographs were plotted by using Joel JSM-5800 SEM.

The SEM study of all the grains of ilmenite, magnetite and quartz, shows variety of micro textures developed by mechanical and chemical processes acting in the coastal area. Mechanically formed grooves are predominant features followed by V marks and concoidal fractures. Rounded grains and smoothening of edges indicates high energy zones, etch V's and solution pits are dominant features by precipitation of chemical processes. Evaporation and exposure of grains in dry intervals increase the pH and aid etching process. In this observation of the sub rounded grains with high impact marks indicates high energy condition is a characteristic feature in coastal areas. V-Shaped triangular pits and etch V's indicates chemical action in pocket beaches. The mechanical breakage blocks indicate nearby source of sediments and arc shaped furrows are in fluvial environment. Development of precipitation indicates calm environment with low energy. The grains from offshore area show lines and pits and impact marks are observed in river samples at high energy environment.



Fig. 4: Rutile and tourmaline
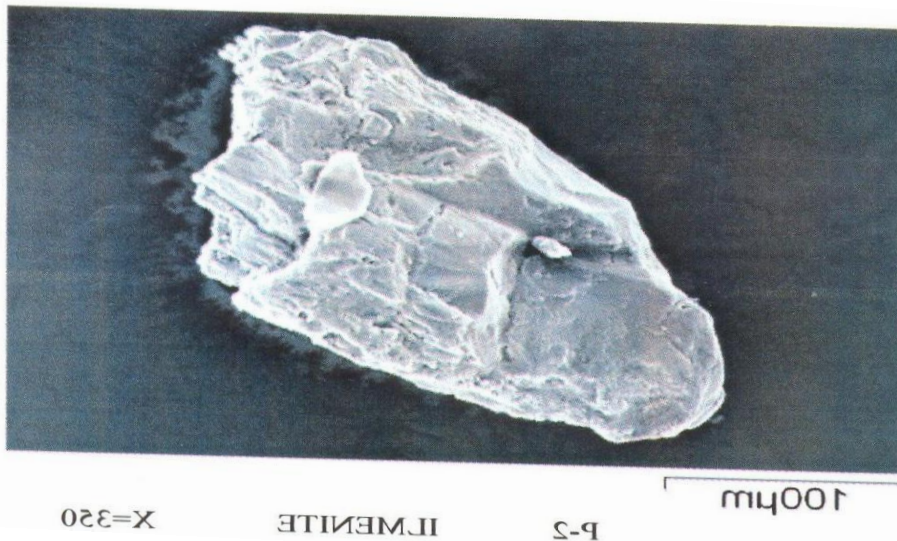


Fig 5: Elongated sub angular, sub rounded grains showing concoidal fractures, grooves, pits of limonite
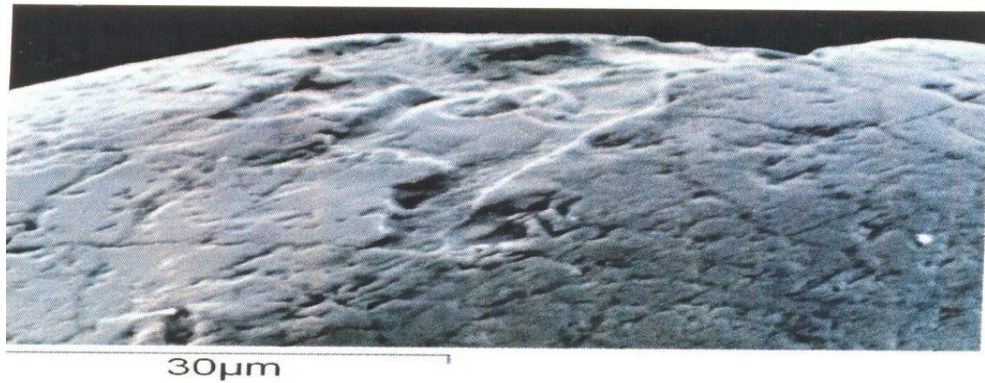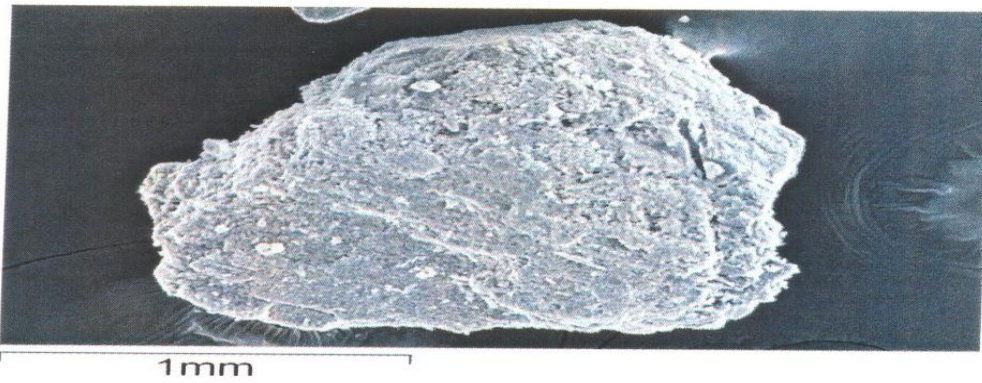
Fig. 6: The ilmenite showing irregular surface with more impact, rounded edges and sub rounded grains effect of chemical action,
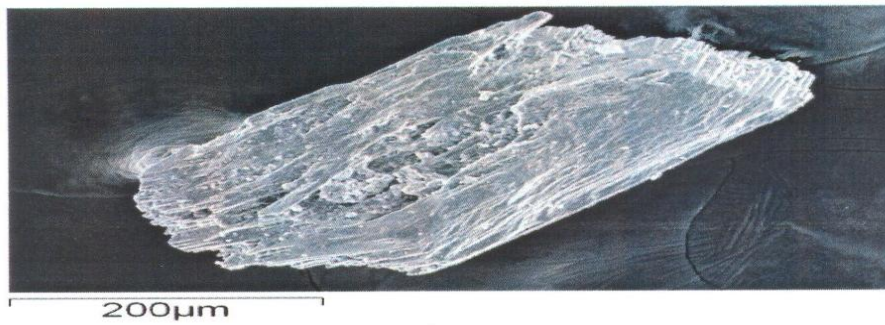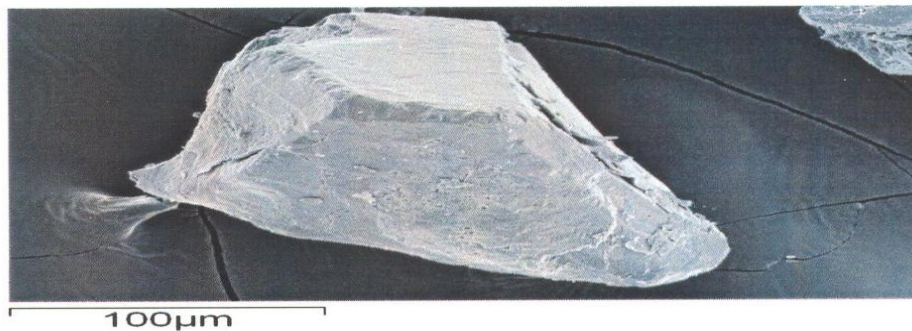


Fig. 7: The magnetite shows elongated sub angular grain scratch marks, impact pits and effect of solution

Fig. 8: The quartz shows step like grooves, secondary precipitation and sub concoidal fractured surface.

## VII.  Results and Discussion

From the above investigations the study of heavy minerals from beach sands of  vagathor,  North  Goa reveals the following aspects regarding their genesis.

- The X-ray diffractogram of ilmenite shows the intergrowth of other minerals along with ilmenorutile and titanite major peaks.
- The heavy mineral suite comprises of opaque (magnetite and ilmenite) and transparent minerals like hornblende, epidote, garnet, rutile, zircon, enstatite and minor amounts of tourmaline.
- The light minerals mainly quartz and feldspars, magnetite concentration ranges between 2.01 to 56.86 percent, ilmenite between 2.83 to 41.04 percent and non magnetic  between 1.18 to 44.81 percent.
- Mechanical process leads to form the concoidal fracture pitted surface, groves and furrows.
- Dissolution chemical process generates concavities, solution pits, etch V marks.
- A chemical process develops silica precipitation.
- The SEM study of all the grains of ilmenite, magnetite and quartz, shows variety of micro textures developed by mechanical and chemical processes acting in the coastal area.
- Mechanically formed grooves are predominant features followed by V marks and concoidal fractures. Rounded grains and smoothening of edges indicates high energy zones, etch V's and solution pits are dominant features by precipitation of chemical processes.
- Evaporation and exposure of grains in dry intervals increase the pH and aid etching process. In this observation of the sub rounded grains with high impact marks indicates high energy condition is a characteristic feature in coastal areas. V-Shaped triangular pits and etch V's indicates chemical action in pocket beaches.
- The mechanical breakage blocks indicate nearby source of sediments and arc shaped furrows are in fluvial environment. Development of precipitation indicates calm environment with low energy.
- The grains from offshore area show lines and pits and impact marks are observed in river samples at high energy environment.
- River sample is fresher then beach sample which are more weathered. They show primary features most of the beach sample overlapping by secondary precipitation.
- The highest concentration of heavy minerals in Vagator beach is in fine fractions, range of 16.58 to 97.49 percent. The heavy minerals concentration in left bank of Chapora River close to the low tide level of Vagator beach.
- The mineral with high specific gravity are winnowed by the retreating currents of the plunging waves.
- The non magnetic heavy mineral varies in degrees of transformation and size from euhedral to subhedral hornblende show elongated edges involving some chemical action in the depositional basin.
- Garnets seems to be undergone etching by the pits and depressions.
- The observed mineral assemblage on the surface features collectively suggest the derivation of   source rocks like mixtures of igneous and metamorphic rocks, crystalline gneisses and schist's.

# REFERENCES

[1].  Ambre N.V, A.R. Gujar, P.G. Mislankar: Surface textures of Quartz grains from Goa coast – An application of the scanning electron microscope (2005).

[2].  Anon (1981); Powder diffraction file inorganic phase alphabetical index of chemical and mineral name published by JCPDS, USA.

[3].  Cronan D.S (1980): underwater minerals, academic press, London P.362.

[4].  Exploration Task Group, March 2007 – Origin, distribution, Evolution of placers of south Maharashtra and Goa, NIO published.

[5].  Folk R.L (1968): petrology of sedimentary rocks. Hemohil, Austin, Texas p 182.

[6].  Friedman G.M (1962): on sorting, sorting coefficients and the log normality of the grain size distribution of sandstones. Jour. Geol. V. 70, pp 737 -753.

[7].  Gokul A.R et.al. (1985): stratigraphy and structure of Goa in Earth resource for Goa's development, Geological survey of India, pp 1-13.

[8].  Gine V.T (1979): Gazetteer of the Union Territory of Goa, Daman and Diu, 1 pp. 222.

[9].  Hails J.R and Hoyt Z.H. (1969): the significance and limitations of statistical parameters for the distinguishing ancient and modern sedimentary environment of lower Georgia coastal plains, jour. Sedimentary petrology, V -39. Pp 559 – 580.

[10]. Iyer S.D. and Wagle B.G (1987): Morphometric analysis of the river basins in Goa; Geographical review of India V-49, pp 11-18.

[11]. Kidwai R.M. And Wagle B.G. (1975): mineralogy of beach and dune sands of Morji Arambol beach on Goa coast, India jour. of Marine Sciences V- 4, pp 128 -130.

[12]. Komar P.D. and Wang C. (1984): process of selective grain transport and formation of placers on beaches, Jour. of Geol V-92, pp 637 – 655.

[13]. Krinsley D.H. and Doornkamp J.C. (1973): Atlas of quartz sand surface texture. Cambridge University press. p 91.

[14]. Loveson V.J and Misra D.D (2004): sustainable develo9pment of Coastal placer minerals, allied publishers pvt.Ltd p. 308.

[15]. Moila R.J. and Wieser D. (1968): Textural parameters an evaluation, Jour. Sedimentary petrology, V 38, pp 45-53.

[16]. Milner H.B. (1962): Sedimentary petrography. George Allen and Union Ltd, London, p 715.

[17]. Rajamanickam G.V. (1993): Geological investigations offshore heavy mineral placers Konkan Coast, Maharashtra, India, Indian School of Mines, Dhanbad (PhD Thesis unpublished) p 258.

[18]. Rajamanickam G.V. (2001): hand book of mineral placer deposits, first edition, New Academic publishers, Delhi, p 235.

[19]. Rosenblum S. (1958): magnetic susceptibility of mineral in the Frantz isodynamic magnetic separator. Am mineralogist V – 43, pp 170 – 173.

[20]. Veerayya M. and Varadachari V.V.R (1975): depositional environments of coastal sediments of Calangute, Goa, sedimentary Geology, V -14 pp 63-74.

[21]. Williams H and Turner F. and Gilbert C.M. (1954): an introduction to the study of rocks in thin sections, W.H.Freeman & Co. Pub, San Francisco, p 406.

# An Experimental Analysis of Performance, Combustion and Emission Characteristics of Simarouba Biodiesel and Its Blends on CI Engine

## Vishwanath Kasturi[1], M. C. Navindgi[2]

[1]*PG Student, Thermal Power Engineering PDACE Gulbarga, Karnataka, India*
[2]*Associate professor, Dept of Mechanical Engineering PDACE Gulbarga, Karnataka, India*

**Abstract:** *Bio-diesel is one of the most promising alternatives for diesel needs. Use of edible oils may create shortage of oil for daily food. This required identification of new kinds of non-edible vegetable oil. With this objective, the present work has focused on the performance, combustion and emission characteristics of diesel engine using simarouba oil and its blends with diesel. In this investigation, the blends of varying proportions of simarouba biodiesel with diesel (S20, S40, S60, S80 & S100) were prepared, analyzed, and compared the performance, combustion and exhaust emission with diesel using 5.2 kW Single cylinder, 4stroke diesel engine. The performance, combustion and emission characteristics of blends are evaluated at variable loads and constant rated speed of 1500 rpm and found that the performance of S20 blend of simarouba oil gives result, that is near to the diesel and also found that the emission CO, HC, & NO$_X$ of this blend is less than the diesel.*
**Keywords:** *Biodiesel, Simarauba, Alternate fuel, CI Engine*

## I. Introduction

According to the present scenario diesel engines are commonly used as prime movers in the transportation, industrial and agricultural sectors because of their high brake thermal efficiency and reliability. Energy conservation and efficiency have always been the quest of engineers concerned with internal combustion engines. In this work, we have adopted Simarauba glauca oil. S*imarouba glauca* belongs to family simarubaceae.

## II. Materials And Methods

The extraction of biodiesel is carried out by base catalyzed transesterification method.
### 2.1. Process of Extracting



Fig 2.1: The flow chart for biodiesel production

To a one liter of raw Simaroauba oil is heated up to $70^0$C. 300 ml of methanol & 5-7gms of NaOH (catalyst) is added and the mixture is maintained at 65-70$^0$C is about 1½ hours and stirred continuously. The mixture is allowed to settle for 20-30 min until the formation of biodiesel and glycerin layers. The glycerin is removed from the bio-diesel in a separating funnel. The bio diesel produced from Simarouba oil is ready to use.

**2.2. Transesterification**

It is most commonly used and important method to reduce the viscosity of vegetable oils. In this process triglyceride reacts with three molecules of alcohol in the presence of a catalyst producing a mixture of fatty acids, alkyl ester and glycerol. The process of removal of all the glycerol and the fatty acids from the vegetable oil in the presence of a catalyst is called esterification.

```
CH2COOR1                                          CH2OH        R1COOR
|                                                 |            |
CHCOOR2                                           CHOH         R1COOR
|               +  3ROH        ⟷                  |        +   |
CH2COOR3                                           CH2OH        R1COOR
                               Catalyst
                               (NaOH)


Cottonseed Glyceride       Alcohol                Glycerin     Biodiesel
```

Chemical reaction

Physical and chemical properties are more improved in esterified vegetable oil because esterified vegetable oil contains more cetane number than diesel fuel. These parameters induce good combustion characteristics in vegetable oil esters. So unburnt hydrocarbon level is decreased in the exhaust. It results in lower generation of hydrocarbon and carbon monoxide in the exhaust than diesel fuel. The vegetable oil esters contain more oxygen and lower calorific value than diesel. So, it enhances the combustion process and generates lower nitric oxide formation in the exhaust than diesel fuel.

## III.  Properties Of Diesel And Some Blends

After transesterification the properties of Simarouba oil blends was determined. It was found that the properties of Simarouba oil blends were similar to diesel. Simarouba oil blends were similar to diesel.

Table 3.1: Properties of Simarouba oil blends

| Properties | Diesel | S20 | S40 | S100 |
|---|---|---|---|---|
| Kinematic viscosity at 400C (Cst) | 2.54 | 3.104 | 3.891 | 5.6 |
| Calorific value (kJ/Kg) | 42500 | 42270 | 41949 | 37933 |
| Density (kg/m3) | 840 | 838 | 846 | 875 |
| Flash Point ($^0$C) | 54 | 79 | 98 | 165 |
| Fire Point ($^0$C) | 64 | 89 | 110 | 185 |

## IV.  Experimental Setup

The experimental setup enables study performance, combustion and emission characteristics. The experiments have been carried out on a DI compression ignition engine for various blends of simarouba oil with diesel (S20, S40, S60, S80, and S100) with varying brake power. The experiment is carried out at constant compression ratio of 17.5:1 and constant injection pressure of 200 bar by varying brake power.



Fig 4.1: Photograph of engine setup

Table 4.1: Engine specifications

| | |
|---|---|
| Manufacturer | Kirloskar oil engines Ltd, India |
| Model | TV-SR, naturally aspirated |
| Engine | Single cylinder, DI |
| Bore/stroke | 87.5mm/110mm |
| Compression Ratio | 17.5:1 |
| speed | 1500r/min, constant |
| Rated power | 5.2kw |
| Working cycle | 4 stroke |
| Injection pressure | 200bar/23 def TDC |
| Type of sensor | Piezo electric |
| Response time | 4 micro seconds |

## V.   Result And Discussion

### 5.1   Performance characteristics
### 5.1.1  Specific fuel consumption



Fig 5.1  The variation of the specific fuel consumption with brake power for diesel and simarouba blends

        The variation of  specific fuel consumption with brake power for diesel, and simarouba biodiesel oil and it's blend  are shown in figure 5.1. Specific fuel consumption for simarouba biodiesel blends are higher than diesel for certain lower loads, but for higher loads, consumption rate remains  almost constant as evident from the graph. This may be due to fuel density, viscosity and heating value of the fuels. The main reason for this could be that percent increase in fuel required to operate the engine is less than the percent increase in brake power due to relatively less portion of the heat losses at higher loads.

### 5.1.2  Air fuel ratio



Fig 5. 2  The variation of the air fuel ratio with brake power for diesel and simarouba blends

The variation of air fuel ratio with brake power for diesel and simarouba biodiesel blends are shown in figure 5.2. It can be observed that air fuel ratio of pure diesel is higher than other simarouba biodiesel and its blends, and we can also see that the air fuel ratio decreases as the load increases. Because the reason is air fuel ratio decreases due to increase in load because of the compensation of load can only be done with increasing the quantity of fuel injection to develop the power required to bare the load.

### 5.1.3  Brake thermal efficiency
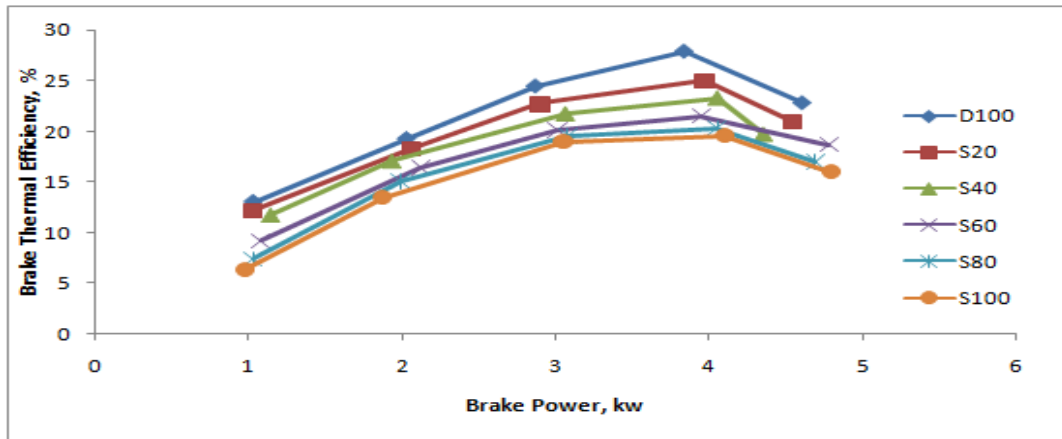


Fig 5. 3  The variation of the brake thermal efficiency  with brake power for diesel and simarouba blends

The variation of  brake thermal efficiency with brake power for diesel, and simarouba biodiesel and its blend are shown in figure 5. 3. shows the break thermal efficiency of simarouba biodiesel and its blends with respect to brake power. It shows that brake thermal efficiencies of all the blends are lower at almost all load levels. Among the blends S20 is found to have the maximum thermal efficiency of 25.01% at a brake power of 3.97 kW while for diesel it is 27.84%. The decrease in brake thermal efficiency with increase in simarouba biodiesel concentration is due to the poor atomization of the blends due to their high viscosity and reduction in heat loss and increase in power with increase in load.

### 5.1.4  Exhaust gas emission
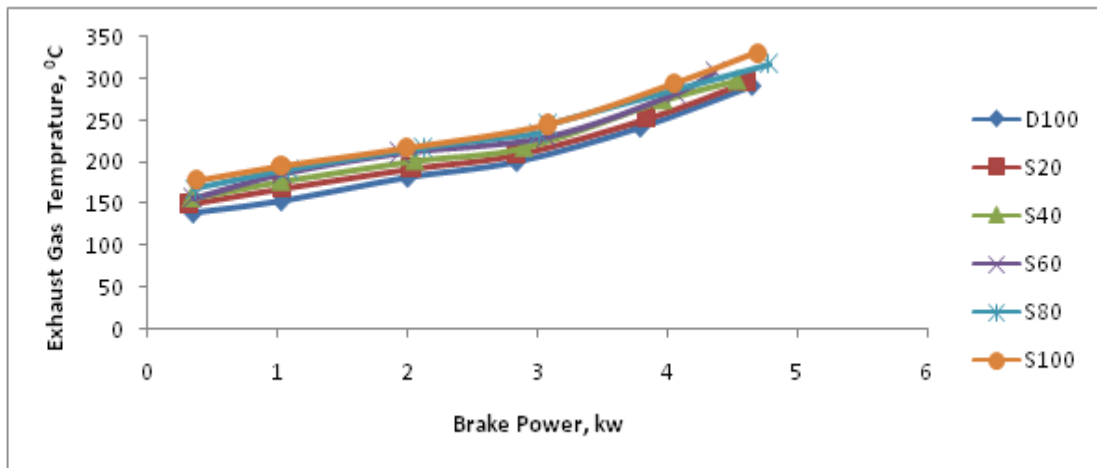


Fig 5.4  The variation of the exhaust gas temperature  with brake power for diesel and simarouba blends

The comparisons of exhaust emission temperature with brake power for diesel, and other blends of simarouba biodiesel are shown in figure 5.4 the exhaust emission temperature of all the biodiesel are higher than the diesel as it is evident from the graph. The exhaust gas temperatures for 100% diesel and 20%, 40%, 60%, 80%, 100%  blends for varying loads can be observed and stated as they are slightly parallel to each other. The exhaust gas temperature of all the blends and 100% diesel increase as the load increases. It is observed that, at full load the exhaust gas temperature is maximum, this is because; at full load the chemically correct ratio of air and fuel is used, due to chemically correct ratio of air and fuel, high heat is generated inside the cylinder.

## 5.2 Emission characteristics
### 5.2.1 Carbon monoxide



Fig 5.5 The variation of the carbon monoxide with brake power for diesel and simarouba blends

Fig 5.5 shows the comparison of brake power with carbon monoxide for different biodiesel blends. The CO emission depends upon the strength of the mixture, availability of oxygen and viscosity of fuel. It is observed that the CO emission initially decreases at lower loads sharply increases after 4 kW of power for all test fuels. And the diesel and simarouba oil with 80%blend has more emission of CO compared with blends of simarouba oil like S20, S40, S60 and S100. This due to incomplete combustion at higher loads which results in higher CO emissions. It is also seen that the CO Emission decreases with increase in percentage of additive in the blends. From this graph it is revealed that S100 (pure simarouba oil) shows lowest carbon monoxide emission compare to all other test fuels up to 4kw of power and then increases due to incomplete combustion. Because the reason is high viscosity and small increase in specific gravity suppresses the complete combustion process, which produces small amount of CO.

### 5.2.2 Hydro carbon
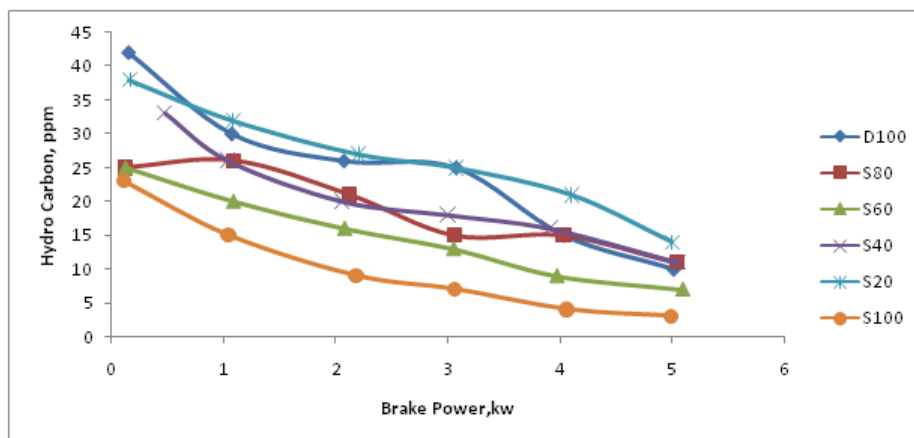


Fig 5.6 The variation of the hydro carbon with brake power for diesel and semarouba blends

Figure 5.6 shows the variation of emission of hydrocarbon with brake power for different blends of simarouba biodiesel and pure diesel. The emission of HC is decreasing with increase of loads, but the blend S20 exhibits emission of HC similar to diesel. And we observe that the S100 has the least emission of HC compared to other blends. Thus, it can be confirmed that both conventional diesel and biodiesel had the same functional group of C–H. However, the conventional diesel had no oxygen group, whereas biodiesel showed oxygen functional group. Therefore, the biodiesel with the existence of oxygen could be promoted cleaner and complete combustion. On the other hand, the conventional diesel without any oxygen produced more black smoke and incomplete combustion during burning. Because the reason is as the Catani number of ester based fuel is higher than diesel, it exhibits ashorter delay period and results in better combustion leading to low HC emission. Also the intrinsic oxygen contained by the biodiesel was responsible for the reduction in HC emission.

### 5.2.3 Nitrogen oxide
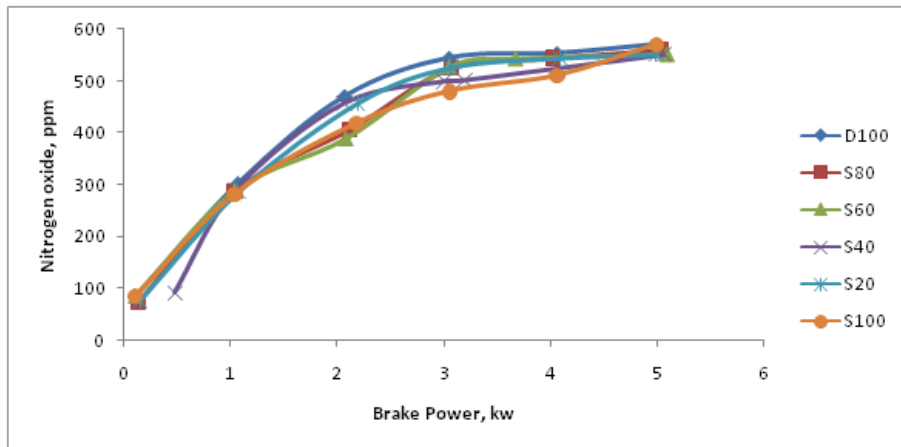


Fig 5.7 The variation of the nitrogen oxide with brake power for diesel and semarouba blends

The average percentage of change in NOx emission for S20, S40, S60, S80, and S100 are shown in the graph. This shows that the NOx emission increased with the increase of percentage ratio of biodiesel. NOx emission is primarily a function of total oxygen inside the combustion chamber, temperature, pressure, compressibility, and velocity of sound. Invariably biodiesel has S20 level of oxygen bound to its chemical structures. Thus, oxygen concentration in biodiesel blends fuel might have caused the formation of NOx . Furthermore, the increase of NOx emission is due to the higher cetane number of biodiesel which will reduce the ignition delay. The increase of NOx emission is a result of the reduced ignition delay. However, the NOx emissions can be reduced through engine tuning or using exhaust catalytic converter. At any rate, the NOx still can be reduced with the advanced technologies such as catalytic converter, EGR and engine tuning.

The NOx emission for biodiesel and its blends is higher than that of diesel except S20 at lower loads. It is increased with the increase in engine load. The maximum NOX values were obtained at full load conditions and were 570, 560,550,550,550,570 ppm with respect t0 D100, S80, S60, S40, S20, S100.The reason for higher NOx emission for blends is due to the higher peak temperature and the biodiesel had S oxygen content in it, which facilated $NO_X$ formation.

### 5.3 Combustion Characteristics
### 5.3.1 Variation of crank angle versus cylinder pressure
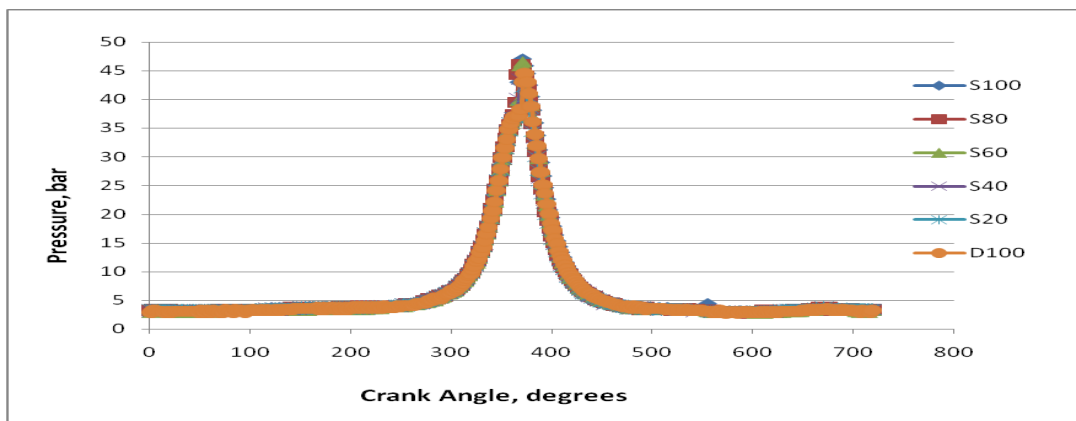


Fig 5.8 Variation of crank angle versus cylinder pressure

In a CI engine the cylinder pressure is depends on the fuel-burning rate during the premixed burning phase, which in turn leads better combusion and heat release. The variation of cylinder pressure with respective crange angle for diesel and different blends of simarouba biodiesel are presented in fig 5.8 peak pressure of 44.54bar and 43.69bar are found for puer diesel and S40 respectively. From the test results it is observed that the peak presure variations are less since the properties such as calorific value, viscosity and density are brought closer to diesel after transestirification of vagitable oil, no magare variation in the pressure are found.

### 5.3.2  Variation of crank angle versus heat release rate
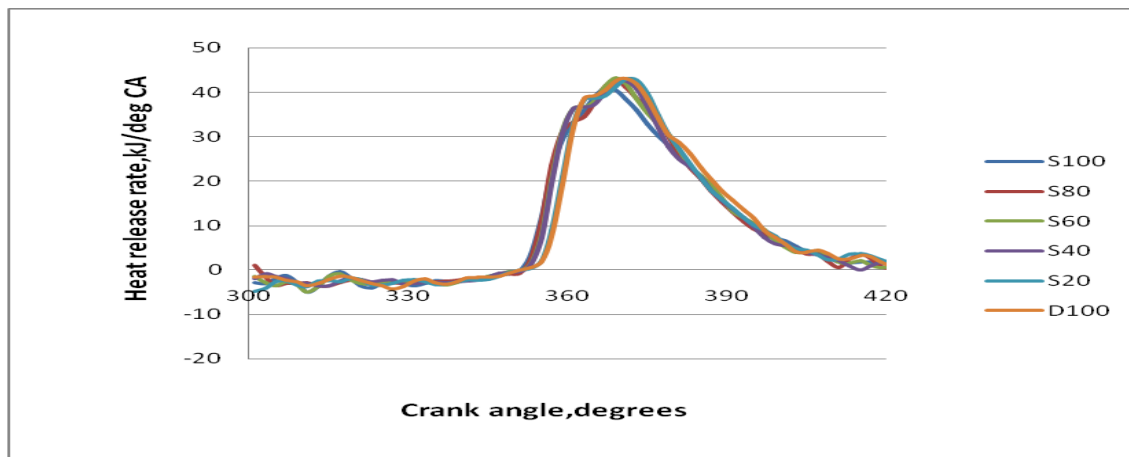


Fig 5.9 Variation of crank angle versus heat release rate

The fig-5.9 shows that the variation of the heat release rate with crank angle.It is observed that all theblends of simarouba oil traces the path of pure diesel and S60 are 43,11044kj and 43,2087kj at 3710.

### 5.3.3 Variation of crank angle versus cumulative heat release rate
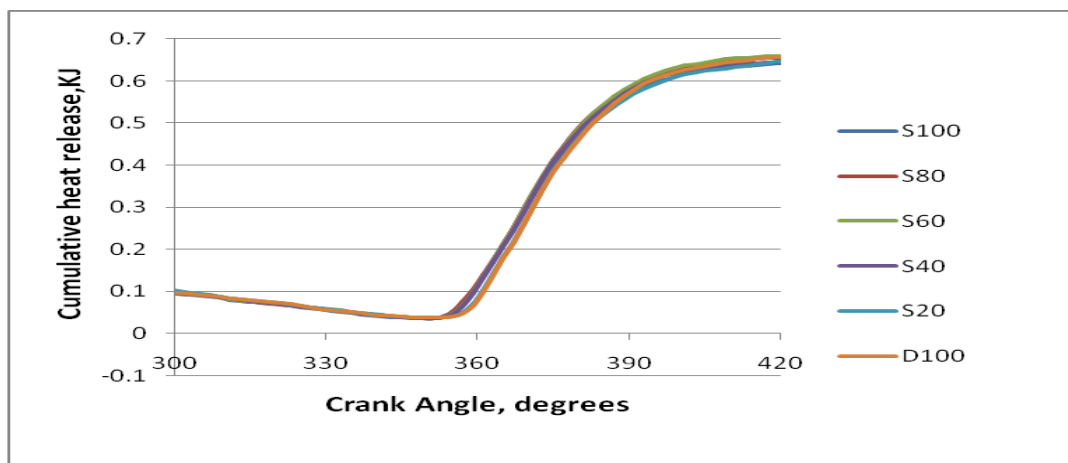


Fig 5.10  Variation of crank angle versus cumulative heat release rate

The fig-5.10 shows the variation of comulative heat transfer with crank angle. It is observed that from the fig-5.10 that all blends of simarouba biodiesl traces the same path as that of the diesel.initially the cumulative heat transfer decreases at first cycle and then increases in the second cycle as shown in the fig-5.3.3.

## VI.  Conclusion

- Specific fuel consumption increases as the concentration of simarouba biodiesel increases so we can observe that with 20% simarouba biodiesel blend almost matches with diesel fuel.
- Air fuel ratio for diesel is lower than simarouba biodiesel and its blends which is evident from the graph.
- The mechanical efficiency of diesel is slightly higher than the simarouba biodiesel blends and D100 and S20 are seen to be almost nearer to each other also from the graph.
- Brake thermal efficiency of simarouba biodiesel at 20% blend has slightly higher efficiency than diesel .
- The exhaust emission temperature of all the biodiesel are higher than the diesel and It is observed that, at full load the exhaust gas temperature is maximum, due to chemically correct ratio of air and fuel.
- The S20 has lower average percentage of change in CO, and HC compared to Diesel. Yet, S20 is producing higher NOx emission. Nevertheless, the S20 is still the suitable biodiesel blend amongst all as the NOx emission can be reduced with the advanced technologies.
- It is conclude that the combustion characteristics of all blends of simarouba oil is almost same as that of diesel.

# REFERENCES

[1]     Ambarish Datta and Bijan Kumar Mandal. Biodiesel production and its emissions and performance: a review. IJSER, Volume 3, Issue 6, June-2012, ISSN 2229-5518.

[2]     Zankruti Patel and Krishnamurthy R. Biodiesel: source materials and future prospects. C G Bhakta Institute of Biotechnology, Uka Tarsadia University, Maliba Campus, Bardoli, Dist. Surat, Gujarat, India-394350, International Journal of Geology, Earth and Environmental Sciences ISSN: 2277-2081, 2013 Vol. 3 (2) May-August, pp.10-20/ Patel and Krishnamurthy.

[3]     Amruth. E, Dr. R. Suresh, Yathish K V. Production of simarouba bio-diesel using mixed base catalyst, and its performance study on CI engine. Department of Mechanical Engineering, SIT  Tumkur , Karnataka, May – 2013.

[4]     A.K. Dash, R.C.Pradhan, L.M. Das, and S.N. Naik. Some physical properties of simarouba fruit and kernel, Centre for Energy Studies, Centre for Rural Development and Technology, Indian Institute of Technology, Delhi, Hauz Khas, New Delhi 110 016, India Received January 28, 2008; accepted April 4, 2008.

[5]     Patil Manasi S. and Gaikwad D. K. A critical review on medicinally important oil yielding plant laxmitaru (simarouba glauca DC). Department of Botany, Shivaji University, Kolhapur416004 (MS) India, Vol.3(4), 2011,1195-1213, ISSN:0975-1459.

[6]     Sharun Mendonca, John Paul Vas. Influence of injection timing on performance and emission characteristics of simarouba biodiesel engine. M.Tech Student, Mechanical Engineering Department, Srinivas Institute of Technology, Valachil, Mangalore,  April 2013. ISSN 2250-3153.

[7]     M. C. Navindgi, Maheswar Dutta, B. Sudheer Prem Kumar. Performance of a CI engine with different blends of mahua (Madhuca Longifolia) biodiesel under varying operating conditions. m PDA College of Engineering, Gulbarga, 585105, Karnataka, India, College of Engineering & Technology, Sangareddy, Medak District, AP, India, Department of Mechanical Engineering, JNTU, Hyderabad, A.P, India,  International Journal of Engineering and Technology Volume 2 No. 7, July, 2012, ISSN 2049-3444.

[8]     O.D. Hebbal, K. Vijaykumar Reddy, K. Rajagopal. Performance characteristics of a diesel engine with deccan hemp oil. Assistant Professor, Poojya Doddappa Appa College of Engineering, Gulburga, India, Controller of Examinations, Jawaharlal Nehru Technological University, Hyderabad, India, Vice chancellor, Jawaharlal Nehru Technological University, Hyderabad, India, 18 April 2006, Fuel 85(2006) 2187-2194.

# International Journal of Modern Engineering Research (IJMER)

## Contents :

# Contra $\alpha$ * Continuous Functions in Topological Spaces

S. Pious Missier[1], P. Anbarasi Rodrigo[2]

***Abstract:*** *In [3], Dontchev introduced and investigated a new notion of continuity called contra-continuity. Recently, Jafari and Noiri [5] introduced new generalization of contra-continuity called contra $\alpha$ continuity . The aim of this paper is to introduce and study the concept of a contra $\alpha$ * continuous and almost contra $\alpha$ * continuous functions are introduced*
***MATHEMATICS SUBJECT CLASSIFICATIONS: 54AO5***
***Keywords And Phrases:*** *contra $\alpha$ * continuous functions, almost contra $\alpha$ * continuous functions, contra $\alpha$ * graph , and locally $\alpha$ * indiscrete space.*

## I. Introduction

Dontchev[3] introduced the notion of contra continuity. Later Jafari and Noiri introduced and investigated the concept of contra $\alpha$ continuous and discussed its properties. Recently, S.Pious Missier and P. Anbarasi Rodrigo [9] have introduced the concept of $\alpha$ * -open sets and studied their properties. In this paper we introduce and investigate the contra $\alpha$ * continuous functions and almost contra $\alpha$ * continuous functions and discuss some of its properties.

## II. Preliminaries

Throughout this paper (X, τ), (Y, σ ) and (Z, $\eta$ ) or X , Y , Z represent non-empty topological spaces on which no separation axioms are assumed unless otherwise mentioned. For a subset A of a space (X, τ), cl(A) and int(A) denote the closure and the interior of A respectively. The power set of X is denoted by P(X).

**Definition 2.1:** A subset A of a topological space X is said to be a $\alpha$ ***open*** [9] if A $\subseteq$ int* ( cl ( int* ( A ))).

**Definition 2.2:** A function f: (X, τ) $\longrightarrow$ (Y, σ ) is called a $\alpha$ * ***continuous*** [10] if f$^{-1}$(O) is a $\alpha$ *open set of (X, τ) for every open set O of (Y, σ ).

**Definition 2.3:** A map f: (X, τ) $\longrightarrow$ (Y, σ ) is said to be ***perfectly $\alpha$ * continuous*** [11] if the inverse image of every $\alpha$ *open set in (Y, σ ) is both open and closed in (X, τ) .

**Definition 2.4:** A function f: (X, τ) $\longrightarrow$(Y, σ) is said to be $\alpha$ ***Irresolute*** [10] if f$^{-1}$(O) is a $\alpha$ *open in (X, τ) for every $\alpha$ *open set O in (Y, σ ).

**Definition 2.5:** A function f: (X, τ) $\longrightarrow$ (Y, σ ) is called a ***contra g continuous*** [2] if f$^{-1}$(O) is a **g - closed** set [6] of (X, τ) for every open set O of (Y, σ ).

**Definition 2.6:** A function f: (X, τ) $\longrightarrow$ (Y, σ ) is called a ***contra continuous*** [3]if f$^{-1}$(O) is a closed set of (X, τ) for every open set O of (Y, σ ).

**Definition 2.7:** A function f: (X, τ) $\longrightarrow$ (Y, σ) is called a ***contra $\alpha$ continuous*** [5] if f$^{-1}$(O) is a $\alpha$ closed set of (X, τ) for every open set O of (Y, σ ).

**Definition 2.8:** A function f: (X, τ) $\longrightarrow$ (Y, σ) is called a ***contra semi continuous*** [4] if f$^{-1}$(O) is a semi closed set of (X, τ) for every open set O of (Y, σ ).

**Definition 2.9:** A function f: (X, τ) $\longrightarrow$ (Y, σ) is called a ***contra g$\alpha$ continuous*** [1] if f$^{-1}$(O) is a g$\alpha$ -closed set of (X, τ) for every open set O of (Y, σ ).

**Definition 2.10:** A Topological space X is said to be $\alpha$ ***$T_{1/2}$ space or $\alpha$ *space*** [9] if every $\alpha$ * open set of X is open in X.

**Definition 2.11:** A Topological space X is said to be a ***locally indiscrete*** [7] if each open subset of X is closed in X.

**Definition 2.12:** Let A be a subset of a topological space (X, τ ). The set ∩{U ∈ τ | A ⊂ U} is called the ***Kernel of A*** [7] and is denoted by ker(A).

**Lemma 2.13:** [6] The following properties hold for subsets A,B of a space X:
1. x ∈ ker(A) if and only if A ∩ F≠ $\phi$ ,for any F ∈ C(X, x);

2. A ⊂ ker(A) and A = ker(A) if A is open in X;
3. If A ⊂ B, then ker(A) ⊂ ker(B).

**Theorem 2.14: [10]** Let f: (X, τ) →(Y, σ ) be a function. Then the following are equivalent:
1.  f is   $\alpha$ * continuous
2.  The inverse image of closed set in Y is $\alpha$ * closed in X.
3.  f ( $\alpha$ * cl (A) )  $\subseteq$  f(cl(A)) for every subset A in X.
4.   $\alpha$ * cl(f$^{-1}$ (G))  $\subseteq$  f$^{-1}$ ( cl(G)) for every subset G of Y.
5.  f$^{-1}$( int (G))  $\subseteq$  $\alpha$ * int (f$^{-1}$(G)) for every subset G of Y.

**Theorem 2.15[9]:**
(i)      Every open set is $\alpha$ *- open and every closed set is $\alpha$ *-closed set
(ii)     Every $\alpha$ -open set is $\alpha$ *-open and every $\alpha$ -closed set is $\alpha$ *-closed.
(iii)    Every g-open set is $\alpha$ *-open and every g-closed set is $\alpha$ *-closed.

## III.   Contra $\alpha$ * continuous functions

**Definition 3.1:** A function f: (X, τ) → (Y, σ) is called **Contra $\alpha$ * continuous functions** if f$^{-1}$ (O) is $\alpha$ * closed in (X, τ) for every open set O in (Y, σ).

**Example 3.2:** Let X = Y= {a, b, c, d}, τ = {ϕ,{a},{b},{c},{ab},{ac},{bc},{abc}, X} and σ = {ϕ, {a},{ab},{abc},Y}. $\alpha$ *C(X, τ) = {ϕ ,{d},{ad},{bd},{cd},{abd},{acd},{bcd},X}Let f: (X, τ) →(Y, σ ) be defined          by f(b) = a = f(d) ,  f(c) = b , f(a) = c. clearly, f is contra $\alpha$ * continuous .

**Theorem 3.3:** Every contra continuous function is a contra $\alpha$ * continuous.

**Proof:** Let f: (X, τ) → (Y, σ) be a function. Let O be an open set in (Y, σ). Since, f is contra continuous , then f$^{-1}$ (O) is closed in (X, τ) . Hence by thm [2.15] , f$^{-1}$ (O) is $\alpha$ * closed in (X, τ) . Therefore, f is contra $\alpha$ * continuous.

**Remark 3.4 :** The converse of the above theorem need not be true.

**Example 3.5: :** Let X = Y= {a, b, c, d}, τ = {ϕ,{a},{ab},{abc}, X}, τ$^{c}$ = {ϕ,{d},{cd},{bcd},X}  and σ = {ϕ, {a},{b},{c},{ab},{ac},{bc},{abc},Y}. $\alpha$ *C(X, τ) = {ϕ , {b} , {c} , {d} , {ad} ,{bc} , {bd} , {cd} , {abd} , {acd} , {bcd} , X }. Let f: (X, τ) →(Y, σ ) be defined  by f(a) = a = f(d) ,  f(b) = b , f(c) = d. clearly, f is contra $\alpha$ *       continuous , but f$^{-1}$({a}) = {ad} is not closed in X.

**Theorem 3.6:** Every contra g continuous map is contra $\alpha$ * continuous.

**Proof:** Let f: (X, τ) → (Y, σ) be a contra g continuous map and O be any open set in Y. Since, f is contra g continuous, then f$^{-1}$ (O) is g - closed in (X, τ) .  Hence by thm [2.15] , f$^{-1}$ (O) is $\alpha$ * closed in (X, τ) . Therefore, f is contra $\alpha$ * continuous.

**Remark 3.7:** The converse of the above theorem need not be true.

**Example 3.8: :** Let X = Y= {a, b, c, d}, τ = {ϕ,{a},{ab},{abc}, X}, g-closed (X, τ) = {ϕ,{d},{ad} , {bd} {cd},  {abd} ,{bcd}, {acd} ,X}  and σ = {ϕ,  {a},{b},{c},{ab},{ac},{bc},{abc},Y}. $\alpha$ *C(X, τ) = {ϕ , {b} , {c} , {d} , {ad} ,{bc} , {bd} , {cd} , {abd} , {acd} , {bcd} , X }. Let f: (X, τ) →(Y, σ ) be defined  by f(a) = a = f(d) ,  f(b) = b , f(c) = d. clearly, f is contra $\alpha$ * continuous , but f$^{-1}$ ({b}) = {b} is not g-closed in X.

**Theorem 3.9:** Every contra $\alpha$ continuous map is contra $\alpha$ * continuous.

**Proof:** Let f: (X, τ) → (Y, σ) be a contra $\alpha$  continuous map and O be any open set in Y. Since, f is contra $\alpha$ continuous, then f$^{-1}$ (O) is $\alpha$  - closed in (X, τ) .  Hence by thm [2.15] , f$^{-1}$ (O) is $\alpha$ * closed in (X, τ) . Therefore, f is contra $\alpha$ * continuous.

**Remark 3.10:** The converse of the above theorem need not be true.

**Example 3.11:** Let X = Y= {a, b, c, d}, τ = {ϕ,{a}, {b},{ab}, {bc} ,{abc}, X}, and σ = {ϕ, {a},{b},{c},{ab},{ac},{bc},{abc},Y}. $\alpha$ *C(X, τ) = {ϕ , {c} , {d} , {ad} ,{bd}, {cd} , {abd} , {acd} , {bcd} , X }. $\alpha$ C(X, τ) = {ϕ , {c} , {d} , {ad} , {cd} , {acd} , {bcd} , X}.Let f: (X, τ) →(Y, σ ) be defined  by f(b) = a = f(d) ,  f(c) = b , f(a) = d. clearly, f is contra $\alpha$ * continuous , but f$^{-1}$ ({a}) = {bd} is not $\alpha$ -closed in X.

**Remark 3.12:** The concept of contra semi continuous and contra $\alpha$ * continuous are independent.

**Example 3.13:** Let X = Y= {a, b, c, d}, τ = {ϕ,{a},{ab},{abc}, X}, SC(X, τ) = {ϕ,{b} , {c} ,{d},{bc} , {bd} {cd},  {bcd},X}  and σ = {ϕ,  {a},{b},{c},{ab},{ac},{bc},{abc},Y}. $\alpha$ *C(X, τ) = {ϕ , {b} , {c} , {d} , {ad} ,{bc} , {bd} , {cd} , {abd} , {acd} , {bcd} , X }. Let f: (X, τ) →(Y, σ ) be defined  by f(a) = a = f(d) ,  f(b) = b , f(c) = d. clearly,     f is contra $\alpha$ * continuous , but f$^{-1}$ ({a}) = {ad} is not semi-closed in X.

**Example 3.14:** Let X = Y= {a, b, c, d}, τ = {ϕ,{a}, {b} , {c} ,{ab}, {ac} , {bc} ,{abc}, X}, SC(X, τ) = {ϕ, {a} ,{b} , {c} ,{d}, {ab} , {bc} , {ac} , {ad} , {bd} {cd}, {abd} , {acd}, {bcd},X}    and σ = {ϕ, {a},{ab},{ac},{abc},Y}. $\alpha$ *C(X, τ) = {ϕ , {b} , {c} , {d} , {ad} ,{bc} , {bd} , {cd} , {abd} , {acd} , {bcd} ,

X }. Let f: (X, τ) →(Y, σ ) be defined  by f(a) = a,  f(b) = b , f(c) = d., f(d) = c. Clearly,     f is semi closed, but f$^{-1}$ ({a}) = {a} is not $\alpha$ *closed in X.

**Remark 3.15:** The concept of contra g$\alpha$ continuous and contra $\alpha$ * continuous are independent.

**Example 3.16:** Let  X = Y = {a, b, c, d},  τ = {ϕ,{a}, {b},{ab}, {bc} ,{abc}, X}, and σ = {ϕ, {a},{b},{c},{ab},{ac},{bc},{abc},Y}. $\alpha$ *C(X, τ) = {ϕ , {c} , {d} , {ad} ,{bd}, {cd} , {abd} , {acd} , {bcd} , X }. g$\alpha$ - Closed(X, τ) = {ϕ , {c} , {d} , {ad} , {cd} , {acd} , {bcd} , X}.Let f: (X, τ) →(Y, σ ) be defined  by f(b) = a = f(d) ,  f(c) = b , f(a) = d. clearly, f is contra $\alpha$ * continuous , but f$^{-1}$ ({a}) = {bd} is not g$\alpha$ -closed in X. Therefore, f is not contra g$\alpha$ continuous.

**Example 3.17:** Let  X = Y = {a, b, c, d}, τ = {ϕ,{a}, {b},{ab},{abc}, X}, and σ = {ϕ, {a},{b},{ab},{bc},{abc},Y}. $\alpha$ *C(X, τ) = {ϕ , {c} , {d} , {ad} ,{bd}, {cd} , {abd} , {acd} , {bcd} , X }. g$\alpha$ - Closed(X, τ) = {ϕ , {c} , {d} , {ac} , {ad} , {bc} , {bd}  , {cd} , {acd} , {bcd} , X}.Let f: (X, τ) →(Y, σ ) be defined  by f(a) = a = f(c) ,  f(d) = b , f(b) = d. clearly, f is contra  g$\alpha$ continuous , but f$^{-1}$ ({a}) = {ac} is not $\alpha$ *- closed in X. Therefore, f is not contra $\alpha$ * continuous.

**Remark 3.18:**  The concept of  $\alpha$ * continuous and contra $\alpha$ * continuous are independent.

**Example 3.19:** Let X = Y= {a, b, c, d}, τ = { ϕ , {a} , {b} , {ab} , {abc} , X } and σ = { ϕ , {a} , {b} {ab},{bc},{abc},Y}, $\alpha$ *O (X,τ)={ϕ, {a} , {b} , {c} , {ab} , {ac} , {bc} , {abc} , {abd} , X}   $\alpha$ *C (X, τ) = { ϕ , {c} , {d} , {ad} ,{bd} , {cd} , {abd} ,{acd}, {bcd}, X} . Let f: (X, τ) →(Y, σ ) be a map defined by f (c) = a, f(a) = f(b) = b,f(d) = c , clearly, f is $\alpha$ * continuous but f is not contra $\alpha$ * - continuous because f$^{-1}$ ({b}) = {ab} is not $\alpha$ * - closed.

**Example 3.20:** Let  X = Y = {a, b, c, d},  τ = {ϕ,{a}, {b},{ab}, {bc} ,{abc}, X}, and σ = {ϕ, {a},{b},{c},{ab},{ac},{bc},{abc},Y}. $\alpha$ *C(X, τ) = {ϕ , {c} , {d} , {ad} ,{bd}, {cd} , {abd} , {acd} , {bcd} , X }. $\alpha$ *O(X, τ) = {ϕ , {a} , {b} , {c} , {ab} , {ac} , {bc} , {abc} , {abd} , X}.Let f: (X, τ) →(Y, σ ) be defined  by f(b) = a = f(d) ,  f(c) = b , f(a) = d. clearly, f is contra $\alpha$ * continuous , but f$^{-1}$ ({a}) = {bd} is not $\alpha$ *- open in X. Therefore, f is not $\alpha$ * continuous.

**Remark 3.21:** The composition of two contra $\alpha$ * continuous need not be contra $\alpha$ * continuous.

**Example 3.22:** Consider  X = Y = Z = {a, b, c }, τ = {ϕ,{a},{ab},{ac}, X} and σ = {ϕ, {a},{b} ,{ab},Y}, $\eta$ ={ϕ,{a},{ab},Z}, $\alpha$ *C(X, τ) = {ϕ,{b},{c},{bc},X}, $\alpha$ *C (Y, σ ) = {ϕ , {b}, {c},{ac},{bc}, Y}. Let f: (X, τ) →(Y, σ ) be defined by f(b) = a , f(c) = b, f(a) = c. Clearly, f is contra $\alpha$ *continuous. Consider the map  g: Y → Z defined  g(b) = a, g(c) = b, g(b) = c , clearly g is contra $\alpha$ *continuous. But g ∘f : X → Z is not a contra $\alpha$ *continuous, ( g ∘f)$^{-1}$ ({ab} ) = f$^{-1}$ (g$^{-1}${ab}) = f$^{-1}$ (bc) = ac which is not a $\alpha$ *closed in X.

**Theorem 3.23:** Let f: (X, τ) → (Y, σ) be a map. The following are equivalent.
1.   f is contra $\alpha$ * continuous.
2.   The inverse image of a closed set F of Y is $\alpha$ * open in X

**Proof:** let F be a closed set in Y . Then Y\F is an open set in Y. By the assumption of  (1), f$^{-1}$(Y\F) = X \ f$^{-1}$ (F) is $\alpha$ * closed in X . It implies that f$^{-1}$ (F) is $\alpha$ * open in X. Converse is similar.

**Theorem 3.24:** The following are equivalent for a function f: (X, τ) → (Y, σ). Assume that $\alpha$ *O(X, τ) ( resp $\alpha$ *C (X, τ)) is closed under any union ( resp; intersection ).
1.   f is contra $\alpha$ * continuous.
2.   The inverse image of a closed set F of Y is $\alpha$ * open in X
3.   For each x ∈ X and each closed set B in Y with f(x) ∈ B , there exists an $\alpha$ * open set A in X such that x ∈ A and f(A) ⊂B
4.   f( $\alpha$ *cl (A))⊂ ker (f(A)) for every subset A of X.
5.   $\alpha$ *cl ( f$^{-1}$ (B)) ⊂f$^{-1}$ ( ker B ) for every subset B of Y.

**Proof:**
**(1)** ⇒ **(3)** Let x ∈ X and B be a closed set in Y with f(x) ∈ B. By (1), it follows that f$^{-1}$ ( Y\B) = X\ f$^{-1}$ (B) is $\alpha$ * closed and so f$^{-1}$ (B) is $\alpha$ * open. Take A = f$^{-1}$ (B). We obtain that x ∈ A and f(A) ⊂B.

**(3)** ⇒ **(2)** Let B be a closed set in Y with x ∈ f$^{-1}$ (B). Since,  f(x) ∈ B, by (3), there exist an $\alpha$ * open set A in X containing x such that f(A) ⊂B. It follows that x ∈ A ⊂f$^{-1}$ (B). Hence, f$^{-1}$ (B) is $\alpha$ * open.

**(2)** ⇒ **(1)** Follows from the previous theorem

**(2)** ⇒ **(4)** Let A be any subset of X. Let y ∉ ker ( f(A)). Then there exists a closed set F containing y such that f(A) ∩F = ϕ. Hence, we have  A ∩f$^{-1}$ ( F) = ϕ and  $\alpha$ *cl (A) ∩f$^{-1}$ ( F) = ϕ. Hence, we obtain f( $\alpha$ *cl (A)) ∩F = ϕ and y ∉ f( $\alpha$ *cl (A)). Thus, f( $\alpha$ *cl (A))⊂ ker (f(A)).

**(4)** ⇒ **(5)** Let B be any subset of Y. By (4) and lemma [2.13] f( $\alpha$ *cl ( f$^{-1}$ (B))) ⊂ ( ker B ) and $\alpha$ *cl ( f$^{-1}$ (B))    ⊂ f$^{-1}$ ( ker B )

---

**(5)** $\Rightarrow$ **(1)** Let B be any open set in Y. By (5) and lemma [2.13] $\alpha$ *cl ( f $^{-1}$ (B)) $\subset$ f $^{-1}$ ( ker B ) = f $^{-1}$ (B) and $\alpha$ *cl ( f $^{-1}$ (B)) = f $^{-1}$ (B). We obtain that f $^{-1}$ (B) is $\alpha$ * closed in X.

**Theorem 3.25:** If f: (X, τ) $\rightarrow$ (Y, σ) is $\alpha$ *irresolute and g: (Y, σ) $\rightarrow$ (Z, $\eta$ ) is contra $\alpha$ * continuous , then their composition g ∘ f: (X, τ) $\rightarrow$ (Z, $\eta$ ) is contra $\alpha$ * continuous.

**Proof:** Let O be any open set in (Z, $\eta$ ). Since, g is contra $\alpha$ * continuous, then g$^{-1}$(O) is $\alpha$ * closed in (Y, σ) and since f is $\alpha$ *irresolute , then f $^{-1}$( g $^{-1}$ (O)) is $\alpha$ * closed in (X, τ) . Therefore, g ∘ f is contra $\alpha$ * continuous.

**Theorem 3.26:** If f: (X, τ) $\rightarrow$ (Y, σ) is contra $\alpha$ * continuous g: (Y, σ) $\rightarrow$ (Z, $\eta$ ) is continuous, then their composition g ∘ f: (X, τ) $\rightarrow$ (Z, $\eta$ ) is contra $\alpha$ * continuous.

**Proof:** Let O be any open set in (Z, $\eta$ ). Since, g is continuous, then g$^{-1}$(O) is open in (Y, σ) and since f is contra $\alpha$ * continuous, then f$^{-1}$( g $^{-1}$ (O)) is $\alpha$ * closed in (X, τ). Therefore, g ∘ f is contra $\alpha$ * continuous.

**Theorem 3.27:** If f: (X, τ) $\rightarrow$ (Y, σ) is contra $\alpha$ continuous g: (Y, σ) $\rightarrow$ (Z, $\eta$ ) is continuous, then their composition g ∘ f: (X, τ) $\rightarrow$ (Z, $\eta$ ) is contra $\alpha$ * continuous.

**Proof:** Let O be any open set in (Z, $\eta$ ). Since, g is continuous, then g$^{-1}$(O) is open in (Y, σ) and since f is contra $\alpha$ continuous, then f$^{-1}$( g $^{-1}$ (O)) is $\alpha$ closed in (X, τ).Hence by thm [2.15], every $\alpha$ closed set is $\alpha$ * closed. We have f$^{-1}$( g $^{-1}$ (O)) is $\alpha$ * closed in (X, τ). Therefore, g ∘ f is contra $\alpha$ * continuous.

**Theorem 3.28:** If f: (X, τ) $\rightarrow$ (Y, σ) is contra $\alpha$ * continuous g: (Y, σ) $\rightarrow$ (Z, $\eta$ ) is g-continuous, then their composition g ∘ f: (X, τ) $\rightarrow$ (Z, $\eta$ ) is contra $\alpha$ * continuous.

**Proof:** Let O be any open set in (Z, $\eta$ ). Since, g is g- continuous, then g$^{-1}$(O) is g- open in (Y, σ) and since f is contra $\alpha$ * continuous, then f$^{-1}$( g $^{-1}$ (O)) is $\alpha$ * closed in (X, τ). Therefore, g ∘ f is contra $\alpha$ * continuous.

**Theorem 3.29:** If f: (X, τ) $\rightarrow$ (Y, σ) is strongly $\alpha$ * continuous and g: (Y, σ) $\rightarrow$ (Z, $\eta$ ) is contra $\alpha$ * continuous , then their composition g ∘ f: (X, τ) $\rightarrow$ (Z, $\eta$ ) is contra continuous.

**Proof:** Let O any open set in (Z, $\eta$ ). Since, g is contra $\alpha$ * continuous, then g$^{-1}$(O) is $\alpha$ * closed in (Y, σ) and since f is strongly $\alpha$ * continuous, f$^{-1}$( g $^{-1}$ (O)) is closed in (X, τ). Therefore, g ∘ f is contra continuous.

**Theorem 3.30:** If f: (X, τ) $\rightarrow$ (Y, σ) is perfectly $\alpha$ * continuous, and g: (Y, σ) $\rightarrow$ (Z, $\eta$ ) is contra $\alpha$ * continuous, then their composition g ∘ f: (X, τ) $\rightarrow$ (Z, $\eta$ ) is .

**Proof:** Let O any open set in (Z, $\eta$ ). By thm [2.15] every open set is $\alpha$ * open set which implies O is $\alpha$ * open in (Z, $\eta$ ). Since, g is contra $\alpha$ * continuous, then g$^{-1}$(O) is $\alpha$ * closed in (Y, σ) and since f is perfectly $\alpha$ * continuous , then f $^{-1}$ ( g $^{-1}$(O)) is both open and closed in X, which implies (g ∘ f) $^{-1}$ (O) is both open and closed in X . Therefore, g ∘ f is perfectly $\alpha$ * continuous.

**Theorem 3.31:** Let f: (X, τ) $\rightarrow$ (Y, σ) is surjective $\alpha$ *irresolute and $\alpha$ * open and g: (Y, σ) $\rightarrow$ (Z, $\eta$ ) be any function. Then g ∘ f: (X, τ) $\rightarrow$ (Z, $\eta$ ) is contra $\alpha$ * continuous if and only if g is contra $\alpha$ * continuous.

**Proof:** The if part is easy to prove. To prove the only if part , let F be any closed set in (Z, $\eta$ ). Since g ∘ f is contra $\alpha$ * continuous, then f $^{-1}$( g $^{-1}$ (F)) is $\alpha$ * open in (X, τ) and since f is $\alpha$ * open surjection, then f(f$^{-1}$( g $^{-1}$ (F))) = g$^{-1}$ (F) is $\alpha$ * open in (Y, σ). Therefore, g is contra $\alpha$ * continuous.

**Theorem 3.32:** Let f: (X, τ) $\rightarrow$ (Y, σ) be a function and X a $\alpha$ * T$_{1/2}$ space. Then the following are equivalent:
1. f is contra continuous
2. f is contra $\alpha$ * continuous

**Proof:**
(1) $\Rightarrow$ (2) Let O be any open set in (Y, σ). Since f is contra continuous, f$^{-1}$ (O) is closed in (X, τ) and since Every closed set is $\alpha$ *closed, f$^{-1}$ (O) is $\alpha$ *closed in (X, τ). Therefore, f is contra $\alpha$ * continuous.
(2) $\Rightarrow$ (1) Let O be any open set in (Y, σ). Since, f is contra $\alpha$ * continuous, f$^{-1}$ (O) is $\alpha$ *closed in (X, τ) and since X is $\alpha$ * T$_{1/2}$ space, f$^{-1}$ (O) is closed in (X, τ). Therefore, f is contra continuous.

**Theorem 3.33:** If f: (X, τ) $\rightarrow$ (Y, σ) is contra $\alpha$ * continuous and (Y, σ) is regular , then f is $\alpha$ *continuous.

**Proof:** Let x be an arbitrary point of X and O be any open set of Y containing f(x). Since Y is regular, there exists an open set U in Y containing f(x) such that cl(U) $\subset$ O. Since, f is contra $\alpha$ * continuous, so by thm[3.24] , there exists N $\in$ $\alpha$ *O (X, τ) , such that f(N) $\subset$ cl(U) . Then, f(N) $\subset$ O. Hence by thm[2.14], f is $\alpha$ *continuous.

**Theorem 3.34:** If f is $\alpha$ *continuous and if Y is locally indiscrete, then f is contra $\alpha$ *continuous.

**Proof:** Let O be an open set of Y. Since Y is locally discrete, O is closed. Since, f is $\alpha$ *continuous, f $^{-1}$(O) is $\alpha$ * closed in X. Therefore, f is contra $\alpha$ *continuous.

**Theorem 3.35:** If a function f : (X, τ) →(Y, σ ) is continuous and X is a locally indiscrete space, then f is contra $\alpha$ *continuous.

**Proof:** Let O be any open set in (Y, σ ). Since f is continuous f $^{-1}$ (O) is open in X. and since X is locally discrete, f $^{-1}$ (O) is closed in X. Every closed set is $\alpha$ * closed. f $^{-1}$ (O) is $\alpha$ * closed in X. Therefore, f is contra $\alpha$ *continuous

**Theorem 3.36:** Let f: (X, τ) → (Y, σ) be a function and g: X → X × Y the graph function, given by g(x) = ( x,f(x)) for every x ∈ X . Then f is contra $\alpha$ * continuous if g is contra $\alpha$ * continuous.

**Proof:** Let F be a closed subset of Y. Then X × F is a closed subset of X × Y. Since g is a contra $\alpha$ * continuous, then g $^{-1}$(X × F) is a $\alpha$ *open subset of X. Also, g $^{-1}$(X × F) = f $^{-1}$(F). Hence, f is contra $\alpha$ * continuous.

**Theorem 3.37:** Let {$X_i$ / i ∈ I}be any family of topological spaces. If f : X → ΠX$_i$ is a contra $\alpha$ * continuous function. then $\pi_i$ ∘ f : X → X$_i$ is contra $\alpha$ * continuous for each i ∈ I, where $\pi_i$ is the projection of ΠX$_i$ onto X$_i$ .

**Proof:** Suppose U$_i$ is an arbitrary open sets in X$_i$ for i ∈ I. Then $\pi_i$ $^{-1}$(U$_i$)is open in ΠX$_i$. Since f is contra $\alpha$ * continuous, f $^{-1}$ ( $\pi_i$ $^{-1}$(U$_i$)) = ( $\pi_i$ ∘ f ) $^{-1}$ (U$_i$ ) is $\alpha$ * closed in X. Therefore, $\pi_i$ ∘ f is contra $\alpha$ * continuous.

For a map f: (X, τ) → (Y, σ), the subset {( x , f(x) ): x ∈ X} ⊂ X × Y is called the graph of f and is denoted by G(f).

## IV. Contra $\alpha$ * closed graph

**Definition 4.1:** The graph G(f) of a function f: (X, τ) → (Y, σ) is said to be ***Contra $\alpha$ * closed graph*** in X × Y if for each (x,y) ∈ (X × Y) - G(f) there exists U ∈ $\alpha$ *O (X, τ) and V∈ C (Y, y) such that ( U × V) ∩ G(f) = ϕ.

**Lemma 4.2:** The graph G(f) of a function f: (X, τ) → (Y, σ) is $\alpha$ * closed in (X × Y) if and only if for each (x,y) ∈ (X × Y) - G(f) , there exists an U∈ $\alpha$ *O (X, x) and an open set V in Y containing y such that f(U) ∩ V = ϕ.

**Proof:** We shall prove that f(U) ∩ V = ϕ ⇔ ( U × V) ∩ G(f) = ϕ. Let ( U × V) ∩ G(f) ≠ ϕ. Then there exists (x,y) ∈ (X × Y) and (x,y) ∈ G(f). This implies that x ∈ U, y ∈ V and y = f(x) ∈ V. Therefore, f(U) ∩ V ≠ ϕ. Hence the result follows.

**Theorem 4.3:** If f: (X, τ) → (Y, σ) is contra $\alpha$ * continuous and Y is Urysohn, G(f) is a contra $\alpha$ * closed graph in X × Y.

**Proof:** Let (x,y) ∈ (X × Y) - G(f), then y ≠ f(x) and there exist open sets A and B such that f(x) ∈ A , y ∈ B and cl(A) ∩ cl(B) = ϕ. Since f is contra $\alpha$ * continuous, there exist O∈ $\alpha$ *O (X, x) such that f(O) ⊂ cl(A). Therefore, we obtain f(O) ∩ cl(B) = ϕ. Hence by lemma [4.2], G(f) is contra $\alpha$ * closed graph in X × Y.

**Theorem 4.4:** If f: (X, τ) → (Y, σ) is $\alpha$ * continuous and Y is T$_1$, then G(f) is Contra $\alpha$ * closed graph in X × Y.

**Proof:** Let (x,y) ∈ (X × Y) - G(f), then y ≠ f(x) and since Y is T$_1$ there exists open set V of Y, such that f(x) ∈ V, y∉ V. Since f is $\alpha$ * continuous, there exist $\alpha$ * open set U of X containing x such that f(U) ⊂ V. Therefore, f(U) ∩ ( Y – V ) = ϕ and Y –V is a closed set in Y containing y. Hence by lemma [4.2], G(f) is Contra $\alpha$ * closed graph in X × Y.

**Definition 4.5** A function f: (X, τ) → (Y, σ) is called ***almost contra $\alpha$ * continuous*** if f $^{-1}$(O) is $\alpha$ *closed set in X for every regular open set O in Y.

**Theorem 4.6** Every contra $\alpha$ *continuous function is almost contra $\alpha$ *continuous.

**Proof**: Let O be a regular open set in Y. Since, every regular open set is open which implies O is open in Y. Since f : (X, τ) → (Y, σ) is contra $\alpha$ *continuous then f $^{-1}$ (O) is $\alpha$ * closed in X. Therefore, f is almost contra $\alpha$ *continuous.

**Remark 4.7:** The converse of the above theorem need not be true.

**Example 4.8:** Let X = Y = {a, b, c}, σ = {ϕ, {a},{b},{ab},Y}.RO(Y, σ) = { ϕ, {a},{b},Y}, $\alpha$ *C(X, τ) = {ϕ , {a},{b},{c} , {ab} ,{bc}, {ac} , X }. Let f : (X, τ) →(Y, σ ) be defined by f(a) = a , f(b) = b = f(c). clearly, f is contra $\alpha$ * continuous , but f $^{-1}$ ({b}) = {bc} is not regular open in X. Therefore, f is not almost contra $\alpha$ * continuous.

**Theorem 4.9:** The following are equivalent for a function f: (X, τ) → (Y, σ)
1.  f is almost contra $\alpha$ *continuous.
2.  f $^{-1}$(F) is $\alpha$ *open in X for every regular closed set F in Y.

3. for each x ∈ X and each regular open set F of Y containing f(x), there exists U ∈ $\alpha$ \*O(X,x) such that f(U) ⊂ F

4. for each x ∈ X and each regular open set V of Y non – containing f(x), there exists an $\alpha$ \* closed set K of X non – containing x such that f$^{-1}$(V) ⊂ K

**Proof:**

(1) ⇔ (2) Let F be any regular closed set of Y. Then ( Y – F ) is regular open and therefore f$^{-1}$( Y – F ) = X - f$^{-1}$(F ) ∈ $\alpha$ \*C (X). Hence, f$^{-1}$(F ) is $\alpha$ \* open in X. The converse part is obvious.

(2) ⇒ (3) Let F be any regular closed set of Y containing f(x). Then f$^{-1}$(F ) is $\alpha$ \* open in X and x ∈ f$^{-1}$(F ). Taking U = f$^{-1}$(F ) we get f(U) ⊂ F .

(3) ⇒ (2) Let F be any regular closed set of Y and x ∈ f$^{-1}$(F ). Then there exists U$_x$ ∈ $\alpha$ \*O (X,x) such that f(U$_x$) ⊂ F and so U$_x$ ⊂ f$^{-1}$(F) .Also, we have f$^{-1}$(F) ⊂ ∪ $_{x ∈ f^{-1}(F)}$U$_x$. Hence, f$^{-1}$(F ) is $\alpha$ \* open in X.

(3) ⇔ (4) Let V be any regular open set of Y non containing f(x). Then ( Y – V ) is regular closed set in Y containing f(x). Hence by (c) , there exists U∈ $\alpha$ \*O (X,x) such that f(U) ⊂ ( Y – V ). Hence, U ⊂ f$^{-1}$(Y – V) ⊂ X - f$^{-1}$(V ) and so f$^{-1}$(V ) ⊂ ( X – U ). Now, since U∈ $\alpha$ \*O (X), (X-U) is $\alpha$ \* closed set of X not containing x. The converse part is obvious.

**Definition 4.7:** A space X is said to be *locally $\alpha$ \* indiscrete* if every $\alpha$ \*open set of X is closed in X.

**Theorem 4.8:** A contra $\alpha$ \*continuous function f : (X, τ) →(Y, σ ) is continuous when X is locally $\alpha$ \* indiscrete.

**Proof:** Let O be an open set in Y. Since, f is contra $\alpha$ \*continuous then f$^{-1}$(O) is $\alpha$ \* closed in X. Since, X is locally $\alpha$ \* indiscrete which implies f$^{-1}$(O) is open in X. Therefore, f is continuous.

**Theorem 4.9:** Let f : (X, τ) →(Y, σ ) is $\alpha$ \*irresolute map with Y as locally $\alpha$ \* indiscrete space and g: (Y, σ) → (Z, $\eta$ ) is contra $\alpha$ \*continuous, then g ∘ f is $\alpha$ \*continuous.

**Proof:** Let B be any closed set in Z. Since g is contra $\alpha$ \*continuous, g$^{-1}$(B) is $\alpha$ \* open in Y. But Y is locally $\alpha$ \* indiscrete, g$^{-1}$(B) is closed in Y. Hence, g$^{-1}$(B) is $\alpha$ \*closed in Y. Since, f is $\alpha$ \*irresolute, f$^{-1}$(g$^{-1}$(B)) = (g ∘ f )$^{-1}$(B) is $\alpha$ \*closed in X. Therefore, g ∘ f is $\alpha$ \*continuous.

**Definition 4.10:** A map f : (X, τ) →(Y, σ ) is said to be *pre $\alpha$ \*open* if the image of every $\alpha$ \*open set of X is $\alpha$ \*open in Y.

**Theorem 4.11:** Let f : (X, τ) →(Y, σ ) be surjective $\alpha$ \* irresolute pre $\alpha$ \*open and g: (Y, σ) → (Z, $\eta$ ) be any map. Then g ∘ f: (X, τ) → (Z, $\eta$ ) is contra $\alpha$ \*continuous if and only if g is contra $\alpha$ \*continuous.

**Proof:** The if part is easy to prove. To prove the " only if " part , let g ∘ f: (X, τ) → (Z, $\eta$ ) be contra $\alpha$ \*continuous and let B be a closed subset of Z. Then (g ∘ f) $^{-1}$ (B) is $\alpha$ \*open in X which implies f$^{-1}$(g$^{-1}$(B)) is $\alpha$ \*open in X. Since, f is pre $\alpha$ \*open, f(f$^{-1}$(g$^{-1}$(B))) is $\alpha$ \*open of X. So, g$^{-1}$(B) $\alpha$ \*open in Y. Therefore, g is contra $\alpha$ \*continuous.

# REFERENCE

[1] K.Alli , **Contra g#p-Continuous Functions,** International Journal of Mathematics Trends and Technology- Volume 4 Issue 11- Dec 2013

[2] M. Caldas, S. Jafari, T. Noiri, M. Simeos, **A new generalization of contra-continuity** via Levines g-closed sets, Chaos Solitons Fractals 42 (2007), 1595–1603.

[3] J. Dontchev, **Contra-continuous functions and strongly S-closed spaces**, Internat. J.Math. Math. Sci. 19 (1996), 303–310.

[5] J. Dontchev, T. Noiri, **Contra-semicontinuous functions,** Math. Pannon. 10 (1999),159–168.

[6] S. Jafari, T. Noiri, **Contra $\alpha$ continuous functions between topological spaces**, Iran.Int. J. Sci. 2 (2001), 153–167.

[7] S. Jafari, T. Noiri, **Contra-super-continuous functions**, Ann. Univ. Sci. Budapest 42(1999), 27–34.

[8] M. Mrsevic, **On pairwise R0 and pairwise R1 bitopological spaces**, Bull. Math. Soc.Sci. Math. R.S. Roumanie 30(78) (1986), 141–148.

[9] Pious Missier .S and P.Anbarasi Rodrigo, **Some Notions of nearly open sets in Topological Spaces**, International Journal of Mathematical Archive 4(12), 2013, 1-7

[10] Pious Missier .S and P.Anbarasi Rodrigo, **On $\alpha$ \*-Continuous** , Outreach Multi Displinary Research Journal ( Accepted)

[11] Pious Missier .S and P.Anbarasi Rodrigo, **Strongly $\alpha$ \*-Continuous functions in topological spaces,** International Organization of Scientific Research

# Modal Analysis of Fibre Reinforced Composite Beams with a Transverse Crack Using ANSYS

Syed Ayesha Yasmeen[1], Anantha Abhijit P [2], Dr. D. Srinivasa Rao[3]

*[1,2] Graduate Students, Department of Mechanical Engineering, DMSSVH College of Engineering, Machilipatnam, India*

*[3] Professor, Department of Mechanical Engineering, DMSSVH College of Engineering, Machilipatnam, India*

***Abstract:*** *In many structures like high speed machineries, aircrafts and light weight structures composite beams and beam like structures are main constituent elements. Cracks induced in these structural elements cause serious failure and monitoring of these cracks is essential. The presence of these cracks influences the dynamic characteristics of the structural elements. Hence the changes in natural frequencies and mode shapes have been the subject of interest of many investigations. In the present work two Fiber- Reinforced Plastic (FRP) materials, Graphite Fibre Reinforced Polyamide and E-Glass Fibre Reinforced Polymer have been selected as beam materials for modal analysis using ANSYS 13.0. The analysis is carried out for these two beams in different ways. Initially the analysis is carried out for different orientation of fibres for two beams. Later the effect of dimensions is analyzed by varying one dimension of the beam at a time by keeping the other two constant. In the next step the analysis is performed for constant dimensions of each beam for same layer orientation and constant volume fraction of fibre by introducing transverse cracks of different depths at various positions along the length of the beam. The results obtained are analyzed.*

***Keywords****: ANSYS, Crack, Fibre- Reinforced Composite beams, Modal Analysis, Natural frequency.*

## I. Introduction

In the modern decades, different engineering fields like automobile, aerospace, naval, and civil use fiber reinforced composite materials by some means. The various properties of composite materials like high strength, low weight, resistance to corrosion, impact resistance, and high fatigue strength increase their reputation. Fiber-reinforced composite beams include the major collection of structural members, which are extensively used as movable elements, such as robot arms, rotating machine parts, and helicopter and turbine blades. Structural damage recognition has gained increasing deliberation from the scientific society since unexpected major hazards, most with human losses, have been reported. Aircraft crashes and the catastrophic bridge failures are a few illustrations. The cracks can be present in structures due to their limited fatigue strengths or due to the manufacturing processes. These cracks open for a part of the cycle and close when the vibration reverses its direction.

These cracks will grow over time, as the load reversals persist, and may reach a point where they pose a peril to the integrity of the structure. As a consequence, all such structures must be cautiously maintained and more generally, SHM denotes a consistent system with the aptitude to detect and interpret adverse "change" in a structure due to damage or normal operation. This was studied by Ramanamurty[5] . The greatest confront in designing a SHM system is to recognize the emphasize changes due to damage or defect. Lots of damage recognition techniques have been proposed for structural health monitoring. Some of the nondestructive evaluation approaches that exploit technologies such as X-ray imaging, ultrasonic scans, infrared thermograph, and eddy current can recognize damages. However, they are somehow complicated to implement, and some of them are unfeasible in many cases such as in service aircraft testing and in-site space structures. Hence, the vibration-based damage identification method as a global damage recognition technique is developed to surmount these difficulties.

A composite material is defined as a material system which consists of a mixture or combination of two or more specifically dissimilar materials which are insoluble in each other and vary in form or chemical composition. Composite materials of two phase system are classified into two widespread groups. They are particulate composites and fiber-reinforced composites. Particulate composites are those particles having assorted shapes and sizes are dissipated with in a matrix in a random fashion examples are mica flakes reinforced with glass, lead particles in copper alloys and silicon carbon particles in aluminum. Particulate composites are used for electrical applications, welding, machine parts and other purposes.

Fiber-reinforced composite material consists of fibers of significant strength and stiffness embedded in a matrix with perceptible boundaries between them. Both fibers and matrix maintain their physical and chemical characters, as their combination achieves a function which cannot be done by each constituent acting individually. Fibers of fiber-reinforced plastics (FRP) may be short or continuous. FRP'S having continuous fibers appear to be more efficient indeed. According to the type of the matrix used FRP composite materials are classified in to four broad categories. They are polymer matrix composites, metal matrix composites, ceramic composites and carbon/carbon composites. Polymer matrix composites are made of thermo plastics or thermo set resins reinforced with fibers such as glass, carbon or boron. A metal matrix composite consists of a matrix of metals or alloys reinforced with metal fibers such as boron or carbon. Ceramic matrix composites consist of ceramic matrices reinforced with ceramic fibers such as silicon carbide alumina of silicon nitrate. Their applications are more effectual at elevated temperatures.

Nikpur and Dimargonas[1] developed the local compliance matrix for unidirectional composite materials. The extent of anisotropy in composites found as a function for increase of interlocking deflection modes were shown in their works. Manivasagam and Chandrasekaran [2] found reduction in fundamental frequency of layered composite materials due to presence of cracks. Krawczuk and Ostachowicz [3] examined Eigen frequencies of a cantilever beam prepared form Graphite Fiber-Reinforced Polyimide with a transverse open crack by generating two models of the beam, the effect of various parameters, the crack location, the crack depth, the volume fraction fibers and fiber's orientation were premeditated upon the deviations of natural frequencies of the beam. Ghoneam [4] investigated the dynamic characteristics of laminated composite beams with an assortment of fiber orientations and dissimilar boundary conditions in non existence and existence of cracks. The possessions of assorted crack depths and positions, boundary conditions were studied both by mathematical development and experimental analysis. The accord among the experimental and theoretical results was established well during analysis.

In the present work modal analysis using ANSYS was carried out for two composite beams of Graphite Fibre- Reinforced Polyamide and E-glass Fibre- Reinforced polymer for the purpose of study by modeling which enables saving of time and cost. Initially by modeling the beams in ANSYS and analyzing them the first three natural frequencies were estimated for different fibre orientations for same volume fraction and then the dependency of the first three natural frequencies of the beams were studied by varying the dimensions of the beams in individual directions. In the next step the variations in the first three natural frequencies due to presence of crack of different depths at various locations on the beam were studied by taking constant volume fraction and constant angle of orientation.

## II. Theoretical Analysis

Considering mid –plane symmetry the differential equation of a beam for bending, when there is no bending- stretching coupling and no shear deformation in transverse direction.

$$IS_{11} \frac{d^4\omega}{dx^4} = q(x) \dots\dots\dots\dots\dots (1)$$

If the beam involves only one layer i.e. isotropic, under the above mentioned conditions.

$$IS_{11} = EI = \frac{Ebh^3}{12} \dots\dots\dots\dots\dots (2)$$

The Poisson's ratio effects are disregarded for the beam of rectangular cross-section in beam theory.
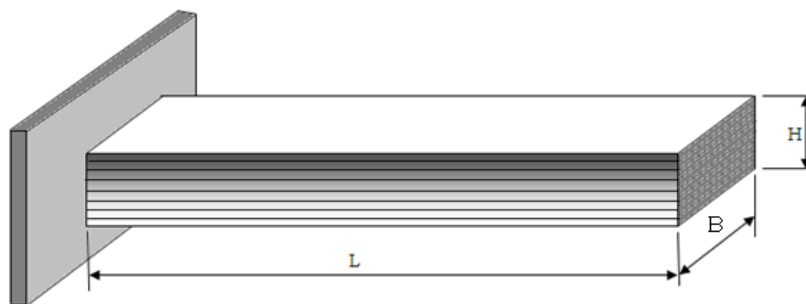


Length(L)=1000mm, Width(B)= 50mm & Height(H)=25mm
Layer Orientation ($0^0$,$45^0$, $60^0$,$90^0$,$-45^0$,$-60^0$,$-90^0$,$0^0$ )

**Figure1: Schematic diagram of composite beam of standard dimensions.**

The imposed static load is written as force per unit length in "equation1". By applying D' Alembert's principle the inertia force is applied and the "equation 1" becomes

$$IS_{11} \frac{d^4 \omega(x,t)}{dx^4} = q(x,t) - \rho F \frac{\partial^2 \omega(x,t)}{\partial x^2} \dots \dots \dots \dots (3)$$

Here $\omega$ and $q$ are the functions of time and space and their derivates become partial derivatives $\rho$ is the mass density of the beam material, and F is the cross- sectional area of the beam. The term q(x, t) is spatially varying time-dependent forcing function causing the dynamic response.

For the composite beam of rectangular cross-section having different lamina and different mass densities the above equations are used.

$$\rho F = \rho b h = \sum_{K-1}^{N} \rho b (h_k - h_{K-1}) \dots \dots \dots \dots (4)$$

By the forcing functions the natural frequencies, material properties and geometry of the beam are not affected and therefore the term q(x, t) be zero.

For the mid-plane symmetrical composite beam the natural vibration equation is given as

$$IS_{11} \frac{d^4 \omega(x,t)}{dx^4} + \rho F \frac{\partial^2 \omega(x,t)}{\partial x^2} = 0 \dots \dots \dots \dots (5)$$

The natural frequency in radians/unit time is prearranged as

$$\omega_n = \alpha^2 \sqrt{IS_{11} / \rho F L^4} \dots \dots \dots \dots (6)$$

Here $\alpha^2$ is the co- efficient $\omega_n$ is the natural frequency in cycles per second (Hertz) is prearranged as

$$f_{n=} \omega_n / 2\pi \dots \dots \dots \dots (7)$$

In common, the governing equation of the beam for free vibration is expressed as

$$[K] - \omega^2 [M]\{q\} = 0 \dots \dots \dots \dots (8)$$

K= Stiffness matrix, M= Mass matrix and q= degrees of freedom.

### III.   Modeling And Analysis Of Composite Beam Using ANSYS

Modal analysis of ANSYS is used to determine natural frequencies and mode shapes which are essential parameters in design of a structure for dynamic load conditions. The beam chosen initially is a composite beam of rectangular cross section for the purpose of analysis in two ways. The first one is for the purpose of variation in fiber orientation and the second one is for varying of the dimensions the beam. The two materials considered for compostie beam models are Graphite Fibre-Reinforced Polyamide and E-Glass Fibre-Reinforced Polymer. The orthotropic material properties of the two beams are mentioned in table1.

**Table 1**: *Properties Of Compotie Beam Materials*

| Graphite Fibre-Reinforced Ployamide | E-Glass Fibre Reinforced Polymer |
|---|---|
| $E_1$=129.207 GPa | $E_1$=57.502 GPa |
| $E_2$=$E_3$= 9.42512 GPa | $E_2$=$E_3$= 18.802 GPa |
| $G_{xy}$ = 5.15658 GPa | $G_{xy}$ = 7.446 GPa |
| $G_{xz}$=4.3053 GPa | $G_{xz}$=7.446 GPa |
| $G_{yz}$=2.5414 GPa | $G_{yz}$=7.239 GPa |
| $\nu_{xy}$=0.3 | $\nu_{xy}$=0.25 |
| $\nu_{yz}$=0.218 | $\nu_{yz}$=0.29 |
| $\nu_{yx}$=0.218 | $\nu_{yx}$=0.29 |
| $\rho$=1550.0666 Kg/m3 | $\rho$=1910 Kg/m3 |

The second model chosen for analysis is a cantilever composite beam of uniform cross-section, having an open transverse crack of depth 'a' at position $L_1$ from fixed end is shown in "Fig.2".
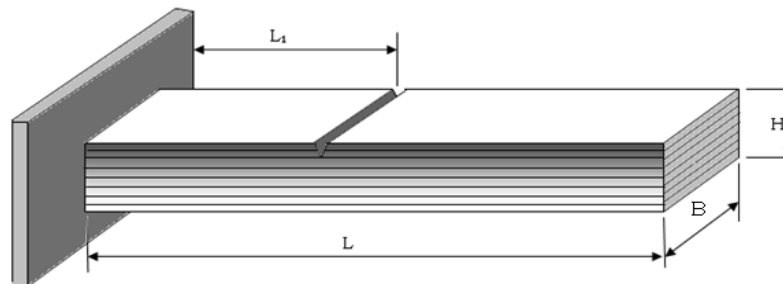


**Figure 2: Schematic Diagram of Cantilever Composite Beam with a Transverse Crack**.

**3.1 Modeling Procedure by ANSYS 13**

The ANSYS procedure for any type of problem consist of mainly three stages, namely preprocessing, solution stage and post processing stage. In preprocessing stage the element type, material properties and real constants are specified. In the solution stage the boundary conditions and loads are defined. The ANSYS postprocessor stage provides a powerful tool for viewing results. The flow chart of the ANSYS procedure is represented in "Fig.2".In the present work "SOLID SHELL190" has been selected. To create layered composites the layer thickness, material, orientation and number of integration points were specified. The beam was then created by using key points and the lines of the beam were obtained by joining these key points. These lines were then joined to obtain area. This area then extruded to get the 3dimensional beam. The boundary conditions were then applied to fix one end of the beam to make it clamped free. Modal analysis was then performed by using Block Lonczos method and the required first three natural frequencies were obtained from general post processor. The same procedure was repeated to obtain the frequencies by changing the dimensions of the composite beams of two materials considered.

The same procedure was adopted for the composite beams with a crack, by modifying the selection of key points in the initial stage to suit the generation of the crack of required dimensions at various locations on the beam.
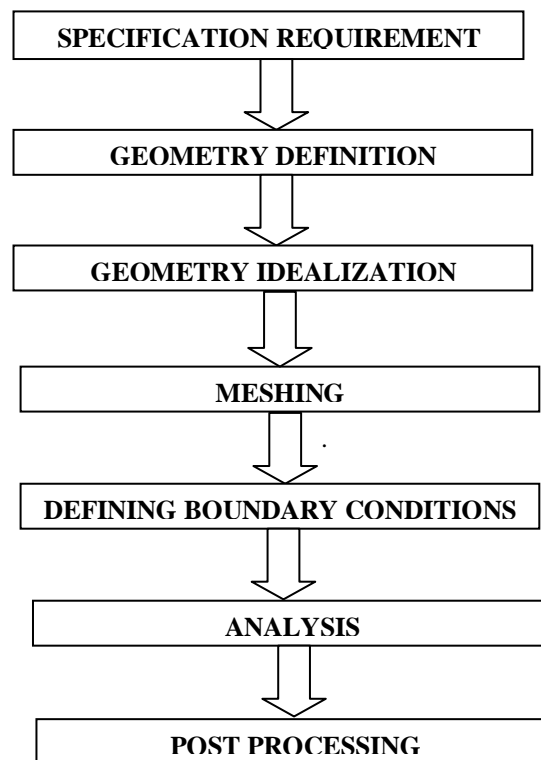


Figure 3: Flow chart representing ANSYS procedure
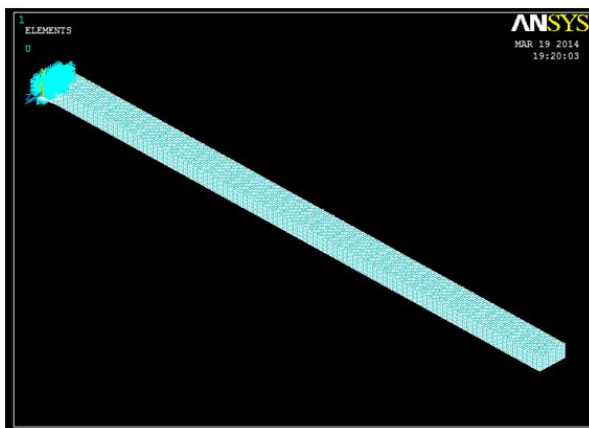


| **Figure 4: Image of the beam after applying the boundary conditions** | **Figure 5: Composite beam with crack in ANSYS** |
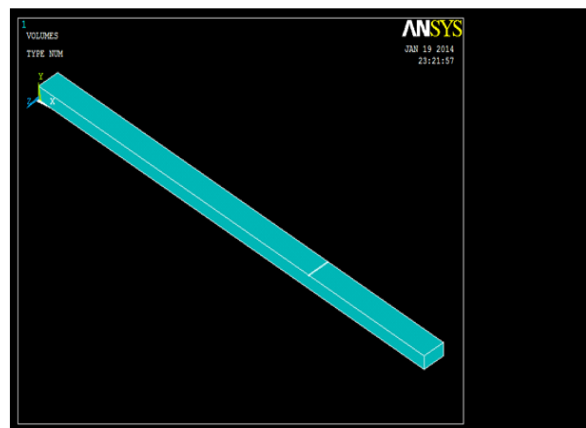
## IV. Results And Discussions

Dynamic analysis of composite beams of two different materials of Fibre -reinforced Plastics (FRP) are considered for the purpose of analysis and comparison. One is Graphite Fibre-Reinforced Polyamide and the other one is E-Glass Fibre-Reinforced Polymer. Modal analysis is done using ANSYS13.0 on these beams by generating different models of the beams for the calculation of first three Natural frequencies of the beams. The analysis is carried out for different fibre orientations of the composite beams of same fibre volume fraction of 0.4. Later the analysis is continued by varying the dimensions of the beam in one direction from standard size of the beam (1000mmx50mmx25mm), by keeping the other two constant. This process is done for all three dimensions i.e. for length, width and height of the beam.

In the next step the modal analysis is also carried out for two beams of standard size considered by introducing a transverse crack of certain Crack Depth Ratio (CDR) at a particular Crack Position Ratio (CPR). The process is repeated for different CDRs at various CPRs.When the orientation of the fibres is changed from $0^0$ to $90^0$ it is observed that the natural frequency decreases with increase in the orientation of the fibres. This is shown in the from "Fig.6"to "Fig.8". When the fibres are lying along the length of the beam they support maximum share of the load on the beam. Hence the strength of the beam increases, which in turn increases the stiffness of the beam. After $70^0$ the change in all these frequencies is unaltered. Therefore it can be concluded that the natural frequencies of a composite beam is a function of angle of fibres.
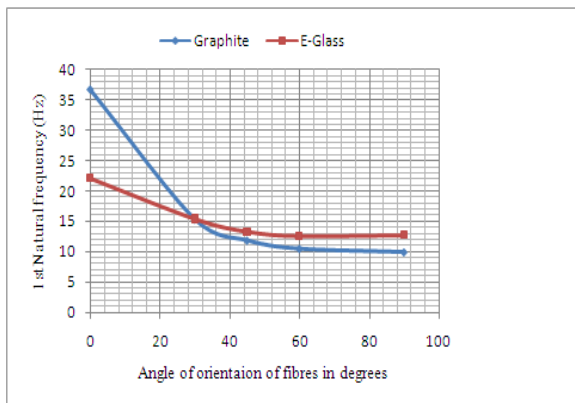


**Figure 6: Variation of 1<sup>st</sup> natural frequency with angle of orientation of fibres**
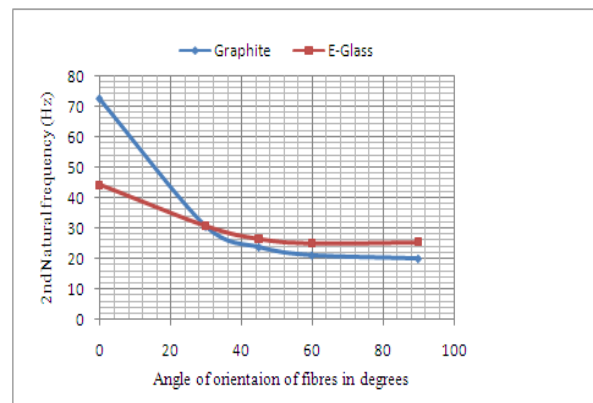


**Figure 7: Variation of 2<sup>nd</sup> natural frequency with angle of orientation of fibres**
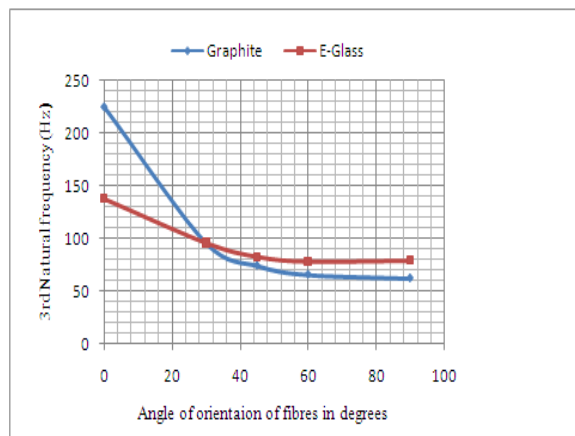


**Figure 8: Variation of 3<sup>rd</sup> natural frequency with angle of orientation of fibres**
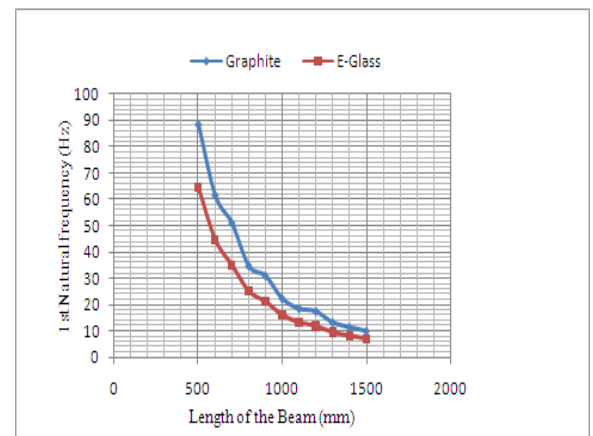


**Figure 9: Variation of 1st natural frequency with length of the beam**
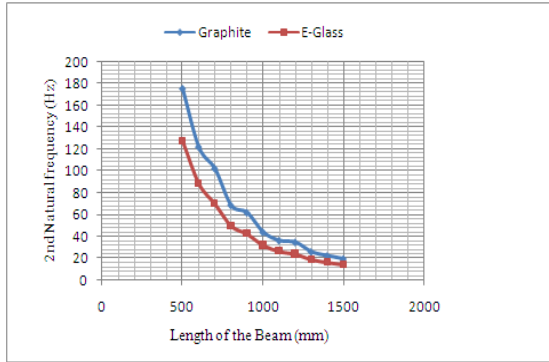
**Figure 10: Variation of 2<sup>nd</sup> natural frequency with length of the beam**
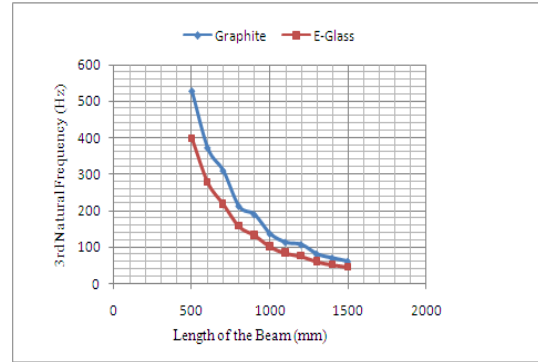


**Figure 11: Variation of 3<sup>rd</sup> natural frequency with length of the beam**
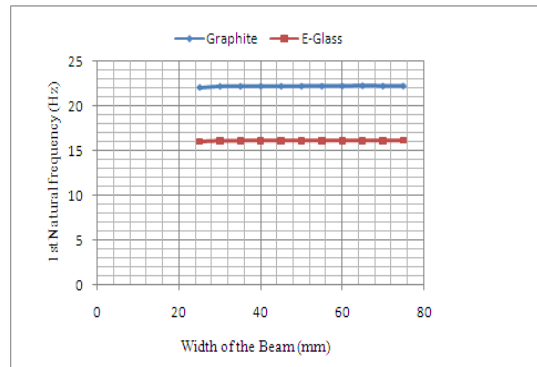


**Figure 12: Variation of 1<sup>st</sup> natural frequency with width of the beam**
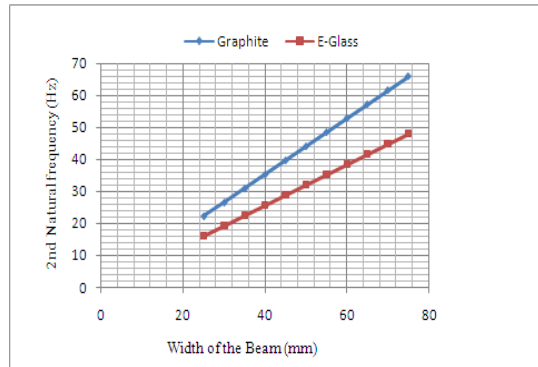


**Figure 13: Variation of 2<sup>nd</sup> natural frequency with width of the beam**
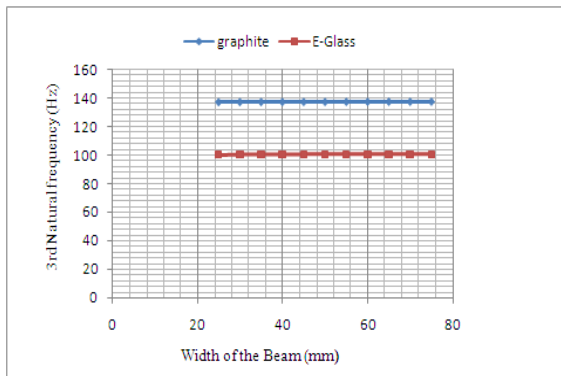


**Figure 14: Variation of 3<sup>rd</sup> natural frequency with width of the beam**
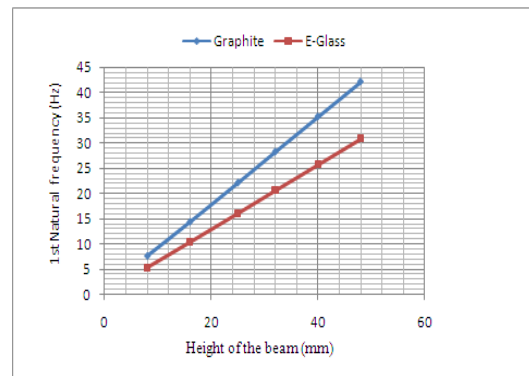


**Figure 15: Variation of 1<sup>st</sup> natural frequency with height of the beam**
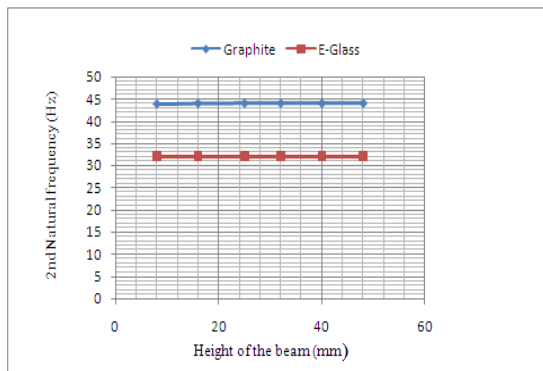


**Figure 16: Variation of 2<sup>nd</sup> natural frequency with height of the beam**
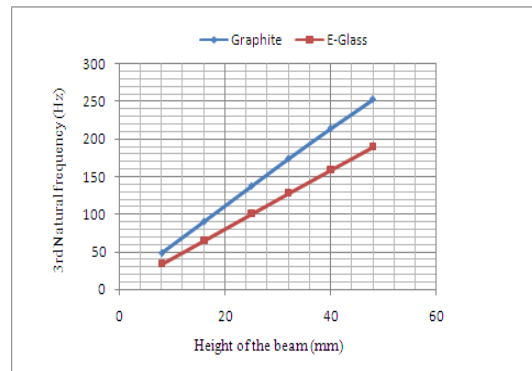


**Figure 17: Variation of 3<sup>rd</sup> natural frequency with height of the beam**
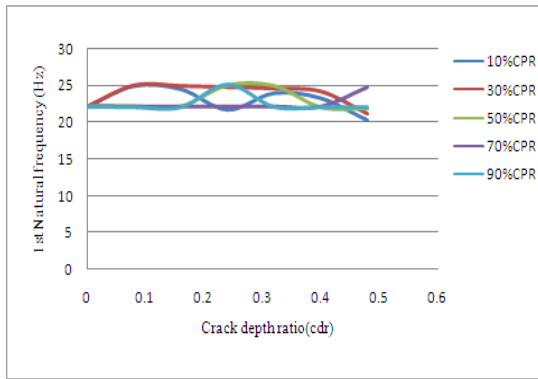
**Figure18: CDR Vs 1st natural frequency for various crack positions (graphite)**
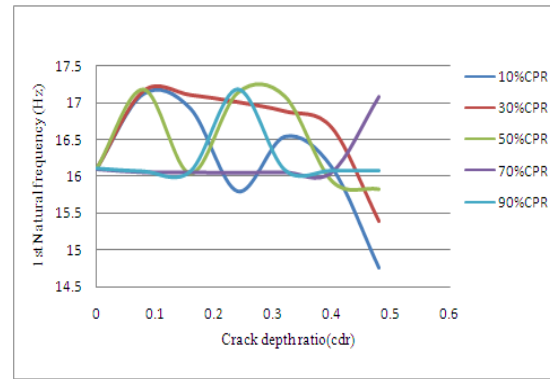


**Figure19: CDR Vs 1st natural frequency for various crack positions (E-glass)**
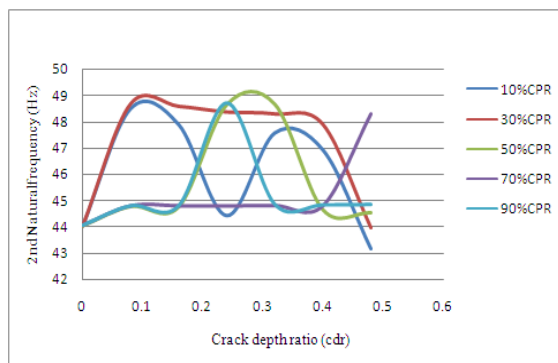


**Figure20: CDR Vs 2nd natural frequency for various crack positions (graphite)**
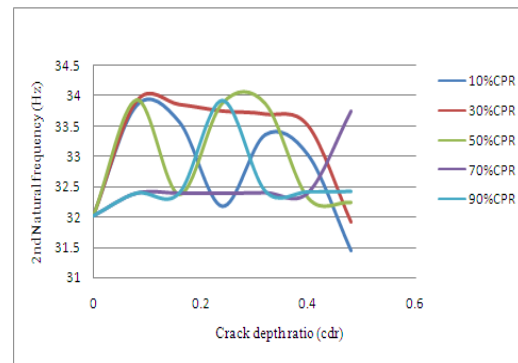


**Figure21: CDR Vs 2nd natural frequency for various crack positions (E-glass)**
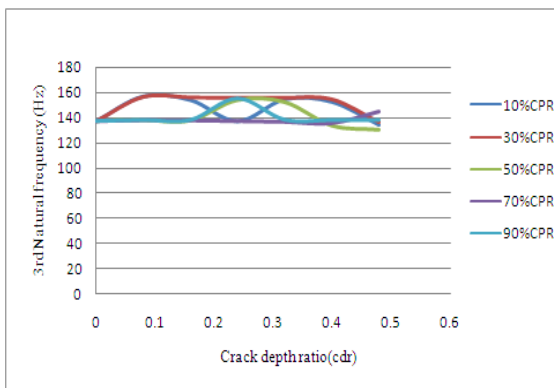


**Figure22: CDR Vs 3rd natural frequency for various crack positions (graphite)**
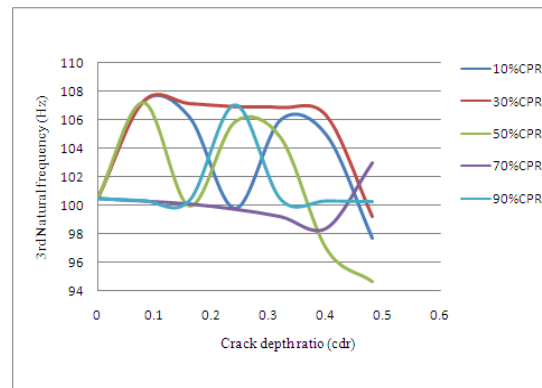


**Figure23: CDR Vs 3rd natural frequency for various crack positions (E-glass)**

The next analysis is carried out for variation of natural frequencies for length of the beam. It is observed that as the length of the composite beam increases the 1st three natural frequencies decreases. This is because the natural frequency is directly proportional to square root of stiffness of the beam and the stiffness of the beam is inversely proportional to cube of length. These variations are shown form "Fig. 9" to "Fig.11".

It is observed from the first three natural frequencies obtained, the variation in natural frequency with width of the composite beams shows similar pattern for 1st and 3rd and another same pattern for 2nd natural frequencies. These variations are shown in from "Fig.12" to "Fig14". The natural frequency is proportional to square root of stiffness of the beam and the stiffness is directly proportional to the width of the beam. The variation of the pattern may be due to different fibre orientation. As the height of the composite beam increases the first three natural frequencies increase. As height increases for constant length and width, the stiffness of the beam increases and in turn results in increase of natural frequency as stiffness is directly proportional to the cube of the height of the beam. In the second natural frequency this variation is not that much significant and fibre orientation may be one of the reasons.

There is no significant change in variation of the natural frequencies for intact and cracked beam when the crack depth ratio (CDR) is small. In general for a beam of uniform cross section of same material as the crack depth increases the natural frequency decreases and as the position of crack of constant depth shifts from fixed to free end the natural frequency increases. But in composite beams considered here interestingly a variety of pattern is observed. In both Graphite Fibre-Reinforced Polyamide and E-Glass Fibre-Reinforced Polymer beams when the crack is located nearer to clamped end (at 30% CPR) and when the position of crack is at free end (at 70% CPR), the patterns obtained are similar i.e. the frequencies decrease with increase in depth of crack and when the CDR crosses 0.4 they exhibit opposite nature with same type of variation. When the crack is located very nearer to clamped end (at 10% CPR), in the mid way of the beams (at 50%CPR) and at the end of the beam (at 90% CPR) the variation of natural frequencies with crack positions follows a wavy nature depending upon its depth. These variations are shown from the "Fig.18" to "Fig.23". The pattern obtained follows a systematic way for each position of the crack. This may be due to variation in the flexibility of the beam. The non-uniformity of material of the beam and the different orientation of the fibres may cause another reason. These variations can be used to identify the presence of cracks in composite beams. This can be applied to various composite beams of various fibre volumes fractions with various fibre orientations.

## V. Conclusions

The following conclusions can be drawn from the present investigations of the composite beam having transverse open crack. The in-plane bending frequencies decrease, in general, as the fiber angle increases; the maximum frequency occurs at $\alpha = 0°$ and decrease gradually with increasing the fibre angle up to a minimum value obtained for $\alpha = 90°$. It is found that all the first three natural frequencies of composite beams of the two materials decrease as the length of the beam increases. It is observed from the first three natural frequencies obtained, the variation in natural frequency with width of the composite beams shows similar pattern for 1st and 3rd and another same pattern for 2nd natural frequency and the variation is linear.

It is also found that the height of the composite beam increases the first three natural frequencies increases. The effect of cracks is more pronounced near the fixed end than at far free end. It is concluded that the first three natural frequencies are most affected when the crack is located nearer to the fixed end, the middle of the beam and the free end, respectively.

The analysis can be used to identify the presence of cracks in various composite beams by analyzing the first three frequency patterns of intact and cracked composite beams.

The analysis can be carried out for different volume fractions of fibres and different boundary conditions of composite beams. The mode shapes can be extracted and the analysis of the mode shapes can be used to locate the intensity of depth and location of the crack. Various other types of analysis can be carried out using MATLAB. The vibration results obtained using ANSYS 13 can be verified by conducting experiments on composite beams using FFT analyzer for various boundary conditions.

## REFERENCES

[1]   Nikpour and Dimarogonas, Local compliance of composite cracked bodies, Journal of Composite Science and Technology, 32, 1988, 209-223.
[2]   Manivasagam and Chandrasekharan, Characterization of damage progression in layered composite, Journal of Sound and Vibration, 152, 1992, 177-179.
[3]   M. Krawczuk , and W.M.Ostachowicz, Modeling and Vibration analysis of a cantilever composite beam with a transverse open crack. Journal of Sound and Vibration  183(1), 1995, 69-89.
[4]   S. M. Ghoneam, Dynamic analysis of open cracked laminated composite beams, Journal of Composite Structures, 32, 1995, 3-11.
[5]   Ramanamurthy, Damage detection in composite beam using numerical modal analysis. International Journal on Design  and Manufacturing Technologies, 2008,Vol.2,No.1.
[6]   ANSYS Release 13.0, ANSYS Inc 2010
[7]   W.T.Thomson., Theory of vibrations with Applications (CBS Publisher 2002)

# Wavelet Analysis of Vibration Signature of a Bevel Gear Box in a Stand of Steel Rolling Mill of a Steel Plant

Md. Faridha Khanam[1], P. Ravi Kumar[2], Dr. D. Srinivasarao[3]

*1 M.Tech. Student, 2 Assistant Professor, Department of Mechanical Engineering, PVP Siddhartha Institute of Technology, Vijayawada, Andhra Pradesh, India*
*3 Professor, Department of Mechanical Engineering, DMS SVH College of Engineering, Machilipatnam, Andhra Pradesh, India*

**Abstract:** *In manufacturing industry Gear boxes are one of the important components in power transmission. Consequently any damage in the gearbox can lead to unprecedented downtime. In machines the gear trains vibrate due to many reasons such as the non regular nature of load, the manufacturing error of the gear teeth, gear back lash, misalignment of the connecting shaft and also due to continuous usage. As a common rule machines do not stop working or fail without some form of caution, which is indicated by an increased vibration level. The most effective instruments which are used in reading the root cause of the trouble are the Vibration analyzers, which collects the vibration signature at the problematic source. In the present work the vibration analysis of bevel gear box in a vertical rolling stand of Light and Medium Merchant Mill (LMMM) at Vizag steel plant is considered for the purpose of condition monitoring. The vibration signatures of input and output shafts of bevel gear box in vertical, horizontal and axial directions are collected at input and output shafts of the gear box using Vb8 instrument. The signatures so collected were further analyzed using wavelet analysis. The analysis is carried out at no-load and loaded conditions at regular intervals of operation for monitoring the gear box and results are discussed.*

*Keywords: Bevel gear box, MATLAB, Vibration Signature, Wavelet Analysis,*

## I. Introduction

In manufacturing industry the crucial power transmission components are gears they are very robust in operation and extremely dependable. The vibration in gear trains causes due to alteration of external load, error of gear teeth during manufacturing, impact meshing, error in shape of gear teeth profile and gear backlash due to wearing. The power transmission between intersecting shafts can be accomplished using bevel gears, they can function at high loads and speeds with considerable precision rating. The better option for the usage of Bevel gears is for right angle drive of low velocity ratios extensive application of straight Bevel gear drives points in automotive differentials, right angle drives or conveyors

The health of rotating machinery is dynamically determined by means of a consistent method termed as periodic vibration monitoring [1].Generally machinery problems can be isolated and detected earlier by the process of analysis of overall vibration levels and associated vibration frequency signatures. Along with other problems imbalance, improper clearances, mechanical looseness, misalignment and anti-friction bearing defects are some included. This early detection allows corrective maintenance to be prioritized and scheduled during non-critical periods, resulting in increased machinery availability and significant savings in both replacement parts and labor costs [2].Therefore the risk of premature failure diminished and the production is also maximized.

Industrial practice equipment normally in service speeds ranging from several 100's to nearly 20000rpm. Which are generally rated more than 100KW Vibration data and vibration frequency signatures collected, processed and analyzed using vibration analyzer's assists the maintenance engineer to identify the faults associated with machinery components as a part of prognostic maintenance system [2]. Historical information or spectral data cannot be obtained by offline monitoring system and hence most of the crucial machinery requires permanently established vibrating monitoring systems [3].

At Vizag Steel Plant steel blooms of cross section(320mmx320mm) are wrecked into billets of cross section(125mmx125mm) each in Light Medium Merchant Mill(LMMM) these billets are then turn rolled into rounds, re bars ,angles and channels correspondingly. These billets are also supplied as input to the Wire Rod Mill(WRM).The LMMM steel plant consists of 7 rolling stands for the above mentioned purpose some of them are horizontal rolling stands and remaining are vertical each vertical stand consists of a prime mover(motor), bevel gear box, transmission shaft, and a top gear box. The of output top gear box supply power to the two

vertical rollers and ensure that both rollers rotate at constant speed and avert the slippage of the hot steel ingot. The present work main emphasis is given to identify the fault by vibration signature analysis of the gear box using wavelet analysis.

## II.  Wavelet Transform

Signal Analysis of Vibration Data – Key for Fault Detection & Monitoring. Signals with sharp sudden changes could be better analyzed with an irregular and asymmetric wavelet than with a smooth sinusoid. Wavelets have limited duration that has an average value of zero.

Wavelets are functions that satisfy certain mathematical requirements and are used in representing data or other functions. This idea is not new. Approximation using superposition of functions has existed since the early 1800's, when Joseph Fourier discovered that he could superpose sines and cosines to represent other functions. However, in wavelet analysis, the scale that we use to look at data plays a special role. Wavelet algorithms process data at different scales or resolutions. If we look at a signal with a large "window, we would notice gross features. Similarly, if we look at a signal with a small "window," we would notice small features. The result in wavelet analysis is to see both the forest and the trees, so to speak.

This makes wavelets interesting and useful. For many decades, scientists have wanted more appropriate functions than the sines and cosines which comprise the bases of Fourier analysis, to approximate choppy signals. By their definition, these functions are non-local (and stretch out to infinity). They therefore do a very poor job in approximating sharp spikes. But with wavelet analysis, we can use approximating functions that are contained neatly in finite domains. Wavelets are well-suited for approximating data with sharp discontinuities.

The wavelet analysis procedure is to adopt a wavelet prototype function, called an analyzing wavelet or mother wavelet. Temporal analysis is performed with a contracted, high-frequency version of the prototype wavelet, while frequency analysis is performed with a dilated, low-frequency version of the same wavelet. Because the original signal or function can be represented in terms of a wavelet expansion (using coefficients in a linear combination of the wavelet functions), data operations can be performed using just the corresponding wavelet coefficients. And if you further choose the best wavelets adapted to your data, or truncate the coefficients below a threshold, your data is sparsely represented. This sparse coding makes wavelets an excellent tool in the field of data compression. Mother wavelet is a prototype for generating the other window functions.All the used windows are its dilated or compressed and shifted versions.
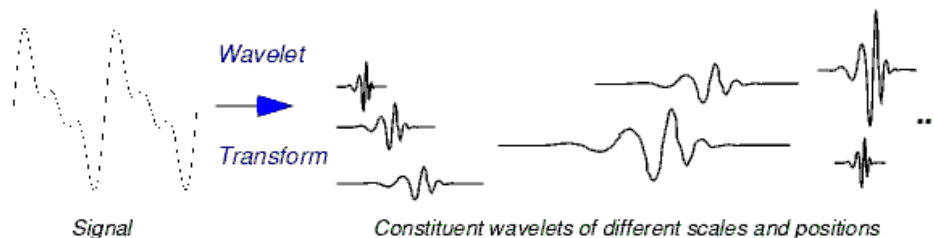


**Figure 1:  Description of wavelet transform**

Signal broken into a series of local basis functions called wavelets, which are scaled and shifted versions of the original (or Mother) wave let**.** Wavelet transforms are most broadly classified into the discrete wavelet transform (DWT) and the continuous wavelet transform (CWT). The DWT is used for signal coding whereas the CWT is used for signal analysis. Consequently, the DWT is commonly used in engineering and computer science and the CWT is most often used in scientific research. In this project work continuous wavelet transform (CWT) is used.
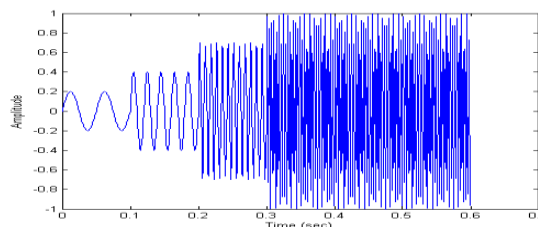


**Figure 2: Example of Continuous wavelet Transform**

### 2.1. Functions of Wavelet Transform
1. Convert a signal into a series of wavelets.
2. Provide a way for analyzing waveforms, bounded in both frequency and duration.

3. Allow signals to be stored more efficiently than by Fourier transform.
4. Be able to better approximate real-world signals.
5. Well-suited for approximating data with sharp discontinuities.

**2.2. Scaling (S)**
 S > 1 dilate the signal.
 S< 1 compress the signal.
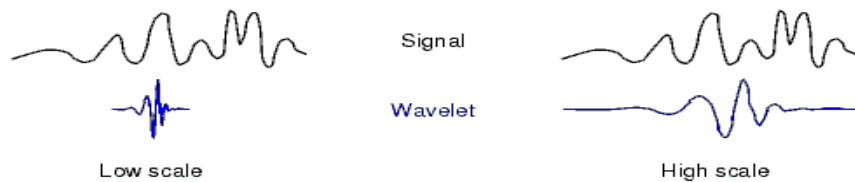


**Figure 3: Scaling**

1)      Low Scale -> High Frequency -> Detailed View Last in Short Time..
2)      High Scale -> Low Frequency -> Non-detailed Global View of Signal -> Span Entire Signal.
3)      Only Limited Interval of Scales is Necessary.

**2.3. Wavelet Applications**
Typical Application Fields
    Astronomy, acoustics, nuclear engineering, sub-band coding, signal and image processing, neurophysiology, music, magnetic resonance imaging, speech discrimination, optics, fractals, turbulence, earthquake-prediction, radar, human vision, and pure mathematics applications. Some of the typical applications are
1)      Identifying pure frequencies.
2)      De-noising signals.
3)      Detecting discontinuities and breakdown points.
4)      Detecting self-similarity.

### III.   Problem Depiction And Experimentation
        The layout of vertical stand 5 LMMM is shown in "Fig.4", in which the gear unit transmits motion from motor to top gear box. The main function of it is to afford variation in speed and torque and also change of the direction of the flow. The bevel wheels are made from case-hardened steel. The teeth of the wheels are case-hardened and lapped. The input and output shafts are mounted with spherical roller bearing(23234C3),Cylindrical roller bearing(NU-232) and 4-point thrust bearing(QJ 232)[4].The necessary contact pattern of gear mesh and adjustment of backlash are done via a set of collar rings provided with the input shaft system as shown in "Fig .5".
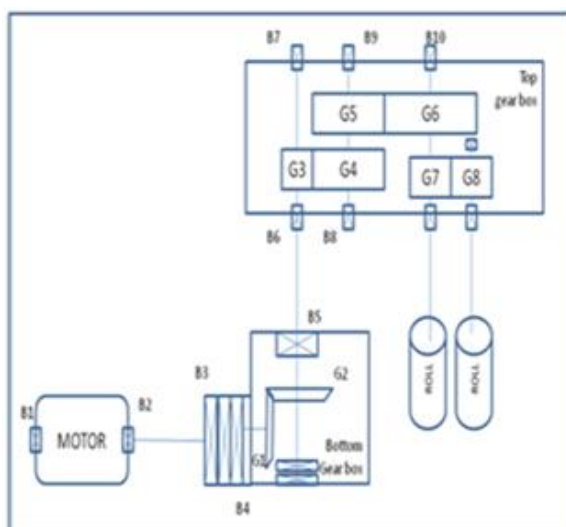


**Figure 4: Layout of stand in LMMM**
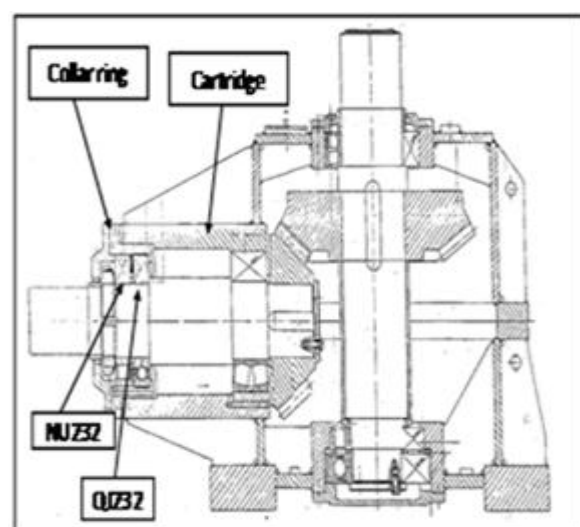


**Figure 5: Arrangement of bottom bevel gear box**

**3.1 Specifications of bottom gearbox**

Motor Speed: 440-880 rpm                          motor rating: 1100 kW
Weight: 2805 kgs                                  Oil pressure: Min =1.2 bar, Max= 1.8 bar
Gear teeth: 22/33                                 Design root clearance: 0.50 mm
Normal output torque: 24.36 kN-m                  Design Back lash: 0.33 mm

Installation of a new indigenous bottom bevel gear box was done at stand 5 on 13/2/2014. The velocity vibration signatures were collected in vertical, horizontal and axial directions at different intervals in loaded and unloaded conditions of the gear box at input side and output side using Vb8 instrument. These signatures for both damaged and undamaged condition are shown from "Fig. 6" to "Fig. 11".The signatures so obtained were further subjected to wavelet transform, a powerful signal processing technique available with MATLAB using "SYM2" wavelet. The wavelet coefficients obtained at different scales are shown from "Fig. 12" to "Fig. 17". The vibration signature of the stand at various predefined points has been constantly examined to establish by usual functioning of the gear box. On incessant monitoring it has been observed that there is a continuing augmentation in the overall RMS velocity value of the vibration signature. It is observed a significant increase in radial component of input side of the bottom gearbox.
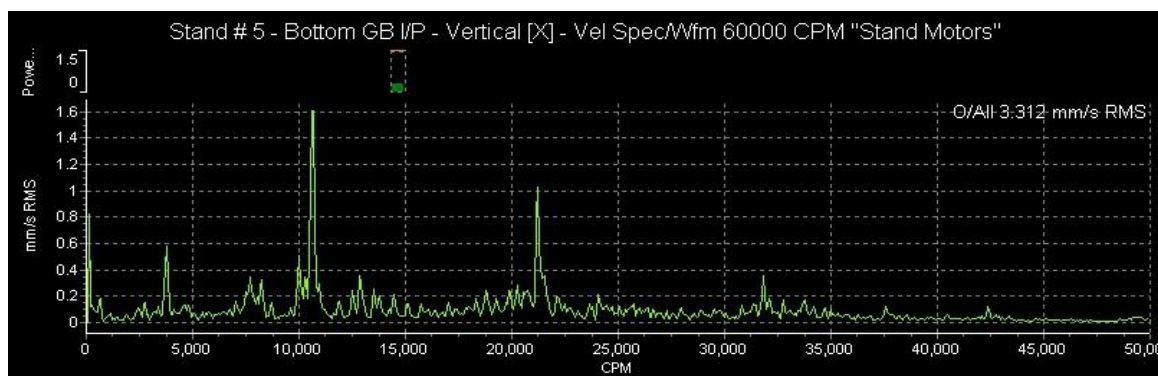

**Figure 6: Vibration spectrum at input side of BGB in vertical direction in damaged condition.**
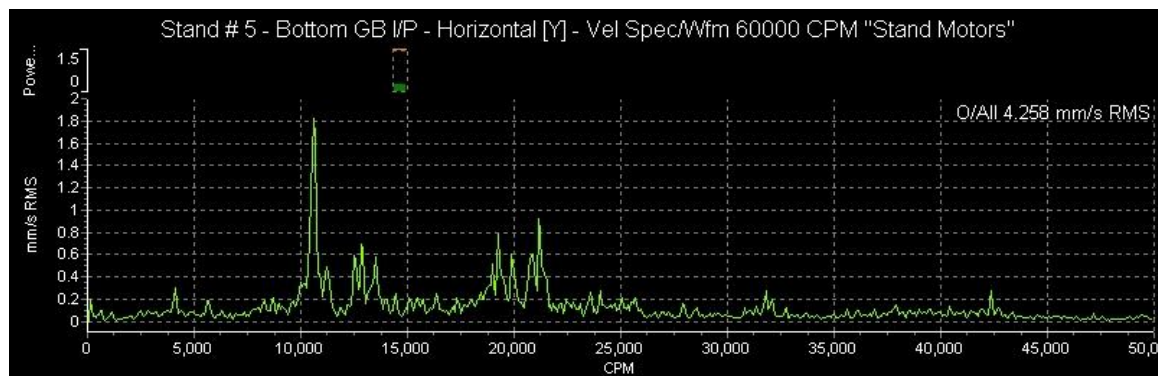

**Figure7: Vibration spectrum at input side of BGB in horizontal direction in damaged condition.**
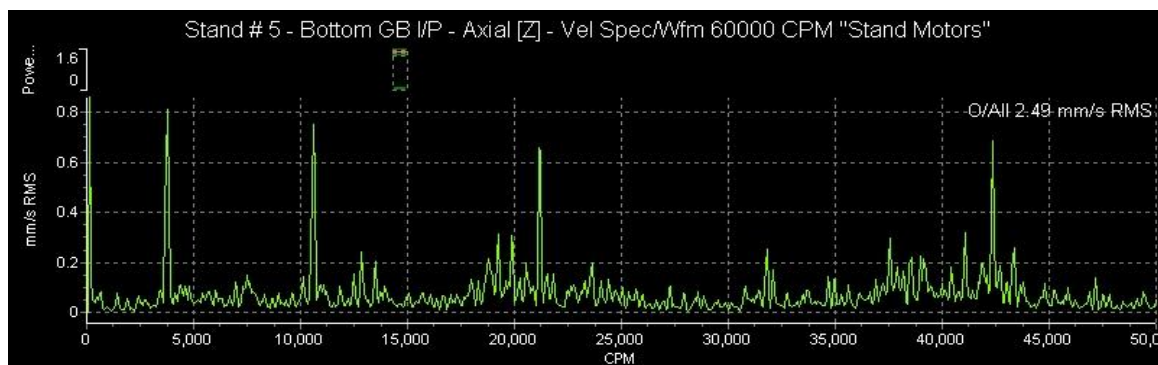

**Figure 8: Vibration spectrum at input side of BGB in axial direction in damaged condition.**
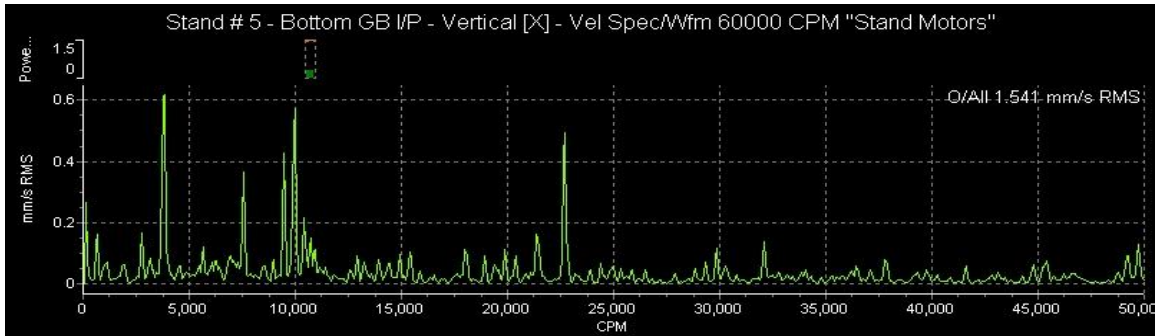
**Figure9: Vibration spectrum at input side of BGB in vertical direction in undamaged condition.**
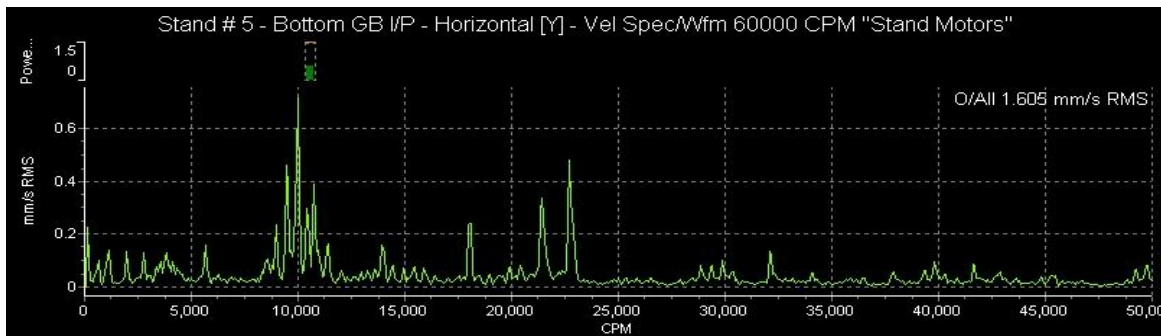


**Figure10: Vibration spectrum at input side of BGB in horizontal direction in undamaged condition.**
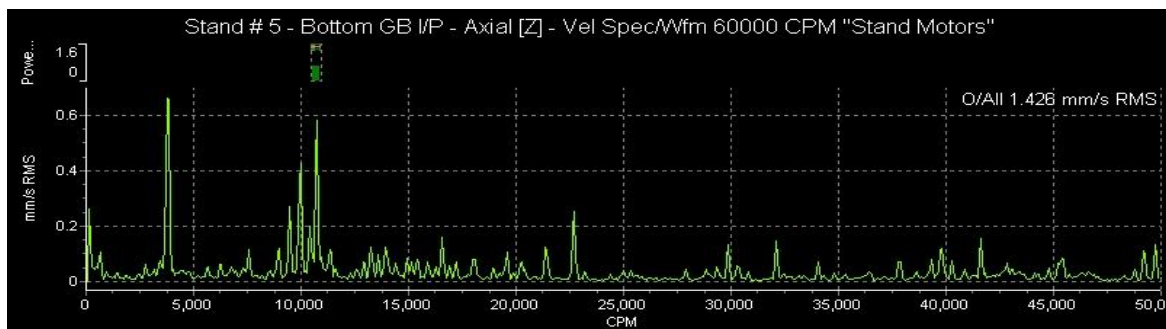


**Figure 11: Vibration spectrum at input side of BGB in axial direction in undamaged condition.**

## IV.        Results And Discussion
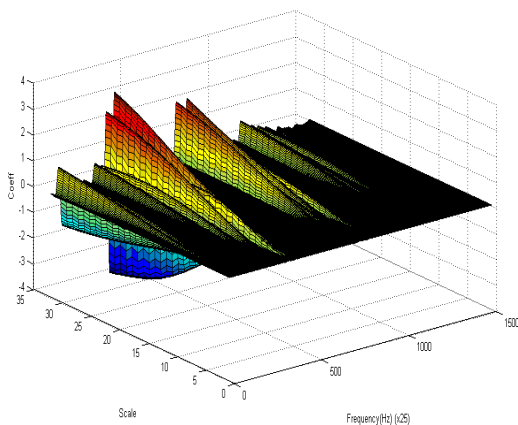


**Figure 12: Wavelet coefficients of vertical vibration spectrum at input side of BGB in damaged condition**
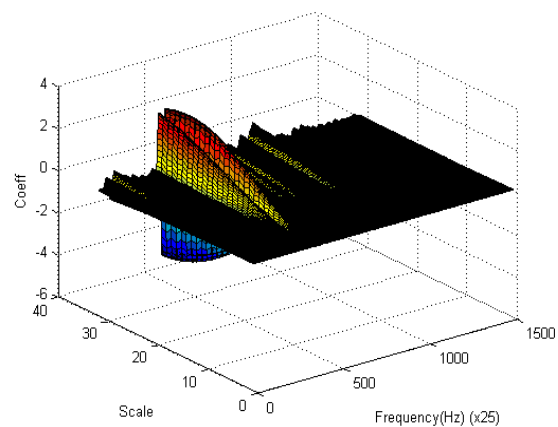


**Figure13: Wavelet coefficients of horizontal vibration spectrum at input side of BGB in damaged condition**
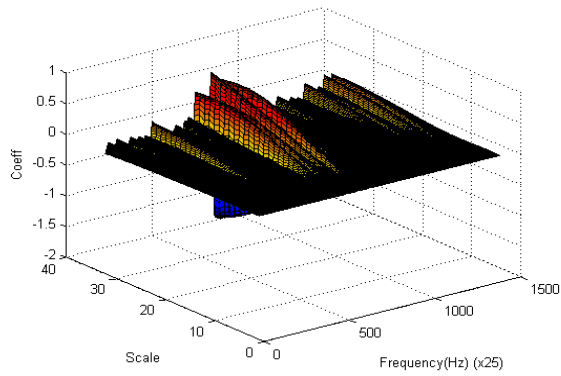
**Figure14: Wavelet coefficients of axial vibration spectrum at input side of BGB in damaged condition**
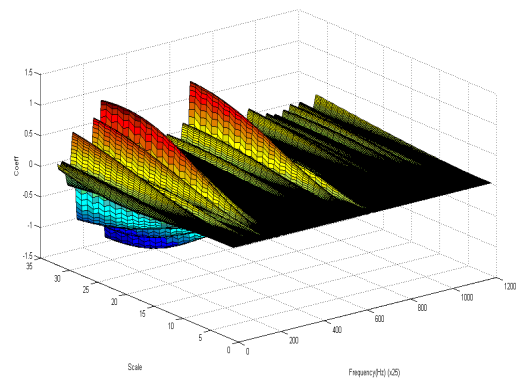


**Figure15: Wavelet coefficients of vertical vibration spectrum at input side of BGB in undamaged condition**
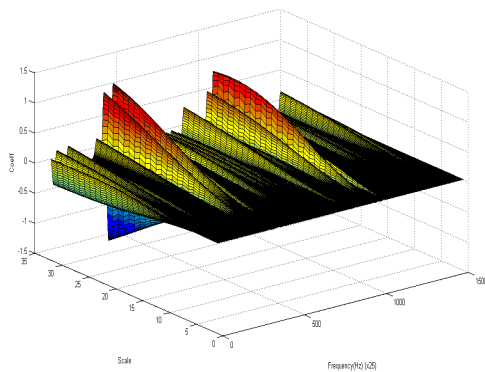


**Figure16: Wavelet coefficients of horizontal vibration spectrum at input side of BGB in undamaged condition**
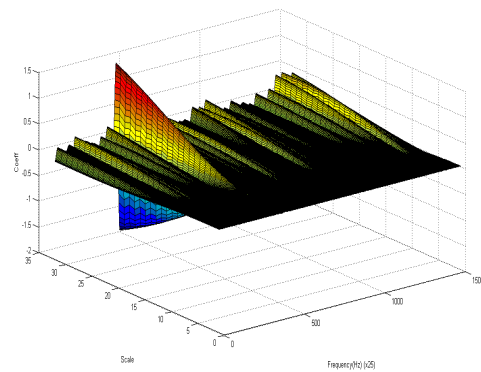


**Figure17: Wavelet coefficients of horizontal vibration spectrum at input side of BGB in undamaged condition**
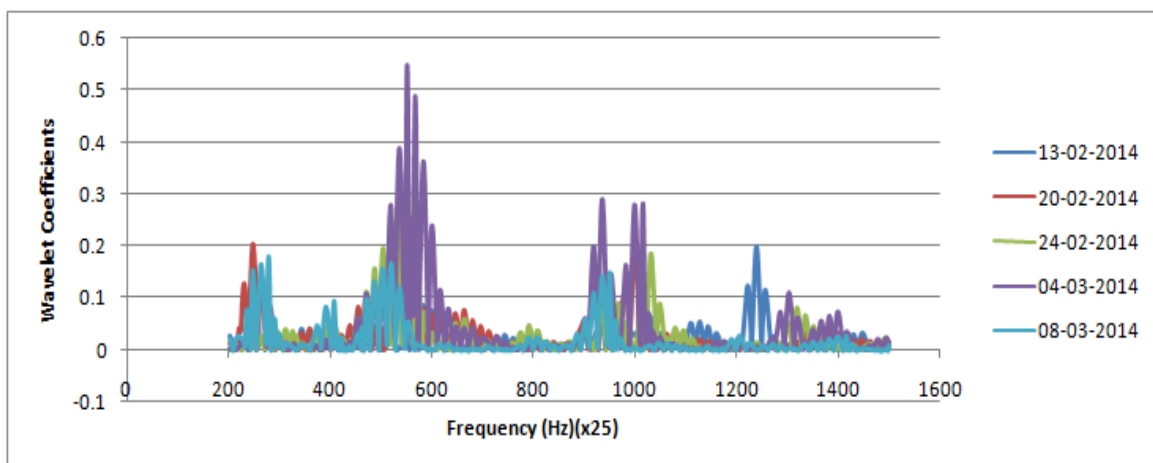


**Figure18: Frequency versus wavelet coefficients of vertical signature at various time intervals for scale 8**
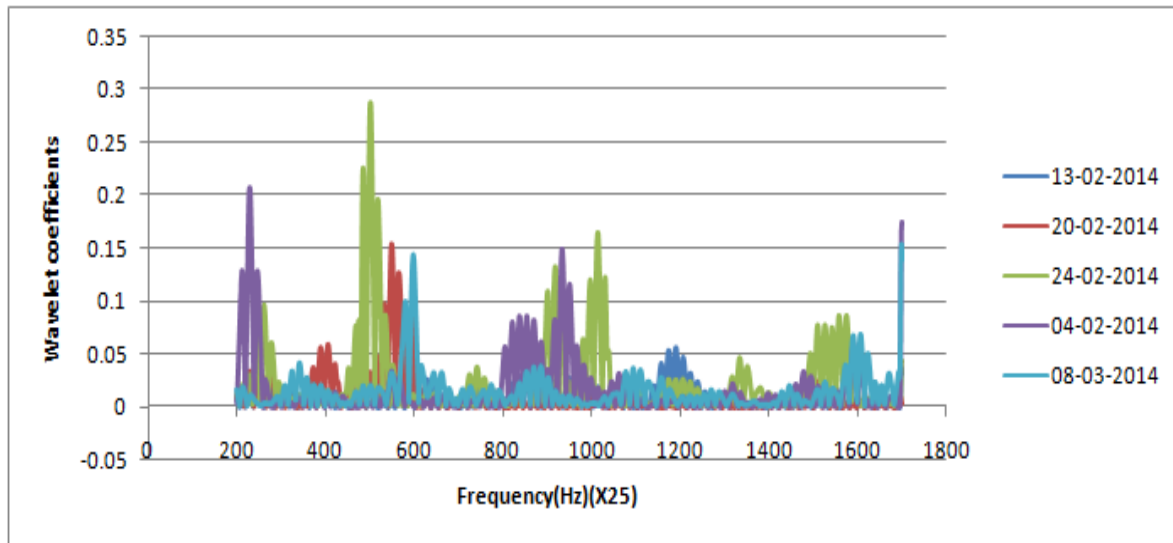
**Figure19: Frequency versus wavelet coefficients of horizontal signature at various time intervals for scale 8**
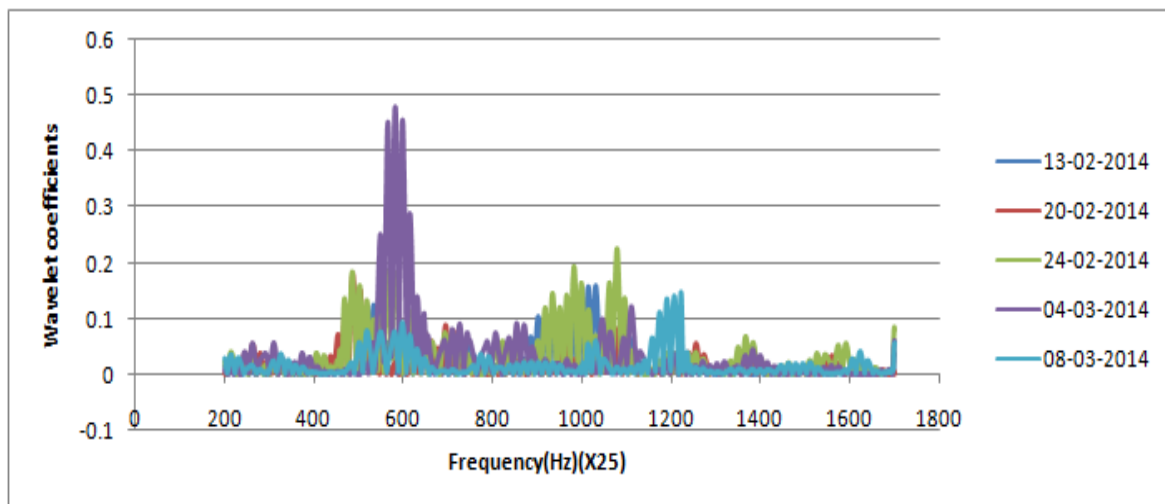


**Figure20: Frequency versus wavelet coefficients of axial signature at various time intervals for scale 8**

The performance of the gear box was observed form date of installation to date of severe damaged condition. i.e., from 13/02/2014 to 04/03/2014.During these periods of operation in general loaded condition the performance is as shown in the "Fig 12" to "Fig.20". The wavelet coefficients of vibration signatures of three directions are shown in form "Fig.18" to "Fig.20" at 'scale 8'.The wavelet coefficients show significant values for the vertical vibration signature in damaged condition. This can be observed in "Fig.18" which was drawn for a particular 'scale 8'for severely damaged condition on 04/03/2014. The gear box shaft alignment test was also carried out to ascertain any misalignment of the gearbox input shaft. But the alignment test results ruled out the possibility. In the gear box assembly a collar ring and a cartridge are provided so that the contact pattern of the meshing gears can be alter as per requirement. The bearing is seated upon the cartridge .Actually an interference fit is to be present between the outer race of the bearing and inner periphery of the cartridge. The concentricity of the gear meshing can be affected by any sort of disorder in cartridge/bearing interferences which could result in misalignment of gears. Hence the gear misalignment was suspected due to cartridge as the temperature of casing has raised to $85^{0}$C against normal operating temperature of $65^{0}$.After dismantling the dimensions of the cartridge and bearing outer diameter were measured and compared with drawing (Table 1).

**Table1: Dimensions of cartridge, bearing**

| S. No | As per drawing | | After dismantling | |
|---|---|---|---|---|
| 1 | OD of Bearing(mm) | ID of Cartridge(mm) | OD of Bearing(mm) | ID of Cartridge(mm) |
| 2 | 290 | $290.0^{-0.02}$ | 290 | 290.05 |

The revealing of incorporation of transition fit during assembly, in place of interference fit between cartridge-bearing interface was done by the indigenous gearbox supplier when the design parameters were traced back to them. An interference fit was supposed to be provided at the particular zone. During operation of the gear box under loaded condition the continuous load cycle must have brought the fit from transition to clearance zone. The cartridge was replaced and the vibration readings of the rectified gear box can be ascertained from the wavelet coefficients of vibrations signatures taken on 08/03/2014 which were also shown in "Fig 18" to "Fig.20".

## V. Conclusion

Analyzing the cartridge dimensions after dismantling the gearbox, it illustrated that there is an increase in the diameter of the cartridge which introduced looseness in between bearing outer race and the cartridge. On re-tracking the installation parameters of the subject gearbox from the supplier, it was found out that a transition fit has been achieved at the input bearing as against an interference fit. Continuous cyclic nature of load resulted in the fit to go into the clearance fit range gradually, which further got augmented and resulted in high vibrations of the shaft. It is proposed to procure a test rig to perform tests on newly purchased gear boxes to run for $2 – 3$ days to demonstrate their fault proof operation. Wavelet analysis of Vibration signatures can be considered as a powerful tool in fault diagnosis in any industry and can reduce unnecessary overheads in terms of breakdowns and manpower costs.

## Acknowledgements

## REFERENCES

[1]   Henry C. Pusey & Salle C. Pusey Current practices and trends in Mechanical failure prevention, Virginia Beach, Virginia April 3-5, 1990.
[2]   Brian C. Howes, A Gearbox vibration - factor fiction, Beta Machinery Analysis Ltd. Calgary AB, Canada, T3C 0J7
[3]   Mitchell Lebold, Katherine McClintic, Robert Campbell, Carl Byington, and Kenneth Maynard, Review of Vibration analysis methods for gearbox diagnostics and prognostics
[4]   U.V.V.Janardhan, Technical Services, Improving the reliability of bevel gearbox by re-engineering, NCCM 2009.
[5]   MATLAB 7.10.0(R2010a)
[6]   Ronald L. Eshleman, Basic Machinery Vibrations (An Introduction to Machine Testing, Analysis, and Monitoring.

# Experimental Investigation of Vertical Downward Flow Boiling Heat Transfer inside Horizontal Mini Rectangular Channel

Satish Reddy[1], Lohith N[2], Manu S[3]

[1](M.Tech 4th sem, Mechanical Engineering, Sri Siddhartha Institute of Technology, Tumkur Karnataka, India)
[2] (Assistant Professor, Department of Mechanical Engineering, Sri Siddhartha Institute of Technology, Tumkur Karnataka, India)
[3](Assistant Professor, Department of Mechanical Engineering, Sri Siddhartha Institute of Technology, Tumkur Karnataka, India)

**Abstract:** *The present work is carried to determine the two phase heat transfer coefficient during flowing vertical downward in the minichannel. The minichannel test section is made up of aluminum having hydraulic diameter 1.33mm. The experiments were carried out by varying mass flow rate from 0.1g/sec to 0.3g/sec of steam at three different vapour qualities of 0.2, 0.4 and 0.6. The result showed as the heat flux increases there is an increase in two phase heat transfer coefficient upto $20000W/m^2\ {}^0C$. In addition to that there is a decrease in treand of heat transfer coefficient for vapour quality.*
**Keywords:** *Heat transfer coefficient, Heat flux, Mass flow rate.*

## I. INTRODUCTION

Rapid development in science and technology resulted in increase in the heat flux in electronic device. The traditional cooling technique facing difficulties in exhacting the heat at the limited allocated surface. Two phase cooling showed the promising to overcome the problem. Experimental results for small diameter tubes also obtained the heat transfer coefficients that are high or less independent of vapor quality and mass flux. And it is depend on saturation pressure and heat flux, the demand of increasing in flow boiling is that high heat fluxes have once again gained importance in an application such as electronics cooling and Micro-Electro Mechanical Systems (MEMS) devices. One of the first explores the works demonstrating the potential of small passages for heat transfer enhancement was performed by Bergles [1].Recent advances in very large-scale integration (VLSI) technology and Micro-Electro Mechanical Systems (MEMS) have resulted in the ability to construct many heretofore unimagined mechanical devices on a single silicon wafer. Because microchannels with noncircular cross-sections comprise an integral part of these silicon-based Microsystems and may be heated asymmetrically, functional designs require that the fluid flow and heat transfer characteristics in these microchannels be known and understood. In addition, the microminiaturization of electronic devices and resulting increased packaging density and associated high heat fluxes [2].Evaluated the heat transfer coefficient in rectangular microchannels in $50*25m^2$. He predicted thermal profile on the chip and compared with experiments. He shows the pressure drop predictions using homogenous flow model were in good agreement with data. Experimentally studied critical heat flux in circular channels with diameters of 2.54 mm and 0.510 mm. The length of the heated channels is 10mm. And the working liquid is R-113. In this, critical heat flux is found to be independent of the inlet sub cooling at low flow rates because of fluid reaching the saturation temperature in a short distance into the heated channels. The author correlation was used for predicting the heat transfer coefficient. Number of reasherers like Bergles, A. E[1], I. Mudawar[2], P.A. Kew, K. Cornwell[3], M.W. Wambsganss.et al[4], Y.Y. Yan, T.F. Lin[5], G. Hetsroni.et al[6], Weilin Qu, Issam Mudawar[7], Bowers and Mudawar [8],Buasubranian Koo.et al, [9].

## II. EXPERIMENTAL SETUP

The flow diagram of experiment setup as shown in fig (1). It consists of pump, digital pressure gauge preheater and thermocouples and two take initially the dimineral heater is filled into the steam. The water is pumped into the preheater where it reaches to the saturation state of the water. The saturated water was then pumped into the test specimen. The wall temperature was measured at different point as shown in fig. The steady state is identified when the readings of the thermocouples remains unchanged. After reaching the steady state all the temperature, pressures were measured.
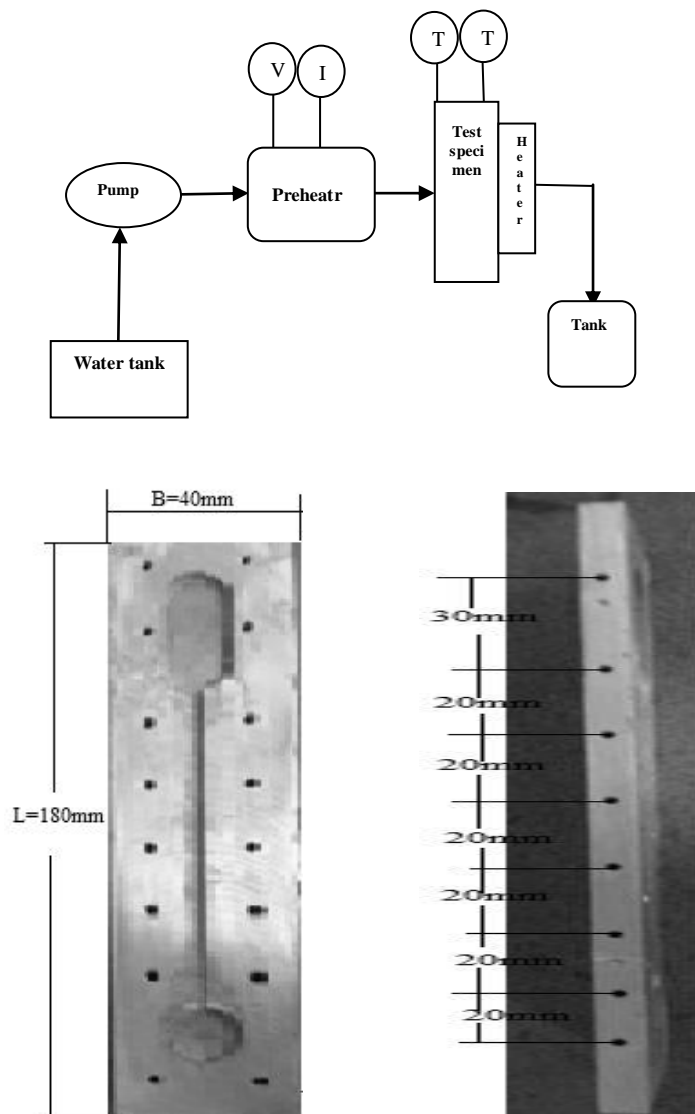
**Figure1:** Fig shows Experimental set up

## III.   FIGURES AND TABLES

**1. Operating Parameter**

**Table -1:** Operating Conditions

| Mass flow rate(g/sec) | Dryness fraction (X) | Heat (Q in Watts) | | | |
|---|---|---|---|---|---|
| | | Q1 | Q2 | Q3 | Q4 |
| 0.1 | 0.2 | 10 | 20 | 30 | 40 |
| | 0.4 | 10 | 20 | 30 | 40 |
| | 0.6 | 10 | 20 | 30 | 40 |
| 0.2 | 0.2 | 10 | 20 | 30 | 40 |
| | 0.4 | 10 | 20 | 30 | 40 |
| | 0.6 | 10 | 20 | 30 | 40 |
| 0.3 | 0.2 | 10 | 20 | 30 | 40 |
| | 0.4 | 10 | 20 | 30 | 40 |
| | 0.6 | 10 | 20 | 30 | 40 |

## 2. Results and Discussions
### 2 (a) Effect of heat flux on wall temperature for m=0.1g/sec, 0.2g/sec and 0.3g/sec.
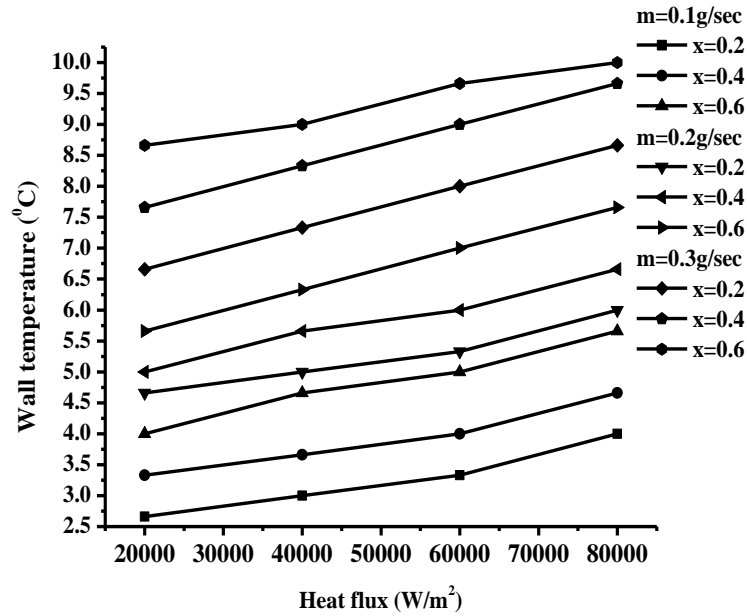


Fig (a)

FigIII.2 (a) shows the variation of heat flux on wall temperature for three different dryness fractions i.e. x=0.2, 0.4 and 0.6 with mass flow rates of m=0.1, 0.2 and 0.3g/sec respectively. It can be noticed from the figure that heat flux increases with increasing wall temperature due to the lower surface tension. Highest wall temperature was found at highest dryness fraction x=0.6.

### 2 (b) Effect of heat flux on heat transfer coefficient for m=0.1g/sec, 0.2g/sec and 0.3g/sec.
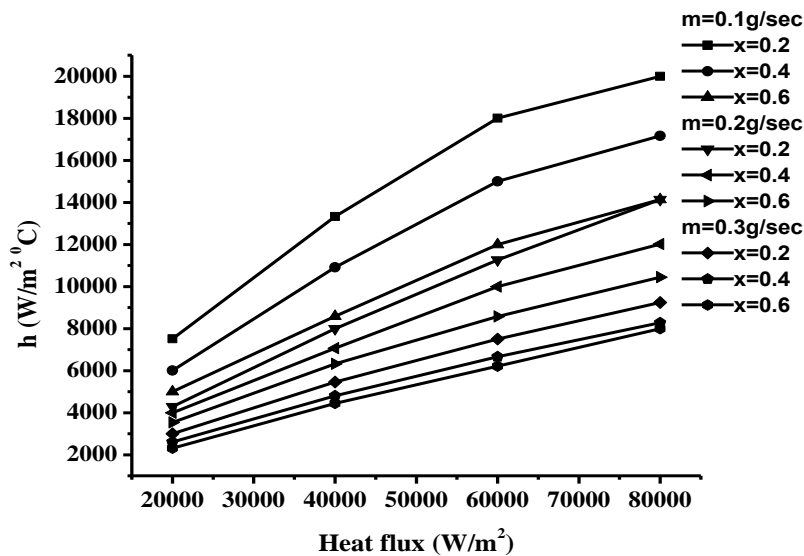


Fig (b)

FigIII.2 (b) shows the variation of heat flux on heat transfer coefficient for three different dryness fractions i.e. x=0.2, 0.4 and 0.6 with mass flow rates of m=0.1, 0.2 and 0.3g/sec respectively. It can be noticed from the figure that heat transfer coefficient increases with increase in the heat flux, because increase in the heat flux increases the wall super heating temperature and at higher wall super heating temperature higher heat transfer will takes place in both cases. Highest heat transfer coefficient was found at lower dryness fraction x=0.2.

**2 (c) Effect of dryness fraction on heat transfer coefficient for m=0.1g/sec, 0.2g/sec and 0.3g/sec**



Fig (c)
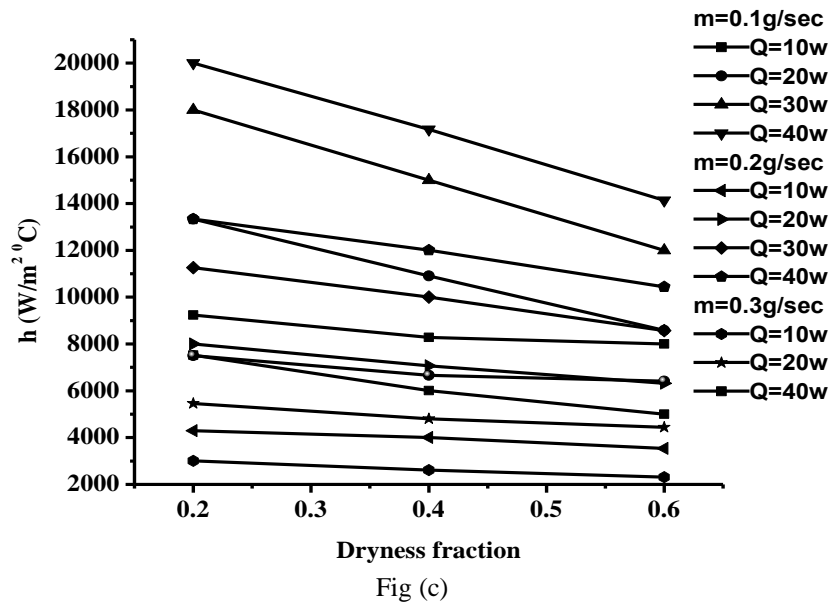
FigIII.2 (c) shows the variation of dryness fraction on heat transfer coefficient for the different heat input i.e. Q=10W, 20W, 30W and 40W with mass flow rates of m=0.1g/sec, 0.2g/sec and 0.3g/sec respectively. It is observed from the above figure that heat transfer coefficient decreases with increasing dryness fraction due to the lower shear stress at the wall surface and increase in thermal resistance. Higher heat transfer coefficient is obtained at higher heat input.

## IV.  CONCLUSION

As heat flux increases there was an increase in wall temperature. For high heat flux there was greater heat transfer coefficients upto 20000W/m$^2$ $^0$C. And also at higher heat fluxes there was slow increase in two phase heat transfer coefficient. The heat transfer coefficient decreases with increasing dryness fraction due to the lower shear stress at the wall surface and increase in thermal resistance. Higher heat transfer coefficient is obtained at higher heat input.

## REFERENCES

Bergles, A. E., 1964, "Burnout in Tubes of Small Diameter." ASME Paper No. 63-WA-182, pp.1-9.

[1]  I. Mudawar, Assessment of high-heat-flux thermal management schemes, IEEE. Trans. Compon. Pack. Technol. 24 (2) (2001) 122–141.

[2]  P.A. Kew, K. Cornwell, Correlations for the prediction of boiling heat transfer in small-diameter channels, Appl. Therm. Eng. 17 (1997) 705–715.

[3]  M.W. Wambsganss, D.M. France, J.A. Jendrzejczyk, T.N. Tran, Boiling heat transfer in a horizontal small-diameter tube, J. Heat Transfer 115 (1993) 963–972.

[4]  Y.Y. Yan, T.F. Lin, Evaporation heat transfer and pressure drop of refrigerant R-134a in a small pipe, Int. J. Heat Mass Transfer 41 (1998) 4183–4194.

[5]  G. Hetsroni, A. Mosyak, Z. Segal, G. Ziskind, A uniform temperature heat sink for cooling of electronic devices, Int. J. Heat Mass Transfer 45 (2002) 3275–3286

[6]  Weilin Qu, Issam Mudawar" Prediction and measurement of incipient boiling heat flux in micro-channel heat sinks" Received 2 November 2001; received in revised form 6 March 2002, International Journal of Heat and Mass Transfer Vol,45 (2002),pp 3933–3945.

[7]  Bowers, M. B., and Mudawar, I., 1994, "High Flux Boiling in Low Flow Rate, Low Pressure Drop Mini-Channel and Micro-Channel Heat Sinks," Int. J. Heat Mass Transfer, 37, pp. 321 332.

[8]  Buasubranian, p; kandlikar,s.g "high speed photographic observation of flow boiling in single rectangular minichannels". Proceeding the ASME summer heat transfer conference. 2003. pp1-7

# Analysis and Improved Operation of PEBB Based 5-Level Voltage Source Converter for Facts Applications

Dineesha .V[1], Sravanthi C. L[2]

*[1,2] Department of Electrical and Electronics Engineering, JNTU Anantapur*

**Abstract:** *The paper presents the power-electronic devices are increasing in several applications, and power-electronic building blocks (PEBBs) are a strategic concept to increase the reliability of the power-electronic converters and to minimize their cost. Magnetic elements, such as zigzag transformers, phase-shifted transformers (PST), or zero-sequence blocking transformers (ZSBT), are used to interconnect the PEBBs. In this paper, by using 5-level voltage source converter the operation of multi-pulse converters will be analyzed, describing the harmonic cancellation and minimization techniques that could be used in these multi-pulse converters, focusing on the power-electronics flexible ac transmission systems devices installed at the NYPA Marcy substation. In order to improve the dynamic response of this system, the use of selective harmonic elimination modulation is proposed and implemented.*

**Index Terms:** *AC–DC power conversion, power conversion harmonics, Selective harmonic elimination, pulse width modulation*

## I.  Introduction

The development of self-commutated switches and multilevel topologies has allowed increasing the power rate of voltage-source converters (VSCs). Due to the flexibility and controllability of the VSCs, they are used in flexible ac transmission systems (FACTS) applications, such as STATCOMs or synchronous static series compensators (SSSCs). Some objectives of these kinds of installations are to control the power flow and ensure voltage stability of the utility grids. Due to the fact that the power rate of the power-electronic devices tends to increase, high-power VSCs are needed. On the one hand, the use of multilevel converter is a suitable alternative to design high-power electronic converters. On the other hand, the power-electronic building blocks (PEBBs) can be associated, generally by using magnetic elements, in order to increase the power rate of the converters. One of the problems in FACTS applications is the output voltage harmonic quality.

The harmonic content of the voltage must satisfy the legislation requirements at the point of common coupling (PCC). Multipulse converters are used to improve the output voltage quality without increasing the switching frequency. In high-power applications, full-wave modulation is commonly used, where the switching frequency has the same value of the fundamental frequency of the output voltage.

The FACTS device installed at the New York Power Authority (NYPA) Marcy substation is presented in Section II. Three different techniques are used in this device in order to reduce the output voltage harmonic content: the harmonic cancellation, the harmonic minimization, and the use of ZSBTs. In order to control the fundamental amplitude of the output voltage, the dc bus voltage $(V_{DC})$ is controlled, exchanging active power.
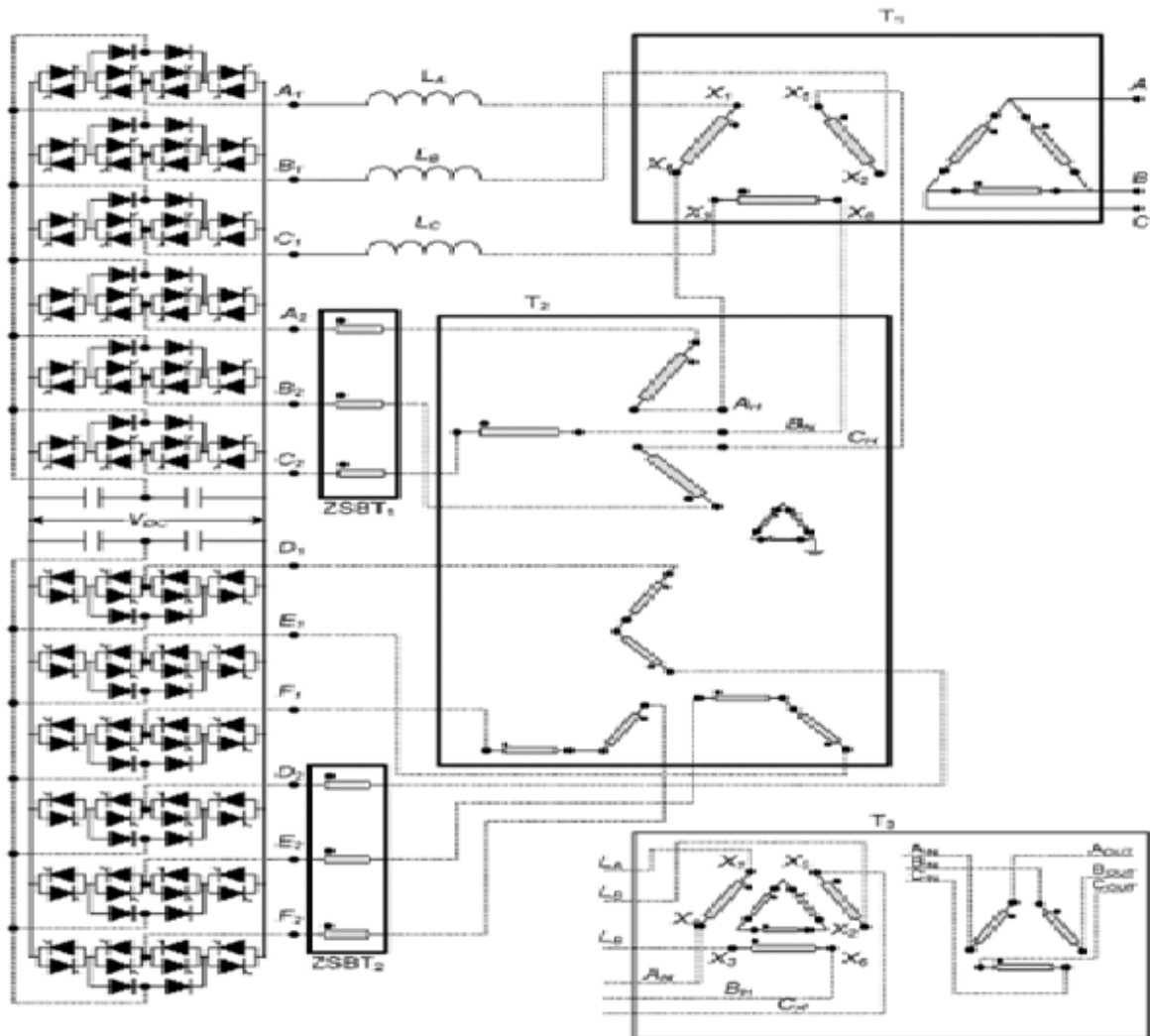
Fig No.1 Circuit diagram For Shunt and Series connected inverters

## II.    Proposed Five Level Voltage Source Converter

**a) Harmonic Minimization by Using the Phase-Shifted Transformer:**
        In the previous paragraph, a method for harmonic optimization is presented where some specific harmonics are eliminated. There is another method for optimizing the harmonic content of the output voltage, where harmonics are minimized instead of eliminated, connecting in series the inverters without using the PSTs.
        The same modulation is used in both inverters, so the output waveform of the inverters is exactly the same Cn . But in the first converter the waveform Cn has been shifted by∝ and inthe second converter by−∝ (all the angles are expressed in degrees), obtaining the voltage Vx :

$$V_x = \sum_{n=1}^{\infty} \left( C_n \cdot e^{\left(j \cdot n \cdot \frac{\alpha\pi}{180}\right)} + C_n \cdot e^{\left(-j \cdot n \cdot \frac{\alpha\pi}{180}\right)} \right)$$

$$= \sum_{n=1}^{\infty} \left( C_n \cdot 2 \cdot \cos(n \cdot \alpha) \right)$$

(2.1)

Where thecos$(n \propto)$ term is called the minimization rate. Thisminimization rate is the percentage of the th harmonic of theoutput voltage with respect to the original value of this th harmonic in the Cn waveform.
        In Table1, the minimization rate for each harmonic, is illustrated for four different values of . The highest minimizations for a given have been highlighted.
        For example, if two signals are phase shifted by +75 and -75, respectively, and then they are added, the resulting signal will have minimized harmonics 11th, 13th, 35th and 37th to the13% of the original value.

The main drawback of this harmonic minimization method is that apart from the harmonic components, the fundamental component is slightly reduced.

TABLE I
HARMONICS MINIMIZATION FOR DIFFERENT α (IN PER UNIT)

| n | α=15° | α=7.5° | α=5° | α=3.75° |
|---|-------|--------|------|---------|
| 1 | 0.96 | 0.99 | 0.99 | 0.99 |
| 5 | 0.25 | 0.79 | 0.90 | 0.94 |
| 7 | -0.25 | 0.60 | 0.81 | 0.89 |
| 11 | -0.96 | 0.13 | 0.57 | 0.75 |
| 13 | -0.96 | -0.13 | 0.42 | 0.65 |
| 17 | -0.25 | -0.60 | 0.08 | 0.44 |
| 19 | 0.25 | 0.79 | -0.08 | 0.32 |
| 23 | 0.96 | -0.99 | -0.42 | 0.06 |
| 25 | 0.96 | -0.99 | -0.57 | -0.06 |
| 29 | 0.25 | -0.79 | -0.81 | -0.32 |
| 31 | -0.25 | -0.60 | -0.90 | -0.44 |
| 35 | -0.96 | -0.13 | -0.99 | -0.65 |
| 37 | -0.96 | 0.13 | -0.99 | -0.75 |
| 41 | -0.25 | 0.60 | -0.90 | -0.89 |
| 43 | 0.25 | 0.79 | -0.81 | -0.94 |
| 47 | 0.96 | 0.99 | -0.57 | -0.99 |
| 49 | 0.96 | 0.99 | -0.42 | -0.99 |

**b) Blocking of Zero-Sequence Voltage Components by Using Magnetic Elements:**

Magnetic elements, such as zero-sequence blocking transformer (ZSBT) or [zero-sequence blocking reactor (ZSBR)], can be used to filter common-mode or zero-sequence harmonics. The impedance that ZSBT imposes to positive or negative sequences is relatively low whereas the impedance for zero sequence is relatively high.

Commonly used ZSBT with "E"-type magnetic core is shown. The three phases are wired in the central limb. The magnetic flux generated by zero-sequence currents of each phase flows through the magnetic core. However, magnetic flux generated by differential currents is cancelled out and, therefore, no flux flows through the magnetic core. The voltage drop in the ZSBT for the phase is

$$V_a = L_{LK} \cdot \frac{d\vec{i}_a}{dt} + L_{CM} \cdot \frac{d\left(\vec{i}_a + \vec{i}_b + \vec{i}_c\right)}{dt}.$$

( 2.2 )

According to for differential mode currents, them impedance imposed by the ZSBT is the leakage impedance$L_{lk}$, which is relatively low. Otherwise, the inductance for zero-sequence currents is relatively high$L_{lk} + 3L_{CM}$ .

**c) QUASI 48-PULSE OUTPUT VOLTAGE:**

The output voltage of the FACTS device shown in Fig. 1 can be a quasi 48-pulse voltage waveform. This voltage waveform is obtained by using previously described harmonic elimination and minimization techniques.
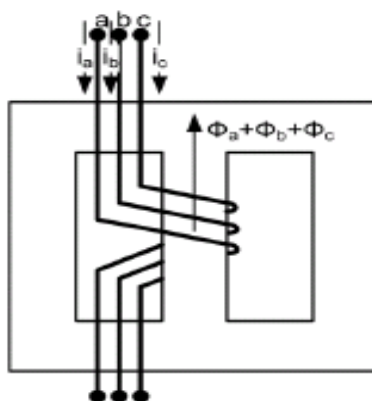


Fig 2.  Zero-sequence blocking transformer with an "E" magnetic core.
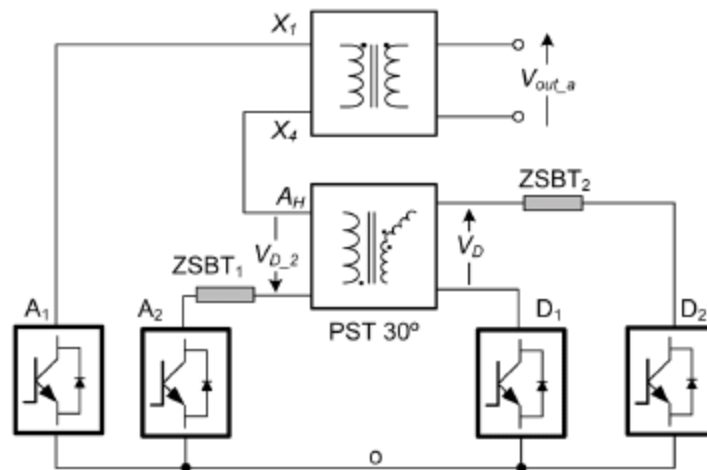
Fig.3 .Simplified single-phase circuit.

As stated previously, three techniques are used in order to eliminate harmonics: ZSBT for triplen harmonics elimination, the PST to eliminate harmonics of order $n = 6k \pm 1$ where k=1,3,5……and harmonic minimization for 11th, 13th, 23rd,25th, 35th, and 37th harmonics . In this way, the quasi 48-pulsewaveform voltage is obtained.

Voltages VA and VD-2 are added and as explained in harmonics of order $n = 6k \pm 1$where k=1, 3, 5,etc. are cancelled.
The relations between angles of the voltages shown in Fig. 7are

$$\alpha_2 = 180 - \alpha_1 \quad \alpha_3 = \alpha_1 - 30 \quad \alpha_4 = 180 + \alpha_3.$$

(2.3)

The angle determines which harmonic is minimized as shown in Table I. If$\alpha_1$ is 7.5 , then 11th, 13th, 35th and 37$^{th}$harmonics are minimized. Otherwise, if$\alpha_1$ is 3.75, 23rd and25th harmonics are minimized.

The voltage waveform in all of the PEBB outputs is the same (Vx) but they are phase shifted by the angles$\alpha_1, \alpha_2, \alpha_3, \alpha_4$. The voltage VD-2 is defined as given by

$$V_{D\_2} = \sum_{n=1}^{\infty} (V_{D1o} - V_{D2o}) \cdot \frac{1}{\sqrt{3}} \cdot \left(1 - e^{-j\frac{2\pi}{3} \cdot n}\right)$$
$$n = 1, 5, 7, 11, 13 \ldots .$$

(2.4)

This equation has taken into account the effect of the ZSBT so common-mode harmonics have not been included.

Defining the value of the angle (the angle that corresponds to the period where the voltage is zero) as , the harmonics 23rd and 25th are minimized. The angle (the phase-shift angle of the voltage with respect to the reference) is 7.5 and 11th, 13th, 35th, and 37th harmonics are minimized in the voltage across the ZSBT is

$$V_{\text{ZSBT 1}} = \frac{V'_A + V'_B + V'_C}{3}$$
$$V_{\text{ZSBT 2}} = \frac{V'_D + V'_E + V'_F}{3}.$$

(2.5)

And the voltage VD-2 is

$$V_{D\_2} = \frac{V_D - V_C}{\sqrt{3}}.$$

(2.6)

The output voltage is a quasi 48-pulse waveform and it has21 different voltage levels, 10 levels in the positive semi-period, the zero level, and 10 levels in the negative semi-period.

To summarize, in the voltage, 23rd and 25th harmonics have been minimized by imposing the angle. After that, the 11th, 13th, 35th, and 37th harmonics are minimized by setting the angle to Nevertheless, there is another option with which the same output voltage is obtained.

The 11th, 13th, 35th, and 37th harmonics of the voltage can be minimized, giving a value .The 23rd and 25th harmonics can be minimized by setting the angle. In both cases, the output voltage has the same quasi 48-pulsewaveform.

### III. Use Of Advanced Modulation Strategies

The convertible static compensator implementation at the NYPA Marcy Station has been described and analyzed in the previous sections. As has been described, full-wave modulation is used by minimizing the switching power losses of the PEBBs, and harmonic elimination and minimization techniques are used in order to optimize the harmonic content of the output voltage. But the drawback of this modulation strategy is the control of the amplitude of the fundamental output voltage. There are two ways to control the amplitude of the output voltage:

1) Changing the angle; but the change of this angle means that the harmonics are not going to be minimized;
2) Changing the dc bus voltage; the dynamic response of the converter is very slow and the system becomes nonlinear using this alternative..

In the SHE modulation, the switches of the power converters are switched several times per period producing notches in the output voltage of each PEBB, Controlling the angle at which the switches are commutated, the amplitude of several harmonics can be controlled. These degrees of freedom are used to control the amplitude of the fundamental component, and to cancel different harmonics. The following equation defines the amplitude of the output voltage harmonic for a three-level converter:

The studied application is based on three-level NPC PEBBs. Therefore SHE modulation is focused on three-level signals. The first quadrant is defined by the three angles whereas the second quadrant and the third and fourth quadrants are obtained by applying quarter-wave and negative half-wave symmetries, respectively.

One of the disadvantages of SHE is that nonlinear equations must be solved. Moreover, the complexity tends to increase when more angles are introduced and when higher order harmonic equations must be solved.

Instead of eliminating specific harmonics, they can be reduced by using selective harmonic mitigation (SHM) modulation. This method has the advantage that more than one harmonic can be reduced for each commutation angle .Three possible modulation alternatives are analyzed in the following paragraphs, using selective harmonic elimination or mitigation techniques with three angles.

### A. Elimination of 11th and 13th Harmonics by Applying SHE Modulation (SHE I):

SHE modulation with three angles is applied to each PEBB in order to control the fundamental component and to eliminate the 11th and 13th harmonics. Consequently, the switching frequency

is three times higher compared to full-waveform modulation, but in this case, the fundamental amplitude is controlled by the modulation and not by the level of the dc bus voltage.

Another degree of freedom is available that is the angle shown given , the value of 3.75 , 23rd and 25th harmonics is minimized up to 6.5%.

As stated previously, all the harmonics of order $n = 6k \pm 1$ where k=1, 3, 5, etc are eliminated by the phase shifted transformerT2 of Fig. 1. Therefore, the first significant harmonics of are harmonics of order 35 and 37.

### B. Elimination of 23rd and 25th Harmonics by Applying SHE Modulation (SHE II):

As in the previous section, SHE modulation with three angles is applied to each PEBB output voltage. In this case, the first angle is used to control the fundamental amplitude and the other two angles are used to eliminate harmonics of order 23 and 25.

The angle is 7.5 with which harmonics of order 11, 13,35, and 37 are minimized up to 13%. All harmonics of order $n = 6k \pm 1$, where k=1, 3, 5, etc. are eliminated by the phase-harmonics shifted transformer T2 of Fig. 1. Thus, the first relevant harmonics of output voltage are harmonics of order 47 and 49.

### C. Elimination of 11th and 13th and Minimization of the 23rd and 25th Harmonics by Applying SHE Modulation (SHE III):

In this third alternative, the amplitude of the fundamental component is not controlled by the SHE modulation angles. Instead, the SHE modulation works with fixed pre calculated angles that eliminate the 11th and 13th harmonics. Different families of angles that eliminate these two harmonics are calculated, and the optimal operation point is selected among all of these families, choosing the angles that, with a high modulation index, generate very small amplitude 23rd and 25th harmonics.

The "optimum" angles selected in our case generate a fundamental amplitude of 0.88 p.u., eliminate the 11th and 13th harmonics, and minimize the amplitude of the 23rd and 25th harmonics. Thus, the SHE modulation works at a fixed point. The selected three angles of the SHE modulation are shown

$$\beta_1 = 21.08° \quad \beta_2 = 54.08° \quad \beta_3 = 57.46°.$$

(2.6)

The amplitude of the fundamental component is controlled by shifting the angle $\propto_1$. As stated previously, all harmonics of order $n = 6k \pm 1$ where k=1, 3, 5, etc are eliminated by the phase-shifted transformer T2.

## IV. Simulation Results

In this section, simulation results with the proposed modulation strategies have been carried out in Mat lab7.8 version and in the Simulink. The optimum working point of each modulation, taking into account the THD and the modulation index, has been chosen as a working point for the simulation. The angles of the SHE modulations and the modulation index are mentioned.
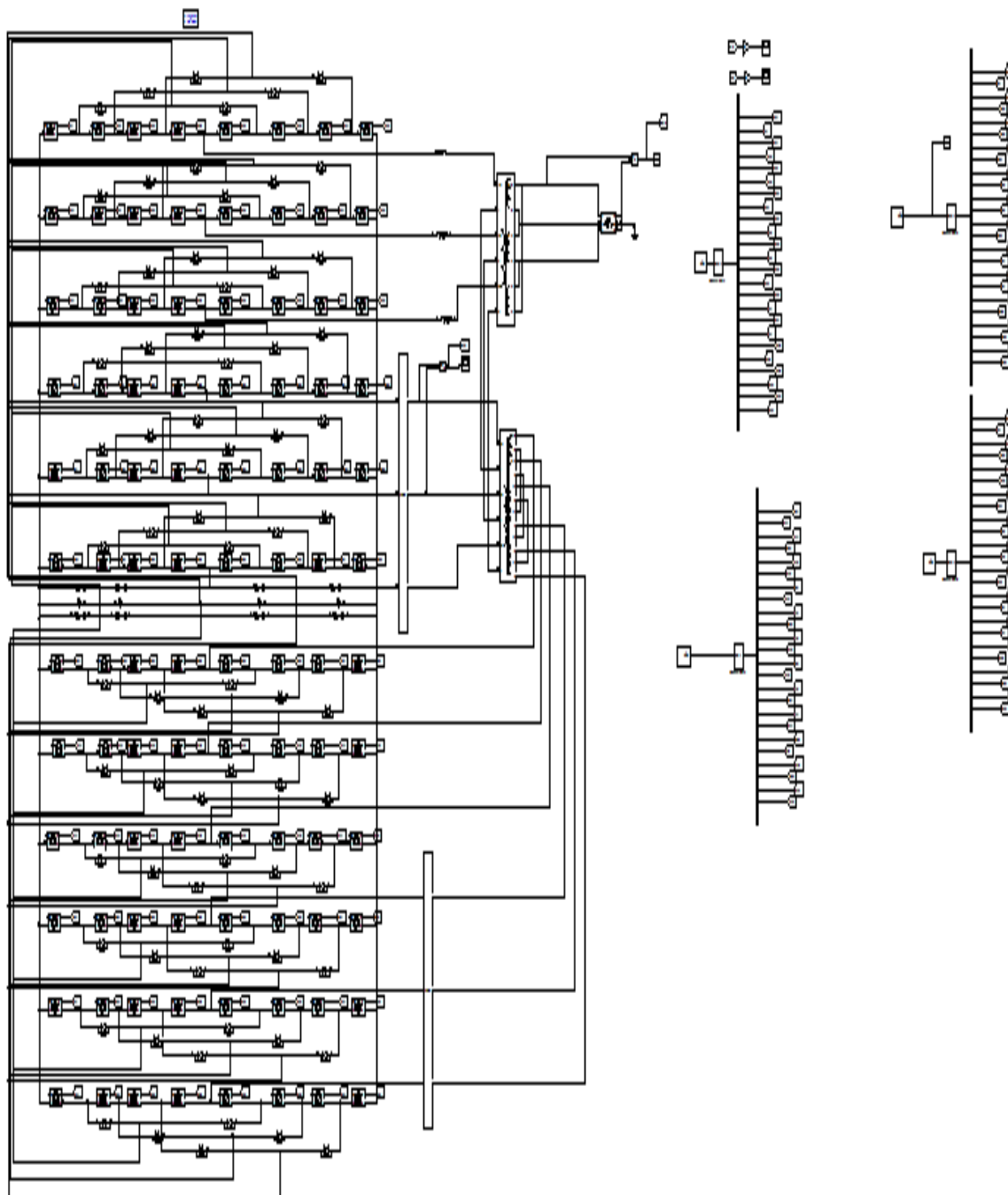


Fig 5. Simulation Circuit Diagram for Five-level Voltage Source Converter Based PEBB

## V. Output Waveforms Of Propsed System
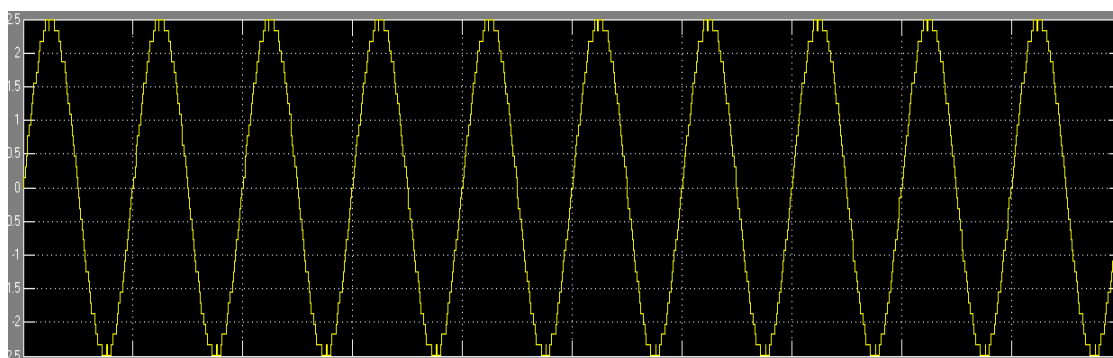

Fig 6. Vout Voltage normalized with respect to voltage Vdc for given modulation.
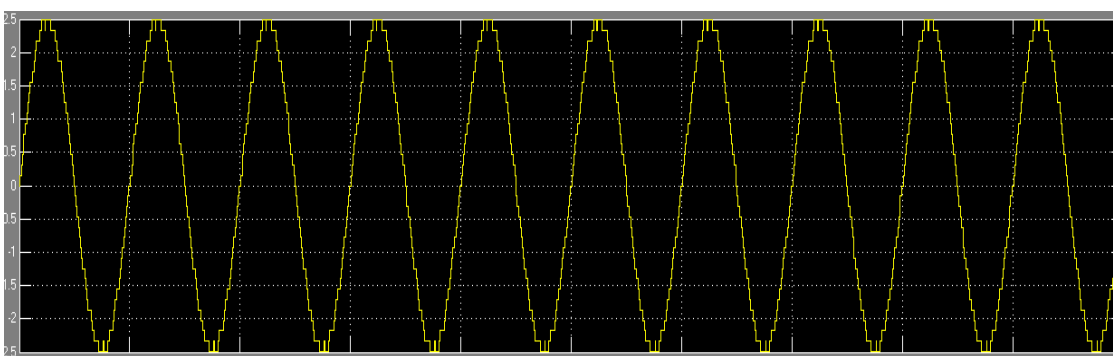

Fig 7.Vzsbt Voltage normalized with respect to voltage Vdc for given modulation
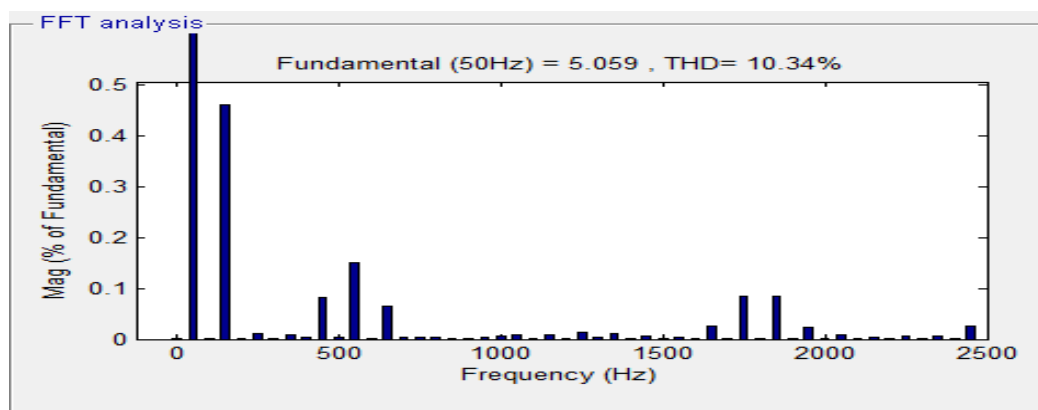

Fig 8. Vout Total harmonic content with respect to Vdc for given modulation
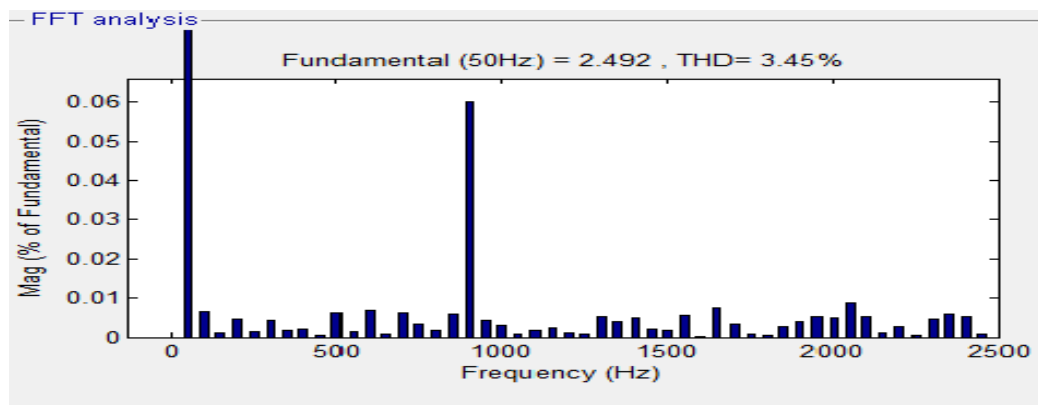

Fig 9. Vzsbt Total harmonic content with respect to Vdc for given modulation

## VI. Conclusion

In this paper a  by using five level voltage source converter is used to new the harmonic cancellation and minimization in multipulse converters has been analyzed and described, focusing on VSC power-electronics converters using PEBBs for FACTS applications. The convertible static compensator implementation at the NYPA Marcy Station has been described and analyzed for this purpose. The harmonic elimination and minimization techniques used in this multipulse VSC have been explained. In this system the total harmonic content and can be used and increase the performance of the system.

The study can be used as a base to understand the association of PEBBs by using magnetic elements and increase the dynamic response of the system and improve facts applications.

## REFERENCES

[1]     J. V. Milanovic and Z. Yan, "Modeling of FACTS devices for voltage sag mitigation studies in large power systems," IEEE Trans. Power Del., vol. 25, no. 4, pp. 3044–3052, Oct. 2010.
[2]     J. A. Barrena, L. Marroyo, M. A. R. Vidal, and J. R. T. Apraiz, "Individual voltage balancing strategy for PWM cascaded H-bridge converter-based STATCOM," IEEE Trans. Ind. Electron., vol. 55, no. 1, pp. 21–29, Jan. 2008.
[3]     S. Kouro, M. Malinowski, K. Gopakumar, J. Pou, L. G. Franquelo, B. Wu, J. Rodriguez, M. A. Perez, and J. I. Leon, "Recent advances and industrial applications of multilevel converters," IEEE Trans. Ind. Electron., vol. 57, no. 8, pp. 2553–2580, Aug. 2010.
[4]     N. Hatano and T. Ise, "Control scheme of cascaded H-bridge STATCOM using zero-sequence voltage and negative-sequence cur-rent," IEEE Trans, Power Del., vol. 25, no. 2, pp. 543–550, Apr. 2010.
[5]     T. Ericsen, "The second electronic revolution (it's all about control)," IEEE Trans. Ind. Appl., vol. 46,      no. 5, pp. 1778–1786, Sep./Oct. 2010. B. Han, B. Bae, S. Baek, and G. Jang, "New configuration of UPQC for medium-voltage application," IEEE Trans. Power Del., vol. 21, no. 3, pp. 1438–1444, Jul. 2006.
[6]     J. Chivite-Zabalza, M. A. Rodriguez, P. Izurza, G. Calvo, and D. Madariaga, "A large power, low-switching frequency voltage source converter for FACTS applications with low effects on the transmission line," IEEE Trans. Power Electron., vol. 27, no. 12, pp. 4868–4879, Dec. 2012.
[7]     X. Zhengping and S. Bhattacharya, "STATCOM control and operation with series connected transformer based 48-pulse VSC," in Proc. 33rd Annu. IEEE Ind. Electron. Soc. Conf., 2007, pp. 1714–1719.
[8]     F. J. Chivite-Zabalza, A. J. Forsyth, and D. R. Trainer, "A simple, passive 24-pulse AC-DC converter with inherent load balancing," IEEE Trans. Power Electron., vol. 21, no. 2, pp. 430–439, Mar. 2006.
[9]     Convertible Static Compensator (CSC) for New York Power Authority EPRI, Palo Alto, CA, and New York Power Authority, White Plains, NY: 2001. 1001970.
[10]    Convertible Static Compensator (CSC) for New York Power Authority EPRI, Palo Alto, CA, and New York Power Authority, White Plains, NY: 2001. 1001970.
[11]    P. S. Sensarma, K. R. Padiyar, and V. Ramanarayanan, "Analysis and performance evaluation of a distribution STATCOM for compensating voltage fluctuations," IEEE Trans. Power Del., vol. 16, no. 2, pp. 259–264, Apr. 2001.
[12]    C. Schauder, "Vector analysis and control of advanced static VAr compensators," in Proc. Int. Conf. AC DC Power Transm. , 1991, pp. 266–272.
[13]    C. Ben-Sheng and H. Yuan-Yih, "A minimal harmonic controller for a STATCOM," IEEE Trans. Ind. Electron., vol. 55, no. 2, pp. 655–664, Feb. 2008.

# Dynamic Structural Optimization with Frequency Constraints

## Qasim H. Bader

*(Department Mechanical Engineering, College of Engineering, University of Babylon, Iraq)*

**Abstract:** *The present work introduces a new method of structural optimization based on frequency constraints by using FEM in conjunction with Evolution optimization. First able as in any structure using this type of optimization the structure is meshed by very small element and the Eigen value (natural frequencies) of the whole structure is find. Then for each element removal the same eigenvalue analysis is done and a new natural frequency is calculated and assigned to an element removed. The sensitivity of structure to this removal of material for each element will be calculated. The question now what will do to control the natural frequency of the structure based on this removal of each element alone. The answer for this question and based upon the sensitivity value, all natural frequencies can be shift towards the required value, this include increasing or decreasing the frequency value and also increasing or decreasing the gap between any pair of natural frequencies.*

**Keywords:** *Structural Optimization, Plate, Frequency Constraints, FEM*

## I. INTRODUCTION

Design optimization has long been sought by engineer. The established classic method of optimization demanded large scale computing facilities met only by the main frame computers till 1980. Two important development of the last three decades hsvr changed the course of events. First the large capacity computers and rapid-processing computing capability. Second, the method of optimization has been joined by new approaches based on concepts of evolutionary or genetic progression.      .

The optimum design of any structure including frequency constraints is very importance, especially in mechanical engineering like aeronautical industries. Also the structure response depends strongly upon the first six natural frequencies of structure.In practice we will be care to avoid a resonance phenomenon or excessive vibration when the excitation forces are near to one of the natural frequencies of the structure.

In the last two decades, there are many researches dealing with the structural optimization based on frequency constraints.Suzuki and Kikuchi[1] , One of the most challenging tasks in the field of structural optimization, where the topology of a structure is not constant and internal holes can be created during the optimization process. An important recent development in layout and shape optimization is the homogenization method in which a material with voids is introduced and the optimization is seeking the optimal porosity of such media.Pan & Wang[2], in this paper adaptive genetic algorithm (AGA) is applied to topology optimization of structure with frequency constraints.

Qasim H. Bader[3], introduce an Evolutionary structural optimization for static analysis for both isotropic and orthotropic shell structure.X.Y.Yong, presents an efficient harmony search (HS) based algorithm for solving the shape optimization subjected to multiple natural frequencies constraints[4].

Reference [5] introduced the same object to achieving the optimum design of beam based on frequency constraints. In this works the optimum design for structure is found and the approximation is done to calculate the value of sensitivity number.A new technique for multiple constraints environments by using of evolutionary structural optimization [6]. Grandhi, presents the same topic for frequency constraints. In this works it is based on changing the thickness of the parts only (i.e. the size of the structure)[7].

Tenk and Hagiwara investigated a vibration shape and topology optimization method for dynamic problems by using homogenization method[8].

In this paper the optimization technique used can applied to a wide range of problems and easy to use in conjunction with ANSYS program as a solution program. The benefit of this method is can be overcomes all difficult may be happen in the previous techniques and also can achieve the required result easy with low cost and without approximation.

## II. OPTIMIZATION CRITERIA

By using an evolution technique, the material removal form the structure is firstly done. The problem here is where we can remove the element and how. The sensitivity equation is required to decide the location of element removal and must join the element removal with the required response. Usually this equation is complicated especially for dynamic analysis.

In this paper a sensitivity equation can be calculated in simple way which indicate the change happen in the value of frequency due to effect of remove material on the frequencies of structure Xie[3].

After finished mesh the structure by fine element, the natural frequencies of the structure is calculated based upon the eigenvalue problem.

$$([K] - \omega_i^2 [m]\{ k_i = \{0\} \qquad (1)$$

Where [K] is the global stiffness matrix, [M] is the global mass matrix, $\omega_i$ is the natural frequency and $\{u_i\}$ is the eigenvector corresponding to natural frequencies.

Form equation (1), the natural frequency equation:

$$\omega i = ki/mi \qquad (2)$$

where $\omega i$ is the eigenvalue of the whole structure for mode i without removing any material.
ki is the modal stuffiness and is defined as:

$$ki = \{ui\}^T[K]\{ui\} \qquad (3)$$

And $m_i$ is the modal mass and is defined as:

$$mi = \{ui\}^T[M]\{ui\} \qquad (4)$$

Now assume we remove one element e from the structure whose natural frequency for mode i is $\omega_i$, the new natural frequency of the structure due to remove element e is for mode i is $\omega_{ie}$.

So the change between these values is known as sensitivity parameters and is defined as:

$$\beta i^e = \omega i - \omega i_e \qquad (5)$$

Where $\beta_i^e$ is the sensitivity parameters for mode i due to remove element number e.

Equation (5) is used for optimization of mode i alone and the others i[th] modes remain unchanged or kept at the same values.

Hence , when we need to optimize the structure including the relation between i and j modes, in this case the two direction sensitivity parameters needs to find and as follow.

$$\alpha ij^e = \beta i^e - \beta j^e i \# j \qquad (6)$$

Where $\alpha_{ij}^e$ is the two direction sensitivity parameters between mode i and j when element number e is removed.

### III. OPTIMIZATION PROCEDURE

By using evolution procedure, the optimum design of the structure start with removing some element of the structure depends on the sensitivity value and also the direction required.

**3.1 Change the value of mode i**
1- Apply the finite element model with a fine mesh.
2- Apply the solution to the model to get the eigenvalue.
3- For each element removed, find the sensitivity parameters $\beta_{ie}$ as described in eq.(5).
4- Remove some element whose sensitivity parameters is positive (the bigger values) when we needs to *increase* the value of natural frequency or remove some element whose sensitivity parameters is negative (the lowest values) when we needs to *decrease* the value of mode i.
5- Step 2 to step 4 is repeated until the optimal value reached or until the percentage of element removal is reached.Now when the designer wants to keep the natural frequency for mode i at constant value and wish to decrease the total weight of the structure. In this case remove elements whose sensitivity value near to zero (i.e. the elements have no change on mode umber i).

**3.2 Change the gap between two modes i and j**
In this case the two direction sensitivity parameter $\alpha_{ij}^e$ is used as described in equation (7). So this parameters indicate the difference between natural frequency i and natural frequency j due to remove element number e, and from this definition it is clear that when the designer needs to increase the gap between mode i and mode j, we will remove the element whose absolute value of $\alpha_{ij}^e$ is lowest. But when the designer wants to decrease the gap between the two modes i and j, then he must remove the elements whose absolute value of $\alpha_{ij}^e$ is highest.

**3.3 Optimization criteria with multiple frequency constraints.**

The optimum design of structure for this case including multiple frequency constraints is similar to one direction sensitivity parameters $\beta_i^e$ described in eq. (5). Assume the objective is to increase the value of mode one and keep the other five mode as soon as possible with same values. In this case we will remove the elements whose positive value of $\beta_1^e$ among $\beta_2^e$ to $\beta_6^e$ near to zero value. This means that the removal of element will increase mode number one and at the same time the effect of this removal on the others five modes is approximately zero.The ANSYS program is used as analytical program to calculate the natural frequency of each mode, and also the natural frequency due to removal of each element and for all modes. The advance programming language APDL was used to write the optimization program to works together with Ansys model. By this program the one dimension sensitivity parameters is calculated for each removal of element and for each mode, this represent a two dimensions array vector of {i$^{th}$ by NE}, where i represent the natural frequency for mode number i and NE represent the total element. The two dimensional sensitivity parameters represents a three dimensions array vector of{ i$^{th}$ x j$^{th}$ x NE}.The remove of an element is done by assign the material number to zero or by killing element. This action will reduce the total global mass matrix and stiffness matrix due to remove these elements and also the time required for solution become smaller. The number of iterations depends on reaching the required value of objective function or the iteration umber is finished or the percentage of material reduction from the original structure is reached.

## IV. EXAMPLES

In this papers the two dimensional cantilever plate of 2 meters length and 1 meter width, the thickness of plate is 0.1 meter. Modulus of elasticity E = 2.1e11 N/m$^2$ and poisons ratio $\upsilon$ = 0.3 and density 7800 Kg/m$^3$. The plate is fixed at one edge and free to move at the other three edges.

The model is divided into 80 x 40 elements. The type of element used is quadrilateral element.

**1. Increasing the value of mode number one.**

The finite element model of the plate is shown in fig.1 including boundary conditions and mesh element. In this case we will try to increase the first natural frequency and keep the other two frequencies at the same value as soon as possible. Fig.2 shows the evaluation history of the first three modes of the plate. In this figure the iterations is terminated when the volume reduction was reached to 6% from the original volume of the structure. For each iteration the total element removed kept with 2 elements maximum and removes the element has the highest value of sensitivity numbers as described in equation 5.

Fig.3 shows the final design model corresponding to 4.4% element removal. At the end of this stage of optimization the first natural frequency if changed from 417 Mhz to 450 MHz with an increasing of 15%.

The result obtained here is similar to the result obtained by Xie& Steven [1].

**2. Reducing the value of mode one**

The same finite model is used as shown in fig.1, the main difference in this case when we required reducing the value of first natural frequency is the type of element removal depends on the sensitivity value which have. In this case the element has the minimum value of sensitivity parameters as described in equation 5 is removed.

Fig.4 shows the evolution history of optimization for the first 3-modes, the other two modes kept constant as soon as possible.

Fig.5 shows the new design of the cantilever plate corresponding to 3.5% of the total element removal. The first natural frequency changed from 417 MHz to 390 MHz with a decrease of 12%. The result obtained here is similar to the result obtained from Tnek& Hagiwara [8]by using homogenization method.

**3. Changing the gap between chosen frequencies.**

To increase the gap between the first natural frequency and the second natural frequency for the same model shown in fig.1, in this case the element removed which has the highest absolute value of two dimensional sensitivity parameters $\alpha_{ij}^e$ as described in eq.6.

Fig.6 shows the evolution history for the first two natural frequencies. For the total element removal of 6%, the final difference between first natural frequency and the second natural frequency by 24% from 220 Hz to 250 Hz.
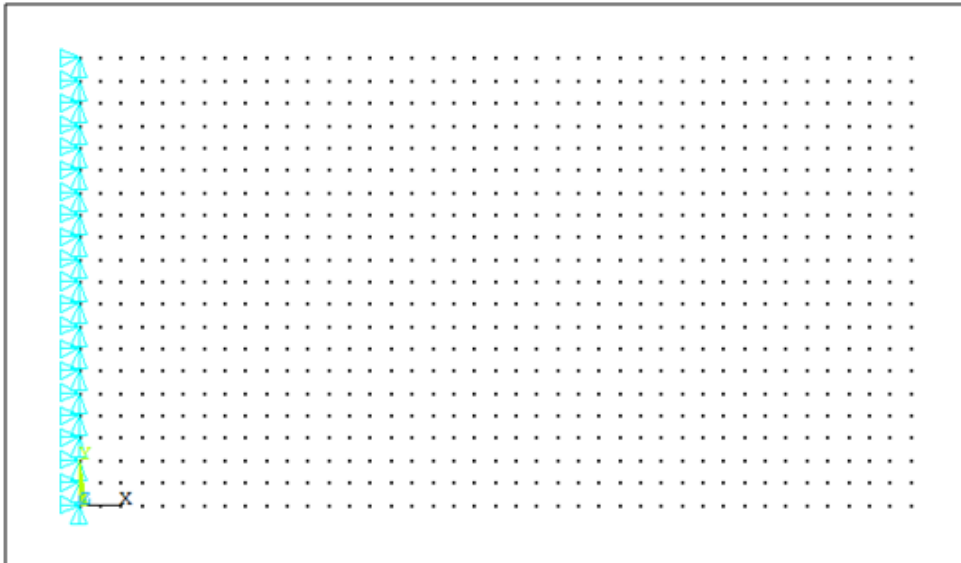
**Fig.1** Finite element model mesh with boundary conditions
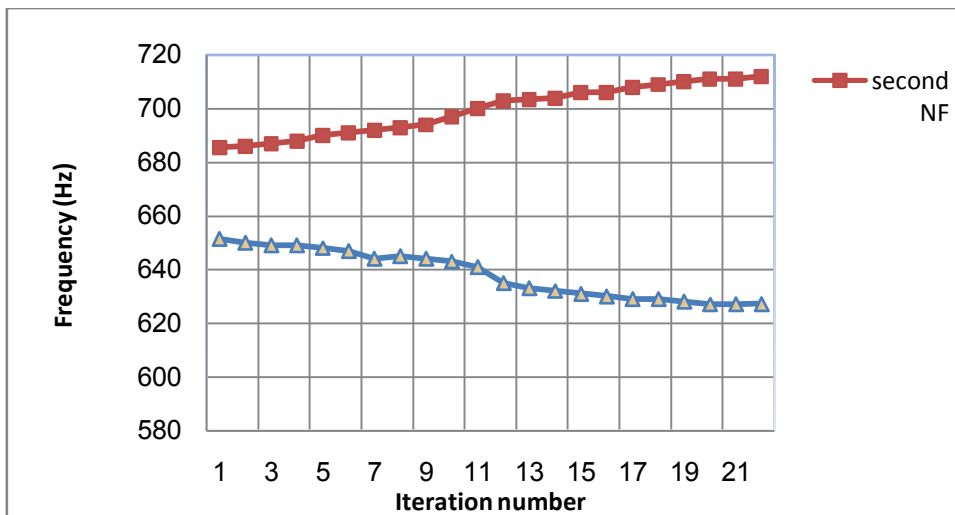


**Fig.2** Natural frequencies versus iteration number
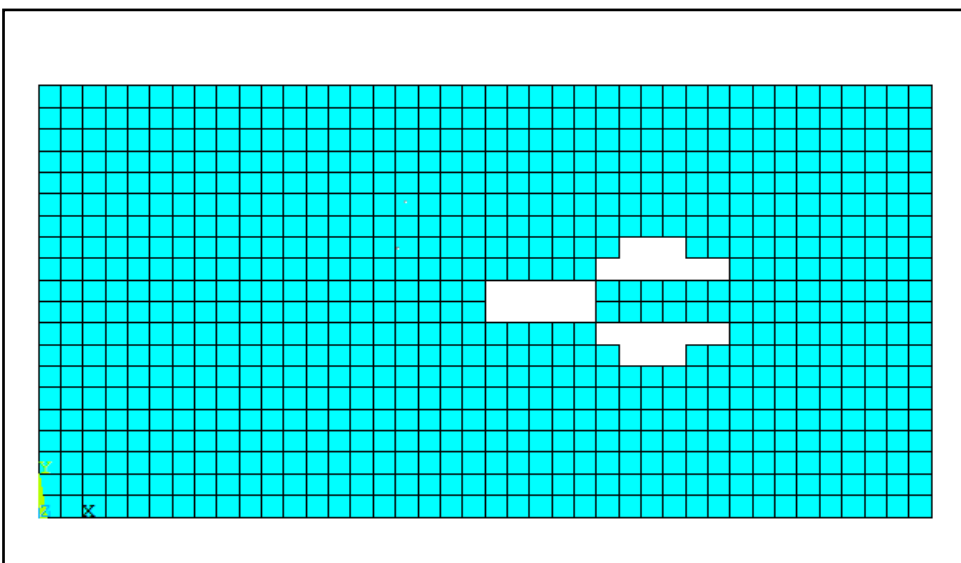


**Fig.3** Final design model of 4.4% element removal
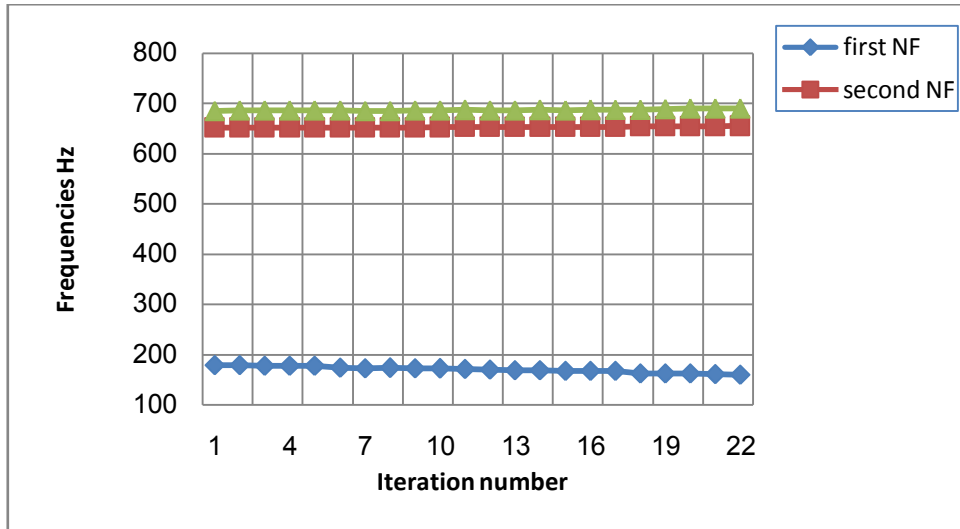
**Fig.4** Evaluation history for the first three NF versus iteration number
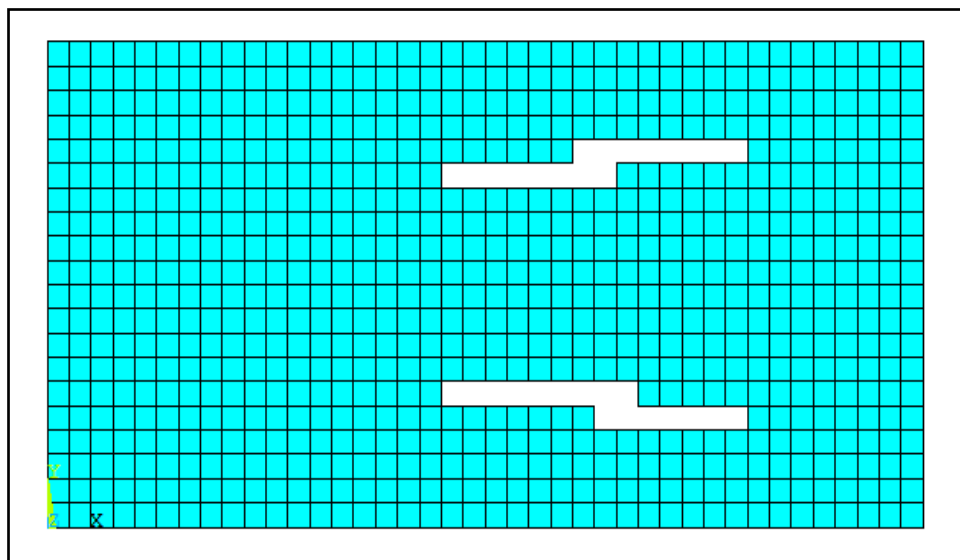


**Fig.5** Final design model for 3.5% of element removal
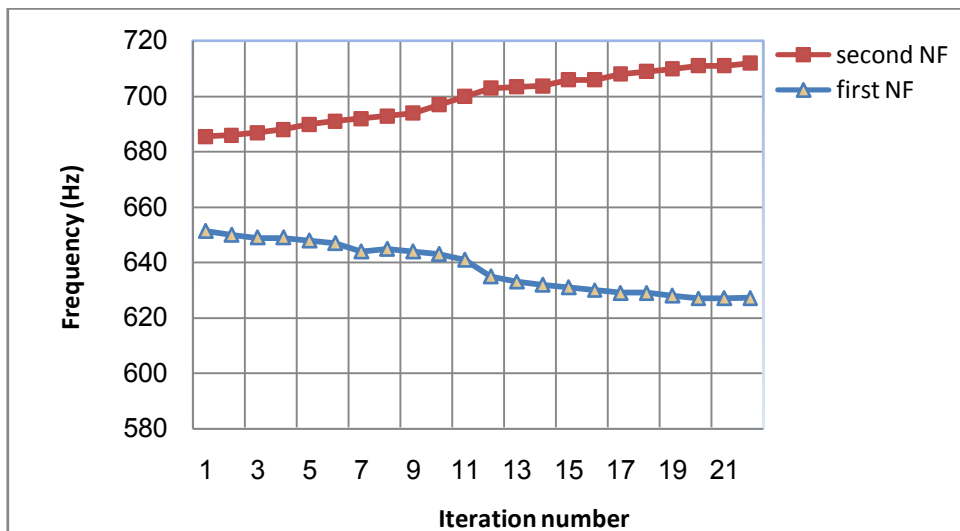


**Fig.6** Evaluation history for the first two NF$^s$ versus iteration number

## V. CONCLUSION REMARKS

Due to existing the finite element solution and software and also to the rapid change in this software comparing to the optimization program and also because the complexity and difficult that producing from the traditional methods.

By this a new technique used (evolution structural optimization)  and by use ANSYS Programming language (APDL) the optimization program can easily be written and works together with the ANSYS program as analytical program only.

So compare to Homogenization method by Hagiwara (8) this method has more simplicity and from using this method, the designer has the ability to control the dynamic characteristics of the structure, and comparing with new technique was introduce by Xie(3), this method is more accurate and precise due to use two dimensional sensitivity parameters when we needs to change the gap between any chose frequencies which is not used in the method of this author.

Also by this technique the new design topology of the structure can easily be calculated from the fine element removal with smooth change by the model.

Finally by using this technique in conjunction with any FEM solution no way to miss the goal required even the structure is complex or simple.

From the result mentioned to this research, for example the first natural frequency can be increased by 14% with removing of 3.5% volume, when the objective is to increase the first natural frequency and when needs to decrease the first natural frequency to 12%, the element removal of 4.4% is required.

Also when required to increase the gap between two natural frequency and kept the others near constant, the gap increase about 13% with removing of 6% from the original volume.

## REFERENCES

[1]     Suzuki and Kikuchi,, Homogenization method for shape and topology optimization, comp. meth. Appl. Mech. Eng. Vol. 93, pp291-318, 1991
[2]     Pan jin and Wang De-Yu, Topology optimization of truss structure with fundamental frequency and frequency domain response constraints,ActaMechanicasolidasinica ,Vol. 19, Sep. 2006, PP.231-240
[3]     Qasim H. Bader, Evaluation of evolutionary optimization technique of multi layered shell structure, PHD thesis, 2003, UOB
[4]     X.Y. Young, Topology optimization for structure with frequency constraints using evolutionary method. Journal of structural engineering, Vol.25, No.12,1999
[5]     Xie and Steven ," evolutionary structural optimization for dynamic problems, computers and structures , Vol. 58, no.6,pp 1067-1073, 1996
[6]     Steven &Querin , optimal design of multiple load case structures using an evolutionary procedure, Engineering computations , Vol. 11, 295-302, 1994
[7]     Grandihi, structural optimization with frequency constraints, AIAA, J.31, 2296-2303. 1993.BikashJoadder, Jagabandhu Shit, SanjibAcharyya, Fatigue Failure of Notched Specimen-A Strain-Life Approach, Materials Sciences and Applications, 2011.
[8]     Tenk and Hajiwara, Static and vibration shape and topology optimization using homogenization and mathematical programming, computers and meth. Applied mechanics engineering, 109, 143-154,1993.

# Implementation scheme of the Direct Torque Control strategy to Four Switch Three Phase Inverter fed Induction Motor drives

## G. Chitra[1], P. R. Muralimohan[2]

[1]*PG Student (PE&ED) Department of Electrical & Electronics Engineering S.V.C.E.T., Chittoor*
[2]*Associate Professor Department of Electrical & Electronics Engineering S.V.C.E.T., Chittoor*

***Abstract:*** *This paper proposes a novel direct torque control (DTC) strategy for induction motor (IM) drives fed by a four switch three-phase inverter (FSTPI). The introduced strategy is based on the emulation of the operation of the conventional six switch three-phase inverter (SSTPI). This has been achieved thanks to a suitable combination of the four unbalanced voltage vectors intrinsically generated by the FSTPI, leading to the synthesis of the six balanced voltage vectors of the SSTPI.*

*This approach has been adopted in the design of the vector selection table of the proposed DTC strategy which considers a subdivision of the Clarke plane into six sectors. Simulation results have revealed that, thanks to the proposed DTC strategy, FSTPI-fed IM drives exhibit interesting performance. These have been experimentally validated and compared to the ones yielded by the Takahashi and the basic DTC strategies dedicated to the SSTPI and to the FSTPI, respectively.*

## I. Introduction

IN RECENT years, direct torque control (DTC) strategies of induction motor (IM) drives have been widely implemented in industrial variable speed applications. Introduced in the middle of the 1980s, the first DTC strategy involves a simple control scheme which makes it possible rapid real time implementation. Since then, several investigations carried out in order to improve the performance of the original DTC strategy.

The major focused features are the uncontrolled switching frequency of the inverter and the high torque ripple resulting from the use of flux and torque hysteresis controllers.

Currently and more than two decades of investigation, several DTC strategies have been proposed so far. These could be classified within four major categories: 1) strategies considering variable hysteresis band controllers 2) strategies with space vector modulation (SVM)-based control of the switching frequency 3) strategies using predictive control scheme and 4) strategies built around intelligent control approaches. Nevertheless, the gained performance is allied to significant increase of implementation schemes.

Commonly, the voltage source inverter (VSI) feeding IM under DTC is the six-switch three-phase inverter (SSTPI). This said, some applications such as electric and hybrid propulsion systems, should be as reliable as possible. Within this requirement, the reconfiguration of the SSTPI into a four-switch three-phase inverter (FSTPI), in case of a switch/leg failure, is currently given an increasing attention . A DTC strategy dedicated to FSTPI-fed IM drives has been proposed . In spite of its simplicity, this strategy is penalized by the low dynamic and the high ripple of the torque. These drawbacks are due to the application of unbalanced voltage vectors to control flux and torque with a subdivision of the Clarke plane limited to four sectors.

Recently, an attempt to discard the previously described disadvantages has been proposed where a DTC scheme using a 16-sector vector selection table has been implemented. Nevertheless, it has been noted that the drive performance remains relatively low due to the increase of the CPU time which is linked to the complexity of the involved vector selection table. In order to achieve a constant switching frequency and to decrease the torque ripple, many DTC schemes based on SVM, using the FSTPI as a VSI, dedicated to control induction and permanent-magnet synchronous motors have been reported in the literature . These strategies offer high performance in terms of torque ripple reduction allied to the control of the inverter switching losses. However, these performances are compromised by the complexity of their implementation schemes.

This paper proposes a new DTC strategy dedicated to FSTPI- fed IM drives. It is based on the emulation of the SSTPI operation thanks to the synthesis of an appropriate vector selection table, which is addressed by hysteresis controllers. The resulting simplicity of the implementation scheme makes the strategy very attractive in many applications, such as the automotive one.

## II.  DTC Of FSTPI-Fed IM Drives: Background

### A. DTC Basis

DTC strategies allow a direct control of the motor variables through an appropriate selection of the inverter control signals, in order to fulfil the requirements as whether the stator flux and torque need to be increased, decreased, or maintained. These decisions are achieved according to the output $C_\emptyset$ of the flux hysteresis controller, the output $C_\tau$ of the torque hysteresis controller, and the angular displacement $\theta_s$ of the stator flux vector $\Phi_s$ in the Clarke ($\square$ $\square$) plane.
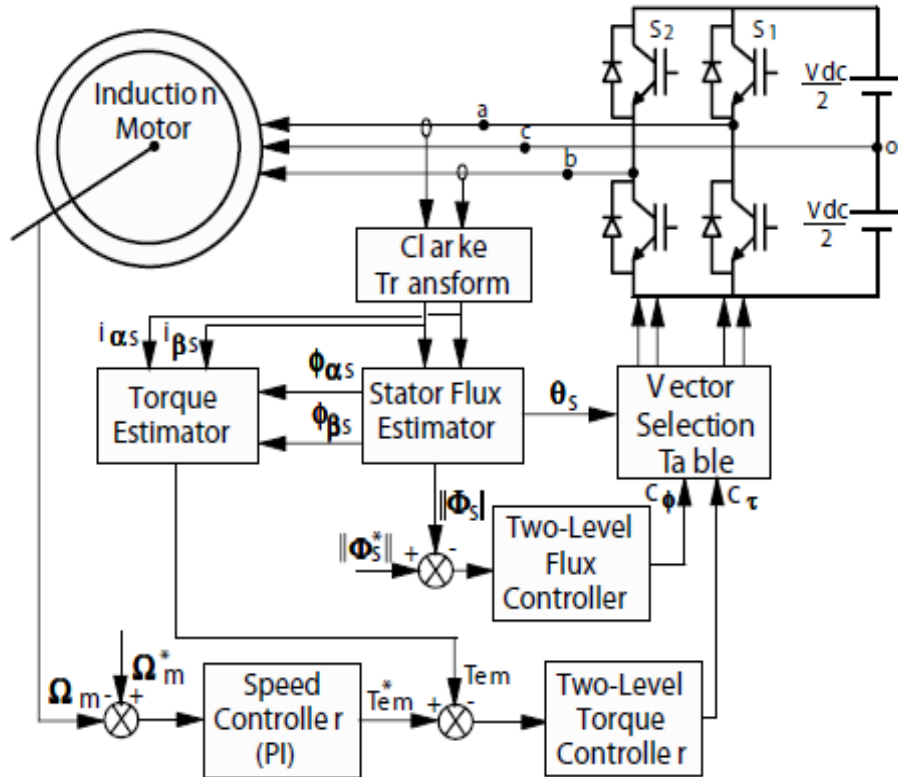


Fig.1. Implementation scheme of the DTC strategy dedicated to FSTPI-fed IM drives.

The dynamic of $\Phi_s$ is governed by the stator voltage equation expressed in the stationary reference frame, as follows:

$$\frac{d}{dt}\Phi_s = V_s - r_s I_s$$

where $\mathbf{Vs}$ , $I_s$ , and rs are the stator voltage vector, current vector, and resistance, respectively. Neglecting the voltage drop $r_s I_s$ across the stator resistance, and taking into account that the voltage vector is constant in each sampling period T$_s$ , the variation of the stator flux vector turns to be proportional to the applied voltage vector. Maintaining the stator flux constant, the variation of the electromagnetic torque Tem depends on the direction of the applied voltage vector, such that:

$$T_{em} = N_P \frac{M}{l_s l_r - M^2} \|\Phi s\| \|\Phi_r^s\| \sin\delta$$

where $\Phi_r^s$ is the rotor flux vector referred to the stator, $\square$ is the angular shift between the stator and rotor fluxes, $\mathbf{Np}$ is the pole pair number, and $I_s$ ,$I_r$ , and M are the stator self-inductance, the rotor self-inductance, and the mutual inductance, respectively. The implementation scheme of the DTC strategy dedicated to a FSTPI-fed IM, shown in Fig. 1, has the same layout as the one of the basic DTC strategy initially proposed, except that,

1) the SSTPI inverter is reconfigured to a FSTPI. Such a reconfiguration is carried out by adding        to the former three extra TRIACs with three fast acting fuses,

2) the three-level hysteresis controller in the torque loop is substituted by a two-level hysteresis   controller. As will be depicted in Section III, this substitution is motivated by the fact that no zero voltage vector is involved in the proposed DTC scheme

**TABLE I:**

Switching states, Stator phase Voltages, their Clarke Components and their corresponding Voltage Vectors

| $(S_1 S_2)$ | $V_{as}$ | $V_{bs}$ | $V_{cs}$ | $V_{\alpha s}$ | $V_{\beta s}$ | $V_1$ |
|---|---|---|---|---|---|---|
| (0 0) | $\dfrac{-V_{dc}}{6}$ | $\dfrac{-V_{dc}}{6}$ | $\dfrac{V_{dc}}{3}$ | $\dfrac{-V_{dc}}{2\sqrt{6}}$ | $\dfrac{-V_{dc}}{2\sqrt{2}}$ | $V_1$ |
| (1 0) | $\dfrac{V_{dc}}{2}$ | $-\dfrac{V_{dc}}{2}$ | 0 | $\dfrac{3V_{dc}}{2\sqrt{6}}$ | $\dfrac{-V_{dc}}{2\sqrt{2}}$ | $V_2$ |
| (1 1) | $\dfrac{V_{dc}}{6}$ | $\dfrac{V_{dc}}{6}$ | $\dfrac{V_{dc}}{3}$ | $\dfrac{V_{dc}}{2\sqrt{6}}$ | $\dfrac{-V_{dc}}{2\sqrt{2}}$ | $V_3$ |
| (0 1) | $-\dfrac{V_{dc}}{2}$ | $\dfrac{V_{dc}}{2}$ | 0 | $-\dfrac{3V_{dc}}{2\sqrt{6}}$ | $\dfrac{V_{dc}}{2\sqrt{2}}$ | $V_4$ |
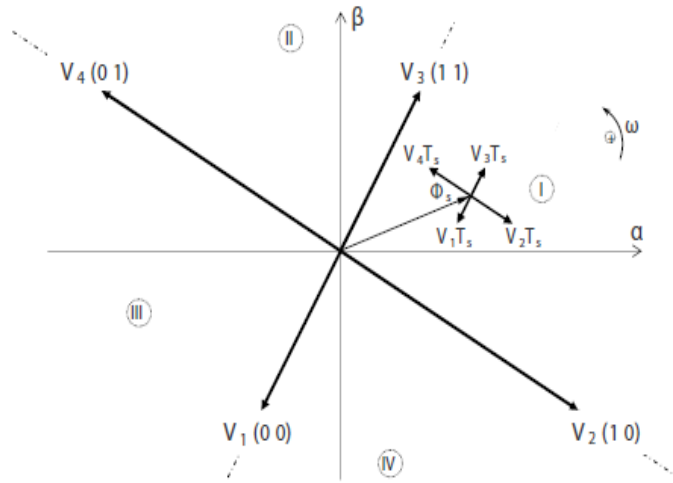


**Fig.2 Unbalanced active voltage vectors generated by the FSTPI**

**B. Intrinsic Voltage Vectors of the FSTPI**

The FSTPI topology consists of a two-leg inverter as illustrated in Fig. 1. Two among the three phases of the motor are connected to the FSTPI legs, while the third one is connected to the middle point of the dc-bus voltage.

Let us assume that the states of the four insulated-gate bipolar transistors (IGBTs) of the FSTPI are denoted by the binary variables S1 to S4 , where the binary "1" corresponds to an ON state and the binary "0" indicates an OFF state. The IM stator voltages are expressed in terms of the states (S1 and S2) of the upper IGBTs, as follows:

$$\begin{bmatrix} V_{as} \\ V_{bs} \\ V_{cs} \end{bmatrix} = \frac{V_{dc}}{6} \begin{bmatrix} 4 & -2 & -1 \\ -2 & 4 & -1 \\ -2 & -2 & 2 \end{bmatrix} \begin{bmatrix} S_1 \\ S_2 \\ 1 \end{bmatrix} \qquad (3)$$

The Clarke transform applied to the stator voltages yields:

$$\begin{bmatrix} V_{\alpha s} \\ V_{\beta s} \end{bmatrix} = \sqrt{\frac{2}{3}} \begin{bmatrix} 1 & -\frac{1}{2} & -\frac{1}{2} \\ 0 & \frac{\sqrt{3}}{2} & -\frac{\sqrt{3}}{2} \end{bmatrix} \begin{bmatrix} V_{as} \\ V_{bs} \\ V_{cs} \end{bmatrix} \qquad (4)$$

Four combinations of the states of the upper IGBTs are characterized by four active voltage vectors (V1 to V4) in the αβ plane, which are given in Table I.

Fig.2 shows the four active voltage vectors represented in the αβ plane. These vectors have unbalanced amplitudes and are shifted by an angle of   π/( 2) . Indeed, vectors V1 and V3 have an  amplitude of Vdc/ √ 6, while vectors V2 and V4 have amplitude of Vdc/√2

**TABLE II**

**Vector selection table of the basic   DTC strategy**

| $C_\emptyset$ $C_r$ | +1 +1 | +1 -1 | -1 +1 | -1 -1 |
|---|---|---|---|---|
| **Sector  I** | $V_3$ | $V_2$ | $V_4$ | $V_1$ |
| **Sector II** | $V_4$ | $V_3$ | $V_1$ | $V_2$ |
| **sector III** | $V_1$ | $V_4$ | $V_2$ | $V_3$ |
| **Sector IV** | $V_2$ | $V_1$ | $V_3$ | $V_4$ |

**C. Limitations of the Basic DTC of a FSTPI-Fed Induction Motor:**

The basic DTC of an IM fed by the FSTPI is based on the subdivision of the αβ plane into four sectors, limited by the four active voltage vectors as shown in Fig. 2. The vector selection table corresponding to the basic strategy is presented in Table II.

Accounting for the symmetry of the four sectors, the following analysis of the torque and flux variations, will be limited to sector I, considering two cases:
1) the initial stator flux vector Φs1 is held by vector     $V_2$ ;
2) the initial stator flux vector Φs1 is held by vector     $V_3$ .
Equation (1) could be rewritten as follows:

$$\Phi_{s2}^i = \Phi_{s1} + (V_i - r_s I_s)T_s \qquad (5)$$

Where $V_i$ ($1 \le i \le 4$) is the voltage vector generated by the FSTPI.
Fig. 3 shows different phasor diagrams of (5), considering both cases previously cited with four scenarios selected from the vector selection table, for each. One can notice the following remarks which deal with the torque dynamic:
1) The application of voltage vectors     $V_1$ or $V_3$ leads to a low torque dynamic if:
    a) $\Phi_{s1}$ is close to vector $V_2$ due to the low amplitude $V_1$ and $V_3$ [see Fig. 3(a1) and (a3)];
    b) $\Phi_{s1}$ is close to vector  $V_3$ due to the low angular shift of the flux vector [see Fig. 3(b1) and (b3)]. It is to be noted that the torque command $C_\tau$ of the control combinations ($C_\emptyset = -1$, $C_\tau = +1$) corresponding to sector II and ($C_\emptyset = +1$, $C_\tau = +1$) corresponding to sector I could not be achieved by the application of    vectors  $V_1$ and $V_3$ , respectively.
  2) The application of voltage vectors  $V_2$ or $V_4$ leads to a low torque dynamic if $\Phi_{s1}$ is close to vector $V_2$ due to the low angular shift of the flux vector [see Fig. 3(a2) and (a4)]. One can notice that the control combinations ($C_\emptyset = +1$, $C_\tau = +1$) corresponding to sector IV and ( $C_\emptyset = -1$, $C_\tau = +1$) corresponding to sector I could not be achieved with the application of voltage vectors $V_2$ and $V_4$, respectively.
  3) The application of voltage vectors $V_2$ or $V_4$ leads to a high torque dynamic if $\Phi_{s1}$ is located near vector $V_3$ [see Fig. 3(b2) and (b4)].

From the previous analysis, one can clearly notice that the basic DTC strategy presents different limitations. These could be eradicated considering the introduced DTC strategy which will be developed in the following section.

**PROPOSED DTC STRATEGY**
**A. Approach to Generate Balanced Voltages by the FSTPI**

The proposed DTC strategy is based on the emulation of SSTPI operation by the FSTPI. This has been achieved through the generation of six balanced voltage vectors using the four intrinsic ones of the FSTPI. The generated vectors have the same amplitude and angular shift as those of the SSTPI. Basically, the active voltage vectors $V_k$, with $1 \le k \le 6$, yielded by the SSTPI have an amplitude $V_k$ equal to $\sqrt{(2/3)}\,V_{dc}$, where $V_{dc}$ is the dc-bus voltage. For the same value of $V_{dc}$, the voltage vectors $V_i$ , with   $1 \le i \le 4$, generated by the FSTPI, present unbalanced amplitudes $V_i$, such that:

$$\begin{cases} V_1 \quad = V_3 \quad = \dfrac{V_{dc}}{\sqrt 6} = \quad \dfrac{1}{2} V_k \\ V_2 \quad = V_4 \quad = \dfrac{V_{dc}}{\sqrt 2} = \quad \dfrac{\sqrt 3}{2} V_k \end{cases} \qquad (6)$$

therefore, a dual application of the voltage vector $V_1$ (respectively, $V_3$ ) of the FSTPI, leads to the generation of the   voltage   vector    $V_{11}$ (respectively,  $V_{33}$), as shown in Fig. 4. It is to be noted that $V_{11}$ and $V_{33}$ are identical to two vectors among the six generated by the SSTPI. Now, let us call Vij the voltage vectors

resulting from the sums of successive voltage vectors Vi and Vj , with $1 \leq i \leq 4$ and $1 \leq j \leq 4$. As far as the angular shift between two successive voltage vectors is equal to   $\pi/2$ , the amplitude   $\mathbf{V_{ij}}$ of vectors   $\mathbf{V_{ij}}$ can be expressed as follows:

$$\mathbf{V_{ij}} = \sqrt{V_i^2 + V_j^2} = \sqrt{\frac{1}{6} + \frac{1}{2}}\mathbf{V_{dc}} = \sqrt{\frac{2}{3}}\mathbf{V_{dc}} = \mathbf{V_k} \quad (7)$$
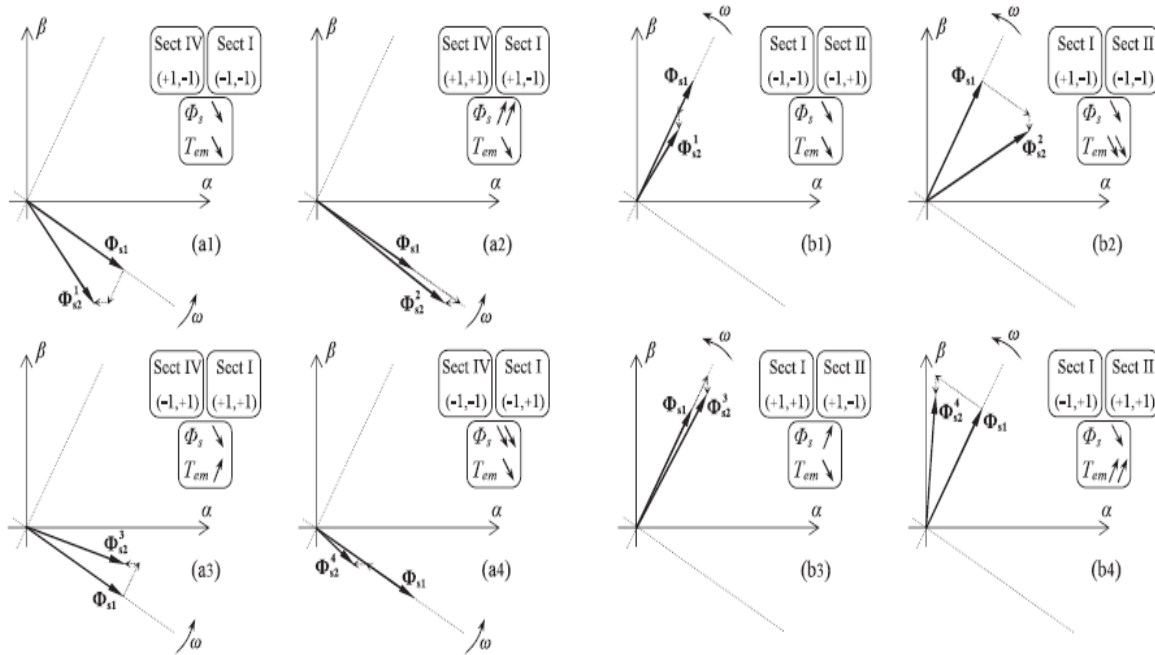


**Fig. 3. Phasor diagrams describing the evolution of the stator flux vector in the case where it is located in the limits of sector I. Legend:  (a) initial flux vector □ s1 held by the voltage vector V2 (b) initial flux vector □ s1 held by the voltage vector  V3**.
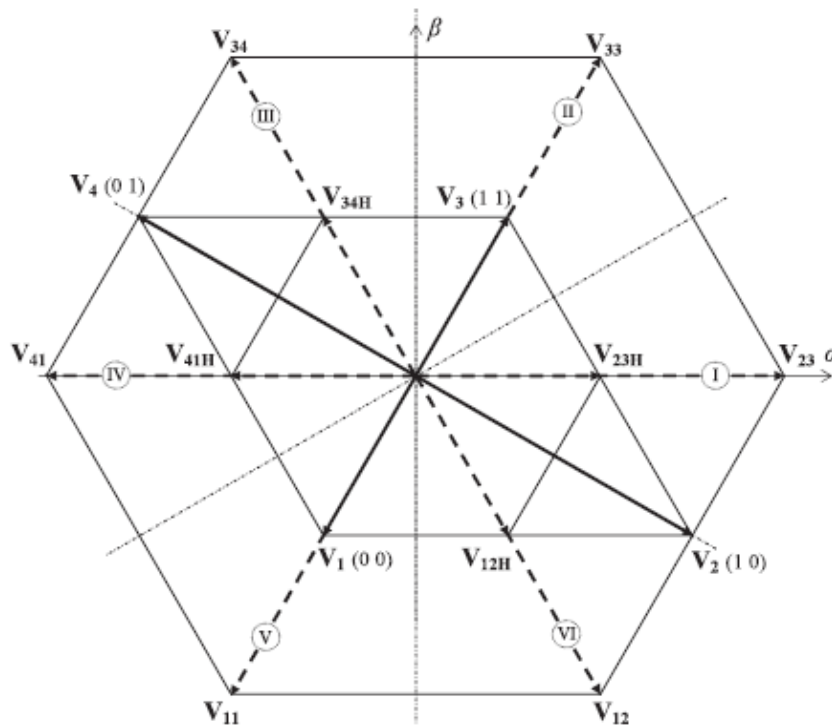


.**Fig.4. Generation of the SSTPI active voltage vectors using the four unbalanced voltage ones of the FSTPI**

One can notice that the voltage vectors Vij have the same amplitude as the ones generated by the SSTPI. Beyond the amplitude, the four generated vectors, named $V_{12}$, $V_{23}$, $V_{34}$, and $V_{41}$, as shown in Fig. 4, share the same phases with the four remaining active voltage vectors of the SSTPI. Table III summarizes the Clarke components of the six voltage vectors generated by the FSTPI considering the previously described approach.

**TABLE III**
**Clarke COMPONENTS OF THE GENERATED VOLTAGE VECTORS**

| $V_{ij}$ | $V_{23}$ | $V_{33}$ | $V_{34}$ | $V_{41}$ | $V_{11}$ | $V_{12}$ |
|---|---|---|---|---|---|---|
| $V_{\alpha s}$ | $\sqrt{\dfrac{2}{3}}V_{dc}$ | $\dfrac{V_{dc}}{\sqrt{6}}$ | $\dfrac{-V_{dc}}{\sqrt{6}}$ | $-\sqrt{\dfrac{2}{3}}V_{dc}$ | $\dfrac{-V_{dc}}{\sqrt{6}}$ | $\dfrac{V_{dc}}{\sqrt{6}}$ |
| $V_{\beta s}$ | $0$ | $\dfrac{V_{dc}}{\sqrt{2}}$ | $\dfrac{V_{dc}}{\sqrt{2}}$ | $0$ | $-\dfrac{V_{dc}}{\sqrt{2}}$ | $-\dfrac{V_{dc}}{\sqrt{2}}$ |

Following the generation of six balanced active voltage vectors ($V_{23}$, $V_{33}$, $V_{34}$, $V_{41}$, $V_{11}$, and $V_{12}$), the αβ plane turns to be subdivided into six symmetric sectors as illustrated in Fig. 4. Moreover, zero voltage vectors can be achieved through the application of two opposite intrinsic ones. The previously described approach represents a great control benefit so far as several DTC strategies implemented in SSTPI fed IM drives could be applied to FSTPI-fed IM ones.

**B. Vector Selection Table of the Proposed DTC Strategy**
The proposed DTC strategy is inspired from the earlier one introduced by Takahashi [1]. For the sake of reduction of the switching frequency as well as the torque ripple, the control combinations ($C_{\emptyset} = \pm 1$, $C_{\tau} = 0$) are omitted using a two-level hysteresis controller in the torque loop.
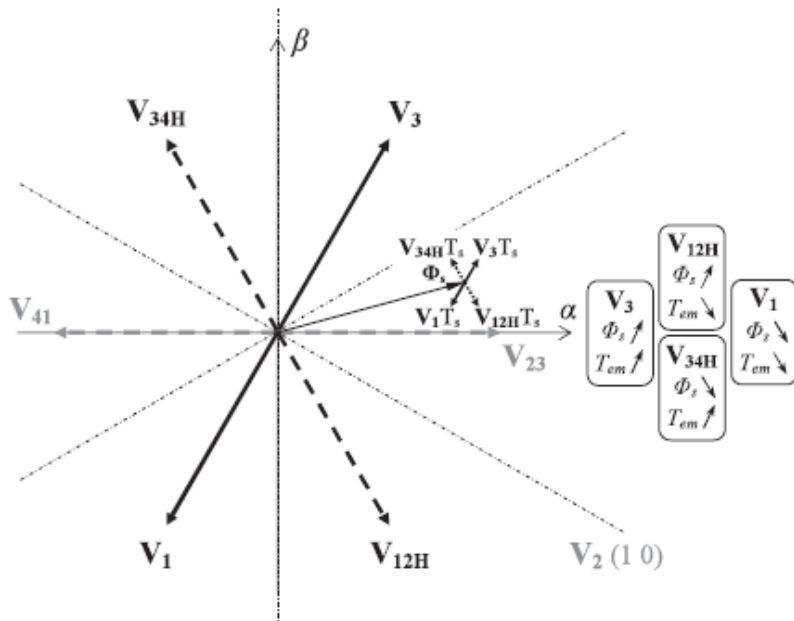


**Fig. 5 Applied voltage vectors in the case where $\Phi_s$   is located in sector I.**

The synthesis of the vector selection table of the proposed DTC strategy is based on the approach described in the previous paragraph. how the control combinations ($C_{\emptyset}=\pm 1$, $C_{\tau}= \pm 1$) could be achieved applying the generated balanced voltage vectors?.
1) The application of $V_{11}$ ( respectively , $V_3$ ) during two successive sampling periods $2T_s$ allows the generation of $V_{11}$ (respectively, $V_{33}$),
2) The application of two consecutive voltage vectors $V_i$ and $V_j$ during two successive sampling periods leads to the generation of $V_{ij}$ .
As a result, the equivalent voltage vectors per sampling period $T_s$ generated by the FSTPI, considering the adopted approach, can be expressed as:

$$\begin{cases} \mathbf{V_{11}\,H} = \frac{1}{2}\,\mathbf{V_{11}} = \mathbf{V_i} \\ \mathbf{V_{33}\,H} = \frac{1}{2}\,\mathbf{V_{33}} = \mathbf{V_3} \qquad\qquad (8) \\ \mathbf{V_{ij}\,H} = \frac{1}{2}\,\mathbf{V_{ij}} \end{cases}$$

where subscript H indicates the half of the corresponding voltage vector. In what follows, the synthesis of the vector selection table will be limited to sector I ($-\pi/6 \leq \theta s \leq \pi/6$ ). In this case and as shown in Fig. 5, the following voltage vectors are applied during a sampling period, according to the corresponding control combinations:

$$\begin{cases} \mathbf{V_3} \ \ \mathbf{for} \ (\mathbf{C_\emptyset} = +1\,, \mathbf{C_\tau} = +1) \\ \mathbf{V_{12}} \ \ \mathbf{for}(\mathbf{C_\emptyset} = +1, \mathbf{C_\tau} = -1) \\ \mathbf{V_{34}} \ \ \mathbf{for}(\mathbf{C_\emptyset} = -1, \mathbf{C_\tau} = +1) \\ \mathbf{V_1} \ \ \mathbf{for}(\mathbf{C_\emptyset} = -1, \mathbf{C_\tau} = -1) \end{cases}$$

In order to emulate the operation of the SSTPI, each control combination ($\mathbf{C_\emptyset}$ , $\mathbf{C_\tau}$ ) should be maintained during two sampling periods 2Ts , which yields the application of:

$$\begin{cases} \mathbf{V_{33}} \ \ \mathbf{for}(\mathbf{C_\emptyset} = +1\,, \mathbf{C_\tau} = +1) \Rightarrow \mathbf{V_3} \ \text{then} \ \mathbf{V_3} \\ \mathbf{V_{12}} \ \ \mathbf{for}(\mathbf{C_\emptyset} = +1, \mathbf{C_\tau} = -1) \Rightarrow \mathbf{V_1} \ \text{then} \ \mathbf{V_2} \\ \mathbf{V_{34}} \ \ \mathbf{for}(\mathbf{C_\emptyset} = -1, \mathbf{C_\tau} = +1) \Rightarrow \mathbf{V_3} \ \text{then} \ \mathbf{V_4} \\ \mathbf{V_{11}} \ \ \mathbf{for}(\mathbf{C_\emptyset} = -1, \mathbf{C_\tau} = -1) \Rightarrow \mathbf{V_1} \ \text{then} \ \mathbf{V_1} \end{cases}$$
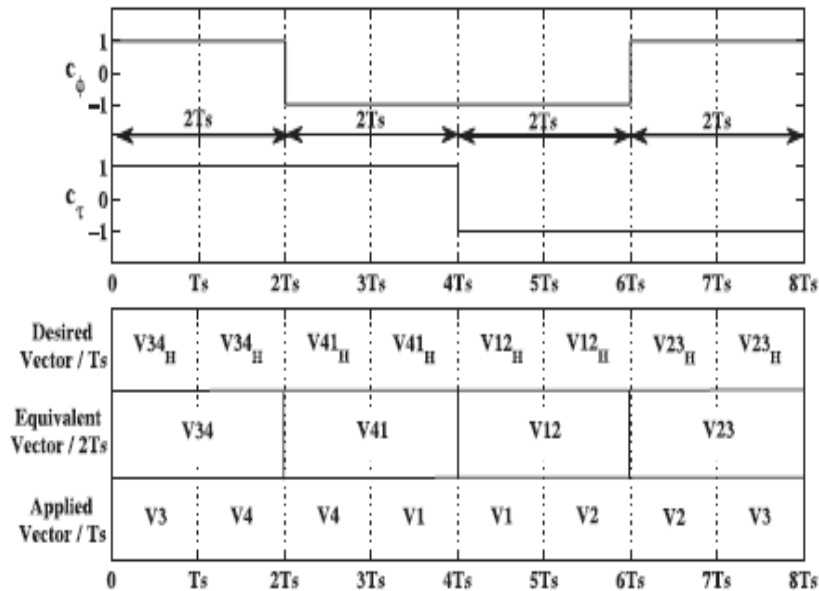


**Fig. 6. Control combinations (c □ , c □), desired voltage vectors per Ts , equivalent voltage vectors during 2Ts , and applied voltage vectors per Ts**

**TABLE IV**

**DESIRED VECTOR SELECTION TABLE**

| $C_\emptyset$ | +1 | +1 | -1 | -1 |
|---|---|---|---|---|
| $C_r$ | +1 | -1 | +1 | -1 |
| Sector I | $V_3$ | $V_{12H}$ | $V_{34H}$ | $V_1$ |
| Sector II | $V_{34H}$ | $V_{23H}$ | $V_{41H}$ | $V_{12H}$ |
| Sector III | $V_{41H}$ | $V_3$ | $V_1$ | $V_{23H}$ |
| Sector IV | $V_1$ | $V_{34H}$ | $V_{12H}$ | $V_3$ |
| Sector V | $V_{12H}$ | $V_{41H}$ | $V_{23H}$ | $V_{34H}$ |
| Sector VI | $V_{23H}$ | $V_1$ | $V_3$ | $V_{41H}$ |

**TABLE V**

**IMPLEMENTED VECTOR SELECTION TABLE**

| $c_\phi$ | +1 | | +1 | | −1 | | −1 | |
|---|---|---|---|---|---|---|---|---|
| $c_\tau$ | +1 | | −1 | | +1 | | −1 | |
| Periods $T_s$ | $1^{st}$ | $2^{nd}$ | $1^{st}$ | $2^{nd}$ | $1^{st}$ | $2^{nd}$ | $1^{st}$ | $2^{nd}$ |
| Sector I | $V_3$ | | $V_1$ | $V_2$ | $V_3$ | $V_4$ | $V_1$ | |
| Sector II | $V_3$ | $V_4$ | $V_2$ | $V_3$ | $V_4$ | $V_1$ | $V_1$ | $V_2$ |
| Sector III | $V_4$ | $V_1$ | $V_3$ | | $V_1$ | | $V_2$ | $V_3$ |
| Sector IV | $V_1$ | | $V_3$ | $V_4$ | $V_1$ | $V_2$ | $V_3$ | |
| Sector V | $V_1$ | $V_2$ | $V_4$ | $V_1$ | $V_2$ | $V_3$ | $V_3$ | $V_4$ |
| Sector VI | $V_2$ | $V_3$ | $V_1$ | | $V_3$ | | $V_4$ | $V_1$ |

The inputs ($C_\emptyset$ , $C_\tau$ , and $\theta_s$ ) of the vector selection table should be maintained during 2Ts which yields the implemented vector selection table provided in Table V. It is to be noted that both intrinsic and compounded voltage vectors are involved in sectors  I, III, IV, and VI, while in sectors II and V, only the compounded voltage vectors are applied. Thus, one can expect an increase of the switching frequency in sectors II and V, with respect to the one in the remaining sectors.

**TABLE VI:** RATIO OF THE AMPLITUDES HARMONICS WITH RESPECT TO FUNDAMENTAL ONE

| Harmonic | $i_{as}$ | | | $i_{cs}$ | | |
|---|---|---|---|---|---|---|
| | $2^{nd}$ | $3^{rd}$ | $5^{th}$ | $2^{nd}$ | $3^{rd}$ | $5^{th}$ |
| $f_s = 2.5HZ$ | 8% | 13.8% | | 9.5% | 11% | |
| $f_s = 20HZ$ | 12% | 13% | 12.5% | 7% | 4% | 8.5% |

**TABLE VII**

**INDUCTION MACHINE RATINGS**

| Power | 0.37 KW | Efficiency | 77% |
|---|---|---|---|
| Voltage | 230V/400V | Current | 1.7A/1A |
| Torque | 2.56 N.m | Stator Flux (Rms) | 640 wb |
| Speed | 1380 rpm | Frequency | 50 HZ |

**Simulation circuit:**



---
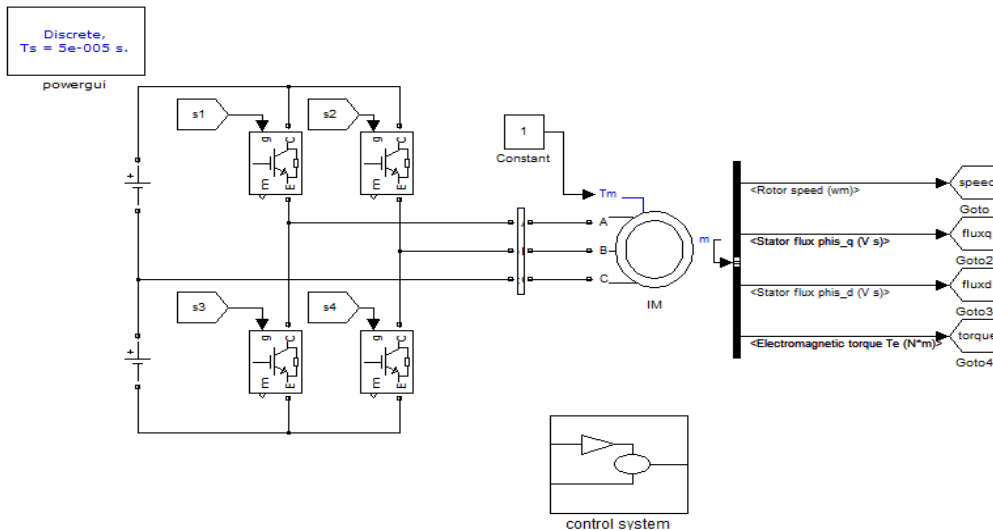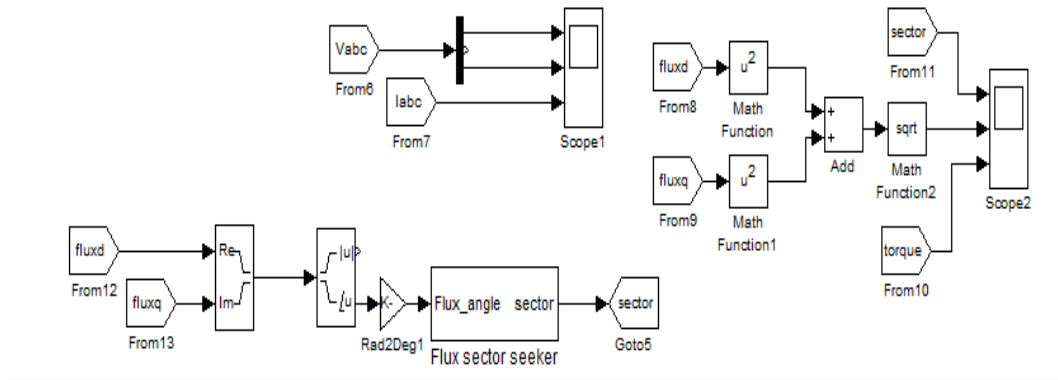
**Simulation results:**
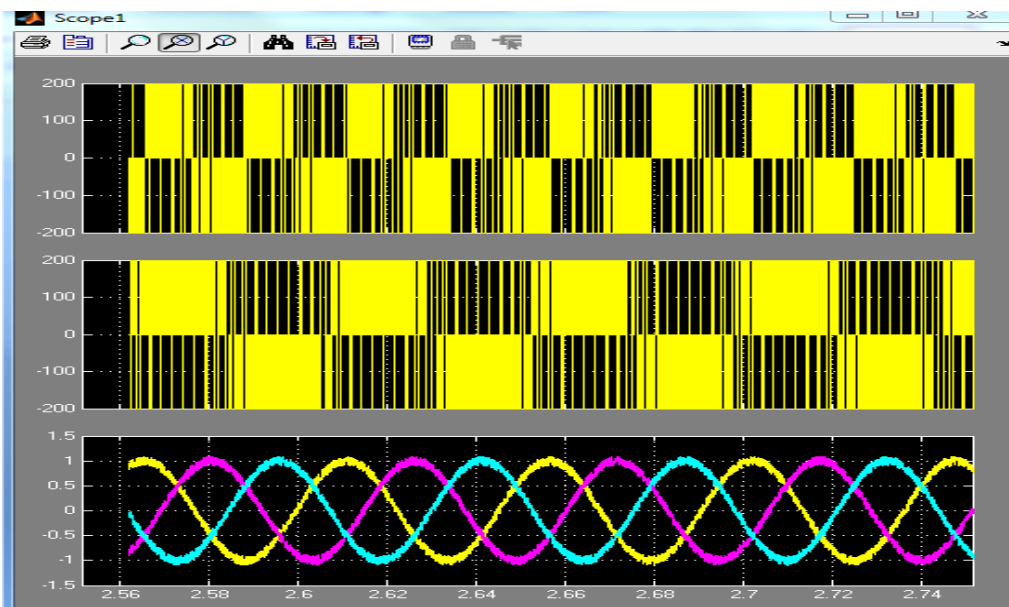


**Fig: Stator a-phase voltage , Stator c-phase voltage, Stator phase currents**
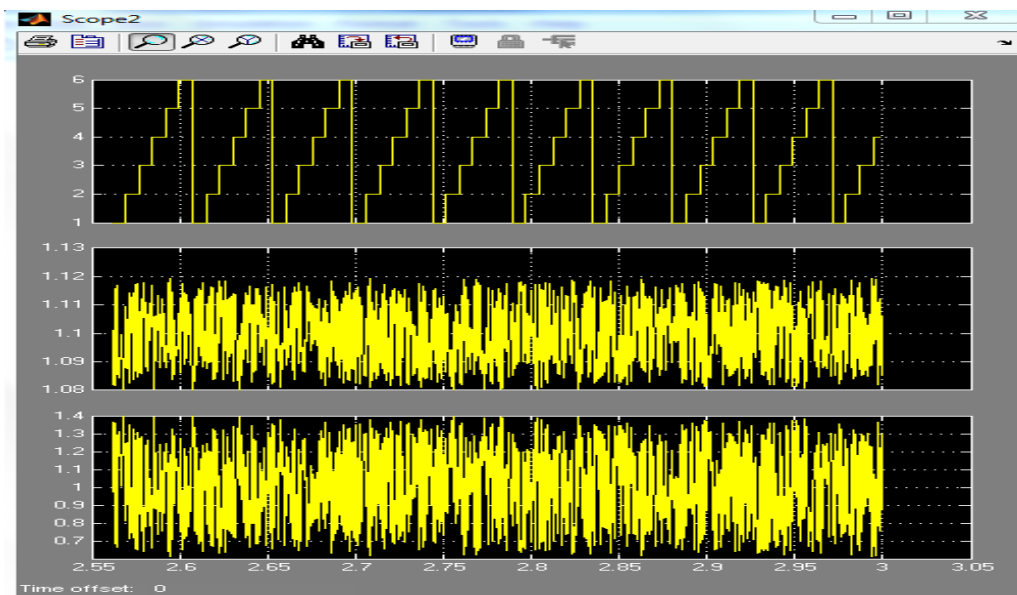


**Fig: Sector section described in alpha,beta plane,stator flux amplitude and its   reference and electromagnetic torque**

## III.  Conclusion

This paper dealt with a new DTC strategy dedicated to FSTPI fed IM drives. The proposed DTC strategy is based on the emulation of the operation of the conventional SSTPI. This has been achieved thanks to suitable combinations of the four unbalanced voltage vectors intrinsically generated by the FSTPI, leading to the synthesis of the six balanced voltage vectors yielded by the SSTPI. This approach has been adopted in the design of the vector selection table which is simply addressed by hysteresis controllers, considering a subdivision of the Clarke plane into six sectors.

Simulation-based investigations of the IM steady-state features have revealed the high performance of the introduced DTC strategy. These performances have been the subject of an experimental validation along with a comparison against those yielded by Takahashi and the basic DTC strategies dedicated to the SSTPI and to the FSTPI, respectively.

## REFERENCES

[1]  I. Takahashi and T. Noguchi, "A new quick-response and high-efficiency  control strategy of an induction motor," IEEE Trans. Ind. Appl., vol. 22,  no. 5, pp. 820–827, Sep. 1986.

[2]  Y. Zhang and J. Zhu, "Direct torque control of permanent magnet synchronous motor with reduced torque ripple and commutation frequency," IEEE Trans. Power Electron., vol. 26, no. 1, pp. 235–248, Jan. 2011.

[3]  Y. Zhang, J. Zhu, Z. Zhao, W. Xu, and D. G. Dorrell, "An improved direct torque control for three-level inverter-fed induction motor sensor-less drive," IEEE Trans. Power Electron., vol. 27, no. 3, pp. 1502–1513, Mar.2012.

[4]  A. Taheri, A. Rahmati, and S. Kaboli, "Efficiency improvement in DTC of six-phase induction machine by adaptive gradient descent of flux," IEEE Trans. Power Electron., vol. 27, no. 3, pp. 1552–1562, Mar. 2012.

[5]  A. B. Jidin, N. R. B. N. Idris, A. H. B. M. Yatim, M. E. Elbuluk, and T. Sutikno, "A wide-speed high torque capability utilizing over modulation strategy in DTC of induction machines with constant switching frequency controller," IEEE Trans. Power Electron., vol. 27, no. 5, pp. 2566–2575, May 2012.

[6]  J. K.Kang, D. W. Chung, and S. K. Sul, "Direct torque control of induction machine with variable amplitude control of flux and torque hysteresis  bands," in Proc. Int. Elect. Mach. Drives Conf., Seattle, Washington, May 1999, pp. 640–642.

[7]  K. B. Lee and F. Blaabjerg, "Sensor less DTC-SVM for induction motor driven by a matrix converter using a parameter estimation strategy," IEEE Trans. Ind. Electron., vol. 55, no. 2, pp. 512–521, Feb. 2008.

[8]  Z. Zhifeng, T. Renyuyan, B. Boadong, and X. Dexin, "Novel direct torque control based on space vector modulation with adaptive stator flux observer for induction motors," IEEE Trans. Magn., vol. 48, no. 8, pp. 3133–3136, Aug. 2010.

[9]  J. Beerten, J. Verveckken, and J. Driesen, "Predictive direct torque control for flux and torque ripple reduction," IEEE Trans. Ind. Electron., vol. 57, no. 1, pp. 404–412, Jan. 2010.

[10]  T. Geyer, "Computationally efficient model predictive direct torque control," IEEE Trans. Power Electron., vol. 26, no. 10, pp. 2804–2816, Oct. 2011.

[11]  H. Zhu, X. Xiao, and Y. Li, "Torque ripple reduction of the torque predictive control scheme for permanent-magnet synchronous motors," IEEE Trans. Ind. Electron., vol. 59, no. 2, pp. 871–877, Feb. 2012.

[12]  S. K. Sahoo, S. Dasgupta, S. K. Panda, and J. X. Xu, "A Lyapunov function-based robust direct torque controller for a switched reluctance motor drive system," IEEE Trans. Power Electron., vol. 27, no. 2, pp. 555–564, Feb. 2012.

[13]  M. N. Uddin and M. Hafeez, "FLC-based DTC scheme to improve the dynamic performance of an IM drive," IEEE Trans. Ind. Appl., vol. 48, no. 2, pp. 823–831, Mar./Apr. 2012.

[14]  M. B. R. Correa, C. B. Jacobina, E. R. C. da Silva, and A. M. N. Lima, "A  general PWM strategy for four-switch three-phase inverters," IEEE Trans. Power Electron., vol. 21, no. 6, pp. 1618–1627, Nov. 2006.

[15]  K. D. Hoang, Z. Q. Zhu, andM. P. Foster, "Influence and compensation of inverter voltage drop in direct torque-controlled four-switch three-phase PM brushless AC drives," IEEE Trans. Power Electron., vol. 26, no. 8, pp. 2343–2357, Aug. 2011.

[16]  R. Wang, J. Zhao, and Y. Liu, "A comprehensive investigation of fourswitch three-phase voltage source inverter based on double fourier integral analysis," IEEE Trans. Power Electron., vol. 26, no. 10, pp. 2774–2787, Oct. 2011.

[17]  M. Azab and A. L. Orille, "Novel flux and torque control of induction motor drive using four switch three phase inverter," in Proc. IEEE Annu.  Conf. Ind.  Electron. Soc., Denver, CO, Nov./Dec. 2001, vol. 2, pp. 1268– 1273.

[18]  B. Bouzidi, B. El Badsi, and A. Masmoudi, "Investigation of the performance of aDTCstrategy dedicated to the control ofB4 fed induction motor drives," Comput. Math. Elect. Electron. Eng., vol. 31, no. 1, pp. 224–236, 2012.

[19]  D. Swierczynski, P. Kazinierkowski, and F. Blaabjerg, "DSP based direct torque control of permanent magnet synchronous motor (PMSM) using space vector modulation (DTC-SVM)," in Proc. IEEE Int. Symp. Ind. Electron., Aquila, Italy, Jul. 2002, vol. 3, pp. 723–727.

[20]  S. Kazemlou and M. R. Zolghadri, "Direct torque control of four-switch three phase inverter fed induction motor using a modified SVM to compensate DC-link voltage imbalance," in Proc. IEEE Int. Conf. Electr.  Power  Energy Convers. Syst., Sharjah, UAE, Nov. 2009, pp. 1–6.

[21]  Q. T. An, L. Z. Sun, K. Zhao, and L. Sun, "Switching function modelbased fast-diagnostic method of open-switch faults in inverters without sensors," IEEE Trans. Power Electron., vol. 26, no. 1, pp. 119–126, Jan. 2011.

[22]  R. R. Errabelli and P. Mutschler, "Fault-tolerant voltage source inverter for permanent magnet drives," IEEE Trans. Power Electron., vol. 27, no. 2, pp. 500–508, Feb. 2012.

[23]  M. D. Hennen, M. Niessen, C. Heyers, H. J. Brauer, and R. W. De Doncker, "Development and control of an integrated and distributed inverter for a fault tolerant five-phase switched reluctance traction drive," IEEE Trans. Power Electron., vol. 27, no. 2, pp. 547–554, Feb. 2012.

[24]  U. M. Choi, H. G. Jeong, K. B. Lee, and F. Blaabjerg, "Method for detecting an open-switch fault in a grid-connected NPC inverter system," IEEE Trans. Power Electron., vol. 27, no. 6, pp. 2726–2739, Jun.

# Photovoltaic-Biomass Gasifier Hybrid Energy System for a Poultry House

Faten Hosney Fahmy[1], Hanaa Mohamed Farghally[2], Ninet Mohamed Ahmed[3]

[1,2,3,] *Photovoltaic Department, Electronics Research Institute, Giza, Egypt.*

***Abstract:*** *Availability and sustainability of energy and food production are the biggest challenge facing the world. Find out how to integrate poultry and animal farms with renewable energy technologies will lead to a greater energy security and food production.The main objective of this paper is to obtain the optimal suited configuration of a hybrid renewable energy system from various combinations to meet the poultry house load requirement reliably, economically, continuously and sustainably. This paper presents an optimal design of hybrid solar PV-biomass gasifier system to fulfill the requirements of 250 kWh/day primary loads with 19 kW peak load for poultry house located at El-fayoum governorate, Egypt. Using HOMER simulations, the optimal sizing of solar photovoltaic (PV) and biogas generating system is obtained on the basis of the minimized cost of the obtained energy (COE) generation, HOMER results show that the solution is sustainable and techno economically viable. The simulation results show that PV (12 kW) - biomass gasifier (20 kW) - battery (270 kWh) hybrid system is most economically feasible with a least cost of energy about $0.224/Kwh. Also, this system is characterized by the minimum percentage of carbon dioxide and the other greenhouse gases emissions.*
***Keywords****: Biomass, HOMER, Hybrid, Photovoltaic, Poultry House, Renewable Energy.*

## I. INTRODUCTION

Energy, Economy and environment are the three inter related areas having direct correlation for development of any nation [1]. In the rapidly growing economies of the developing countries the demand for electricity is constantly increasing. Electricity is one of the driving forces in a growing economy and increasing demand puts incredible pressure on the countries' energy infrastructure to match that demand. Depleting oil and gas reserves, combined with growing concerns of atmospheric pollution, have made the search for energy from renewable sources inevitable [2-3].

As well energy plays a crucial role in poultry housing. Where, energy is used for several applications; most importantly for lighting, heating, ventilation and cooling, and running electric motors for feed lines [4]. Therefore, to electrify the previously mentioned house equipments, it is necessary to use a well designed renewable energy systems. Several renewable energy sources, notably wind, waves, tidal, biomass and solar are either intermittent by nature or vary greatly according to time of day or season. In order to achieve reliability, it is necessary to integrate two or more energy sources such as solar photovoltaic, wind, biomass, micro hydro or diesel generators together in an optimal way as hybrid energy system [5].

Poultry products can be considered as one of the most important sources of cheap protein, where the white meat (poultry meat) is very cheap as compared with the red meat (animal meat). In addition to, poultry production is characterized by its high economic return due to its short production cycle, the capital cycle is very rapid in the case of poultry production as compared with the capital cycle in other types of animal production where the production cycle of poultry production takes 7–8 weeks meanwhile the production cycle of bovine takes from 3 to 12 months. Therefore, in the case of poultry production the capital cycle can be repeated 7 times a year. Also, Poultry production needs small area in comparison with other animals. Poultry production can contribute to the solution of the unemployment problem [6-8]. Poultry production can contribute to the state food security policy and strategy. The design of the poultry house based on hybrid renewable energy system is realized by satisfying the load demand, non-linear seasonal variations and equipment constraints. The system's sizing and the design optimization has been done by application of the National Renewable Energy Laboratory's (NREL) software "Hybrid Optimization Model for Electric Renewable (HOMER) version 2.68 betas".

The current situation of energy in Egypt clearly indicates that, the future energy demand cannot be met by traditional energy sources. In coming years it would be a necessity to switch from conventional sources to renewable energy resources to fulfill the energy demand for multiple areas and differing applications. Therefore, coupling of renewable energy with cattle and poultry houses holds great promise for increasing food supplies with natural energy source that does not produce air pollution or contribute to the global problem of climate especially in the food sector. The main objective of the present study is to determine the optimum size of hybrid

renewable energy system that able to fulfill the requirements of 250 kWh/day primary load with 19 kW peak load to feed one of the poultry house located at El-fayoum governorate, Egypt.

## II.  LOCATION

El-Fayyum governorate is chosen as the location of this study. Its Geographic coordinates are; Latitude: 29°18′28″ N, Longitude: 30° 50′23″ E and Elevation above sea level: 40 m [9]. El-fayoum governorate contributes to enhancing the industrial activity through many industries, the most important of which are foodstuffs. It is one of the main producers of meats and dairy products. Poultry field is considered one of the main economic activities in the governorate. Therefore, it is chosen as the site under consideration for the poultry house installation.

## III.  PV-BIOMASS POULTRY HOUSE SYSTEM DESCRIPTION

Modern poultry house made of steel construction and the average growing season is 55 days. The size of the house is approximately 14 meter by 150 meter which holds 28,000 birds [4]. The average bird density is 0.07m2/bird. Figure 1 shows the block diagram of the suggested photovoltaic-biomass gasifier hybrid system. The main components of the system are namely PV array, biomass generator, battery, inverter and load.
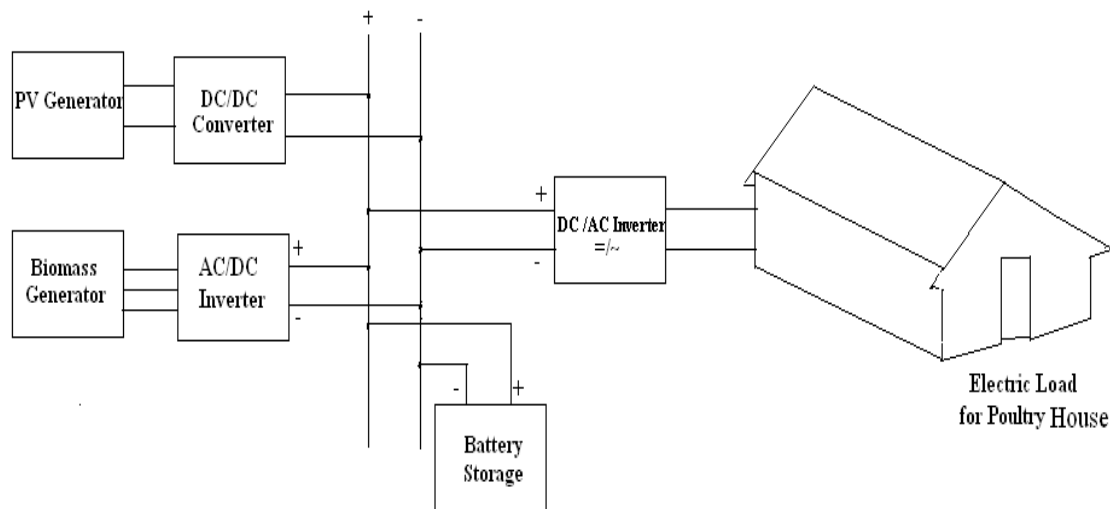


Fig. 1  The proposed block diagram of the standalone PV-biomass poultry house system.

Hybrid renewable energy system is designed based upon the certain important variables to optimize the cost & size effectively. The use of hybrid off-grid electricity depends on the comparative costs, affordability, quality of service, and accessibility of other energy options which are locally available. Therefore, before simulation, certain parameters like solar irradiation, available biomass and load profile must be evaluated.

## IV.  HOMER SIMULATION

HOMER is used to assist in the design of power systems and to facilitate the comparison of power generation technologies across a wide range of applications. HOMER models a power system's physical behavior and its life-cycle cost, which is the total cost of installing and operating the system over its life span. HOMER allows the modeler to compare many different design options based on their technical and economic merits. Also, it is capable of selecting an optimized hybrid model to serve the given electrical load. In a decentralized electricity generation the COE depends on the selection of various renewable energy technologies and their resources. It contains a number of energy component models and evaluates suitable technology options based on cost and availability of resources. Analysis with HOMER requires information on resources, the data of the component types, their numbers, costs, efficiency, longevity, etc. It compares a wide range of equipments to optimize the system design [10-14]. The following subsections will describe the various input parameters that HOMER requires to model the system: The energy load demand (poultry house) that the system has to serve, the selected energy components to generate electricity, the various energy resources associated to the selected components, and how this hybrid combination operates to serve the loads.

# V. METHODOLOGY

## 5.1 Hybrid Energy System Resources
### 5.1.1 Solar Radiation

Solar energy has been deemed clean, inexhaustible, unlimited, and environmental friendly. Such characteristics have attracted the energy sector to use this energy source on a larger scale. Solar Profile represents the solar resource data for the location of interest, indicating the amount of global solar radiation that will incident on the PV array. Solar radiation strongly depends on latitude and climate conditions. The monthly average solar radiations are directly taken by HOMER using latitude and longitude of the El-fayoum governorate. Figure 2 shows the solar resource profile considered over a span of one year; it illustrates the monthly global solar radiation of El-fayoum governorate. The average solar radiation for this location is 5.842 kWh/m2/d, and the average clearness index was found to be 0.664. The graph plot in Fig.2 shows that, solar radiation is available throughout the year; therefore a considerable amount of PV power output can be obtained [14].
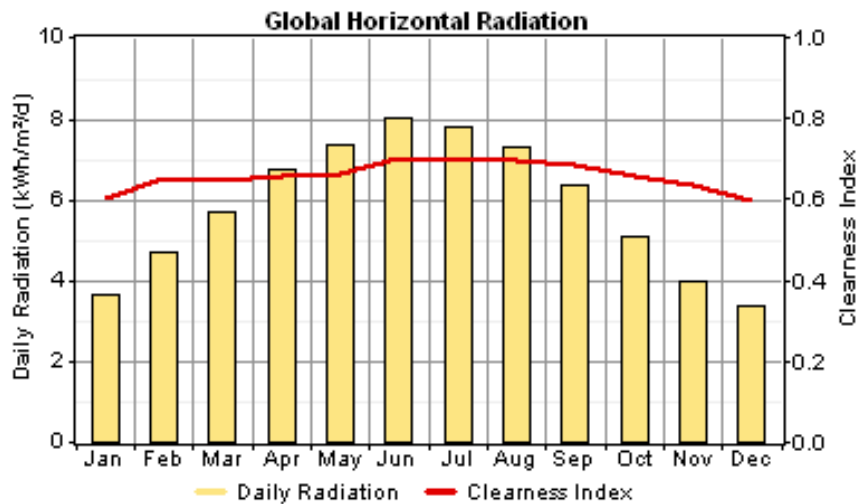


Fig. 2 Global solar radiation of El-fayoum governorate.

### 5.1.2 Biomass

Biomass represents an important source of energy which includes a large variety of different fuels with different chemical compositions and combustion characteristics. Its utilization as a source of energy is important from an energetic as well as an environmental viewpoint. There are four main types of biomass sources which represent the potential of biomass energy sources in Egypt and include: agricultural residues (dedicated bioenergy crop residues), municipal solid wastes, animal wastes, and sewage sludge. The potential biomass quantity and its theoretical energy content were computed according to statistical reports, literature reviews, and personal investigations. The results show that Egypt produces a considerable amount of biomass with a total theoretical energy content of $416.9\times1015$J. The dry biomass produced from bioenergy crop residue sources has been estimated at about 12.33 million tons/year, of which 63.75% is produced from rice straw. This source represents the highest percentage (44.6%) of the total theoretical potential energy in Egypt, followed by municipal solid wastes, which could produce 41.7% from an annual amount of 34.6 million tons. Meanwhile, the rest of the total theoretical potential energy could be produced from animal and sewage wastes [15]. Biomass gasifier is considered. Using the produced biogas, a generator is included in the hybrid system to generate electricity. The average data of the available of biomass supply is a bout 8 ton per day.

## 5.2 System Components
### 5.2.1 PV Array

The cost of solar electricity with solar photovoltaic (PV) panels has become economically feasible in recent years. A monocrystalline PV 75 Wp, Imp= 4.4A and Vmp = 17V modules is selected in this study. The capital cost and replacement cost for a 1kW PV is taken as $2000 and $2000 respectively. As there is very little maintenance required for PV, only $10/year is taken for O&M costs. Solar PV panels of different capacities are considered,e.g.1,2,3,4,5,5,7,8,9,10,11,12,13,14,15,16,17,18,19,20,21,22,23,24,25,26,27,28,29,30,31,32,37,38,39 ,40,45and 50 kW for optimization and the lifetime considered is 20 years [16].

### 5.2.2 Biomass Generator

Biomass gasification converts solid biomass into more convenient gaseous form. This process is done in gasifier mainly comprised of a reactor, where the combustible gas is generated and the gas is made available for power generation/thermal application after the required cleaning and cooling process. The capital and replacement costs are the same $ 628 while M&O cost is $0.08/h. The sizes to consider are 0, 20, 25, 30, 35, and 40 KW and the lifetime is 20 years. Figure 3 illustrates the monthly biomass resource [9].
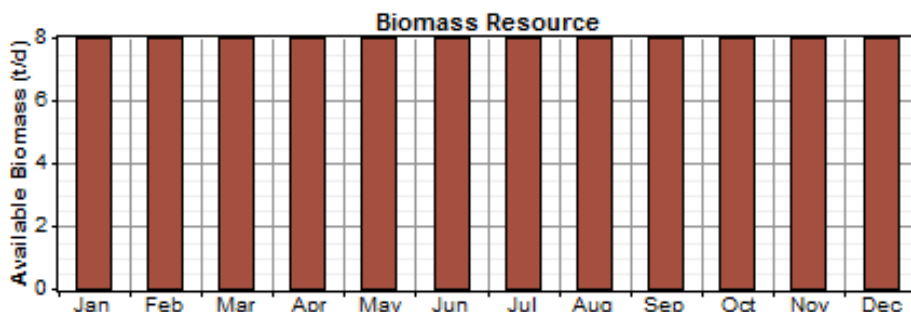


Fig.3   Biomass input in tones/day.

### 5.2.3 Buttery

Storage battery is essential to make the renewable energy system dependable. The battery bank serves as an energy source entity when discharging and a load when charging. The net energy balance to the battery determines its state-of-charge (SOC). The battery has to be protected against overcharging. It is also necessary to guard the battery against excessive discharge. Therefore, the SOC at any period t should be greater than a specified minimum SOC, SOCmin as given by (1) [5]:

$$1 \geq SOC(t) \geq SOC_{min} \qquad (1)$$

A Trojan T-105 battery is used in this system. The nominal voltage is 24V, nominal capacity is 225 Ah (5.4 kWh). The lifetime throughput is 5 year. The capital cost and replacement costs are taken as $145 [16]. The considered quantities are: 0, 1,2,3,4,5,6,7,8,9,10,20,50.

### 5.2.4 Inverter

Inverter is an electronic power device that is required in a hybrid system to maintain the energy flow between AC and DC electrical components. The capital cost, replacement cost and O&M costs for 1kW systems, are considered as $700, $550, and $100/year respectively. The lifetime of the inverter is 15 years and efficiency of 90%. The   proposed hybrid renewable energy system which consists of a photovoltaic array, biomass generator, storage battery, inverter and load is shown in Fig.4. The estimated lifetime of this system is about 20 years [17].
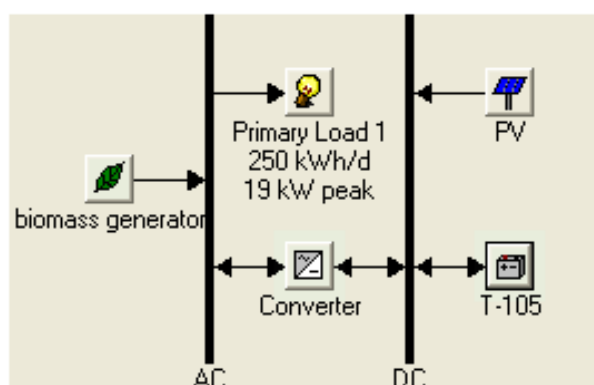


Fig. 4 Schematic of the proposed poultry house hybrid energy system in HOMER code.

### 5.2.5 Load Estimation:

Birds are very sensitive to their environment and extreme heat or cold will result in greatly increased mortality in the house.  Hot and humid weather conditions and poor management practices increase the mortality, reduce the growth and make poultry production to be uneconomical. Heat stress is the major problem in poultry housing. Being a tropical country the temperature reaches over 40°C during summer which is not

suitable for poultry housing. Temperature of the poultry houses varies from 25-33°C depending on the growth stage of the birds. The conditioned environment of poultry houses is completely reliant on electricity; power outages will cause changes in temperatures and increasing concentrations of ammonia and germs. Due to the aforementioned factors, security of electricity supply is critical to poultry production; any unexpected loss of power can affect the health and growth and in extreme cases can prove fatal to the birds.

Therefore, optimum temperatures and ventilation are required to maximize productivity. Adequate air conditions are provided through heating and ventilation to attain proper temperature. Therefore, Energy plays a crucial role in poultry production. Energy needs were determined in terms of all actual electrical equipments used in the house. In a typical commercial poultry house, energy is used for several applications; most importantly for lighting, heating, ventilation and cooling, and running electric motors for feed line [10, 18].

Electrical equipments used in the poultry house are presented in Table 1. This Table illustrates the categorized poultry house data; it lists the number of units, voltage, operation periods (hour) and power rating for each equipment.

Table1: Electrical Equipments which are used in the Poultry House.

| .Equipment | Number of units | Voltage (V) | Operation periods (hour) | Rated Power (watt) | Total power(watt) |
|---|---|---|---|---|---|
| 36-inch wall side fan | 6 | 220 | 24 | 300 | 1800 |
| 48-inch tunnel fan | 4 | 220 | 24 | 1000 | 4000 |
| Lighting | 50 | 220 | 24 | 9 | 450 |
| Feed line motors | 2 | 220 | 24 | 500 | 1000 |
| Water pump | 1 | 220 | 12 | 1000 | 1000 |
| Total (summer) | | | | | 8250 |
| Additional winter equipments | | | | | |
| Electrical oil radiator | 5 | 220 | 12 | 2000 | 10000 |
| Pump for heater | 2 | 220 | 11 | 500 | 1000 |
| Total (Winter) | | | | | 19250 |

The poultry house is considered to have an average energy consumption of about 250 kWh/d, with a peak demand of 19 kW as indicated in Fig. 4. The daily load profile of poultry house for winter and summer seasons is shown in Fig. 5. Also, a seasonal load profile for poultry house is indicated in Fig. 6. It is observed that the electrical power consumption in winter months is higher than that in summer months due to heating load in these months.
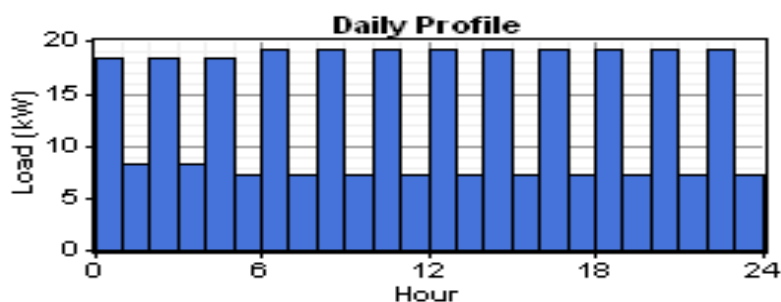

Fig.5 Daily load profile for poultry house.
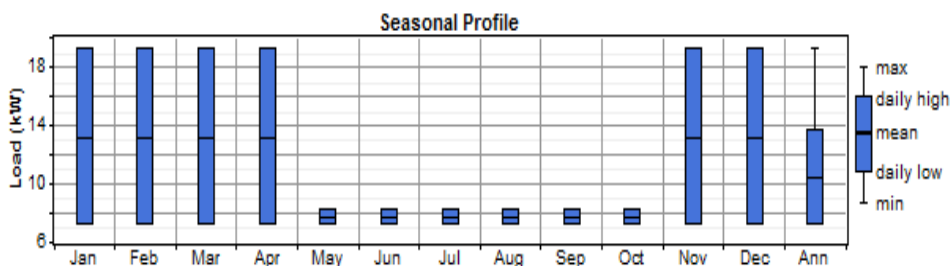

Fig. 6 Seasonal load profile for poultry house.

# VI. Economical Model

HOMER's main financial output is the total net present cost (NPC) and cost of energy (COE) of the examined system(s) configurations. NPC analysis is an appropriate gauge or scale for the purpose of economic comparison of different energy systems classification and configuration, the reason is that NPC balances widely divergent cost characteristics of renewable and non-renewable sources. As well, it explores and summaries all the relevant associated costs that occur within the lifetime of the energy project. The economic performance parameters of a photovoltaic-biomass hybrid power system with storage and converter in El-fayoum governorate is calculated through modeling the system. For economic aspect, (NPC) and (COE) of the system are investigated. HOMER uses total net present cost (NPC) to represent the system's life cycle cost. The NPC is calculated by (2) [19-20]:

$$NPC(\$) = \frac{TAC}{CRF} \tag{2}$$

Where, TAC is the total annualized cost; CRF is the capital recovery factor which can be calculated by the following equation:

$$CRF(\$) = \frac{i(1+i)^N}{(1+i)^N - 1} \tag{3}$$

Where, N is the number of years and $i$ is the annual real interest rate (%).

Cost of energy (COE), which is the average cost per kilowatt-hour ($/KWh) of electricity produced by the concerned system is estimated as in (4):

$$COE(S) = \frac{C_{ann,tot}}{E} \tag{4}$$

Where, $C_{ann,tot}$ is the annual total cost, $. $E$ is the total electricity consumption, KWh/Year.

# VII. PV-Biomass System Sizing

## 7.1 PV Array Sizing

Estimation of the sizing parameters of the PV array is very useful to conceive an optimal and economic PV system.

### 7.1.1 Estimation the Number of Solar Modules

Estimating the number of PV modules $N_{pv}$ which required for a given daily energy requirement depends on the amount of daily PV energy requirement $PV_{wp}$ and the chosen module peak power $PV_{wp,module}$. $N_{pv}$ can be obtained using the following equation [12]:

$$N_{PV} = \frac{PV_{wp}}{PV_{wp,module}} \tag{5}$$

### 7.1.2 Determination the Number of Series Connected Modules

The number of modules Ns to be connected in a series string is determined by the nominal voltage of the module Vn and the chosen DC bus voltage Vpv as given in following equation [12]:

$$Ns = V_{pv}/Vn \tag{6}$$

### 7.1.3 Determination the Number of the Modules Parallel-Connected

The number of strings in parallel ($N_P$) is determined by dividing the designed array output $PV_{array}$ by the selected module output $PV_{wp,module}$ and the number of series modules $N_S$ as indicated in the following equation [12]:

$$N_P = \frac{PV_{array}}{N_S PV_{wp,module}} \tag{7}$$

## 7.2 Design of Biomass Generator
### 7.2.1. Gasification

Gasification can be broadly defined as the thermochemical conversion of solid or liquid carbon based feedstock (biomass) into combustible gaseous fuel by partial oxidation of the biomass using a gasification agent.

The process is carried out at high temperatures of around 800 ℃ – 900 ℃. Biomass gasification using air as the gasifying agent, yields syngas which contains $CO_2$, CO, $H_2$, $CH_4$, $H_2O$, trace amounts of hydrocarbons, inert gases present in the air and biomass and various contaminants such as char particles, ash and tars. Fuel Bound organic Nitrogen (FBN) can also be converted into nitrogen oxides (NOx) during gasification [21].

### 7.2.2 The Suggested Gasifier

Gasifiers are available in different types and sizes. Downdraft gasifiers are one among the fixed bed gasification systems. Downdraft gasification technology has an increased interest among researchers worldwide due to the possibility to produce mechanical and electrical power from biomass in small-scale to an affordable price. The producer gas obtained from a downdraft reactor contains less tar because the gasses are passed through the hot oxidation zone. The downdraft gasifier is also known as Co-Current Moving Bed is shown in Fig. 7. Its fuel is fed from the top and gravitates in the packed bed where it is gasified. Air, oxygen or a mixture of air and steam is fed either from the top or the middle of the reactor and the gasification zones are similar to the updraft reactor. The producer gas is, however, removed from the bottom part of the reactor. Devolatilization of the biomass occurs in the pyrolysis zone, which is heated by convection and radiation from the lower hearth zone. The hearth zone is embedded on top of the reduction zone, to which char is transferred and gasified [21].
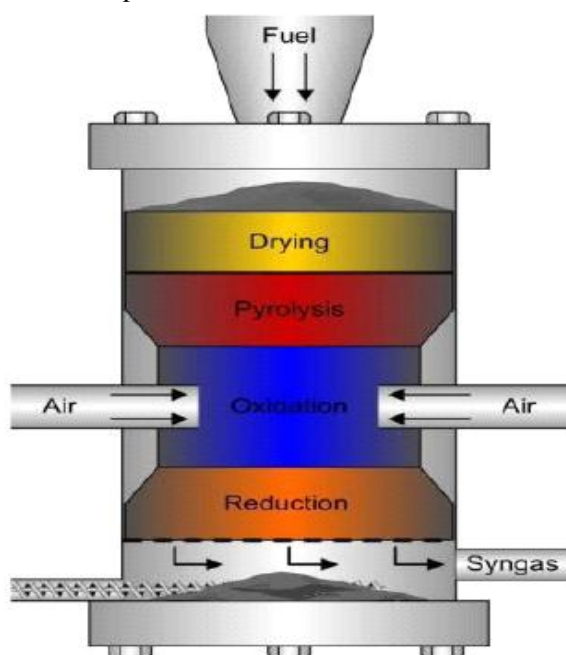


Fig. 7 Down-draft biomass gasifier

### 7.2.3 Biomass Material

The study focused on the use of agricultural crop residues, specifically maize residues. Maize residues (cobs, leaves and stalks) are abundantly available renewable materials that can be used as an energy source in gasification and combustion systems. Cobs, leaves and stalks are important residues of maize processing and consumption. For every 1 kg of dry maize grains produced, about 0.15 kg of cobs, 0.22 kg of leaves and 0.50 kg of stalks are produced [22]. Maize generates a substantial amount of residues, maize residues consist of the non-edible parts of the plant that are left in the farm after harvesting the targeted crop such as stalks, leaves and cobs. A minimum quantity of these residues are used locally for heating purposes such as water heating, fish smoking, small scale smelting and palm kernel oil processing while a significant quantity is left in the farms to rot. The maize residues available as bioenergy resources were estimated from the annual quantities of the crop produced followed by field verification and the application of the appropriate crop-to-residue ratio as presented in Table 2 [23]. Also, Lower Heating Value (LHV), and moisture content (%) of the maize residues is presented in Table 2.

Table 2: Crop to Residue Ratio, Moisture Content and LHV of Maize Crop.

| Commodity | Residue type | Crop to residue ratio | Moisture content (%) | LHV (MJ/kg) |
|---|---|---|---|---|
| Maize | Maize stalk | 1.00 | 15.5 | 15 |
| | Maize cob | 0.25 | 8 | 15 |

**7.2.4 Biomass Fuel Estimation**

The amount of maize stalks required to fuel the plant for a year can be estimated using the following procedure:

The annual generated residues in tones, $G_A$, can be obtained by multiplying Annual Production in tones and Crop to Residue Ratio as it pears (8)[23].

$$G_A = A_P \times CRR \tag{8}$$

where $A_p$ is annual production in tones and CRR is crop to residue ratio. To obtain the Annual Available residues in tons $A_A$, the annual generated residue in tons $G_A$, is multiplied by 60% as indicated in (9) [23].

$$\tag{9}$$

$$A_A = G_A \times 60\%$$

The annual dry maize residues, $D_A$ is given by (10) [23], where MC is the moisture content.

$$D_A = A_A - [A_A \times MC] \tag{10}$$

Similarly, the total energy, ET, in (T J/yr) is given by (11) [23], where LHV is Lower Heating Value of the maize residues

$$E_T = D_A \times \frac{LHV}{100} \tag{11}$$

To obtain the Electricity produced annually, MWh, an average conversion of 1.5 MWh per ton of dry biomass was considered and the final expression is indicated in (12) [23].

$$MWh = D_A \times \frac{1.5MWh}{1tone} \tag{12}$$

## VIII. Results And Discussions

The methodology applied provides a useful and simple approach for sizing and analyzing the hybrid systems using HOMER. The output of the simulation helps to choose the optimal system configuration. The aim is to identify a configuration among a set of systems that meets the desired system reliability requirements with the lowest electricity unit cost. HOMER uses the total net present Cost (NPC) and COE as their main selection tools. All the possible hybrid system configurations are listed in ascending order of their total NPC is shown in Fig. 8. Four system configurations are obtained; PV –biomass-battery, biomass, biomass-battery, PV-biomass. The feasible system and economical details of all the configurations of the four hybrid systems resulted from the optimization process are shown in Fig. 8. When these configurations are compared in terms of NPC and COE; the hybrid PV/biomass/battery generation system was found to be the most economically feasible one, which ensures the continuity of power supply and able to fully meet load demands at the lowest possible total NPC of $261,720 and cost of energy $0.224/kWh. Biomass configuration has higher NPC but slightly lower COE ($0.220/kWh) than the optimal configuration ($0.224/kWh). Both the biomass-battery and PV-biomass configurations have higher NPC and COE. The combination of optimal system components are a 12kW PV-Array, 20kW Biomass, 50 T- 105 Battery, 20 kW Inverter. The total NPC, capital cost, replacement cost, operation & maintenance cost, and COE for such a hybrid system are $261,720, $55,250, $96,796, $103,821 and $0.224/kWh, respectively. Figure 9 shows the cash flow summary of each components of photovoltaic-biomass-battery system. The most costs are for the biomass generator and the minimum cost for the PV array.

Fig.8 Optimization results for the PV and Biomass generator configuration for poultry house.
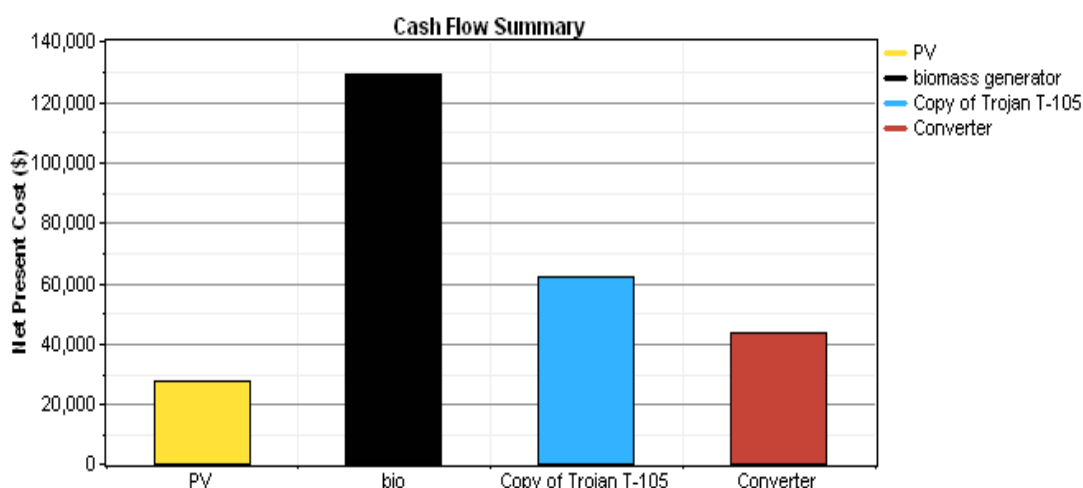


Fig. 9 Cost summary of PV-biomass -battery system

Figure10 shows the monthly average distribution of the electricity produced in kW from the PV and biomass components. If we go towards the electricity produced by that system, it is observed that, the total electrical production of the hybrid system is 102,403 kWh/yr operating for 8760 h/yr. PV array contributes 30,796 kWh/yr of energy which is about 30% of the total energy supplied to the load by the hybrid energy system and biomass gasifier contributes 71,607 kWh/ yr of energy which is about 70% of the total energy supplied to the load by the hybrid energy system. Both the unmet electric load and capacity shortage values equal zero. The consumption is about 91,247 kWh yr and excess electricity is about 8, 68 kWh /yr as shown in Fig. 10. Therefore, the proposed hybrid energy system can supply the poultry house through 24 hour by a reliable power supply throughout the year. Based on the optimization results, it is observed that, during the winter months (from November to April) the biomass energy generator contributes a bigger proportion of energy generation than the PV array. Also, during the summer months (from May to October), the load demand is met nearly by approximate contribution from the PV array and the biomass generator. The COE obtained from the optimal hybrid system is $0.224/KWh. The cost of the different elements of the optimal system configuration is shown in Table 3. The batteries have a low impact on the capital and O&M costs. PV shares the maximum portion of the capital investment. Only biomass generator has the fuel costs.

Table 3: The Cost of the Different Elements of the Optimal System Configuration.

| Component | Capital ($) | Replacement ($) | O&M ($) | Fuel ($) | Salvage ($) | Total ($) |
|---|---|---|---|---|---|---|
| PV | 24,000 | 7,483 | 0 | 0 | -4,194 | 27,289 |
| biomass generator | 10,000 | 29,070 | 78,255 | 13,161 | -1,452 | 129,033 |
| Copy of Trojan T-105 | 7,250 | 55,653 | 0 | 0 | -808 | 62,095 |
| Converter | 14,000 | 4,590 | 25,567 | 0 | -854 | 43,302 |
| System | 55,250 | 96,796 | 103,821 | 13,161 | -7,308 | 261,720 |
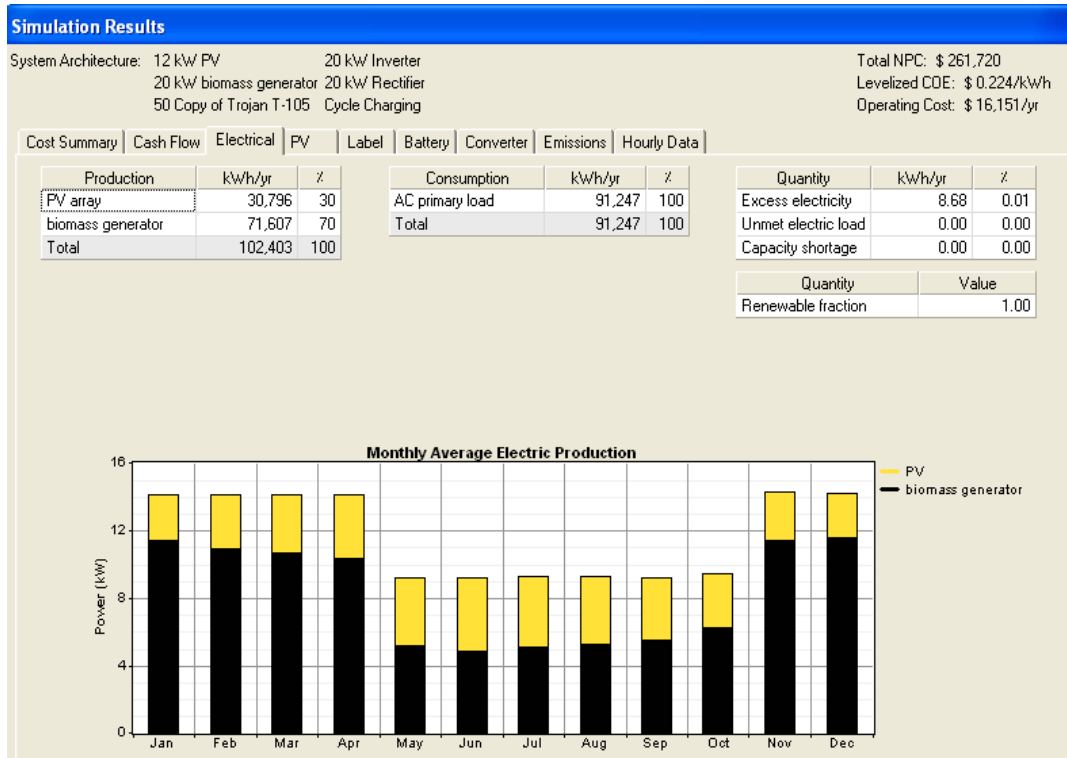


Fig. 10 Monthly average electricity production of the optimal system configuration.

In this study, the emissions from the four energy system configurations were evaluated. A comparison between types of greenhouse gas emission and their quantity within one year of operation for these energy systems is illustrated in details in Table 4. Carbon dioxide, carbon monoxide, unburned hydrocarbons, particular matter, sulfur dioxide and nitrogen oxides are the emitted pollutions. Emission is measured as yearly emissions of the emitted gases in *kg/ yr*. It is observed that, PV-biomass-battery system generates the minimum values of pollution emissions.

Table 4 : A comparisons of the Emissions from Different Configurations of Hybrid Power Systems.

| Emission / System | Carbon dioxide (Kg/yr) | Carbon monoxide (Kg/yr) | Unburned hydrocarbons (Kg/yr) | Particular matter (Kg/yr) | Sulfur dioxide (Kg/yr) | Nitrogen oxides (Kg/yr) |
|---|---|---|---|---|---|---|
| PV/Biomass/ Battery | 2.16 | 0.223 | 0.0247 | 0.0168 | 0 | 1.99 |
| Biomass | 3.32 | 0.342 | 0.0379 | 0.0258 | 0 | 3.05 |
| Biomass/ Battery | 3.14 | 0. 323 | 0.0358 | 0.0244 | 0 | 2.88 |
| PV/Biomass | 2.44 | 0.251 | 0.0278 | 0.0189 | 0 | 2.44 |

Semines Solar SP 75 PV with 75 Wp ($PV_{WP}$,module =75 W) module was selected for the proposed PV array. This PV module is a mono-crystalline silicon type with nominal maximum power of 75W, each module contains 36 silicon cell connected in series. Table 5 shows the Semines Solar SP 75 PV module electrical specifications. For the daily peak power requirement of 12 kW, if the DC bus voltage V*pv* is chosen to be 24V,

160 modules are needed to supply the load with required energy. The number of modules to be connected in a series string Ns is obtained to be 2 modules and the number of strings in parallel $N_P$ is equal 80 modules.

Table 5: Semines Solar SP75 Photovoltaic Module specifications

| Characteristics | Rating |
|---|---|
| Maximum power (Pmax) | 75 W |
| Voltage at Pmax | 17 V |
| Current at $P_{max}$ | 4.4 A |
| Short-circuit current (Isc) | 4.8 A |
| Open-circuit voltage(Voc) | 21.7 V |
| Height | 1200 (mm) |
| Width | 572 (mm) |
| Efficiency | 15% |

The moisture content and the Lower Heating Value (LHV) for the maize stalks are 15.5 and 15 respectively. This implies that for the 24 hours a day that the gasifier will be operating for 365 days in a year, it will consume a 840960 kg maize stalks annually, equivalent to 840.960 tons for the daily peak power requirement of 20 kW contributed by the biomass generator.

## IX. Conclusion

Hybrid energy system has the advantage of providing power on a reliable and environmental friendly basis. The main objective is to meet the electricity demand of a poultry house. This can be achieved by making proper utilization of resources like biomass and solar. Also, this work determine the optimal size of a hybrid renewable energy system which able to fulfill the requirements of 250 kWh/day load with 19 kW peak load for a poultry house located at El-fayoum governorate, Egypt. The proposed hybrid system can supply the poultry house for 24 hour by a reliable power supply throughout the year. In this study, a resource assessment and demand calculation have been carried out and the COE has been ascertained for different systems and configurations. The optimization and simulation by HOMER shows that, on the basis of lowest COE and NPC, a combination of PV, biomass generator and battery system has been identified as the cheapest and most dependable solution with a NPC and COE of $261,720 and $0.224/kWh respectively. The complete sizing procedure of the PV system is presented. The number of series connected PV modules is 2, while the number of parallel strings is 80. It is found that, for the 24 hours a day that the gasifier will be operating for 365 days in a year, it will consume 840960 kg of maize stalks. The simulations' results prove that the combination of PV-biomass-battery system configuration is the best solution to guarantee the reliable supply without interruption of the load under the climatic data change.

## REFERENCE

[1]  Kanwardeep Singh, Study of Solar /Biogas Hybrid Power Generation, M. Sc. in Power System and Electric Derive, Thapar University, Patiala, 2010.

[2]  Rohit Sen, Off-Grid Electricity Generation with Renewable Energy Technologies in India; An application of HOMER., M .Sc. Renewable Energy & Environmental Modeling, University of Dundee, 2011.

[3]  Balachander Kalappan, Dr. Vijayakumar Ponnudsamy, Modeling, Simulation and Optimization of Hybrid Renewable Power System for Daily Load demand of Metropolitan Cities in India, American Journal of Engineering Research, Vol. 2, No. 11, 2-013 , pp-174-184.

[4]  John Byrne, Leigh Glover, Steve Hegedus, Garrett VanWicklen, Melissa Weitz, Hideyuki Hiruma, The Potential For Solar Electric Applications For Delaware's Poultry Houses, Final Report of A Renewable Energy Applications for Delaware Yearly (READY) Project, 2005.

[5]  P. Balamurugan, S. Kumaravel, and S. Ashok, Optimal Operation of Biomass Gasifier Based Hybrid Energy System, International Scholarly Research Network, 2011, pp. 1-7.

[6]  John Sheffield, Coordinator, Evaluation of comprehensive Approaches Needed to Improve the Handling of Farm Animal Manure and Benefit the Environment and the Farming Industry, JIEE REPORT NO. 2000-07

[7]  Nassar Ali Grepay, ,The Main Factors Affecting Poultry Production in Libya , Oeconomia, Vol. 8, No. 4, 2009, pp. 43–49.

[8]  Banshi Sharma, MVSc, Poultry Production, Management and Bio-Security Measures, Journal of Agriculture and Environment, Vol. 11, Jun.2010, pp. 120-125.

[9]  Latitude and Longitude of the El El-fayoum City city of Egypt, www.newstrackindia.com/.../latitudelongitude/.../city-el-El-fayoum-city-663545. htm

[10]  Rahul Mishra, Shakti Singh, Sustainable Energy Plan for a Village in Punjab for Self Energy Generation, International Journal of Renewable Energy ,Vol. 3, No. 3, 2013, pp. 640-646.

[11]    Gabriele Seeling, Hochmuth, Optimization of hybrid Energy Systems Sizing and Operation control, Candidacy for the Degree of Dr.-Ing, University of Kassel, 1998.

[12]    Aicha Soufi,  Ali Chermitti, Nacereddine Bibi Triki,   Sizing and Optimization of a Livestock Shelters Solar Stand-Alone Power System, International Journal of Computer Applications, Vol. 71, No.4, May 2013, pp. 40-47.

[13]    Mahmud Abdul Matin Bhuiyan, Anand Mandal, Ujwal Kumar Thakur, Optimum Use of Renewable Energy Resources to Generate Electricity Via Hybrid System, Kathmandu University Journal of Science, Engineering and Technology Vol. 9, No.1, 2013, pp. 212-221.

[14]    www.HOMERenergy.com , version 2.68 beta.

[15]    N. Said, S. A. El-Shatoury, L. F. Díaz, M. Zamorano, Quantitative Appraisal of Biomass Resources and Their Energy Potential in Egypt, Renewable and Sustainable Energy Reviews, Vol. 24, Issue C, 2013, pp. 84-91.

[16]    Angshuman Patra, Design and Economic Analysis of Standalone Photovoltaic, Biomass Gasifier and Photovoltaic biomass Gasifier Hybrid System, M. Sc. of Technology In Energy Science and Technology, Faculty of Engineering and Technology,  Jadavpur University, Kolkata, 2012.

[17]    O.J.Onojo, G.A. Chukwudebe, E.N.C. Okafor, S.O.E. Ogbogu, Feasibility Investigation of a Hybrid Renewable Energy System as a Back Up Power Supply for an Ict Building in Nigeria,  Part-1:Natural and Applied Sciences, Vol. 4, No. 3, 2013,  pp.149-169 .

[18]    Niharika Varshney, M. P. Sharma, D. K. Khatod, Sizing of Hybrid Energy System using HOMER, International Journal of Emerging Technology and Advanced Engineering, Vol. 3, No. 6, June 2013,  pp. 436-442.

[19]    G. Liu, M. G. Rasul, M. T. O. Amanullah, M. M. K. Khan, Economic and Environmental Modeling of a Photovoltaic-Wind-Grid Hybrid Power System in Hot Arid Australia , Int. J. of Thermal & Environmental Engineering Vol. 1, No. 1,  2010, pp. 15-22.

[20]    Yasser Maklad, An Introduction and Costing of a Biomass/Wind/Pv Hybrid Energy System for Electricity Micro-Generation to Domestic Buildings in Armidale Nsw, Australia, Global journal of research Analysis, Vol.3 , No.4, 2014, pp. 70-74 .

[21]    Geoffreey osoro mosiori , thermo – chemical characteristics of potential gasifier fuels in selected regions of the lake victoria basin, M.Sc.,  kenyatta university,  october, 2013.

[22]    Yaning Zhang, A.E. Ghaly and Bingxi Li, Physical Properties of Maize Residues, American Journal of Biochemistry and Biotechnology, Vol. 8, No. 2, 2012, pp. 44-53.

[23]    G. Otchere-Appiah, E. B. Hagan, Potential for Electricity Generation from Maize Residues in Rural Ghana: A Case Study of Brong Ahafo Region, International Journal of Renewable Energy Technology Research, Vol. 3, No. 5, 2014, pp. 1 – 10.

# Isolation and Identification High-Biological Activity Bacteria in Yogurt Quality Improvement

Huong H. L. Ly[1], Huong T. Ha[2], Huong T. Nguyen[3]

[1,2,3](*Department of Biotechnology – Ho Chi Minh City University of Technology*)

***Abstract:*** *Six strains of lactic bacteria and seven strains of acetic bacteria which were isolated from fermented food. The screening secured one strain of lactic acid bacterium LB4 which carried strong probiotic activity and one strain of acetic acid bacterium AB7 which was capable to generate high glucuronic acid. Activities of probiotic and glucuronic acid were useful biological activities for health protection and enhancing. The results of DNA sequencing showed LB4 was similar to Lactobacillus acidophilus and AB7 was similar to Gluconacetobacter nataicola with 100% of similar proportion. Both of these bacteria were safe that could be used in food fermentation.*

***Keywords:*** *probiotic, glucuronic acid, Lactobacillus acidophilus, Gluconacetobacter nataicola.*

## I. Introduction

The biological activity of yogurt was considered about probiotic activity - the popular biological activity in fermented milk products by lactic acid bacteria. The effects of probiotic in fermented milk products have been known for a long time [1]. Some recent researches have showed that lactic acid bacteria could be combined simultaneously with acetic acid bacteria in micro-aerobic condition. This combination significantly increased the concentration of glucuronic acid which was biosynthesized by acetic acid bacteria [2]. Glucuronic acid contained high biological activity, useful effects on human health. It reduced cholesterol in blood, eliminated the oxidizing agents and excreted toxins in human body. Nowadays, glucuronic acid has also been studied in combination with fucose sulfate and manose sulfate in the structure of U-fucoidan that promoted the Apoptosis which controlled cancer cells self-destroying. The combination of lactic acid bacteria and acetic acid bacteria have been considered significantly in a number of recent studies [3,4].

With the good effects of probiotic bacteria and glucuronic acid for human health. In this study, many strains of lactic acid bacteria which has high active probiotic and many strains of acetic acid bacteria which has high active glucuronic were isolated for the purpose of contribution these strains in yogurt production that was added high activity of glucuronic acid activity besides traditional probiotic activity.

## II. Materials And Methods

### 2.1. Isolates and culture media

Lactic acid bacteria isolated from kimchi, pickled cucumber, tofu water, pickled vegetable, "com me" - Vietnam traditional fermented cooked rice, and "nem" - traditional fermented meat. The culture medium to isolate and reserve lactic acid bacteria was Man Rogosa Sharpe agar (MRS).

Acetic acid bacteria isolated from fermented coconut juice, fermented grape juice, vinegar, tea Kombucha. The culture media to isolate and reserve acetic acid bacteria was Heschin-Schramm agar (HS) medium.

### 2.2. Antibacterial activities evaluation

Probiotic activity is evaluated by antibacterial ability by agar spot test and well diffusion agar test. Raw bacteriocin concentration of lactic acid bacteria (AU/mL) was determined by the formula:

$$AU/mL = D_{FI} \times 1 / V_{bacteriocin} \text{ [5]}$$

The ability to survive in harsh conditions of human gastro-intestinal system of lactic acid bacteria were evaluated in terms of pH 2 and 0.3% bile salts.

Evaluation of the intestinal harmful bacteria resistant by bacteriocin which produced by lactic acid bacteria.

### 2.3. Method of measuring concentration of glucuronic acid of acetic acid bacteria

Glucuronic acid concentration was determined by K-Uronic acid kits and measured absorption at 340nm by UV-Vis spectro 6000 spectrophotometer [4].

### 2.4. Method of identification of microorganisms

Lactic acid bacteria and acetic bacteria that obtained high biological activity were identified by the method 16S rDNA sequencing procedure with the primers [NK]16s-F and [NK]16s-R which were supplied by Nam Khoa Biotek Company.

## III.   Results And Discussion

### 3.1. Isolation and screening of lactic acid bacteria

#### 3.1.1. Isolation of lactic acid bacteria

Lactic acid bacteria were isolated based on characteristics such as negative catalase, negative oxidase and the change of reagent U-ferment color would be selected for screening. The strains included rod-shaped, non-spore and Gram-positive will be selected for probiotic activity evaluation.

There were 6 strains that appropriated requirements could be identified as lactic acid bacteria. These strains were described in Table 1:

**Table 1:** Characteristics of isolated lactic acid bacteria strains

| No. | Strain | Morphological Characteristics | |
|---|---|---|---|
| | | **Macroscopic** | **Microscopic** |
| 1 | LB1 |  Milky color, circular, convex and entire of colonies, smooth surface. |  Gram-positive, sedentary and short rod cells, discrete or small group arrangement. |
| 2 | LB2 |  Milky color, circular, convex and entire of colonies, smooth surface. |  Gram-positive bacteria, sedentary, spherical cells, single or double arrangement. |
| 3 | LB3 |  Milky color, circular, convex and entire of colonies, smooth surface. |  Gram-positive bacteria, sedentary, spherical cells, discrete or group of many cells arrangement. |

| 4 | LB4 |  Milky color, circular, convex and entire of colonies, smooth surface. |  Gram-positive bacteria, sedentary, long rod cells, discrete arrangement. |
|---|---|---|---|
| 5 | LB5 |  Milky color, circular, convex and entire of colonies, smooth surface. |  Gram-positive bacteria, sedentary, spherical cells, discrete or group of many cells arrangement. |
| 6 | LB6 |  Milky color, circular, convex and irregular of colonies, smooth surface. |  Gram-positive bacteria, sedentary, single spherical cells. |
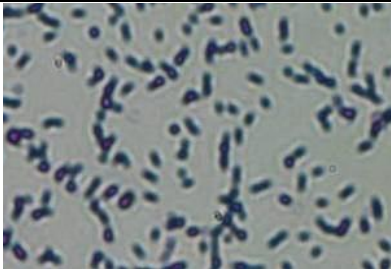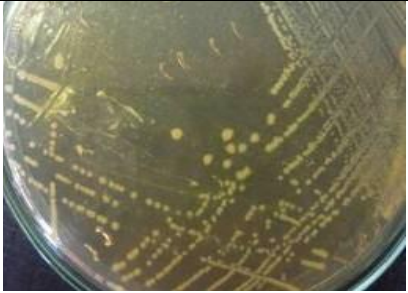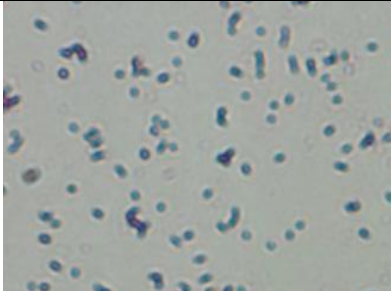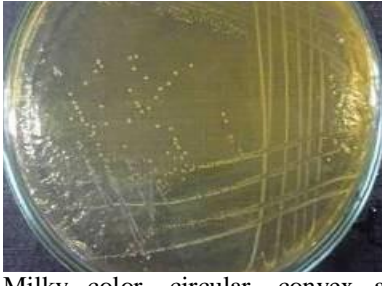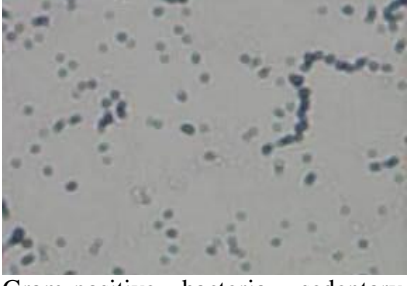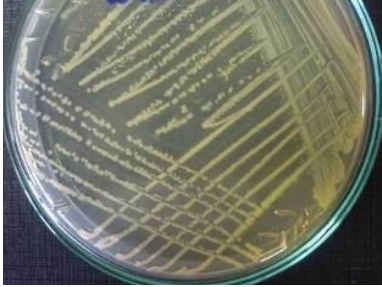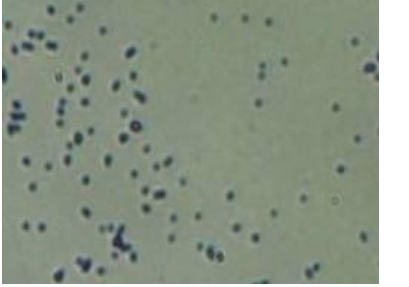
*Note:* LB1 was isolated from kimchi, LB2 was isolated from sour water of tofu, LB3 from pickled vegetable, LB4 from pickled cucumber, LB5 from fermented cooked rice, LB4 from meat fermented.

Thus, there were 6 strains of bacteria had been isolated and identified as lactic acid bacteria by biochemical tests and morphological test. These bacterial strains were screened to select strain of high probiotic activity.

### 3.1.2. Screening of lactic acid bacteria which secured high probiotic activity

Six strains of isolated lactic acid bacteria were capable to resistant the bacteria indicator *Bacillus subtilis* (Table 2). Both of strains LB1 and LB4 obtained strong of antibacterial ability; the strain LB2 had average antibacterial ability; LB3, LB5 and LB6 secured weak antibacterial ability.

**Table 2:** The antibacterial property of strains lactic bacteria

| No. | Strain | Sterile loop diameter (mm) | Antibacterial activity | No. | Strain | Sterile loop diameter (mm) | Antibacterial activity |
|---|---|---|---|---|---|---|---|
| 1 | LB1 | 12 | +++ | 4 | **LB4** | 15 | +++ |
| 2 | LB2 | 7 | ++ | 5 | LB5 | 4 | + |
| 3 | LB3 | 4 | + | 6 | LB6 | 3 | + |

*Note:* Sterile loop diameter > 10mm (+++): high antibacterial activity, 5-10mm (++): average antibacterial activity, <5 mm (+): weak antibacterial activity, 0mm (-): no antibacterial activity.

Thus, there were two strains which obtained high antibacterial ability were LB1 isolated from kimchi and LB4 was isolated from pickled cucumber. Two strains would be studied in bacteriocin production, ability to exist in low pH and high bile salts concentration.

The results about the ability to survive in harsh conditions of the digestive system and bacteriocin generation of LB1 and LB4 were illustrated in Table 3.

**Table 3:** The ability to exist in harsh conditions and bacteriocin production

| Bacteria strain | Bacteriocin concentration (AU/mL) | Proportion of survival (%) | |
|---|---|---|---|
| | | pH 2 | 0.3% bile salt |
| LB1 | 60 | 10.14 | 22.34 |
| **LB4** | **100** | **43.01** | **42.4** |

After incubating about 24 hours with these conditions at 37°C, LB4 synthesized highest bacteriocin which concentration bacteriocin was 100 AU/mL and the bacteriocin concentration of LB1 was 60 AU/mL. At the same time, the strain LB4 also showed the ability to survive in harsh conditions of the digestive system with a proportion was over 40%, higher than the result of LB1 in the same survey condition. Specifically, the ability to exist in pH 2 of LB4 was 43.01%, higher than the strain LB1 4 times (10.14%); survival ability in 0.3% bile salts was 42.4%, doubled the survival ability of LB1. Bacteriocin concentration was generated by LB4 strain equivalent the research of Ogunbanwo et al. (2003) and Sarika et al. (2010) [6,7]. The survival ability of this strain is also higher than the other lactic acid bacteria had been studied [2]. Therefore, LB4 could be confirmed as a powerful probiotic strain. However, the biological activity of this strain should be further confirmed by the ability to inhibit pathogenic bacteria commonly exist in the digestive system of the human.

Th results of inhibition of intestinal bacterial pathogenic by bacteriocin by lactic acid bacteria LB1 and LB4 discharged were presented in Table 4 with bacteriocin generation to resistant bacteria is indicated by diameter of inhibition loop.

**Table 4:** Results of inhibition of intestinal bacterial pathogenic

| Lactic acid bacteria strain | Diameter of inhibition loop (mm) | | | | | |
|---|---|---|---|---|---|---|
| | *E.coli* | *Sal* | *Shi* | *Sta* | *Vib* | *Lis* |
| LB1 | 9 | 4 | 3 | 0 | 0 | 0 |
| **LB4** | 14 | 9 | 10 | 2 | 3 | 7 |

*Note:*  *E.coli: Eschrichia coli, Sal: Salmonella,*
*Shi: Shigella, Sta: Staphylococcus aureus*
*Vib:Vibrio parahaemolyticus, Lis: Listeria monocytogenes*
Diameter of inhibition loop > 10mm: high of bacterial pathogenic ability,
Diameter of inhibition loop 5 - 10mm: average of bacterial pathogenic ability,
Diameter of inhibition loop <5 mm: low of bacterial pathogenic ability,
Diameter of inhibition loop 0mm: could not inhibit bacterial pathogenic ability.

The strain LB4 resisted more harmful bacteria than the strain LB1. The ability of harmful bacteria resistance of LB4 also showed that it was more sensitive with harmful bacteria than the results of Ouwehand et al. (2004) [40]. The lactic acid bacteria were isolated by Ouwehand et al. were almost only sensitive with *E. coli* and *L. monocytogenes* and some strains were sensitive with *S. aureus* and *Salmonella.*

Thus, the strain LB4 was highest about probiotic activity in six isolated strains, and this activity was also higher than the results of other studies as mentioned above. Therefore, the strain LB4 could be asserted as a strong probiotic activity strain.

### 3.2. Isolation and screening of acetic acid bacteria
#### 3.2.1. Isolation of acetic acid bacteria
Acetic acid bacteria were isolated from HS medium which was added 1% CaCO3 and 4% ethanol, the positive catalase test and halo-degradation ring would be selected for microscopic inspection. The rod-shaped bacteria, non spore-forming and Gram-negative staining will be selected to prepare test for ability to discharge glucuronic acid.

There are 7 isolated strains which are satisfied the conditions of test were confirmed as acetic bacteria. These strains are described in Table 5:

**Table 5:** Chracteristics of isolated acetic acid bacteria strains

| No. | Strain | Morphological Charateristics | |
|---|---|---|---|
| | | **Macroscopic** | **Microscopic** |
| 1 | AB1 |  Opalescent, punctiform, raised and mucus of colonies, 0.3-0.5mm of diameter, the old was yellow and darker than the young. |  Gram-negative, long rods, sedentary, no spore-forming, arranged in clusters 2-4 concentrate bacteria. |
| 2 | AB2 |  Circular and raised colonies, smooth surface, 0.5-1.5 mm of diameter, young colonies was limpid like the aerosol, the old became darker. |  Gram-negative, short rods, sedentary, no spore-forming, discrete arrangement. |
| 3 | AB3 |  White and flat colonies, around 0.1 mm of diameter. |  Gram-negative, long rods, no spore-forming, discrete arrangement. |
| 4 | AB4 |  White and flat colonies, smooth surface, the old colonies was slightly mucilaginous, the young was limpid like the aerosol, small of diameter, about 0.1mm. |  Gram-negative short rods, no spore-forming, usually discrete arrangement. |

| 5 | AB5 | White and flat colonies, smooth surface, very small size of diameter 0.1-0.2mm. | Gram-negative, long rods, sedentary, no spore-forming, and arranged in clusters or 2 discrete cells put together. |
|---|-----|---|---|
| 6 | AB6 | Yellowish, entire and raised colonies, smooth surface, diameter 1-2mm, the center of old colonies was dark. | Gram-negative, long rods, sedentary, no spore-forming, discrete arrangement. |
| 7 | AB7 | White, entire and flat colonies, smooth surface, small size of diameter 0.3-0.5mm. | Gram-negative, long rods, slightly curved rod cells, no spore-forming, discrete or clustered arrangement in 2 cells. |
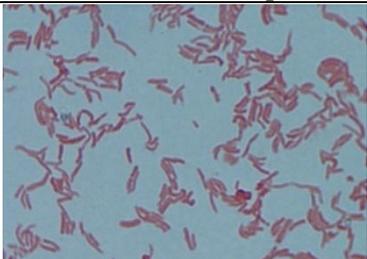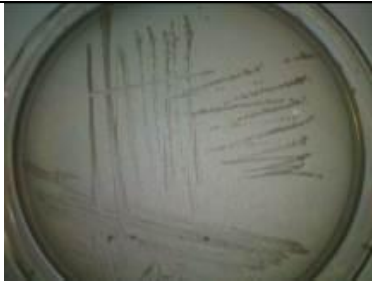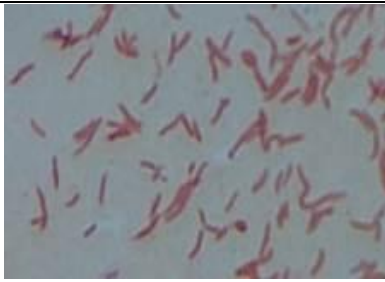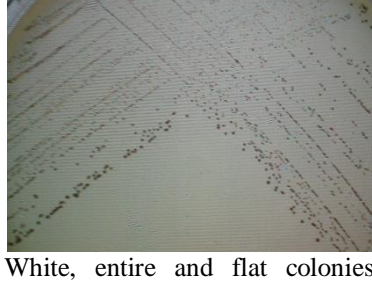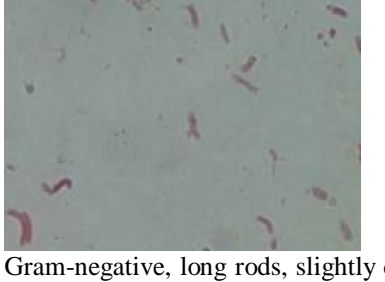
*Note:* AB1, AB2 and AB3 old isolated from fermented coconut juice, AB4 isolated from fermented grape juice, AB5 from vinegar, AB6 and AB7 from tea Kombucha.

So, there were 7 strains of acetic acid bacteria had been isolated and identified based on biochemical and microscopic characteristics. These strains were screened by glucuronic acid generation.

### 3.2.2. Screening acetic bacteria capable of high glucuronic acid

Seven strains of isolated acetic bacteria were cultured at 30°C in 36 hours in fresh milk for screening strains that produced high glucuronic acid concentration to increase biological activity of yogurt (Table 6) .

**Table 6:** Result of screening acetic bacteria

| No. | Strain bacteria | Concentration of glucuronic acid (mg/L) |
|-----|-----------------|------------------------------------------|
| 1 | AB1 | 22,19[c] |
| 2 | AB2 | 9,13[f] |
| 3 | AB3 | 0[g] |
| 4 | AB4 | 12,04[d] |
| 5 | AB5 | 11,52[e] |
| 6 | AB6 | 25,37[b] |
| 7 | **AB7** | **28,04[a]** |

*Note:* The letters from a to g showed the differences at 95% of reliability

In 7 isolated acetic acid bacteria strains, only 6 strains was capable in fermenting to generate glucuronic acid were AB1, AB2, AB4, AB5, AB6 and AB7. The strain AB3 was incapable of glucuronic acid production in milk. In 6 strains of bacteria that produced glucuronic acid, concentration of glucuronic acid was

generated by AB7 that was isolated from tea Kombucha was the highest and difference significantly to the others.

Thus, AB7 was the the highest glucuronic acid concentration strain in isolated acetic acid bacteria.

### *3.3. Identification of high biological activity bacteria strains*
#### *3.3.1. The results of 16S rDNA gene sequencing of LB4 strain*
The isolated strain LB4 were identified by 16S rDNA sequencing. The sequence of 16S rDNA gene of LB4:

AGCTAGTTGGTAGGGTAACGGCCTACCAAGGCAATGATGCATAGCCGAGTTGAGAGAC TGATCGGCCACATTGGGACTGAGACACGGCCCAAACTCCTACGGGAGGCAGCAGTAGGGAATCTT CCACAATGGACGAAAGTCTGATGGAGCAACGCCGCGTGAGTGAAGAAGGTTTTCGGATCGTAAAG CTCTGTTGTTGGTGAAGAAGGATAGAGGTAGTAACTGGCCTTTATTTGACGGTAATCAACCAGAAA GTCACGGCTAACTACGTGCCAGCAGCCGCGGTAATACGTAGGTGGCAAGCGTTGTCCGGATTTATT GGGCGTAAAGCGAGCGCAGGCGGAAGAATAAGTCTGATGTGAAAGCCCTCGGCTTAACCGAGGA ACTGCATCGGAAACTGTTTTTCTTGAGTGCAGAAGAGGAGAGTGGAACTCCATGTGTAGCGGTGG AATGCGTAGATATATGGAAGAACACCAGTGGCGAAGGCGGCTCTCTGGTCTGCAACTGACGCTGA GGCTCGAAAGC

| Description | Max score | Total score | Query cover | E value | Ident | Accession |
|---|---|---|---|---|---|---|
| Lactobacillus acidophilus gene for 16S rRNA, partial sequence, strain: JCM 7711 | 952 | 952 | 100% | 0.0 | 99% | AB911464.1 |

**Figure 1:** Comparison of 16S rDNA gene of LB4 strain with *Lactobacillus acidophilus* (accession number AB911464.1)

The sequence included 525bps and this gene was compared with sequences in the bacterial database by using NCBI BLAST Search tool. The results showed that 16S rDNA gene of strain LB4 was similar up to 100% in comparison with the DNA sequence of *Lactobacillus acidophilus* that had accession number AB911464.1 in International Gene bank. This probiotic bacteria were applied widely in fermented foods such as yogurt, kimchi ... and used in medical products such as digestive enzymes. So, this was useful microorganism and safe for health.

#### *3.3.2. The results of 16S rDNA gene sequencing of AB7 strain*
The isolated strain AB7 were identified by 16S rDNA sequencing. The sequence of 16S rDNA gene of AB7:

TGGCTCAGAGCGAACGCTGGCGGCATGCTTAACACATGCAAGTCGCACGAACCTTTCGGG GTTAGTGGCGGACGGGTGAGTAACGCGTAGGGATCTGTCCACGGGTGGGGGATAACTTTGGGAAA CTGAAGCTAATACCGCATGACACCTGAGGGTCAAAGGCGCAAGTCGCCTGTGGAGGAACCTGCGT TCGATTAGCTAGTTGGTGGGGTAAAGGCCTACCAAGGCGATGATCGATAGCTGGTCTGAGAGGAT GATCAGCCACACTGGGACTGAGACACGGCCCAGACTCCTACGGGAGGCAGCAGTGGGGAATATTG GACAATGGGCGCAAGCCTGATCCAGCAATGCCGCGTGTGTGAAGAAGGTTTTCGGATTGTAAAGC ACTTTCAGCGGGGACGATGATGACGGTACCCGCAGAAGAAGCCCCGGCTAACTTCGTGC

| Description | Max score | Total score | Query cover | E value | Ident | Accession |
|---|---|---|---|---|---|---|
| Gluconacetobacter nataicola strain LMG 1536 16S ribosomal RNA gene, partial sequence | 821 | 821 | 100% | 0.0 | 100% | NR_041012.1 |

**Figure 2:** Comparison of 16S rDNA gene of AB7 and *Gluconacetobacter nataicola* (accession number NR_041012.1)

The sequence included 444bps and this gene was compared with sequences in the bacterial database by using NCBI BLAST Search tool. The results showed that 16S rDNA gene of strain AB7 similar to the DNA sequence of *Gluconacetobacter nataicola* that had accession number NR_041012.1 on the International Gene bank with the similar proportion up to 100%. This was the traditional microorganism that was used in many fermented foods such as vinegar, tea Kombucha... So, this identified strain was safe for human health.

## IV.    Conclusion
In this research, there were 6 lactic acid bacteria strains and 7 acetic acid bacteria strains from traditional fermented foods were isolated for biological activity improvement of yogurt. The strain LB4 showed the strongest of probiotic activity, the sequence of LB4 was identified as *Lactobacillus acidophilus* in comparison with data on Gene Bank. AB7 was capable of production of the highest glucuronic acid in all

isolated strains. The sequence of this strain was similar to *Gluconacetobacter nataicola*. Both strains were safe microorganisms for human health and could be used in food fermentation.

## REFERENCES

[1] Anukam, C. K. et al., 2007, Probiotics: 100 years (1907-2007) after Elie Metchnikoff's Observation. Communicating Current Research and Educational Topics and Trends in Applied Microbiology, A. Méndez-Vilas (Ed.).

[2] Zhiwei Yang, Feng Zhou, Baoping Ji, Bo Li, Yangchao Luo, Li Yang, Tao Li. 2010. Symbiosis between Microorganisms from Kombucha and Kefir: Potential Significance to the Enhancement of Kombucha Function. Appl Biochem Biotechnol DOI 10.1007/s12010-008-8361-6.

[3] Nguyen K. Nguyen, Ngan T.N. Dong, Phu H. Le, Huong T. Nguyen. 2014. Evaluation of the Glucuronic Acid Production and Other Biological Activities of Fermented Sweeten-Black Tea by KBC Layer and the Co-Culture with Different Lactobacillus Sp. Strains. International Journal Of Modern Engineering Research (IJMER), vol.4, iss.5, ISSN: 2249–6645.

[4] Huong H.L Ly, Huong T. Nguyen. 2014. Optimization of Factors Affecting Glucuronic Acid Production in Yogurt Fermentation. International Journal Of Modern Engineering Research (IJMER), vol.4, iss.6, ISSN: 2249–6645.

[5] Nguyen Thuy Huong, Tran Thi Tuong An, 2008. Bacteriocin collection by fermentation with Lactococcus lactic sedentary-cells on bacterial cellulose (BC) and application in fresh meat preservation. Journal of Science and Technology, vol 11, pp. 100 – 109. Vietnam National University of Hochiminh City.

[6] Ogunbanwo, S.T., A.I. Sanni and A.A. Onilude. 2003. Influence of cultural conditions on the production of bacteriocin by Lactobacillus brevis OG1. African Journal of Biotechnology. Vol. 2 (7), pp. 179-184.

[7] Sarika, A. R., A. P. Lipton and M. S. Aishwarya. 2010. Bacteriocin production by a new isolate of Lactobacillus rhamnosus GP1 under different culture conditions. Advance Journal of Food Science and Technology, 2: pp. 291 – 297.

## BIOGRAPHY

**Huong H.L. Ly** is currently MSc Researcher in Department of Biotechnology, Ho Chi Minh City University of Technology, Vietnam National University of Ho Chi Minh City. She received Bachelor degree in 2011 in Advanced Biotechnology program that was corporation between Can Tho University - Vietnam and Michigan State University – USA. In 2014, she graduated MSc degree in Biotechnology at Ho Chi Minh City University of Technology, Vietnam National University of Ho Chi Minh City, Vietnam. Her main research includes food and environmental biotechnology, microbiology and bio-medicine.

**Huong T. Ha** is pursuing her MSc degree in Biotechnology at Ho Chi Minh City University of Technology, Vietnam National University of Ho Chi Minh City. She received Bachelor degree in Biotechnology in BiRDI, Can Tho University, Vietnam in 2012. Her main research includes food biotechnology and microbiology.

**Huong T. Nguyen** is presently working as Associate Professor in Biotechnology in Ho Chi Minh City University of Technology, Vietnam. She is Head of Department of Biotechnology, Ho Chi Minh City University of Technology, Vietnam National University of Ho Chi Minh City. Her main research includes microbiological engineering and genetics engineering.

# Regression techniques to study the student performance in post graduate examinations - A case study

Ananth. Y. N[1], Narahari. N. S[2]

[1]*Associate Professor &Ph.D student- Dept of Computer Science- School of Graduate Studies, Jain University, Bangalore-India*
[2]*Professor and Head, Dept of Industrial Engineering & Management, R.V.College of Engineering Autonomous-VTU - Bangalore-India*

***Abstract****: Aptitude of students entering into Post graduate courses in INDIA is an aspect to be studied. Entrance Examinations do test the aptitude but to a certain extent. Post graduate students are expected to have a certain level of aptitude and this aptitude should be sustained till the end of their course and beyond. Therefore, it is a necessity to examine to what extent their aptitudes are getting tested. The marks scored by the students in the entrance examination is an indicator of the aptitude but does not speak of the ability of the students in all the aspects or the subject of their specialization in the post graduate courses.It has been observed that a causal dependency exists between the degree marks and the entrance test marks. This paper tries to investigate this dependency with linear regression techniques. On the whole , categories of students are identified by studying the distribution of marks. A mapping between the marks and the questions are being studied. Linear regression technique is being used to identify the groups of students and to predict the expected marks that the future students would score.*

***Keywords****: Aptitude, Dependent variable, Performance, Predictor, Regression*

## I. INTRODUCTION

Testing students' aptitude is a challenging area – given the wide variety of the questions in the degree and the entrance test examinations. Students' abilities are also varied – Some will be good in quantitative techniques, some in reasoning and analytical abilities and so on. The undergraduate degree examinations test mainly the knowledge level of the students-habitual learning methods directed at memorizing ,learning the facts and so on .The reasoning power and the spirit of enquiry at a higher level blooms by the finishing years of graduation. Hence it is imperative to study the progression of students. In this context, not all the students will have the same sustainable ability to persue post graduate courses. In this regard, setting the right kind of questions across all kinds of students is a difficult task .Therefore it is good to consider the marks in the undergraduate examinations and study the dependency of the entrance test marks on that. Taking this as an indicator, sectors of students could be identified .This information could be used to correlate to what kind of questions that would be suitable for students' groups-Doing statistical studies among the groups, the right kind of questions can be set for the right kind of groups. With this perspective, this paper discusses linear regression and its use. Although this techniques has its own limitations, this technique is an useful one. The particular case study that has been considered is the Karnataka –Post Graduate Common Entrance Test examinations

## II. LITERATURE SURVEY

Many techniques do exist in order to study the distribution and patterns of marks in examinations. Reliability issues of the questions has been studied by S. O. Bandele and Dr. A. E. Adewale in [1]**.**Requirement of prerequisites for Masters programmes can be very clearly seen as in [2]

What can be inferred from this data is that the stream of the undergraduate degree is quite important for the choice of the subjects in post graduate courses.

Regression techniques are quite a powerful technique of analysis in many areas like market survey; understanding of customer behavior .The main use of regression techniques is that they can be used for investigating the causal dependencies between variables. These techniques are being used in education to study the causal factor analysis in many situations. For example regression techniques are used in analyzing the influence of peer pressure in secondary schools, upon the scores of the students. Multiple regression can be to understand whether exam performance can be predicted based on revision time, test anxiety, lecture attendance, and gender. This has also been used in analyzing the advantages of high ranked schools in moulding the students in an indirect way, by considering the marks scored by the students of such schools. The study of the effect of good teachers, good teaching aids upon student performance have also employed to a good extent the technique

of regression. On the whole it can be said that wherever there is a study of causal factors relating to student performance in schools /colleges, regression techniques can be employed.

## III. BRIEF METHODOLOGY

Linear regression is a modelling technique in which the relationship between a scalar dependent variable y and one or more explanatory variable X is being studied. The case of a single explanatory variable is called as linear regression and when there are more than one explanatory variable, it is called as multiple linear regression.

In linear regression, datasets are modelled by using linear predictor functions and unknown parameters are modelled using "predictor variables". More commonly, the conditional dependency of Y given X is what is being depicted here.The technique can be used for prediction where in a model to describe the behavior of Y given X can be developed. This model can be used in order to predict the data values Y for a new set of X.

The actual mathematical model for regression can be given as follows. Given a data set $\{y_i, x_{i1}, x_{i2}, \ldots \ldots x_{ip}\}$ i=1to n,the regression model assumes that the relationship between the dependent variable y and the regressors x is linear.This relationship is modelled with a set of regression coefficients and an error term which is also called as noise. The regression coefficients give the extent to which a particular regressor $x_i$ affects y.The relationship may not be perfect always and the difference between the actual relationship and the observed relationship is modelled using the error term or the noise term. Thus the model takes the form:

$Y_i = \beta_1 x_{i1} + \beta_2 x_{i2} + \ldots \ldots \beta_i x_{ip} + \varepsilon_i = [X_i]^T \beta + \varepsilon_i$ i= 1to n. where T denotes the transpose so that $[X_i]^T\beta$ is the inner product between $x_i$ and $\beta$

This model can take the compact form
Y = xβ + ε where,

$$
\mathbf{y} = \begin{pmatrix} y_1 \\ y_2 \\ \vdots \\ y_n \end{pmatrix}, \quad
\mathbf{X} = \begin{pmatrix} \mathbf{x}_1^T \\ \mathbf{x}_2^T \\ \vdots \\ \mathbf{x}_n^T \end{pmatrix} = \begin{pmatrix} x_{11} & \cdots & x_{1p} \\ x_{21} & \cdots & x_{2p} \\ \vdots & \ddots & \vdots \\ x_{n1} & \cdots & x_{np} \end{pmatrix}, \quad
\boldsymbol{\beta} = \begin{pmatrix} \beta_1 \\ \beta_2 \\ \vdots \\ \beta_p \end{pmatrix}, \quad
\boldsymbol{\varepsilon} = \begin{pmatrix} \varepsilon_1 \\ \varepsilon_2 \\ \vdots \\ \varepsilon_n \end{pmatrix}.
$$

## IV. THE CONTEXT

Karnataka -PGCET examination –The area of study for this paper is the study of the marks distributions and considerations of the dependent and independent factors in the Karnataka PGCET examination. InKarnataka , seats for the Post graduate Courses in Engineering, MCA and MBA are conducted by Karnataka examination Authority-(This year it has been changed).The examination is taken by nearly a lakh students and the rank is allocated to them based on their score in the entrance examination –Previously the ranks were decided by considering the students' marks in their respective degrees also-equal weightage was being given to both the marks. Now a study of the dependency of the ranks upon these  is made .For regression analysis , the entrance examination marks field is considered to be the dependent variable and the degree marks is considered to be the independent variable. A sample output from Excel for this case is given below. The data is taken from the MCA results and the number of data points is 1000.The actual data consists of only the entrance test marks but for the analysis, the degree marks is derived by taking into consideration the equal weightage given to both the marks.This has been generated by running a formula involving the rank and the entrance test marks.
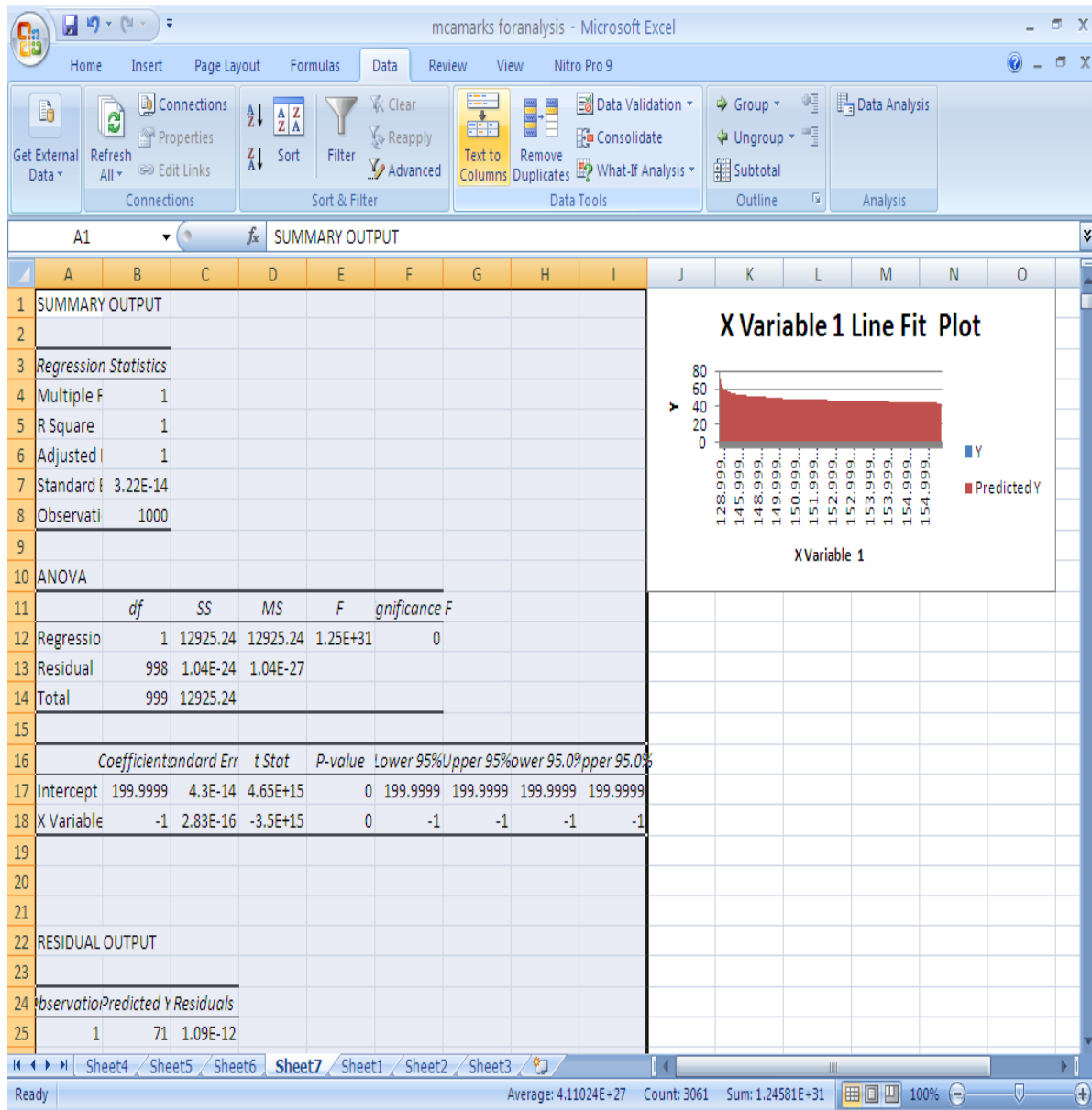
## V. REGRESSION OUTPUT EXPLAINED

The regression output shows both the $R^2$ and the adjusted $R^2$ values are equal to 1- which shows that there is perfect correlation between the two sets of marks. In reality this would not be possible because of the different kinds of scoring patterns practiced in different universities and colleges and they cannot be reduced to one single uniformscale. The observed results are due to the fact that the degree marks is generated from the program. The degree marks is generated taking into consideration that there is a 50% component of the degree marks and the entrance test marks and evolving a suitable formula to generate them by using the rank and the entrance test marks. But the marks is indeed following the given pattern which can be verified by observing the rank field. There is a difference of not more than 1 mark in the entrance test for the current and the next rank. Therefore, effectively the marks distribution follows the applied pattern. The same applies to the regression equation which can be taken from the output. It reads

$$Y = 199.99 - X$$

The confidence interval is set to 95% which means that the rejection region is only 5% and the predicted Y value falls within that range only.

This technique can be further extended to contain more explanatory variables where in multiple regression can be used. The analysis done hitherto considers the dependency only upon the degree marks but other causal factors like peer pressure, test anxiety and so on.

## VI. DECIDING ABOUT THE QUESTIONS IN THE ENTRANCE EXAMINATION

When this output is subjected to a more thorough analysis going into details of why a particular student group has scored a particular set of ranks- the questions in the entrance examination have to be analyzed. These have to be analyzed with a perspective of the aptitude of the students taking up the examination. The nature of the questions in the degree examinations and those in the entrance examination has to be matched in order to bring about a suitable testing of the aptitude. The regression outputs give us a quantitative measure of the impact of the marks of the students – which can be used to derive to what extent the marks is determining the aptitude of the student. The same degree marks in the future examinations can be used with these coefficients to predict what could be the marks in the entrance examination that a particular student community would score-Of course , a stringent study of the types of questions has to be done to determine the aptitude of the students in a particular area of the questions.

The questions in the entrance examination can also be categorized, each one testing a particular aspect of the student ability. The post graduate entrance exams are expected to test the students' ability in quantitative ability, reasoning and so on. By studying the pattern of marks in the entrance examination and the groups given by the regression output, one can decide what kind of questions best measure the aptitude of the student groups.With a perspective of what is required to pick up the right kind of candidates , this information could be used to decide about the questions .The analysis of marks , combined with the comparisons of the questions and answers in both the examinations , this could be used as a predictive technique in deciding the right question needed for the current year.

## VII. LIMITATIONS

Linear regression, as has been explained here is testing only one aspect of the scenario. The causal factors for a student scoring a certain marks are many, including peer pressure, test anxiety, future expectations , motivation and so on. Some of these are easy to be quantified some and some are not.Linear regression is best useful when there is a linear relationship between the dependent and the independent variables.Better techniques like genetic algorithms and partial least square methods can be used for better analysis.

## VIII. CONCLUSIONS

This paper discusses a mathematical model to study the marks distributions in the Karnataka PGCET examinations. The technique of linear regression can be applied to a large sets of records also and this is where the usefulness of the method can be seen. As the number of students taking up the examination is very large , deriving a knowledgeable pattern of marks distribution becomes essential when a change of question paper is the issue. Other probabilistic techniques and statistical techniques can be used along with linear regression to better know of the clusters of the students and devise the question papers accordingly.

### REFERENCES

[1]     http://www.mcser.org/journal/index.php/jesr/article/viewFile/186/171.
[2]     http://www20.csueastbay.edu/ecat/graduate-chapters/g-stat.html

## Contents :

# Optimized Projected Strategy for Enhancement of WSN Using Genetic Algorithms

Er. Dinesh Randhawa[1], Er. Manit Kapoor[2], Er. Kuldeep Sharma[3]

[1]*Electronics and Communication, Ramgarhia College of Engg. and Technology, Phagwara, Punjab, India*
[2, 3] *Assistant Professor, Ramgarhia Institute of Engineering and Technology, Phagwara, Punjab*

**Abstract:** *This paper put forward a new strategy for selecting the most favorable cluster head in Stable Election Protocol (SEP). The planned approach selects a node as cluster head if it has the maximum energy among all the available nodes in that particular cluster. It considers diverse nodes and divides nodes among normal, transitional and advance nodes. To handle the heterogeneity of the nodes, different optimized probability density functions are selected. First node dead time explain the network stability period and last node dead explain the overall network lifetime. The main pressure is to increase the time when first node dies and also when last node dies. The projected strategy is designed and implemented in the Matlab using mathematics toolbox. The projected algorithm is also compared with the some prominent protocols like leach, E-LEACH, SEP and extended SEP.*
**Keywords:** *LEACH, SEP, WSN, Energy, Network Lifetime, Throughput.*

## I. INTRODUCTION

Wireless sensor networks (WSN) composed of a huge number of small self-sufficient devices with computational, sensing and wireless communication capabilities. These sensors measure ambient conditions e.g. speed, temperature, pressure, humidity etc and transform the data into electrical signals which can be processed to reveal some characteristics about the phenomena. These analog signals are then changed into digital signals which are further processed in processing unit. Transmission between the sensor nodes is wireless which is the most power consuming movement in the sensor networks. For this, clustering of the sensor nodes is done. Cluster-based routing algorithm has a better energy utilization rate compared with non-cluster routing algorithm. The basic idea of clustering routing is to use the information aggregation mechanism in the cluster head to reduce the amount of data transmission, thereby, reduce the energy dissipation in communication. In clustering, every node sends data to its selected cluster head & this cluster head further sends data to the sink node or base station. Hence energy utilization is compact in comparison to the case where each node would have send data directly to the base station as the radio activity consumes more energy.

There is an increasing need for the nodes to handle more complex functions in data acquisition and processing, and energy saving solutions remains a major requirement for these battery-powered sensor nodes. Three major functions are performed by sensor; the data processor that performs local computations on the data sensed; and the communicator that performs information exchange between neighboring nodes. Each sensor is usually limited in their energy, processing power and sensing ability. However, networks of these sensors give rise to a robust, reliable and accurate network. The sensors can collaborate and cooperate among each other, elect leaders or heads, gather their data and then transmits a more results from the sensing. WSN systems are increasingly demanding with new applications in various areas wireless sensor networks are consisted of thousands of small sensors that span a large geographical region.

These sensors are able to commune with each other to collaboratively detect objects, collect information and transmit messages. However, as sensors are usually small in size, they have many physical limitations such as battery, computational power and memory. Because of those limitations, energy-efficient techniques are main research challenges in wireless sensor networks. A number of techniques have been proposed to solve these challenges. Leach (low-energy adaptive clustering hierarchy) is one of the famous techniques in wireless sensor networks. This is a cluster-based protocol that utilizes randomized rotation of local cluster base stations (cluster-heads) to evenly distribute the energy load among the sensors in the network. This technique can reduce a number of transmissions in Clusters. However, The Intense Data Flow Can Be Harmful, Especially In Wireless Sensor Networks, Since Congestions And Collisions May Be Occurred. Traditional server/client-based techniques like a leach cannot utilize autonomous-repair and scalability and so on. And also it gives too much burden on base-station. Wireless sensor networks (WSNS) are networks of light-weight sensors that are battery powered used majorly for monitoring purposes. The advances in micro-electromechanical technologies have made the improving of such sensors a possibility. However, while WSNS are increasingly equipped to handle some of these complex functions, in-network processing such as data

aggregation, information fusion, computation and transmission activities requires these sensors to use their energy efficiently in order to extend their network life time. Sensor nodes are prone to energy drainage and failure, and their battery source might be irreplaceable, instead new sensors are deployed. This can negatively impact the stability and performance of the network system if the extra energy is not properly utilized. Leach protocol and the likes assume a near to perfect system; an energy homogeneous system where a node is not likely to fail due to uneven terrain, failure in connectivity and packet dropping. But more recent protocols like SEP is considered the reverse that is energy heterogeneity where the factors mentioned above are a possibility, which is more applicable to real life scenario for WSN. Thus, energy heterogeneity should therefore be one of the key factors to be considered when designing a protocol that is robust for WSN. The goal is to present a modified protocol design that is more robust and can ensure longer network life-time while taking other performance measures into consideration. Sensor network should be adaptive and sensitive to the dynamic environment where they are deployed. Since nodes are battery-powered and communications are radio-based, nodes are more susceptible to failures. The information collected by individual node should be aggregated to give more accurate and reliable results. Sensor network should be reliable and be able to provide relevant data through information gathering techniques. The hardware design should incorporate methods to conserve energy using low powered processors and the system software should use minimal power as possible. A sensor network algorithm should be distributed and self-organizing, since WSN is infrastructure-less. The security of the network should also be considered. Scalability is another important factor to be considered when designing a topology for WSN.

## II. LITERATURE SURVEY

Since the nodes of wireless sensor networks are in the condition of a highly-limited and unreplenish able energy resource such as battery power, computation, and storage space, the energy efficiency is the most important key point of the network routing designing. [1]

Wireless sensor networks (WSNS) have been considered as a promising method for reliably monitoring both civil and military environments under hazardous or dangerous conditions. Due to such environments, the power supplies for sensors in the network are not usually rechargeable or replaceable. Therefore, the energy efficiency is critical for the lifetime and cost of WSN. Numerous mechanisms have been proposed to reduce the impact of communication protocols on the overall energy dissipation of WSN. The low-energy adaptive clustering hierarchy (leach) and another improved centralized leach deploy randomized rotation of cluster-heads to evenly distribute the energy load among all sensors in a WSN. [2]

The effect of coding on the energy consumption in wireless embedded networks. An analytical model of the radio energy consumption is developed to study how different dc balanced codes affect the energy consumption for the one-hop case. A Rayleigh fading channel is assumed, the analysis is extended to include multihop scenarios in order to study the tradeoff between coding overhead and energy consumption. [3]

Adopting biologically inspired approaches for wireless sensor networks. Agent operates automatically with their behavior policies as a gene. Agent aggregates other agents to reduce communication and gives high priority to nodes that have enough energy to communicate. Agent behavior policies are optimized by genetic operation at the base station. Simulation results show that our proposed framework increases the lifetime of each node. Each agent selects a next-hop node with neighbor information and behavior policies. [3]

A distributed, energy efficient algorithm for collecting data from all sensor nodes with minimum latency called delay-minimized energy-efficient data aggregation algorithm (DEDA). The DEDA algorithm minimizes data aggregation latency by building a delay-efficient network structure. At the same time, it also considers the distances between network nodes for saving sensor transmission power and network energy. Energy consumption is also well balanced between sensors to achieve an acceptable network lifetime. [5]

Wireless sensor network is composed of hundreds of sensor nodes involving in limited energy, efficient and low-energy consuming routing algorithm is the crucial problem to the routing design. [6]

Recent advances in wireless sensor networks have led to many new protocols specifically designed for sensor networks where energy awareness is an essential consideration. Clustering is a key routing technique used to reduce energy consumption. Clustering sensors into groups, so that sensors communicate information only to cluster heads and then the cluster-heads communicate the aggregated information to the base station, saves energy and thus prolonging network lifetime. [7]

Routing protocols like EEE leach, leach and direct transmission protocol (DTX) in wireless sensor network (WSN) and a comparison study of these protocols based on some performance matrices. Addition to this an attempt is done to calculate their transmission time and throughput. To calculate these, MATLAB environment is used. Finally, on the basis of the obtained results from the simulation, the above mentioned three protocols are compared. [8]

Algorithm considers the sensor nodes are static and randomly distributed in the heterogeneous network, the coordinates of the sink and the dimensions of the sensor field are known. [9]

The main problem with the leach lies in the random selection of cluster heads. There exists a probability that cluster heads formed are unbalanced and may remain in one part of network making some part of network unreachable. Here our main purpose is to select a cluster head depending upon its current energy level and distance from the sink node. This increases the energy efficiency and hence network lifetime. [10]

Leach (low energy adaptive clustering hierarchy) protocol randomly selects a few nodes as cluster heads based on a probability model. The probabilistic approach leads to the formation of unequally sized clusters which leads to imbalance in energy consumption across the network and thereby reduces the efficiency and network lifetime. [11]

The largest energy consumption for a single cluster head in the next round will be estimated, and all nodes with residual energy larger than the calculated consumption will be taken to a new round of simulated annealing to find a better solution. Thus, loss of the cluster head for each round can be minimized, and the WSN lifetime can be extended ultimately. [12]

SEP (stable election protocol) so every sensor node in a heterogeneous two-level hierarchical network independently elects itself as a cluster head based on its initial energy relative to that of other nodes. [13]

Wireless sensor network (WSN) is a hopeful approach for a variety of applications. Because of limitation of energy resource, memory space and processing capability of sensor nodes, it is very difficult to implement IP-based routing protocols in WSN. Recently, many research focus on developing special routing protocols for WSNS with the main design criteria: energy efficiency, load balance and reliability. [14]

As the use of wireless sensor networks (WSNS) has grown enormously in the past few decades, the need of scalable &energy efficient routing and data aggregation protocol for large scale deployments has also risen. Leach is a hierarchical clustering protocol that provides an elegant solution for such protocols. [15]

The non cluster-heads choose optimal cluster-head, they consider comprehensive nodes' residual energy and distance to base-station then compare their performance, the simulation results show that the new strategy of cluster-heads election achieve great advance in sensor and networks' life-time. [16]

An analytical model for the study of energy consumption in multihop wireless embedded and sensor networks where nodes are extremely power constrained. Low power optimization techniques developed for conventional ad hoc networks are not sufficient as they do not properly address particular features of embedded and sensor networks. It is not enough to reduce overall energy consumption, it is also important to maximize the lifetime of the entire network, that is, maintain full network connectivity for as long as possible. [17]

## III.   Experimetal Setup

Assume a three-level hierarchical clustered heterogeneous sensor network with 100 sensor nodes which are randomly distributed over the 100×100 m2 area. The sink or base station is located at point (90×90). The packet size that the nodes send to their cluster heads as well as the aggregated packet size that a cluster head sends to the sink is set to 4000 bits. The initial energy of each normal node is set to 0.5 joule. The proposed approach has been implemented in matlab and the performance has been evaluated by simulation. We have measured the lifetime of the network in terms of rounds when the first sensor node dies. All the parameter values including the first order radio model characteristic parameters are mentioned in the table 1 below:

**Table 1: Various Parameters and Their Values**

| PARAMETERS | VALUES |
|---|---|
| Sensor Field | 100×100 |
| Sink Position | 90×90 |
| N | 100 |
| Packet Size | 4000 |
| EFS | $10pj/Bit/M^2$ |
| EMP | $0.0013pj/Bit/M^4$ |
| $E_{DA}$ | 50nj/Bit |
| $E_O$ | 0.5 J |
| P | 0.1 |
| A | 2 |
| B | 1 |
| M | 0.3 |
| X | 0.3 |

## IV.   Heterogeneous WSN Model

In This Section, The Heterogeneous Wireless Sensor Network Model Which Includes Cluster Formation And Maintaining Optimum Number Of Clusters Is Mentioned.

**A. Creation of a Cluster**

Consider a three stage hierarchical clustered network. The low energy adaptive clustering hierarchy (leach) is a protocol which is hierarchically clustered where clusters are re-established in each round. In this protocol, new cluster heads get elected in each round and as a result the load becomes well distributed and balanced among the nodes of the network. An optimal percentage of nodes $P_{opt}$ are considered that has to become cluster head in each round. We have assumed the same distributed algorithms to form clusters in the network. To decide whether a node to become cluster head or not a threshold t(s) is addressed in which is as follows:

$$T(s) = \begin{cases} \dfrac{p_{opt}}{1 - p_{opt}.(r.\bmod.\dfrac{1}{p_{opt}})}, if s \in G' \\ 0, otherwise \end{cases} \quad (1)$$

Where r is the current round number and g is the set of nodes that have not become cluster head within the last $1/p_{opt}$ rounds. At the beginning of each round, each node which belongs to the set g selects a random number 0 or 1. If the random number is less than the threshold t(s) then the node becomes a cluster head in the current round.

**B. Optimum Number of Clusters**

According To The Radio Energy Model Addressed In [2], In Order To Achieve An Adequate SNR In Transmitting An L Bit Message Over A Distance D, The Energy Dissipated By The Radio Is Given By:

$$E_{Tx}(l,d) = \begin{cases} L.E_{Elec} + L.\in_{fs}.d^2, if d \le d_0 \\ L.E_{Elec} + L.\in_{mp}.d^4, if d \ge d_0 \end{cases} \quad (2)$$

Where $E_{elec}$ Is The Energy Dissipated Per Bit To Run The Transmitter Or Receiver Circuit, $\in_{fs}$ (Free Space Fading) And $\in_{mp}$ (Multi Path Fading) Are The Energy Expenditure Of Transmitting One Bit Data To Achieve An Acceptable Bit Error Rate And D Is The Distance Between A Cluster Member Node And Its Cluster Head. By Equating the Two Expressions at $D = D_0$, We Get

$$d_0 = \sqrt{\dfrac{\in_{fs}}{\in_{mp}}} \quad (3)$$

So According To [2], The Optimum Number Of Clusters $K_{opt}$ For Our Cluster Based Network, Having N Sensor Nodes Distributed Randomly In A (Mxm) Sensor Field Is As Follows:

$$k_{opt} = \sqrt{\dfrac{n}{2\pi}}.\sqrt{\dfrac{\in_{fs}}{\in_{mp}}}.\dfrac{M}{d^2} \quad (4)$$

Again, The Optimal Probability Of A Sensor Node To Become Cluster Head Can Be Calculated As:

$$p_{opt} = \dfrac{k_{opt}}{n} \quad (5)$$

## V. Proposed Protocol

We have analyzed a three-tier node scenario in a diverse sensor network environment. There are p is the percentage of advance, intermediate and normal nodes having a times more energy than the normal nodes that are distributed randomly over the sensor field. A cluster head election process is considered based on the battery power and residual energy of the node. In our approach, intermediate and advanced nodes have higher probabilities to become a cluster head in a particular round than the normal nodes. The proposed heterogeneous network model doesn't effect on the spatial density of the network but changes the total initial energy of the network. We have individual initial energy equations for intermediate and advanced nodes as follows:

$$E_1 = E_0.(1+a) \quad (6)$$
$$E_2 = E_0.(1+b) \quad (7)$$

Where, $E_0$=energy of a normal node, $E_1$=energy of a intermediate node, $E_2$=energy of an advanced node

The total initial energy of three types of nodes is as follows:

$$E_{t0} = n.E_0.(1 - p - k) \tag{8}$$

$$E_{t1} = n.p.E_0.(1 + a) \tag{9}$$

$$E_{t2} = n.k.E_0.(1 + b) \tag{10}$$

Where, $E_{t0}$=total initial energy of normal nodes, $\mathbf{E_{t1}}$=total initial energy of intermediate nodes, $E_{t2}$=total initial energy of advanced nodes

The total initial energy of the new heterogeneous sensor network model is given by equation (11):

$$E_t = n.E_0.(1 - p - k) + n.p.E_0.(1 + a) + n.k.E_0.(1 + b)$$

$$E_t = n.E_0.(1 + p.a + k.b) \tag{11}$$

In this work, we have approached to allocate a weight to the optimal probability of a sensor node ($p_{opt}$) to become cluster head in a particular round. This weight must be equal to the division of the initial energy of each node by the initial energy of a normal node. If all the nodes are homogeneous, all the nodes will become cluster head once every $1/p_{opt}$ round which is coined as epoch of the network. In order to maintain the minimum energy consumption in each round within an epoch, the average number of cluster heads per round per epoch must be constant and equal to $p_{opt}.n$. In our approach the average number of cluster heads per round per epoch is equal to n. (1+p.a+k.b). In [2], the weighted election probabilities for normal and advanced nodes are defined. In our three tier node scenario, the weighted election probabilities for the normal, moderate and advanced nodes are as follows:

$$P_{nrm} = \frac{p_{opt}}{1 + p.a + p.b} \tag{12}$$

$$P_{adv} = \frac{p_{opt}}{1 + p.a + p.b} . (1 + a) \tag{13}$$

We further define the thresholds $t(s_{nrm})$, $t(s_{adv})$ for the normal, advanced nodes. In equation (1) we have replaced $p_{opt}$ by the weighted probabilities of normal and advanced nodes to get the threshold that is used to elect the cluster head in each round. Thus, the threshold for the normal nodes to become cluster head can be evaluated by the following equation:

$$T(s_{nrm}) = \begin{cases} \dfrac{p_{nrm}}{1 - p_{nrm}.(r.\mathrm{mod}.\dfrac{1}{p_{nrm}})}, & if s \in G' \\ 0, & otherwise \end{cases} \tag{14}$$

Where r is the current round number, g' is the set of normal nodes that have not become cluster head within the last $1/p_{nrm}$ rounds of the epoch. $T(s_{nrm})$ is the threshold applied to a population of n.(1-p-k) that are normal nodes. This ensures that each normal node will become a cluster head exactly once every (1+p.a+k.b)/$p_{nrm}$ rounds per epoch and that the average number of cluster heads that are normal nodes per round per epoch is equal to n. (1-p-k). Similarly, thresholds $t(s_{int})$ and $t(s_{adv})$ for intermediate and advanced nodes are also evaluated.

## VI. Performance Analysis

**A. WSN in active stage**

Figure 1 is showing the wsn in active mode where all nodes are active. Nodes correspond to by circles are normal nodes and nodes with circle and star (*) are cluster heads. Nodes represent by triangle are intermediate nodes and nodes with triangle and star (*) are cluster heads. Nodes represent by diamond are advance nodes and nodes with diamond and star (*) are cluster heads. The entire network has a base station that is responsible for the collection of data from all other nodes.
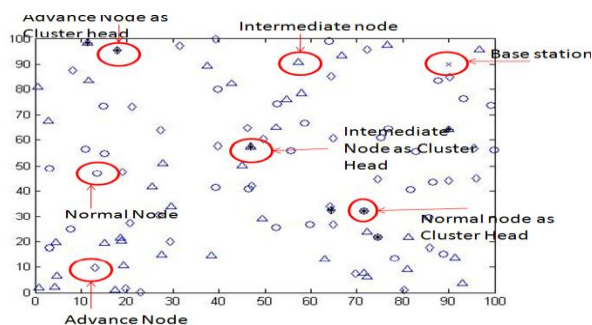


Fig 1: Initial Configuration of WSN

**B. First Dead Nodes**

        Figure 2 is indicating the leach with active as well as with some dead nodes represent by red diamond. Figure 2 shows the dimension area of 100*100, there are 100 nodes in total in which some are active represent by circles (o), some are cluster head represent by using circle and star (*) , triangle and star (*) , diamond  and star (*) and also red diamonds represent the node dead so far during the life cycle of wireless sensor network.
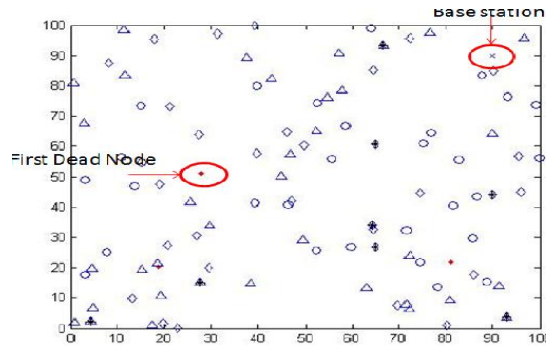

Fig 2: First Dead Node

**C. ALL Dead Nodes**

        Figure 3 is representing all dead nodes represent by red diamond. Figure 3 also shows the dimension area of 100*100, there are 100 nodes and red diamonds represent the node dead so far during the life cycle of wireless sensor network. The entire network has a base station that is responsible for the collection of data from all other nodes.
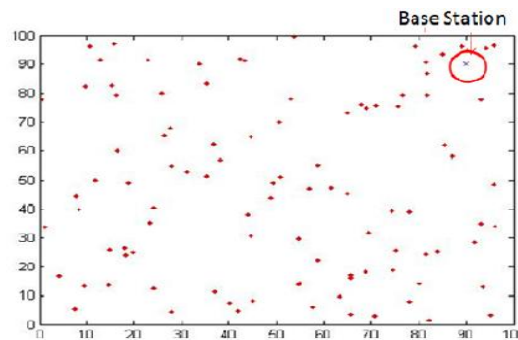

Fig 3:  All Dead Nodes

**Table II: Comparison With The Earlier Research**

| Name Of Algorithm | Parameter | *A | *B |
|---|---|---|---|
| Leach* | First Dead Node | 1000 | 920 |
|  | Last Dead Node | 1400 | 1420 |
| Eleach* | First Dead Node | 1500 | 1560 |
|  | Last Dead Node | 2700 | 2800 |
| SEP^ | First Dead Node | 900 | 969 |
|  | Last Dead Node | 3000 | 3350 |
| ESEP^ | First Dead Node | 1800 | 1854 |
|  | Last Dead Node | 3500 | 3414 |
| Proposed | First Dead Node |  | 2343 |
|  | Last Dead Node |  | 3750 |

*A - Analytic Study of Various Algorithm in WSN by Reetika Munjal[*], M M Islam[^]
*B – Results of Proposed Study

**D. Packet Send to Cluster Head**

        Figure 4 is signifying the packets that are sent to cluster head in leach protocol during the lifetime of the leach protocol. It shows the throughput from 0 rounds to 1420 as 1420 is the overall lifetime of leach in our experiment. Here y axis shows the amount of packets sent during running time. It is clearly shown that the

packets goes down rapidly recently after the first node dead, which clearly shows the benefits of the stability period of wireless sensor network.
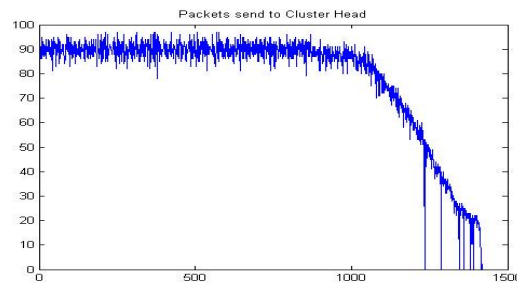


Fig.4 packet send to cluster head of leach protocol

Figure 5 is viewing the packets that are sent to cluster head in energy leach protocol during the lifetime of the energy leach protocol. It illustrates the throughput from 0 rounds to 2800 as 2800 is the overall lifetime of leach in our experiment. Here y axis shows the amount of packets sent during running time. It is clearly shown that the packets goes down rapidly recently after the first node dead, which clearly shows the benefits of the stability period of wireless sensor network. However it also shows the progress in terms of network life time and stability period than the simple leach protocol.
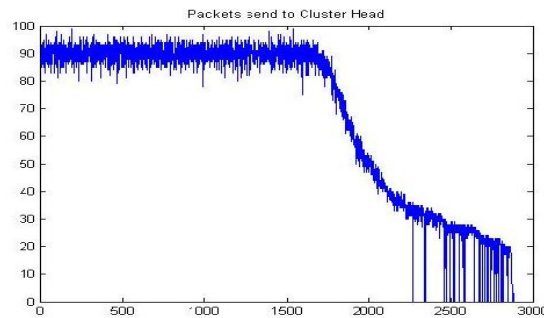


Fig.5 Packet Send To Cluster Head Of Eleach Protocol

Figure 6 is screening the packets that are sent to cluster head in energy leach protocol during the lifetime of the energy leach protocol. It illustrates the throughput from 0 rounds to 3750 as 3750 is the overall lifetime of leach in our experiment. Here y axis shows the amount of packets sent during running time. It is clearly shown that the packets goes down rapidly recently after the first node dead, which clearly shows the benefits of the stability period of wireless sensor network. However it also shows the progress in terms of network life time and stability period than the simple LEACH, ELEACH Protocol.
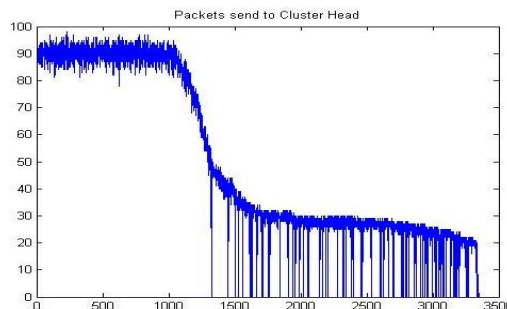


Fig.6 Packet Send To Cluster Head Of SEP Protocol

Figure 7 is viewing the packets that are sent to cluster head in energy leach protocol during the lifetime of the energy leach protocol. It illustrates the throughput from 0 rounds to 3414 as 3414 is the overall lifetime of leach in our experiment. Here y axis shows the amount of packets sent during running time. It is clearly shown that the packets goes down rapidly recently after the first node dead, which clearly shows the benefits of the stability period of wireless sensor network. However it also shows the progress in terms of network life time and stability period than the simple LEACH, ELEACH, SEP  protocol.
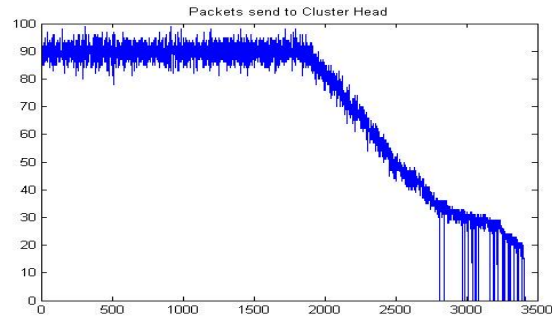
Fig.7 Packet Send To Cluster Head Of ESEP Protocol

Figure 8 is showing the packets that are sent to cluster head in energy leach protocol during the lifetime of the energy leach protocol. It illustrates the throughput from 0 rounds to 2450 as 2450 is the overall lifetime of leach in our experiment. Here y axis shows the amount of packets sent during running time. It is clearly shown that the packets goes down rapidly recently after the first node dead, which clearly shows the benefits of the stability period of wireless sensor network. However it also shows the progress in terms of network life time and stability period than the simple leach, ELEACH, SEP, ESEP protocol.
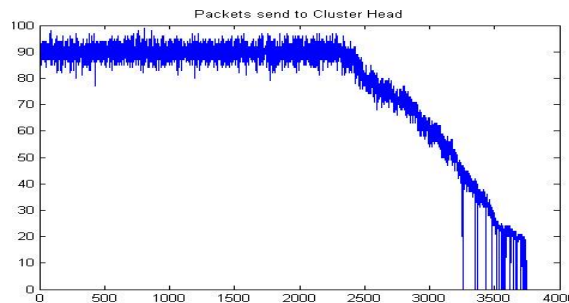

Fig.8 Packet Send To Cluster Head Of Proposed SEP Protocol

## VII. Conclusion
The Proposed Algorithm Has Revealed A Significant Enhancement Over LEACH, E-LEACH, SEP And Extended SEP. The Only Difference Among Existing Protocols And Proposed Algorithm Is That Projected Algorithm Selects A Node As Cluster Head Only If It Has Maximum Energy Among Other Nodes In Cluster During Run Time. The Proposed Algorithm Is Seems To Be Justified As Heterogeneity Of WSN Nodes Is Also Well Thought-Out By Introducing The Normal, Advance And Intermediate Nodes. The Comparisons Of Proposed Algorithm With Existing Algorithm Are Better In With Respect To Packets Sent To Cluster Heads, When The First Node Dies And When All Node Become Dead I.E. Network Life Time. In Near Prospect We Will Extend This Work By Introducing The Genetic Algorithms To Improve The Decision Making Of Cluster Head Selection.

## REFERENCE
[1]     Guisheng Yin1, Guang Yang1,2, Wu Yang1,2, Bingyang Zhang1,2, Wenjin Jin1,2 "An Energy-Efficient Routing Algorithm For Wireless Sensor Networks", International Conference On Internet Computing In Science And Engineering (IEEE) (2008),28-29 Jan; Harbin, Pp.181-186.
[2]     Haosong Gou And Younghwanyoo, "An Energy Balancing LEACH Algorithm For Wireless Sensor Networks", Seventh International Conference On Information Technology (IEEE) (2010),12-14 April; Lasvegas, NV, Pp.822-827.
[3]     Heikkikarvonen, Zach Shelby, Carlos Pomalaza-Rae.Z, "Coding For Energy Efficient Wireless Embedded Networks", International Workshop On Wireless Ad-Hoc Networks (IEEE) (2004), 31 May-3 June, Pp.300-304.
[4]     Hongjoong Sin, Jangsoo Lee, Sungju Lee, Seunghwanyoo, Sanghyuck Lee, Jaesik Lee, Yongjunlee, And Sungchun Kim, "Agent-Based Framework For Energy Efficiency In Wireless Sensor Networks", World Academy Of Science, Engineering And Technology 22, 2008, Pp.305-309.
[5]     Huu Nghia Le, Vyacheslav Zalyubovskiy, Hyunseung Choo "Delay-Minimized Energy-Efficient Data Aggregation In Wireless Sensor Networks", International Conference On Cyber-Enabled Distributed Computing And Knowledge Discover (IEEE) (2012),10-12 Oct; Sanya, Pp.401-407.
[6]     Linlin Wang, Jieliu , Wei Wang "An Improvement And Simulation Of LEACH Protocol For Wireless Sensor Network", First International Conference On Pervasive Computing, Signal Processing And Applications (IEEE) (2010), 17-19 Sept; Harbin, Pp.444-447.

[7] Ma Chaw Mon Thein, Thandarthein "An Energy Efficient Cluster-Head Selection For Wireless Sensor Networks", International Conference On Intelligent Systems, Modelling And Simulation (IEEE) (2010), 27-29 Jan ; Liverpool, Pp.287-291.

[8] Meenakshi Sharma And Anil Kumar Shaw "Transmission Time And Throughput Analysis Of EEE LEACH, LEACH And Direct Transmission Protocol: A Simulation Based Approach", Advanced Computing: An International Journal ( ACIJ ),Vol.3, No.5, September 2012.

[9] M M Islam1, M A Matin2, T K Mondol1 "Extended Stable Election Protocol (SEP) For Threelevel Hierarchical Clustered Heterogeneous WSN", (IEEE) (2012),18-19 June; London, Pp.1-4.

[10] Reetika Munjal, Bhavneesh Malik "Approach For Improvement In LEACH Protocol For Wireless Sensor Network", Second International Conference On Advanced Computing & Communication Technologies (IEEE) (2012),7-8 Jan; Rohtak, Haryana, Pp.517-521.

[11] Rupesh Mehta, Abhishek Pandey& Pratik Kapadia "Reforming Clusters Using C-LEACH In Wireless Sensor Networks", International Conference On Computer Communication And Informatics (IEEE) (ICCCI -2012),10-12 Jan;Coimbatore, Pp.1-4.

[12] Shuo Shi, Xinning Liu And Xuemaigu "An Energy-Efficiency Optimized LEACH-C Forwireless Sensor Networks", 7th International ICST Conference On Communications And Networking In China (CHINACOM) (IEEE) (2012),8-10 Aug; Kun Ming, Pp.487-492.

[13] Smaragdakis, Georgios, Ibrahim Matta, And Azer Bestavros. "SEP: A Stable Election Protocol For Clustered Heterogeneous Wireless Sensor Networks", Boston University Computer Science Department, 2004.

[14] Thu Ngo Quynh1, Kieu-Ha Phung2,3, Hoan Vu Quoc1 "Improvement Of Energy Consumption And Load Balance For LEACH In Wireless Sensors Networks", (IEEE) (2012),15-17 Oct; Jeju, Island, Pp.583-588.

[15] Vivek Katiyar, Narottam Chand, Gopal Chand Gautam,Anil Kumar "Improvement In LEACH Protocol For Large-Scale Wireless Sensor Networks", (IEEE) (2011),23-24 March; Tamil Nadu, Pp.1070-1075

[16] Yuhua Liu Yongfeng Zhao Jingju Gao "A New Clustering Mechanism Based On LEACH Protocol", International Joint Conference On Artificial Intelligence (IEEE) (2009), 25-26 April; Hainan, Island, Pp.715-718.

[17] Zach Shelby, Carlos Pomalaza-Ra, Heikki Karvonen, And Jussi Haapola,"Energy Optimization In Multihop Wireless Embedded And Sensor Networks", Springer Science+Business Media International Journal Of Wireless Information Networks, Vol. 12, No. 1, January 2005.

# Groundwater Arsenic Contamination and its Implications: A Case Study of Shahpur Block of Bhojpur District, Bihar

Amardip Singh[1], A. K. Ghosh[2]

*[1]Xavier Institute of Social Service, Ranchi, Jharkhand, India*
*[2]A. N. College, Patna, Magadh University, Bodh Gaya, Bihar, India*

**Abstract:** *Bhojpur district is one of the 36th districts in Bihar composed of 14 blocks. Out of 14 blocks, 06 blocks namely Ara, Barhara, Bihia, Koilwar, Shahpur and Udwant Nagar, situated along the bank of Ganga river are severely affected by ground water arsenic contamination. In the present study, Shahpur block has taken into consideration for assessment of groundwater arsenic contamination, impact of arsenic on grain quality and human health, average daily consumption of arsenic by inhabitants of affected villages and total agricultural area affected due to irrigation through arsenic contaminated groundwater. Shahpur block is composed of 86 revenue villages. Out of 86 revenue villages, 30 villages were selected for assessment of arsenic contamination in groundwater. Study findings reveals that out of total 30 selected revenue villages, 27 villages are severely affected by groundwater arsenic contamination. Maximum concentration of arsenic findings was obtained in hand pump of village Karnamepur where the level of arsenic was 598 ppb. Out of 30 revenue villages, only three villages namely Harkhi Pipra, Suhiya and Domariya were arsenic free. Study findings shows that 2137.11 hectares irrigated agricultural land (43.76 % of blocks irrigated land) of 27 revenue villages in Shahpur block is irrigated by arsenic contaminated groundwater. These agricultural land and crops cultivated in the affected area are vulnerable to assimilation of groundwater arsenic through irrigation. The elevated level of arsenic in food grains may result since crops receiving arsenic contaminated groundwater as a source of irrigation can uptake arsenic during the phyto-extraction process and bio-accumulate in different degrees in different parts of plants. The present study findings also reveals that the average per capita consumption of arsenic by children, young person, adults and old persons are 0.227 mg/L, 0.489 mg/L, 0.559 mg/L and 0.568 mg/L respectively. The identified per capita arsenic consumption in arsenic affected villages has exceeded the maximum allowable limit of arsenic consumption through water and food.*
*Key words: agricultural field, groundwater arsenic, irrigation, arsenic in food grains*

## I. Introduction

Arsenic (As) is a metalloid element (atomic number 33) with one naturally occurring isotope of atomic mass 75, and four oxidation states (-3, 0, +3, and +5) [1]. In the aqueous environment, the +3 and +5 oxidation states are most prevalent, as the oxyanions arsenite ($H_3AsO_3$ or $H_2AsO_3^-$ at pH ~9-11) and arsenate ($H_2AsO_4^-$ and $HAsO_4^{2-}$ at pH ~4-10) [1]. In soils, arsine gases (containing $As_3^-$) may be generated by fungi and other organisms [2].

There are about 24 As-bearing minerals that are commonly found in hydrothermal veins, ore deposits, and rocks. Most primary As minerals are sulfides, of which arsenopyrite is the most common [3]. Secondary minerals tend to be less common arsenates and oxides. Arsenic in crustal rocks also has an affinity for, and is associated with, pyrite or Fe hydroxides and oxides [4] for which chemical formulas are $FeS_2$, $FeOOH$, $Fe_2O_3$, and $Fe_3O_4$, respectively.

High As concentrations have been found in both surface waters and shallow groundwater from the area around the mining activity as a result of natural oxidation of arsenopyrite, mining activity and release following post-mining groundwater rebound [5]. It is reported that concentrations of As in the surface waters reaching up to 580 µg/L. [6].

There is no proof regarding the natural emission of As in the Ganga–Brahmaputra plains so far. However, the release of As, by the natural processes in groundwater, has been recognized, from the Holocene sediments comprising sand, silt and clay [7,8] in parts of the Bengal Delta Plains (BDP), West Bengal and in the Gangetic plains of Bihar. Several isolated geological sources of As have been recognized, viz. Gondwana coal seams in Rajmahal basin (200 mg/kg of As), Bihar mica-belt (0.08–0.12% of As), pyrite-bearing shale from the

Proterozoic Vindhyan range (0.26% of As), Son valley gold belt (2.8% of As) and Darjeeling Himalayas belt (0.8% of As) [9,10,11,12]. The contaminated aquifers are of Quaternary age and comprise micaceous sand, silt and clay derived from the Himalayas and basement complexes of eastern India. These are sharply bound by the River Bhagirathi-Hooghly (distributaries of the River Ganges) [13] in the west, the rivers, Ganges and Padma in the north, the flood plain of the River Meghna (tributary of the River Padma), and the River Yamuna in the northeast [14].

The actual source of groundwater arsenic contamination, in the Ganga–Brahmaputra basin, is yet to be established. The sources of arsenic are natural or may partly stem from anthropogenic activities like intense exploitation of groundwater, application of fertilizers, burning of coal and leaching of metals from coal-ash tailings. The hypotheses about the sources of arsenic in the BDP are as follows:

  (i)  Arsenic, transported by the River Ganges and its tributaries from the Gondwana coal seams in the Rajmahal trap area located at the west of the basin can be of the order of 200 ppm. [15].

  (ii) Arsenic is transported by the north Bengal tributaries of Bhagirathi and Padma from near the Gorubathan base-metal deposits in the eastern Himalayas [16].

  (iii) Arsenic is transported with the fluvial sediments from the Himalayas [8]. This is the most accepted hypothesis at present.

Several studies suggested that the groundwater arsenic contamination is mostly restricted to the alluvial aquifers of the Ganges delta comprising sediments carried from the sulphide-rich mineralized areas of Bihar and elsewhere surrounding the basin of deposition [17].

The first case of arsenic in India was reported in 1976 from Chandigarh [18]. Since then widespread arsenic contamination has been reported in groundwater from many parts of India  including West Bengal, Bihar, Chhattisgarh, Jharkhand, Uttar Pradesh and Assam and other regions of Punjab, Haryana, and Himachal Pradesh, surroundings of New Delhi, the union territory of Chandigarh, and the state of Rajasthan [19]. Among them, the most severely contaminated state is West Bengal where 12 districts and 26,00,000 people are affected [18,19,20].

In West Bengal, India, cases of arsenic poisoning were first noted in 1983-84 [21], although in the year of 1978 arsenicosis (skin lesions) and groundwater contamination were first noticed in West Bengal [22]. Since the 1980s, extensive sampling of well water in West Bengal has revealed levels of As that exceed 50 μg/L concentrations in some samples exceeding 1000 μg/L [21]. In 1983-84, several patients treated for arsenicosis in West Bengal came from neighbouring Bangladesh. Sampling in Bangladesh during the early 1990s from tube wells (installed two decades earlier to provide what was thought to be safe, pathogen-free drinking water) revealed elevated concentrations of As [23].

In the recent study on assessment of arsenic contamination in groundwater of Bihar a number of districts of Bihar namely Begusarai, Bhagalpur, Bhojpur, Buxar, Darbhanga, Katihar, Khagaria, Kishanganj, Lakhiserai, Munger, Patna, Purnea, Samastipur, Saran, Vaishali are arsenic effected districts [24].

In Bhojpur district, out of total 14 blocks, 06 blocks namely Ara, Barhara, Behea, Koilwar, Shahpur and Udwant Nagar, situated along the Ganga river bank are affected by groundwater arsenic contamination. In the present study, out of 86 revenue villages of Shahpur block, 30 revenue villages were selected for assessment of arsenic contamination in groundwater. Out of 30 selected revenue village of block, only three villages namely Harkhi Pipra, Suhiya and Domariya are free from groundwater arsenic contamination. Further, 27 revenue village of block having 73,775 people and 11,792 (15.98%) children (0-6 years) are vulnerable by consuming arsenic contaminated groundwater (50 and over 50 ppb). The concentration of groundwater arsenic consuming by the villagers is much higher than the World Health Organisation (WHO) limit (10 ppb).

## II.  Study Area

Shahpur is one of the 14th blocks of Bhojpur district situated on the bank of river Gnaga and located at $25^0 35.972$'N latitude and $84^0 24.108$'E longitude. The block is approximately 27.5 km (aerial distance) away from the Ara town (distract headquarter) of Bhojpur. The block is composed of 23 panchayats, 86 villages and 99 habitations. The study area in the block is spread over a 10 km. belt running roughly parallel to the river Ganga. Most of the selected villages and their tolas in the study area are known as flood affected area. The main sources of livelihood of the area are agriculture and livestock.
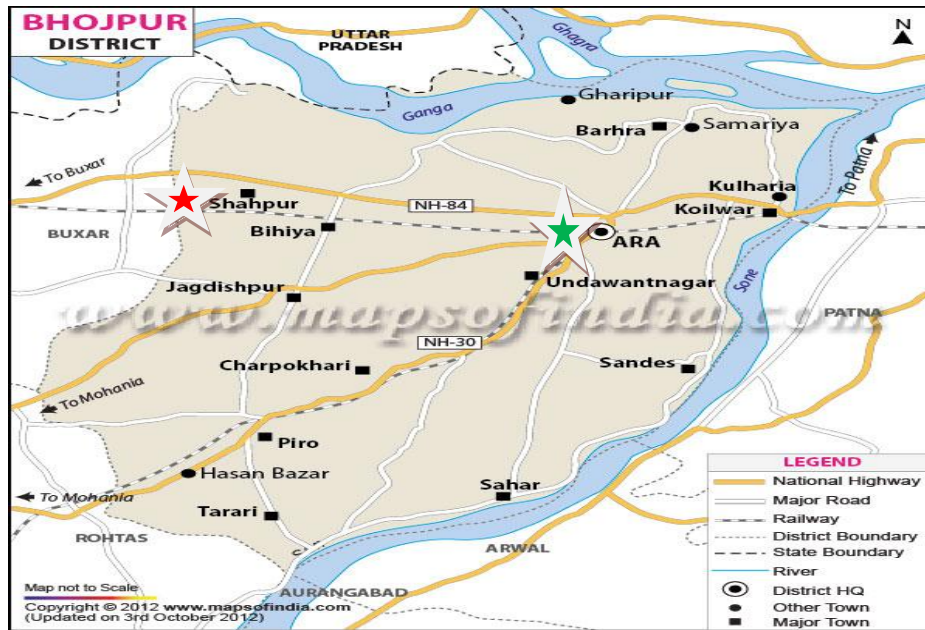
**Fig.1.1: Map of Bhojpur district showing location of Ara and Shahpur block**

In the present study, 27 revenue villages of the block were selected to assess the extent of groundwater arsenic contamination, area of agricultural field irrigated by arsenic contaminated groundwater, quality of food grains and vegetables cultivated in the area and also to identify the daily consumption of arsenic by the villagers from various sources. The assumptions about food grains and vegetables containing arsenic which are grown in the arsenic affected area is based on the previous study undertaken by the researchers.

## III. Materials And Methods

In the present study, testing of groundwater samples of the study area has done by reliable laboratory-based testing methods i.e., UV/VIS Spectrophotometry and Atomic Absorption Spectrophotometry (AAS) methods. However, Field Test Kits [FTKs] are essential for quick preliminary survey, and met the immediate priority of identifying the most contaminated groundwater sources. All the hand pumps of the villages under study were tested for Arsenic content by FTKs. 10% of random verification of FTK results was done by UV (Ultra Violet) Spectrophotometer. Thereafter, all the results above 40 μg/L were retested using Atomic Absorption Spectrophotometer (AAS).

## IV. Results And Discussions

**Arsenic Contaminated Hand Pumps in Bhojpur District**

In Bhojpur district total 5,917 water samples of public hand pumps were assessed by FTK (Field Test Kit) to know the approximate level of arsenic content in the groundwater. Out of total 5,917 water samples of public hand pumps, 2,806 (47.42%) samples were contaminated with arsenic. Taking into account the permissible limit of 10 μg/L set by WHO 1993 [25], Table 1.1 shows the percentage of arsenic contaminated groundwater in selected bocks of Bhojpur districts. However, the selected blocks in the district show considerable number of safe or below detectable limit (BDL) marked hand pumps. Comparing to all selected blocks of the district, maximum number of contaminated hand pumps were identified in Barhara block (Table 1.1).

**Table 1.1: Percentage arsenic affected blocks of Bhojpur district (FTK Readings)**

| Sl. No. | Name of Block | Arsenic Concentration 11 ppb and above |
|---------|---------------|----------------------------------------|
| 1 | Barhara | 55.35 % |
| 2 | Shahpur | 37.97 % |
| 3 | Bihia | 33.37 % |
| 4 | Udwant Nagar | 55.69 % |
| 5 | Ara | 15.23 % |
| 6 | Koilwar | 26.12 % |
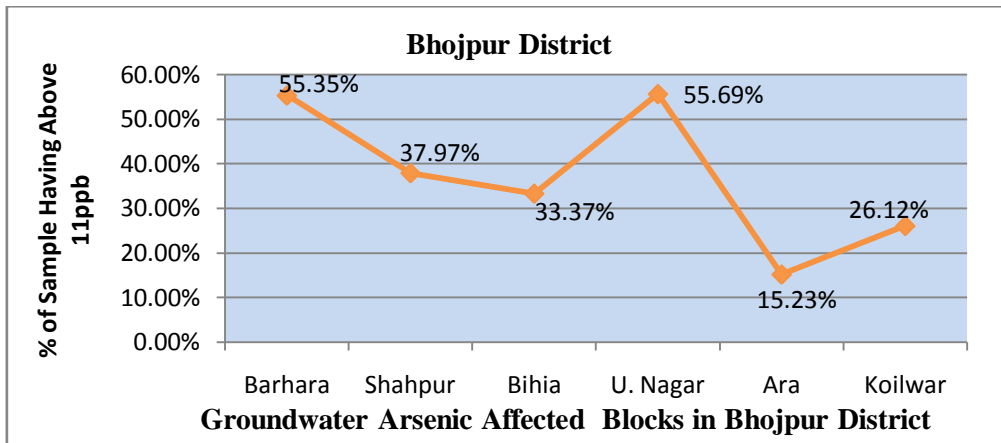
**Fig.1.2: Status of percentage arsenic contaminated blocks of Bhojpur district**

A base map of arsenic hot spots (block-wise) in the district was prepared on the basis of FTK data of 5,917 groundwater samples. In the base map, red coloured dots (>101 μg/L arsenic) showing alarming level of arsenic contamination in affected revenue villages and their tolas of the blocks. The Global Positioning System (GPS) data were used during preparation of the base map of arsenic affected areas (Fig. 1.3).
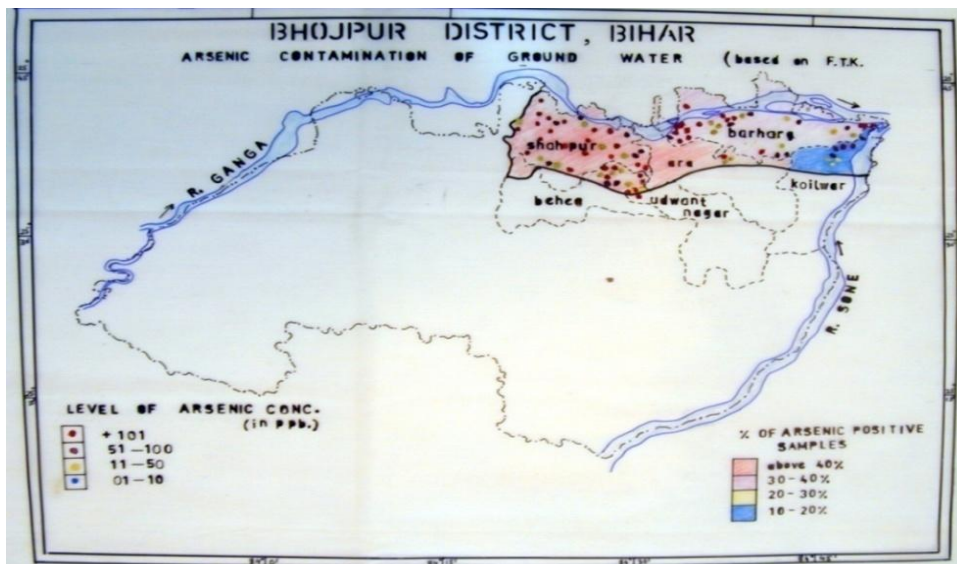


**Fig. 1.3: Arsenic contaminated blocks of Bhojpur district, based on FTK data & GPS fixes**

**Arsenic Affected Villages in Shahpur Block**

In Shahpur block of Bhojpur district total revenue villages are 86. Out of 86 revenue villages, 30 revenue villages were selected for assessment of arsenic contamination in groundwater. All selected villages of the block are located along the southern boundary of Ganga river distanced up to 10 km from the bank.

The study findings reveals that out of 30 selected revenue villages, only three villages namely Harkhi Pipra, Suhiya and Domariya are free from groundwater arsenic contamination. Remaining 27 revenue villages towards the southern part from the bank of the Ganga river were identified as arsenic contaminated villages. The details of groundwater arsenic contaminated revenue villages with population are shown in Table 1.2.

**Table 1.2: Groundwater arsenic contaminated villages of Shahpur block**

| S. No. | Block | Arsenic Affected Revenue Villages (50 and over 50 ppb by FTK) | Total Population | Population (0-6 Years) |
|---|---|---|---|---|
| 1 | Shahpur | Parsonda | 1,967 | 292 |
| 2 | Shahpur | Ramdatahi | 3,131 | 473 |
| 3 | Shahpur | Sonbarsa | 3,070 | 526 |
| 4 | Shahpur | Sarna | 5,568 | 844 |
| 5 | Shahpur | Isharpura | 4,254 | 628 |
| 6 | Shahpur | Milki Gopalpur | 1,254 | 194 |

| 7 | Shahpur | Karnamenpur | 4,402 | 710 |
|---|---------|-------------|-------|-----|
| 8 | Shahpur | Chakki Nauranga Ojhwalia Diara | 836 | 112 |
| 9 | Shahpur | Ram Karhi (Ditto) | 629 | 141 |
| 10 | Shahpur | Mirchaiya Ka Dera (Ditto) | 1,328 | 174 |
| 11 | Shahpur | Misrauliya | 759 | 104 |
| 12 | Shahpur | Gashainpur | 834 | 141 |
| 13 | Shahpur | Bishunpur | 317 | 71 |
| 14 | Shahpur | Dudh Ghat | 1,285 | 261 |
| 15 | Shahpur | Nargada | 1,226 | 136 |
| 16 | Shahpur | Barsaun | 8,586 | 1,338 |
| 17 | Shahpur | Semariya Palti Ojha | 5,788 | 976 |
| 18 | Shahpur | Bahoranpur Dakhinwar | 2,326 | 411 |
| 19 | Shahpur | Karja | 3,453 | 519 |
| 20 | Shahpur | Paharpur | 1,822 | 345 |
| 21 | Shahpur | Jhaua | 11,459 | 1,995 |
| 22 | Shahpur | Dhauri | 1,724 | 246 |
| 23 | Shahpur | Pakri | 1,645 | 236 |
| 24 | Shahpur | Dumariya | 3,265 | 460 |
| 25 | Shahpur | Abatana | 346 | 51 |
| 26 | Shahpur | Dewaich Kundi | 1,281 | 223 |
| 27 | Shahpur | Bansipur | 1,220 | 185 |
| **Total** | | | **73,775** | **11,792** |

**Source:** Census 2011

In Shahpur block, total 1,018 groundwater samples of public hand pumps were tested through (FTK). Out of total 1,018 groundwater samples of public hand pumps, 102 samples shown arsenic concentration in between 01 to 10 ppb, 386 samples shown arsenic concentration in between 11 to 50 ppb and remaining 530 samples shown arsenic concentration in between 51 to 110 ppb respectively (Table 1.3).

**Table 1.3: Number of F.T.K tested drinking water samples in Shahpur block**

| Sl. No. | Arsenic contamination (in ppb) | No. of samples |
|---------|-------------------------------|----------------|
| 1 | 01 to 10 ppb. | 102 |
| 2 | 11 to 50 ppb. | 386 |
| 3 | 51 to 110 ppb. | 530 |
| **Total** | | **1,018** |

A base map of arsenic affected areas (village-wise) in the block was prepared on the basis of FTK data of 1,018 groundwater samples. In the base map, red coloured dots (over 50 μg/L arsenic) showing alarming level of arsenic contamination in affected villages of the block. The GPS data were used during preparation of base map of As affected villages (Fig. 1.4).
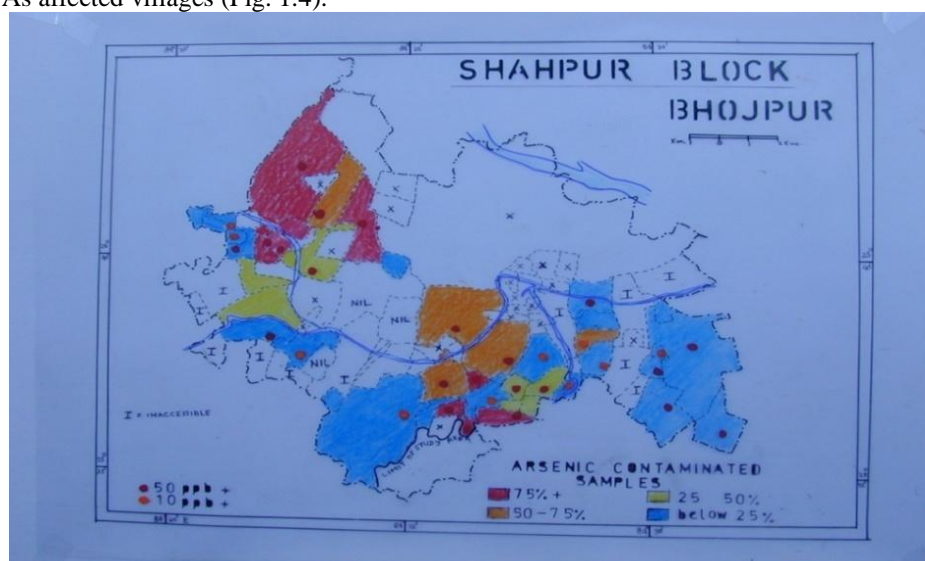


**Fig. 1.4: Arsenic contaminated village of Shahpur block, based on FTK data & GPS**

Further, out of total 1,018 groundwater samples of public hand pumps, 308 samples were tested through AAS-HG by Sriram Institute of Industrial Research (SIIR), New Delhi. The selected 308 groundwater samples has already shown the high arsenic content during FTK testing in the field environment were sent to the SIIR for final confirmation and data base. Maximum concentration of arsenic findings was obtained in hand pump of village Karnamepur where the level of arsenic was 598 ppb. The details of the arsenic content (range-wise) in 308 groundwater samples of selected 27 revenue villages of Shahpur block are shown in Table 1.4.

**Table 1.4: Number of ASS-HG tested drinking water samples in Shahpur block**

| Sl. No | Arsenic content (µg/L) | No. of samples containing arsenic in a specific range |
|--------|------------------------|-------------------------------------------------------|
| 1 | BDL | 50 |
| 2 | 1-9 | 23 |
| 3 | 10-49 | 69 |
| 4 | 50-99 | 70 |
| 5 | 100-199 | 61 |
| 6 | 200-299 | 20 |
| 7 | 300-399 | 07 |
| 8 | 400-499 | 05 |
| 9 | 500-599 | 03 |
| **Total** | | **308** |

Out of 1,018 hand pumps surveyed in the block, 166 hand pumps in various villages of block shows more than 50 ppb concentration of groundwater arsenic. The villages which show more than 50 ppb concentration of arsenic were Karnamenpur, Isharpura, Ram Karhi, Sonbarsa, Mirchaiya Ka Dera, Milki Gopalpur, Chakki Nauranga Ojhwalia Diara, Bansipur, Sarna, Parsonda and Ramdatahi.

Based on 308 tested and identified groundwater samples of public hand pumps by AAS-Hg in Shahpur block, Table 1.4 shows the specific number of samples having specific range of arsenic concentration. Out of total 308 groundwater sample of the study area, 50 samples shown the arsenic content Below Detectable Limit (BDL) and 01 sample shown the highest arsenic level of 598 ppb (Karnamepur village).
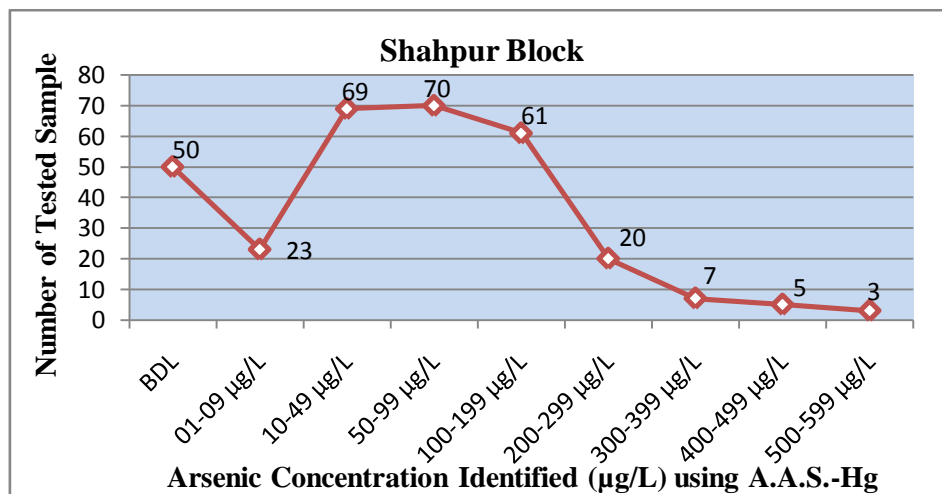


**Fig. 1.5: Status of ASS-HG tested drinking water samples in Shahpur block**

**Arsenic Content in Food Grains**

Arsenic concentration in uncontaminated soils in some Bangladesh districts ranged between 0.10 and 2.75 mg/kg. In contrast, in areas where irrigation is carried out with contaminated groundwater, the soil As level is reported to be up to 81 mg/kg [26, 27]. The elevated level of As in soil has resulted in elevated concentrations of As in food since crops receiving arsenic contaminated irrigated water can uptake As during the phyto-extraction process and bio-accumulated in different degrees in different parts of plants (e.g. roots, stems, and grains). Several research studies have found high concentrations of arsenic in vegetables and rice in areas where concentrations of arsenic in soil and water are also high.

Higher concentrations of arsenic were also reported in rice plants (*boro* rice) in the following orders: rice roots > rice stem > rice leaf > rice grain > rice husk [26]. It is therefore evident that, the food chain could be a significant pathway of As ingestion by the people of Bangladesh [28]. The arsenic-contaminated irrigation

water (0.318– 0.643 mg/L) and soil (5.70–9.71 mg/ kg) considerably influenced in the accumulation of arsenic in rice, pulses, and vegetables in West Bengal, India [29].

In previous study, for identification of arsenic content in food grains, seeds of wheat, maize, rice, lentils and rice husk were selected. The samples of seeds and rice husk were taken from village Rampur Diarra of Maner block in Patna district. The village is well known arsenic hot spot of the block. For assessing arsenic content in food grains, the hybrid variety of wheat, maize and rice were Ub-2338, K-H-101 and Sonam. For lentil, locally available lentil seeds were selected. Besides, the food grains, rice husk of Sonam variety was selected for estimation of arsenic contents for comparing its concentration with rice grain [30].

Laboratory findings showed that selected food grains and rice husk have substantial concentration of arsenic contents. The highest value of arsenic contents was shown in wheat grain and minimum in maize seeds. Rice husk has shown comparatively more arsenic content than the rice grain. In comparison with the Australian Food Standard (AFS) i.e., 0.1 mg/kg, the arsenic value in different food grains were within the limit but cumulative effect of arsenic along with arsenic contaminated drinking water significantly affects human health. Details of the exact arsenic concentration in each selected food samples are shown in Table 1.5.

**Table 1.5: Arsenic in food samples (Maner block, Patna)**

| S. No. | Sample Id | Village | Food Item | Variety | As(mg/kg) |
|---|---|---|---|---|---|
| 1 | 10/28/0001/900/PMRDF001 | Rampur Diara | Wheat | Ub-2338 | 0.024 |
| 2 | 10/28/0001/900/PMRDF002 | Rampur Diara | Maize | K-H-101 | 0.011 |
| 3 | 10/28/0001/900/PMRDF004 | Rampur Diara | Rice | Sonam | 0.019 |
| 4 | 10/28/0001/900/PMRDF004 | Rampur Diara | Rice husk | Sonam | 0.022 |
| 5 | 10/28/0001/900/PMRDF005 | Rampur Diara | Lentil | N.A | 0.015 |

**Source:** Singh, K.S. & Ghosh, K.A. 2011
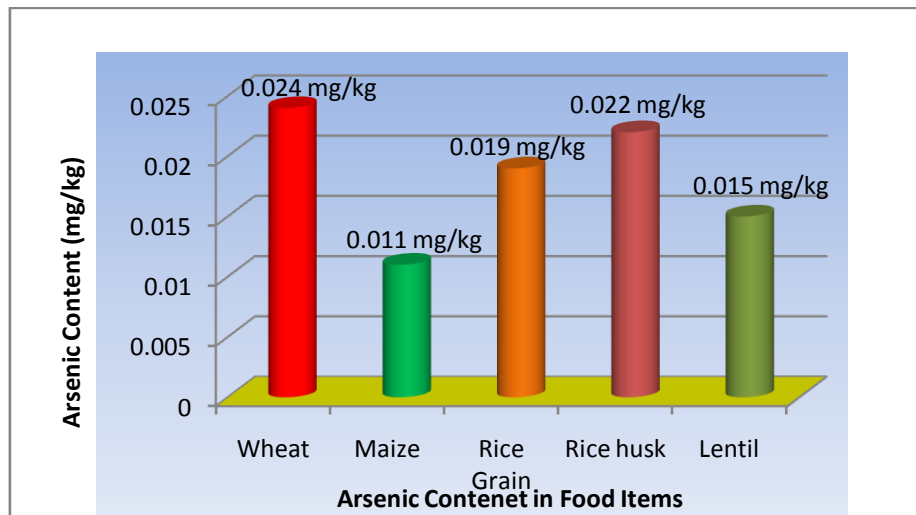


**Fig. 1.6: Arsenic in food samples, Maner, Patna (Singh, K.S. & Ghosh, K.A. 2011)**

Findings of the above mentioned study carried out in Maner block of Patna district further correlates strongly with chances of findings of substantial amount of arsenic in food grains cultivated in arsenic affected villages of Brahara block.

**Daily Consumption of Arsenic**

To assess per capita average daily consumption of arsenic from various sources such as drinkable water, cooked foods (rice, pulses, chapatti and vegetables), a survey study was conducted in selected revenue villages (27 village) of Shahpur block (20% sample survey). The average per capita consumption of arsenic from various sources by children, young person, adults and old persons are 0.227mg/L, 0.489 mg/L, 0.559 mg/L and 0.568 mg/L respectively (Table 1.6).

The above findings reveals that per capita arsenic consumption in arsenic affected villages of Shahpur block has exceeded the maximum allowable limit of arsenic consumption through water and food (0.2 mg/kg/day). Hence, the cumulative effect of high arsenic consumption for long duration would be fatal for the habitants of arsenic affected villages.

**Table 1.6: Consumption of arsenic from various sources**

| Village | Type of Person | Consumption of Water | | | | | Consumption of Water/Day (Lit.) | Avg. As in Water (mg/L) | Intake of As/Day (mg/L) |
|---------|----------------|---------------------------------|------|------|------|------|---|---|---|
| | | Drinking Water (Lit.) | Rice (Lit.) | Pulse( Lit.) | Chapati (Lit.) | Veg. (Lit.) | | | |
| 26 selected revenue villages | Children | 2.25 | 0.180 | 0.095 | 0.035 | 0.025 | 2.585 | 0.088 | 0.227 |
| | Young | 4.85 | 0.355 | 0.150 | 0.090 | 0.115 | 5.56 | 0.088 | 0.489 |
| | Adult | 5.70 | 0.300 | 0.155 | 0.090 | 0.110 | 6.355 | 0.088 | 0.559 |
| | Old | 5.90 | 0.280 | 0.130 | 0.055 | 0.100 | 6.465 | 0.088 | 0.568 |

**Source**: Field Survey
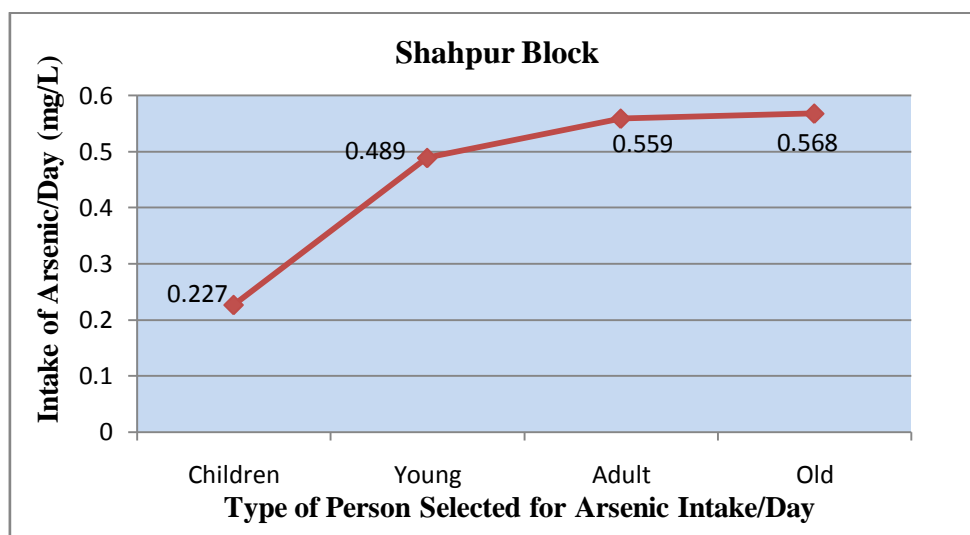


**Fig. 1.7: Daily consumption of arsenic from various sources in Shahpur block**

**Vulnerability of Agricultural Land and Crops Due to Groundwater Arsenic**

In Shahpur block, agriculture is the main economic activity of the people, and major crops are wheat, maize, rice, marua, arhar, mung, massor, urad, khesari, mustered, ground nut, lentil, turmeric, zinger, potato, sweet patato, bringal, ladiys finger, beans, tomato, cauliflower, cabbage, onion etc.

The total agricultural land of Shahpur block is 10,722.57 hectare. Total agriculture land of arsenic contaminated villages (27 villages) in block is 5,648.39 hectares which constitute 52.67 % of block's agricultural land, out of this, irrigated and un-irrigated land is 2,137.11 and 3,511.28 hectares which constitute 19.93 % and 32.74 % of total agricultural land respectively (Table 1.7).

**Table 1.7: Land use pattern in arsenic contaminated villages (in hectares)**

| Village | Forest Land | Agricultural Land | | | Cultivable Waste Land | Area Not Available for Cultivation | Total |
|---------|-------------|-------------------|-------------|-------|---|---|---|
| | | Irrigated | Un-irrigated | Total | | | |
| Parsonda | 0.00 | 246.00 | 5.00 | 251 | 1.33 | 1.00 | 253.33 |
| Ramdatahi | 0.00 | 10.10 | 2.83 | 12.93 | 0.00 | 5.28 | 18.21 |
| Sonbarsa | 0.00 | 220.24 | 20.26 | 240.5 | 22.06 | 45.00 | 307.56 |
| Sarna | 0.00 | 278.00 | 208.00 | 486 | 9.00 | 18.54 | 513.54 |
| Isharpura | 0.00 | 0.00 | 1,061.48 | 1,061.48 | 0.00 | 0.00 | 1,061.48 |
| Milki Gopalpur | 0.00 | 8.09 | 3.14 | 11.23 | 5.26 | 1.72 | 18.21 |
| Karnamenpur | 0.00 | 20.00 | 40.05 | 60.05 | 2.02 | 3.08 | 65.15 |
| Chakki Nauranga Ojhwalia Diara | 0.00 | 0.00 | 0.00 | 0 | 0.00 | 0.00 | 0 |
| Ram Karhi  (Ditto) | 0.00 | 0.00 | 0.00 | 0 | 0.00 | 0.00 | 0 |
| Mirchaiya Ka Dera | 0.00 | 0.00 | 0.00 | 0 | 0.00 | 0.00 | 0 |
| Misrauliya | 0.00 | 28.32 | 5.67 | 33.99 | 10.12 | 4.05 | 48.16 |

| | | | | | | |
|---|---|---|---|---|---|---|
| Gashainpur | 0.00 | 25.60 | 44.45 | 70.05 | 9.25 | 3.25 | 82.55 |
| Bishunpur | 0.00 | 13.96 | 0.00 | 13.96 | 24.89 | 7.28 | 46.13 |
| Dudh Ghat | 0.00 | 15.56 | 39.94 | 55.5 | 2.35 | 2.45 | 60.3 |
| Nargada | 0.00 | 21.65 | 43.95 | 65.6 | 15.35 | 18.20 | 99.15 |
| Barsaun | 0.00 | 49.05 | 304.38 | 353.43 | 12.00 | 0.00 | 365.43 |
| Semariya Palti Ojha | 0.00 | 0.00 | 164.98 | 164.98 | 8.23 | 81.74 | 254.95 |
| Bahoranpur Dakhinwar | 0.00 | 100.30 | 504.00 | 604.3 | 0.00 | 10.00 | 614.3 |
| Karja | 0.00 | 236.74 | 0.00 | 236.74 | 0.00 | 0.00 | 236.74 |
| Paharpur | 0.00 | 195.00 | 5.00 | 200 | 0.00 | 6.79 | 206.79 |
| Jhaua | 0.00 | 267.45 | 578.65 | 846.1 | 25.25 | 10.45 | 881.8 |
| Dhauri | 0.00 | 20.45 | 39.56 | 60.01 | 0.75 | 0.35 | 61.11 |
| Pakri | 0.00 | 115.45 | 156.23 | 271.68 | 11.30 | 5.15 | 288.13 |
| Dumariya | 0.00 | 165.35 | 177.25 | 342.6 | 12.15 | 4.20 | 358.95 |
| Abatana | 0.00 | 44.35 | 38.00 | 82.35 | 16.00 | 10.10 | 108.45 |
| Dewaich Kundi | 0.00 | 15.35 | 30.14 | 45.49 | 15.45 | 16.35 | 77.29 |
| Bansipur | 0.00 | 40.10 | 38.32 | 78.42 | 3.28 | 2.88 | 84.58 |
| **Total** | **0.00** | **2,137.11** | **3,511.28** | **5,648.39** | **206.04** | **257.86** | **6,112.29** |
| **Block Total** | **15.30** | **4,883.23** | **5,839.34** | **10,722.5** | **1,083.43** | **881.63** | **23,425.5** |

**Source:** Census of India-2001, Village Directory

Based on the Census of India, 2001, 2137.11 hectares (43.76 % of blocks irrigated land) of agricultural land in Shahpur block is irrigated by arsenic contaminated groundwater. These agricultural land and the cultivable crops are vulnerable due to assimilation of arsenic through plant roots by irrigation of arsenic contaminated groundwater. Previous laboratory findings supports that the samples of food grains collected from Rampur Diara village of Maner block in Patna district have substantial amount of arsenic. This study strongly supports the hypothesis that if the crops area irrigated by the arsenic contaminated groundwater, a substantial amount of arsenic will be assimilated by the crop plants and will be available in food gains also.

## V.  Impact of Arsenic on Human Health

Arsenic is a global health concern due to its toxicity and the fact that it occurs at unhealthful levels in water supplies, particularly groundwater, in more than 70 countries [31] of six continents. Chronic exposure to As can cause harm to the human cardiovascular, dermal, gastrointestinal, hepatic, neurological, pulmonary, renal and respiratory systems [32] and reproductive system [33]. The different forms of As have different toxicities, with arsine gas being the most toxic form. Of the inorganic oxyanions, arsenite is considered more toxic than arsenate, and the organic (methylated) arsenic forms are considered least toxic [33].

Inorganic arsenic is one of the few substances that have been shown to cause cancer in humans through consumption of drinking-water. Cancer usually takes more than 10 years to develop. Arsenic can cause cancers of the skin, bladder and lungs, and there is limited evidence that it may also cause cancers of the kidney, liver and prostate [34]. The International Agency for Research on Cancer (IARC) has classified arsenic and arsenic compounds as carcinogenic to humans (Group 1), which means that there is sufficient evidence for their carcinogenicity in humans [35]. The organic arsenic compounds monomethylarsonic acid and dimethylarsinic acid are the active ingredients of some herbicides and are metabolites of inorganic arsenic. On the basis of sufficient evidences of cancer in experimental animals and because monomethylarsonic acid is extensively metabolized to dimethylarsinic acid, both compounds are classified as possibly carcinogenic to humans (Group 2B). Arsenobetaine and other organic compounds that are not metabolized in humans are not classifiable as to their carcinogenicity (Group 3) [34]. Furthermore, IARC has stated that arsenic in drinking-water is carcinogenic to humans (Group 1) [36].

Arsenic exposure from contaminated drinking water of more than 50μg/l is a significant cancer risk. The exposure of human to arsenic contaminated water and foods can lead to some physical changes on the skin such as the appearance of small black or white marks (melanosis), then thickening of the skin on the palms and the feet (keratosis), followed by skin lesions and eventually skin cancer. The development of internal cancer in humans may take 10 years to develop and is often the result of long term exposure to arsenic. The long term ingestion or exposure (10-15 years) of arsenic can lead to a disease called 'Arseniasis, arsenicosis, and arsenicism' [28]. Chronic exposure to arsenic has been linked to carcinogenic effects in both humans and animals. These include cancer of the various skin and various internal organs (lung, bladder, liver and kidney) reproductive and developmental effects; cardiovascular disease; reduced intellectual function in children and

mortality. Non-cancer endpoints include hyper-pigmentation, hypo-pigmentation, keratosis of skin, peripheral vascular disease (black foot disease), cardiovascular disease, hypertension and neurotoxicity. There are some claims that chronic exposure of arsenic may also cause diabetes development and prostate cancer [37, 38, 39].

Considering the above facts and figures, the population of selected 27 revenue villages of Shahpur block is critically vulnerable to high arsenic exposure. Out of total population, 15.98 % children (below 06 years age), 13.01 % SC, 1.57 % ST and 85.40 % other category population is vulnerable to arsenic exposure (Table 1.8).

**Table 1.8: Population vulnerable to arsenic exposure in selected villages of Shahpur block**

| S. N. | Particulars | Male | Female | Total |
|---|---|---|---|---|
| 1 | **Population Distribution and Sex Ratio** | | | |
| 2 | Population | 38,247 (100) | 34,879 (100) | 73,775 (100) |
| 3 | Children below 6 yrs | 6,142 (16.05) | 5,650 (16.19) | 11,792 (15.98) |
| 5 | **Caste Distribution** | | | |
| 6 | Schedule Caste | 5,038 (13.17) | 4,564 (13.08) | 9,602 (13.01) |
| 7 | Schedule Tribes | 630 (1.64) | 534 (1.53) | 1,164 (1.57) |
| 8 | Others | 32,579 (85.18) | 29,781 (85.38) | 63,009 (85.40) |
| **9** | **Total population** | **38,247 (100)** | **34,879 (100)** | **73,775 (100)** |

**Source:** Census of India 2001, Figures within parentheses are in percentage
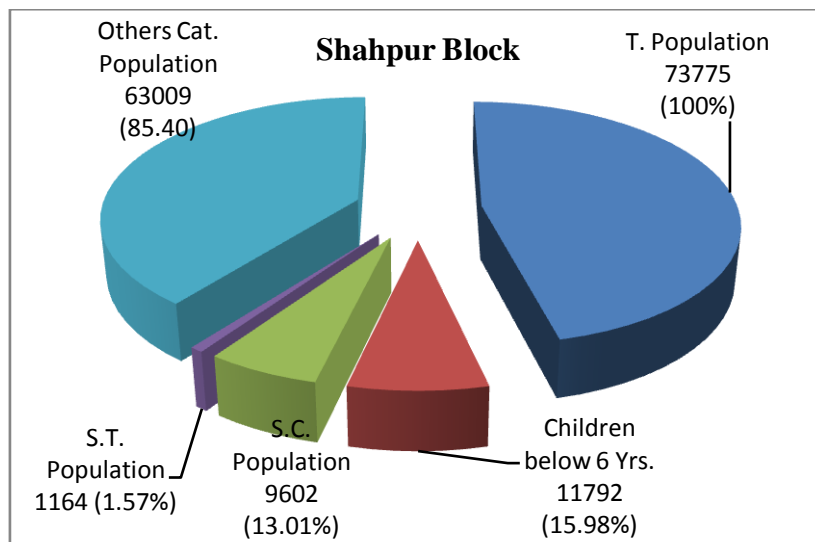


**Fig: 1.8: Population vulnerable to arsenic exposure in selected villages of Shahpur block**

## VI. Food Safety And Security

In the present study, the most well-known concern is entering of arsenic in food chain, affecting food safety. This poses a potential dietary risk to human health in addition to the risk from drinking of contaminated groundwater. Less well known but potentially more serious is the risk of arsenic to crop production. Continuous build up of arsenic in the soil from arsenic contaminated groundwater irrigation reduces crop yields in the long term.

Impact of green revolution resulted in installation of numerous shallow tube wells in the study area over the last three decades. This has caused in a sharp increase of groundwater extraction for irrigation. Based on census 2001, 2,137.11 hectares irrigated agricultural land (43.76 % of blocks irrigated land) in selected 27 revenue village of block is irrigated by arsenic contaminated groundwater especially for cultivation of Rabi and Zaid crops. These agricultural land and the cultivable crops are vulnerable due to assimilation of arsenic through the plant roots by irrigation of arsenic contaminated groundwater. In addition, widespread use of arsenic contaminated irrigation water ultimately leads to issues of food security, food safety and degradation of the environment.

In contrast, based on the general discussions among the villagers of the arsenic affected villages, they says that "even though the villages are suffering from groundwater arsenic contamination but the productivity of various crops are very good and almost equal in comparison of other nearby villages which are free from groundwater arsenic contamination. Further, it is recommended that the assessment of arsenic content in various

crops and vegetables grown in the present study area should be undertaken immediately to identify the exact concentration of arsenic content in various food grains and vegetables.

## VII. Conclusion

On the basis of overall findings of the present study it is observed that out of total 30 selected revenue villages of Shahpur block in Bhojpur district, 27 revenue villages situated along the bank of the Ganga river are severely affected by groundwater arsenic contamination. Maximum concentration of arsenic findings was obtained in hand pump of village Karnamepur where the level of arsenic was 598 ppb. In selected 27 revenue villages, arsenic free revenue villages were Harkhi Pipra, Suhiya and Domariya only. Present study findings reveals that average per capita consumption of arsenic from all sources i.e., from drinking water, rice, pulses, chapatti and vegetable by children, young person, adults and old persons are 0.227 mg/L, 0.489 mg/L, 0.559 mg/L and 0.568 mg/L respectively. The identified per capita arsenic consumption in arsenic affected villages has exceeded the maximum allowable limit of arsenic consumption through water and food (0.2 mg/kg/day).

Consumption of arsenic greater than its permissible limit though drinking water and foods is fatal for human health. Chronic exposure to arsenic can cause harm to the human cardiovascular, dermal, gastrointestinal, hepatic, neurological, pulmonary, renal and respiratory systems and reproductive system. The exposure of human to arsenic contaminated water and foods can lead to some physical changes on the skin such as the appearance of small black or white marks (melanosis), then thickening of the skin on the palms and the feet (keratosis), followed by skin lesions and eventually skin cancer. The long term ingestion or exposure (10-15 years) of arsenic can lead to a disease called 'arseniasis, arsenicosis, and arsenicism'. Non-cancer endpoints include hyper-pigmentation, hypo-pigmentation, keratosis of skin, peripheral vascular disease (black foot disease), cardiovascular disease, hypertension and neurotoxicity. Most of the symptoms of above mentioned diseases were observed in the field during the study. In the present study out of total population, 15.98% children (below 06 years age), 13.01% SC, 1.57% ST and 85.40% other category population is vulnerable to arsenic exposure.

In addition, 2,137.11 hectares agricultural land (43.76 % block's irrigated land) of 27 revenue villages in Shahpur block is irrigated by arsenic contaminated groundwater. These agricultural land and the cultivable crops are vulnerable due to assimilation of arsenic through plant roots by irrigation of arsenic contaminated groundwater. The justification in support of the vulnerability of agricultural land and the cultivable crops towards arsenic assimilation is the previous study undertaken in village Rampur Diarra of Maner block in Patna district. Study findings of the previous study shows that food grains such as seeds of wheat, maize, rice, lentils and rice husk containing substantial amount of arsenic (Maner block is declared as arsenic hotspot). The elevated level of arsenic in food grains resulted since crops receiving arsenic contaminated groundwater as a source of irrigation can uptake arsenic during the phyto-extraction process and bio-accumulated in different degrees in different parts of plants.

## Acknowledgement

## REFERENCES

[1]    Smedley, P.L. & Kinniburgh, D.G. (2002). A review of the source, behaviour and distribution of arsenic in natural waters. Applied Geochemistry, 17:517-568.
[2]    Woolson, E.A. (1977). Fate of arsenicals in different environmental substrates. Environmental Health Perspectives., 19:73-81
[3]    Ehrlich, H.L. & Newman, D.K. (2009). Geomicrobiology, Fifth ed., CRC Press, Boca Raton, FL.
[4]    Nordstrom, D.K. (2002). Worldwide occurrences of arsenic in ground water. Science., 296: 2143-2145.
[5]    Williams, M. (1997). Mining-related arsenic hazards: Thailand case-study. British Geological Survey Technical Report, WC/97/49.
[6]    Williams, M., Fordyce, F., Paijitprapapon, A. & Charoenchaisri, P. (1996). Arsenic contamination in surface drainage and groundwater in part of the southeast Asian tin belt, Nakhon Si Thammarat Province, southern Thailand. Environmental Geology., 27:16-33.
[7]    Bhattacharya, P., Chatterjee, D. & Jacks, G. (1997). Occurrence of As contaminated groundwater in alluvial aquifers from the Delta Plains, eastern India: option for safe drinking water supply. Int. J. Water Res. Dev., 13:79-92.
[8]    McArthur J.M., Banerjee, D.M., Hudson-Edwards, K.A., Mishra, R., Purohit, R., Ravenscroft, P., Cronin, A., Howarth, R.J., Chatterjee, A., Talukder, T., Lowry, D., Houghton, S. & Chadha, D.K. (2004). Natural organic matter in sedimentary basins and its relation to arsenic in anoxic groundwater: the example of West Bengal and its worldwide implications. Appl. Geochem., 19:1255-1293.

[9]     Bhattacharya, P., Jacks, G., Ahmed, K.M., Khan, A.A. & Routh, J. (2002). Arsenic in groundwater of the Bengal Delta Plain aquifers in Bangladesh. Bull. Environ. Contam. Toxicol., 69:538-545.

[10]    Acharyya, S.K., Lahiri, S., Raymahashay, B.C. & Bhowmik, A. (1993). Arsenic toxicity of groundwater in parts of the Bengal basin in India and Bangladesh: the role of Quaternary stratigraphy and Holocene sea-level fluctuation. Environ. Geol., 39:1127-1137.

[11]    Acharyya, S.K., Chakraborty, P., Lahiri, S., Raymahashay, B.C., Guha, S. & Bhowmik, A. (1999). Arsenic poisoning in the Ganges delta. Nature., 401:545-546.

[12]    BGS/MML. (1999). Groundwater Studies for Arsenic Contamination in Bangladesh. Final report, Department of Public Health Engineering, Govt. of Bangladesh Dhaka. British Geological Survey, Mott MacDonald Ltd.

[13]    Bhattacharyya, R., Jana, J., Nath, B., Sahu, S.J., Chatterjee, D. & Jacks, G. (2005). Groundwater As mobilization in the Bengal Delta Plain. The use of ferralite as a possible remedial measure: a case study. Appl. Geochem., 18:1435-1451.

[14]    Acharyya, S.K., Lahiri, S., Raymahashay, B.C., Bhowmik, A. (2000). Arsenic toxicity of groundwater in parts of the Bengal basin in India and Bangladesh: the role of Quaternary stratigraphy and Holocene sea-level fluctuation. Environ. Geol., 39:1127-1137.22

[15]    Saha, A.K. (1991). Genesis of arsenic in groundwater in parts of West Bengal. Center for Studies on Man and Environment, Annual Volume, Calcutta,

[16]    Ray, A.K. (1999). Chemistry of arsenic and arsenic minerals relevant to contamination of groundwater and soil from subterranean source. Everyman's Science 35(1).

[17]    Bhattacharya, P., Mukherjee, A.B., Bundschuh, J., Zevenhoven, R. & Loeppert, R.H. (2007). Trace Metals and other Contaminants in the Environment. In Bhattacharya, P., Mukherjee, A.B., Bundschuh, J., Zevenhoven, R. & Loeppert, R.H. (Eds.). Volume 9. Elsevier BV

[18]    Thakur, B.K., Gupta, V. & Chattopadhyay, U. (2013). Arsenic groundwater contamination related socio-economic problems in India: Issues and Challenges. In Nautiyal, S., Rao, K.S., Kaechele, H., Raju, K.V., Schaldach, R. (eds.), Knowledge Systems of Societies for Adaptation and Mitigation of Impacts of Climate Change, Environmental Science and Engineering, DOI:10.1007/978-3-642-36143-2_10, p.163-182, Springer-Verlag Berlin Heidelberg.

[19]    Chakraborti, D., Rahman, M. M., Das, B., Nayak, B., Pal, A., Sengupta, M. K., Hossain, M.A., Ahamed, S., Sahu, M., Saha, K.C., Mukherjee, S.C., Pati, S., Dutta, R.N. & Quamruzzaman, Q. (2013). Groundwater arsenic contamination in Ganga–Meghna–Brahmaputra plain, its health effects and an approach for mitigation. Environ Earth Sci., Special issue. DOI 10.1007/s12665-013-2699-y.

[20]    Chakraborti, D., Rahman, M.M., Das, B., Matthew Murrill, M., Dey, S., Mukherjee, S.C., Dhar, R.K., Biswas, B.K., Chowdhury, U.K., Roy, S., Sorif, S., Selim, M., Rahman, M., Quazi Quamruzzaman, Q. (2010). Status of groundwater arsenic contamination in Bangladesh: A 14-year study report. Water Research, 4 (4):5789-5802.

[21]    Rahman, M.M., Sengupta, M.K., Ahamed, S., Lodh, D., Das, B., Hossain, M.A., Nayak, B., Mukherjee, A., Mukherjee, S.C., Pati, S., Saha, K.C., Palit, S.K., Kaies, I., Barua, K., Asad, K.A. (2005). Murshidabad-One of the nine groundwater arsenic-affected districts of West Bengal, India, Part I: Magnitude of contamination and population at risk. Clinical Toxicology, 43:823-834.

[22]    Mandal, B.K., Chowdhury, T.R., Samanta, G., Mukherjee, D.P., Chanda, C.R., Saha, K.C. & Chakraborti, D. (1998). Impact of Safe Water for Drinking and Cooking on Five Arsenic-Affected Families for 2 Years in West Bengal, India. The Science of Total Environment., 218: 185-201.

[23]    Smith, A.H., Lingas, E.O. & Rahman, M. (2000). Contamination of drinking-water by arsenic in Bangladesh: a public health emergency. Bulletin of the World Health Organization., 78:1093-1103.

[24]    Task Force/State Agencies, Central Ground Water Board, Ministry of Water Resources, Government of India.

[25]    WHO (1993). Guidelines for Drinking Water Quality. Recommendations, 2nd Ed., World Health Organization, Geneva.

[26]    Huq, S.M.I., Correl, R. & Naidu, R. (2006a). Arsenic accumulation in food sources in Bangladesh. In Naidu, R., Smith, E., Owens, G., Bhattacharya, P., Nadebaum, P. (eds.), Managing arsenic in the environment from soil to human health, p.283-293, CSIRO, Victoria, Australia.

[27]    Huq, S.M.I., Joarder, J.C., Parvin, S., Correll, R. & Naidu, R. (2006b). Arsenic contamination in food-chain: Transfer of Arsenic into food materials through groundwater irrigation. J. Health Population and Nutrition., 24(3):305-316.

[28]    Kibria, G., Haroon, A.K.Y., Nugegoda, D. & Rose, G. (2010). Climate change and chemicals: Environmental Biological aspects., p.470, New India Publishing Agency, New Delhi.

[29]    Bhattacharya, P., Mukherjee, A. & Mukherjee, A. B. (2011). Arsenic in groundwater of India. Elsevier B.V.

[30]    Singh, K.S. & Ghosh, K.A. (2011). Entry of arsenic into food material - a case study. World Applied Sciences., 13 (2): 385-390.

[31]    Ravenscroft, P., Brammer, H., & Richards, K. (2009) Arsenic Pollution: A Global Synthesis. Wiley-Blackwell, p.588.

[32]    ATSDR (2000). Toxicological profile for arsenic. U.S. Department of Health & Human Services, Public Health Service Agency for Toxic Substances and Disease Registry, p.428.

[33]    Mandal, B.K. & Suzuki, K.T. (2002). Arsenic round the world: a Review. Talanta., 58:201-235.

[34]    IARC (in preparation). A review of human carcinogens. C. Metals, arsenic, dusts, and fibres. Lyon, International Agency for Research on Cancer (IARC Monographs on the Evaluation of Carcinogenic Risks to Humans, Vol. 100)

[summary in Straif, K., Benbrahim-Tallaa, L., Baan, R., Grosse, Y., Secretan, B., Ghissassi EL, F., Bouvard, V., Guha, N., Freeman, C., Galichet, L., Cogliano, V. (2009)]. A review of human carcinogens-Part C: Metals, arsenic, dusts, and fibres. The Lancet Oncology, 10:453–454.

[35]   IARC (1987). Summaries & evaluations: Arsenic and arsenic compounds (Group 1). Lyon, International Agency for Research on Cancer, p. 100 (IARC Monographs on the Evaluation of Carcinogenic Risks to Humans, Supplement 7; http://www.inchem.org/documents/iarc/suppl7/arsenic.html).

[36]   IARC (2004). Summaries & evaluations: Arsenic in drinking-water (Group 1). Lyon, International Agency for Research on Cancer, p. 39 (IARC Monographs on the Evaluation of Carcinogenic Risk to Humans, Vol. 84.

[37]   Naidu, R., Smith, E., Owens, G., Bhattacharya, P. & Nadebaum, P. (2006). Managing arsenic in the environment from soil to human health. In Naidu, R., Smith, E., Owens, G., Bhattacharya, P. & Nadebaum, P. (eds.), CSIRO, Victoria, Australia.

[38]   Brammer, H. & Ravenscroft, P. (2009). Arsenic in groundwater: A threat to sustainable agriculture in south and south-east Asia. Environment International., 35: 647-654.

[39]   George, C.M., Factor-Litvak, P., Khan, K., Islam, T., Singha, A., Moon-Howard., Van Geen, A. & Graziano, J.H. (2013). Approaches to increase arsenic awareness in Bangladesh: An evaluation of an arsenic education program. Health Education & Behaviour., 40(3):331-338.

# Analysis of Temperature loss of Hot Metal during Hot Rolling Process at Steel Plant

K. K. Anantha Kirthan[1], S. Sathurtha Mourian[2], M. Vignesh[3], A. Nisanth[4]

[1,2,3,4] *Department Of Mechanical Engineering (SW), PSG College of Technology, Coimbatore, India*

*Abstract: Hot metal is travelling a long distance (around 126 m) between roughing mill and a Steckel finishing mill during hot rolling process in a steel plant which resulted in heat loss. Since, the metallurgical qualities of finished product are closely related to the accurate control of temperature of the material during the hot rolling process, the heat in the furnaces maintains the slab temperature at high level at the cost of more fossil fuels. Temperature of the work piece influences spread appreciably. Lower the temperature of raw material input, greater is the spread. Similarly, higher the temperature, lesser is the spread. Lesser speed of rolling results in greater spread and vice-versa. Hence, temperature is playing a vital role in hot rolling process.*

*Temperature loss of semi finished work pieces between the mill stand is inevitable until it protected from the open atmosphere. If a low-emissivity material (radiation shield) is placed between two surfaces, the radiation heat transfer can be considerably reduced. The shield increases the thermal resistance to radiation heat flow. Because radiation is a major source of heat loss at the temperatures involved (around 1060° C.) Thermal shields may be fixed over the path of the hot strip to reduce heat loss and in particular such heat shields can be employed to reduce the head-to-tail temperature variation along the length of a transfer bar. The result of this study is the development of an effective procedure for computer calculation of processes of hot rolling to optimize its parameters*

*Key words: Heat loss, Convection and radiation heat transfer, thermal shield, temperature gain*

## I. Introduction

The semi-finished steel products from the casting operations are further processed to produce finished steel products in a series of shaping and finishing operations in the rolling mills. Rolling mills are either hot or cold processes. Mechanical forces for cold rolling will create much more force and energy needs, while hot rolling happens much faster with less force. However, there are significant energy costs to heat the metal to near eutectic temperatures. Hence, this study is concern with TWO main objectives:

- To minimize temperature loss of hot metal while it is conveyed from rougher to finishing mill.
- To decrease the temperature difference of head and tail end of hot metal on entering the finishing train.
  In order to achieve the proposed objective, the following main tasks are included in this study:
- Calculating the heat loss of the hot metal from the walking beam furnace.
- Calculating the heat loss of the hot metal (Transfer Bar) travelling between the Reheat furnace and roughing Mill which includes the:
- Temperature drop due to radioactive heat transfer between the slab and the surrounding environment.
- Temperature drop due to heat Convection between the slab and air.
- Calculating the **EXPECTED** Heat loss from **Transfer Bar** if the **THERMAL SHIELD** is placed over the distance between Roughing Mill and finishing mill.
- Comparing the results and calculating the exact amount of heat gain by introducing this innovative technique.

## II. Heat Transfer Calculation

*Radiation shield and the radiation effect*

Radiation heat transfer between two surfaces can be reduced greatly by inserting a thin, (low-emissivity) sheet of material between the two surfaces. Such highly reflective thin plates or shells are called **radiation shields.** The role of the radiation shield is to reduce the rate of radiation heat transfer by placing additional resistances in the path of radiation heat flow.

Radiation heat transfer between two large parallel plates of emissivity's $\varepsilon_1$ and $\varepsilon_2$ maintained at uniform temperatures $T_1$ and $T_2$:

A thin carbon steel sheet with an emissivity of 0.56 is placed between the hot slab and atmosphere that are maintained at uniform temperatures    $T1 = 1050°C$ and $T_2 = 30°C$ and have emissivities $\varepsilon_1 = 0.56$ and $\varepsilon_2 = 0.56$, respectively. Determine the net rate of radiation heat transfer between the hot slab and atmosphere and compare the result to that without the shield.

***DATA of the hot metal slab considered for Analysis***
Size of the hot metal slab  = 1.275 m X 60 m
Area of the slab           = 76.5 m$^2$
Approximate distance travelling by hot metal Transfer bar between roughing mill and a STECKEL finishing mill                       =  126 m
Velocity of the hot metal  = 3.5 m/sec
Weight of the material     = 15,000 kg
 Mean specific heat         = 0.483 kJ/kg°K
Temperature of the coming out of Roughing mill   =1050$^o$C
Ambient temperature        =30°C
The quantity of heat available with hot slab coming out of roughing Mill (Q) can be found from the formula (Assuming ONE DIMENSIONAL heat flow).

**$Q = m \ x \ C_p \ (t_1 − t_2)$**

Where
Q   = Quantity of heat in kJ
m   = Weight of the material in kg
$C_p$ = Mean specific heat, kJ/kg°K
$t_2$   = Ambient temperature, °K
t1  = Temperature of the slab coming out of the roughing mill °K
Hence, The quantity of heat available with hot slab coming out of roughing Mill
(Q) = m  x  $C_p$ $(t_1 − t_2)$
    = 15,000 X 0.483 (1050 – 30)
    **= 73,89,900 kJ**

## III.  Calculation Of Heat Loss Without Thermal Shield

Researchers working in the field of hot rolling have classified the heat transfer mechanism involved in the process are as follows:

1. Temperature drop due to radiation  heat  transfer between  the  slab  and  the  surrounding environment.
2. Temperature drop due  to heat convection   between the slab and air

***Heat loss due to radiation heat transfer between the hot metal and the surrounding environment:***
If a hot object is radiating energy to its cooler surroundings the net radiation heat loss rate can be expressed as
*$q = \varepsilon \ \sigma \ (T_h^4 - T_c^4) \ A$*
    *where*
*$T_h$ = hot body absolute temperature (K)*
*$T_c$ = cold surroundings absolute temperature (K)*
*$A$ = area of the object  (m$^2$)*
The emissivity of steel at *390 $^o$F (199 $^o$C) > $\varepsilon = 0.64$*
*$\sigma = 5.6703 \ 10^{-8} \ (W/m^2K^4)$ - The Stefan-Boltzmann Constant*
In our case to calculate heat loss rate on both sides of hot metal
**q  = 2 X $\varepsilon \ \sigma$  $(T_h^4 - T_c^4)$ A**
    = 2 X 0.64 X *5.6703 $10^{-8}$ $W/m^2K^4$ X* $(1323^4 – 303^4)$  X 76.5
**$\simeq$ 16964 KW    ----------- (a)**

***Heat loss due  to  heat convection between the  hot metal  and air;***
Let us assume the FORCED CONVECTION FOR FLAT PLATE for our case:

### *Flow over flat plate*

The friction and heat transfer coefficient for a flat plate can be determined by solving the conservation of mass, momentum and energy equations (either approximately or numerically). They can also be measured experimentally. It is found that the Nusselt number can be expressed as:

$$Nu = \frac{hL}{K} = C\ Re^{m}\ Pr^{n}$$

Where C, m and n are constants and L is the length of the flat plate. The properties of the fluid are usually evaluated at the film temperature defined as:

$$T_f = \frac{TS + T\alpha}{2}$$

### *Turbulent flow*

For isoflux plates, the local Nusselt number for turbulent flow can be found from

$$Nu = \frac{hL}{K} = 0.037 \times Re^{4/5} \times Pr1^{/3},$$

$$0.6 \leq Pr \geq 60,\ 5 \times 10^5 \leq Re \geq 10^7$$

(The above relationships have been obtained for the case of isothermal surface but could also be used approximately for the case of non-isothermal surface. In such cases assume the surface temperature be constant at some average value)

*Reynolds number:* Ratio of inertia forces to viscous forces in the fluid

$$Re = \frac{\rho\ LV}{\mu}$$

Properties of Air, (1050 + 30)/2 = 540°C

*From the HMT Table for Air temperature 540ºC;*

Density ($\rho$)  = 0.4352 kg/m$^3$
Specific heat (**Cp**)  = 1.101 kJ/kg ºk
Coefficient of viscosity ($\mu$) = 37.37 X 10$^{-6}$ kg/ms
Kinematic viscosity ($\vartheta$)  = 86.38 X 10$^{-6}$ m$^2$/sec
Thermal conductivity (**k**)  = 59.36 X 10$^{-3}$ W /m ºk
Prandtl Number (**Pr**)  = 0.704
Hence,

$$Re = \frac{\rho\ LV}{\mu}$$

$$= \frac{0.432\ X\ 60\ X\ 3.5}{37.37\ X\ 10^{-6}} = 2.45\ X\ 10^6$$

Flow is TURBULENT, since the Re is > the critical Reynolds number 5 X 10$^5$
For isoflux (uniform heat flux) plates, the local Nusselt number for turbulent flow:

$$Nu = 0.037\ X\ Re^{4/5}\ x\ Pr^{1/3}$$

$$= 0.0308\ X\ (2.45\ X\ 10^6)^{4/5}\ X\ (0.704)^{1/3}$$

$$= 4258$$

$$Nu = \frac{hL}{K} = 0.037\ X\ Re^{4/5}\ x\ Pr^{1/3}\ (\text{ for cooling})$$

$$\frac{hL}{K} = 4258$$

$$h = \frac{4258\ X\ 59.36\ X\ 10^{-3}}{60} = 4.21\ W\ /\ ºC$$

Therefore the HEAT loss on both sides of Hot metal due to convection:

$$Q_{con} = 2\ X\ h\ X\ A\ (\square T)$$

$$= 2\ X\ 4.21\ X\ 76.5\ X\ (1050 - 30)$$

$$= 657\ kW\ \text{-------------------- (b)}$$

**For Total Heat Loss from hot metal**
= **(a) + (b)** = 16964 + 657 = **17621 kJ/sec.**

## IV. Calculation Of Heat Loss With Thermal Shield

*Specification of Thermal shield:*
Shape of the shield proposed: Rectangular shield Size of the shield:1.5 m (W) X 2.0 m (L) X0.5 m (H)
Area covered under the shield : Length of the transfer
bar (60 m)

**Heat loss due to radiation heat transfer between the h o t m e t a l and the surrounding environment:**
To calculate radiation exchange we must take into account surface areas, surface geometries and position in relation to each other.

This is done by the *shape factor F12*
*F12 = Fraction of Radiation leaving surface 1 and interrupted by surface 2*
*Net exchange of RADIATION between the surfaces of **two parallel infinite plates***
If Emissivity's are equal

$$\frac{q}{A} = \frac{\sigma (T_1{}^4 - T_2{}^4)}{\frac{1}{\varepsilon_1} + \frac{1}{\varepsilon_2} - 1}$$

Where
Stefan Boltzmann's Constant (σ )
$= 5.67 \, X10^{-8}$ Wsk$^{-4}$/m$^2$
*Emissivity of Steel slab* $\varepsilon_1$        = 0.56,
Temperature $T_1$                = 1050ºC
*Emissivity of Steel plate* $\varepsilon_2$        = 0.56,
Temperature $T_2$                = 930ºC
**Area of the shield      (A)**
**= (1.5 X 62) + (0.5 X 62) + (0.5 X 62)= 155 m$^2$**

$$\frac{q}{A} = \frac{5.67 \, X10^{-8} (1323^4 - 1203^4)}{\frac{1}{0.56} + \frac{1}{0.56} - 1}$$

q = 155 X $\frac{5.67 \, X \, 10^{-8} \, X \, 9692 \, X \, 10^8}{2.57}$ = 3314325

Heat loss on both side of Hot metal (q)
= 2 X 3314325 = 6628649 watts
*Radiation heat loss (q) = 6628 K --------- (c)*

**Heat loss due to heat convection between the hot metal and air;**
Properties of Air, (1050 + 930)/2 = 990ºC
From the HMT Table for Air temperature 1000ºC ;
Density (**ρ**) = 0.277 kg/m$^3$
Specific heat (**Cp**) = 1.185 kJ/kg ºk
Coefficient of viscosity (**μ**) = 49.03 X 10$^{-6}$ kg/ms
Kinematic viscosity (**ϑ**)   = 178.00 X 10$^{-6}$ m$^2$/sec
Thermal conductivity (**k**) = 80.71 X 10$^{-3}$ W /m ºk
Prandtl Number (**Pr**)        = 0.719
Velocity of Transfer bar    = 3.5 m/sec
Hence, **Re**    = $\frac{\rho \, LV}{\mu}$ = $\frac{0.277 \, X \, 62 \, X \, 3.5}{49.03 \, X \, 10^{-6}}$ = **1.225 X 10$^6$**
Flow is TURBULENT, since the Re $_{is}$ > the critical Reynolds number 5 X 10$^5$
For isoflux (uniform heat flux) plates, the local **Nusselt number for turbulent** flow:
**Nu = 0.037 X Re$^{4/5}$ x Pr$^{1/3}$**
= 0.037 X (1.225 X 10$^6$)$^{4/5}$ X (0.719)$^{1/3}$ = 2463
**Nu = $\frac{hL}{K}$** = 0.037 X Re$^{4/5}$ x Pr$^{1/3}$ ( for cooling)
$\frac{hL}{K}$ = 2463
h = $\frac{2463 \, X \, 80.71 \, X \, 10^{-3}}{62}$ = **3.20 W / ºC**
Therefore the HEAT loss on both sides of Hot metal due to convection:

**Q $_{con}$ = 2 X h X A ($\Box$T)**
  = 2 X 3.20 X 155 X (1050 – 930)
  **= 119 kW ----------------------- (d)**
**For Total Heat Loss from hot metal**
= (c) + (d) = 6628 + 119 = 6747 Kw  **= 6747 kJ/sec.**

## V. Temperature Available In The Transfer Bar *Without* Thermal Shield

Time taken by the Head end to reach Steckel mill (T$_h$) = $\frac{126}{3.5}$ sec = 36 Sec
Time taken by the Tail end to reach Steckel mill (T$_t$)   = 53 sec
*Heat Loss in Transfer Bar Head end*
= 17621 X 36 sec = **634356 KJ**

*Heat Loss in Transfer Bar Tail*
= 17621 X 53 sec = **933913 KJ**

*Temperature available in the transfer bar at head end*
**(Q)= m C$_p$ $\Delta T$**
The quantity of heat available with hot slab coming out of roughing Mill
(Q) = m x Cp (t$_1$ – t$_2$)
  = 15,000 X 0.483 (1050 – 30)
  **= 73, 89,900 kJ**
Hence, 7389900 (-) 634356
= 15,000 X 0.483 (T$_h$ – 30), Th = **962** ℃

*Temperature available in the transfer bar at tail end*
(Q) = m C $\Delta T$
Hence, 7389900 (-) 933913
= 15,000 X 0.483 (T$_t$ – 30), **T$_t$ = 921** ℃

## VI. Temperature Available In The Transfer Bar *With* Thermal Shield

Time taken by the Head end to reach Steckel mill (T$_h$) = $\frac{126}{3.5}$ sec = 36 Sec
Time taken by the Tail end to reach Steckel mill (T$_t$)   = 53 sec
*Heat Loss in Transfer Bar Head end*
  = 6747 X 36 sec = **242892 KJ**
*Heat Loss in Transfer Bar Tail end*
  = 6747 X 53 sec = **357591 KJ**

*Temperature available in the transfer bar at head end is*

**(Q)= m C$_p$ $\Delta T$**
The quantity of heat available with hot slab coming out of roughing Mill
**(Q)  = m x Cp (t$_1$ – t$_2$)**
 = 15,000 X 0.483 (1050 – 30)  **= 73,89,900 kJ**
Hence,  7389900 (-) 242892
= 15,000 X 0.483 (T$_h$ – 30), **T$_h$ = 986** ℃

*Temperature available in the transfer bar at tail end*
Hence, 7389900 (-) 357591
= 15,000 X 0.483 (T$_t$ – 30), **T$_t$ = 970** ℃

## VII.  Result Abstract

| | Heat loss due to **Radiation** | Heat loss due to **Convection** | Temp of Head End ($T_{head\ end}$) | Temp of Tail End ($T_{tail\ end}$) | Temp variation along the Length of Transfer bar |
|---|---|---|---|---|---|
| *Transfer Bar without Thermal shield* | 169 64 KW | 657 KW | 962 ℃ | 921 ℃ | 41 ℃ |
| *Transfer Bar with Thermal shield* | 486 0 KW | 119 KW | 986 ℃ | 970 ℃ | 16 ℃ |
| *Heat / Temp GAIN by placing Thermal shield* | **121 04 KW** | **538 KW** | **24 ℃** | **49 ℃** | **25 ℃** |

From the above table, it could be seen that by introducing the Thermal shield
- *The radiation heat transfer from the Transfer bar reduces to* ***one third.***
- *The head-to-tail temperature variation along the length of a transfer bar got reduced to about* ***one third.***

## VIII.  Conclusion

This study is an attempt to reduce the heat loss taking place during the rolling process in Hot Rolling Mill (HRM) of a Steel Plant.  Radiation heat transfer between two surfaces can be reduced greatly by inserting a thin, (low-emissivity) sheet of material between the two surfaces. Hence, it is proposed to cover the transfer roller table between rough & Steckel mill with THERMAL SHIELDS to minimize temperature loss of hot metal while it is conveyed from rougher to finishing mill and to decrease the temperature difference of head and tail end of hot metal on entering the finishing train. Furthermore, this technique has an environment impact such as reduction in fuel cost, reduced energy consumption and less emission in the furnace provided before & after the finishing Steckel mill.

## REFERENCES

[1]    S.V. Patankar Numerical Heat Transfer and Fluid Flow, McGraw-Hill, New York
[2]    S.Sohal Manohar and R.Howell John, Int.J. Heat and Mass Transfer. 8 (1973),
[3]    W.L.Roberts, Hot Rolling of Steel, Marcel dekker INC., New York, (1983)
[4]    Cengel, Y.A. and Boles, M.A (2007) Thermodynamics  an Engineering Approach, McGraw-Hill, Singapore
[5]    R.K. Rajput,  Heat and Mass transfer, TATA McGraw Hill, New Delhi
[6]    C.P. Kothandaraman, S.subramanyan Heat and Mass Transfer DATA BOOK, Wiley Eastern Ltd, New Delhi
[7]    Hot Flat Rolling Mills Division, Germany Steckel Mills Manual (Source -Online)

**Author 1:**

Name : ANANTHA KIRTHAN K K
Place : Coimbatore
Date of birth : 11th may, 1994. Age : 20
Gender :  Male
Degree : Bachelor of Engineering
Field : Mechanical Engineering (SW)
Institution : PSG College of Technology
City : Coimbatore
State : Tamil nadu
Country : India
E mail : cubicalwisdom99@gmail.com

**Author 2:**
Name : SATHURTHA MOURIAN S
Place : Coimbatore
Date of birth : 22th december, 1994. Age : 20
Gender :  Male
Degree : Bachelor of Engineering
Field : Mechanical Engineering (SW)
Institution : PSG College of Technology
City : Coimbatore
State : Tamil nadu
Country : India
E mail : mouri.sath93@gmail.com

**Author 3:**
Name : VIGNESH M
Place : Coimbatore
Date of birth : 12th march, 1994. Age : 20
Gender :  Male
Degree : Bachelor of Engineering
Field : Mechanical Engineering (SW)
Institution : PSG College of Technology
City : Coimbatore
State : Tamil nadu
Country : India
E mail : vigneshthebbm@gmail.com

**Author 4:**
Name : NISANTH A
Place : Coimbatore
Date of birth : 14th september, 1994. Age : 20
Gender :  Male
Degree : Bachelor of Engineering
Field : Mechanical Engineering (SW)
Institution : PSG College of Technology
City : Coimbatore
State : Tamil nadu
Country : India
E mail : nisanth63@gmail.com

# Design, Analysis and Optimization of a 6 cylinder Engine Crank shaft

V. Mallikarjuna Reddy[1], T. Vijaya Devi [2]

[1]*M.Tech student, Dept of Mech. Engg, CMR Institute of Technology, Hyderabad, India*
[2] *Asst. prof, Dept of Mech. Engg, CMR Institute of Technology, Hyderabad, India*

***Abstract:*** *This paper deals with; the problem occurred in six cylinders four stroke engine crankshaft. It consist of static structural analysis of six cylinder engine crank shaft. It identifies and solves the problem by using the modelling and simulation techniques. The main work was to model the crankshaft with dimensions and then simulate the crankshaft for static structural analysis. The topic was chosen because of increasing interest in higher payloads, lower weight, higher efficiency and shorter load cycles in crankshaft. The modelling software used is Unigraphics-NX7.5 for modelling the crankshaft. The analysis software ANSYS is used for structural analysis of crankshaft. The objective involves modelling and analysis of crankshaft, so as to identify the effect of stresses on crankshaft, to compare various materials and to provide possible solution. Results obtained from the aforementioned analysis were then used in optimization of the crankshaft. The first step in the optimization process was weight reduction of the component considering static loading. This required the stress range under static loading not to exceed the magnitude of the stress range in the original crankshaft. Possible weight reduction options and their combinations were considered. The optimization process resulted in a weight reduction, increased strength and a reduced cost of the crankshaft.*
***Keywords:*** *6 cylinder Engine Crankshaft, Unigraphics, Finite element analysis, Stress Analysis, optimization.*

## I. Introduction

Crankshaft is one of the most important moving parts in internal combustion engine. Crankshaft is a large component with a complex geometry in the engine, which converts the reciprocating displacement of the piston to a rotary motion with a four link mechanism. Since the crankshaft experiences a large number of load cycles during its service life, fatigue performance and durability of this component has to be considered in the design process. Design developments have always been an important issue in the crankshaft production industry, in order to manufacture a less expensive component with the minimum weight possible and proper fatigue strength and other functional requirements. These improvements result in lighter and smaller engines with better fuel Efficiency and higher power output. Crankshaft must be strong enough to take the downward force of the power stroke without excessive bending. So the reliability and life of the internal combustion engine depend on the strength of the crankshaft largely. And as the engine runs, the power impulses hit the crankshaft in one place and then another. This study is conduct on a six cylinder engine crank shaft. The modelling of six cylinder engine crankshaft is done by using Unigraphics-NX7.5 software. The finite element analysis has been performed on crankshaft in order to optimize the weight and manufacturing cost. The material for crankshaft is Cast Iron. Other alternate materials on which analysis has been done are, Forged steel, high carbon steel.

## II. Literature Review

Solanki et al. [1] presented literature review on crankshaft design and optimization. The materials, manufacturing process, failure analysis, design consideration etc. were reviewed. The design of the crankshaft considers the dynamic loading and the optimization can lead to a shaft diameter satisfying the requirements of the automobile specifications with cost and size effectiveness. They concluded that crack grows faster on the free surface while the central part of the crack front becomes straighter. Fatigue is the dominant mechanism of failure of the crankshaft. Residual imbalances along the length of the crankshafts are Crucial to performance.

Meng et al. [2] discussed the stress analysis and modal analysis of a 4 cylinder crankshaft. FEM software ANSYS was used to analyse the vibration modal and distortion and stress status of crank

throw. The relationship between frequency and the vibration modal was explained by the modal analysis of crankshaft. This provides a valuable theoretical foundation for the optimization and improvement of engine design. Maximum deformation appears at the centre of the crankpin neck surface. The maximum stress appears at the fillet between the crankshaft journal and crank cheeks, and near the central point journal. The crankshaft deformation was mainly bending deformation was mainly bending deformation under the lower frequency. Maximum deformation was located at the link between main bearing journal and crankpin and crank cheeks. So, the area prone to appear the bending fatigue crack.

Montazersadgh and Fatemi [3] choose forged steel and a cast iron crankshaft of a single cylinder four stroke engine. Both crankshafts were digitized using a CMM machine. Load analysis was performed and verification of results by ADAMS modelling of the engine. At the next step, geometry and manufacturing cost optimization was performed. Considering torsional load in the overall dynamic loading conditions has no effect on von mises stress at the critically stressed location. Experimental stress and FEA results showed close agreement, within 7% difference. Critical locations on the crankshaft are all located on the fillet areas because of high stress gradients in these locations. Geometry optimization results in 18% weight reduction of the forged steel. Fillet rolling induces compressive residual stress in the fillet areas, which results in 165% increase in fatigue strength of the crankshaft.

### III. Design Calculation For Crankshaft
The specification of diesel engine for crankshaft is TABULATED below:

| No of cylinders | 6 |
|---|---|
| Bore/Stroke | 86 mm/ 68 mm |
| Compression Ratio | 18 : 1 |
| Max. Power | 8.1 HP @ 3600rpm |
| Max. Torque | 16.7 Nm@ 2200rpm |
| Maximum Gas pressure | 25 Bar |

**Table 1**: Specification of engine

Deign of crankshaft when the crank is at an angle of Maximum bending moment. At this position of the crank, the maximum gas pressure on the piston will transmit maximum force on the crankpin in the plane of the crank causing only bending of the shaft. The crankpin as well as ends of the crankshaft will be only subjected to bending moment. Thus, when the crank is at the dead center, the bending moment on the shaft is maximum and the twisting moment is zero.

Let, D = Piston diameter or cylinder bore in mm, p = Maximum intensity of pressure on the piston in N/mm2The thrust in the connecting rod will be equal to the gas load on the piston ($F_p$ ). We know that gas load on the piston,

Force on the piston:
Bore diameter (D) =86mm,
$F_p$= Area of the bore ×$P_{max}$
$F_p = \pi/4 \times D^2 \times P\ max = 14.52$ KN
Distance between two bearings is given by,

$$b = 2D = 2 \times 86 = 172mm$$
$$\text{Therefore } b_1 = b_2 = b/2 = 86mm$$

Due to this piston gas load ($F_P$) acting horizontally, there will be two horizontal reactions $H_1$ and $H_2$ at bearings 1 and 2
Respectively, such that

$$H_1 = H_2 = F_p/2 = 7.26KN$$

Design of crank pin against loading
According to distortion energy theory, the Von-Misses stress induced in the crank-pin is,
$M_{ev} = \sqrt{(K_b \times M_c)^2 + 3/4(K_t \times T_c)^2}$
Where,
Kb = combined shock and fatigue factor for bending (Assume Kb=2)
Kt = combined shock and fatigue factor for torsion (Assume K t =1.5)
Putting the values in above equation we get

---

$M_{ev} = 1568$ KN-mm

Also we know that

$M_{ev} = \pi/32 \times \sigma_v \times 44^3$

$1568 \times 10^3 = \pi/32 \times \sigma_v \times 44^3$

Von-Mises stress $\sigma_v = 187.49$ N/mm$^2$

## IV. Modeling Of Crankshaft

The software used for Modelling of crankshaft is Unigraphics-NX7.5 and software it is developed by SIEMENS.

This is CAD/CAM/CAE software but we are using this for only 3-D part modelling (CAD).

This CAD includes.

1. Sketcher
2. Part modelling (part design)
3. Surface Design
4. Assembly Design
5. Drafting
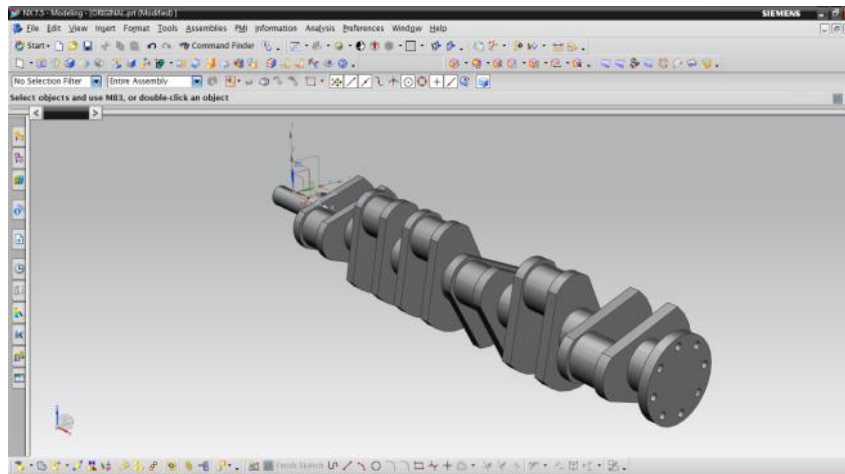


**Figure 1**: 3-D model of Crankshaft using Unigraphics-Design 1-Original

## V. Meshing Of Crankshaft

The Figure.2 shows the meshed model of crankshaft. The Discretization (Mesh generation) is the first step of Finite Element Method. In this step the component or part is divided into number of small parts. In discretization the no of elements are 59971. The effect of force on each portion of the component is not same. The purpose of discretization is to perform the analysis on each small division separately.
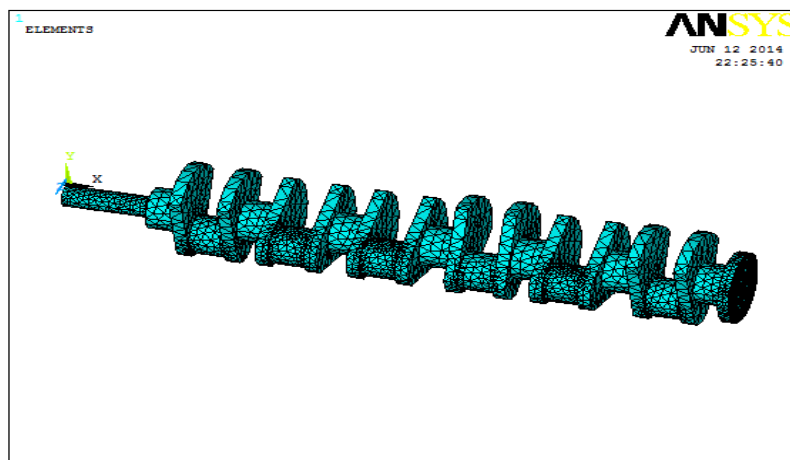


**Figure 2**: Meshed model of crankshaft

## VI. Loading And Boundary Conditions

Crankshaft is a constraint with a ball bearing from one side and with a journal on the other side. The ball bearing is press fit to the crankshaft and does not allow the crankshaft to have any motion other than rotation about its main axis. Since only 180 degrees of the bearing surfaces facing the load direction constraint the motion of the crankshaft.
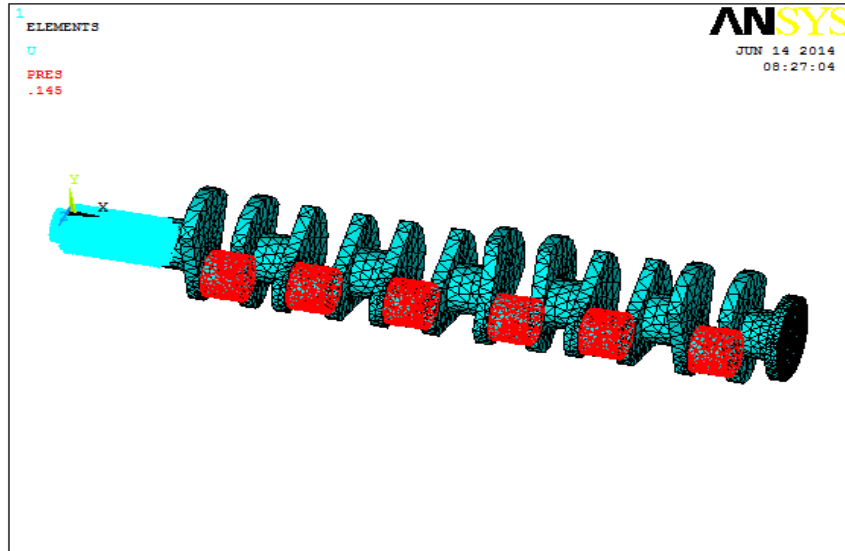


**Figure 3**: Load applied on crankshaft

This constraint is defined as a fixed semi-circular surface as wide as ball bearing width. The other side of the crankshaft is journal bearing. Therefore this side was modeled as a semi-circular edge facing the load at the bottom of the fillet radius fixed in a plane perpendicular to the central axis and free to move along central axis direction.

## VII. Static Structural Analysis For Crankshaft Design 1-Original

After the application of boundary conditions and force, the next step is to perform the structural analysis of crankshaft. In this structural analysis, we are mainly concern with the total deformation and the stresses acting on the crankshaft (von-mises stresses). When the force is applied, the slight deformation and also the stresses take place in the crankshaft. The total deformation of crankshaft is shown in Figure.4. The deformation in the crankshaft is not same throughout. The portion in red colour shows that the deformation at that region is maximum and the portion in blue colour shows that the deformation is minimum in that region. The maximum displacement is 12.77 mm.
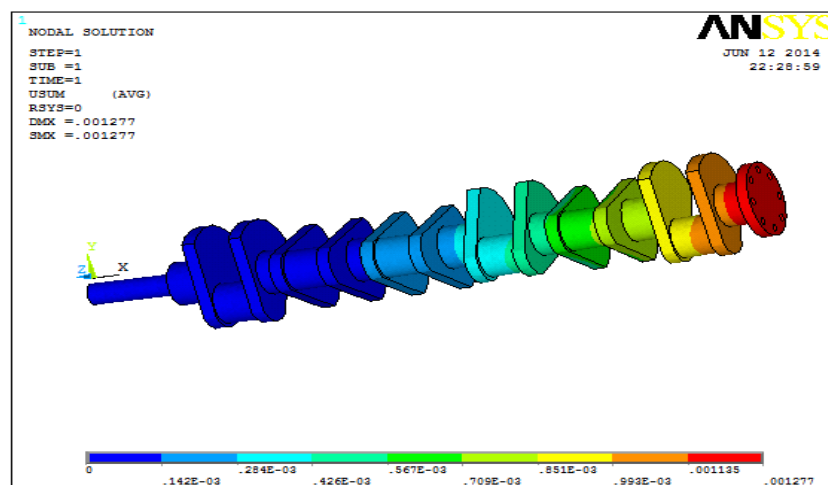


**Figure: 4**: Deformation of crankshaft
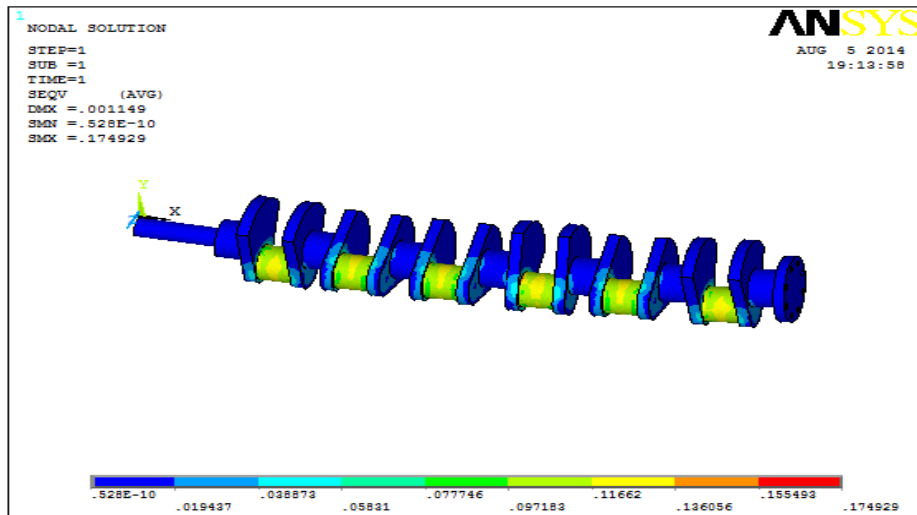
**Figure5**: Von Misses stress for Cast Iron 174.92MPa
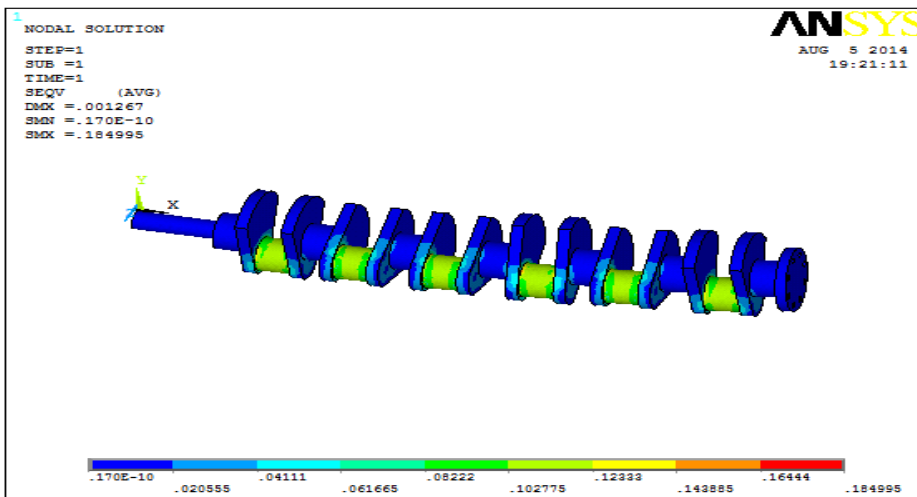


**Figure6**: Von Misses stress for Forged steel 184.99 MPa
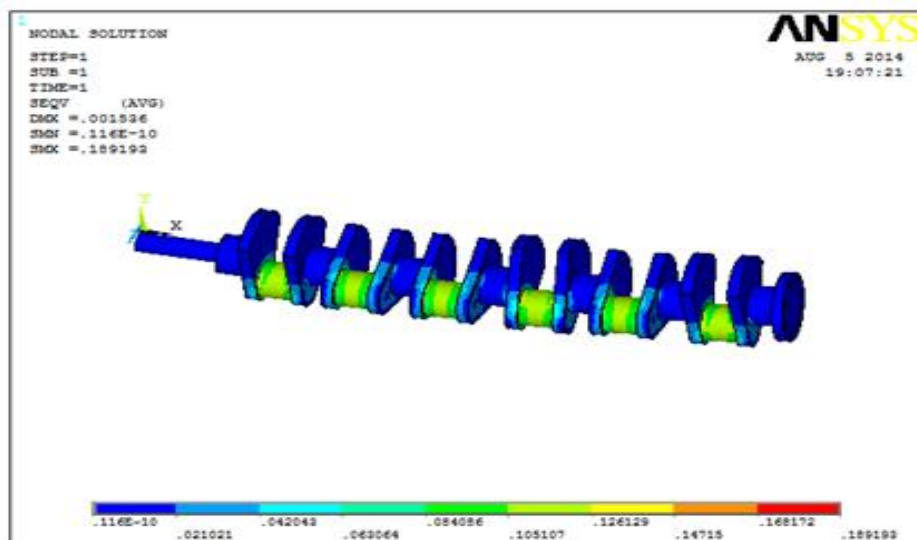


**Figure: 7**: Von Misses Stress for High Carbon Steel 189.19 MPa

The stress acting on the Design1Original crankshaft is shown in Figure.5, 6, and 7

## VIII. Geometry Optimization

In order to achieve the objectives various changes in the initial design of the crankshaft were done and they were analysed among them two cases showed the most effective results. Design 1-Original is 4180032.9702 mm3 and the weight of the Design 1-Original is 33.23kg.In Design 2 Volume of the modified design after modification is 4051869.7021 mm3and the weight of the modified Design 2-Modified is 32.21kg. After designing, the load and boundary conditions were assigned to the new model. After applying the loading and boundary conditions, equivalent stress, equivalent strain, and total deformation diagrams are obtained. And then the various stress, strain and deformation of the different designs are then compared, analysed and the best results give the final optimized design.
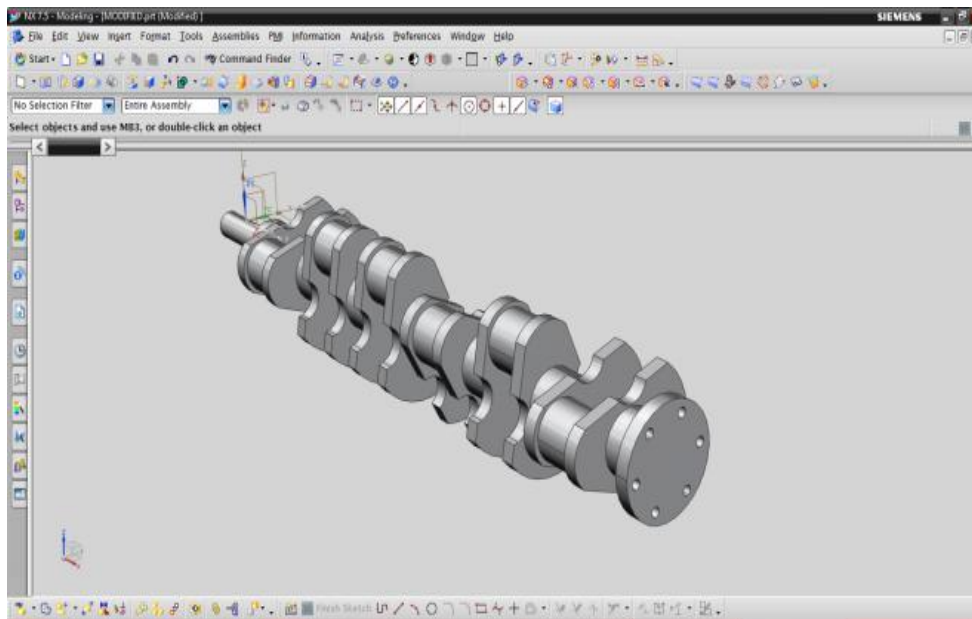


**Figure 8:** Modified 3-D model of Crankshaft using Unigraphics Design 2-Modified

## IX. Static Structural Analysis For Crankshaft Design 2-Modified

The total deformation for a modified crankshaft is shown in Figure.9. The deformation in the crankshaft is not same throughout. The portion in red colour shows that the deformation at that region is maximum and the portion in blue colour shows that the deformation is minimum in that region. The maximum displacement is 11.57 mm.
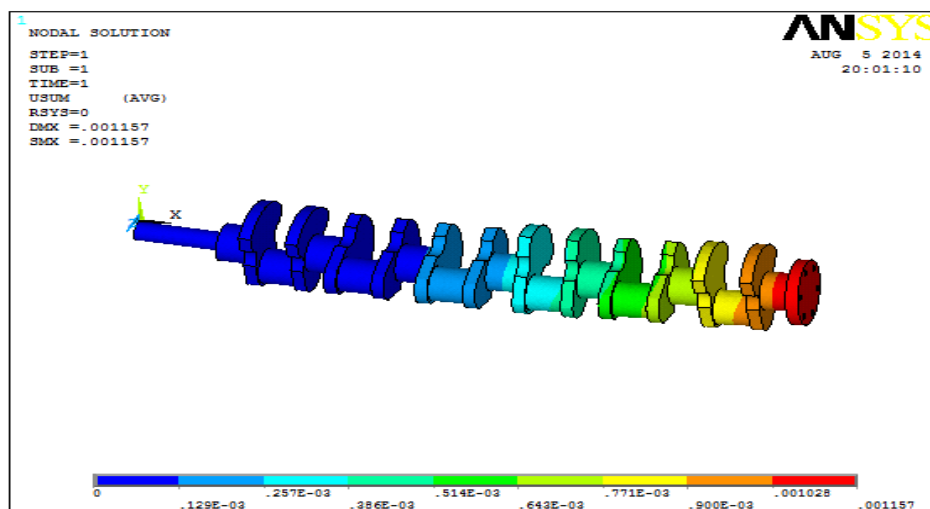


**Figure: 9**: Deformation of crankshaft
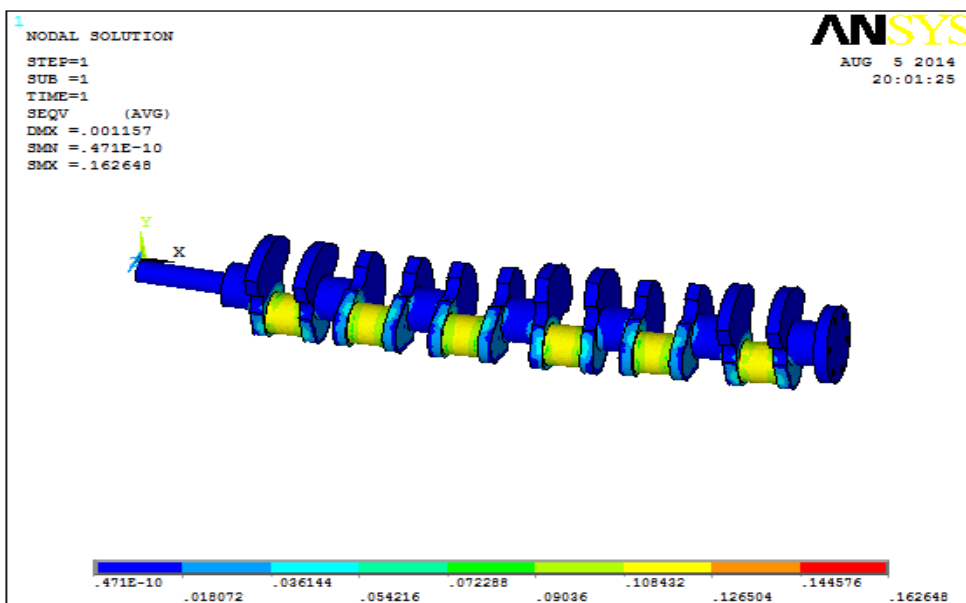
**Figure10:** Von Misses stress for Cast Iron 162.64MPa
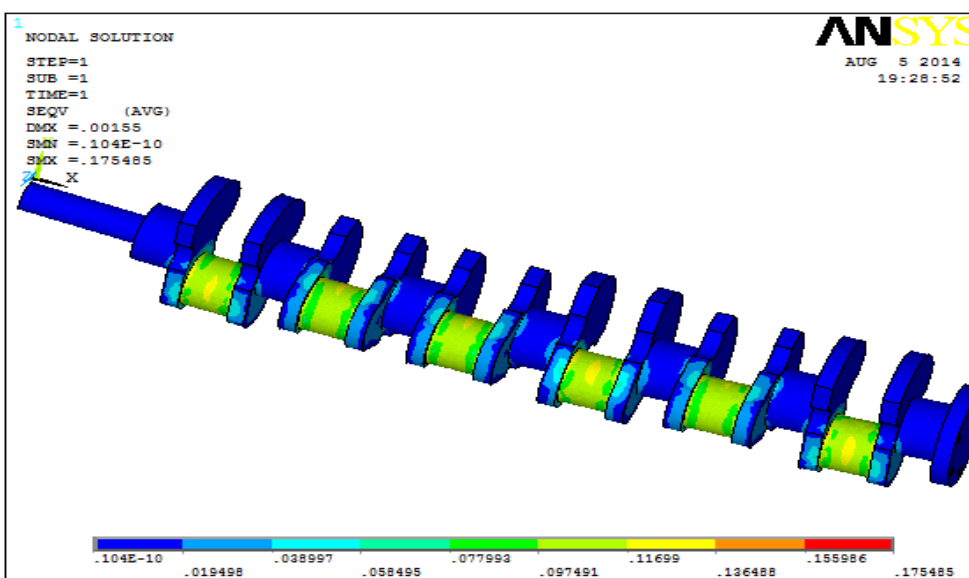


**Figure: 12**: Von Misses Stress for High Carbon Steel 175.48MPa

The stress acting on the Design 2-Modified crankshaft is shown in Figure.10, 11, 12

## X.    Comparison Of Results

After applying loading and boundary conditions results from ansys were obtained and compiled in table

| Model | Design 1-Original | | Design 2-Modified | |
|---|---|---|---|---|
| Material | Von-Misses Stress ($\sigma$)MPa | Weight (kg) | Von-Misses Stress ($\sigma$)MPa | Weight (kg) |
| Cast Iron | 174.92 | 33.23 | 162.64 | 32.21 |
| High Carbon Steel | 189.19 | 33.43 | 175.48 | 32.41 |
| Forged Steel | 184.99 | 35.168 | 171.64 | 34.04 |

**Table 2**: Results obtained from ANSYS

## XI. Conclusion

Finite Element analysis of the six cylinder crankshaft has been done using FEA tool ANSYS. From the results obtained from FE analysis, many discussions have been made.

1. Results show the improvement in the strength of the crankshaft as the maximum limits of stresses. The value of von-misses stresses that comes out from the analysis is far less than material yield stress so our design is safe.
2. The weight of the crankshaft is also reduced by 1133g (5% of weight Reduction) from Design 1-Original to Design 1-Modified. Thereby, reduces the inertia force.
3. As the weight of the crankshaft is decreased this will decrease the cost of the crankshaft and increase the engine performance
4. Above Results shows that FEA results conformal matches with the theoretical calculation so we can say that FEA is a good tool to reduce the time consuming theoretical work.
5. 

### Acknowledgements

### REFERENCES

[1]. A. Solanki, K. Tamboli,M.J, M.J, M.J, M.J. Zinjuwadia, (2011), "Crankshaft Design and Optimization- A Review" National Conference on Recent Trends in Engineering & Technology.
[2] J. Meng, Y. Liu, R. Liu, (2011), "Finite Element analysis of 4-Cylinder Diesel Crankshaft" I.J. Image, Graphics and Signal Processing, vol 5, pp. 22-29
[3]. F. H. Montazersadgh, A. Fatemi, (2007), "Project Report on Stress Analysis and Optimization of Crankshafts Subject to Dynamic Loading" The University of Toledo
[4]. Y. Gongzhi, Y. Hongliang, D. Shulin, (2011), "Crankshaft Dynamic Strength Analysis for Marine Diesel Engine" Third International Conference on Measuring Technology and Mechatronics Automation, pp. 795-799
[5]. G. Yingkui, Z. Zhibo, (2011), "Strength Analysis of Diesel Engine Crankshaft Based on PRO/E and ANSYS" Third International.

# Energy Management of Distributed Generation Inverters using MPC Controller in a MICROGRID Applications

Mohana. P[1], Sivanagaraju. S. V[2]

[1,2] *Department of Electrical and Electronics Engineering, JNTU Anantapur*

***Abstract:*** *This paper presents a microgrid consisting of different distributed generation (DG) units that are connected to the distribution grid. An energy-management algorithm is implemented to coordinate the operations of the different DG units in the microgrid for grid-connected and islanded operations. The proposed microgrid consists of a photovoltaic (PV) array which functions as the primary generation unit of the microgrid and a proton-exchange membrane fuel cell to supplement the variability in the power generated by the PV array. A lithium-ion storage battery is incorporated into the microgrid to mitigate peak demands during grid-connected operation and to compensate for any shortage in the generated power during islanded operation. The control design for the DG inverters employs a new model predictive control algorithm which enables faster computational time for large power systems by optimizing the steady-state and the transient control problems separately. The design concept is verified through various test scenarios to demonstrate the operational capability of the proposed microgrid, and the obtained results are discussed.*

***Index Terms:*** *Distributed generation (DG), energy management, microgrid, model predictive control (MPC).*

## I. Introduction

Over the last decade, efficient and reliable communication and control technologies, coupled with an increase in smarter electrical facilities, such as electric vehicles and smart meters, have resulted in an increasing number of consumers participating in demand response management (DRM) [1]–[5]. The current research is also focused on achieving a smarter grid through demand-side management (DSM), increasing energy reserves and improving the power quality of the distribution system, such as harmonic compensation for nonlinear loads [5]–[8]. These new trends enable higher levels of penetration of renewable generation, such as wind and solar power into the grid. The integration of renewable sources can supplement the generation from the distribution grid. However, these renewable sources are intermittent in their generation and might compromise the reliability and stability of the distribution network. As a result, energy-storage devices, such as batteries and ultra-capacitors, are required to compensate for the variability in the renewable sources. The incorporation of energy-storage devices is also critical for managing peak demands and variations in the load demand. In this paper, a microgrid consisting of a photovoltaic (PV) array, a proton-exchange membrane fuel cell (PEMFC), and a lithium-ion storage battery (SB) is proposed. The PEMFC is used as a backup generator unit to compensate for the power generated by the intermittent nature of the PV array. The SB is implemented for peak shaving during grid-connected operation, and to supply power for any shortage in generated power during islanded operation and to maintain the stability of the distribution network. An energy-management algorithm is designed for the microgrid to coordinate the sharing of power among different DG units. The proposed controller for the inverters of DG units is based on a newly developed model predictive control (MPC) algorithm, which optimizes the steady-state and the transient control problems separately. In this way, the computation time is greatly reduced. In what follows, this paper provides a comprehensive solution for the operation of a microgrid which will simultaneously dispatch real and reactive power during both grid-connected and islanded operations, compensate for harmonics in the load currents, and perform peak shaving and load shedding under different operating conditions.

## II. System Description And Modeling

### A. System Description

Fig. 1 shows the configuration of the microgrid proposed in this paper that is designed to operate either in the grid-connected or islanded mode. The main DG unit comprises a 40-kW PV array and a 15-kW PEMFC, which are connected in parallel to the dc side of the DG inverter 1 through dc/dc boost converters to regulate the

dc-link voltage of the DG inverter at the desired level by delivering the necessary power. The PV array is implemented as the primary generation unit and the PEMFC is used to back up the intermittent generation of the PV array. When there is ample sunlight, the PV array operates in the MPPT mode to deliver maximum dc power $P_{pv}$ which is discussed in detail in [9] and [10], and the output voltage of the PV array is permitted to vary within an allowable

TAN *et al.*: COORDINATED CONTROL AND ENERGY MANAGEMENT OF DG INVERTERS IN A MICROGRID
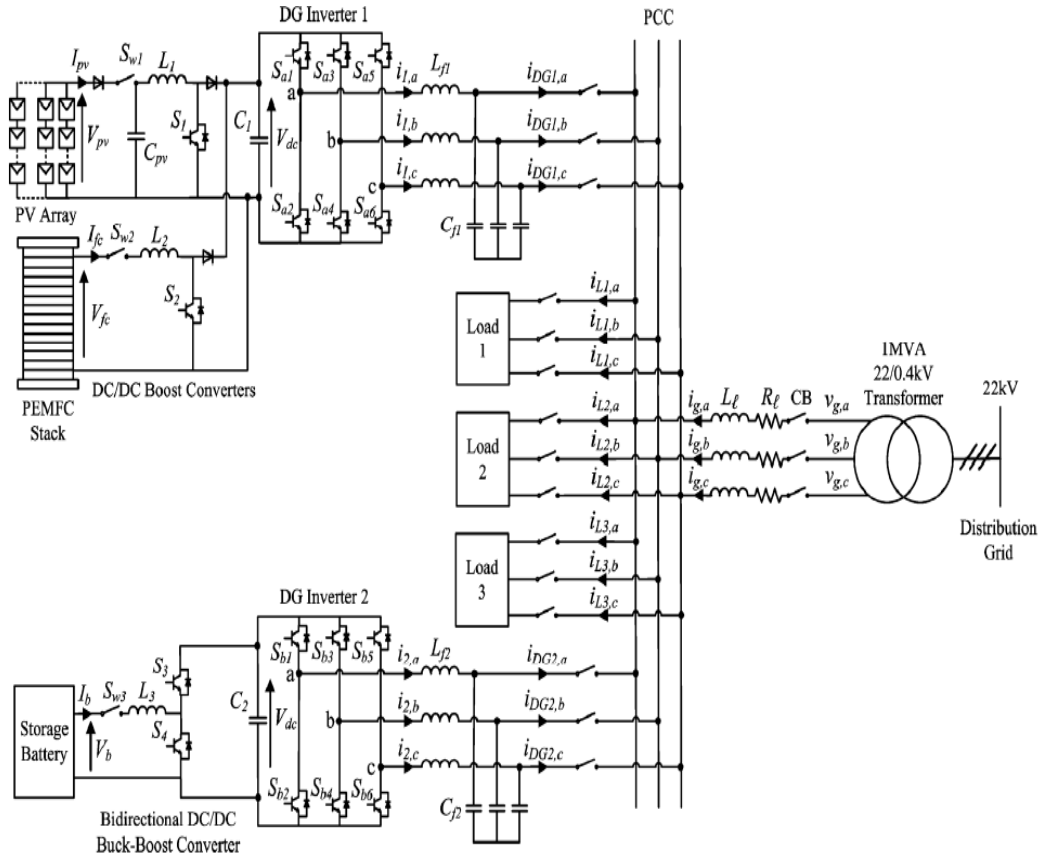


Fig. 1. Overall configuration of the proposed microgrid architecture.
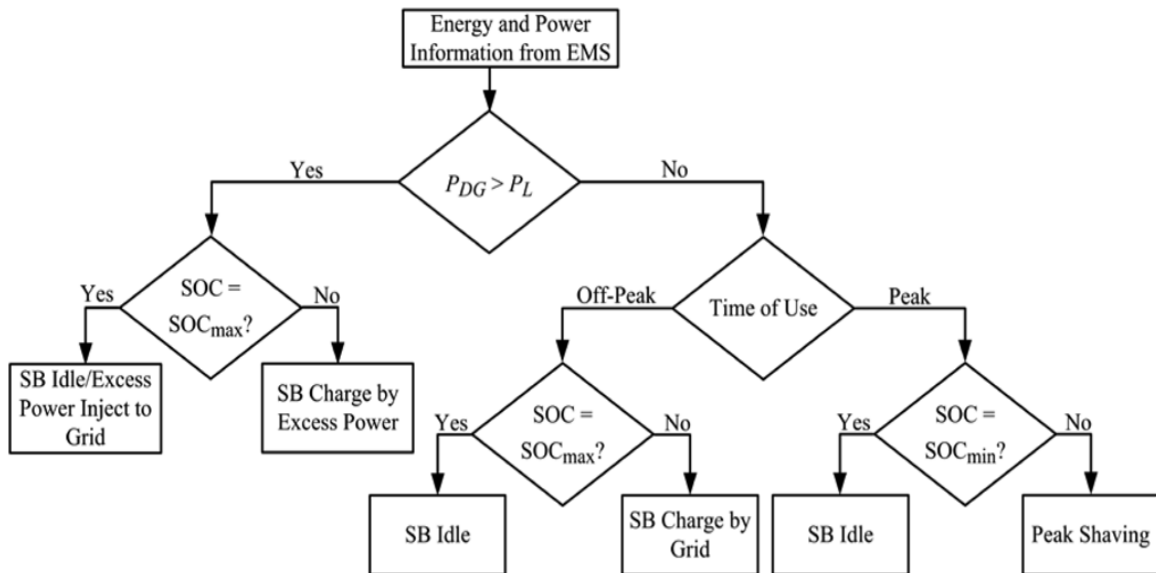


Fig. 2. Operation of the SB during grid-connected operation
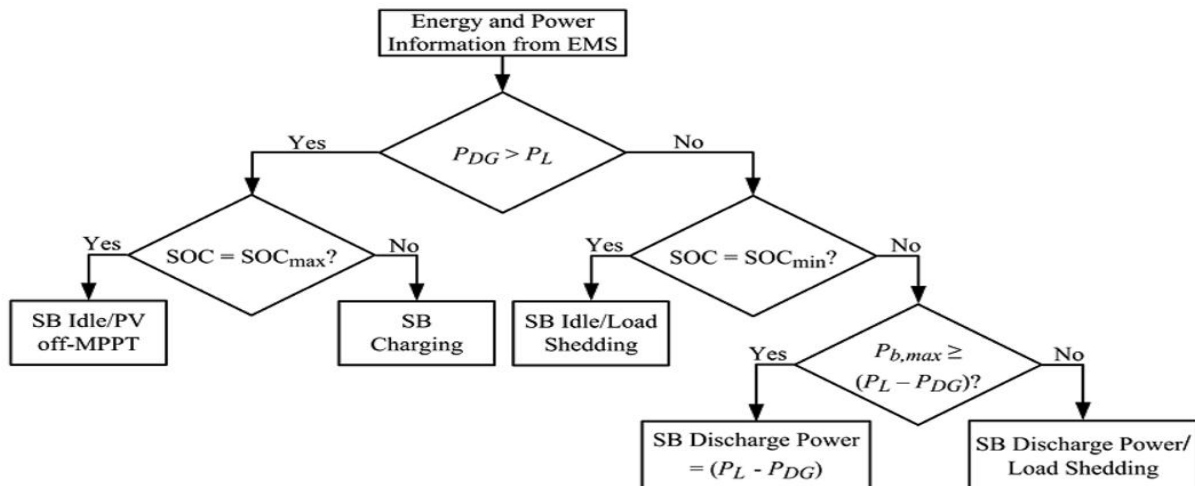
. Fig. 3. Operation of the SB during islanded operation

Range to ensure proper operation of the DG inverter. To maintain the level of the dc-link voltage at the required level, the PEMFC supplements the generation of the PV array to deliver the necessary $P_{fc}$. when the output voltage of the PV array falls below a preset limit, the PV array is disconnected from the DG unit and the PEMFC functions as the main generation unit to deliver the required power. A 30-Ah lithium-ion SB is connected to the dc side of DG inverter2 through a bidirectional dc/dc buck-boost converter to facilitate the charging and discharging operations. During islanded operation, the role of the SB is to maintain the power balance in the microgrid which is given by

$$P_{DG} + P_b = P_L \qquad (1)$$

Where $P_{DG}$ is the power delivered by the main DG unit, $P_b$ is the SB power which is subjected to the charging and discharging constraints given by

$$P_b \leq P_{b,max} \qquad (2)$$

And $P_L$ is the real power delivered to the loads. The energy constraints of the SB are determined based on the state-of-charge (SOC) limits which are given as

$$SOC_{min} < SOC < SOC_{max} \qquad (3)$$

Although the SOC of the battery cannot be measured directly, it can be determined through several estimation methods presented in [11] and [12]. When the microgrid operates islanded from the distribution grid, the SB can operate in the charging, discharging, or idle mode depending on its SOC and $P_b$. The flowcharts in Figs. 2 and 3 summarize the operation of the SB based on the output information provided by an energy-management system (EMS) during grid-connected and islanded operation, respectively. The EMS controls and monitors different aspects of power management, such as load forecasting, unit commitment, economic dispatch, and optimal power flow through a centralized server. Important information, such as field measurements from smart meters, transformer tap positions, and circuit- breaker (CB) status are all sent to the centralized server for processing through Ethernet. During grid-connected operation, the distribution grid is connected to the microgrid at the point of common coupling (PCC) through a circuit breaker (CB). The role of the main DG unit functions to provide local power and voltage support for the loads and, hence, reduces the burden of generation and delivery of power directly from the distribution grid. With the proliferation of power-electronics equipment being connected to the microgrid, the load currents could be distorted due to the presence of harmonic components. The DG units also function to compensate for any harmonics in the currents drawn by nonlinear loads in the microgrid, so that the harmonics will not propagate to other electrical networks connected to the PCC. Generally, there are variations in the power generated by the PV array and that demanded by the loads. If the power generated by the main DG unit is greater than the total load demand in the microgrid, the excess power can be used to charge the SB or injected into the distribution grid, depending on the SOC of the SB, as shown in Fig. 2. Conversely, when the total load demand is greater than the power generated by the main DG unit, the SB can be controlled to achieve different energy-management functions depending on its SOC and the time of use (TOU) of electricity. During off-peak periods as shown in Fig. 2, when the cost of generation from the grid is low and if the SB's SOC is below the maximum SOC limit , the SB can be charged by the grid and the loads will be supplied by the main DG unit and the grid. During peak periods, when the cost of generation from the grid is high and if the SB's SOC is above the minimum SOC limit , the SB can deliver

power to the grid to achieve peak shaving. When a fault occurs on the upstream network of the distribution grid, the CB operates to disconnect the microgrid from the distribution grid. The main DG unit and the SB are the sole power sources left to regulate the loads. In the case when the generation capacity of the main DG unit is unable to meet the total load demand, the SB is required to provide for the shortage in real and reactive power to maintain the power balance and stability of the microgrid as shown in Fig. 3. When the total load demand exceeds the generation capacity of the main DG unit and the SB, the EMS detects a drop in the system frequency and load shedding for noncritical loads is required to restore the system frequency and maintain the stability of the microgrid.
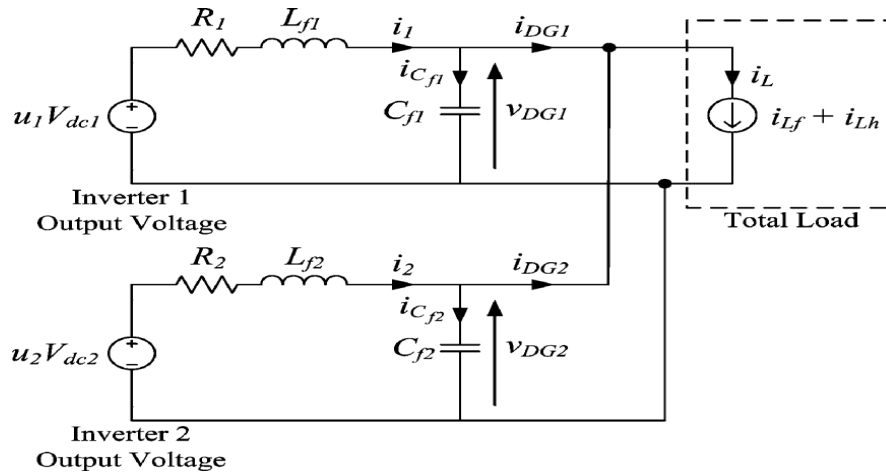


Fig. 4. Equivalent single-phase representation of the DG inverters for Grid connected operation
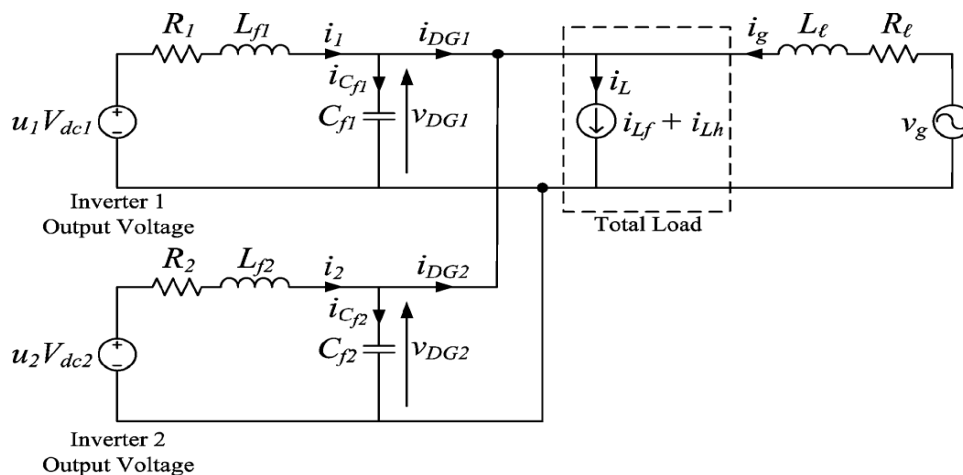


Fig. 5. Equivalent single-phase representation of the DG for islanded operation.

**B. DG Inverter Modeling**
        Figs. 4 and 5 show the equivalent single-phase representation of the DG inverters for grid-connected and islanded operation, respectively [13]–[15]. The switched voltage across the output of the th DG inverter is represented                                                                                                                          by $u_i V_{dcj}$ where $u_i$ is the control input and $j = 1,2$ The output of the DG inverter is interfaced with an LC filter represented by $L_{fi}$ and $C_{fi}$ to eliminate the high switching frequency harmonics generated by the DG inverter. The resistance $R_i$ models the loss of the DG inverter. The total load current $i_L$, which is the sum of the currents delivered to the load k, is given by

$$i_L = \sum_{k=1,2,3} i_{LK} = i_{L1} + i_{L2} + i_{L3} \qquad (4)$$

and can be modeled as two components consisting of fundamentals $i_{Lf}$ and harmonic $i_{Lh}$ with their peak amplitudes $I_{Lf}$ and $I_{Lh}$ respectively, and is represented by

$$i_L = i_{Lf} + i_{Lh} = I_{Lf} \sin(\omega t - \varphi_{Lf})$$
$$+ \sum_{h=3,5,...}^{N} I_{Lh} \sin(h\omega t - \varphi_{Lh})$$

---

$$=I_{Lf} \sin \omega t \cos \varphi_{Lf} - I_{Lf} \cos \omega t \sin \varphi_{Lf}$$
$$+\sum_{h=3,5...}^{N} I_{Lh} \sin(h\omega t - \varphi_{Lh})$$
$$=i_{Lf,p}+i_{Lf,q}+i_{Lh} \tag{5}$$

where $\varphi_{Lf}$ and $\varphi_{Lh}$ are the respective phase angles of the fundamental and harmonic components of $i_L$ , and $i_{Lf,p}$ and $i_{Lf,q}$ are the instantaneous fundamental phase and quadrature components of $i_L$ . To achieve unity power factor at the grid side, compensate for the harmonics in the load currents and concurrently achieve load sharing, the inverter of the DG unit supplies a current $i_{DGj}$ that is given by

$$i_{DGj}=(i_{Lf,p} - i_g)+i_{Lf,q}+i_{Lh} \tag{6}$$

where $i_g$ is the grid current. As shown in Fig. 4, the distribution grid is supplied by a utility substation represented by a voltage source $u_g$ during grid-connected operation, and is connected to the microgrid and the loads via a distribution line with resistance $R_l$ and inductance $L_l$ . In the grid-connected mode, the grid voltage is known and the microgrid shares the load demand with the grid. Hence, to
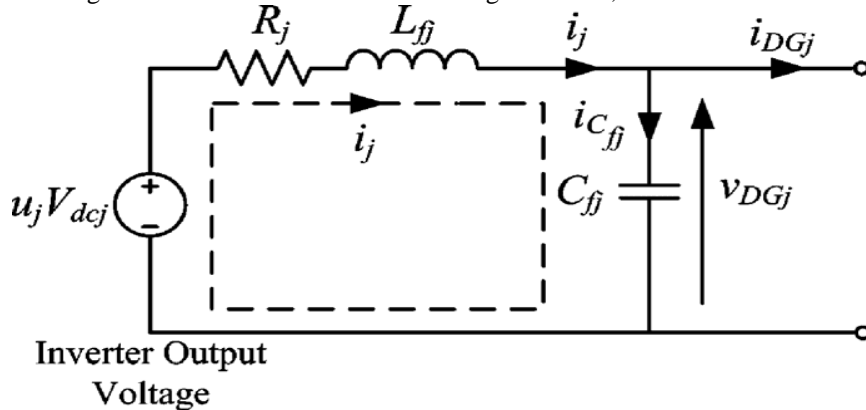


Fig. 6. Single-phase representation of the the DG inverter for grid-connected and islanded operations

Control the power delivered to the loads, the output current of the DG inverter is controlled using the current control mode (CCM). During islanded operation, the microgrid will supply the overall load demand as shown in Fig. 5, and it is required that the output voltage be regulated to a pure sine wave with a fixed magnitude. This can be achieved through the voltage-control mode (VCM). The control design for the DG inverter will be elaborated on further in Section III. To derive a state-space model for the DG inverter during both grid-connected and islanded operations, Kirchhoff's voltage and current laws are applied to the current loop $i_j$ as shown in Fig. 6, and the following equations are obtained:

$$\frac{di_j}{dt} = -\frac{R_j}{L_{fj}}i_j - \frac{1}{L_{fj}}u_{DGj}+\frac{V_{dcj}}{L_{fj}}u_j \tag{7}$$

$$\frac{du_{jDGj}}{dt} =-\frac{1}{C_{fj}}i_j+\frac{1}{C_{fj}}i_{DGj} \tag{8}$$

where $i_j$ is the current passing through $L_{fj}$ . Hence, the gridconnected DG inverter model can be written as

$$\dot{x}_{gj} = A_{gj}x_{gj} + B_{gj1}u'_j + B_{gj2}u_j \tag{9}$$

$$y_{gj} = C_{gj}x_{gj} + D_{gj1}u'_j + D_{gj2}u_j \tag{10}$$

where the subscripts $g$ and $j$ represent the model of DG inverter $j$ during grid-connected operation and

$$A_{gj} = -\frac{R_j}{L_{fj}} \; ; B_{gj1} = [-\frac{1}{L_{fj}} \quad 0] \; ; B_{gj2} = \frac{V_{dcj}}{L_{fi}} \; ; C_{gj}=1$$

$$D_{j1} = [0 \quad -C_{fj}]; D_{gj2} = 0$$

$x_{gj} = i_j$ is the state; $u'_j = [u_{DGj} \quad du_{dgj}/dt]^T$ exogenous input; $u_j$ is the control input, with -1≤ $u_j$ ≤1; and $y_{gj} = i_{DGj}$ is the output, which will be regulated to track the desired periodic reference waveform. During islanded operation, the frequency will change due to power imbalance in the microgrid. This change in frequency is detected by the EMS of the microgrid, which is used to manage and monitor the power dispatch by each DG unit. Based on the frequency change information, the EMS will require the main DG unit and the SB to generate the necessary power to meet the overall load demand in the microgrid as shown in the flowchart of Fig. 3, such that (1) is satisfied. During islanded operation, it follows from (7) and (8) that DG inverter can be modeled as

$$\dot{x}_{ij} = A_{ij}x_{ij} + B_{ij1}i'_j + B_{ij2}u_j \tag{11}$$

$$y_{ij} = C_{ij}x_{ij} + D_{ij1}i'_j + D_{ij2}u_j \tag{12}$$

where the subscript $i$ denotes the model of the DG inverter $j$ during islanded operation( $j$ =1,2) and

$$A_{ij} = \begin{bmatrix} -\frac{R_j}{L_{fj}} & -\frac{1}{L_{fj}} \\ \frac{1}{C'_f} & 0 \end{bmatrix} ; B_{ij1} = \begin{bmatrix} 0 \\ -\frac{1}{C'_f} \end{bmatrix} ; B_{ij2} = \begin{bmatrix} \frac{V_{dcj}}{L_{fj}} \\ 0 \end{bmatrix}$$

$$C_{ij} = \begin{bmatrix} 0 & 1 \\ 1 - \frac{C_{fj}}{C'_f} & 0 \end{bmatrix} ; D_{ij1} = \begin{bmatrix} 0 \\ \frac{C_{fj}}{C'_f} \end{bmatrix} ; D_{ij2} = \begin{bmatrix} 0 \\ 0 \end{bmatrix}$$

With $C'_f = \sum_{j=1}^{2} C_{fj}$ ; $x_{ij} = [i_j \quad u_{DGj}]^T$ is the state vector; $i'_j = i_L - \sum_{n \neq j} i_n$ is the exogenous input of the DG inverter $j$; $u_j$ is the control input, with -1≤ $u_j$ ≤1 and $y_{ij} = [u_{DGj} \quad i_{DGj}]^T$ is the output, which will be regulated to track the desired reference waveform. Note that although the emphasis is on the voltage $u_{DGj}$, both $u_{DGj}$ and $i_{DGj}$ will be regulated in the VCM to ensure that the power is delivered. Furthermore, it is assumed that the exogenous input $i'_j$ in the model is not directly measurable by the DG inverter $j$ since it involves quantities outside that inverter. Precisely, $i'_j$ represents the sum of all load currents $i_L$ minus the sum of all $i_n$ from the other DG inverters $n \neq j$ in the microgrid. Although only one other inverter has been presented in the proposed microgrid, the model is extendable to more DG inverters.

## III.   Control Design

With the mathematical model presented in Section II-B, this paper proposes a novel MPC algorithm for the control of the DG inverters of the microgrid. The proposed algorithm is a newly developed MPC algorithm specifically designed for fast-sampling systems, to track periodic signals so as to deal with the dual-mode operation of the microgrid. The algorithm decomposes the MPC optimization into a steady-state sub-problem and a transient sub-problem, which can be solved in parallel in a receding horizon fashion. Furthermore, the steady-state sub problem adopts a dynamic policy approach in which the computational complexity is adjustable. The decomposition also allows the steady-state sub-problem to be solved at a lower rate than the transient sub-problem if necessary. These features help to achieve a lower computational complexity and make it suitable for implementation in a fast-sampling system like our microgrid applications. In the simulation studies in this paper, the sampling interval is chosen as 0.2ms, which is considered pretty small in conventional MPC applications, but necessary for the high order of harmonics being tackled for our problem. According to [16], sampling in the range of tens of kHz is possible with state-of-the-art code generation techniques. It is noted that in either the grid-connected or the islanded operation, the state-space model of Section II-B after time-discretization will take the form

$$x^+ = Ax + B_1 w + B_2 u \qquad (13)$$
$$y = Cx + D_1 w + D_2 u \qquad (14)$$

where the superscript + represents the time-shift operator (with sampling interval $T_s$ ), and the exogenous signal $\omega$ is periodic. In general, any periodic signal with a finite number of harmonics can be written as the output of an autonomous finite-dimensional linear time-invariant state-space model. Furthermore, the initial state of this autonomous model determines the magnitude and phase angle of this periodic signal. Hence, the exogenous signal in (13) and (14) together with the reference that in (14) desires to track can be modeled by

$$\varepsilon^+ = A_\epsilon \varepsilon \qquad (15)$$
$$\omega = C_\omega \varepsilon$$
$$d = C_d \varepsilon \qquad (17)$$

for some $A_\epsilon$ , $C_\omega$ and $C_d$ as described above. For the CCM during grid-connected operation, $y = i_{DG}$  and the current reference for $i_{DG}$ to track consist of the same order of harmonics as $i_L$ and is derived from the desired active and reactive power outputs of the DG units generated by the EMS. On the other hand, for the VCM as described in Section II-B during islanded operation, $y = [u_{DG} \; i_{DG}]^T$  for the DG unit and the reference $d = [du_{DG} \quad di_{DG}]$ consists of a voltage reference and a current reference. The voltage reference $du_{DG}$ for $u_{DG}$ to track is typically a pure sine wave, which is derived from the monitored prior to islanding. To ensure that the respective DG units deliver the necessary power for stable operation of the microgrid during islanded operation, the current reference $i_{DG}$ for $di_{DG}$ to track is regulated according to the power reference generated by the EMS.

The state-space model given by (15)–(17) is known as the exogenous system in this paper. Although only odd harmonics up to the 29th order have been considered, the methodology can be easily extended to include even harmonics. The exogenous state $\epsilon$, which essentially represents the sets of Fourier coefficients of $\omega$ and $d$ , can be automatically identified using a Kalman-based observer known as the exogenous Kalman filter once the signal $\omega$ is measured and the reference d  is specified. The exogenous Kalman filter is given by

$$\widetilde{\xi}^+ = A_\xi \widetilde{\xi} + L_w(w - \widetilde{w}) + L_d(d - \widetilde{d}) \qquad (18)$$
$$\widetilde{w} = C_w \widetilde{\xi} \qquad (19)$$
$$\widetilde{d} = C_d \widetilde{\xi} \qquad (20)$$

where is the estimated exogenous state $L_w$, and $L_d$ are the observer gain matrices of the Kalman filter, and the terms $(\omega - \widetilde{\omega})$ and $(d - \widetilde{d})$ are essentially the difference between the actual $\omega, d$ and the estimated $\widetilde{\omega}, \widetilde{d}$ generated from the Kalman filter, such that $(\omega - \widetilde{\omega})$ and $(d - \widetilde{d})$ should tend to zero asymptotically. Since is actually a Fourier decomposition of the periodic signals $\omega$ and $d$, the exogenous Kalman filter given by (18)–(20) functions like a harmonic extraction circuit from the power system point of view [17], [18]. In what follows, the control $u$ in (13) and (14) is decomposed into a steady-state control $u_s$ and a transient control $u_t$ as

$$u = u_s + u_t \qquad (21)$$

such that $u \to u_s$ and $u \to u_t$ asymptotically. Both $u_s$ and $u_t$ will employ aMPC strategy, but the formerwill adopt a dynamic MPC policy whereas the latter will adopt a more conventional finite-horizon approach.
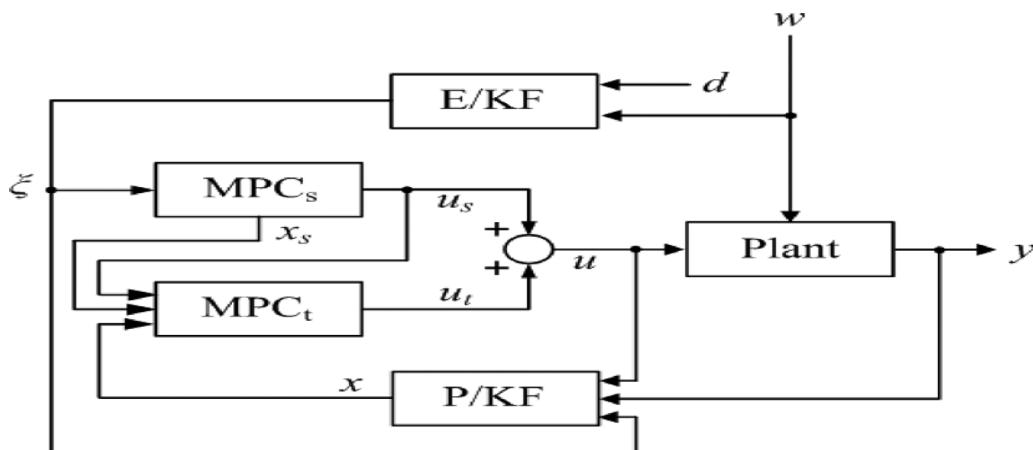


Fig. 7. Overall MPC controller for the DG inverter with E/KF denoting the exogenous Kalman filter and P/KF denoting the plant Kalman filter
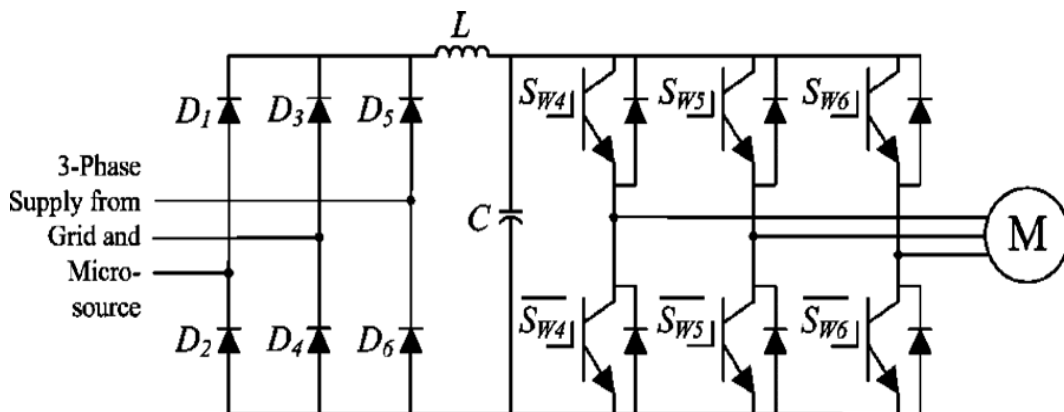


Fig. 8. Configuration of a 15-kVA three-phase ASD.. and (14). Similar to the case of the exogenous Kalman filter, the plant Kalman filter is given by

$$\widetilde{x} = A\widetilde{x} + B_1 w + B_2 u + L_y(y - \widetilde{y})$$
$$\widetilde{y} = c\widetilde{x} + B_1 w + B_2 u$$

where$\widetilde{x}$ is the estimated plant $L_y$ state and is the observer gain matrix of the plant Kalman filter, and the term $(y - \widetilde{y})$ is the difference between the actual measured output and the estimated output . The overall configuration of the proposed control algorithm combining the steady-state control and the transient control is shown in Fig. 7.

## IV. Simulation Studies

The simulation model of the microgrid shown in Fig. 1 is realized in Matlab/Simulink. The microgrid is tested under various conditions to evaluate its capabilities when operating connected and islanded from the distribution grid. Three different load types consisting of linear and nonlinear loads are considered in the studies. For load 1, a 15-kVA three-phase PWM adjustable speed drive (ASD) with its configuration as shown in Fig. 8 is used and load 2 is made up of a three-phase RL load rated at $P_{L2}$= 28 kW and $Q_{L2}$= 18.5 kVAr. Load 3 is a noncritical three-phase dimmer load rated at $P_{L3}$=18 kW and $Q_{L3}$= 12.3 kVAr, which is nonlinear in nature and will be shed under emergency conditions when the generation of the microgrid is unable to meet the load demand. The per-phase currents, $i_{L1}$, $i_{L2}$ and $i_{L3}$ drawn by loads 1, 2, and 3 for $0 \leq t < 0.2s$ are shown in Fig. 9. The system parameters are given in Table I. The impedances of the DG inverters and distribution line have been coarsely estimated since these values are not precisely known in practice.
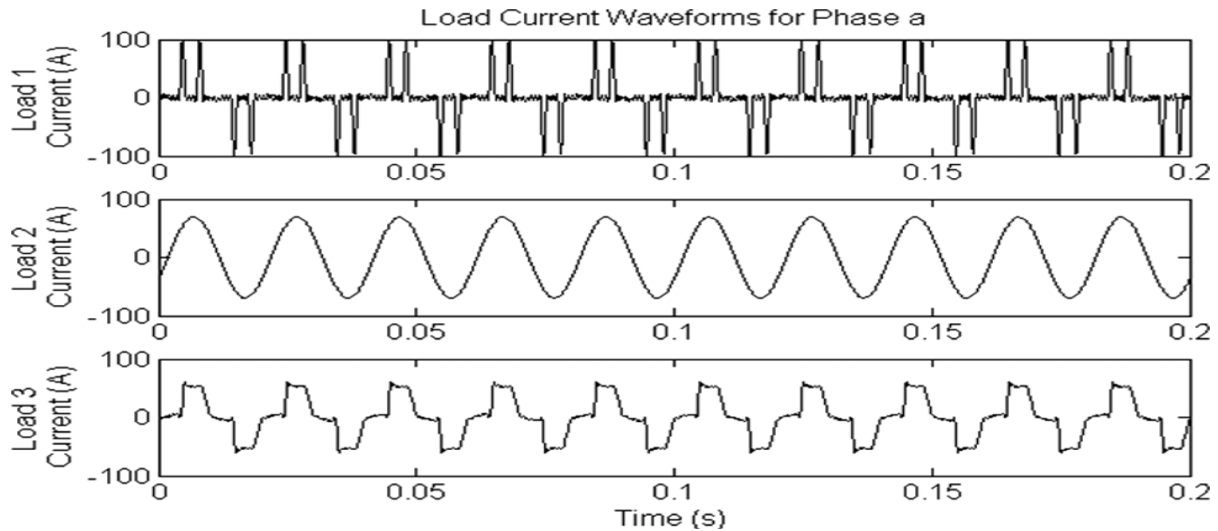


Fig. 9. Per-phase currents drawn by loads 1, 2, and 3.

TABLE
PARAMETERS OF THE PROPOSED SYSTEM

| Parameter | Value |
|---|---|
| Distribution grid voltage | $v_g$ =230V (phase) |
| DC link voltage | $V_{dc}$ =400V |
| Distribution line impedance | $R_\ell = 0.0075\Omega$, $L_\ell = 25.7\mu H$ |
| LC filter | $L_f$= 1.2mH, $C_f$= 20$\mu$F |
| DG inverter loss resistance | $R_f$=0.01 $\Omega$ |
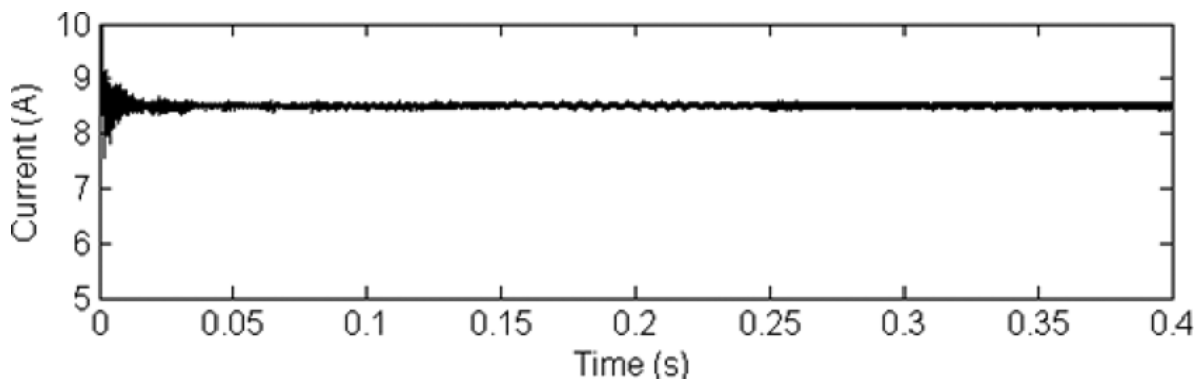


Fig. 10. Waveform of the SB current during charging

**A. Test Case 1:** *Power Quality Improvement With Load-Sharing During Grid-Connected Operation*

The first test case demonstrates the capability of the microgrid to improve the power quality of the distribution network by compensating for the harmonics in the total load current due to the nonlinear loads that are connected to the distribution network, such that the harmonics will not propagate to the rest of the distribution network during grid-connected operation. In this test case, the main DG unit accounts for 20% of the total load demand. The SB is operating in the charging mode to store energy during off-peak period where the cost of generation from the grid is low to meet future sudden demands for power. The SB current (as shown in Fig. 1) and the SOC during charging for $0 \leq t < 0.4$ s are shown in Figs. 10 and 11, respectively. The waveforms of the total load current , the current supplied by the main DG unit and grid current under this test case are shown in Fig. 12. The unsteady measurements in and as shown in Fig. 12(middle) and Fig. 12(bottom) respectively during initialization for $0 \leq t < 0.06s$ are due to the factthat the controller needs a period of 3 cycles to track the generated references. During steady-state condition, the total harmonic distortion (THD) value of $i_L$ is 42.1% as shown in Fig. 12 (top). With the main DG unit compensating for the harmonic currents as shown in Fig. 12 (middle), the THD value of $i_g$ is improved to about 0.4% as shown in Fig. 12 (bottom). To achieve power factor correction at the grid side, the main DG unit is also controlled to provide the reactive component $i_{Lf,q}$ of the current $i_L$ as given in (5). Fig. 13 shows closed-up waveforms of the grid voltage $v_g$ and $i_g$ of phase a for $0.2 \leq t < 0.24s$ . It is observed that the waveform of $i_g$ is in phase with $v_g$ that of with power factor correction.
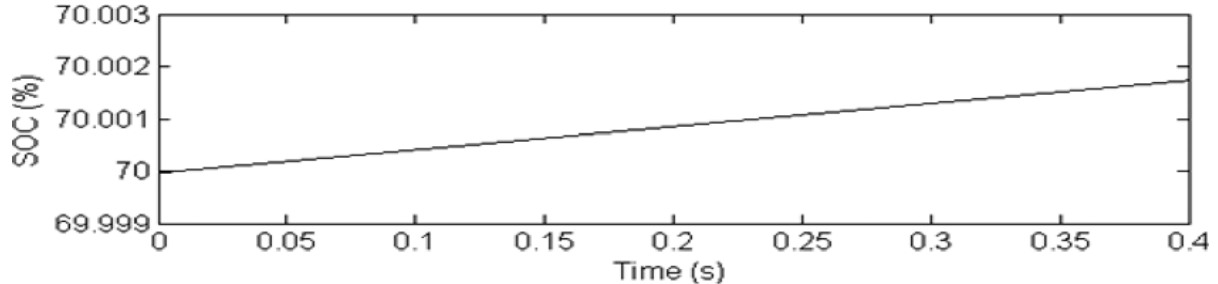

Fig. 11. SOC of the SB during charging
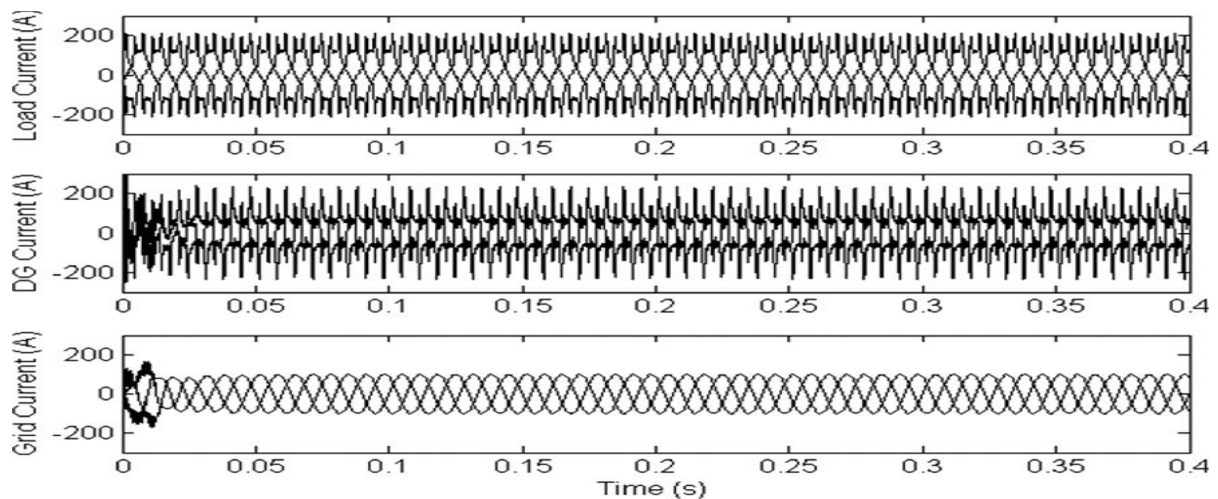

Fig. 12. Waveforms of three-phase load current (top), three-phase DG current (middle), and three-phase grid current (bottom)
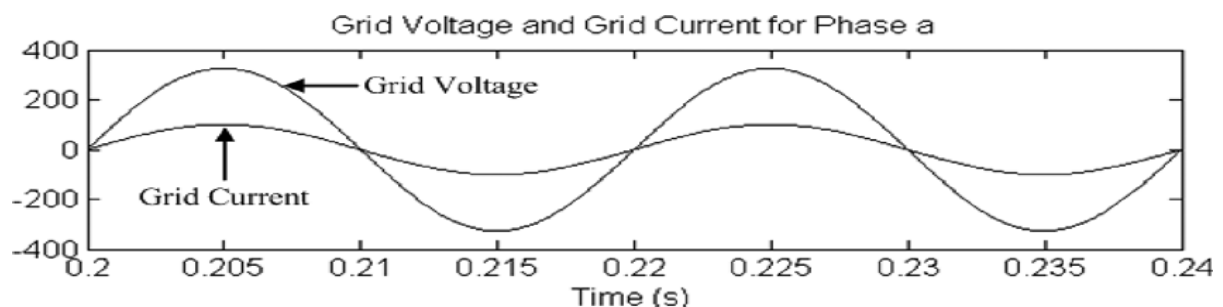

Fig. 13. Waveforms of grid voltage and grid current for phase a

The total real and reactive power delivered to the loads is about 58 kW and 35 kVAr as shown in the power waveforms of Fig. 14. The real power dispatched by the main DG unit is 11.6 kW (20% of the real power consumed by the loads) as shown in Fig. 15, which demonstrates the capability of the main DG unit to dispatch the required power. The main DG unit also delivers all of the reactive power required by the loads to achieve unity power factor at the grid side. The real and reactive power delivered by the grid is shown in Fig. 16. It can be observed from Fig. 16 that the grid supplies 80% (46.4 kW) of the total real power delivered to the loads and dispatches an additional power of about 3 kW to charge the SB. It is also observed that the reactive power supplied by the grid is zero, resulting in unity power factor at the grid side.
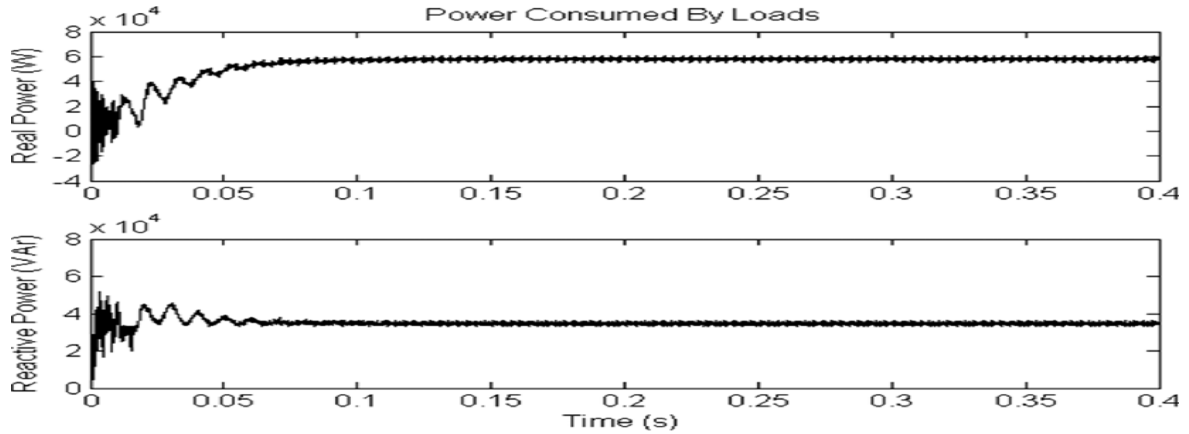
Fig. 14. Real (top) and reactive (bottom) power consumed by loads
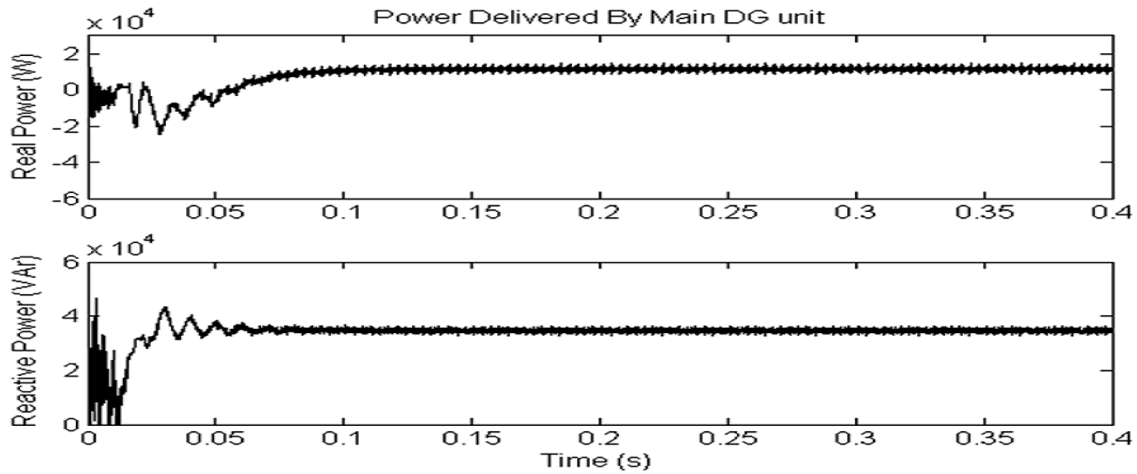
Fig. 15. Real (top) and reactive (bottom) power delivered by the main DG unit
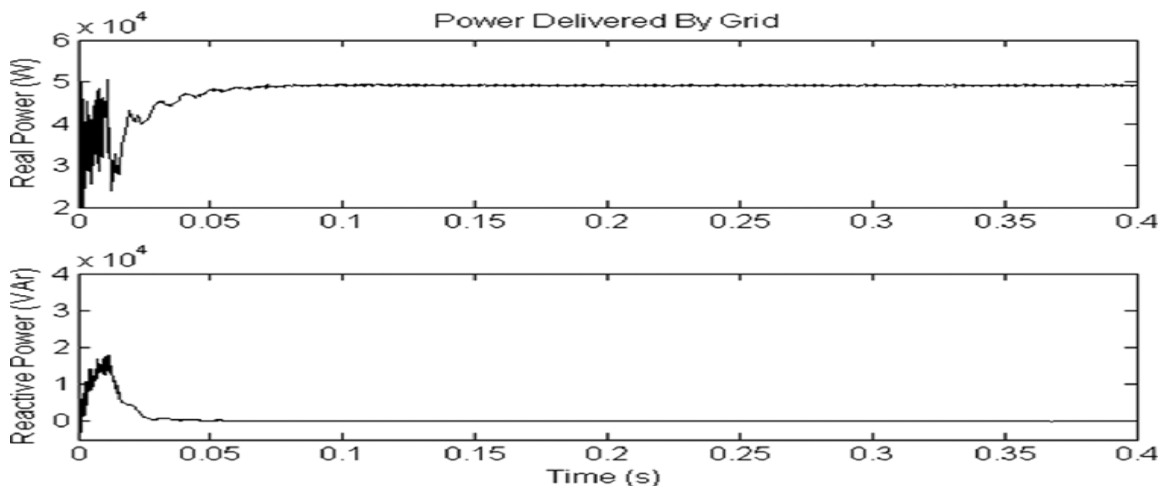
Fig. 16. Real (top) and reactive (bottom) power delivered by the grid

**B. Test Case 2:** *Peak Shaving of Loads During Peak Periods*

The electricity pricing in many countries is impacted by the TOU tariffs. In DSM, energy-storage devices can be used to reduce the burden of generation of power directly from the distribution grid during peak periods. The second test case demonstrates the operation of the microgrid to achieve peak shaving in order to reduce the cost of generation from the grid when consumers practice DSM. Fig. 17 shows a typical hourly demand response curve in a day indicated by the solid line. As in test case 1, the main DG unit is controlled to deliver 20% of the load demand. To achieve peak shaving at 11:00 h, the SB is operating in the discharge mode to provide 20% (11.6 kW) of the load demand. With a further reduction of 20% in the power supplied by the grid, the total load demand at 11:00 h is reduced by a total of 40% as shown by the dotted line in Fig. 17. The power waveforms of the grid for $o \leq t < 0.4$ s are shown in Fig. 18. It can be seen from Fig. 18 that the real power deliveredby the grid is 60% (34.8 kW) of the load demand with peak shaving, and the reactive power supplied is zero with the main DG unit compensating for the reactive components of the load currents. The real power waveform delivered by DG inverter 2 (as shown in Fig. 1) of the SB during discharging is shown in Fig. 19. It can be observed from Fig. 19 that the SB delivers the required real power of about 20% (11.6 kW) of the load demand during peak shaving.
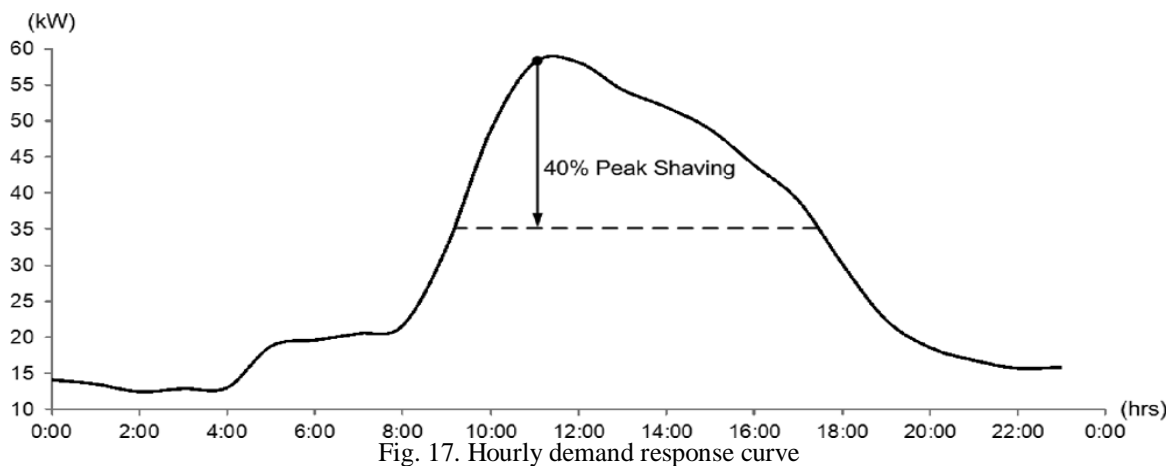

Fig. 17. Hourly demand response curve
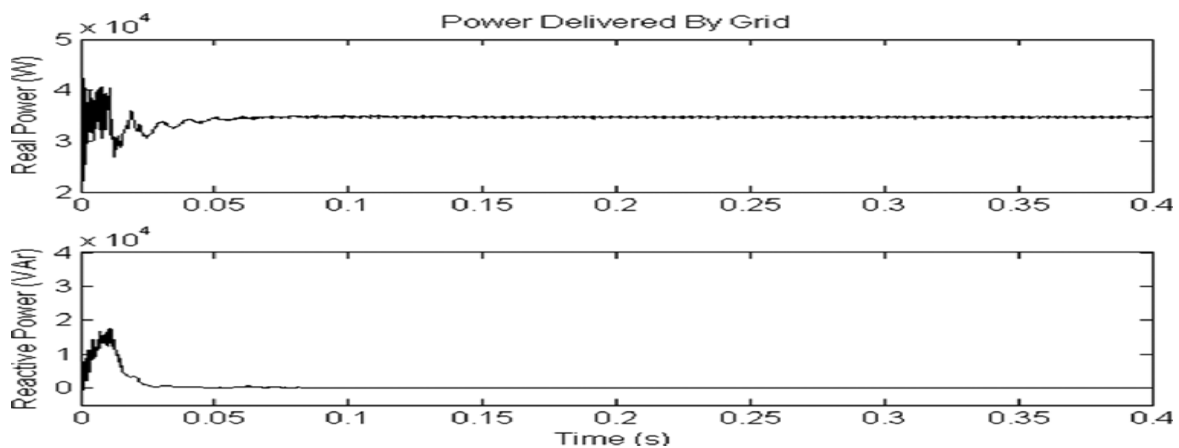

Fig. 18. Real (top) and reactive (bottom) power delivered by the grid
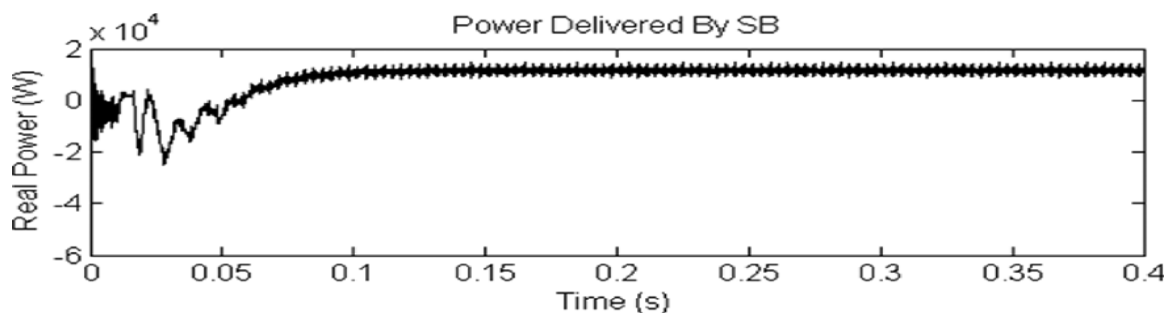

Fig. 19. Real power delivered by SB

**C. Test Case 3:** *Load Shedding During Islanded Operation*

During islanded operation, the total generation of the microgridmight not be able to sustain its generation tomeet the power demand of the loads. Under such circumstances, consumers participating in DRM will allow the non-critical load to be shed so as to maintain the stable operation of the microgrid. The third test case demonstrates the operation of the microgrid when it islands from the grid. In this test case, the microgrid is initially operating in the grid-connected mode for $o \leq t < 0.2$ s. The SB is initially operating in the idle mode and its SOC is 80%. A fault occurs on the upstream network of the distribution grid and the CB operates to disconnect the microgrid from the distribution grid at t=0.2 s.Fig. 20 shows the waveforms of the real and reactive power supplied by the grid. It can be seen from Fig. 20 that the CBmanages to fully isolate the microgrid from the distribution grid in about half a cycle, resulting in zero real and reactive power delivered by the grid for $0.2 \leq t < 0.6$ s. The real power delivered by DG inverter 2 of the SB is shown in Fig. 21. For $0 \leq t < 0.2$ s, the SB is in the idle mode. After the initiation of the islanding operation at t= 0.2 s, theDGinverter 2 is tasked by theEMS to increase its generation to provide real power of about 12.5 kW to the loads which reach steady-state operation in about 3 cycles. With only the main DG unit and the SB supplying for the loads, the power imbalance results in a decrease in the system frequency, which is detected by the EMS. To maintain the stability of the microgrid during islanded operation, the shedding of load 3 $P_{L3=}$18 kW and $Q_{L3}=$ 12.3 kVAr) is also initiated at t= 0.4 s by the EMS such that the total generation from the main DG unit ( $P_{DG}$=27.5 kWand $Q_{DG}$ =22.7 kVAr) and the SB ( $P_{b}$=12.5 kW) can meet the power demand by the loads. A delay of $0 \leq t < 0.2$ s is introduced between islanding of the microgrid and load shedding to cater for frequency transients that might occur momentarily due to the energization of large motor loads. The waveforms of the real and reactive power delivered to the loads for 0 0.6 s are shown in Fig. 22. It can be observed from Fig. 22 that when load 3 is shed at t=0.4s, the total real and reactive power delivered to the loads gradually decreases to settle and operate stably at about 40 kW and 22.7 kVAr, respectively, in about 3 cycles.
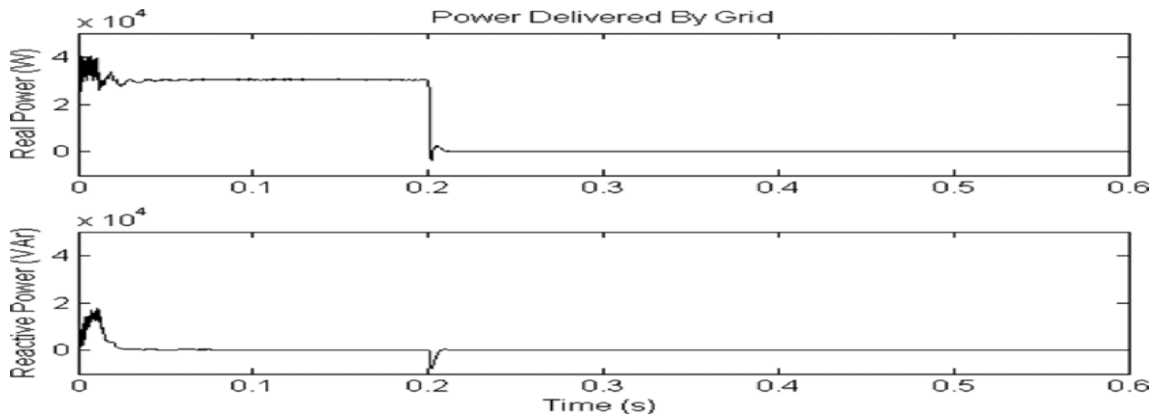

Fig. 20. Real (top) and reactive (bottom) power delivered by the grid
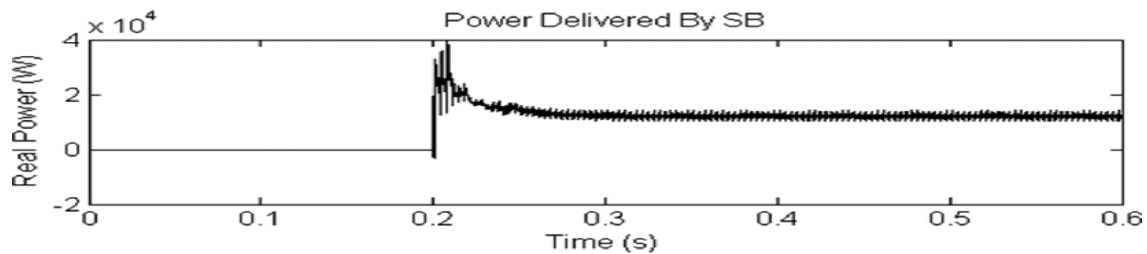

Fig. 21. Real power delivered by SB.
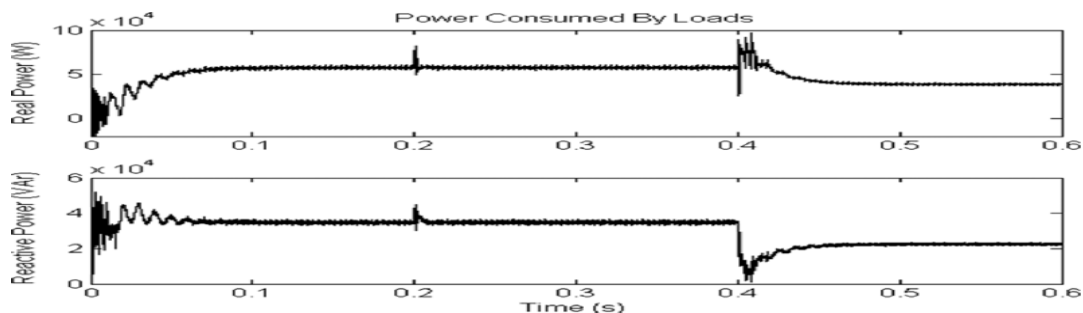

Fig. 22. Real (top) and reactive (bottom) power consumed by loads

## V.  Conclusion

In this paper, a control system that coordinates the operation of multiple DG inverters in a microgrid for grid connected and islanded operations has been presented. The proposed controller for the DG inverters is based on a newly developed MPC algorithm which decomposes the control problem into steady-state and transient subproblems in order to reduce the overall computation time. The controller also integrates Kalman filters into the control design to extract the harmonic spectra of the load currents and to generate the necessary references for the controller. The DG inverters can compensate for load harmonic currents in a similar way as conventional compensators, such as active and passive filters, and, hence, no additional equipment is required for power-quality improvement. To realize the smart grid concept, various energy-management functions, such as peak shaving and load shedding, have also been demonstrated in the simulation studies. The results have validated that the microgrid is able to handle different operating conditions effectively during grid-connected and islanded operations, thus increasing the overall reliability and stability of the microgrid.

## REFERENCES

[1]     S. Braithwait, "Behaviormanagement," IEEE Power and EnergyMag., vol. 8, no. 3, pp. 36–45, May/Jun. 2010.
[2]     N. Jenkins, J. Ekanayake, and G. Strbac, Distributed Generation. London, U.K.: IET, 2009.
[3]     M. Y. Zhai, "Transmission characteristics of low-voltage distribution networks in China under the smart grids environment," IEEE Trans. Power Del., vol. 26, no. 1, pp. 173–180, Jan. 2011.
[4]     G. C. Heffner, C. A. Goldman, and M. M. Moezzi, "Innovative approaches to verifying demand response of water heater load control," IEEE Trans. Power Del., vol. 21, no. 1, pp. 1538–1551, Jan. 2006.
[5]     R. Lasseter, J. Eto, B. Schenkman, J. Stevens, H. Vollkommer, D. Klapp, E. Linton, H. Hurtado, and J. Roy, "Certs microgrid laboratory test bed, and smart loads," IEEE Trans. Power Del., vol. 26, no. 1, pp. 325–332, Jan. 2011.
[6]     A. Molderink, V. Bakker, M. G. C. Bosman, J. L. Hurink, and G. J. M. Smit, "Management and control of domestic smart grid technology," IEEE Trans. Smart Grid, vol. 1, no. 2, pp. 109–119, Sep. 2010.
[7]     A. Mohsenian-Rad, V. W. S.Wong, J. Jatskevich, R. Schober, and A. Leon-Garcia, "Autonomous demand-side management based on gametheoretic  energy consumption scheduling for the future smart grid," IEEE Trans. Smart Grid, vol. 1, no. 3, pp. 320–331, Dec. 2010.
[8]     S. Chowdhury, S. P. Chowdhury, and P. Crossley, Microgrids and Active Distribution Networks. London, U.K.: IET, 2009.
[9]     A. Yazdani and P. P. Dash, "A control methodology and characterization of dynamics for a photovoltaic (PV) system interfaced with a distribution network," IEEE Trans. Power Del., vol. 24, no. 3, pp. 1538–1551, Jul. 2009.
[10]    K. T. Tan, P. L. So, Y. C. Chu, and K. H. Kwan, "Modeling, control and simulation of a photovoltaic power system for grid-connected and stand-alone applications," in Proc. Int. Power Energy Conf., 2010, vol. 56, pp. 608–613.
[11]    M. Charkhgard and M. Farrokhi, "State-of-charge estimation for lithium-ion batteries using neural networks and EKF," IEEE Trans. Ind. Electron., vol. 57, no. 12, pp. 4178–4187, Jun. 2010.
[12]    M. Coleman, C. K. Lee, C. Zhu, and W. G. Hurley, "State-of-charge determination from EMF voltage estimation: Using impedance, terminal voltage, and current for lead-acid and lithium-ion batteries," IEEE Trans. Ind. Electron., vol. 54, no. 5, pp. 2550–2557, Oct. 2007.
[13]    A. Gosh and G. Ledwich, Power Quality Enhancement Using Custom Power Devices. Norwell, MA: Kluwer, 2002, pp. 380–406.
[14]    J.M.Guerrero, J. Matas, L. Garcíade Vicuña, M. Castilla, and J.Miret, "Decentralized control for parallel operation of distributed generation inverters using resistive output impedance," IEEE Trans. Ind. Electron., vol. 54, no. 2, pp. 994–1004, Apr. 2007.
[15]    C. L. Chen, Y. B.Wang, J. S. Lai,Y. S. Lai, and D. Martin, "Design of parallel inverters for smooth mode transfer of microgrid applications," IEEE Trans. Ind. Electron., vol. 25, no. 1, pp. 6–15, Jan. 2010.
[16]    J. Mattingley, Y. Wang, and S. Boyd, "Receding horizon control: Automatic generation of high-speed solvers," IEEE Control Syst. Mag., vol. 31, no. 3, pp. 52–65, Jun. 2011.
[17]    J. A. Macias and A. Gomez, "Self-tuning of Kalman filters for harmonic computation," IEEE Trans. Power Del., vol. 21, no. 1, pp.  501–503, Jan. 2006.
[18]    V. Moreno, A. Pigazo, and R. I. Diego, "Reference estimation technique for active power filters using a digital Kalman algorithms,"

# Experimental Investigation on Performance, Emission and Combustion Characteristics of A LHR Single Cylinder Diesel Engine Operating On Mahua Biodiesel and Diesel Fuel

Sharankumar[1], Prakash.S.Patil[2], Dr. Omprakash Hebbal[3]

[1] *M.Tech Scholar, Department of Mechanical Engineering, PDA College of Engineering, Gulbarga, Karnataka/(INDIA)*
[2] *Associate Professor Department of Mechanical Engineering, PDA College of Engineering, Gulbarga, Karnataka/(INDIA)*
[3] *Professor Department of Mechanical Engineering, PDA College of Engineering/ Gulbarga/Karnataka/ (INDIA)*

**Abstract:** *Diesel is a fossil fuel that is getting depleted at a fast rate. So an alternative fuel is necessary and a need of the hour. Rice bran oil, which is cultivated in India at large scales, has a high potential to become an alternative fuel to replace diesel fuel. Direct use of mahua oil cannot be done, as its viscosity is more than the diesel fuel, and hence affects the combustion characteristics. The mahua oil is esterified to reduce the viscosity and it is blended with diesel on volume basis in different proportions. The use of thermal barrier coatings (TBCs) to increase the combustion temperature in diesel engines has been pursued for over 20 years. Increased combustion temperature can increase the efficiency of the engine. However, TBCs have not yet met with wide success in diesel engine applications because of various problems associated with the thermo-mechanical properties of the coating materials. Although, the in-cylinder temperatures that can be achieved by the application of ceramic coatings can be as high as 850-9000C compared to current temperatures of 650-7000C. The increase in the in-cylinder temperatures helped in better release of energy in the case of biodiesel fuels thereby reducing emissions at, almost the same performance as the diesel fuel. Here the effort has been made to determine the performance, emission and combustion characteristics of MOME blend with diesel in conventional engine and LHR engine.*

*Keywords:* *LHR Engine, normal engine Biodiesel, mahua oil, MOME, Performance, Emission and combustion Characteristics, Thermal barrier coating.*

## I. Introduction

India is one of the fastest developing countries with a stable economic growth, which multiplies the demand for transportation in many folds. Fuel consumption is directly proportionate to this demand. India depends mainly on imported fuels due to lack of fossil fuel reserves and it has a great impact on economy. India has to look for an alternative to sustain the growth rate. Bio-diesel is a promising alternative for our Diesel needs. With vast vegetation and land availability, certainly bio-diesel is a viable source of fuel for Indian conditions. Recent studies and research have made it possible to extract bio-diesel at economical costs and quantities. The blend of Bio-diesel with fossil diesel has many benefits like reduction in emissions, increase in efficiency of engine, higher Cetane rating, lower engine wear, low fuel consumption, reduction in oil consumption etc. It can be seen that the efficiency of the engine increases by the utilization of Bio-diesel. This will have a great impact on Indian economy.Diesel fuels have deep impact on the industrial economy of a country. These are used in heavy trucks, city transport buses, locomotives, electrical generators, farm equipments, underground mine equipments etc. The consumption of diesel fuels in India for the period 2007-08 was 28.30 million tons, which was 43.2% of the consumption of petroleum products. This requirement was met by importing crude petroleum as well as petroleum products. The import bill on these items was 17,838 crores. With the expected growth rate for diesel consumption more than 14% per annum, shrinking crude oil reserves and limited refining capacity, India is likely to depend more on imports of crude petroleum and petroleum products.[1]

## II.  Materials And Methods
The extraction of biodiesel is carried out by base catalyzed transesterification method.

**2.1 Extraction of biodiesel from crude mahua oil:**
To a one liter of crude mahua oil is heated up to 70$^o$C.  300 ml of methanol & 5-7gms sodium methoxide of (catalyst) is added and the mixture is maintained at 65-70$^0$C is about 1½ hours and stirred continuously. The mixture is allowed to settle for 20-30 min until the formation of biodiesel and glycerin layers. The glycerin is removed from the bio-diesel in a separating funnel. The bio diesel produced from mahua biodiesel is ready to use.

**2.2. Transesterificatio**:
It is most commonly used and important method to reduce the viscosity of vegetable oils. In this process triglyceride reacts with three molecules of alcohol in the presence of a catalyst producing a mixture of fatty acids, alkyl ester and glycerol. The process of removal of all the glycerol and the fatty acids from the vegetable oil in the presence of a catalyst is called esterification.



Physical and chemical properties are more improved in esterified vegetable oil because esterified vegetable oil contains more Cetane number than diesel fuel. These parameters induce good combustion characteristics in vegetable oil esters. So unburnt hydrocarbon level is decreased in the exhaust. It results in lower generation of hydrocarbon and carbon monoxide in the exhaust than diesel fuel. The vegetable oil esters contain more oxygen and lower calorific value than diesel. So, it enhances the combustion process and generates lower nitric oxide formation in the exhaust than diesel fuel

**3. The Properties of Diesel and Mahua Biodiesel:**
The different properties of diesel fuel and mahua biodiesel are determined and shown in table.3.2 After transesterification process the fuel properties like kinematic viscosity, cv, density, flash and fire point get improved in case of biodiesel. The calorific value of mahua biodiesel is lower than that of diesel because of oxygen content. The flash and fire point temperature of biodiesel is higher than the pure diesel fuel this is beneficial by safety considerations which can be stored and transported without any risk.

**Table 3.2 Fuel properties**

| properties | D100 | B10 | B20 | B30 | B100 | Apparatus used |
|---|---|---|---|---|---|---|
| Kinematic viscosity at 40$^0$C (cSt) | 4.6 | 4.8 | 4.95 | 5.05 | 5.2 | Redwood viscometer |
| Calorific value(kJ/kg) | 42600 | 42408.39 | 42212.64 | 41500.54 | 38848.08 | Bomb calorimeter |
| Density (kg/m$^3$) | 828 | 830 | 835 | 840 | 880 | Hydrometer |
| Flash point ($^0$C) | 51 | 62 | 70 | 80 | 155 | Pensky-martien's apparatus |
| Fire point($^0$C) | 57 | 75 | 83 | 94 | 165 | Pensky-martien's apparatus |

# III. Experimental Setup

The experimental setup enables study performance, combustion and emission characteristics. The experiments have been carried out on a DI compression ignition engine for various blends of mahua biodiesel with diesel (MB10%, MB20%, MB30%, and MB100) with varying brake power. The experiment is carried out at constant compression ratio of 17.5:1 and constant injection pressure of 200 bars by varying brake power.



| | |
|---|---|
| Manufacture : | Kirlosker oil engines Ltd, India |
| Model : | TV-SR, naturally aspirated |
| Engine | Single cylinder, DI |
| | |
| Bore/stroke | 87.5mm/110mm |
| Compression Ratio | 17.5:1 |
| speed | 1500r/min, constant |
| Rated power | 5.2kw |
| Working cycle | 4 stroke |
| Injection pressure | 200bar/23 def TDC |
| Type of sensor | Piezo electric |
| Response time | 4 micro seconds |

Fig 4.1: Photograph of engine setup           Table 4.1: Engine specification

# IV. Results And Discussions

**4.2 Performance, emission and combustion characterstics of mahua bio-diesel and its blends on diesel engine:**

**4.2.1 Variation of brake thermal efficiency with brake power**
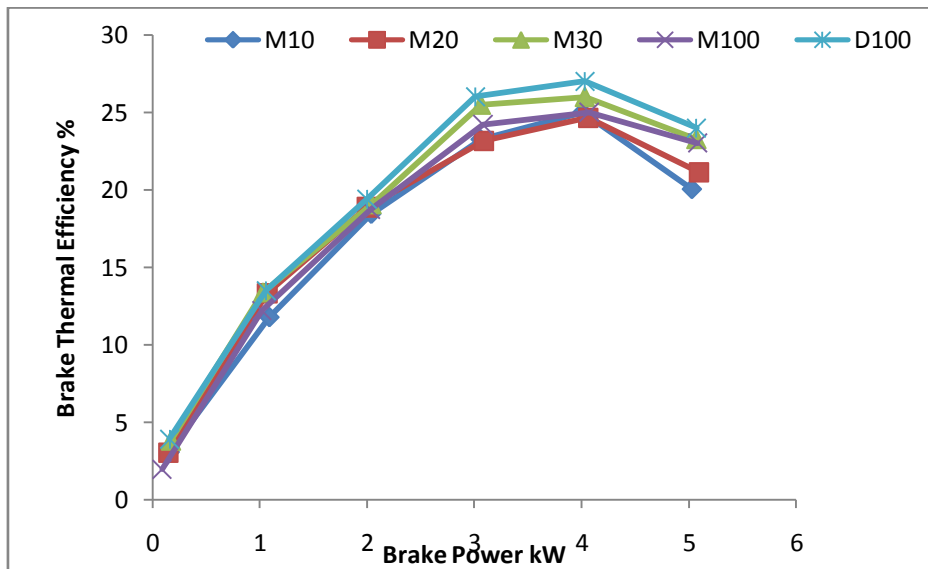


Fig- 4.1 Variation of brake thermal efficiency with brake power

The variation of brake thermal efficiency with brake power for diesel, mahua biodiesel and their blends are shown in fig.4.1. Brake thermal efficiency of 30% blend is very close to diesel for entire range of operation. Maximum brake thermal efficiency diesel oil is 27% against 26% of 30% blend which is lower by 1% we can say that of brake thermal efficiency of 30% blend is well comparable with diesel oil. Brake thermal efficiency of other blends follows in order of 10%, 20%, blend and mahua biodiesel. The maximum brake thermal efficiency of 20% and mahua biodiesel are 24.65% and 25% against 25.62% of diesel oil. And minimum brake thermal efficiency is 1.95% of mahua biodiesel at 0.09kw brake power.

**4.2.2 Variation of specific fuel consumption with brake power**
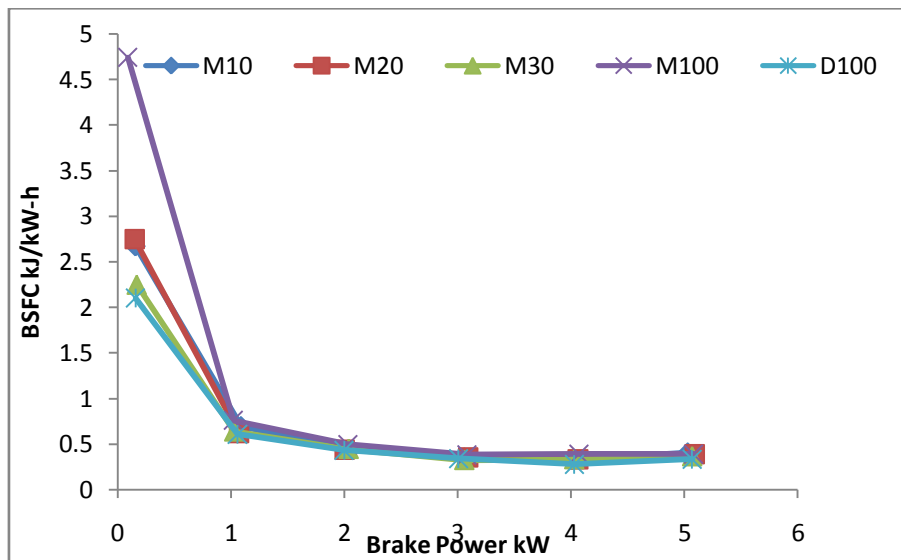


Fig- 4.2 Variation of specific fuel consumption with brake power

The variation of specific fuel consumption with brake power for diesel, mahua biodiesel and their blends are shown in fig.4.2.As the power developed increases the specific fuel consumption decreases for all the tested fuels. This may be due to fuel density, viscosity and heating value of the fuels. BSFC of 30% blend closely matches with diesel oil. Minimum BSFC of 10% blend 20% blend and 100% blend are 0.33 kg/kW-h, 0.336 kg/kW-h, and 0.388 kg/kW-h against 0.28 kg/kW-h of diesel oil. The specific fuel consumption of all blends is more than that of diesel oil.

**4.2.3Variation of exhaust gas temperature with brake power**
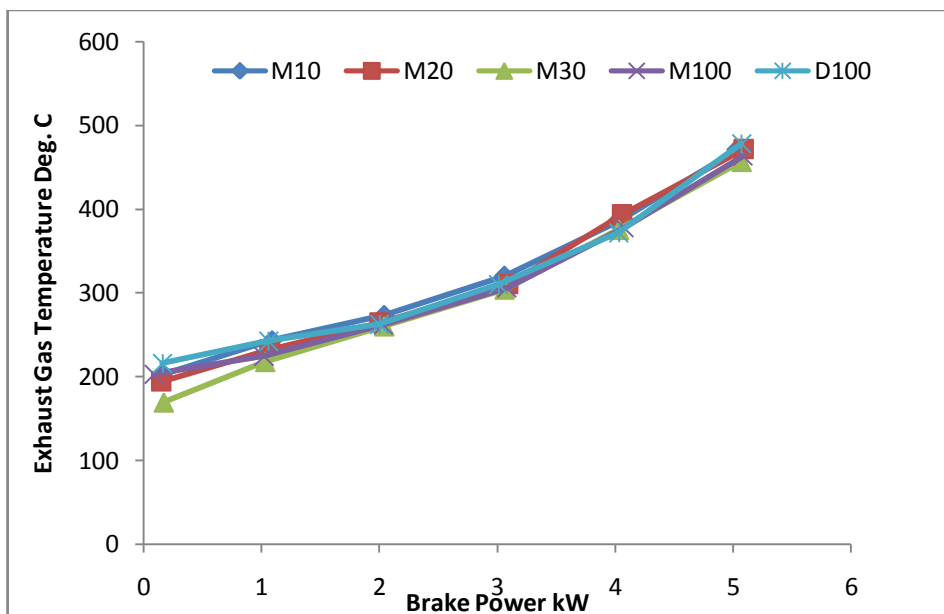


Fig- 4.3 Variation of exhaust gas temperature with brake power

The variation of exhaust gas temperature with brake power for diesel, mahua biodiesel and their blends are shown in fig.4.2. The exhaust gas temperature of 30% blend has lower values compared with all other blends and is well comparable with diesel oil. The exhaust gas temperature of all blends with diesel increases with increases in operating loads. The 30% blend has higher performance than other blends due to reduction in exhaust loss.

**4.2.4 Variation of carbon monoxide emission with brake power**
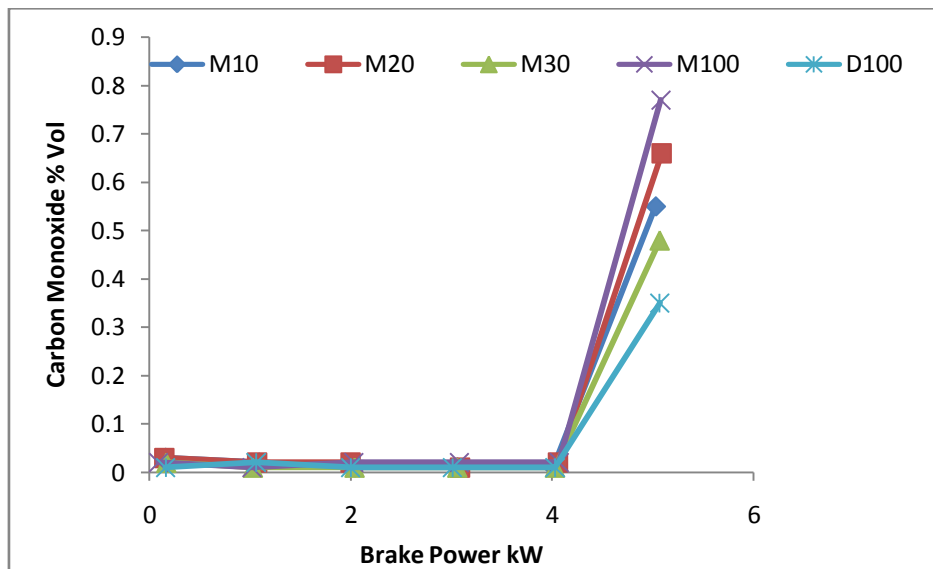


Fig-4.4 Variation of CO emission with brake power

The variation of carbon monoxide emission with brake power for diesel, mahua biodiesel and their blends are shown in fig.4.4.CO emission of all blends is higher than that of diesel. Among the blends, 30 % blend has a lower CO emission followed by 10%, 20% blend. CO emission of 10%, 20% and 30% blends at maximum load is 0.55, 0.66 and 0.48 % volume against 0.35 % volume of diesel oil. CO emission of neat mahua biodiesel is higher than all other blends for entire operating range and the maximum value is 0.77 % volume occurs at rated load.

**4.2.5 Variation of hydrocarbon emission with brake power**
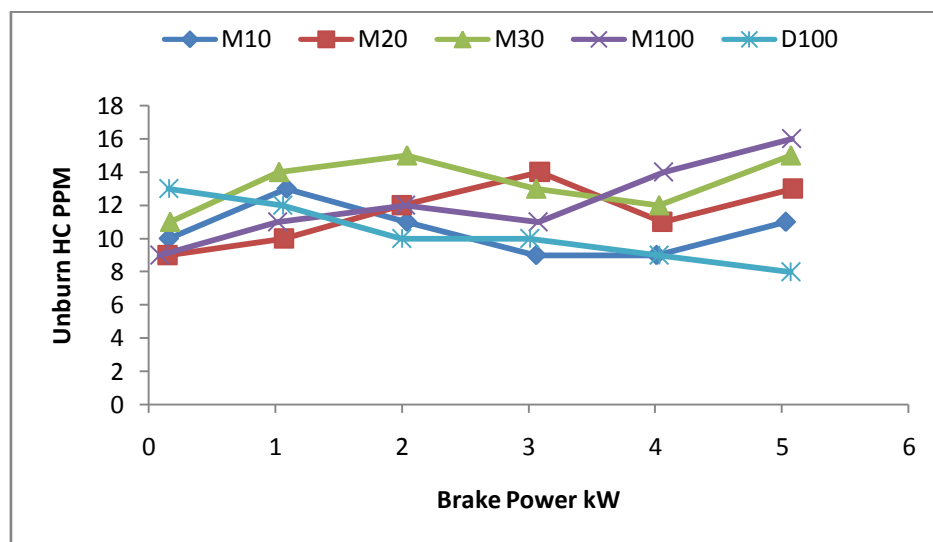


Fig-4.5 Variation of hydrocarbon emission with brake power

The variation of carbon monoxide emission with brake power for diesel, mahua biodiesel and their blends are shown in fig.4.5.Unburnt HC emission of all blends is lower than that of diesel for low and part load operation. However at maximum load unburnt HC is more for 30 % blend and 20% blend. Maximum unburnt HC of neat mahua biodiesel is 16 ppm compared with 8 ppm of diesel at 5.07kW brake power.

### 4.2.6 Variation of NOₓ emission with brake power
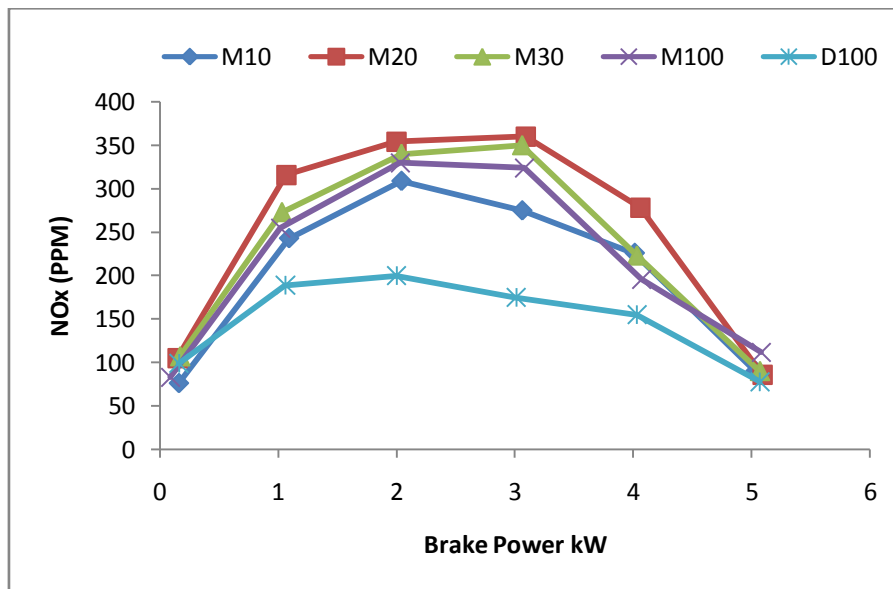


Fig-4.6 Variation of NOₓ emission with brake power

The variation of NOₓ emission with brake power for diesel, mahua biodiesel and their blends are shown in fig.4.6. NOₓ Emission of 30 % blend is lower compared with other blends followed by 20% blend. However smoke emission of 30 % blend is higher than that of diesel. Smoke emission at maximum load for 10%, 20%, 30% and 100% blends are 309,360,350, and 330 ppm against, 200 ppm of diesel oil. For 20% of blend smoke emission is on higher side for entire range of operation and maximum emission of 112 ppm occurs at maximum load.

### 4.2.7 Variation of carbon dioxide emission with brake power
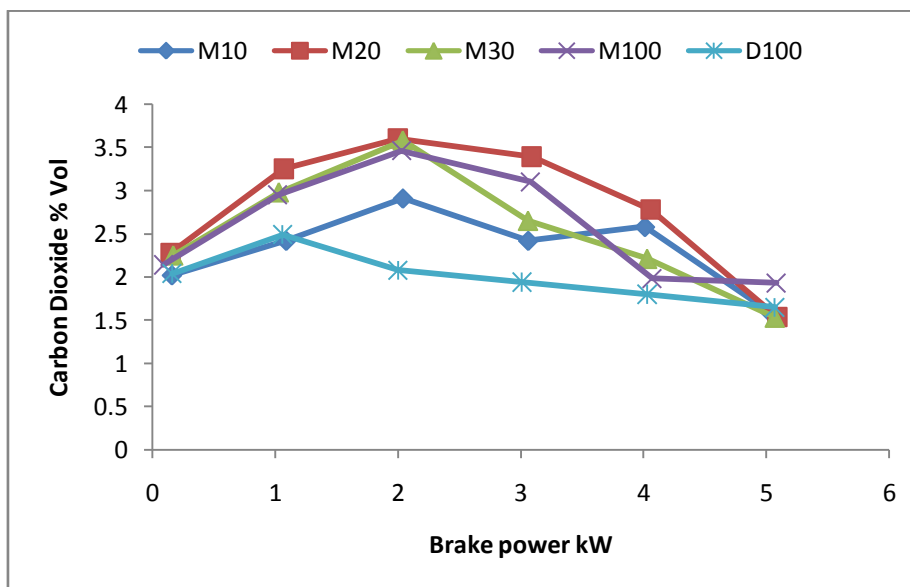


Fig-4.7 Variation of carbon dioxide emission with brake power

The Variation of carbon dioxide emission with brake power for diesel, mahua biodiesel and their blends are shown in fig.4.7. The carbon dioxide emission blend 20% and 30% are up to 3.09 and 3.06kW is same. The 20% blend is increases at 3.09 and 4.07kW and finally at maximum load both are same. Compared to all blends carbon dioxide emission is decreases in diesel oil.

**4.2.8 Variation of crank angle with cylinder pressure**
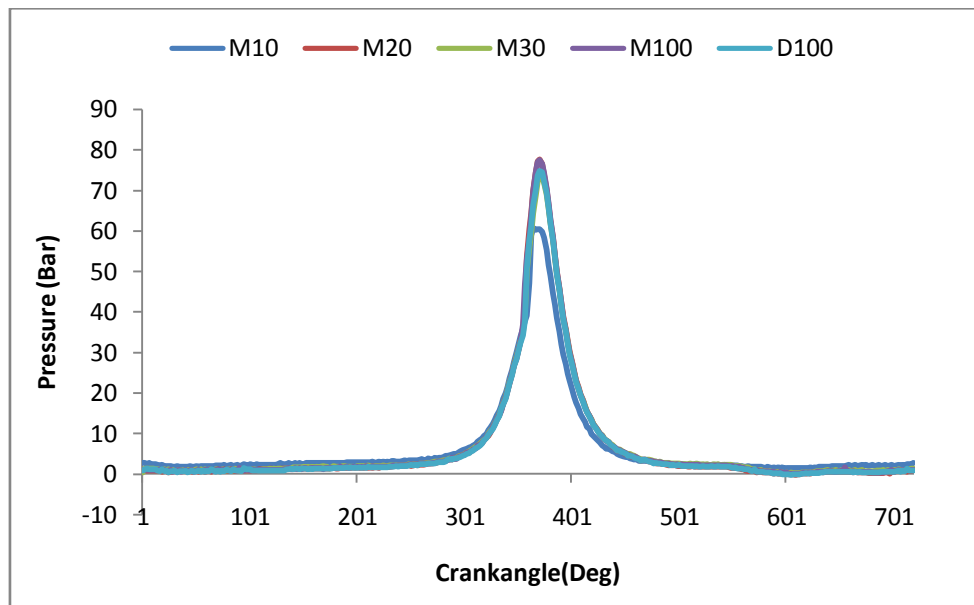


Fig-4.8.Variation of crank angle with cylinder pressure

In a CI engine the cylinder pressure is depends on the fuel-burning rate during the premixed burning phase, which in turn leads better combustion and heat release. The variation of cylinder pressure with respect to crank angle for diesel and different blends of mahua biodiesel are presented in fig-4.8. Peak pressures and crank angle is 77.43 bars and 371.Deg at100% pure biodiesel and diesel oil is 73.55 bars and 369.Deg. respectively. The blend 30% is same for all the pressures and crank angle.

**4.2.9 Variation of crank angle with net heat release rate**
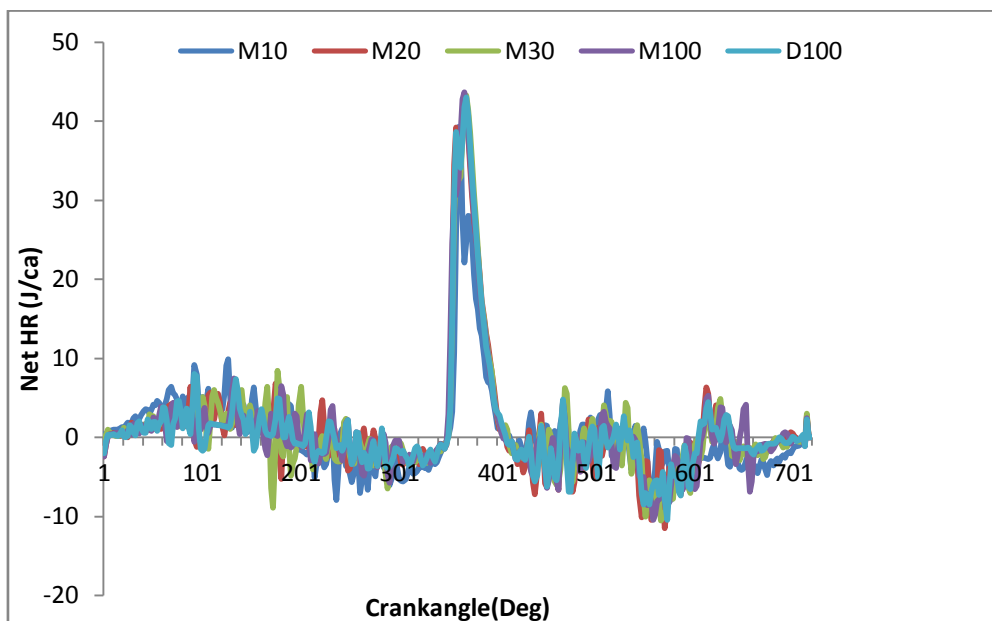


Fig-4.9.Variation of heat release rate with crank angle

The variation of cylinder net heat release rate with respect to crank angle for diesel and different blends of mahua biodiesel are shown in fig.4.9.The peak point of heat release rate with crank angle is diesel oil is 41.38(J/ca) and 367.Deg.

**4.2.10 Variation of crank angle versus cumulative heat release rate**
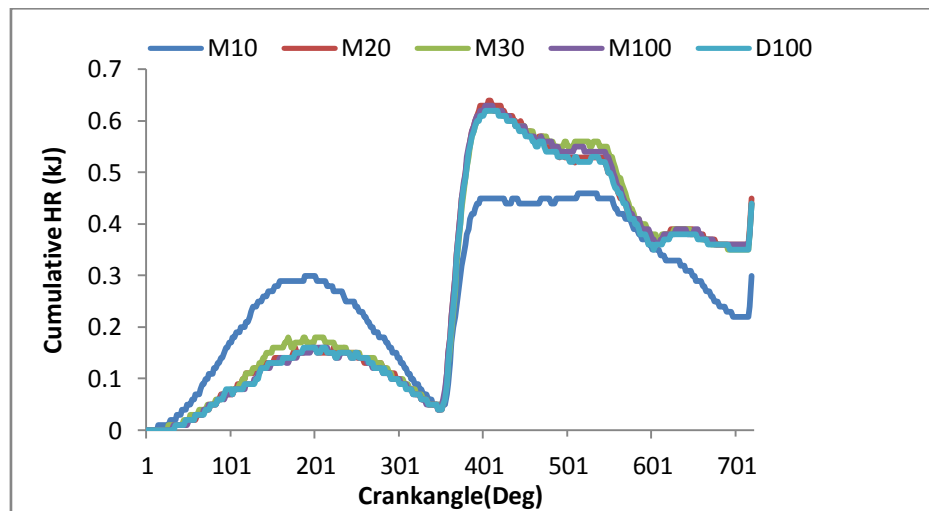


Fig-4.10. Variation of cumulative heat release rate with crank angle

The variation of cumulative heat release rate with crank angle is shown in figure (4.10). The diesel and blend values are same in all loads expect 10% blend. The two main phases of the combustion process, premixed and diffusion are clearly seen in the rate of heat release curve. If all heat losses (due to heat transfer from the gases to the cylinder walls, dissociation, incomplete combustion, gas leakage) are added to the apparent heat release characteristics, the fuel burn characteristics are obtained.

**4.3. Comparison of mahua biodiesel performance and emission with normal engine and LHR engine.**

To ascertain the validity of results obtained, mahua biodiesel LHR engine performance and emission is compared with normal engine results obtained by similar experimental work of Haiter Lenin [16] This person also used the similar engine specification, 5.2kW, 1500rpm, injection pressure 200 bars, and kirlosker make diesel engine.

**4.3.1 Variation of brake thermal efficiency with brake power**
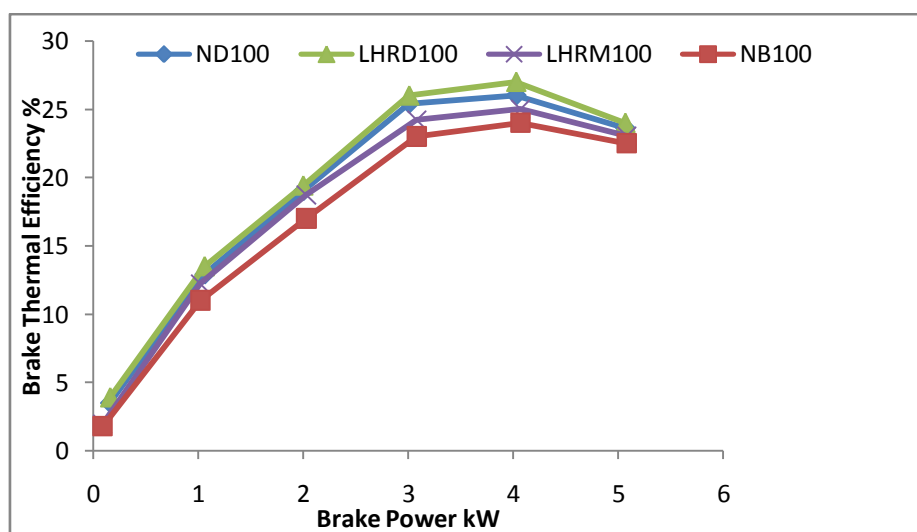


Fig- 4.11 Variation of brake thermal efficiency with brake power

The variation of brake thermal efficiency with brake power for normal engine and LHR engine of diesel, and mahua biodiesel are shown in fig.4.11.The maximum brake thermal efficiency is 27%, 26%, 25%, and 24% for LHRD100, ND100, LHRM100, and NB100. Entire operating loads the LHR engine having maximum brake thermal efficiency compared with normal engine.

**4.3.2 Varisson of specific fuel consumption with brake power**
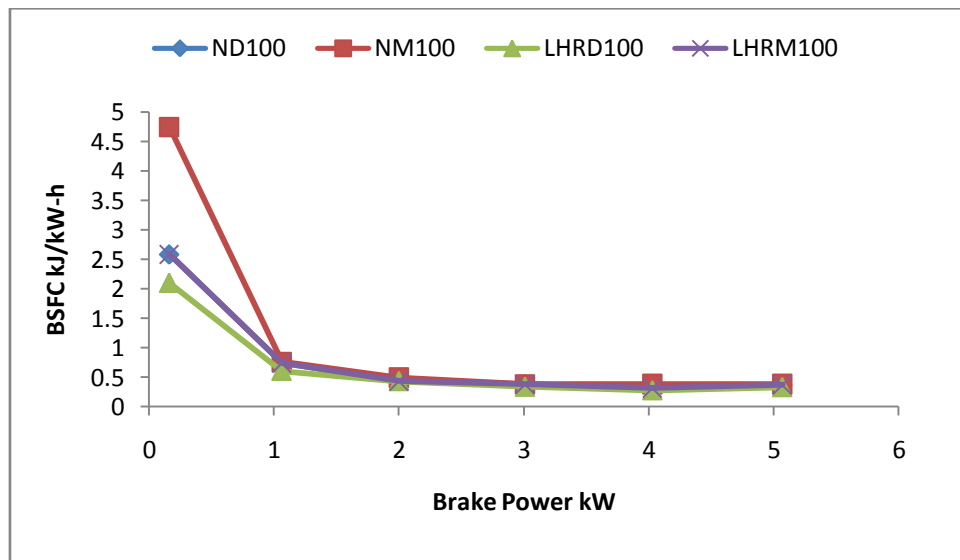


Fig- 4.12 Variation of specific fuel consumption with brake power

The variation of specific fuel consumption with brake power for normal engine and LHR engine of diesel and mahua biodiesel are shown in fig.4.12.The LHRD100 is having minimum specific fuel consumption at maximum load 0.333 kJ/kW-h at 5.07kW. The NM100 and LHRM100 having same specific fuel consumption at entire operating load. The NM100 is having maximum specific fuel consumption of 4.8 kJ/kW-h, at 5.08kW load.

**4.3.3 Variation of exhaust gas temperature with brake power**
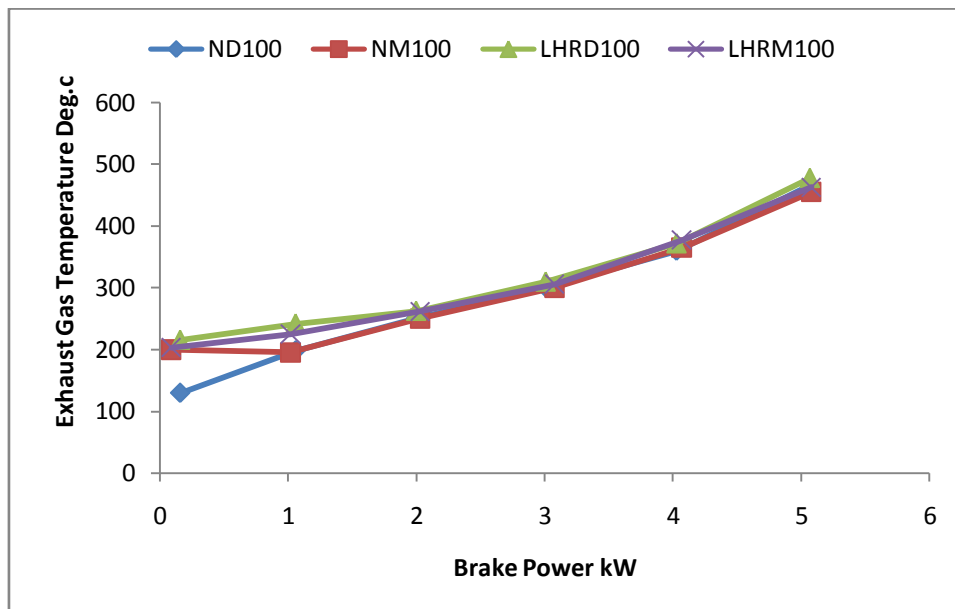


Fig- 4.13. Variation of exhaust gas temperature with brake power

The variation of exhaust gas temperature with brake power for normal engine and LHR engine of diesel and mahua biodiesel are shown in fig.4.13. The exhaust gas temperature is initial two loads are LHRD100 is maximum 215 $^{\circ}$, and 242.47 $^{\circ}$ at 0.16kW, 1.06kW after that four loads LHRD100 and LHRM100 both are same. The minimum exhaust gas temperature is NM100.

**4.3.4 Variation of carbon monoxide emission with brake power**
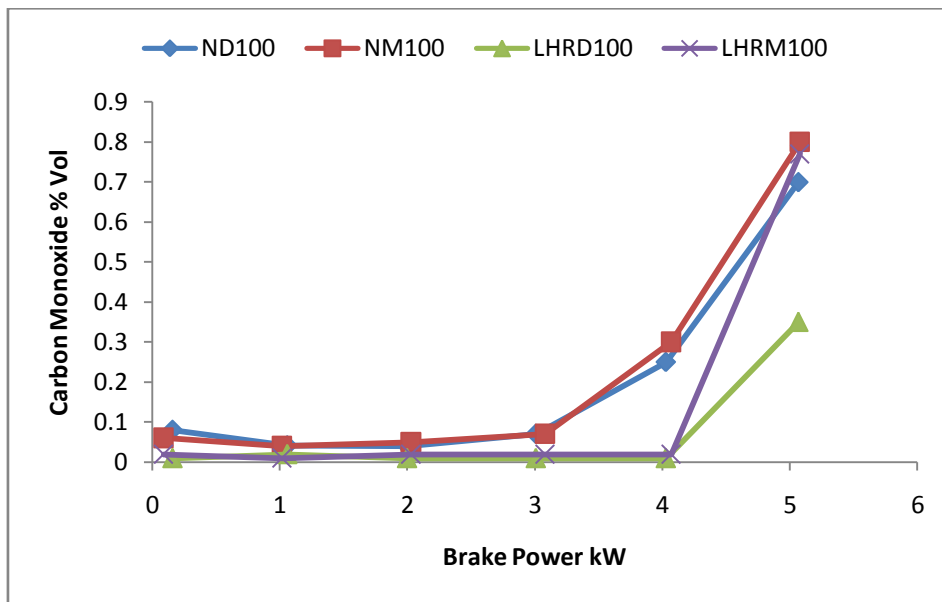


Fig-4.14. Variation of CO emission with brake power

The variation of carbon monoxide emission with brake power for normal engine and LHR engine of diesel and mahua biodiesel are shown in fig.4.14. The carbon monoxide emission gradually increases with increase in load. The carbon monoxide emission of LHRD100, LHRM100 is lower than ND100, NM100.This is because of the availability of oxygen content which makes the combustion better.

**4.3.5 Variation of hydrocarbon emission with brake power**
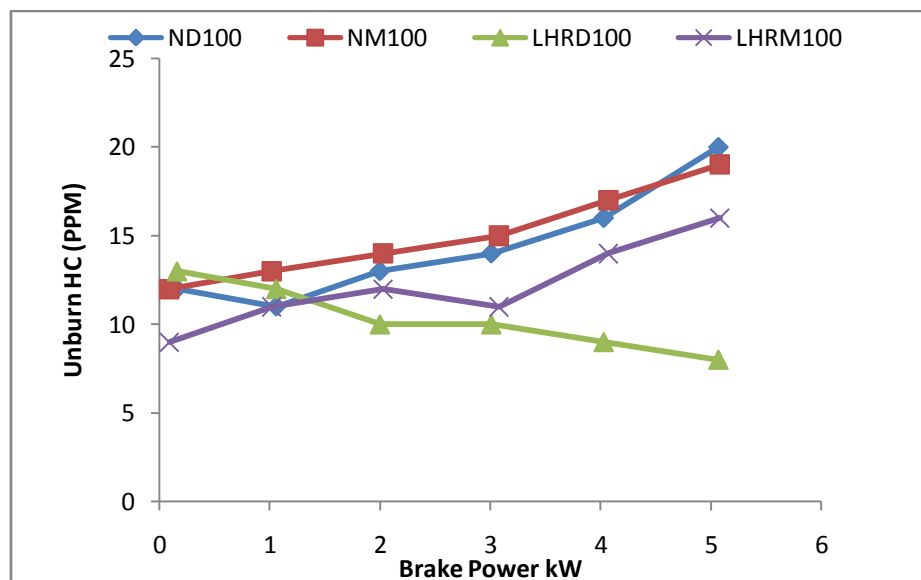


Fig-4.15 Variation of hydrocarbon emission with brake power

The variation of hydrocarbon emission with brake power for normal engine and LHR engine of diesel and mahua biodiesel are shown in fig.4.15. The hydrocarbon emission is low in LHRD100 and LHRM100 when compared with the ND100, and NM100. The decrease in the hydrocarbon in the LHR engine may be due to the increase in after combustion temperature due to decrease in heat rejected to cooling and heat loss to atmosphere due to the MMC coating.

### 4.3.6 Variation of NOx emission with brake power
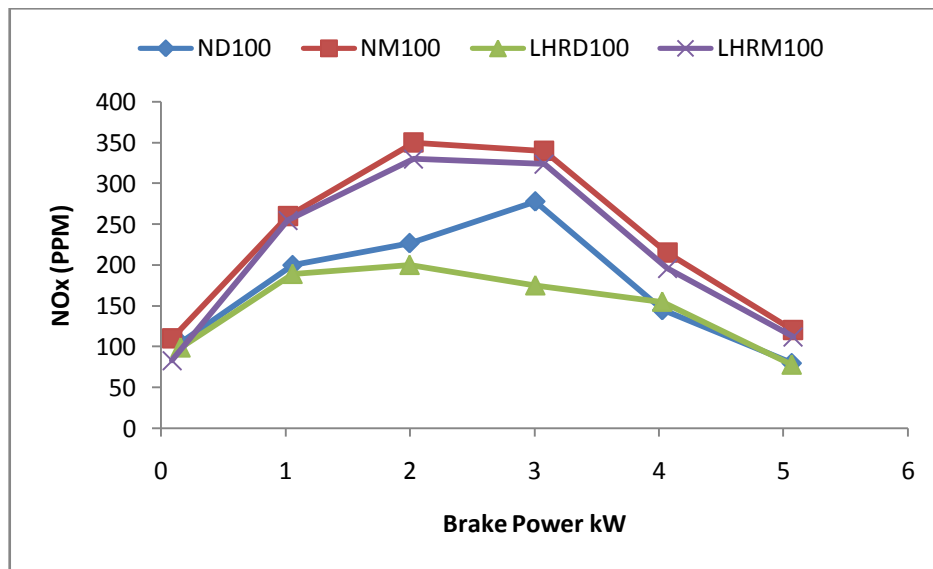


Fig-4.16 Variation of $NO_x$ emission with brake power

The variation of oxides of nitrogen emission with brake power for normal engine and LHR engine of diesel and mahua biodiesel are shown in fig.4.16.The oxides of nitrogen emission gradually increases and decreases with increase in load. And Compared to the normal engine. The Oxides of nitrogen emission in the LHR engine are more because of an increase in after combustion temperature due to the MMC coating.

### 4.3.7 Variation of carbon dioxide emission with brake power
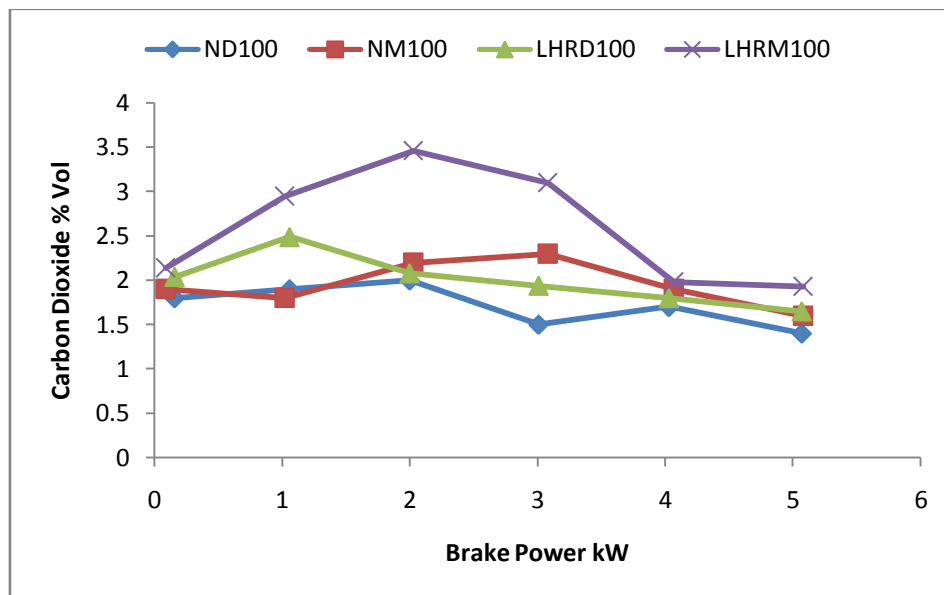


Fig-4.17. Variation of carbon dioxide emission with brake poweer

The variation of carbon dioxide emission with brake power for normal engine and LHR engine of diesel and mahua biodiesel are shown in fig.4.16.The carbon dioxide emission maximum in NM100, and LHRM100. The LHRD100 is having minimum carbon dioxide emission compared with ND100, NM100, and LHRM100. The experimental study was carried out with diesel and mahua oil biodiesel blend. The MMC coating was done on the cylinder head and engine to convert the normal engine into low heat rejection engine. It was observed that the heat transferred to the coolant and surrounding was reduced well due to the thermal barrier coating. The specific energy consumption of LHR engine with biodiesel was higher than diesel oil, but

lower than the normal engine operations. The high operating temperature during combustion in low heat rejection engine makes the combustion process to nearly a complete combustion. At maximum load the carbon monoxide and unburned hydrocarbon emission level decreases for LHR engine with mahua biodiesel blend. The reduction in carbon monoxide and unburned hydrocarbon emission level is due to the high combustion temperature and availability of oxygen in biodiesel blend.

## V.  Conclusions

Experimental conducted on a single cylinder DI- LHR diesel engine to compare the suitability of mahua biodiesel as an alternate fuel.  Then the performance and emission characteristics of blends are evaluated and compared with diesel and optimum blend is determined. For conformation its available results are compared with the results of normal engine mohua biodiesel available in literature for similar work. From the above discussion, the following conclusions are follows.

- The mahua biodiesel is satisfies the important properties like; density, viscosity, flash point, fire point and calorific value as per ASTM standards.
- Mahua biodiesel can be directly used in diesel engines without any engine modifications.
- Engine works smoothly on mahua biodiesel with Performance comparable to diesel operation.
- Brake thermal efficiency of 30% blend is equal  to diesel compared to other blends
- Specific fuel consumption is neared to diesel oil at minimum loads and increases at maximum loads. Minimum BSFC of 10% blend 20% blend and 100% blend are 0.33 kg/kW-h, 0.336 kg/kW-h, and 0.388 kg/kW-h against 0.28 kg/kW-h of diesel oil.
- The exhaust gas temperature of all blends and diesel increases with increases of operating loads.
- Combustion characteristics are all blends of mahua biodiesel is almost same as that of diesel.
- The emission characteristics like CO, HC are increases and $CO_2$, $NO_x$ levels are decrease against diesel oil.
- Performance of LHR mahua biodiesel is validated as results are in well comparison with results normal engine mahua biodiesel.
- Form the above conclusions mahua biodiesel is suitable for normal engine and  as well as LHR engine also.

## REFERENCES

[01]    Ch.S.Naga Prasad  dr. k.vijaya Kumar reddy  " Experimental investigation on performance and emission characteristics of diesel engine using bio-diesel as an alternate fuel "department of mechanical engineering JNTU college of engineering, Hyderabad . Published online -2010

[02]    Ekrem Buyukkaya , Tahsin Engin, Muhammet Cerit "Effects of thermal barrier coating on gas emissions and performance of a LHR engine with different injection timings and valve adjustments"  faculty of department of mechanical engineering, sakarya Published December 2004; June 2005, august 2006

[03]    Sitaramaiah Naramsetty, V. Ranjith Kumar, Y.V.Hanumantha Rao "performance and emission characteristics of diesel engine fuelled with biodiesel of mahua oil & diesel blends with additives."  M.Tech student, mechanical engineering department, Kl University, Vijayawada   vol. 3, issue 4, July-august 2013,

[04]    Ch .S. Naga Prasad , K. Vijay Kumar Reddy, B.S.P. Kumar, E. Ramjee, O.D. Hebbel And M.C. Nivendgi "performance and emission characteristics of a diesel engine with castor oil" Dept. Of Mech. Engg., JNTU College of Engg., Hyderabad- vol.2 no.10 (Oct 2009)

[05]    Hanbey Hazar "cotton methyl ester usage in a diesel engine equipped with insulated combustion chamber" department of automotive, technical education faculty, firat university, elazig 23119, turkey  august 2009

[06]    Siddalingappa R. Hotti, Omprakash Hebbal. Performance and combustion characteristics of single cylinder diesel engine running on karanja oil/diesel fuel blends. PDA College of Engineering, Gulbarga, India. Scientific Reach, Engineering, 2011, 3, 371-375.

[07]    K.Venkateswarlu "effect of engine modifications on performance and emission characteristics of diesel engines with alternative fuels" department of mechanical engineering, kl university, Greenfields, vaddeswaram, Guntur(dist). Andhra Pradesh, India. vol.2, issue 2(2010).

[08]    O.D. Hebbal, K. Vijaykumar Reddy, K. Rajagopal. "Performance characteristics of a diesel engine with Deccan hemp oil". Assistant Professor, Poojya Doddappa Appa College of Engineering, Gulbarga, India, Controller of Examinations, Jawaharlal Nehru Technological University, Hyderabad, India, Vice chancellor, Jawaharlal Nehru Technological University, Hyderabad, India, 18 April 2006, Fuel 85(2006) 2187-2194.

[09]    Prof. Alpesh Mehta, Mehul Joshi , Ghanshyam Patel , Mohammad Juned Saiyad "performance of single cylinder diesel engine using jatropha oil with exhaust heat recovery system" assistant professor, government engineering college, godhra students of 7th semester mechanical government engineering college, godhra,  vol.iii- issue iv oct.-dec., 2012.

[10]    Vinay Kumar D, Veeresh Babu A, Ravi Kumar Puli, "effect of injection pressure on the performance and smoke formation of low heat rejection engine using pongamia methyl ester" research scholar, Dept. of mechanical engineering, NIT, Warangal. India jers/vol.ii/ issue iii/july-September, 2011.

# Swarm Intelligence: An Application of Ant Colony Optimization

A. Ilamaran[1], S. Ganapathiram[2], R. Ashwin Kumar[3], J. Uthayakumar[4]

[1, 2, 3,] *Sri Ganesh College of Engineering and Technology*
[4] *Apollo Computer Education, Puducherry, India*

**Abstract:** *Swarm intelligence, a branch of artificial intelligence is a part which discusses the collective behaviour of social animals such as ants, fishes, termites, birds, bacteria. The collective behaviour of animals to achieve target can be used in practical applications. One of the applications is ant colony optimization. Ongoing research of ACO, there are diverse applications namely data mining, image processing, power electronic circuit design etc. One of that is network routing. By using ACO, we can find the shortest path in network routing.*
**Keywords:** *Swarm intelligence, Artificial Intelligence, Ant colony optimization, Network routing.*

## I. INTRODUCTION

Swarm intelligence is an area of Artificial Intelligence which is, in part, influenced by the collective behaviour of decentralized, self-organized system as social insects. The expression was introduced by Gerardo Beni and Jing Wang in 1989, in the context of cellular robotic systems. SI systems consist typically of a population of simple agents or bodies interacting locally with one another and with their environment. The inspiration often comes from nature, especially biological systems. The agents follow very simple rules, and although there is no centralized control structure dictating how individual agents should behave, local, and to a certain degree random, interactions between such agents lead to the emergence of "intelligent" global behaviour, unknown to the individual agents. Examples in natural systems of SI include ant colonies, bird flocking, animal herding, bacterial growth, and fish schooling. The definition of swarm intelligence is still not quite clear. In principle, it should be a multi-agent system that has self-organized behavior that shows some intelligent actions. The application of swarm principles to robots is called swarm robotics, while 'swarm intelligence' refers to the more general set of algorithms and also used to forecasting problems.

### 1.1 Applications of Swarm Intelligence
- Ant colony optimization
- Particle swarm optimization
- Artificial bee colony algorithm
- Differential evolution
- The bees algorithm
- Artificial immune systems
- Grey wolf optimizer
- Bat algorithm
- Gravitational search algorithm
- Self-propelled particles
- Stochastic diffusion search
- Multi-swarm optimization

Individual social insects, do not possess very much cognitive abilities by themselves. In a colony of social insects, such as ants, bees, wasps and termites, each insect usually performs its own tasks independently from other members of the colony. However, the tasks performed by different insects are related to each other in such a way that the colony as a capability of solving complex problems through cooperation. Important, survival-related problems such as selecting and picking up materials, finding and storing food, which require sophisticated planning, are solved by insects colonies without any supervisor or centralized controller. This collective behaviour which emerges from a group of insects has been called "swarm intelligence".

(**Flocking of birds**)      (**Bee colony**)      (**Ant colony**)

**Figure 1**

We are interested in a particular behaviour of real ants, namely the fact that they are capable of finding the shortest path between a food source and the nest without the use of visual information. The ethology discovered that Ants communicate with one another by means of pheromone (a chemical substance) trails. As an ant move, a certain amount of pheromone is dropped on the ground, marking the path with a trail of this substance. The more ants follow a given trial, the more attractive this trail becomes to be followed by other ants. This process can be described as a loop of positive feedback, in which the probability that an ant chooses a path is proportional to the number of ants that have already passed by that path. When an established path between a food source and the ant's nest is disturbed by the presence of an object, ants soon will try to go around the obstacle. Firstly, each ant can choose to go around to the left or to the right of the object with a 50%-50% probability distribution. All ants move roughly at the same speed and deposit pheromone in the trail at roughly the same rate. Therefore, the ants that (by chance) go around the obstacle by the shortest path will reach the original track faster than the others that have followed longer paths to circumvent the obstacle. As a result, pheromone accumulates faster in the shorter path around the obstacle. Since ants prefer to follow trails with larger amounts of pheromone, eventually all the ants converge to the shorter path.
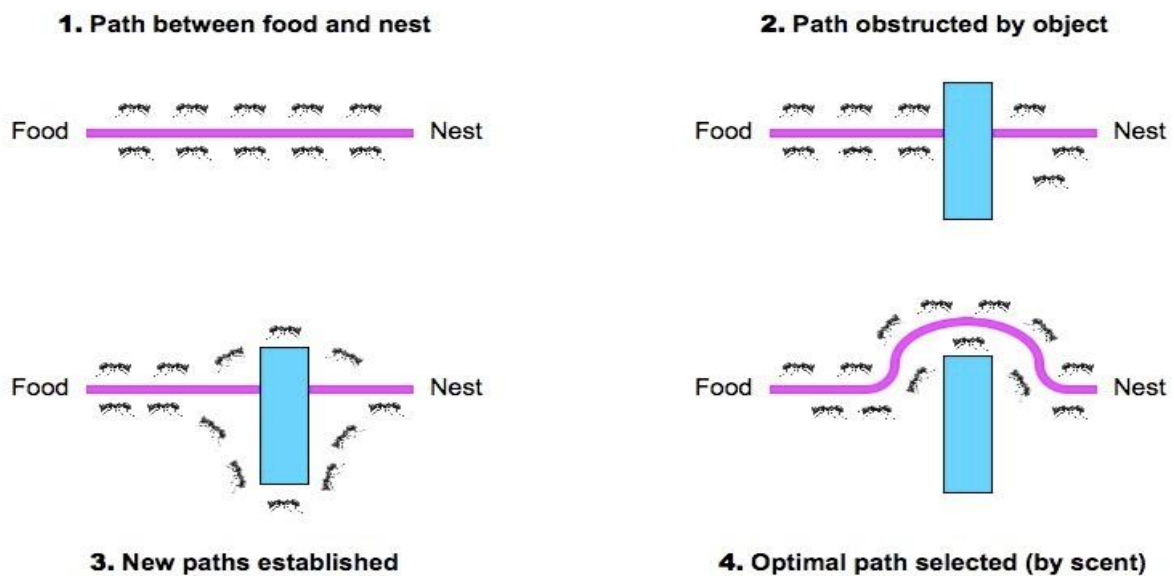


**Figure 2**

## II.   Ant Colony Optimization

ACO, a sub-field of swarm intelligence (Blum & Dorigo, 2004; Dorigo, Di Caro, & Gambardella, 1999). It is the relatively new field of Ant Colony Optimization. Ant Colony Optimization (ACO) is a metaheuristic, originally defined by Dorigo et al, in [Dorigo et al, 1999]. A metaheuristic is a general method of defining heuristics for a wide range of problem areas which is largely influenced by the behaviour of real ants. [Dorigo and Stutzle, 2004].It is a system based on agents which simulate the natural behaviour of ants, including mechanisms of cooperation and adaptation. In the use of this kind of system as a new metaheuristic was proposed in order to solve combinatorial optimization problems.

It is one of the most advanced techniques for approximate optimization (Blum, 2005). It has been employed to solve many problems in real world situations, such as the scheduling problem (Merkle, Middendorf, & Schmeck, 2002),vehicle routing problem (Fuellerer, Doerner, Hartl, & Iori, 2009; Reimann, Doerner, & Hartl, 2004), assignment Problem (Maniezzo, Colorni, & Dorigo, 1994,Stutzle, 1997), subset problem (Leguizamo´n & Michalewicz, 1999), machine learning problem (Parpinelli, Lopes, & Freitas, 2002), Bayesian network problem (de Campos, Ga´mez, & Puerta, 2002) and industrial problem (Corry & Kozan, 2004). The inspiring source of ACO algorithms are the foraging behaviors of real ant colonies. After the observation of ant colonies, scientists discovered how ants find shortest paths between food sources and their nest. Starting from their nest, ants initially explore the lands around at random. While moving ahead, ants can leave pheromone (a kind of chemical substance) trails on the path they are going through. Other ants can smell pheromone and follow a trail. The more a trail is followed, the more pheromone will be left and the path becomes more attractive for other ants to follow. The pheromone trails are the guides helping ants find the food. The indirect communication between the ants via pheromone trails enables them to find the shortest path between their nest and food (Blum, 2005).The below Fig.3 illustrates the shortest path discovering process of ant colonies.
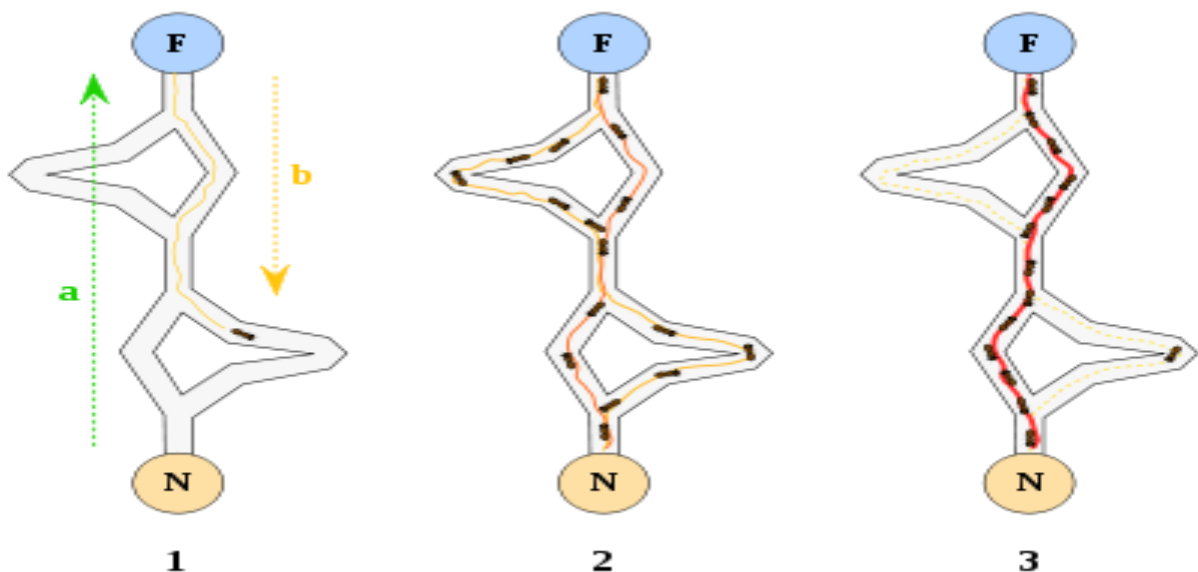


**Figure 3**

### *ACO algorithms are based on the following ideas*

Each path followed by an ant is associated with a candidate solution for a given problem. When an ant follows a path, the amount of pheromone deposited on that path is proportional to the    quality of the corresponding candidate solution for the target problem. When an ant has to choose between two or more paths, the path(s) with a larger amount of pheromone have a greater probability of being chosen by the ant. As a result, the ants eventually converge to a short path, hopefully the optimum or a near-optimum solution for the target problem.
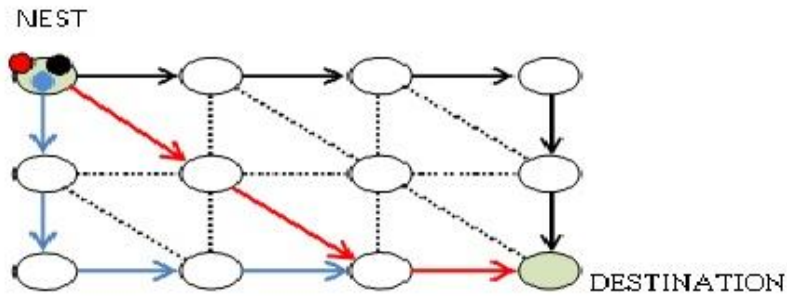
**Figure 4.1**

1. Ants start foraging from their nest. Initially, the selected possibility of each path is equal. So Red ant, which symbolized by red circle, go the shortest path. Other ants which symbolized by blue and black circles goes in the long path.
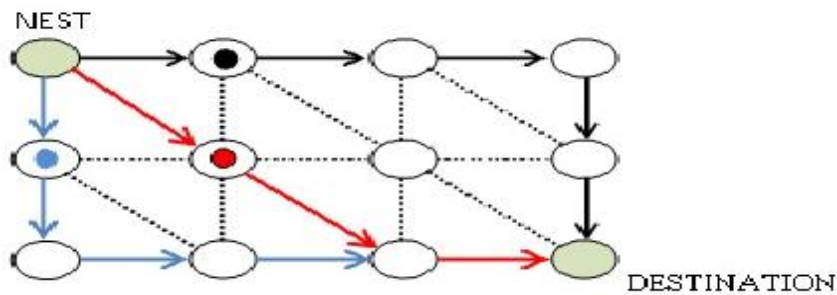


**Figure 4.2**

2. The ants which go the short path arrives their destination (food source) earlier. Thus, when they go back, it has higher possibility for ants to select the shortest path because the short path has stronger pheromone concentration.
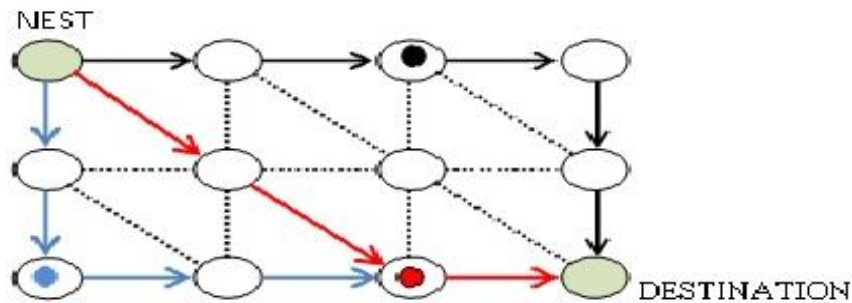


**Figure 4.3**

3. With more ants go the short path; the pheromone trail on it continuously increases. And with the evaporation of the pheromone on the long path, less and less ants will take it.
4.
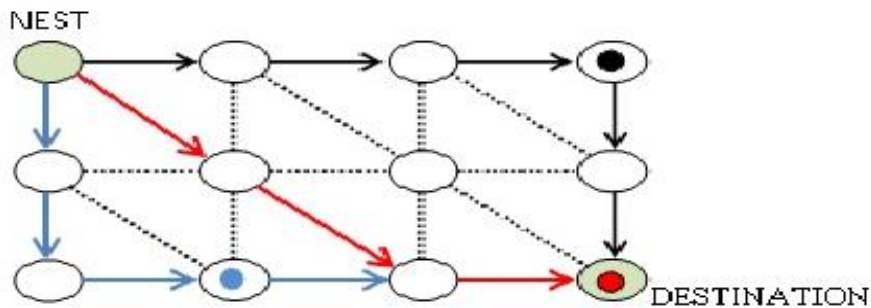


**Figure 4.4**

5. After sufficient round of ants' going and returning between the nest and the food source. All the ants will choose the short path .The possibility they go the long path will be 0.

**2.1applications of ACO**

On-going research of ACO in diverse engineering applications such as,

➢ Network routing
➢ Data mining
➢ Discounted cash flows in project scheduling
➢ Grid work flow scheduling problem
➢ Image processing
➢ Intelligent testing system
➢ System identification
➢ Protein folding
➢ Power electronic circuit design

### III.  ACO IN NETWORK ROUTING

Computer scientists began researching the behaviour of ants in the early 1990's to discover new routing algorithms. The result of these studies is Ant Colony Optimisation (ACO), and in the case of well implemented ACO techniques, optimal performance is comparative to existing top-performing routing algorithms.

Electronic communication networks can be categorised as either circuit-switched or packet-switched. Circuit-switched networks rely on a dedicated connection from source to destination, which is made once at start-up and remains constant until the tear-down of the connection. An example of a circuit switched network would be the British Tele coms telephone network. Packet-switched networks work quite differently, however, and all data to be transmitted is divided into segments and sent as data-packets. Data-packets can arrive out of order in a packet-switched network, with a variety of paths taken through different nodes in order to get to their destination. The internet and office local area networks are both good examples of packet-switched networks.
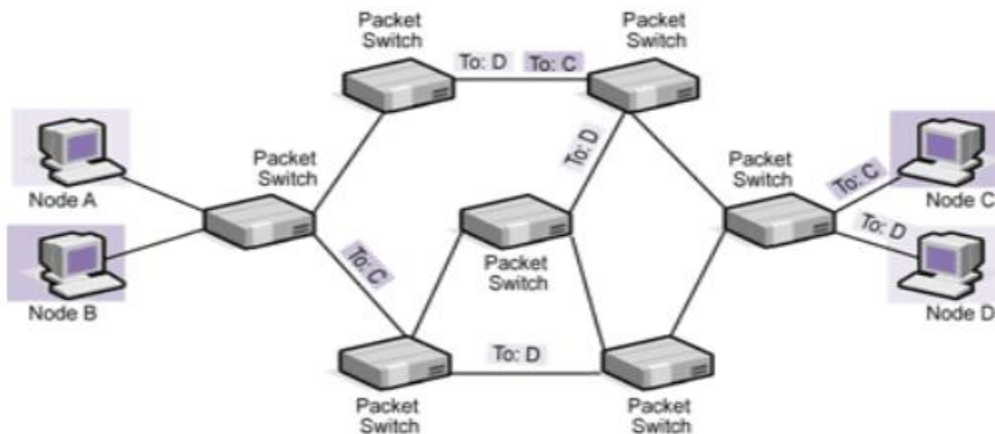


**Figure 5**

A number of techniques can be employed to optimize the flow of traffic around a network. Such techniques include flow and congestion control, where nodes send packet acknowledgements from destination nodes to either ramp-up or decrease packet transmission speed. The area of interest in this report concentrates on the idea of network routing and routing tables. These tables hold information used by a routing algorithm to make a local forwarding decision for the packet on the next node it will visit in order to reach its final destination.

One of the issues with network routing (especially in very large networks such as the internet) is adaptability. Not only can traffic be unpredictably high, but the structure of a network can change as old nodes are removed and new nodes added. This perhaps makes it almost impossible to find a combination of constant parameters to route a network optimally. Packet-switched networks dynamically guide packets to their destination via routing tables stored in a link state and are selected via a link state algorithm. A link state

algorithm works by giving every node in the network a connectivity graph of the network. This graph depicts which nodes are directly connected. Values are stored for connected nodes in a map which represents the shortest path to other nodes. One such link state algorithm used in network routing is Dijkstra's algorithm. When a path between two nodes is found, its weight is updated in the table. Should a shorter path be found, the new optimal weight will be updated to the table, replacing the old value. The algorithm allows traffic to be routed around the network whilst connecting to the least number of nodes as possible. The system works, but doesn't take into account influx of traffic and load balancing.

## IV. CONCLUSION

In this paper ACO based Routing is proposed and implemented on Network Models. The results show that the type of the variations of the ACO that should be applied on the network, obviously depends on the structure, size and the application. For example, from the reliability point of view ACO is better than other methods. This is because the number of packets destroyed during the journey is less in ACO. ACO saves the wastage of time in removing the cycles from the path of the journey of the packets and hence increases the throughput of the system. Future work on this algorithms can be carried out considering more factors that can be applied in a routing problems such a delay factor, congestion control etc.

## REFERENCES

[1.] D. Bertsekas and R. Gallager. Data Networks. Prentice-Hall, Inc, Upper Saddle River, New Jersey, 1992
[2.] K. Oida and M. Sekido, "An agent-based routing system for QoS guarantees", Proc. IEEE International Conference on Systems, Man, and Cybernetics, Oct. 12-15, pp. 833-838, 1999.
[3.] Satyabrata Chakrabarti and Amitabh Mishra, "QoS Issues in Ad Hoc Wireless Networks", IEEE Communication Magazine, February 2001.
[4.] A. Bieszczad, B. Pagurek, and T. White, "Mobile agents for network management", IEEE Communication Surveys, Fourth Quarter 1998.
[5.] Grassé, P.P. 1959. La reconstruction du nid et les coordinations interindividuelles chez Bellicositermes natalensis et Cubitermes sp. La theorie de la stigmergie: Essai d'interpretation des termites constructeurs. Ins. Soc., 6, 41-83.
[6.] E. Bonabeau, M. Dorigo, and G. Théraulaz, Swarm intelligence: from natural to artificial systems, Oxford University Press, 1999.
[7.] G. Di Caro and M. Dorigo, "AntNet: a mobile agents approach to adaptive routing", Tech. Rep. IRIDIA/97-12, Université Libre de Bruxelles, Belgium.
[8.] M. Heusse, D. Snyers, S. Guérin, and P. Kuntz, "Adaptive agent-driven routing and load balancing in communication network", Proc. ANTS'98, First International Workshop on Ant Colony Optimization, Brussels, Belgium, October 15-16, 1998.
[9.] S. Lipperts and B. Kreller, "Mobile agents in telecommunications networks - a simulative approach to load balancing", Proc. 5th Intl. Conf. Information Systems, Analysis and Synthesis, ISAS'99, 1999.
[10.] Raman, L.: OSI system and Network Managements, IEEE Communication: Managements of Heterogeneous Networks, vol. 36, no.3, March 1998.
[11.] R. K. Ahuja, Magnanti T.L., and J.B. Orlin. Network Flows: Theory, Algorithms and Applications. Prentice Hall, Inc., Upper Saddle River, New Jersey, 1993
[12.] Sugawara, K.; Sano, M.; Yoshihara, I.; Abe, K.; Watanabe, Foraging behaviour of multi-robot system and emergence of swarm intelligence, Systems, Man, and Cybernetics, 1999. IEEE SMC '99 Conference Proceedings. 1999 IEEE International Conference on, Volume: 3, 1999 Page(s): 257 -262 vol.3
[13.] Fukuda, T.; Funato, D.; Sekiyama, K.; Arai, F.,Evaluation on flexibility of swarm intelligent system Robotics and Automation, 1998. Proceedings. 1998 IEEE International Conference on , Volume:4,1998 Page(s): 3210 - 3215 vol.4
[14.] Kawabata, K.; Suzuki, T.; Hayama, T.; Kobayashi, H., Distributed intelligent control structure for multi-legged walking robots Advanced
[15.] Motion Control, 1996. AMC '96-MIE. Proceedings. 1996 4$^{th}$ International Workshop on, Volume:1,1996, Page(s): 231 -236 vol.1.
[16.] A. Colorni, M. Dorigo, and V. Maniezzo, "An investigation of some properties of an ant algorithm", Proc. Parallel Problem Solving from Nature Conference (PPSN 92), Brussels, Belgium, pp. 509-520, 1992.
[17.] M. Dorigo, V. Maniezzo, and A. Colorni, "The ant system: optimization by a colony of cooperating agents", IEEE Transactions on Systems, Man, and Cybernetics, Part B, vol. 26, no. 1, pp. 29-41, 1996.
[18.] A. Colorni, M. Dorigo, and V. Maniezzo, "An investigation of some properties of an ant algorithm", Proc. Parallel Problem Solving from Nature Conference (PPSN 92), Brussels, Belgium, pp. 509-520, 1992._
[19.] S. Chen and K. Nahrstedh, "An Overview of Quality-of-Serive routing for the next Generation High-Speed networks" IEEE Network, pp64-79, Nov/Dec 1998_

[20.] R. Schoonderwoerd, O.E. Holland, J. Bruten, L. Rothkrantz, "Ant-based load balancing in telecommunications networks", HP Labs Technical Report, HPL-96-76, May 21, 1996.

[21.] R. Schoonderwoerd, O.E. Holland, J.L. Bruten, "Ant-like agents for load balancing in telecommunications networks", Proc. First ACM

[22.] Bellman, Richard Ernest, "Dynamic programming", PrincetonUniversity Press, 1957

[23.] Dijkstra, E.W.: A Note on Two Problems in Connection with Graphs. In: Numeric Mathematics 1, p. 269 – 271,1959

[24.] G. Navarro Varela and M.C. Sinclair, "Ant colony optimisation for virtual-wavelength-path routing and wavelength allocation", Proc. 1999 Congress on Evolutionary Computation, Washington DC, USA, pp. 1809-1816, July 1999.

[25.] E. Bonabeau, F. Henaux, S. Guerin, D. Snyers, P. Kuntz, and G. Theraulaz, "Routing in telecommunications networks with "smart" antlike agents", Proc. Intelligent Agents for Telecommunications Applications '98._

[26.] G. Di Caro and M. Dorigo, "An adaptive multi-agent routing algorithm inspired by ants behavior", Proc. PART98 - Fifth Annual Australasian Conference on Parallel and Real-Time Systems, Adelaide, Australia, September 28-29, 1998.

[27.] G. Di Caro and M. Dorigo, "Ant colonies for adaptive routing in packet switched communications networks", Proc. PPSN V – Fifth International Conference on Parallel Problem Solving from Nature, Amsterdam, Holland, September 27-30, 1998.

[28.] G. Di Caro and M. Dorigo, "Extending AntNet for best effort quality-of service routing", Proc. ANTS'98 - First International Workshop on Ant Colony Optimization, Brussels, Belgium, October 15-16, 1998.

# Classification Rule Discovery Using Ant-Miner Algorithm: An Application Of Network Intrusion Detection

J. Uthayakumar[1], D. Nivetha[2], D.Vinotha[3], M.Vasanthi[4]

[1]*Apollo Computer Education, Puducherry, India*
[2,3,4] *Department of CSE, Sri Manakula Vinayagar Engineering College, Puducherry, India*

*Abstract: Enormous studies on intrusion detection have widely applied data mining techniques to finding out the useful knowledge automatically from large amount of databases, while few studies have proposed classification data mining approaches. In an actual risk assessment process, the discovery of intrusion detection prediction knowledge from experts is still regarded as an important task because experts' predictions depend on their subjectivity. Traditional statistical techniques and artificial intelligence techniques are commonly used to solve this classification decision making. This paper proposes an ant-miner based data mining method for discovering network intrusion detection rules from large dataset. The obtained result of this experiment shows that clearly the ant-miner is superior than ID3, J48, ADtree, BFtree, Simple cart. Although different classification models have been developed for network intrusion detection, each of them has its strength and weakness, including the most commonly applied Support Vector Machine(SVM)method and the clustering based on Self Organized Ant Colony Network (CSOACN).Our algorithm is implemented and evaluated using a standard bench mark KDD99 dataset. Experiments show that ant-miner algorithm out performs than other methods in terms of both classification rate and accuracy.*
*Keywords: Intrusion Detection, Ant-miner, Artificial Intelligence, Cross validation*

## I. INTRODUCTION

In today's information system management, large-scale data clustering and classification have become increasingly important and challenging area. As a particular application area, Intrusion Detection Systems (IDSs) are designed to defend computer system from various cyber attacks and computer viruses. There are two primary assumptions in the research of intrusion detection: (1) user and program activities are observable by computer systems and (2) normal and intrusion activities must have distinct behaviors.

### 1.1 Data-mining based approaches for IDSs

Researchers have proposed an implemented various models that different measures of system behavior. As it is an energy and time consuming job for security experts to update current IDSs frequently by manual encoding, using data mining approaches to network intrusion detection provides an opportunity for IDSs to learn the behaviors of networks automatically by analyzing the data trials of their activities. Two key advantages of using a data mining approach to IDSs (1) It can be used to automatically generate the detection models for IDSs, so that new attacks can be detected automatically as well. (2) It is general, so it can be used to build IDSs for a wide variety of computing environments. The central theme of data mining approaches is to take a data-centric point of view and consider intrusion detection as a analysis process. This includes four essential steps.

(1) Capturing packets transferred on the network.
(2) Extracting an extensive set of features that can describes network connection or a host session.
(3) Learning a model that can accurately describe the behavior of abnormal and normal activities by applying data mining activities.
(4) Detecting the intrusions by using the learnt models.

We assume that Step (1) and (2) have been developed and are already available for the further training and testing phases. Step (3) in data mining, in general, is by classification, link analysis, and sequence analysis. In the rest of the paper, we will use SVM to denote either the concept or the algorithm when there is no confusion.

---

**1.2 Motivation and Contribution:**

Support Vector Machine (SVMs) have been widely accept as a powerful data classification method. On the other hand, the Self –Organized Ant Colony Network (CSOACN) has been shown to be efficient in data clustering (Section 5). Our work aims to be developed an algorithm that combines the logic of both methods to produce a high-performance IDS.One challenge of developing IDSs is to realize real-time detection in high-speed networks. The machine-learning-based SVM is a good choice for learning with a little volume of data. Clustering in intrusion detection is used to resolve the multiple classification problems. The main contribution of this paper includes the following.

(1) Modifications to the supervised learning SVM and the unsupervised learning CSOACN so they can be used interactively and efficiently.
(2) A new algorithm, CSVAC, that combines the modified SVM and CSOACN to minimize the training dataset while allowing new data points to be added to the training set dynamically. The idea of combining supervised learning and unsupervised learning was applied previously.

**1.3 Related work**

Issues related to intrusion detection can be categorized into two broad cases(1) network security and intrusion detection models and (2) intrusion detection methods and algorithms based on artificial intelligence(mostly machine learning) techniques. In this section we shall briefly review some related works in the second area, and leave area (1) to the next section, when we discuss the background of IDSs .Intrusion detection has been studied for decades using machine learning techniques, including traditional classification methods such as K-Nearest Neighbor (K-NN), Support Vector Machine (SVMs), Decision Trees (DTs).Bayesian, Self –Organized Maps (SOMs), Artificial Neural Networks (ANNs), Generic Algorithm (GAs). A review of using these approaches, was given, which also included in statistics of the use of techniques reported in 55 research articles during the period 2000-2007. Another more recent review provided thorough survey of intrusion detection using computational intelligence. Most recently, an IDSs was introduced by integrating On Line Analytical Processing (OLAP) tools and data mining techniques. It is shown that the association of the two fields produces a good solution to deal with defects of IDSs such as low detection accuracy and high falls alarm rate. As one of the swarm intelligence approaches, Ant Colony Optimization (ACO, has been applied in many fields to solve optimization problems, but its application to the intrusion detection domain is limited. The basic ingredient of their ACO algorithm was a heuristic for probabilistically constructing solutions. Hybrid intrusion detection approaches involving SVM have been studied in the past , that uses Dynamically Growing Self-Organizing Tree (DGSOT) algorithm for clustering to help in finding the most qualified points to train the SVM classifier. Another hybrid intrusion detection approach was recently detected that combines the hierarchical clustering and SVM .The purpose of using the hierarchical clustering algorithm is to provide the SVM classifier with fewer but higher quality training data that may reduce the training time and improve the performance of the classifier .WE use ACO to achieve the goal that is capable of updating the models without a retraining process ,as explained in the previous section about motivations.

**1.4 Background**

In this section, we present some background knowledge about IDSs. We begin with the introduction of basic concepts and technologies of network security.

***1.4.1 Network security***

There are three basic security concerns that are important to information on a network.

• Confidentiality: Loss of confidentiality results when information is read are copied by unauthorized users.
• Integrity: Loss by integrity results when information is modified in unexpected ways.
• Availability: Loss of availability results when information can be erased or become inaccessible by authorized users. On the other hand, there are three security concepts that are related to the people who use the information.
• Authentication: Proving whether a user is who he/she claims to be .
• Authorization: Determining whether a particular user has the privilege to perform a certain action.
• Non-repudiation: Providing protection against an individual falsely denying having performed a particular action.

### 1.4.2 Network intrusion detection:

Intrusion detection is the detection of actions that attempt to compromise the integrity, confidentiality, or availability of a resource. It attempts to detect attacks by examining various data records observed through processes on the same network. Data records are split into two categories host -based data which is audit data that record all system calls in chronologically sorted order; and network- based data, which is the network traffic data. As one of the promising network security technologies, Intrusion Detection Systems (IDSs) detect a possible intrusion as soon as possible and take appropriate actions .An IDSs is a reactive rather than pro-active agent. This paper adapts an advanced AI technique, ACO based ant-miner algorithm into network intrusion detection problem.

## II.   ANT-MINER ALGORITHM FOR CLASSIFICATION RULE DISCOVERY (CRD)

### 2.1 Rule structure

In order to apply the ant-miner algorithm to the problem of classification learning, the classification rule structure can be expressed in the form of IF-THEN as follows:

IF <Predecessor > THEN < Successor >

The predecessor part of the rule consists of several conditions, usually connected by a logical conjunction operator AND. The successor part of the rule shows the classification conclusion. For example, to express a intrusion detection class, a corresponding rule can be expressed as below:

Rule 1: IF dst_host_str_diff_host_rate<=0.035 AND

hot<=25.0 AND

count<=29.5

THEN Class normal

These kinds of rules are based on practical problem-solving knowledge which provides necessary and sufficient conditions for achieving certain goals.

### 2.2 Data structure of rule discovery

The inspiring source of the data structure for discovering rules comes from the foraging path of real ant colonies. In Fig. 1 there is a path taken by an ant which is represented with nodes connected by blue lines: Start->$Val_{1,2}$->$Val_{2,1}$->$Val_{3,3}$-> $C_3$->End. It forms an IF-THEN rules give below. The attributes and selected attribute values forms the predecessor part, and the Class and the Class value forms the successor part. This rule can be expressed as: IF $Attribute_1$ = $Val_{1,2}$ AND $Attribute_2$ = $Val_{2,1}$ AND $Attribute_3$ = $Val_{3,3}$THEN Class = $C_3$. To generate a discovered rule, it should be ensured that enough ants take the same path. The method to obtain a discovered rule will be proposed in Section C.
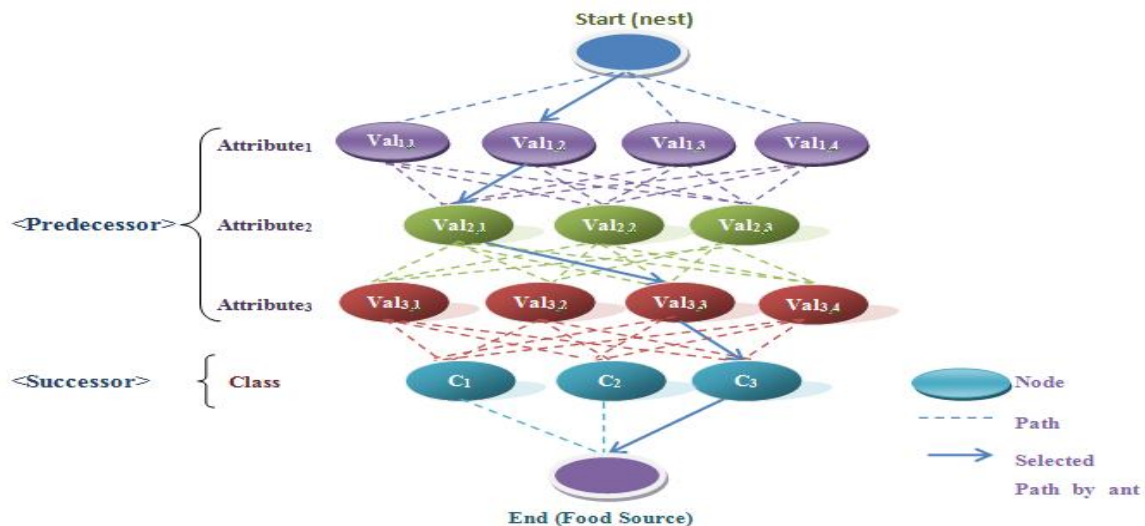


Fig. 1 Data structure for classification rule discovery

The major differences between data structure for discovering classification rules and the foraging paths of real ant colonies can be summarized as below:

---

(1) Real ants go to a food source from their nest and back to the nest later. But artificial ants in our data structure do not return. The movements of artificial ants are transitions from discrete states to discrete states. Unlike real ants, the artificial ants are ''jumping'' from one node to another. Thus, current study only copes with categorical attributes.

(2) For real ants, pheromone updating and path going happen simultaneously. But our artificial ants update pheromone trails only after a rule is generated.

(3) Real ants may travel in group. But in our artificial world, a single ant explores a given data structure. Only after an ant reaches the end node and generates a rule, another ant can start walking.

(4) Pheromone is the only factor to affect the movements of real ants, or else they will move on the ground randomly. To improve the algorithm efficiency, a ''looking-ahead'' characteristic has been added to the artificial ants, which will be introduced in detail below.

**2.3 Description and workflow of ant-miner algorithm**

The ant-miner algorithm has similar basic principle with the shortest path discovery of real ants. The design of the algorithm involves a probability function which describes the possibility of ants path choosing. The function is based on: (1) the amount of pheromone in the trail; and (2) a problem dependent heuristic function .After several ants exploring, more and more ants will take a specific path because the positive feedback mechanism, that is, the path with a larger amount of pheromone and heuristic value have a greater probability of being chosen by an ant. If a path is chosen by the ant, the pheromone on it will increase.Once enough ants take this path, it will be chosen as a candidate rule. If its quality is good enough, it will definitely become a discovered rule. The feedback mechanism is the major characteristic of ant-miner algorithms. It can be considered as the major difference between ant-miner and other CRD methods.

The flowchart of the ant-miner algorithm for rule discovery is given in Fig. 2. The algorithm starts with obtaining a training set which consists of training cases. After that, the main loop will be executed to discover one rule per iteration: (1) It begins with initializing the index of ant (t), the index of converge, ConvergeIndex (j) which is used to test convergence of ants paths and pheromone on all trails. Convergence of path is an important indicator to check if a steady path chosen by ant colony has formed. It tests if ants take the same path one after another and record how many ants take this path. (2) A sub-loop is executed to discover classification rules by a number of artificial ants (No_of_ants) who explore paths in turn. And the discovery process consists of three main steps: rule generation, rule pruning and pheromone updating. The sub-loop will terminate under the condition that all ants have taken their exploration (t≥No_of_ants), or the convergence state has been reached (j≥No_rule_converge). No_rule_converge is the threshold of ConvergIndex (j). It means if there are No_rule_converge ants take the same path one after another, the path is qualified for a discovered rule candidate. If the current ant has constructed a rule that is exactly the same as the rule constructed by previous ants, then it is said the ants have converged to a single rule (path) and the value of ConvergeIndex (j) will increase by 1. (3) The main loop selects the best rule from the discovered rules according to their qualities. (4) The training cases which are covered by the best rule need to be removed from the training set. In other words, the number of training cases in the training set is gradually decreased with continuous matching with the best rules. The loop will end when the number of training cases is greater than the user-specified threshold that is the Max_uncovered_cases (Max_uc).Ant-miner algorithm can meet the requirements of exclusiveness and completeness: (1) It will not happen that multiple rules apply to a case. The rules apply to cases one by one in the same order with that they are discovered. The former discovered rule is used earlier. All the cases which are covered by it will be applied and these cases will not be considered when the later rules are used. This means that only the first rule which can cover the case will apply to it. Therefore, it does not have the situation that multiple rules apply to a case. (2) There will always be one rule matching the conditions of a given case. Ant-miner algorithm discovers rules according to the training cases. If a rule is discovered, all the training cases covered by this rule will be removed from the training set. After that, the algorithm will discover another rule based on the rest cases. This is a circulation process, until the number of uncovered cases is less than the parameter ''Max_uncovered_cases (Max_uc)''.The default rule has the majority class value in the set of uncovered training cases (Parpinelli et al., 2002a, 2002b).

START

Obtain Training Set (TS)

Initialize DiscoveredRuleList

No — TS > Max_uc?

Yes

t = 1

j = 1

Initialize all traits with the same amount of pheromones

No — t ≥ No_of_ants AND j ≥ No_rule_converge

Yes

Generate rule by ant

Prune rule

Update pheromone for trails

rule (t) = rule (t-1) ?

Yes — j = j +1

No — j = 1

t = t +1

Select the best rule among all generated rules

Add the best rule to DiscoveredRuleList

Delete cases which have been covered by the best rule from Training Set

END

Fig. 2 Work flow of Ant-Miner Algorithm for classification rule discovery (Jia Yu et al., (2011)

### 2.3.1 Rule generation

The ants start from the artificial nest and choose a value for each attribute for rule generation. This process is carried out by the probability function (Eq. (1)). It gives the probability ($P_{ij}$) that $V_{ij}$ is selected as the value of $Attribute_i$ ($Attribute_i = V_{ij}$), where Attributei is the $i^{th}$ attribute and $V_{ij}$ is the $j^{th}$ value of $Attribute_i$ (adapted from Parpinelli et al. (2002a)).

$$P_{ij} = \frac{\eta_{ij}.\tau_{ij}(t)}{\sum_{i=1}^{a}(x_i).\sum_{j=1}^{b}(\eta_{ij}.\tau_{ij}(t))} \qquad (1)$$

where, $\eta_{ij}$ is the value of a problem-dependent heuristic function for $term_{ij}$. The higher the value of     the more relevant for classification the $term_{ij}$ is, and so the higher its probability of being chosen. The function that defines the problem-dependent heuristic value is based on information theory. $\tau_{ij}(t)$ is the amount of pheromone associated with $term_{ij}$ at iteration $t$, corresponding to the amount of pheromone currently available in the position $i, j$ of the path being followed by the current ant. The better the quality of the rule constructed by an ant, the higher the amount of pheromone added to the trail segments visited by the ant. Therefore, as time goes by, the best trail segments to be followed – that is, the best terms (attribute-value pairs) to be added to a rule – will have greater and greater amounts of pheromone, increasing their probability of being chosen. a is the total number of attributes. $x_i$ is set to 1 if the attribute $a_i$ was not yet used by the current ant, or to 0 otherwise. $b_i$ is the number of values in the domain of the $i$-th attribute. A $term_{ij}$ is chosen to be added to the current partial rule with probability proportional to the value of Equation (1), subject to two restrictions, namely:(1)The attribute $A_i$ cannot be already contained in the current partial rule. In order to satisfy this restriction the ants must "remember" which terms (attribute-value pairs) are contained in the current partial rule.(2)A $term_{ij}$ cannot be added to the current partial rule if this makes it cover less than a predefined minimum number of cases, called the *Min_cases_per_rule* threshold. Once the rule antecedent is completed, the system chooses the rule consequent (i.e., the predicted class) that maximizes the   quality of the rule. This is done by assigning to the rule consequent the majority class among the cases covered by the rule.

$$\eta_{ij} = \max \left( \frac{freqT^1_{ij}, freqT^2_{ij}............freqT^k_{ij}}{|Tij|} \right) \qquad (2)$$

where $T_{ij}$ is the partition containing the cases where $Attribute_i = V_{ij}$; $|T_{ij}|$ is the number of cases in $T_{ij}$; $freqT^k_{ij}$ is the number of cases in $T_{ij}$ where $Class = C_k$. The higher the value of $\eta_{ij}$, the higher the possibility of $V_{ij}$ to be selected as a new node into the rule. Compared with the heuristic function which was originally proposed by Parpinelli et al. (2002a), this function has lower complexity. $V_{ij}$ is selected to be added to a rule depending on the probability from Eq. (1). But there is an exception that Vij cannot be added to the current partial rule when the rule covers less than a specified minimum number of cases, called the Min_cases_per_rule (minimum number of cases covered per rule). After the ant has explored all attributes (in other words, the predecessor of the rule has been generated), it will choose $C_i$, which is the $i^{th}$ value of the Class (the successor of the rule). The ant selects the $C_i$ which accumulates mostly in the training cases covered by the predecessor of the rule. The whole rule is not generated until the ant has selected the successor.

### 2.3.2 Rule pruning

Rule pruning is a common place technique in data mining. Once a rule is created, the rule pruning operation is invoked. Rule pruning will increase the quality of a rule. It makes the rule simpler and easier to be understood. The rule pruning process tries to remove each node of the rule predecessor in turn, and then computes the quality of the rule. It picks the node whose removal most significantly improves the quality of the rule, and actually removes it from the rule after each node in the rule has been tried. Once a node is removed, the rule has been shortened.

### 2.3.3 Pheromone Updating

Pheromone updating of the ant-miner algorithm is designed to simulate the pheromone ants left that evaporated in the real world. Pheromones on nodes guide artificial ants to find the right ''paths'' (rules). Pheromone updating improves the classification accuracy of ant-miner in this study. It is because that the positive feedback effect of the pheromone updating helps to correct some mistakes made by the short-sightedness of the heuristic measure. Pheromone updating copes better with attribute interactions than entropy measure, because it is based on the performance of a rule as a whole (Parpinelli et al., 2002b). Therefore,

---

pheromone updating helps getting better classification rules. Eq. (3) (Parpinelli et al., 2002a) introduces the definition of rule quality.
Where,

$$Q = \frac{TP}{TP+FN} \cdot \frac{TN}{FP+TN} \quad (3)$$

- *TP* (true positives) is the number of cases covered by the rule that have the class predicted by the rule.
- *FP* (false positives) is the number of cases covered by the rule that have a class different from the class predicted by the rule.
- *FN* (false negatives) is the number of cases that are not covered by the rule but that have the class predicted by the  rule
- *TN* (true negatives) is the number of cases that are not covered by the rule and that do not have the class predicted by the rule.

where Q is the quality of a rule, $0 \leq Q \leq 1$; TruePos (true positive) is the number of training cases in the training set whose antecedent part and consequent part are covered by the rule; FalsePos (false positive) is the number of cases whose antecedent part is covered by the rule and the consequent is not covered; FalseNeg (false negative) is the number of cases whose antecedent part is not covered by the rule but the consequent part covered; TrueNeg (true negative) is the number of cases whose antecedent part and consequent part are not covered by the rule. Q in Eq. (3) decides how much pheromone will be added to the path which has been taken by the ant. The better the quality of a rule (a path taken by ants), the more pheromone will be exposed to the path so as to attract more ants to take this path. Several equations below define how to update pheromone.

### *(1) Pheromone initialisation*
The operation is to ''Initialize all trails with the same amount of pheromone''. It is defined as Eq. (4) (Parpinelli et al., 2002b), where a is the number of attributes; $b_i$ is the number of values of Attribute$_i$; t is the sequence number of iteration.

$$\tau_{ij}(t=0) = \frac{1}{\sum_{l=1}^{a} b_i} \quad (4)$$

### *(2) Pheromone updating for explored nodes*
The amount of pheromone on the nodes which have been used by the current rule will be updated because the artificial ant deposits pheromone during path exploration. Meanwhile, the pheromone evaporation also needs to be simulated. Therefore, the integrative operation is performed according to Eq. (5) (Liu et al., 2004).

$$\tau_{ij}(t) = (1-\rho)\,\tau_{ij}(t-1) + (1-1/1+Q)\,\tau_{ij}(t-1) \quad (5)$$

where $\rho$ is the pheromone evaporation rate which controls how fast the pheromone evaporates from the trails; Q is the quality of the rule which is calculated from Eq. (3); t is the sequence number of iteration. This equation adopted from the pheromone updating function of Ant-Miner (Parpinelli et al., 2002) has higher classification accuracy because Ant-Miner's function does not consider pheromone evaporation for explored nodes.

### *(3) Pheromone updating for unexplored nodes*
The nodes which have not been used by the current rule will only have pheromone evaporation. The evaporation is performed according to Eq. (6):

$$\tau_{ij}(t) = \frac{\tau_{ij}(t-1)}{\sum_{i=1}^{a} \sum_{j=1}^{b_i} b_i=1\,\tau_{ij}(t-1)} \quad (6)$$

where a is the number of attributes; $b_i$ is the number of values of Attribute$_i$; t is the sequence number of iteration. The equation means that the amount of pheromone of unexplored nodes will be decreased as time goes by.

### III. IMPLEMENTATION OF CLASSIFICATION RULE DISCOVERY FOR NETWORK INTRUSION DETECTION

There are mainly three reasons for us to use ant-miner algorithm for bankruptcy prediction purpose. (1)The ant-miner algorithm can achieve CRD problems with good performances. (2) Bankruptcy prediction is a classification based problem, ant-miner algorithm yields better results compare to other algorithm. (3) CRD can help discovering knowledge of bankruptcy prediction classification in large amount of data. ACO, a sub-field of swarm intelligence (Blum & Dorigo, 2004; Dorigo, Di Caro, & Gambardella, 1999). It is one of the most advanced techniques for approximate optimization (Blum, 2005). In this paper, we proposed the solution for network intrusion detection using ant-miner algorithm. The results of the experiment show that the ant-miner method has significantly better performance than other classifiers in terms of rules generation and predictive accuracy.

**3.1 Data and experiment design**

In order to make a reliable comparison we used three benchmark datasets including network intrusion detection dataset. In this research, Network Intrusion Detection dataset is collected by our self from the experts and we donated this to UCI repository. Table 1 shows the variable name, instances.

TABLE 1
Description of datasets

| Dataset | Feature | Instances | Normal/Anomaly |
|---------|---------|-----------|----------------|
| *Network Intrusion Detection* | 41 | 783 | 408/375 |
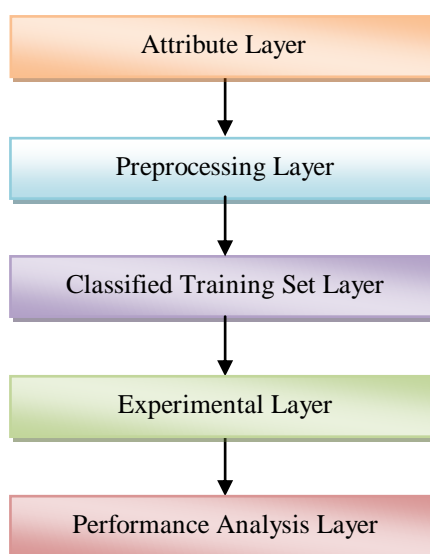


Fig. 3 Framework of Bankruptcy Prediction System

**3.2 Results**

The ant- miner finally extracts 43 rules, 22 of which are anomaly and the others are normal. The simple cart finally extracts 3 rules out of which 2 are anomaly and others are normal. The rules and the corresponding descriptions are illustrated in table 1and 2 for ant- miner and AD tree. The AD tree extracts 10 rules out of which 3 are anomaly and others are normal. J48 finally extracts 4 rules out of which 3 are normal and other is anomaly. BF tree finally extracts 4 rules out of which 2 normal and others are anomaly. The rules and descriptions of BF tree are illustrated in table 5. Overall classification means the accuracy level when the rules are applied to the cases according to the application steps generated from 5 data mining techniques. The results show that the rules of the ant-miner methods are significantly better than those of other data mining techniques. While the rules generated from the AD tree, BF tree, J48. The below results shows that the ant-miner is best than the other data sets.

TABLE 1
The descriptions of the rules generated from Ant-miner

| Rule | Description |
|---|---|
| Rule 1 | IF logged_in=0 AND src_bytes<=28.5 THEN anomaly |
| Rule 2 | IF dst_host_same_src_port_rate<=0.995 AND src_bytes<=1009.0 THEN normal |
| Rule 3 | IF dst_bytes>0.5 AND hot<=1.5 THEN normal |
| Rule 4 | IF dst_host_same_srv_rate>0.395 AND src_bytes>290.0 THEN anomaly |
| Rule 5 | IF dst_host_srv_diff_host_rate<=0.035AND hot<=25.0 AND count<=29.5THENnormal |
| Rule 6 | IF src_bytes>28.5 AND dst_host_same_src_port_rate<=0.995 THEN normal |
| Rule 7 | IF dst_host_srv_count<=84.0 AND count>1.5  THEN anomaly |
| Rule 8 | IFdst_host_same_src_port_rate>0.635ANDdst_host_rerror_rate<=0.845AND dst_host_srv_diff_host_rate>0.095THEN anomaly |
| Rule 9 | IF count<=4.5 AND dst_host_srv_count>2.0 THEN normal |
| Rule 10 | IF dst_host_count>23.0 AND dst_bytes<=2.0 THEN anomaly |
| Rule 11 | IF dst_host_srv_count<=82.5 AND count>1.5  THEN anomaly |
| Rule 12 | IF protocol_type=tcp AND dst_host_diff_srv_rate<=0.125 AND src_bytes <=285.5 THEN Normal |
| Rule 13 | IF dst_host_srv_diff_host_rate>0.09 THEN Anomaly |
| Rule14 | IF dst_host_count>251.0 AND dst_bytes<=2 THEN anomaly |
| Rule 15 | IF flag=SF THEN normal |
| Rule 16 | IF src_bytes> 28.5 AND flag = SF AND hot<= 1.5 THEN normal |
| Rule 17 | IF dst_bytes<= 2.0 AND dst_host_count > 223.5  THEN anomaly |
| Rule 18 | IF srv_count > 2.5 THEN anomaly |
| Rule 19 | IF dst_host_same_srv_rate > 0.025 AND src_byte<= 17.5 AND dst_host_diff_srv_rate <= 0.6899  THEN normal |
| Rule 20 | IF dst_host_same_src_port_rate> 0.03 THEN anomaly |
| Rule 21 | IF count <= 1.5 AND flag = SF THEN normal |
| Rule 22 | IF src_bytes > 28.5 AND hot <= 0.5 THEN normal |
| Rule 23 | IF srv_count > 3.5 THEN anomaly |
| Rule 24 | IF dst_bytes <= 1044.0 AND protocol_ type = tcp AND dst_host_srv_count > 4.5 THEN normal |
| Rule 25 | IF dst_host_rerror_rate > 0.005 THEN anomaly |
| Rule 26 | IF dst_host_same_src_port_rate <= 0.995 AND  src_bytes <= 1009.0 AND is_guest_login = 0  THEN normal |
| Rule 27 | IF count  <= 1.5 AND dst_host_rerror_rate <= 0.005  AND dst_host_srv_diff_host_rate <= 0.095 THEN  Normal |
| Rule 28 | IF duration <= 2.5 AND dst_host_diff_srv_rate <  0. 025 AND dst_host_rerror_rate <= 0.375 THEN anomaly |
| Rule 29 | IF land = 0 THEN normal |
| Rule 30 | IF src_bytes > 28.5 AND hot <= 1.5 THEN normal |
| Rule 31 | IF dst_bytes <= 2.0 AND dst_host_count > 223.5 THEN  Anomaly |
| Rule 32 | IF srv_count > 3.5 THEN anomaly |
| Rule 33 | IF src_bytes <= 17.5 AND dst_host_diff_srv_rate <= 0.06 THEN normal |
| Rule 34 | IFdst_host_rerror_rate>0.005AND dst_host_same_src_port_rate <= 0.3 THEN anomaly |
| Rule 35 | IF protocol _type = tcp AND flag = SF THEN normal |
| Rule 36 | IF  dst_host_same_src_port_rate > 0.5649  AND  dst_host_rerror_rate  <=  0.845  AND  dst_ |

| | bytes <= 0.5THEN anomaly |
|---|---|
| Rule 37 | IF dst_bytes <= 0.5 THEN anomaly |
| Rule 38 | IF src_bytes <= 24.0 AND dst_host_same_srv_rate <= 0.34 THEN anomaly |
| Rule 39 | IF src_bytes <= 399.0 AND dst_host_srv_serror_rate <= 0.135 THEN normal |
| Rule 40 | IF flag = SF AND dst_host_same_src_port_rate <= 0.995 THEN normal |
| Rule 41 | IF dst_host_srv_count <= 82.5 AND src_bytes <= 13.0 AND dst_host_diff_srv_rate > 0.025 THEN anomaly |
| Rule 42 | IF src_bytes > 4.0 AND dst_bytes <= 0.5 THEN anomaly |
| Rule 43 | IF dst_host_srv_serror_rate<=0.035 THEN normal |

TABLE 2
The descriptions of the rules generated from ADTree

| Rule | Description |
|---|---|
| Rule 1 | IF dst_bytes<0.5:0.938 AND dst_bytes>=0.5:-1.688 |
| Rule 2 | IF count>20.5:-0.771 AND count>=20.5:2.391 |
| Rule 3 | IF hot>0.5:-2.06 AND hot>0.5:1.663 |
| Rule 4 | IF src_bytes<28.5:0.511 AND src_bytes>=28.5:-0.744 |
| Rule 5 | IFdst_host_same_src_port_rate<0.985:-0.629AND dst_host_same_src_port_rate>=0.985:0.866 |
| Rule 6 | IF service=http:-1.185 AND service!=http:0.83 |
| Rule 7 | IF dst_host_srv_count<42.5:0.371 AND dst_host_srv_count>=42.5:-0.889 |
| Rule 8 | IF service=ftp_data:-1.006 AND service!=ftp_data: 0.987 |
| Rule 9 | IF dst_host_serror_rate<0.02:-0.949 AND dst_host_serror_rate>=0.02:0.851 |
| Rule 10 | IF dst_host_rerror_rate<0.005:-0.745 AND dst_host_rerror_rate<=0.005:0.958 |

TABLE 3
The descriptions of the rules generated from Simple cart

| Rule | Description |
|---|---|
| Rule 1 | IF service=(ecr_i)|(ftp)|(ftp_data) AND service!=(ecr_i)|(ftp)|(ftp_data) |
| Rule 2 | IFdst_host_serror_rate<0.045:THEN normalAND dst_host_serror_rate>=0.045:THEN anomalySrc_bytes>=28.5ANDdst_host_same_srv_rate<0.455ANDdst_host_same_srv_rate >=0.45:THENanomalyANDsrc_byte<<34167.0:THENnormalANDsrc_bytes>=34167.0: THEN anomaly |
| Rule 3 | IF protocol_type=(icmp) THEN anomaly AND if protocol_type=(icmp) THEN normal |

TABLE 4
The descriptions of the rules generated from J48

| Rule | Description |
|---|---|
| Rule 1 | IFdst_host_count<=235ANDdst_host_count>235ANDdst_host_same_src_port_rate<=0.99AND dst_host_same_src_port_rate > 0.99 |
| Rule 2 | IF srv_count <= 3 AND srv_count >3: THEN anomaly AND dst_host_same_srv_rate <=0.2: THEN anomaly AND dst_host_same_srv_rate > 0.2 AND dst_host_rerror_rate<= 0 AND dst_host_rerror_rate > 0 AND src_bytes <= 241: THEN normal AND src_bytes > 241 |
| Rule 3 | IF protocol_ type = tcp AND protocol_type = udp : THEN normal AND protocol_ type = icmp : THEN anomaly AND dst_bytes <= 4 :THEN anomaly AND dst_bytes > 4 : THEN normal AND protocol_type = tcp : THEN normal AND protocol_type = udp : THEN normal AND protocol_type =icmp AND hot <= 0 : THEN normal AND hot >0 : THEN anomaly AND dst_bytes <= 1 : THEN anomaly AND dst_bytes >1 : THEN normal |
| Rule 4 | IF dst_host_srv_count <= 2 : THEN anomaly AND dst_host_srv_count >2 : THEN normal AND src_bytes <= 570 THEN normal AND src_bytes > 570 : THEN anomaly |

TABLE 5
The descriptions of the rules generated from BFTree

| Rule | Description |
|------|-------------|
| Rule 1 | IF service = ( ecr_i)|(ftp)|(ftp_data) AND service != (ecr_i)|(ftp)|(ftp_data) |
| Rule 2 | IFdst_host_serror_rate<0.045:THENnormalANDdst_host_serror_rate>=0.045:THENanomaly src_bytes >= 28.5 AND dst_host_same_srv_rate < 0.455ANDdst_host_same_srv_rate >= 0.455 : THEN anomaly AND src_bytes < 34167.0 : THEN normal AND src_bytes >= 34167.0 : THEN  anomaly |
| Rule 3 | IF protocol_type = (icmp): THEN  anomaly AND protocol_type!=(icmp) |
| Rule4 | IF hot < 26.0 : THEN normal AND hot >=26.0 THEN normal |

TABLE 6
Comparison of Ant-miner with ID3, Genetic algorithm, neural networks, and Inductive learning methods

| DATA-MINING CLASSIFICATION ALGORITHM | CONFUSION MATRIX | | NUMBER OF RULES | ACCURACY |
|---|---|---|---|---|
| ANT- MINER | 410 | 1 | 43 | 99.61 |
|  | 2 | 370 | | |
| ADTREE | 394 | 14 | 10 | 97.19 |
|  | 8 | 367 | | |
| SIMPLE CART | 396 | 12 | 3 | 97.57 |
|  | 7 | 368 | | |
| J48 | 398 | 10 | 4 | 97.06 |
|  | 13 | 362 | | |
| BFTREE | 396 | 12 | 4 | 97.31 |
|  | 9 | 366 | | |
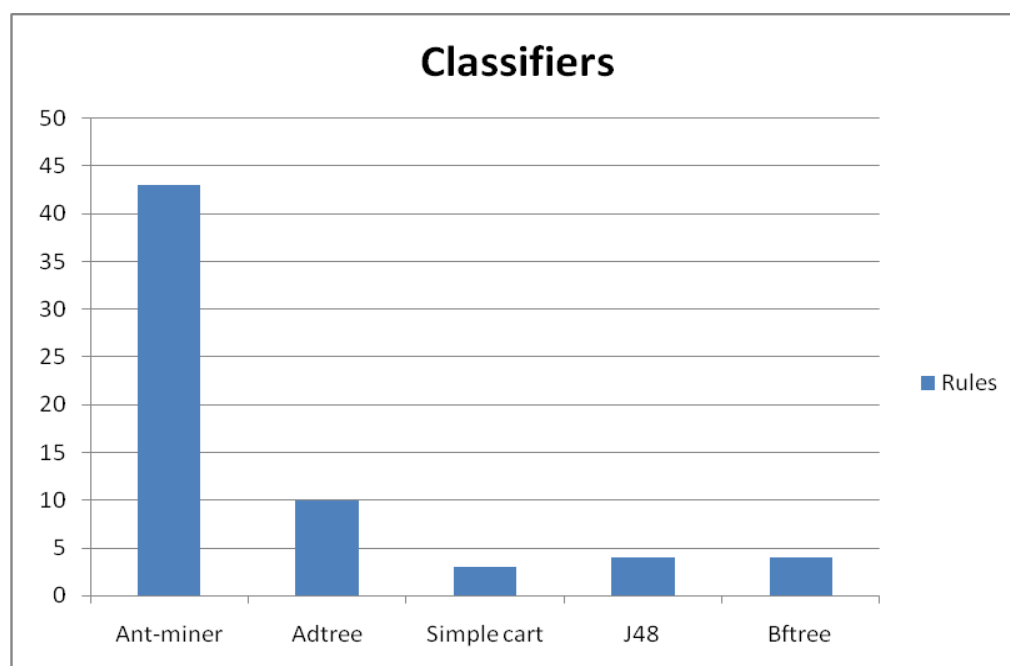


Fig. 4 Rules Generated by Classifiers
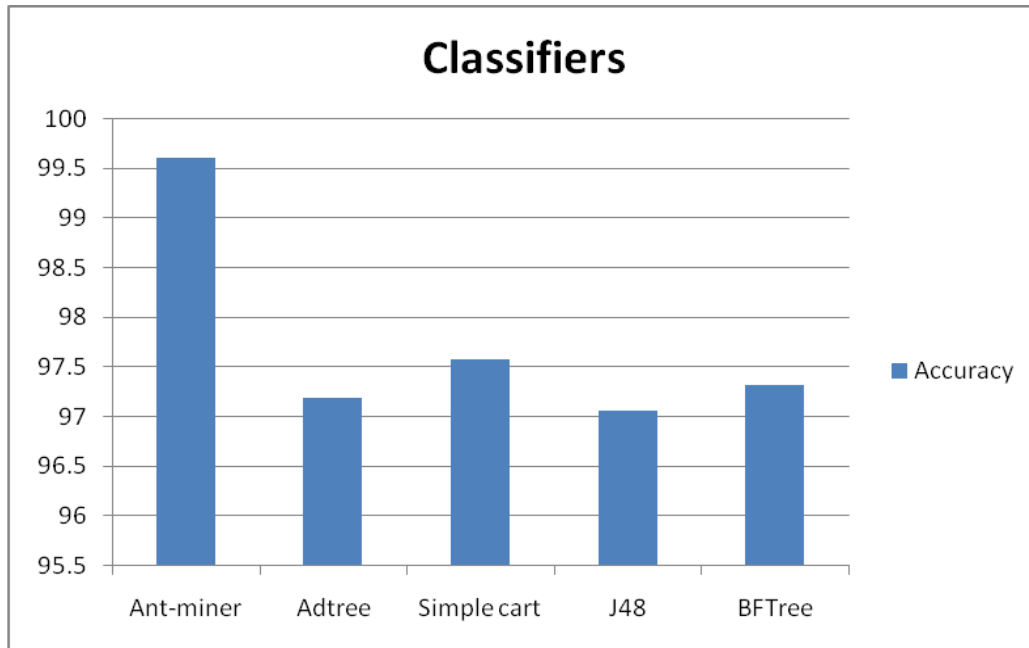
Fig. 5 Accuracy by Classifiers

This paper demonstrated the ant-miner based data mining approach to discover decision rules from experts' decision process. This study is the first work on ant-miner for the purpose of discovering experts' qualitative knowledge on bankruptcy. Four data mining techniques ID3, GA, Neural networks, Inductive learning methods are applied to compare their performance with ant-miner method.

## IV.    CONCLUSIONS

Data mining has been widely applied to discovering Network Intrusion Detection databases. However, few studies have reported the potential of data mining that can investigate the Network Intrusion Detection from experts' decisions. This work proposes a new method of classification rule discovery for Network Intrusion Detection by using ant-miner algorithm. This paper demonstrates ant-miner based data mining approach to discover decision rules from experts' decision process in networking way to predict Intrusion Detection. In performance terms, ant-miner provides more rules but give better predictive accuracy when compare to other techniques. This study has conducted a case study using the dataset Network Intrusion Detection dataset is retrieved from UCI repository in July 2014. Finally this paper suggests that Ant-miner could be a more suitable method than the other classifiers like J48, Simple Cart, ADTree, and BFTree. In future research, additional artificial techniques could also be applied. And certainly researchers could expand the system with more dataset.

## REFERENCES

[1]    Han, J., & Kamber, M. Data mining: Concepts and techniques. San Francisco, CA, USA: Morgan Kaufmann. (2001).
[2]    Brachman, R. J., Khabaza, T., Kloesgen, W., Piatesky-Shpiro, G., & Simoudis, E. Mining business databases. Communication of the ACM, 39(11) (1996) 42-48.
[3]    Hayes-Roth, F. Rule-based systems. Communications of the ACM, 28 (1985) 921-932.
[4]    Alupoaei, S., & Katkoori, S. Ant colony system application to marcocell overlap removal. IEEE Transactions Very Large Scale Integration (VLSI) Systems, 12(10) (2004) 1118-1122.
[5]    Bianchi, L., Gambardella, L.M., & Dorigo, M. An ant colony optimization approach to the probabilistic travelling salesman problem. In J. J. Merelo, P. Adamidis, H. G.Beyer, J. L. Fernandez-Villacanas, and H. P. Schwefel (Eds.), Proceedings of PPSN-VII, seventh international conference on parallel problem solving from nature. Lecture Notes in Comput Science (2002) 883-892. Berlin: Springer.
[6]    Demirel, N. C.,  & Toksari, M. D. Optimization of the quadratic assignment problem using an ant colony algorithm. Applied Mathematics and Computation, 183(1), (2006) 427-435.
[7]    Lina, B. M. T. Lub, C. Y., Shyuc, S. J., & Tsaic, C. Y. Development of new features of ant colony optimization for flowshop scheduling. International Journal of Productions Economics, 112(2),(2008)742-755.
[8]    Ramos, G. N., Hatakeyama, Y., Dong, F., & Hirota, K. Hyperbox clustering with ant colony optimization (HACO) method and its application to medical risk profile recognition. Appied Soft Computing, 9(2), (2009) 632-640.

[9]     Parpinelli, R. S., Lopes, H. S., & Freitas , A. A. An ant colony algorithm for classification rule discovery. In H. A. Abbass, R. A. Sarker, & C. S. Newton (Eds.), Data mining: A heuristic  approach (2002a) 191-208. London: Idea Group Publishing.

[10]   Parpinelli, R. S., Lopes,H.S.,&Freitas,A.A.An ant colony algorithm for classification rule discovery.In H.A.Abbass,R.A.Sarker,&C.S.Newton(Eds.),Data mining:A heuristic approach (2002a) 191-208.London Idea Group Publishing.

[11]   Parpinelli, R.S., Lopes, H.S.,& Freitas, A.A. Data mining with an ant mining optimization Algorithm IEEE Transaction on Evolutionary Computation,6(4),(2002b) 321-332.

[12]   Jiang, W., Xu, Y., & Xu, Y. A novel  data method based on ant colony algorithm. Lecture Notes in Computer Science, (2005) 3584, 284-291.

[13]   Jin, P., Zhu, Y.,  Hu, K., & Li, S. classification rule mining  based on ant colony optimization algorithm. In D. S. Huang, K. Li, & G. W. Irwin (Eds.), Intelligent control and automation, lecture notes in control and information and sciences (2006) 654-663. Berlin: Springer.

[14]   Liu, B., Abbass, H, & Mckay, B. Classification rule discovery with ant colony optimization. IEEE Computational Intelligence Bulletin, 3(1),(2004) 31-35.

[15]   Roozmand, O., & Zamanifar, K. Parallel ant miner 2. In L. Rutkowski et al.(Eds.), Artifical Intelligence and soft computing – ICAISC (2008) 681-692 Berlin: springer.

[16]   Liu, B., Abbass, H.A., & Mckay, B. Density-based heuristic for rule discovery for Ant-Miner .In: The 6th Australia-Japan joint workshop on intelligent and evolutionary system (2002) 180-184 Canberra, Australia.

[17]   Wang, Z. & Feng, B. Classification rule mining with an improved ant colony algorithm. In G. I. Webb & X. Yu (Eds.), AI 2004: Advances in artificial intelligence, lecture notes in computer science (2005) 357-367 Berlin: Springer.

[18]   Blum, C., & Dorigo, M. Deception in ant colony optimization. In M. Dorigo, M. Birattari, C. Blum, L. M. Gambardella, F. Mondada, & T. Stutzle (Eds.), Proc. ANTS 2004, Fourth Internet Workshop on Ant Colony Optimization and Swarm Inteligence, Lecture Notes in Computer Science (2004). Berlin:Springer.

[19]   Nejad, N. Z., Bakhtiary, A. H., & Analoui, M. Classification  using unstructured rules and ant colony optimization. In: Proceedings of the International multi conference of engineers and computer scientists Vol. I, (2008) 506-510. Hong Kong.

[20]   Dorigo, M., Di Caro, G., & Gambardella, L. M. Ant algorithms for discrete optimization. Artificial Life, 5(2), (1999) 137-172.

[21]   Blum,C.Ant colony optimization: introductionnand recent trends.Physics of Life Reviews,2(2005)353-373.

[22]   Merkle, D. Middebdorf, M., & Schmerck, H. Ant colony optimization for resource-constrained project scheduling ,IEEE Transcations on Evolutionary Computation, 6(4)  (2002) 333-346.

[23]   Fuellerer, G., Doerner, K. F., Hartl, R. F., & Iori, M .Ant Colony Optimization for two-dimensional loading vehicle routing problem. Computers  and Operations Research, 36(3), (2009) 655-673.

[24]   Reimann, M., Doerner, K., & Hartl, R.F. D-ants: Savings based ants divide and conquer the vehicle routing problems. Computers & Operations Research, 31(4), (2004) 563-591.

[25]   Colorni, A., Dorigo, M., Maniezzo, V., & Trubian, M. An system for job-shop scheduling. Belgian Journal of Operations Research. Statistics and Computer Science (JORBEL), 34, (1994). 39-52.

[26]   Stutzle, T. MAX-MIN Ant system for the quadratic assignment problem. Technical report AIDA-97-4, FG Intellektik, FB Innformatik, TU Darmstadt, Germany (1997b).

[27]   Leguizamo n, g., & Michalewicz, Z., A new version of Ant System for subset problems. In P. J. Angeline, Z. Michalewicz, M. Schoenauer, X. Yao, & A. Zalzala (Eds,), Proceedings of the 1999 Congresson Evolutionary Computation (CEC'99) (pp. 1459-1464). Piscataway, NJ, IEEE Press.

[28]   De Campos, L. M., Ga'mez, J. A., & Puerta, J. M. Learning Bayesian networks by ant colony optimization: Searching in the space of orderings. Mathware and Soft computing, 9(2-3) (2002b).251-268.

[29]   Corry, P., & Kozan, E.. Ant Colony Optimization for machine layout problems. Computational Optimization and Applications,28(3),(2004) 287-310.

[30]   Jia Yu, Yun Chen, Jianping Wu, Modeling and implementations of classification rule discovery by ant colony optimization for spatial land-use suitability assessment, Computers, Environment and Urban Systems 35 (2011) 308-319.

[31]   W. Lee, S.J. Stolfo, K.W. Mok, A data mining framework for building intrusion detection models, in: Proceedings of IEEE Symposium on Security and Privacy, 1999, pp. 120-132.

[32]   W.Lee, S.J Stolfo, K. W. Mok, Mining audit data to build intrusion detection models, in: Proceedings of the 4th International conference on Knowledge Discovery and Data Mining, AAAI Press, 1998,pp, 66-72.

[33]   L. Khan, M. Awad, B. Thuraisingham, A new intrusion detection systems using support vector machines and hierarchial clustering. The VLDB Journal 16(2007) 507-521.

[34]   X. Xu, Adaptive intrusion detection based on machine learning: feature extraction, classifier construction and sequential pattern prediction, Information Assurance and Security 4(2006) 237-246.

[35]   Y. Feng, J. Zhong, C. Ye, Z. Xiong, Z. Wu Intrusion detection classifier base on self-organizing ant colony networks clustering, Information Assurance Security 4(2006) 247-256.

[36]   C.-F. Tsai, Y. F. Hsu, C.-Y. Lin, W.-Y. Lin, Intrusion detection by machine learning: a review, Expert Systems with Applications 36(2009) 11994-12000.

[37]     S. Kumar, Classification and detection of computer intrusions. Ph.D. Thesis, Purdue University, August 1995.
[38]     B. Mukherjee, L. T. Heberlein, K. N. Levitt, Network intrusion detection, IEEE, Network (1994) 26-41.
[39]     E. H. Spafford D. Zamboni, Intrusion detection using autonomous agents, Computer Networks 34(4) (2000) 547-570.
[40]     F. Klawonn, F. Hoppner What is fuzzy about fuzzy clustering? Understanding and improving the concept of the fuzzifier, in: Cryptographic Hardware Embedded Systems. Vol. 2779, Springer, 2003, pp.254-264.
[41]     J. Han, M. Kamber, J. Pei, Data Mining Concepts Models Methods and Algorithms John Wiley, 2003.
[42]     UCI KDD Archive, KDD Cup 1999 data, 1999.http://kdd.ics.uci.edu/databases/kddcup99/kddcup99.html.

# Steady Resource Selection Model for Housing Projects in Nigeria

Mee-Edoiye M. Andawei

*Department of Civil Engineering, Faculty of Engineering Niger Delta University, Nigeria*

**Abstract:** *One of the primary indicators of any country's level of development is the volume of decent housing stock provided for her citizenry. This could be done by government agencies and the private investors as noticed in many developing countries. Interest of governments of developing countries in this respect is high to attract support from both the public and other development partners. Events of the past show that, housing delivery is pioneered by host governments and their agencies alone in most. The situation is not different in Nigeria, with over 80million in search of decent accommodation. The direct interventionist policy of the Nigerian government have been restricted to the initiation of policy guidelines, leaving the on-site assembly of project resources and its attendant challenges to the direct initiative of developers. Available data shows that a total of NGN4.5billion was spent between the first and fourth development plans with forest of uncompleted projects. The existence of numerous slums in our cities and overcrowding in many homes tells the story that decent accommodation is expensive to provide and beyond the reach of the low-income group. The singular focus of government in initiating policy guidelines and the inability of those who manages the production process of housing units to establish the optimum resource requirement and utilization in the construction process have added more injury to the high cost of housing production. This paper is therefore aimed at determining the resource selection criteria that will optimize resources for housing delivery in Nigeria.*

**Keywords:** *housing, leveling, optimization, project, smoothening.*

## I. Introduction

One of the cardinal objectives of housing policy initiative in Nigeria and indeed other developing countries is to provide her citizenry with decent and affordable accommodation. A review of the Nigerian sub-sector would be necessary to have a glimpse of the success rate and challenges of affordable housing delivery. This review will consider some policy initiatives and actions taken by government from colonial era to the establishment of the National Housing Fund.

### 1.1 Colonial Era

During the colonial era, the public action in housing was confined to layouts and construction of government reserved areas - GRAs. These reserved areas were exclusive meant for the colonial masters, who were only interested in the exportable profits and not the housing challenges faced by the teeming Nigerians. This was evident in the merger provision made for the housing sub-sector in the initial development plan.

### 1.2 First National Development Plan 1967-1968

Housing activities in the first national development which span 1962-1968 was little and savored of colonial legacy. The emphasis of government was on the provision of senior staff housing which led to setting up regional housing corporations in Kaduna-northern Nigeria, Enugu-eastern Nigeria, Ibadan-western Nigeria and Benin City-mid-western Nigeria.

### 1.3 Second National Development Plan 1970-1974

As it was in the first national development plan, housing and town planning were taken together in the second national development 1970-1974. This period coincided with the oil boom and sharp increase in government revenue. In the face of up-surge of the revenue profile, the federal government granted a loan of NGN6milion to the Nigerian Building Society in 1972, to expand the credit facilities to the low income group in the country. The government took a further bold step in setting up the Federal Housing Authority and allocated an initial sum of NGN5million for direct construction of houses in the then twelve states. This historically marked the beginning of government's direct participation in housing delivery.

**1.4 Third National Development Plan 1975-1980**
The period of the third national development plan 1975-1980 saw much greater attention in sphere of public housing than earlier attempts by government. As table below shows, the sum of NGN2million was earmarked for the direct provision of two hundred and two housing units for low and medium income groups in Nigeria. The period also witnessed the construction of many federal and state low cost housing estates and emergence state housing corporations' medium income housing estates. It was during this plan period that the Building Society was acquired by the Federal Mortgage Bank of Nigeria and was given an initial capital of NGN150million to encourage private participation in housing delivery. The government also set up several rent tribunals and enacted the Land Use Decree.

**1.5 Fourth National Development Plan 1980-1985**
This period witnessed high public awareness in housing delivery. Expectedly, housing featured prominently in the manifestos of the then five political parties and the Federal Ministry of Housing and Environment was created and the Nigeria Housing Policy was formulated in 1981. The key points of the policy include:

a. To improve and increase the quantity and quality of housing stock in Nigeria.
b. To give attention to the concept of affordability in housing provision
c. To aid self help housing programmes.
d. To encourage owner occupation by expanding credit facilities.
e. To mobilize both government and private sector financing into housing.

The Nigerian government also earmarked NGN2.645billion for execution of housing programme within the planned period as contained below.

**1.6 National Housing Fund**
The most recent of these policies is the National Housing Fund as contained in Decree 3 of 1992. The policy requires banks, insurance companies and allied financial institutions to compulsorily contribute 10% of their loan-able funds and advances for on-lending to primary mortgage institutions. It stipulates a mandatory monthly contribution of 2.5% of the basic income of every Nigerian earning a minimum of NGN3,000.00 per annum into the fund, which is managed by the Federal Mortgage Bank of Nigeria.

## II.   Literature Review
The target of United Nation Commission for Human Settlements at the global level, to ensure the provision of decent accommodation for the over 750million homeless people in developing countries by the year 2000 was not met due to myriad of problems. Some of the reasons advanced for this abysmal success rate include high cost of housing construction, inadequate funds, ubiquitous land tenure system and the interventionist policies of the governments of these countries. Andawei (2001) in his contribution noted that the inability of performing organizations to determine the best resource combination at any given point in time of the project life also the high cost of housing production. The application of optimal resource selection model during the pre and post-contract stages of the project is required to minimize budget and schedule slips noticed with many housing projects.

**2.1 Scientific Approach**
This resource optimization model has its origin from scientific management. Scientific management has the orientation of scientific analysis of work methods and the development of management principles and practices. They aimed at efficiency and productivity through the reduction of unit cost and increase in output per worker, improved working condition, reduction of physical efforts and the development of the science of work (Jaja and Zeb-Obipi, 1999). One dominant factor in management of resources is the scientific approach in problem solving. It involves the definition and analysis of work, measurement of facts, experimentation, development of work methods and techniques.
These processes in their opinion, will meet the objective of firms which is to achieve optimum efficiency in production, as the survival of the firm in a competitive world like ours, depends largely on their ability to deliver goods and services at a competitive cost. Managers, therefore deals more with physical relation between inputs and outputs in the production chain, which ultimately produces the best input combination to achieve a given output level of a production system for which housing in one.

**2.2 Housing Project Criteria**

The housing production process which involves series of processes requires the utilization of machines, men of various skills, materials and time. This transformation process which primarily utilizes raw materials shares the novel characteristic of a project being managed by project team members. The primary focus of these project team members is to develop selection models to deal with these dynamic and expected project surprises at both the planning and execution stages of these projects to achieve set budget and time which is the baseline of every project success. Though it appears to be very challenging to always complete projects within the planned completion period, such delayed completion have multiplier effect on the cost and other project parameters. In the words of Franklin(1780) to tradesmen: "that every team member is aware that time is money. If the planned time-scale is exceeded, the original cost estimates and budgets are almost certain to be exceeded too. A project costs money during every day of its existence, living or non-living, weekday or weekend." The knowledge of the effect of project time variance on other cost parameters and how cost behaves over time throughout the project life is therefore remains fundamental to success of housing project delivery. Project resources are scarce and can be optimally utilized only when they are available in the right proportion at any given point in time by proper resource planning, allocation, monitoring and control by the project team (Harris and McCaffer 1985).

In their separate arguments, Mazda(2000), Andawei(2001) contended that project time and cost which are the basic project success factors can no longer be open-ended. They then suggested the adoption of traditional procedures to achieve the cost and time needs of these acyclic projects through the use of bills of quantities, two-stage tendering and other cost control mechanisms. They noted that the Nigerian construction environment has exacerbates this situation as project team members are faced with frequent changes in the monetary and fiscal policies, inadequate data and records on productivity levels, imprecise project objectives and uncertain expertise of team members, which accounts for present level of performance of the housing sub-sector.

In agreeing with the above assertion, Spinner(1997) contended that the complexities introduced in the construction industry by technological innovations have made job coordination and resource allocation with traditional methods more difficult, which has made the adoption of better and more efficient techniques in resource planning imperative. Despite the existence of this revenue enhancing approach, it is obvious that its prolonged application in housing production can no longer stand due to the discovery by stakeholders in the housing sub-sector of more sophisticated resource scheduling models that maximizes project resource usage.

**2.3 Resource Scheduling**

Resource scheduling is the process of allocating resource available capacities to jobs and activities. It is the process that helps the team members to determine and make available the resource requirements of the various project activities within pre-determined constraints. The purpose of resource scheduling is to ensure that available capacity of project resources are efficiently used to achieve the objective of the activity and the organization at a broader scale. In practice, resource scheduling results in to a time-based plan which allows the determination of and allocation of resources within the limitations in the best manner. Rogers(1985) opined that the resource schedule that guarantees efficiency is the one that can maintain a high utilization of labour, plant, materials and time. Popescu and Charoenngam(1995) see resource scheduling to be more than resource allocation. They argued that the assumption of unlimited resource availability by some concepts like network techniques, can no longer hold as the constraining indices of the different resource categories are not the same at all points of the project. They instead considered resource availability at the required quantity and time in the project life critical. They concluded by recommending resource levelling and smoothening as the alternative solution for resource and time constrained situations respectively. While I agree totally with their view on the open-ended resource availability assumption of network techniques, I do not completely share the opinion that resource leveling and smoothening techniques as the ultimately solution to the resource dis-equilibrium, but can enhance resource efficiency level which forms the core of this paper.

The basic approach to all scheduling techniques is to form a network of activities and events relationship that pictorially portrays the sequential logic of activities in the project. In supporting this widely held view, Kenzer (1995) and Udosen (1997) considered network as one of the most acceptable and powerful tool for project planning and control as it provides a consistent framework for planning, allocating, monitoring and controlling project resources. Secondly, it shows the activity interdependence and defines the critical activities in any given project and helps to identify floats of project activities.

**2.4 Resource Management**

For the project implementation to proceed efficiently and as scheduled, the project team members must source for the right type of resources, quantities planned for each activity as at the time of execution. While this process appears to be simple and straightforward the resources' need may fluctuate from time to time thus

necessitating hiring and or layoffs to fit in nicely with the daily resource demand. According to Akpan and Chizea(2013), this is not always practically feasible. Even if this could be possible with labour, it may not be possible with fixed assets jointly used in the project execution, they asserted. They further contended that the allocation of resources to a project invariably poses two fundamental problems to the project manager.

Firstly, the determination of maximum level of resources during each time period and secondly is the problem associated with excessive resource demand at certain periods and very low demand almost immediately following a high demand. They identified some of the resource allocation problems and the accompanying scheduling bottlenecks such as when there is excessive fluctuation in resource demand, when resource availability is limited and when resource availability is not a limiting factor.

They further recommended that under excessive resource fluctuation, the project team should endeavour to maintain a steady demand level on available resources so as to avoid inefficiency and wastage inherent in high turnover of resources that accompany excessively high demand at certain periods with low demand immediately following.

When resources are in limited supply, the project team in an attempt to maintaining a steady resource level, should minimize the inevitable increase in project duration, cost due to overheads and possible cost penalties that could result from project delay. Thirdly when resource availability is not a limiting factor, concerted efforts should be made by the project team to stay within the project budget and minimize the cost of idle resources.

**2.5 Determination of the Steady Resource Demand Level**

From the foregoing though Akpan and Chizea(2013) tried to identify some of the key challenges in making supply and demand decisions of project resources, they were unable to give an outright solution. Some of the key issues raised by them which is evident in every resource decision making is the issue of providing the optimum level or steady level of resources to avoid shortage as well as idle time, which this paper intend to address.

Firstly, when the resource demand is more than the resource supply, it will result to resource shortage. The affected project activities have to wait until the resources are made available. The implication on the project is that, the entire project has to wait until when the resources are made available. Worst still if it is an activity that is vulnerable and must to be completed. The total cost to the project resulting from this shortage, amongst others, will include idle time of the waiting resources, likely extension of project completion time and its attendant penalties. Similarly when the resource supply is in excess of demand, the additional idle resources will be counted as additional cost to the project. The question how do one maintain an optimum resource level that would be economical. I considered two key optimization techniques - the greatest resource utilization and the minimum slack heuristics in attempting to solve this daunting resource selection challenge.

**2.5.1 Greatest resource demand**

This heuristics assigns priority on activities on the basis of total resource requirements, with priority given to the activities with the greatest resource demand. The activity priority is computed as

$$\text{priority} = dj \sum_{i=1}^{n} ri, j$$

dj = duration of activity j
rij = per period requirement of resource i by activity j
n = number of resource types

**2.5.2 Minimum slack first**

In this heuristics, activities are ordered by the amount of least slack going first. In this regard resources would be devoted to critical or near critical activities, delaying those with greater slack. Delay of any activity uses some of its slack, as the activity will have a better chance of receiving resources in the next allocation.

**2.5.3 General heuristic features**:

As scheduling heuristic operates, irrespective of the priority rule, one or two events will occur. The routine will run out of activities for the current period before all activities are scheduled or it will run out of resources before all activities are scheduled. If the former occurs, the excess resources are left idle or assigned elsewhere in the project organization. On the other hand if one or two of the resources are exhausted, activities requiring these resources are slowed down or delayed until the next period when resources are re allocated. The main problem facing the project manager under this situation is to find a schedule that satisfies the sequence constraint and minimizing the overall duration of the entire project within the resource ceiling. The resulting optimal resource schedule should be able to indicate when to start any activity and at what level of resources it should maintain while it is alive.

Work of Fendley(1968) focused on the best heuristics for resource scheduling. While their findings vary somewhat because of their different assumptions, the minimum slack rule was found to be the best. The choice according to them was based on the fact that minimum slack heuristic results to minimum project schedule slippage, the best utilization of facilities and minimum total system occupancy time. These results and works of other authors so far have increased the range of uncertainty in the choice of heuristics that should be considered generally suitable and optimal. In an effort to narrow the region of choice the idea of random activity selection was proposed by Akpan(2000).

## III. Methodology

This paper adopted a steady resource level model to establish the resource equilibrium. The model has twelve procedural steps:

1. Draw a network diagram of the project
2. Compute all the critical indices - the earliest and latest times of all the activities
3. Determine the longest - critical path and all the critical activities
4. Prepare a resource demand table for all the activities and allocate resources
5. Determine the total resource demand per time period - daily, weekly or monthly.
6. Compare the total resource demand with the resource availability.
7. Compute the cost of hiring additional resources to meet up the resource demand
8. Level the resources of all the activities within the limits of resource availability
9. Re-determine the new project duration after the resource leveling
10. Compute the cost of delayed completion.
11. Compare the cost of delayed and the cost of hiring additional resources
12. Make your resource allocation decision.

Two sample projects were used to demonstrate the steady resource level model. The project details as shown below.

### Case 1
Resource considered for allocation is A-Labour
Resource ceiling: 7units each

*Table* 3.1 Project Network details for case 1

| Activity | Duration | Resource Demand A |
|----------|----------|-------------------|
| 1-2 | 2 | 3 |
| 2-3 | 3 | 3 |
| 3-4 | 2 | 4 |
| 4-5 | 2 | 3 |
| 4-6 | 3 | 4 |
| 4-7 | 2 | 3 |
| 5-7 | 2 | 4 |
| 6-7 | 3 | 4 |
| 7-8 | 3 | 4 |
| 8-9 | 4 | 3 |

### Case 2
Resource considered for allocation is A-Labour
Resource ceiling: 6units each

Table 3.2 Project Network details for case 2

| Activity | Duration | Resource Demand A |
|----------|----------|-------------------|
| 1-2 | 3 | 3 |
| 2-3 | 3 | 4 |
| 3-4 | 3 | 3 |
| 4-5 | 3 | 4 |
| 4-6 | 2 | 3 |
| 5-7 | 2 | 3 |
| 6-7 | 3 | 3 |
| 7-8 | 3 | 3 |

**Table 3.3 Resource demand for case 1**

| Activity | ACTIVITY DURATION (weeks) | | | | | | | | | | | | | | | | | | | | | |
|---|---|---|---|---|---|---|---|---|---|---|---|---|---|---|---|---|---|---|---|---|---|---|
| | 1 | 2 | 3 | 4 | 5 | 6 | 7 | 8 | 9 | 10 | 11 | 12 | 13 | 14 | 15 | 16 | 17 | 18 | 19 | 20 | 21 | 22 |
| 1-2 | 3 | 3 | | | | | | | | | | | | | | | | | | | | |
| 2-3 | | | 3 | 3 | 3 | | | | | | | | | | | | | | | | | |
| 3-4 | | | | | | 4 | 4 | | | | | | | | | | | | | | | |
| 4-5 | | | | | | | | 3 | 3 | | | | | | | | | | | | | |
| 4-6 | | | | | | | | 4 | 4 | 4 | | | | | | | | | | | | |
| 4-7 | | | | | | | | | | | 3 | 3 | | | | | | | | | | |
| 5-7 | | | | | | | | | | | 4 | 4 | | | | | | | | | | |
| 6-7 | | | | | | | | | | | 4 | 4 | 4 | | | | | | | | | |
| 7-8 | | | | | | | | | | | | | | 4 | 4 | 4 | | | | | | |
| 8-9 | | | | | | | | | | | | | | | | | 3 | 3 | 3 | 3 | | |
| Total Resource Demand | 3 | 3 | 3 | 3 | 3 | 4 | 4 | 7 | 7 | 4 | 11 | 11 | 4 | 4 | 4 | 4 | 3 | 3 | 3 | 3 | — | — |

**Table 3.4 Steady resource level for case 2**

| Activity | RESOURCE DEMAND / DURATION | | | | | | | | | | | | | | | | | | | | | |
|---|---|---|---|---|---|---|---|---|---|---|---|---|---|---|---|---|---|---|---|---|---|---|
| | 1 | 2 | 3 | 4 | 5 | 6 | 7 | 8 | 9 | 10 | 11 | 12 | 13 | 14 | 15 | 16 | 17 | 18 | 19 | 20 | 21 | 22 |
| 1-2 | 3 | 3 | | | | | | | | | | | | | | | | | | | | |
| 2-3 | | | 3 | 3 | 3 | | | | | | | | | | | | | | | | | |
| 3-4 | | | | | | 4 | 4 | | | | | | | | | | | | | | | |
| 4-5 | | | | | | | | 3 | 3 | | | | | | | | | | | | | |
| 4-6 | | | | | | | | 4 | 4 | 4 | | | | | | | | | | | | |
| 4-7 | | | | | | | | | | | 3 | 3 | | | | | | | | | | |
| 5-7 | | | | | | | | | | | 4 | 4 | | | | | | | | | | |
| 6-7 | | | | | | | | | | | | | 4 | 4 | 4 | | | | | | | |
| 7-8 | | | | | | | | | | | | | | | | 4 | 4 | 4 | | | | |
| 8-9 | | | | | | | | | | | | | | | | | | | 3 | 3 | 3 | 3 |
| Total Resource Demand | 3 | 3 | 3 | 3 | 3 | 4 | 4 | 7 | 7 | 4 | 7 | 7 | 4 | 4 | 4 | 4 | 4 | 4 | 3 | 3 | 3 | 3 |

**Table 3.6 Resource demand for case 2**

| Activity | ACTIVITY DURATION (weeks) | | | | | | | | | | | | | | | | | | | | | |
|---|---|---|---|---|---|---|---|---|---|---|---|---|---|---|---|---|---|---|---|---|---|---|
| | 1 | 2 | 3 | 4 | 5 | 6 | 7 | 8 | 9 | 10 | 11 | 12 | 13 | 14 | 15 | 16 | 17 | 18 | 19 | 20 | 21 | 22 |
| 1-2 | 3 | 3 | 3 | | | | | | | | | | | | | | | | | | | |
| 2-3 | | | | 4 | 4 | 4 | | | | | | | | | | | | | | | | |
| 3-4 | | | | | | | 3 | 3 | 3 | | | | | | | | | | | | | |
| 4-5 | | | | | | | | | | 4 | 4 | 4 | | | | | | | | | | |
| 4-6 | | | | | | | | | | 3 | 3 | | | | | | | | | | | |
| 5-7 | | | | | | | | | | | | | 3 | 3 | | | | | | | | |
| 6-7 | | | | | | | | | | | | 3 | 3 | 3 | | | | | | | | |
| 7-8 | | | | | | | | | | | | | | | 3 | 3 | 3 | | | | | |
| Total | 3 | 3 | 3 | 4 | 4 | 4 | 3 | 3 | 3 | 7 | 7 | 7 | 6 | 6 | 3 | 3 | 3 | | | | | |

**Table 3.7 Steady resource level for case 2**

| Activity | ACTIVITY DURATION (weeks) | | | | | | | | | | | | | | | | | | | | | |
|---|---|---|---|---|---|---|---|---|---|---|---|---|---|---|---|---|---|---|---|---|---|---|
| | 1 | 2 | 3 | 4 | 5 | 6 | 7 | 8 | 9 | 10 | 11 | 12 | 13 | 14 | 15 | 16 | 17 | 18 | 19 | 20 | 21 | 22 |
| 1-2 | 3 | 3 | 3 | | | | | | | | | | | | | | | | | | | |
| 2-3 | | | | 4 | 4 | 4 | | | | | | | | | | | | | | | | |
| 3-4 | | | | | | | 3 | 3 | 3 | | | | | | | | | | | | | |
| 4-5 | | | | | | | | | | 4 | 4 | 4 | | | | | | | | | | |
| 4-6 | | | | | | | | | | | | | 3 | 3 | | | | | | | | |
| 5-7 | | | | | | | | | | | | | | | | 3 | 3 | | | | | |
| 6-7 | | | | | | | | | | | | | | | 3 | 3 | 3 | | | | | |
| 7-8 | | | | | | | | | | | | | | | | | | 3 | 3 | 3 | | |
| Total | 3 | 3 | 3 | 4 | 4 | 4 | 3 | 3 | 3 | 4 | 4 | 4 | 3 | 3 | 3 | 6 | 6 | 3 | 3 | 3 | | |

## IV.   Discussion Of Results

Assuming that in each of the cases, the cost of hiring one unit of resource A is $1,600 per 40hour-week and the cost of delayed completion is $4,500 per week for both cases. The best resource decision to take can be established using the above model.

*Case 1*

In meeting the contract duration of twenty weeks as shown in TABLE 3.3, the resource needs of week eleven and twelve is eleven units while the available resource ceiling is seven. If we must meet the original project duration we must as a matter of necessity hire additional four units of resources A for at least weeks 11 and 12, which will cost $12,800. Alternatively the project can be extended by another two weeks and maintain the original resource ceiling of 7units throughout the project. This will attract an additional sum of $9,000 as cost of delayed completion. The optimal resource decision in this case is to maintain the resource ceiling of 7units and extend the project by two weeks.

*Case 2*

In meeting the contract duration of seventeen weeks as shown in TABLE 3.6, the resource needs of week ten to twelve is seven units while the available resource ceiling is six. If we must meet the original project duration we have to as a matter of necessity hire additional one unit of resource A for at least weeks 10, 11 and12, which will cost $4,800. Alternatively the project can be extended by another four weeks and maintain the original resource ceiling of 6units throughout the project. This will attract an additional sum of $13,500 as cost of delayed completion. In this case extending the project by three weeks is not the optimal decision. The best thing to do is to hire additional one unit of resource A to the three week period.

## V.   Conclusion

Project resource demand and supply decision making have been beclouded with uncertainties over the years. Several models have been developed in recent times to correctly predict the meeting point of resource demand and supply chains in the housing project delivery process. The use of Steady Resource Level model, in my opinion will help project managers in the housing and other sectors dealing with resource combination of non-acyclic projects to make a more rational resource decisions at any given activity node point.

## REFERENCE

[1.]    S.A. Jaja and I. Zeb-Obipi, Management: elements and theories (Port Harcourt: Pearl Publishers, 1999). (1)
[2.]    F. Harris and R. McCaffer, Modern construction management, (London: Collins Professional Technical Books, 1985). (2)
[3.]    F. Mazda, Engineering management (Singapore: Addison Wesley Longman, 2000). (3)
[4.]    M.M. Andawei, Application of network-based techniques in the cost control and management of construction works, The Quantity Surveyor, 37(4), 2001, 24-27. (4)
[5.]    M.P. Spinner, Project management principles and practices (New Jersey: Prentice Hall Upper Saddle River, 1997). (5)
[6.]    C.M. Popescu and C. Charoenngam C,  Project planning, scheduling and control in construction. an encyclopedia of terms and applications (New York: Wiley 1995). (6)
[7.]    H. Kernzer, Project management: a systems approach to planning, scheduling and Controlling ( New York: Van Nostrand Reinhold, 1995). (7)
[8.]    U.J. Udosen, The techniques of project planning and control  (Uyo:Classic Nigeria Company, 1997). (8)
[9.]    E.O.P Akpan and E.F Chzea, Project management: theory and practice (Owerri: FUTO Press, 2013). (9)
[10.]   L.G Fendley, Towards the development of a complete multi-project scheduling system, Journal of Industrial Engineering, 19(10), 1968, .505-515. (10)
[11.]   E.O.P Akpan, Priority rules in project scheduling: a case for random activity selection, Journal of Production Planning and Control, 11(2), 2000, 165-170. (11).

# Novel mechanical Whistle Counter Device for Pressure Cooker

Sanyam Saxena[1], Akhil Muralidharan[2], A. Kannan[3], Sanya Joseph[4]

*[1,2,3] SMBS, Vellore Institute of Technology, Chennai Campus, Tamil Nadu, India.*
*[4] Indira Gandhi Delhi Technical University for Women, India*

***Abstract:*** *The domestic pressure cooker is one of the most essential cooking utensils used in kitchens worldwide. It ensures that the food is prepared in time, and still retains the nutritional value of the ingredients used. A major flaw associated with it is the fact that one has to keep an account of the number of whistles generated by the pressure regulator. Otherwise, the food turns out undercooked or Over-cooked and even leads to wastage of fuel. The problem becomes particularly acute for the hearing impaired. The device explained in this paper helpstokeep the track of number of whistles produced by cooker.*

***Keywords:*** *Mechanical counter, pressure cooker, pressure regulator, slider, coupler, crank, rotating disc, bevel gears.*

## I. Introduction

The pressure cookers are extensively used in household for preparing food. The pressure cookers have preference over the conventional cooking utensils due to the advantage of retaining the nutritive value and flavor of the cooked food and less time required for cooking and thus effecting considerable savings in time and fuel. The temperature inside the cooker is increased by increasing pressure inside the vessel. The vessel is completely sealed from all sides, increasing the pressure. This ensures that the water inside the vessel has to reach a higher temperature before it can get converted to steam, due to the additional pressure developed inside the vessel and thus reducing time consumed in cooking. The steam produced has a fairly high heat potential. When the pressure within the cooker /vessel increases beyond a certain limit, steam is let out using the steam regulator. This produces a whistling sound. The whistling sound produced in a pressure cooker indicates the status of the food being cooked.

It can be cumbersome to keep tabs on the number of whistles produced during the cooking process. The situation becomes particularly unsettling for the hearing impaired. The following device counts the number of whistles produced by the pressure regulator, thus, eliminating the above mentioned problem.

---

### NOMENCLATURE

d  – Diameter of the rotating disc
t  – Traverse distance of the whistle/dead load
a  – Distance between pivot point and link (connecting the disc)
b  – Distance between pivot point and link (connecting the whistle)

---

## II. Present Study

There is no such "mechanical device" currently in existence, which can be used to keep track of the number of whistles produced by the pressure regulator in a pressure cooker. Such counting devices will help eliminating the problems faced while using the humble pressure cooker, especially for the hearing impaired and thus, in maintaining the quality of food being prepared.

## III. Description of the device

The following innovation aims to alleviate the problems faced in house hold kitchens, pertaining to the usage of pressure cookers. It involves a counting mechanism which counts the number of whistles produced by the cooker (the number of times the weight is lifted) and helps in keeping tabs on the food being cooked.

A slider crank mechanism is a four bar mechanism used to convert reciprocatory to rotary motion and vice versa. The device is based on the first inversion of the slider crank mechanism. The shortest link is made the

crank (rotary motion). One of the adjacent links is made the coupler. The link opposite to the crank is made the slider (reciprocatory motion).A link that makes a complete rotation is called a crank. A link that reciprocates/rocks is called a slider. The assembly has been illustrated in the following diagram.
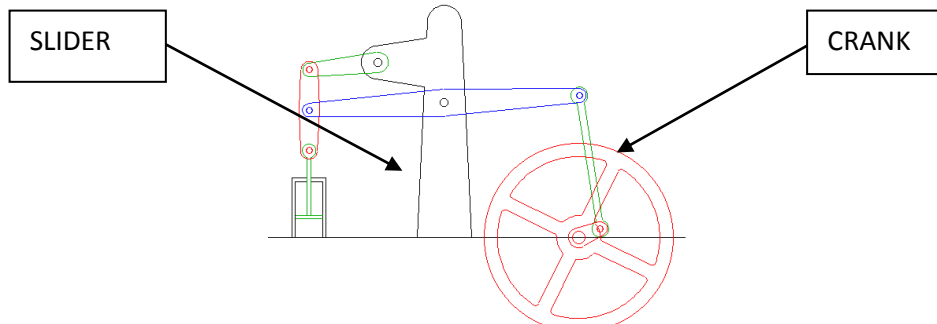


Fig. 1: Conversion of liner to rotary motion

The primary components used in the assembly are as follows:
1.   An alloy steel rod connected to the pressure regulator, acting as the slider. It reciprocates.
2.   An alloy steel rod connected to the slider, acting as the coupler
3.   An alloy steel rod connected to the coupler, acts as a crank. It rotates
4.   A rotating disc connected to the crank.
5.   A mechanical counter
6.   A shaft connecting the rotating disc and mechanical counter
7.   Supports for the coupler, rotating shaft, rotating disc.
8.   Bevel gears (miter gears, in this case), to transfer power between intersecting shafts. (perpendicular, in this case) Bevel gears have been used to connect the shaft connected to the rotating disc and the shaft connected to the mechanical counter. These shafts are so placed so that the counter is placed in such a position that it becomes easier for the user to view/read the output of the counter.
9.   The slider, coupler, crank are inter connected using pin joints.



Fig.2: A mechanical counter
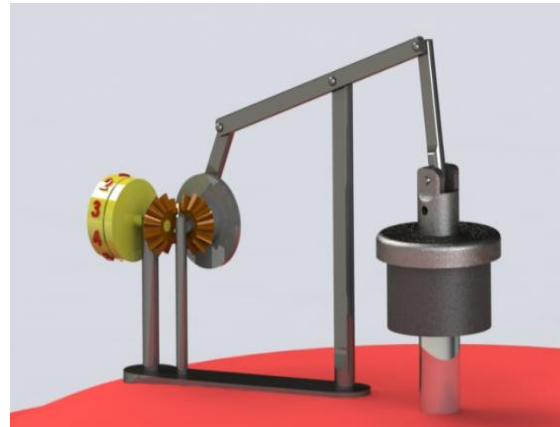


Fig.3: CAD Model of the device
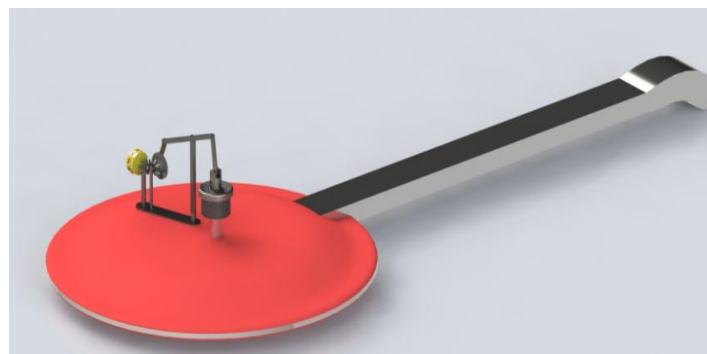


Fig. 4: Device mounted on a cooker top

# IV.  Working

As the pressure in the cooker rises it exerts a force on the regulator/dead weight, making it to traverse from the bottommost point to the topmost point. The link will move the rocker arm and correspondingly the other link will move down leading to a 180 degree rotation of the disc. As pressure is released the whistle falls down to its initial position and the disc covers the remaining 180 degree of rotation.

Thus a complete 360 degree rotation is made by the disc when the whistle travels back to its initial position. The disc is connected to a mechanical counter by means of bevel gears. The number of rotations is equal to the number of times the cooker whistles. So each rotation of disc is calibrated on the counter and the reader will read out the number of rotation made, accounting for the number of whistles made by the cooker.

Since the displacement of the regulator/dead weight "t" is of the order of a few millimeters. This needs the use of a crank with diameter of a few millimeters. Since it is very difficult to manufacture bevel gears of comparable dimensions, a bigger gear needs to be fixed on the crank. This requires the use of a bigger crank in order to generate the required torque to rotate the gears. This is achieved by placing the pivoting point of the connecting rod closer to the whistle end resulting in larger displacement on the disc end. Thus appropriate diameters of the disc and gears can be selected for fabrication.

*Calculation of dimensions of various components used*

Mathematically, total distance traversed by slider/piston = 2 x (radius of the crank), Hence, the distance covered by the pressure regulator from the bottommost position to the topmost position and back to the bottom most position = 2 x radius of the crank In order to prevent the reverse motion of disc, the diameter of disc "d" is kept slightly less than the displacement "t".
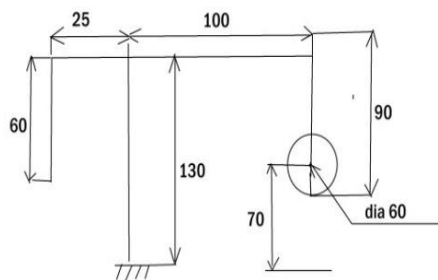


Fig.4: dimensions of all links and parts          Fig.5: to determine the position of pivot point
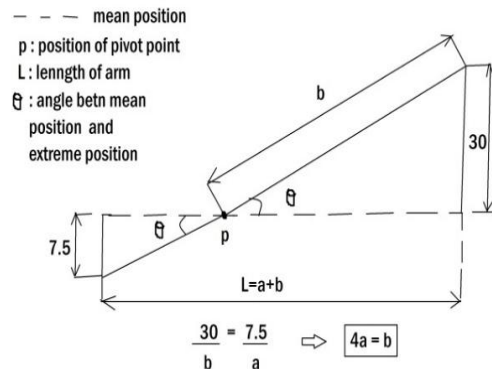
# V.  Thermal Analysis Of Cad Model
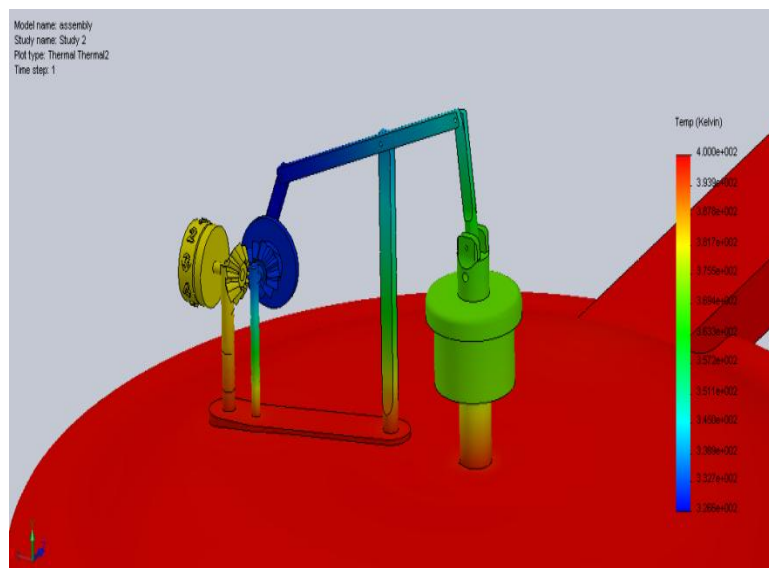


Fig. 6: Thermal analysis

The temperature in the interior part of a pressure cooker can reach up to130 degrees Celsius. Continuous exposure to such temperature can affect the working of the slider crank mechanism and also the mating of the bevel gears due to thermal expansion. Thermal analysis was performed in Solid Works 2013 to evaluate the temperatures attained by each component so that suitable materials can be chosen.

For the analysis the interior temperature of the pressure cooker was assumed to be 400 degree Kelvin, thermal conductivity of stainless steel taken as 17 W/m-K and the convection coefficient was assumed to be 7.9 W/m$^2$K between steel and air, 5.7 W/m$^2$-K between cast iron and air etc. The temperatures were found to vary between 400K to 326K among the components. Accordingly the choice of materials used for links and the counter were modified.

## VI. Issues Involved In Working Of Model And Fabrication, And Their Solutions

1. The device needs to constantly work under high humidity and pressure (kitchen conditions), thus there are fair chances of rusting of components. In order to prevent it, the components and links are made up of aluminum or alloy steel.
2. Resetting of counter: Once a cooking cycle is completed, the counter needs to be reset to 0 value, this can be done by removing the whistle and rotating the counter in anti-clock wise manner. This will set the counter to 0.
3. Chances of jamming of mechanism: The working condition involves emission of oil and food particles from the cooker, coagulation of such particles can jam the moving or rotating parts. Thus the device is well prevented inside a casing, having a window for read out.

## VII. Benefits Of the Device

1. Eliminates the chances of missing the whistle count, thereby preventing the food from under cooking or over cooking
2. Helps the hearing impaired people to cook food.

## VIII. Summary

Thus every time the pressure in the cooker increases the force imparted at the regulator end is transmitted along the different links in the assembly. The displacement is magnified as it reached the crank and the translational input is converted to rotary motion. The number of rotations so produced is computed using a mechanical counter. This gives a fair idea about the status of the food being cooked, thus eliminating the troubles entailed in keeping a check on the conventional pressure cookers used in regular households.

## REFERENCES

[1] Pressure cooker design by Syntens.
[2] A model of heat and mass transfer inside a pressure cooker, journal of Food Engineering
[3] A comprehensive review on pressure cookers, Applied Energy, Volume102, February2013, Pages 1399-1421
[4] Chapter-10 bevel Gear Mechanical Design Engineering Handbook, 2014,Pages 403-438
[5] Introduction of an ewbevel gear measurement standard, CIRP Annals–Manufacturing Technology, Volume 62,Issue 1, 2013, Pages 515-518 [6]Building a mechanical counter.

## Contents :

# Improving overall equipment effectiveness by Implementing Total Productive Maintenance in plastic pipe manufacturing industries

Guide Er. Dinesh Kumar[1], Dashrath kumar[2]

*[1]Assistant Professor, Mechanical Engineering Department, J.C.D.M. College of Engg. Sirsa, Haryana*
*[2]M.tech Mechanical Engg. Final year Reg. no. 1211283005*

**Abstract:** *The global marketplace is highly competitive and organizations who want to survive long-term, have to continuously improve, change and adapt in response to market demands. Improvements in a company's performance should focus on cost cutting, increasing productivity levels, quality and guaranteeing deliveries in order to satisfy customers. Total Productive Maintenance (TPM) is one method, which can be used to achieve these goals. TPM is an approach to equipment management that involves employees from both production and maintenance departments. Its purpose is to eliminate major production losses by introducing a program of continuous and systematic improvements to production equipment. This thesis is aimed at implementation of Total productive maintenance in Shiv Plastic Pvt. Limited.*

## I.  Introduction

**Total Productive Maintenance**

In today's industrial scenario huge losses/wastage occur in the manufacturing shop floor. This waste is due to operators, maintenance personal, process, tooling problems and non-availability of components in time etc. Other forms of waste includes idle machines, idle manpower, break down machine, rejected parts etc are all examples of waste. The quality related waste are of significant importance as they matter the company in terms of time, material and the hard earned reputation of the company. There are also other invisible wastes like operating the machines below the rated speed, start up loss, break down of the machines and bottle necks in process. Zero oriented concepts such as zero tolerance for waste, defects, break down and zero accidents are becoming a pre-requisite in the manufacturing and assembly industry. In this situation, a revolutionary concept of TPM has been adopted in many industries across the world to address the above said problems.

TPM is a unique Japanese philosophy, which has been developed based on the Productive Maintenance concepts and methodologies. This concept was first introduced by M/s Nippon Denso Co. Ltd. of Japan, a supplier of M/s Toyota Motor Company, Japan in the year 1971. Total Productive Maintenance is an innovative approach to maintenance that optimizes equipment effectiveness, eliminates breakdowns and promotes autonomous maintenance by operators through day-to-day activities involving total workforce.

A strategic approach to improve the performance of maintenance activities is to effectively adapt and implement strategic TPM initiatives in the manufacturing organizations. TPM brings maintenance into focus as a necessary and vitally important part of the business. The TPM initiative is targeted to enhance competitiveness of organizations and it encompasses a powerful structured approach to change the mind-set of employees thereby making a visible change in the work culture of an organization. TPM seeks to engage all levels and functions in an organization to maximize the overall effectiveness of production equipment. This method further tunes up existing processes and equipment by reducing mistakes and accidents.

TPM is a world class manufacturing (WCM) initiative that seeks to optimize the effectiveness of manufacturing equipment (Shirose, 1995). Whereas maintenance departments are the traditional center of preventive maintenance programs, TPM seeks to involve workers from all departments and levels, including the plant-floor to senior executives, to ensure effective equipment operation.
TPM as the name suggests consists of three words:
(1) **Total**. This signifies to consider every aspect and involving everybody from top to bottom.
(2) **Productive**. Emphasis on trying to do it while production goes on a minimize troubles for production.
(3) **Maintenance**. Means keeping equipment autonomously by production operators in good position.

### Goals of Total Productive Maintenance

The goal of TPM focuses on improving corporate culture through improvement of human resources and plant equipment. The Japan Institutes of Plant Maintenance (JIPM) has put forward the five goals of TPM which are the minimum requirements for the TPM development.

**1.** Improving equipment effectiveness.
**2.** Improving maintenance efficiency and effectiveness.
**3.** Early equipment management and maintenance prevention.
**4.** Training to improve the skills of all people involved.
**5.** Involving operators in routine maintenance.

### Improving Equipment Effectiveness

Equipment effectiveness is a measure of the value added to production through equipment. This goal is to increase equipment effectiveness so each piece of equipment can be operated to its full potential and maintained at that level. Nakajima describes in his book that TPM maximizes equipment effectiveness though two types of activity to insure that the equipment performs to design specifications which is the true focus of TPM

- *Quantitative*: It increases the equipment's total availability & improving its productivity within a given period of operating time.
- *Qualitative***:** It reduces the number of defective products, stabilizing & improving quality.

Although the equipment must operate at its design speed, produce at the design rate, and produce a quality product at these speeds and rates, there are factors which might obscure efficient utilization of the equipment. Examining, identifying and eliminating all losses which obscure the efficiency of the equipment will increase the efficiency of the equipment

The concept of zero breakdowns and zero defects are inevitable to maximize equipment effectiveness. These equipment losses include: equipment downtime loss, performance loss, and defect loss. Various equipment losses can be quantitatively calculated through measuring equipment effectiveness that ties the '6 major losses' to three measurable.

## II. Literature Review

TPM is a unique Japanese philosophy, which has been developed based on the Productive Maintenance concepts and methodologies. This concept was first introduced by M/s Nippon Denso Co. Ltd. of Japan, a supplier of M/s Toyota Motor Company, Japan in the year 1971.

*Nakajima (1989)* A major contributor of TPM has defined TPM as an innovative approach to maintenance that optimizes equipment effectiveness, eliminates breakdowns, and promotes autonomous maintenance by operators through day-to-day activities involving the total workforce. TPM is not a maintenance specific policy; it is a culture, a philosophy and a new attitude toward maintenance.  He suggests that equipments should be operated at 100 percent capacity 100 percent of the time. *Pirsig et al. (1996)* emphasizes upon seven unique broad elements and four main themes in any TPM implementation program. The key themes in the TPM implementation program include training, decentralization, maintenance prevention and multi-skilling, while the broad elements include asset strategy, empowerment, resource planning and scheduling, systems and procedures, measurement, continuous improvement and processes. Have proposed developed the eight-step approach to the implementation of TPM involving system, measurement, autonomous maintenance, housekeeping, continuous improvement, culture, training, and plant design.  *Maier et al. (1998)* consider preventive maintenance, teamwork shop floor employee competencies, measurement and information availability work environment, work documentation, and extent of operator involvement in maintenance activities as factors reflecting TPM implementation. The basic practices of TPM are often called the pillars or elements of TPM. The entire edifice of TPM is built and stands, on eight pillars *Noon et al. (2000)* explained TPM seeks to maximize equipment effectiveness throughout the lifetime of the equipment. It strives to maintain the equipment in optimum condition in order to prevent unexpected breakdown, speed losses, and quality defects occurring from process activities. There are three ultimate goals of TPM: zero defects, zero accident, and zero breakdowns *Marco Castro (2013)*  Total Productive Maintenance (TPM) is one of the World Class Manufacturing tools that seeks to manage assets by involving everyone in the manufacturing organization. The financial and productivity bane fits of implementing TPM are significant. Many approaches have been proposed regarding TPM implementation procedures, of which logically sequenced implementation procedure is an identified success factor, yet the majority of TPM implementation attempts fail to achieve their intended goals.

## III. Methodology

**Overall Equipment Effectiveness**

Overall Equipment Effectiveness has been developed by the JIPM. OEE is regarded as an important measurement for assessing the performance of equipment. The method distinguishes the six big loss types, and three key performance measurements: availability, performance rate and quality rate that combines into one consolidated metric. The OEE can be used to help focus on improving the performance of machinery and associated processes by identifying those performance opportunities that will have the greatest impact to the bottom line. Improvements in changeovers, quality, machine reliability, working through breaks and more, can be measured and improved utilizing the OEE metric. It is the ratio of actual equipment output to its theoretical maximum output. OEE can be viewed as the percent of time that equipment would need to run at its maximum speed in order to attain the actual output of that tool or machine. It is calculated using the following formula.

$$OEE = Availability \times Performance\ Rate \times Quality\ Rate$$

To find the overall equipment efficiency of the steel Industry, identifying the six major losses of the machines was the first stride by organizing under three key factors. And then data pertinent to those losses was collected for randomly selected machineries. The major losses that are identified and the OEE of the selected machineries presented as follows.

**Calculating Overall Equipment Effectiveness**

Some of the data pertinent to the above loss are difficult to obtain, since the company doesn't apply the overall equipment efficiency concepts in evaluating the performance of the machines at the individual level. It has been attempted to gather some relevant data to estimate the OEE of the typical machinery.

**Availability**

The availability is the ratio of time needed for operating the equipment to the time actually consumed for operation and it is expressed as:

$$Availability = \frac{Actual\ Running\ Time}{Scheduled\ Running\ Time} \times 100$$

Whereas Actual Running Time = Scheduled running time – Unplanned stoppages.

Unplanned stoppage means the period during which the line is stopped due to equipment failure, setup, adjustment, and change over and so forth.

So that:-

$$Availability = \frac{Scheduled\ running\ time - Unplanned\ stoppages}{Scheduled\ running\ time} \times 100$$

**Performance Rate**

The performance rate is the ratio between actual average production and standard production. This factor indicates the ratio of the actual output and the targeted output. Actual output is the actual performance of the operation and is less than the targeted output due to rough running of the equipment, jams and equipment wear. Hence, it is expressed as:

$$Performance\ Rate = \frac{Actual\ average\ production}{Standard\ production} \times 100$$

$$Average\ production\ rate = \frac{Total\ production\ in\ cycle\ period}{No.of\ working\ days\ in\ a\ cycle\ period}$$

**Quality Rate**

This is percentage of good parts out of total produced sometimes called "yield". Quality losses refer to the situation when the line is producing, but there are quality losses due to in-progress production and warm up rejects. We can express a formula for quality like this:

$$Quality\ Rat = \frac{No.of\ Products\ Processed - No.of\ Products\ rejected}{No.of\ Products\ Processed} \times 100$$

## IV. Case Study

**About The Company**

Shiv Plastic Pvt. Limited Company Are a Certified Company Situated In Fatehabad Industrial Area. Company Are Manufacturing Plastic Polythene Pipes Of Different Sizes According To The Demand Of Customers And Uses In Different Area. The Material Are Supplied To Company From Delhi. The Product Are Supplied In Different Area.

**The Different Diameter From 5 Inches To 12 Inches Pipes Are Manufacturing**

| Sr. no. | Dia. in Inches | Dia. In cm | Dia. In mm |
|---|---|---|---|
| 1. | 5 | 13 | 130 |
| 2. | 6 | 15 | 150 |
| 3. | 7 | 18 | 180 |
| 4. | 8 | 20 | 200 |
| 5. | 9 | 23 | 230 |
| 6. | 10 | 25 | 250 |
| 7. | 11 | 28 | 280 |
| 8. | 12 | 30 | 300 |

**Dia. Of pipes to manufacturing in industry**

**Sample of Monthly Production of Pipes Before TPM ( May 2013 To Sept. 2013)**

| S. No | Month | Production(Quintal) |
|---|---|---|
| 1 | May | 2200 |
| 2 | June | 2190 |
| 3 | July | 2150 |
| 4 | August | 2170 |
| 5 | September | 2100 |

**Production and Wastage Before TPM ( May 2013 to September 2013)**

| Months | Production (Quintal) | Waste (Quintal) | % |
|---|---|---|---|
| May | 2200 | 250 | 11.36 |
| June | 2190 | 239 | 10.91 |
| July | 2150 | 235 | 10.93 |
| August | 2170 | 235 | 10.82 |
| September | 2100 | 230 | 10.95 |

**Sample of Monthly Production of Pipes After TPM ( Dec. 2013 To April 2014 )**

| S. No | Month | Production(Tones) |
|---|---|---|
| 1 | December | 2240 |
| 2 | January | 2250 |
| 3 | February | 2160 |
| 4 | March | 2240 |
| 5 | April | 2220 |

**Production and Wastage After TPM( Dec 2013 to April 2014)**

| Months | Production (Tones) | Waste Tones) | % |
|---|---|---|---|
| December | 2240 | 195 | 8.7 |
| January | 2250 | 190 | 8.4 |
| February | 2160 | 170 | 7.8 |
| March | 2240 | 170 | 7.5 |
| April | 2220 | 165 | 7.4 |
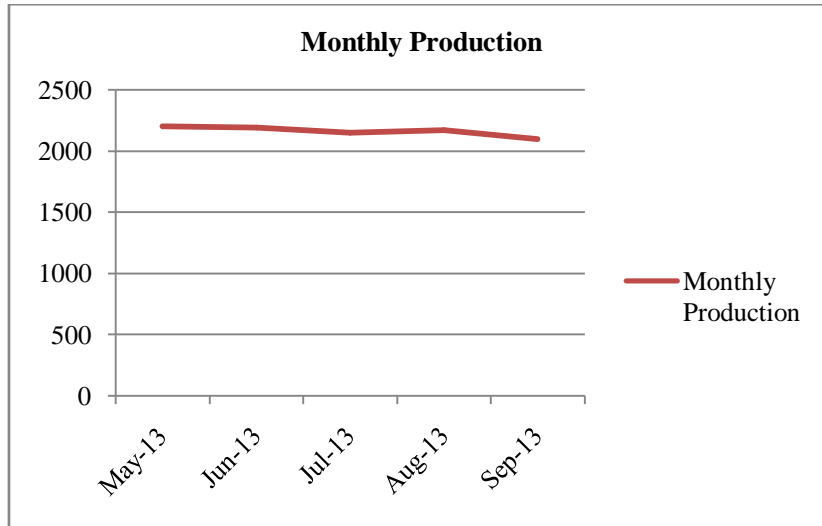
**Monthly Production (Quintal) of Pipes without TPM**
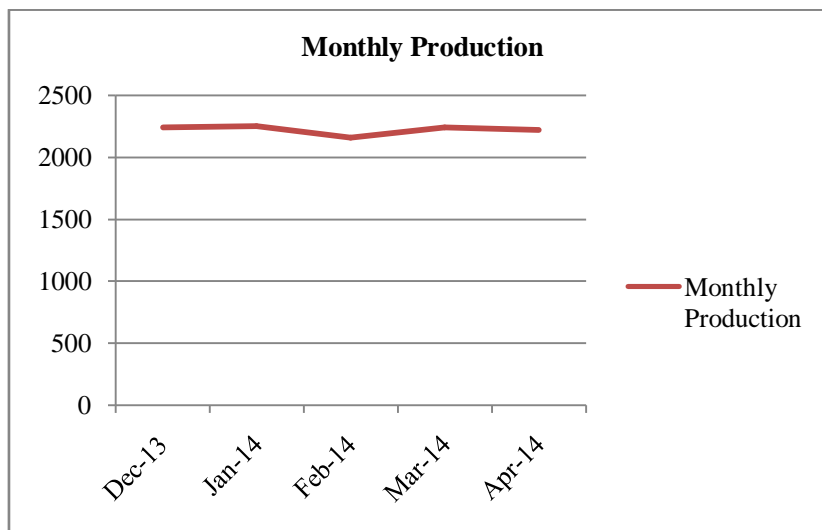


**Monthly Production (Quintal) of Pipes With TPM**
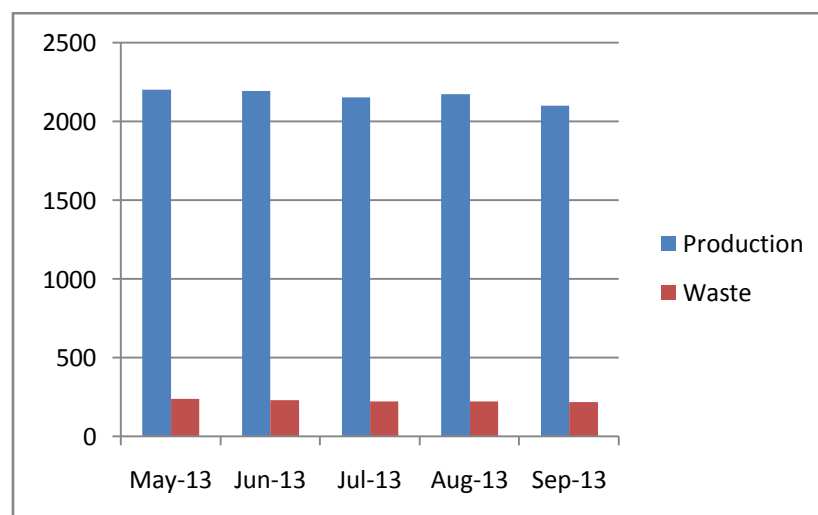


**Waste (Quintal) and production (Quintal) report of the Five months Without Implementation TPM**
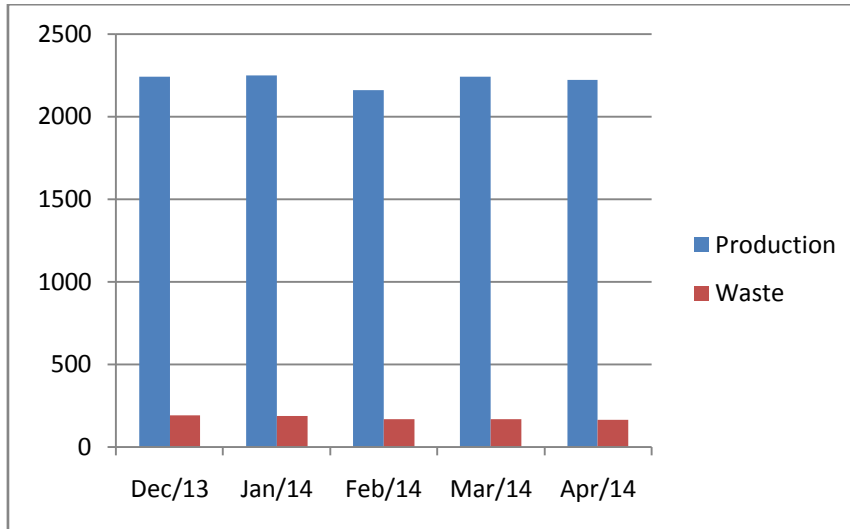
**Waste (Quintal) and production (Quintal) report of the Five months With Implementation TPM**
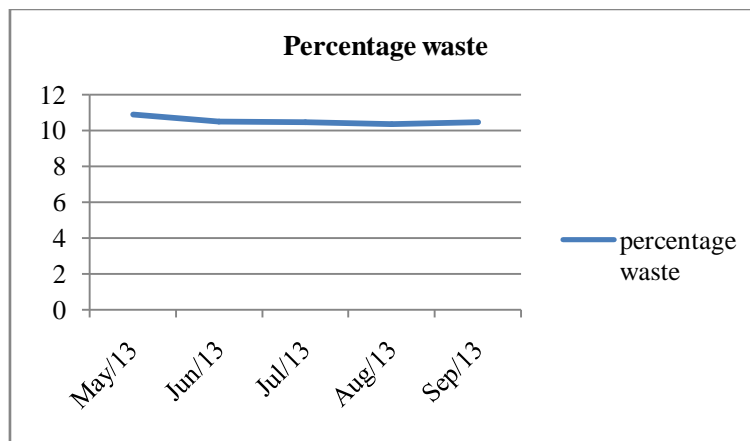


**Percentage waste of the Five months Without TPM**
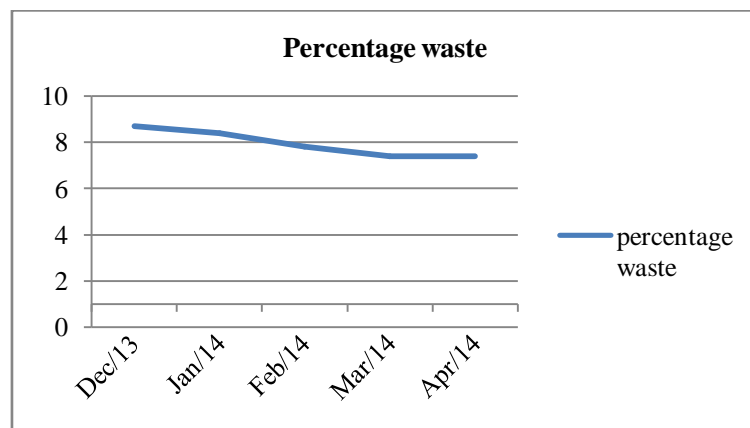


**Percentage waste of the Five months with TPM**

**The major losses that are identified**
1. Equipment failure loss
2. Setup and adjustment loss
3. Startup loss
4. Minor stoppage and idling loss:
5. Speed Loss
6. Quality Defect and rework loss

## V. Conclusion

The main objective of this paper understand TPM concept and to generate awareness among the budding technologies about TPM. During research in Shiv plastic Pvt. limited we have compare before implementing TPM and after implementing TPM data and distort major problems by TPM based corrective action plan we have reduce 60% problems improve OEE. TPM methodology not only increases the effectiveness of the manufacturing system but also increase the effectiveness of the entire organization through mandatory participation and continuously improve Productivity, quality, cost, Delivery, safety health and Morale.

## REFRENCES

[1]. Ravikant V et al. (2011), "International Journal of Advanced Engineering Sciences and Technologies", Vol. 6 No. 2, pp. 270 – 276.
[2]. Ahuja and Khamba (2008), "Strategies and success factors for overcoming challenges in TPM implementation in Indian manufacturing industry", Journal of Quality in Maintenance Engineering, Vol. 14 No. 2, pp. 123-147.
[3]. Wakjira and Ajit Pal Singh, (2012), "Total productive maintenance: A case study in manufacturing industry", Global Journal of Researches in Engineering, Vol 12, pp 25-31.
[4]. Ahuja & Khamba, (2008), "Strategies and success factors in TPM", Vol. 14 No. 2, pp. 123-147.
[5]. Ahuja & Khamba, (2007), "An evaluation of TPM implementation initiatives in an Indian manufacturing", Journal of Quality in Maintenance Engineering, Vol. 13 No. 4, pp. 338-352.

# Thermal Expansivity Behavior and Determination of Density of Al 6061-Sic-Gr Hybrid Metal Matrix Composites

S A Mohan Krishna[1], Dr. T N Shridhar[2], Dr. L Krishnamurthy[3]

[1]*Associate Professor, Department of Mechanical Engineering, Vidyavardhaka College of Engineering, Mysore, India,*

[2, 3]*Dept. of Mechanical Engineering, The National Institute of Engineering, Mysore-570 008, India*

**Abstract:** *Metal Matrix Composites (MMCs) covers a very wide range of materials to simple reinforcements of castings with low cost refractory wool, to complex continuous fires lay-ups in foreign alloys. In particular, many of the considerations arising due to fabrication, processing and service performance of composites are related of processes that take place in the interfacial region between matrix and reinforcement. The thermal characterization of hybrid metal matrix composites is increasingly important in a wide range of applications. In the present scenario, research work is accomplished on hybrid composites based on thermal expansion as limited research has been carried out on hybrid composite based on thermal properties. The coefficient of thermal expansion is one of the most important properties of MMCs. Since nearly all Metal Matrix Composites are used in various temperature ranges, measurement of CTE as a function of temperature is necessary in order to know the behaviour of the material. In this research paper, the thermal expansion behaviour of Al-SiC-Gr composites is investigated and its response are studied between 50°C to 350°C using Horizontal Platinum Dilatometer. The assessment of thermal parameters of composites will benefit to analyze heat capacity, variation in the intensity of heat, heat diffusion and heat release rate. The density of the composites is also determined using water displacement method. The theoretical and experimental values are determined to check the porosity of composites. Using Rule of Mixtures, the theoretical density is determined and the same is compared with the experimental value, which help to understand the distribution of reinforcements.*

**Key words:** *Thermal Characterization, Coefficient of Thermal Expansion, Hybrid Composites, Temperature and Dilatometer.*

## I. Introduction

A composite material is a macroscopic combination of two or more distinct materials having a recognizable interface between them. Composites are used not only for their structural properties, but also for electrical, thermal, tribological and environmental applications [1]. The applications of these materials are absolutely appreciative and applicable in almost all areas of mechanical engineering. Aluminium Silicon alloys in particular finds extensive and increased applications in industries due to their properties viz., high fluidity, low melting point, high strength, corrosion resistance, good casting characteristics and lower coefficient of thermal expansion [2]. Thermal Analysis of Metal Matrix Composites is required to clearly examine the thermal properties viz., Thermal Conductivity, Temperature Difference, Thermal Capacity or Heat Difference, Coefficient of Thermal Expansion and Rate of Heat Transfer. Thermal Analysis is also often used as a term for the study of Heat Transfer to measure Heat capacity and Thermal Conductivity.

The behaviour of composite materials is often sensitive to changes in temperature. This is mainly because, the response of the matrix to an applied load is temperature dependent and changes in temperature can cause internal stresses to be set up as a result of differential thermal contraction and expansion of the constituents. Thermal analysis of hybrid composites is a pragmatic approach to clearly study its thermal characteristics. Most of the thermal studies are mainly concerned with Aluminium matrix composites but minimum information is available on hybrid composites [3].

## II. Literature Review

Aluminium Matrix Composites (AMC) consists of Aluminium or its alloys as the continuous matrix and a reinforcement that can be particle, short fiber or whisker or continuous fiber. Research and development activities of the last decade have resulted in the evolution of a class of MMCs termed as Discontinuously Reinforced Aluminium (DRA) composites. Particle or discontinuously reinforced Aluminium Matrix

Composites have become very important because they are economical when compared to continuous fiber reinforced composites and they have relatively good isotropic properties compared to fiber-reinforced composites. These materials have caught the attention of producers and researchers all over the world because of their outstanding properties such as high-strength-to-weight ratio, improved wear and elevated temperature resistance and low density. In addition these materials are comparatively easier to manufacture than the continuously reinforced composites and have a great potential to be available at low cost [4]. These AMCs, which are high performance materials, have also attracted considerable attention from automotive industries and component suppliers. Though initially aimed only at aerospace and defence products, AMCs have progressively moved into higher volume applications. These materials employ a metallic matrix such as Aluminium to which is added reinforcement materials such as Alumina ($Al_2O_3$) or Silicon Carbide. The net result is a composite material with enhanced mechanical properties particularly with regard to density and stiffness and other mechanical properties [5].

**S Cem Okumus, Sardar Aslam** et al [6] in their paper have studied on Thermal Expansion and Thermal Conductivity behaviour of Al/Si/SiC hybrid composites clearly highlights that Aluminium-Silicon based hybrid composites reinforced with silicon carbide and graphite particles were prepared by liquid phase particle mixing and squeeze casting. The thermal expansion and thermal conductivity behaviour of hybrid composites with various graphite contents (5.0; 7.5; 10 wt.%) and different silicon carbide particle sizes (45 μm and 53 μm) were investigated. Results indicated that increasing the graphite content improved the dimensional stability, and there was no obvious variation between the thermal expansion behaviour of the 45 μm and the 53 μm silicon carbide reinforced composites.

**R Arpon, E Louis** et al [7] have analyzed that thermal expansion behaviour of Aluminium/SiC composites with bimodal particle distributions where it summarizes that The thermal response and the coefficient of thermal expansion (CTE) of Aluminium matrix composites having high volume fractions of SiC particulate have been investigated. The composites were produced by infiltrating liquid Aluminium into preforms made either from a single particle size, or by mixing and packing SiC particulate of two largely different average diameters (170 and 16 μm, respectively). The experimental results for composites with a single particle size indicate that the hysteresis in the thermal strain response curves is proportional to the square root of the particle surface area per unit volume of metal matrix, in agreement with current theories. Instead, no simple relationship is found between the hysteresis and any of the system parameters for composites with bimodal particle distributions. On the other hand, the overall CTE is shown to be mainly determined by the composite compactness or total particle volume fraction; neither the particle average size nor the particle size distribution seems to affect the overall CTE. This result is in full agreement with published numerical results obtained from finite element analyses of the effective CTE of Aluminium matrix composites. The results also indicate that the CTE varies with particle volume fraction at a pace higher than predicted by theory.

**R A Saravanan, J Narciso** et al [8] have investigated on thermal expansion behaviour of particulate metal matrix composites explains that Aluminium-matrix composites containing thermally oxidized SiC particles of controlled diameter ranging from 3 to 40 μm have been produced successfully by vacuum assisted high-pressure infiltration. Their thermal-expansion coefficients (CTEs) were measured between 25°C and 500°C with a high-precision thermal mechanical analyzer (TMA), and compared with the predictions of various theoretical models. The thermal-expansion behavior of the three-phase $Al/SiC/SiO_2$ composite shows no significant deviation from the predictions of elastic analysis, since the measured CTEs lie within the elastic bounds derived by Schapery's analysis. The effect of particle size is quite evident in the pressure-infiltrated composites: the larger the particles, the greater the thermal expansion of the composite. The observed behavior of these composites is discussed in terms of particle size, silica layer formed during oxidation, and thermal stresses developed as a result of the CTE mismatch between the reinforcement and the matrix.

**Tran Nam, Requena** et al. [9] have studied on effect of thermal cycling on the expansion behaviour of Al/SiC composites is carried out where the coefficient of thermal expansion (CTE) and accumulated plastic strain of the pure aluminium matrix composite containing 50% SiC particles during thermal cycling (within temperature range 298–573 K) were investigated. The composite was produced by infiltrating liquid aluminum into a preform made by SiC particles with an average diameter of 14 microns. Experiment results indicated that the relationship between the CTE of Al/SiC and temperature is nonlinear; CTE could reach a maximum value at about 530 K. The theoretical accumulated plastic strain of Al/SiC composites during thermal cycling has also been calculated and compared with the experimental results.

**N Chawla, X Deng** et al [10] comprehensively describes thermal expansion behaviour of Aluminium matrix composites with densely packed SiC particles where the coefficient of thermal expansion (CTE) of Al-based metal matrix composites containing 70 vol.% SiC particles (Al/SiC) has been measured based on the length change from room temperature to 500°C. In the research work, the instantaneous CTE of Al/SiC was studied by thermo-elastic models and micromechanical simulation using finite element analysis in order to explain abnormalities observed experimentally. The CTE was predicted according to analytical thermo-elastic

models of Kerner, Schapery and Turner. The CTE was modeled for heating and cooling cycles from the temperature range $20^0C$ to $500^0C$ considering the effects of microscopic voids and phase connectivity. The finite element analysis is based on a two-dimensional unit cell model comparing between generalized plane strain and plane stress formulations. The thermal expansion behaviour is strongly influenced by the presence of voids and confirms qualitatively that they cause the experimentally observed decrease of the CTE above $250^0C$.

The literature review presented extensively will refer to the work carried out on composite materials pertaining to mechanical, tribological and thermal properties. In the present scenario, work is accomplished on hybrid composites based on mechanical properties but limited research has been carried out on hybrid composite concerned with thermal properties and characterization. Thermal studies on composite materials are getting greater importance in the present scenario. Thermal analysis will help to understand the properties of materials as they change with temperature. It is often used as a term for the study of heat transfer through structures. Metal Matrix Composites can be customized to provide good CTE matching for thermal management and thermal conductivity applications. It is essential to evaluate new materials for the thermal stability and to measure properties including CTE and thermal conductivity for specialty products [6].

## III. Experimental Procedure

In the research work, the coefficient of thermal expansion is determined using Linesis 75 Platinum Horizontal Dilatometer. Fig 3.1 shows a typical Platinum Horizontal Dilatometer. Thermal expansion is the tendency of matter to change in volume in response to change in temperature. The degree of expansion to the change in temperature is called the material's coefficient of thermal expansion and generally varies with temperature. Coefficient of Thermal Expansion is one of the most important properties of MMCs. Since nearly all Metal Matrix Composites are used in various temperature ranges, measurement of CTE as a function of temperature is necessary in order to know the behaviour of the material. Several different systems for measurement of CTE can be used depending on the temperature conditions. One of the most common systems used is a dilatometer. A dilatometer measures the length or the volume changes of the sample, when the sample follows a temperature program and submits a small force. In a push rod dilatometer, the change in length of the sample is detected by an inductive displacement transducer. Calibration and corrections of measurements are done by using various standards and comparison with materials of known expansion. The measurement of the coefficient of thermal expansion (CTE) can be carried out in the temperature range from approximately – 150°C to 1500°C.

Linesis 75 Platinum Horizontal Dilatometer comprises of Thyristor controlled unit, Linear Variable Differential Transformer (LVDT), automatic pressure control unit, variety of sample holders and RCS (Rate Controlled Sintering) software. The coefficient of thermal expansion (CTE) can be controlled by two parameters simultaneously namely wall thickness and volume fraction comprehensively. The CTE values have a stronger dependence on particle volume fraction than the wall thickness in the range of temperatures explored. The thermal expansion results with the variation of temperature for the composites and the matrix are shown for different percentage composition. It is obvious that the CTE of the composites and matrix increases with increase in temperature.

The pushrod dilatometer method for measuring thermal expansion is experimentally simple, reliable and easy to automate. In this method, the relative expansion of the specimen is transmitted referring to cooled or heated zone to a measuring device (an extensometer) by means of tubes and/or rods of a stable reference material. In this technique, the specimen is placed at the end of a tube and a smaller rod is placed in the tube in contact with the specimen. An extensometer has the capability to detect the difference in expansion between the specimen and an equal length of the tube. The most widely used extensometer is the LVDT (Linear Variable Differential Transformer).



**Fig 3.1- Linesis 75 Platinum Horizontal Dilatometer**

## IV.   Results & Discussion

For the determination of CTE, the size of the cylindrical sample is diameter 5 mm and length 10 mm. 5 samples are considered with different percentage compositions. Al 6061 is the base alloy and reinforcements SiC and Gr with different percentage compositions 1.25%, 2.5%, 3.75% and 5% are selected. All the specimens were tested from room temperature to 360°C. This temperature range was selected so as to include the entire usable range of the composites, without the formation of liquid phase in the matrix. The data were obtained in the form of per cent linear change versus temperature. Standard data analysis software was used to evaluate the CTE of the composites tested and was determined at intervals of 20 °C.   Rate Controlled Sintering (RCS) is an asset for standard dilatometer software. During measurement using dilatometer, the change in length of the sample for the required temperature range is considered. The purpose of RCS is to determine the optimal sinter process, especially the optimal temperature-time profile. Some of the salient parameters considered during the determination of CTE are sample length, relative density of the samples and sintering temperature.  The melting point of Aluminium is 560°C. But during the testing process, it was limited to 360 °C, as there is greater possibility of reaching molten condition.

The evaluation of CTE of hybrid metal matrix composites is relatively difficult to predict because several factors namely volume fraction, morphology and distribution of the reinforcements, matrix plasticity, interfacial bondage, and the internal structure of the composites, may influence the results. During the evaluation of CTE, thermal strain can be attributed to thermal stress and higher thermal stress can lead to the generation of strain between the heating and cooling cycles [6]. The thermal expansion behavior of Al alloy reinforced with Silicon Carbide and Graphite were measured at prominent temperatures varying from 20°C to 350°C. The CTE of the hybrid composites are lower than the conventional Al-SiC composites with the same volume fraction of SiC. The thermal expansion behaviour of the hybrid composites depends on the intrinsic thermal expansion properties of SiC and double interpenetrating structure [11].
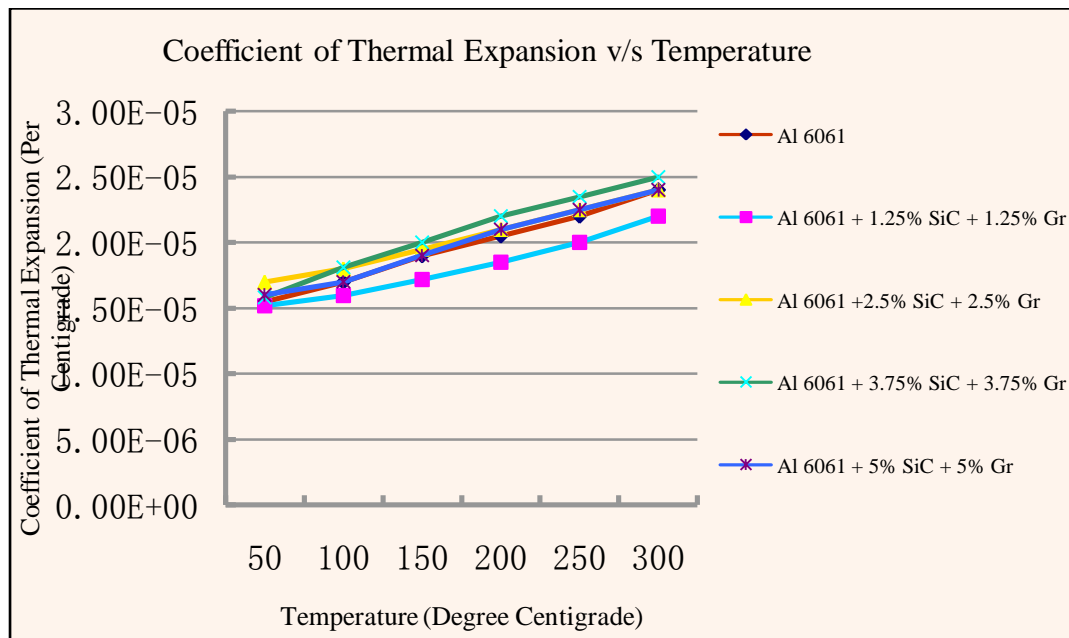


**Fig 4.1: Variation of CTE v/s Temperature for different compositions of MMC**

Fig 4.1 shows the variation of CTE and temperature for different compositions of hybrid MMC. It is noticed that, the CTE of the hybrid composites with different percentage compositions increases with the increase in temperature. There is consistency in the increase of CTE for different temperatures recorded at regular intervals. During the testing of different samples, the elongation was observed to be low, as such the increase in the values of CTE of the mentioned compositions of hybrid MMCs were in endurable limits ranging from $15 \times 10^{-6}/°C$ to $26 \times 10^{-6}/$ °C. Al 6061 + 3.75% SiC + 3.75% Gr exhibited the maximum value of CTE, whereas Al 6061 + 1.25%SiC + 1.25% Gr exhibited lower magnitude of CTE and Al 6061 exhibited normal value of CTE.

The percentage volume fraction of SiC estimated was low, facilitating CTE to increase drastically and exhibits the expected trend. The hybrid composites have lower volume fractions of SiC than conventional Al-SiC composites with the same CTEs [11]. The decrease in the maximum temperature for CTE values for

graphite reinforced composites is considered as a result of relaxation of the compressive stress in the matrix. The reduction in CTE values can be attributed to the lower CTE value of graphite compared to Al-Si matrix alloy and SiC reinforcement and the ability of the reinforcements to effectively constraint the expansion of the matrix. The thermal strain of all hybrid composites increases as the amount of graphite is increased, indicating that introducing a high amount of graphite to Al-Si based composites may not be beneficial to attain dimensional stability [12]. It was examined that the thermal response and the coefficient of thermal expansion (CTE) of Aluminium matrix composites have high volume fractions of SiC particulate. In Al-SiC composites, the thermal expansion behavior will be influenced by the thermal expansion of Aluminium and the tightened restriction of SiC particles. The CTE of the particle reinforced MMCs is usually affected by a variety of factors namely interfacial reactions, plasticity due to CTE mismatch between particle and matrix during heating or cooling processes and residual stresses [13].

**Determination of Density for The Hybrid MMC**

Density of MMC material can be determined using the relationship between volume and mass. A special technique for the determination of the density where pores are taken into account is the determination by using water displacement (Archimedian density).

Table 4.1 shows the determination of density for different compositions This method allows the determination of the density in air compared to its displacement in water or other liquid of known density. Depending upon the nature of the specimen (e.g., open or closed cell), the resultant value may deviate from the true mass. A clean specimen is weighed accurately in air using a laboratory balance. The same specimen is weighed while suspended in water or other liquid of such density that the specimen will sink. Deducting the mass of the suspension wire from the weight in liquid, the volume of the specimen is calculated from the effect of displacement by a liquid of known density (Archimedean principle). This allows the determination of density of specimens with irregular shapes, uneven surfaces, or porosity. Caution must be exercised to assure that no air is trapped within the specimen. Placing the specimen in a vacuum while submerged in the displacement liquid will usually avoid error.

**Table 4.1: Determination of density for different compositions**

| Sl.No. | Material Identification | Density (g/cc) |
|--------|-------------------------|----------------|
| 1 | Al-6061 | 2.7 |
| 2 | Al-6061 with 1.25% SiC + 1.25% Graphite | 2.69 |
| 3 | Al-6061 with 2.5% SiC + 2.5% Graphite | 2.689 |
| 4 | Al-6061 with 3.75% SiC + 3.75% Graphite | 2.681 |
| 5 | Al-6061 with 5% SiC + 5% Graphite | 2.678 |

Using Rule of Mixtures, the density of the composites was calculated and the values were compared with experimental. The variation was very marginal and proved to have negligible porosity.

## V.  Conclusions

The following conclusions are drawn based on the results obtained:

1. It is noticed that, the CTE of the hybrid composites with different percentage compositions increases with the increase in temperature. There is consistency in the increase of CTE for different temperatures recorded at regular intervals.

2. During the testing of different samples, the elongation was observed to be low, as such the increase in the values of CTE of all compositions were in endurable limits.

3. The percentage volume fraction of SiC estimated was low, facilitating CTE to increase drastically and exhibits the expected trend.

4. The hybrid composites have lower volume fractions of SiC than conventional Al-SiC composites with the same CTEs.

5. In Al-SiC composites, the thermal expansion behavior will be influenced by Aluminium and the tightened restriction of SiC particles.

6. Al 6061 + 3.75% SiC + 3.75% Gr exhibited the maximum value of CTE, whereas Al 6061 + 1.25%SiC+ 1.25% Gr exhibited lower magnitude of CTE and Al 6061 exhibited normal value of CTE.

7. The theoretical and experimental values of density of composites were compared and it proved to have negligible porosity.

## REFERENCES

[1] "Introduction to composites", Composites ASM Hand Book, Vol 21, May 2002.
[2] N. R. Habbu "Use of Aluminium Silicon Alloys in Automobile Application" proceedings of one day Industry Institute Interactive Meet on Al-Si alloys, Development and Application for transport sector, IISC Bangalore, September 2000.
[3] D. Hull, T.W. Clyne, "An Introduction to Composite Materials", Cambridge Solid State Science Series, Second Edition.
[4] S.S. Joshi, N. Ramakrishnan & P. Ramakrishnan, "Micro Structural Analysis of Chip formation during Orthogonal Machining of Al/ SiCp Composites" Journal of Engg. Metals. Technology, July 2001, Volume 123, pp 315 – 321.
[5] C.A. Conceicao Antonio, J. Pauio Davim "Optimal cutting conditions in turning particulate metal matrix composites based on experiment and genetic search model". Composites Part A 33 (2002) 213-219.
[6] S Cem Okumus, Sredar Aslan et al, "Thermal Expansion and Thermal Conductivity Behaviors of Al-Si/SiC/graphite Hybrid Metal Matrix Composites (MMCs)", Volume 18, No 4 (2012).
[7] R Arpon, E Louis et al, "Thermal expansion behaviour of aluminium/SiC composites with bimodal particle distributions", Volume 51, Issue 11, 27 June 2003, Pages 3145-3156.
[8] R A Saravanan, J Narciso et al, "Thermal expansion studies on aluminium-matrix composites with different reinforcement architecture of SiC particles" Volume 51, Issue 11, 27 June 2003, Pages 3145-3156.
[9] Tran Nam, Requena et al, "Thermal expansion behaviour of aluminium matrix composites with densely packed SiC particles", Applied Science and manufacturing, Part A 39 (2009) 856-865.
[10] N Chawla, X Deng et al, "Thermal expansion anisotropy in extruded SiC particle reinforced 2080 aluminium alloy matrix composites", Material Science and Engineering, A 426 (2006) 314-322.
[11] Zhang, Wu et al, "Microstructure and thermal conduction properties of an Al-12 Si matrix composite reinforced with dual sized SiC particles", Journal of Materials Science, 2004, 303-305, Volume 39.
[12] Elomari S, San Marchi et al, "Thermal expansion responses of pressure infiltrated SiC/Al MMC", Journal of Material Science, 1997, pp 2312-2140.
[13] Chawla N, Deng X et al, "Thermal expansion anisotropy in extruded SiC particle reinforced 2080 Al alloy matrix composites", Materials Science & Engineering, A426, 2006, pp 314-322.

# Grid fault Control Scheme for Peak Current Reduction in Photovoltaic Inverters during Voltage Sag

Jinu John[1], Alan.M.George[2]

[1]*Student, Department of Electrical &Electronics Engineering, ASIET, MG University, India*
[2]*Assistant Professor, Department of Electrical &Electronics Engineering, ASIET, MG University, India*

***Abstract:*** *In this paper presents a control scheme for grid interactive photovoltaic inverters to minimize peak current during unbalanced voltage sag. Power quality of a photovoltaic (PV) inverter deteriorates due to the presence of grid faults with voltage sag. In grid connected PV important feature is the ride-through capability, which allows the device to remain connected to the grid during different types of grid disturbances and avoid the need to disconnect. But during the voltage sag, the source should operate with increasing converter currents to maintain the injection of the generated power in the system. This abnormal operation may result in undesired system disconnections due to overcurrent during voltage sag. In this paper discuss a control scheme provide, controller for a PV three-phase inverter that ensures minimum peakvalues in the grid- injected currents during voltage sag.*

***Keywords:*** *Renewable energy, photovoltaic (PV) inverter, grid fault, voltage sag, peak current*

## I. INTRODUCTION

The need for renewable energy sources is increases because of the acute energy crisis in the world today. Existing centralized power generation units are insufficient to meet the continuously rising power demand. The wide gap generation and distribution location lead to fail in supplying power to the rural areas. This can be eliminated by the use of advancement in power electronics by providing instantaneous supply to the people by providing flexibility in source by placing the inverters.

One of the most promising renewable energy resources is solar energy. Within a variety of renewable and sustainable energy technologies, photovoltaic technology appears to be one of the most promising ways meeting the future energy demands as well as environmental issues. In the last decades, solar energy has been used as reliable energy for electric distribution. Use of the solar panel is the key component to convert solar energy to electrical energy. In the last decades,solar energy has been used as reliable energy source for electric distribution.

In the past, PV sources were mainly used in isolated and stand-alone applications. Nowadays the majority of the PV power sources are connected to the public grid. International standards are regulating the grid connection of photovoltaic systems, forcing the PV source to remain connected during short-time grid-voltage faults. As a result, during the voltage sag, the source should operate with increasing converter currents to maintain the injection of the generated power. This abnormal operation may result in undesired system disconnections due to overcurrent. These over currents, which can double the nominal values, can damage the power systems and switches as well as the interconnection lines, unless the source is disconnected. The overcurrent will flow until the sag is cleared or the switch that disconnects the source from the grid is opened after the regulated trip time. To avoid this overcurrent reference current generation can be used to inject current during sag.

## II. GRID FAULT CONTROLLERS

Voltage sag has become one of the major power quality concerns in recent years. As applications of power electronics in the commercial and industrial sectors grow rapidly, these sensitive loads can be easily interrupted byvoltage sags and the resulting losses are significant. During voltage sag, one or more phase voltages at the point of common coupling (PCC) are reduced and the currents supplied by the PV source must be increased in order to maintain the same amount of injected power as in nominal conditions. Thus, the PV system can be viewed as a high reliability current source that must inject all the generated power to the grid. The source should be able to override the large currents caused by temporary voltage sags, and continue feeding the grid according to the standards. This overcurrent, affect the nonlinear load connected to the system.
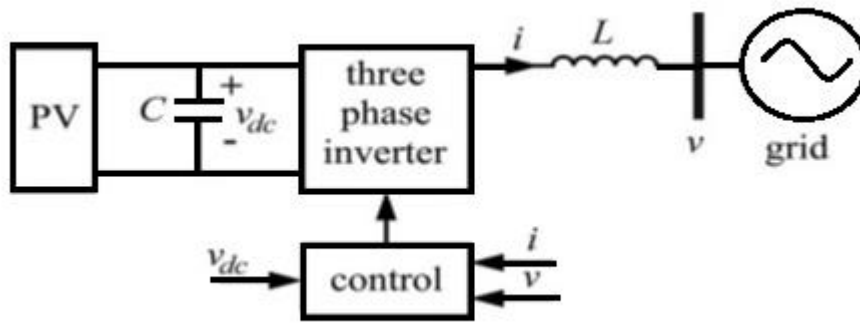
Figure: 2.1 Block diagram of grid-connected three-phase PV inverter

The different methods based on the reference current generation in grid fault controllers are [4],

1. Instantaneous Unity Power Factor Control (IUPFC)
2. Average Unity Power Factor Control (AUPFC)
3. Instantaneous Positive-Sequence Control (IPSC)
4. Average Positive-Sequence control (APSC)
5. Positive-Negative Sequence Compensation Control (PNSCC)

The 1st approach is the instantaneous unity power factor control (IUPFC), which must be used when the injectedcurrent i is required to follow exactly the voltage v. The second approach, the average unity power factor control, is implemented to avoid the appearance of current harmonics that increase the current THD in a grid connected system. Third, the instantaneous positive-sequence control (IPSC) gives an injected current that only follows the positive voltage sequence v+. Fourth, the average positive-sequence control (APSC) provides a current that follows the averaged positive-voltage sequence, avoiding the appearance of current harmonics in the system. And fifth, the positive negative sequence compensation control (PNSCC) gives a constant injected active power and low current THD [9].
Based on the equation α and β are given below,

$$ i_r = \frac{P_r(v^+ + \alpha v^-)}{|v^+|^2 + \beta(1+\alpha)v^+v^- + |v^-|^2} (1) $$

In this, discrete values α and β can be online changed in order to commute between the extreme power From the above five grid fault controllers, obtain ageneralized method for reference current generation;quality characteristics during the voltage sag. However, it isalso possible to use continuous values for α and β in order toachieve intermediate power quality characteristics. Where theinteger variable α takes values 1, 0, or -1, and the Booleanvariable β takes values 0 and 1.

Table 1: Definition of Discrete control parameters α and β

| Strategy | α | β |
|---|---|---|
| IUPFC | 1 | 1 |
| AUPFC | 1 | 0 |
| IPFC | 0 | 1 |
| APSC | 0 | 0 |
| PSNC | -1 | 1 |

### III. Control Strategy

The control scheme for minimize peak current during voltage sag to be design; In order to reduce the peak current to its minimum value, noninteger values areproposed for α and β when computing the expression of the reference currentvector $i_r$ .A simple searching algorithm is used offline to find the optimumvalues of α and β for each unbalance factor n. With each pair alpha, beta fora given unbalance factor, the peak values over a line period are computed. It must be noted that the minimum peak value will be reached when $i_{apeak} = i_{bpeak}$. Then for each n, a single pair alpha, beta giving minimum peakcurrent values is stored in a look-up table. When sag is

detected, n iscomputed online .Then the appropriate values of α and βare retrieved fromthe look-up table and as per the value of n obtain the reference currents.

The voltage unbalance factor can be expressed as;

$$n = \frac{v^-}{v^+} \quad (2)$$

## IV. Designing The Control Scheme

The field of overcurrent reduction solutions that based on the control scheme, which avoid any increase in the number of electronic devices. In the selection of a proper reference current is proposed to override grid faults and achieve different power quality requirements especially peak current during voltage sag. In this method proposes a controller for a PV inverter that ensures minimum peak values in the grid-injected currents during the voltage sag. This study is based on the generalized algorithm and design method is developed in order to search for the control parameter values that minimize the peak currents. Fig 4.1 shows the overview of grid connected pv system under fault.
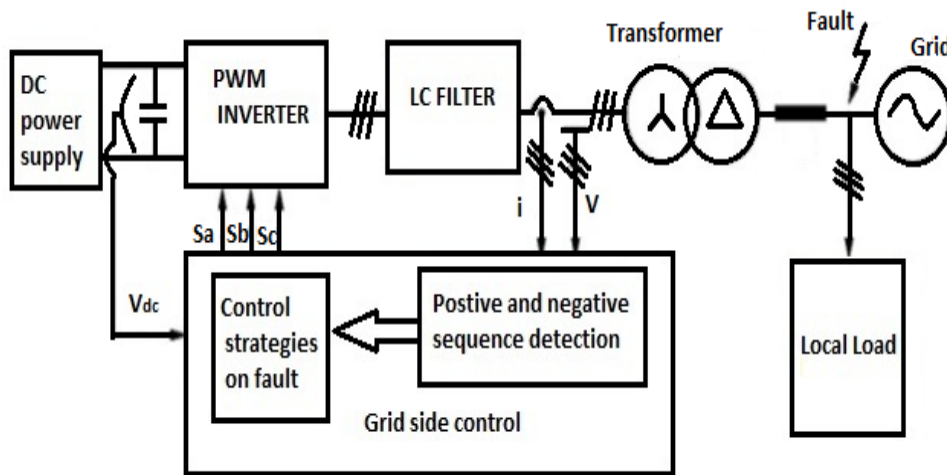


Figure: 4.1 Control strategies at faulty grid conditions

Fig: 4.2 show the control block diagram of the control scheme. When sag occur sag voltage is taken for the generation of reference current. Positive and negative sequence voltage is separated and unbalance factor n is calculated from equation (2).Then appropriative α and β values are retrieved from look up table and based on the value reference current $i_r$calculated from equation (1).Compare the value of $i_r$ with i gating pulses giving to the controller.
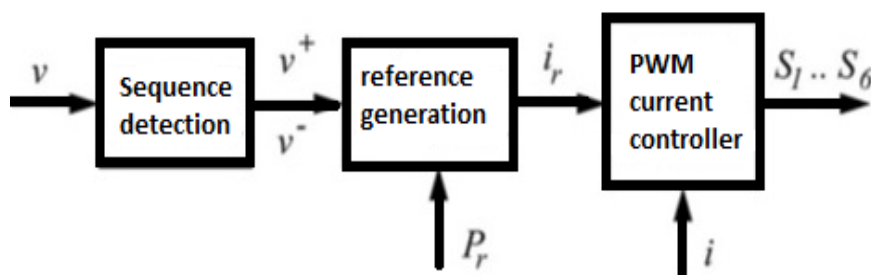


Figure: 4.2 Control block diagram

### 4.1 Detection of Positive and Negative Sequences

The grid voltage is a crucial issue in order to have full control over the power that is delivered from the DPGS to the grid. In this section, characterization is performed by means of a positive and negative sequence voltage detector based on a second-order generalized integrator.The proposed positive- and negative-sequence detection system that provides an effective solution for grid synchronization of power converters in the presence of grid faults. The calculation of the instantaneous symmetrical components on the alpha-beta reference frame makes it possible to use only two SOGIBPF [3]
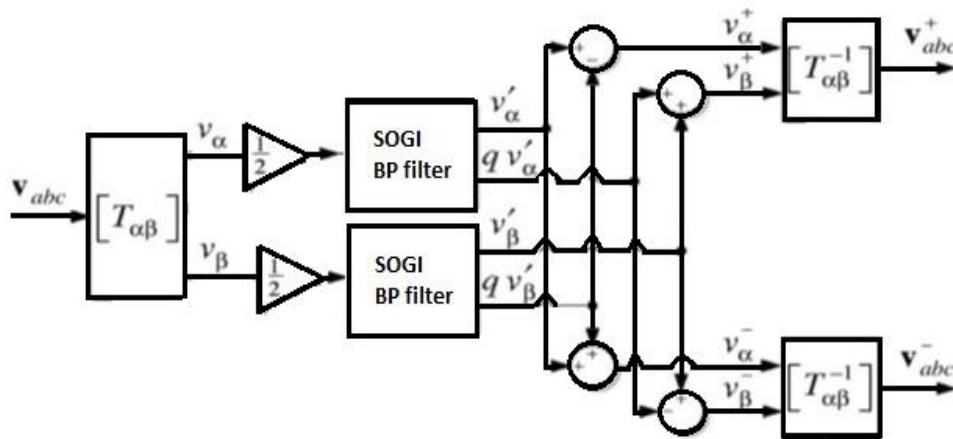
Figure : 4.3 Extracting the positive and negative sequences voltage of the grid

**4.2 Current Controller**

In this hysteresis controller (HCC) for three-phase pulse width modulation (PWM) voltage-source inverters (VSI) is used. The HCC is intrinsically robust to the load parameters variations, exhibits very fast transient performance, and is suitable for simple implementations

**4.3 Circuit Parameters**

Table 2: Simulation Parameters

| Dc voltage | $V_{dc}$ | 230*V* |
|---|---|---|
| Power | $P_r$ | 2.3k |
| Capacitor | C | 1.8mF |
| Inductor | L | 5mH |
| Grid side oltage | V | 380V,50Hz |
| Sampling frequency | $f_s$ | 10KHz |

**4.4 Simulink model**

In the simulation a PV three-phase three-wire inverter full-bridge as the power converter dc source configured to provide an active power of 2.5 kW at its maximum power point. The inverter was connected to the dc source through a dc-link capacitor. The sequence detection algorithm reported in was used in this study to obtain the positive- and negative-voltage sequences.A PWM hysteresis current controller was used as the modulation scheme The switching frequency was set to 10 kHz, according to the limits expected for the insulated gate bipolar transistors (IGBTs) bridge characteristics

When implementing the controller, the amplitudes of the positive and negative sequences $V^+$ and $V^-$, necessary to evaluate the depth of the sag, n, are calculated by on the basis of the stationary reference frame (SRF) theory[3] .The unbalance factor n is easily derived and the optimal values of α and β are given using interpolation in a look-up table and used with equations to obtain the reference current $i_r$.
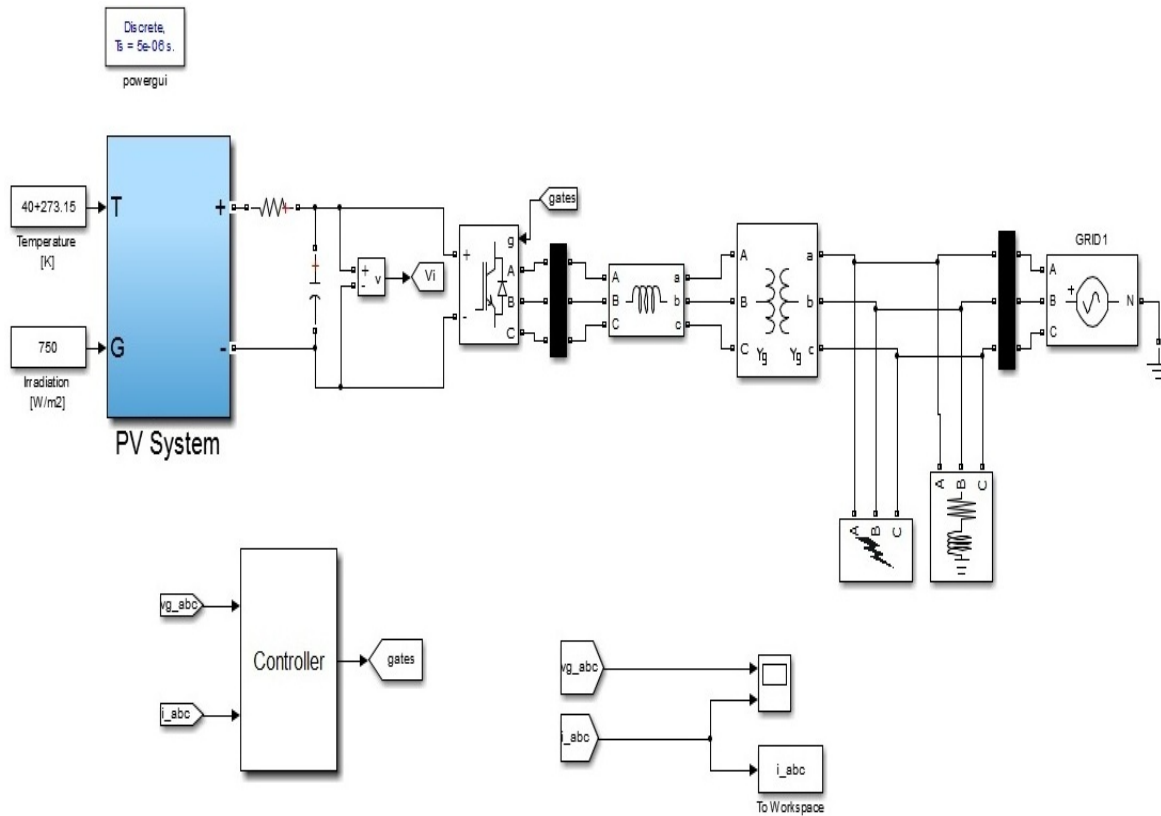
Figure:4.4 Simulation model of generalized control scheme
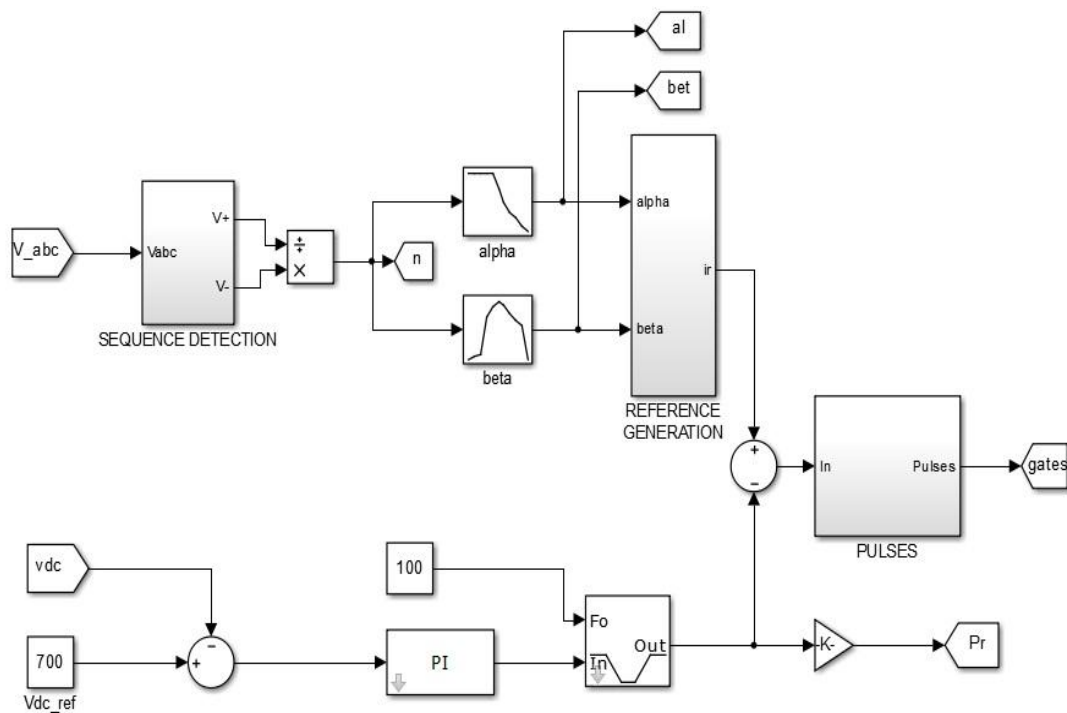


Figure: 4.5 Controller section of reference current generation

**4.5 Result Analysis**

   Result analysis of grid connected pvsystem during voltage sag in uncompensated system and peak currentreduction methods are given below the fig:7& fig:8.
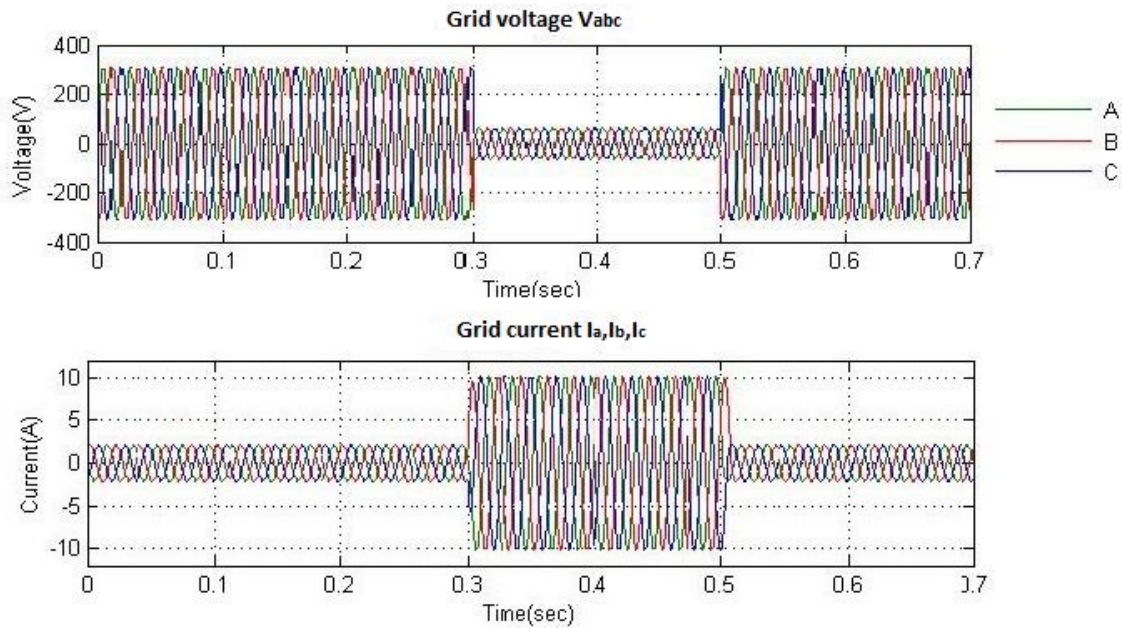
Figure: 4.6 Grid voltages and current during voltage sag without compensation 0.3sec-0.5sec
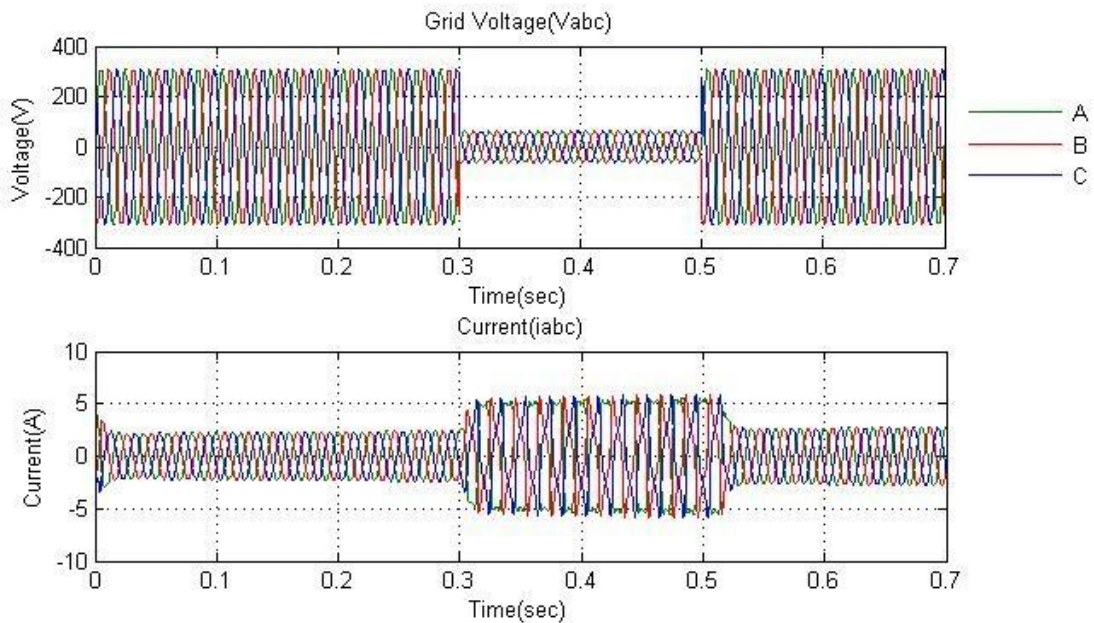


Figure: 4.7 Grid voltage and current during voltage sag with peak current compensation 0.3sec-0.5sec

As per fig: 4.6show the output wave form of grid connected pv inverter without any compensation. From the output it is clear that large peak current is introduced in system. It'sabout 5 times larger than the normal value. These peak current during sag badly affect the system. So that to reduce the peak current during sag a reference current generation method is incorporated to the system to reduce the peak current. By this reference current generation peak current compensation method we can reduce the peak current. The output wave form of voltage and current using the compensation method is shown in the fig: 4.7.From the figure it is clear that the level of peak current during voltage sag is reduced by this compensation method.

## V.  Conclusion

This paper has presented a controller for a PV three-phase inverter, which ensures minimum peak values in the grid-injected currents during voltage sags. The comparison with a reference control shows that the peak current values are considerably reduced by using the control scheme.Positive and negative sequence

separation DSOGI FLL method is used. In this method on the stationary and orthogonal reference frame, permitting elimination of the zero-sequence component, this cannot be controlled in three-phase three-wire power converters. Analyze wave form, distortion is present with the control scheme & reduction of distortion is necessary.

A control scheme for peak current reduction during voltage sag in grid connected PV inverter was analyzed & simulated. The converter can overcome deeper sags without the disconnection caused by harmful overcurrent during grid fault condition.

## REFERENCE

[1] JaumeMiret, Miguel Castilla, Antonio Camacho, LusGarca de Vicuna, and JoseMatas "Control Scheme for Photovoltaic Three-Phase Inverters to Minimize Peak Currents During Unbalanced Grid-Voltage Sags" , IEEE Transactions on Power Electronics , Vol: 27 , No: 10, Oct. 2012

[2] P. Rodriguez, A. V. Timbus, R. Teodorescu, M. Liserre, and F. Blaabjerg, "Flexible active power control of distributed power generation systems during grid faults", IEEE Trans. Ind. Electron., vol. 54, no. 5, pp. 2583 2592, Oct. 2007

[3] P. Rodriguez, A. Luna, R.S. Munoz-Aguilar, I. Etxeberria-Otadui, R.Teodorescu, and F. Blaabjerg, "A stationary reference frame grid synchronization system for three-phase grid-connected power converters under adverse grid conditions", IEEE Trans. Power Electron., vol. 27, no.1,pp. 99112, Jan. 2012

[4] M. Castilla, J. Miret, J.L. Sosa, J. Matas, and L. Garca de Vicuna, "Grid fault control scheme for three-phase photovoltaic inverters with adjustable power quality characteristics", IEEE Trans. Ind. Electron., vol. 25, no. 12,pp. 29302940, Dec. 2010

[5] S. Subramanian and M. K. Mishra, "Interphase AC-AC topology for voltage sag supporter",IEEE Trans. Power Electron., vol. 25, no. 2, pp. 514518,Feb. 2010

[6] J. C. Vasquez, R. A. Mastromauro, J. M. Guerrero, and M. Liserre, "Voltage support provided by a droop-controlled multifunctional inverter", IEEE Trans. Ind. Electron., vol. 56, no. 11, pp. 45104519, Nov. 2009

[7] C. Wessels, F. Gebhardt, and F. W. Fuchs, "Fault ride-through of a DFIG wind turbine using a dynamic voltage restorer during symmetrical and asymmetrical grid faults", IEEE Trans. Power Electron., vol. 26, no. 3, pp. 807815, Mar. 2011

[8] J. H. Enslin and P. J. Heskes, Harmonic interaction between a large number of distributed power inverters and the distribution network, IEEE Trans. Power Electron., vol. 19, no. 6, pp. 15861593, Nov. 2004

[9] F. Wang, J. L. Duarte, and M. A. M. Hendrix, "Pliant active and reactive power control for grid-interactive converters underunbalanced voltage"dips, IEEE Trans. Power Electron., vol. 26, no. 5, pp. 15111521, May 2011

[10] Yalcinkaya, M. H. J. Bollen, and P. A. Crossley, "Characterization of voltage sags in industrial distribution systems",IEEE Trans. Ind. Appl., vol. 34, no. 4, pp. 682688, Jul./Aug 1998

# Microgrid Control Strategy

M Parvathy Nair[1], Sajith RP[2]

[1](Student, Department Of Electrical And Electronics, ASIET / MG University, Kerala, India)
[2] (Assistant Professor, Department of Electrical and Electronics, ASIET, MG University, Kerala, India)

**Abstract:** *The energy sector is moving into the era of distributed generation (DG) and microgrids (MGs). The stability and operation aspects of converter-dominated DG MGs, however, are faced by many challenges. To overcome these difficulties, this paper presents a new large-signal-based control topology for DG power converters that is suitable for both grid connected and islanding modes of operation without any need to reconfigure the control system and without islanding detection. To improve MG stability and to guarantee stability and high performance of the MG system during sudden harsh transients such as islanding, grid reconnection, and large load power changes, a nonlinear MG stabilizer is proposed. We propose a novel control topology for microgrids which can work in both grid connected and islanding modes without reconfiguration so it does not require islanding detection technique, the controller is based on the concept of synchronverter In this paper, a radical step is taken to improve the synchronverter as a self-synchronized synchronverter by removing the dedicated synchronization unit.*

**Keywords:** *Distributed generation(DG),Grid-connected, Microgrid (MG), Point of Common Coupling (PCC), Synchronverter.*

## I. INTRODUCTION

The need of reducing CO2 emissions in the electricity generation, electricity markets restructuring and technological development in the micro generation lead to the growing interest in the use of micro generation. Microgrid is a new type of power systems consisting of generation sources, loads and energy storages. In another words, it is an association of a small modular generation system, a low voltage distribution network and load units inter-faced by means of fast acting power electronics. Microgrids are determined usually in accordance with a few de nitive functions. They are usually used in small urban areas or in small industry. The most common power range for microgrids is from 25 to 100 kW. But the systems with lower and upper power levels are also widely used. As micro energy sources in microgrids, usually, diesel or gas motor driven gen sets, fuel cells or renewable genera-tion such as wind parks, photovoltaic systems and gas or biofuel driven micro turbines are used.

The generating technologies which are used in microgrids have potentially lower cost and lower emissions in comparison with traditional power sources. This assumption is based on the idea of generating heat and electrical power simultaneously in the units. The smaller size of these generating units allows them to be placed in the best position for cooling, energy distribution and maintaining of the installation. The most appropriate way to realize the rising potential of small scale generation is to tie loads and generating units together. This is accomplished in microgrids by using inverters to interface generating units with the distribution system. Such applications can increase the efficiency of the system remarkably, especially if the thermal power of the system may be utilized for heating buildings.

Microgrids operate in two basic modes. They can operate in o -grid mode. In that case the power is generated and stored without assistance from the main low voltage grid. These microgrids comprise one or more energy sources, batteries and local loads which are fed by these sources. In other case a microgrid is connected to the main grid in normal interconnected mode. This operating manner, usually called grid-connected mode, is the main operation mode. In this mode microgrid operate as a back-up system or as a part of the utility system. The purpose of the back-up microgrid system is to feed local loads when the main grid fails for any reason. This mode is also called the emergency mode. The con guration of a microgrid in the grid-connected mode also requires a power source and a large battery bank. Batteries or super capacitors are used in microgrids for storage the excess of the generated energy and support energy sources when the loads increase. The size and type of the batteries are determined by systems requirements. During the normal operation of the main grid, the purpose of the microgrid is to maintain the battery bank in full charged condition so that it should be always ready for emergency operating. When microgrid operates like a part of the utility system, the microsources of the microgrid feed local loads. If the generated power exceeds the demanded power level inside the microgrid,

excess of the energy is supplied to the main grid. In the other way, if microgrid cannot provide full supplying of its local loads the required energy ows from the main grid. Due to the fact that most of the loads require AC power which is opposed to the DC power generated by the sources, the battery inverters intended to invert and control electrical energy ows are required in both operation modes.

The conventional linear controllers and small-signal analysis reported previously only deal with small variations around the operating point or base load; this refers to small-signal stability because it just deals with stability at one specific operating point when small perturbations appear in the system. However, in a MG system with comparable sizes of DG units and due to the absence of physical inertia and due to high penetration level of converter-based DG units, a MG system will be subjected to large transients and power angle swings. Typical large-signal disturbances in a MG system include transition between grid connected and islanding modes, and sudden large load demands. In these situations, linear controllers are not sufficient to guarantee MG stability at different operating conditions; and accordingly, instabilities due to severe transients are expected. On the other hand, non-linear controller with global stability can be designed to guarantee stable and robust operation at different operating conditions. Motivated by the afore-mentioned issues, we propose a novel control topology for microgrids which can work in both grid connected and islanding modes without reconfiguration so it does not require islanding detection technique. The controller involves angle, frequency, and power loops instead of conventional current and voltage loops. The controller is based on the concept of synchronverter which has been recently proposed to emulate the behavior of a synchronous generator (SG) by a virtual rotor.

The synchronverter concept offers some advantages over the conventional converter control strategy as it introduces emulated inertia and controlled frequency dynamics, whereas in the conventional VSC, frequency dynamics is unknown and cannot be controlled directly. Moreover, synchronverters can be easily embedded in a power system or MGs with many conventional SGs since their dynamic performance is similar to SGs. It is evident that synchronverters are one of the most interesting choices for future power systems.

## II. SYSTEM OVERVIEW

Due to fast development of renewable energy resources, the concept of distributed generation (DG) is gaining an important role in future smart power grids [1][3]. DG has many advantages such as closeness to customers, increased efficiency and reduced transmission loss, better reliability, and improved energy management [4]. The majority of DG resources are interfaced to grid/loads via power electronic converters. A cluster of DG units connected to the grid via power electronic interfaces form a microgrid (MG). Fig.1 shows a typical MG. MGs form an important portion of future smart grids and therefore, their roles are vital in power system operation. A microgrid system has two states of operation; namely, they are grid-connected and islanding modes. The islanding is a situation in which the MG is dis-connected from the main grid when a fault is occurred in the grid. Because of power reliability and power quality issues, it is necessary that microgrids continue their operation in autonomous mode when grid is not available.
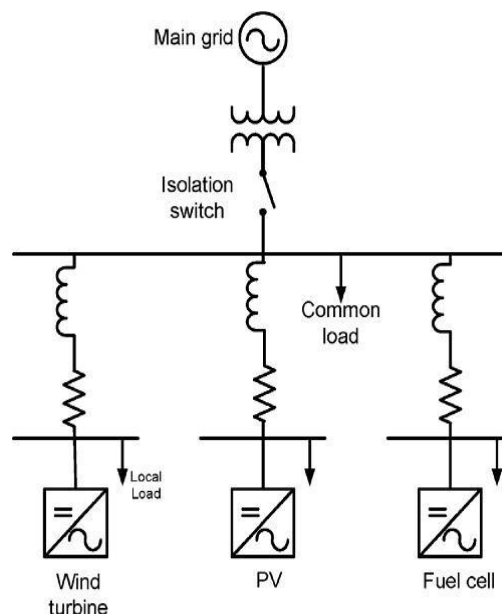


Fig 1: Microgrid Scheme

The existing microgrid control schemes can be divided into droop-based and non-droop based approaches. Controlling DER units based on droop characteristics is the ubiquitous method in the literature. The droop-based approach originates from the principle of power balance of synchronous generators in large interconnected power systems. That is, an imbalance between the input mechanical power of the generator and its output electric real power causes a change in the rotor speed which is translated to a deviation of the frequency. Likewise, output reactive power variation results in deviation of voltage magnitude. The same principle is artificially employed for electronically-interfaced DER units of a microgrid as well. Opposite droop control, i.e., using real power/voltage and reactive power/frequency droop characteristics, has also been applied for low voltage microgrids in view of their low X/R ratios. The main advantage of a droop-based approach is that it obviates the need for communication since the control action is performed merely based on local measurements. This feature gives droop control a significant exibility in that as long as a balance between generation and demand can be maintained, there is no interdependency between the DER unit local controllers.

**2.1 Synchronverter**
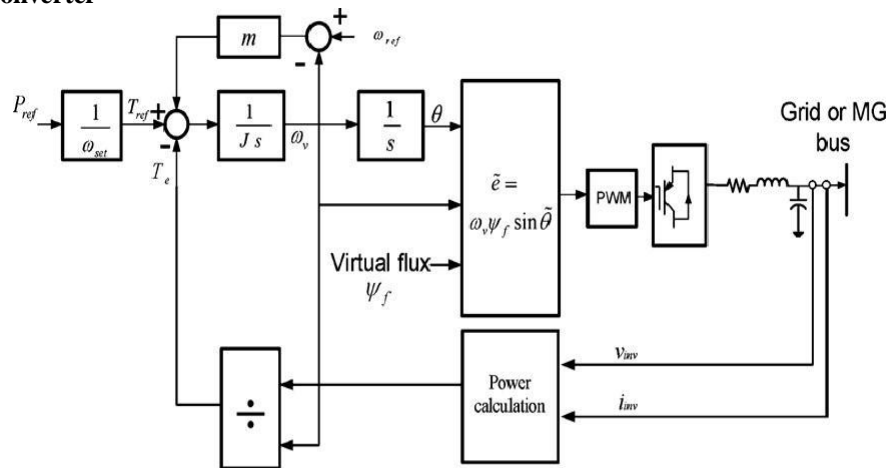


Fig 2: Synchronverter model

Fig. 2 depicts the basic concept of the converter control topology. The basic idea is to mimic back-EMF generation principle and rotor dynamic of a synchronous generator, including its rotor momentum of inertia and friction . The utilization of emulated rotor dynamics improves the converter dynamics and it yields a control structure that is more suitable for MG operation. In this VSC model, the virtual rotor plays the role of controlling the frequency dynamics, which is not accessible in the conventional current/voltage control topology of VSC. The virtual friction is responsible to damp VSC frequency oscillations in grid-connected mode. However, it is proposed to use it as a droop control for power sharing in islanded mode. The voltage generation principle is like back-EMF generation in a typical SG given by,

$$e = \omega_v \, \varphi_f \sin \theta \qquad (1)$$

where e stands for a balanced three-phase voltage. This equation emulates rotational back-EMF generation in an SG. The frequency dynamics of the VSC is given by,

$$J\frac{d\omega_v}{dt} = T_e - T_{ref} - m(\omega_v - \omega_{ref}) \qquad (2)$$

which is directly obtained from Fig.2. Similar to every multiphase electrical system, output power is calculated by inner product of three-phase voltages and currents,

$$P_e = \varphi_f \omega_v < i, \sin \theta > \qquad (3)$$

Thus, (3) is simplified to,

$$P_e = \frac{3}{2}\varphi_f \omega_v i \cos(\theta - \varphi) = \frac{3}{2} \varphi_f \omega_v i \cos \delta \qquad (4)$$

The virtual electrical torque is given by,

$$T_e = \frac{P_e}{\omega_v} = \frac{3}{2}\varphi_f \cos \delta \, i \qquad (5)$$

It is worth noticing that unlike electrical machines, there is no real electrical torque and it is just defined for the sake of the control design of a VSC-based DG unit. Similarly, the reactive power equation is obtained as

$$Q_e = \frac{3}{2}\varphi_f \omega_v i \sin \delta \qquad (6)$$
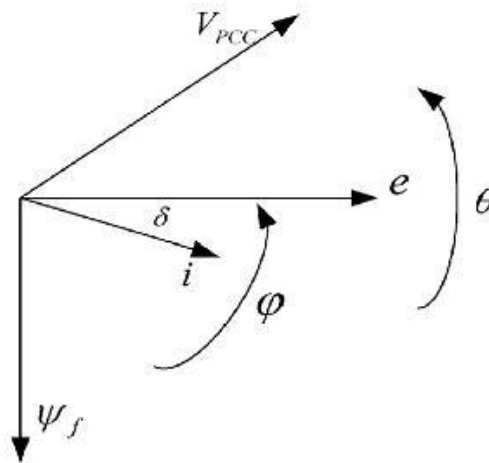
Fig 3:Phasor diagram of system

Fig. 3 exhibits the phasor diagram of a VSC connected to the grid. One of the most attractive features of this VSC topology is the existence of friction coefficient of(m) , which acts like a damper in grid connected mode and is used as a frequency power droop control for power sharing among DG units in islanding. In other words, the term$m(\omega_v - \omega_{ref})$ provides a power sharing tool for DG units. Moreover, the values of and can be selected arbitrarily as a function of design requirements and they can have values which are not feasible in a real SG.The virtual rotor momentum of inertia is obtained by:

$$J = m\tau_f \qquad (7)$$

where $\tau_f$ is the time constant of power-frequency droop loop determined by designer according to acceptable frequency dynamics
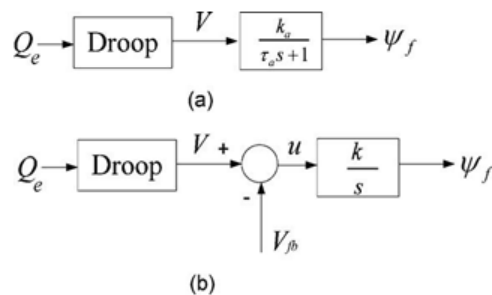


Fig 4 Block diagram of flux control loop

Two different topologies for virtual rotor flux control are proposed as shown in Fig.4, namely they are Model1, which adopts a low-pass filter to generate the virtual rotor flux; and Model2, which adopts a pure integrator. In the first topology, the reference voltage is again generated by a voltage droop function. Processed by the low-pass filter emulating rotor flux decay dynamics of an SG, the rotor ux is obtained. In the latter, the voltage command, which is generated by a reactive power-voltage droop, is compared to the actual voltage and the error is fed into the integrator resulting in the reference rotor ux. It can be noted that in Model2, the low-pass filter behaves like the flux decay equation of a real SG; therefore, in Model 2, the VSC acts as an SG. This helps embedding numerous DG units in a large power system where VSCs and the conventional power plants are seen the same by the power system. The flux decay equation of synchronous generators is due to the fact that applied dc voltage to the rotor excitation appears with a delay in the stator side as a result of rotor winding inductance.T he voltage droop function is as follows:

$$V = V^* - nQ_e \qquad (8)$$

where $V^*$is the no-load voltage and $Q_e$ is DG reactive power. This droop control is used in both modes of operation to share reactive power among DG units. In fact, in ideal case, total reactive power demand is distributed according to static droops constants n .

**2.2 Controller**
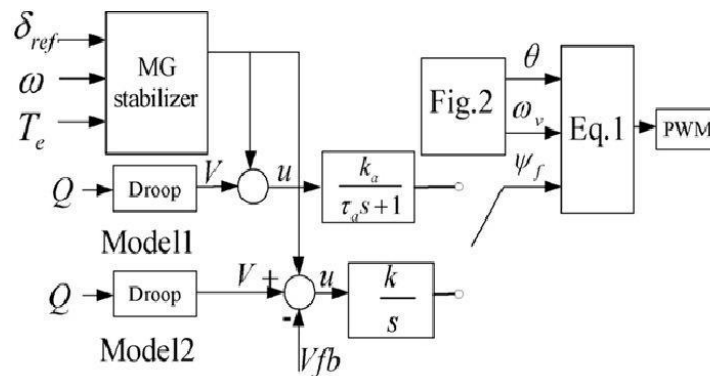


Fig 5 Block diagram of control loop

Fig5 shows the proposed control topology. The controller uses power angle, frequency, and power as control variables instead of conventional cur-rent and voltage control loops. As it is seen, the controller has three control loops, namely angle loop, frequency loop, and torque loop which is afterward called microgrid stabilizer.The first is a power angle tracker in which the controller aims at tracking the desirable power angle by proper frequency and power setting, whereas the latter just tries to damp angle oscillations while there is no de ned angle reference.The nonlinear microgrid stabilizer, which can be considered as torque controller, attempts to set torque error equal to zero using a supplementary voltage control. Simply speaking, in contrast to the conventional current-voltage control, the power is directly controlled by varying power angle and voltage amplitude. That is to say that amplitude of current can be controlled by adjusting power angle $\delta$ and frequency $\omega_v$ via a direct power control strategy.

## III. PROPOSED PLAN

### 3.1 Problem idenfication

The synchronization unit often needs to provide the frequency and the amplitude, in addition to the phase, of the fundamental component of the grid voltage as the references for the power controller. The negative impact of a synchronization unit on control performance is well known. Moreover, because PLLs are inherently nonlinear and so are the inverter controller and the power system, it is extremely di cult and time-consuming to tune the PLL parameters to achieve satisfactory performance. A slow synchronization unit could directly affect control performance and degrade system stability but a complex synchronization unit, on the other hand, is often computationally intensive, which adds significant burden to the controller. Hence, the synchronization needs to be done quickly and accurately in order to maintain synchronism, which makes the design of the controller and the synchronization unit very challenging because the synchronization unit is often not fast enough with acceptable accuracy and it also takes time for the power and voltage controllers to track the references provided by the synchronization unit as well.

### 3.2 Problem solution

A radical step is taken to improve the synchronverter as a self-synchronized synchronverter by removing the dedicated synchronization unit. It can automatically synchronize itself with the grid before connection and track the grid frequency after connection This leads to much improved performance, simplifed controller, reduced demand for computational power, reduced development cost and effort, and improved software reliability. Moreover, it is able to operate in different modes as the original synchronverter but without the need of a dedicated synchronization unit to provide the grid frequency as the reference frequency.

### 3.3 Proposed controller

The proposed controller for a self-synchronized synchronverter is shown in Fig.6, after making some necessary changes to the core of the synchronverter controller shown . It is able to be connected to the grid safely and to operate without the need of a dedicated synchronization unit.
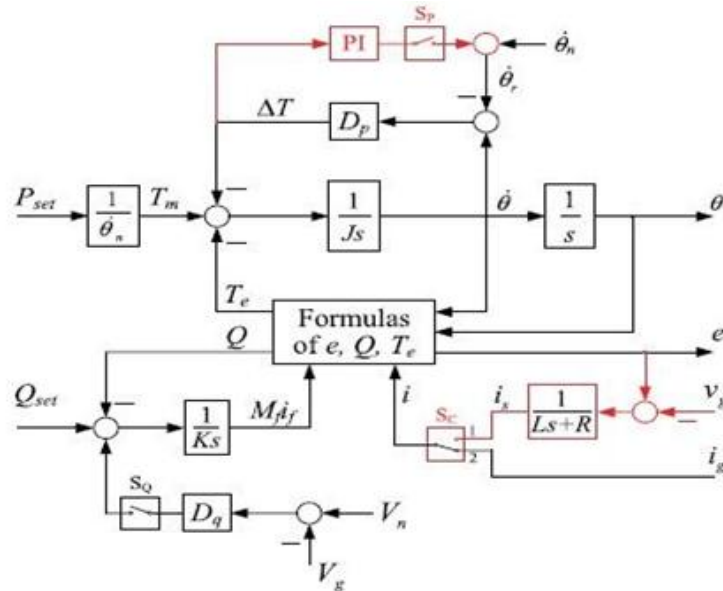
Fig 6 Block diagram of proposed controller of a self- synchronized synchronverter

There are two major changes made: 1) a virtual current is generated from the voltage error between e and $V_g$ is added and the current fed into the controller can be either $i_s$ or the grid current $i_g$ ; 2) a PI controller is added to regulate the output T of the frequency droop block $D_p$ to be zero and to generate the reference frequency $\theta_r$ for the original synchronverter. In order to facilitate the operation of the self-synchronized synchronverter, three switches $S_C$ ,$S_P$ ,$S_Q$ and are added to change the operation mode.

3.4 Operation After Being Connected to the Grid

As mentioned before, the power angle delta of a synchronverter can be controlled by the virtual mechanical torque $T_m$ calculated from the power command $P_{set}$ as,

$$T_m = \frac{P_{set}}{\dot{\Delta\theta}} = \frac{P_{set}}{\dot{\theta}_n} \qquad (9)$$

where $\dot{\theta}_n$ is the nominal grid frequency. When $S_P$ is turned ON, $\Delta T$ is controlled to be 0 in the steady state via the PI controller. Hence, $T_e$ is the same as $T_m$ and $\dot{\theta}$ is controlled as

$$\dot{\theta} = \dot{\theta}_r = \dot{\theta}_r + \dot{\Delta\theta} \qquad (10)$$

where $\dot{\Delta\theta}$ is the output of the PI controller. The power angle settles down at a constant value that results in P = $P_{set}$ . This operation mode is called the set mode in [8]. In order to differentiate the set mode for real power and reactive power, the set mode for the real power is called the P-mode and the set mode for the reactive power is called the Qmode. If $P_{set} = 0$, then $\theta = \theta_g$, in addition to $\dot{\theta} = \theta_r$ .When the switch $S_p$ is turned OFF, the PI controller is taken out of the loop and the synchronverter is operated in the frequency droop mode (called the PD -mode , meaning that the real power P is not the same as $P_{set}$ but deviated from $P_{set}$ ) with the frequency droop coefficient defined as

$$D_p = \frac{\Delta T}{\dot{\Delta\theta}} \qquad (11)$$

Where

$$\dot{\Delta\theta} = \dot{\theta} - \dot{\theta}_n \qquad (12)$$

is the frequency deviation of the synchronverter from the nominal frequency. It is also the input to the frequency droop block $D_p$ (because $S_p$ is OFF). This recovers the synchronverter frequency as

$$\dot{\theta} = \dot{\theta}_n + \dot{\Delta\theta} \qquad (13)$$

which is the same as (10) but with a different $\dot{\Delta\theta}$. Actually, in both cases, $\theta$ converges to the grid frequency $\theta_g$ when the power angle $\delta$ is less than $\frac{\pi}{2}$ rad, as will be shown below. According to [28], the time constant $\tau_F = \frac{J}{D_p}$ of the frequency loop is much smaller than the time constant $\tau_V = \frac{K}{\theta_n D_q}$ of the voltage loop. Therefore, $M_f$ $i_f$ can be assumed constant when considering the dynamics of the frequency loop. Moreover, according to (5), the real power delivered by the synchronverter (or an SG) is proportional to $\sin \delta$. As a result,

the electromagnetic torque $T_e$ is proportional to $\sin \delta$. For $\delta \in \left(-\frac{\pi}{2}, \frac{\pi}{2}\right)$, $T_e$ increases when the power angle increases and $T_e$ decreases when the power angle decreases. If the grid frequency $\dot{\theta}_g$ decreases, then the power angle $\delta$ and the electromagnetic torque $T_e$ increase. As a result, the input to the and the set mode (P -mode) but not in the droop mode (PD -mode) integrator block $\frac{1}{Js}$ in Fig. 6 decreases and the synchronverter frequency $\dot{\theta}$ decreases. The process continues until $\dot{\theta} = \theta_g$. If the grid frequency increases, then a similar process happens until $\dot{\theta} = \theta_g$. Hence, the synchronverter frequency $\dot{\theta}$ automatically converges to the grid frequency $\dot{\theta}_g$ (when $\delta \in \left(-\frac{\pi}{2}, \frac{\pi}{2}\right)$ and there is no need to have a synchronization unit to provide $\dot{\theta}_g$ for the synchronverter as the reference frequency. The proposed controller preserves the reactive power control channel of the original synchronverter, with the added Switch $S_Q$ to turn ON/OFF the voltage droop function. When $S_Q$ is OFF, $M_f i_f$ is generated from the tracking error between $Q_{set}$ and Q by the integrator with the gain $\frac{1}{K}$. Therefore, the generated reactive power Q tracks the set-point $Q_{set}$ without any error in the steady state regardless of the voltage difference between $V_n$ and $V_g$. This operation mode is the set mode for the reactive power, called the Q-mode .When the Switch $S_Q$ is ON, the voltage droop function is enabled and the voltage error $\Delta V = V_n - V_g$ is taken into account while generating $M_f i_f$. Hence, the reactive power Q does not track $Q_{set}$ exactly but with a steady-state error $\Delta Q = Q_{set} - Q$ that is determined by the voltage error $\Delta V$ governed by the voltage droop coefficient

$$D_q = -\frac{\Delta Q}{\Delta V} \qquad (14)$$

This operation mode is the voltage droop mode and is called the $Q_D$ - mode, meaning that the reactive power is not the same as $Q_{set}$ but deviated from $Q_{set}$.

**3.4 Synchronization before Connecting to the Grid**

Before the synchronverter is connected to the grid, its generated voltage e(strictly speaking, v) must be synchronized with the grid voltage $V_g$. More-over, the amplitude E is also required to be equal to the amplitude $V_g$ and the phase sequence of e and $V_g$ must be the same as well. For a conventional SG, a synchroscope is often used to measure the phase difference between e and $V_g$ so that the mechanical torque is adjusted accordingly to synchronize the SG with the grid. For grid-connected inverters, PLLs are often adopted to measure the phase of the grid voltage so that the generated voltage is locked with the grid voltage. As mentioned before, the proposed controller shown in Fig. 6 is able to operate the synchronverter under the set mode with Pset = 0 and $Q_{set} = 0$. As a result, the condition (7) can be satisfied when it is connected to the grid. However, the current $i_g$ owing through the grid inductor is 0 until the circuit breaker is turned on, and hence, no regulation process could happen. In order to mimic the process of connecting a physical machine to the grid, a virtual per-phase inductor $L_s + R$ is introduced to connect the synchronverter with the grid and the resulting current,

$$i_s = \frac{1}{L_s + R}\left(e - V_g\right) \qquad (15)$$

can be used to replace $i_g$ for feedback so that $T_e$ and Q can be calculated according to (2) and (4). This allows the synchronverter to operate in the P-mode for the real power with $P_{set} = 0$ and in the Q-mode for the reactive power with $Q_{set} = 0$ so that the generated voltage e is synchronized with the grid voltage $V_g$. The only difference is that the (virtual) current $i_s$, instead of the grid current $i_g$, is routed into the controller via the switch $S_C$ thrown at Position 1. Since the current is is not physical, the inductance L and resistance R of the virtual synchronous reactance $X_S$ can be chosen within a wide range. Small values lead to a large transient current is to speed up the synchronization process before connection. However, too small L and R may cause oscillations in the frequency estimated. Normally, the L and R can be chosen slightly smaller than the corresponding values of Ls and Rs. Moreover, the ratio R L defines the cut-of frequency of the filter $\frac{1}{sL+R}$, which determines the capability of filtering out the harmonics in the voltage $V_g$. When the virtual current is driven to zero, the synchronverter is synchronized with the grid. Then, the circuit breaker can be turned on at any time to connect the synchronverter to the grid. When the circuit breaker is turned on, the Switch $S_C$ should be turned to Position 2 so that the real current $i_g$ is routed into the controller for normal operation. After the synchronverter is connected to the grid, the switches $S_P$ and $S_Q$ can be turned ON/OFF to achieve any operation mode

## IV. SIMULATIONS AND RESULTS
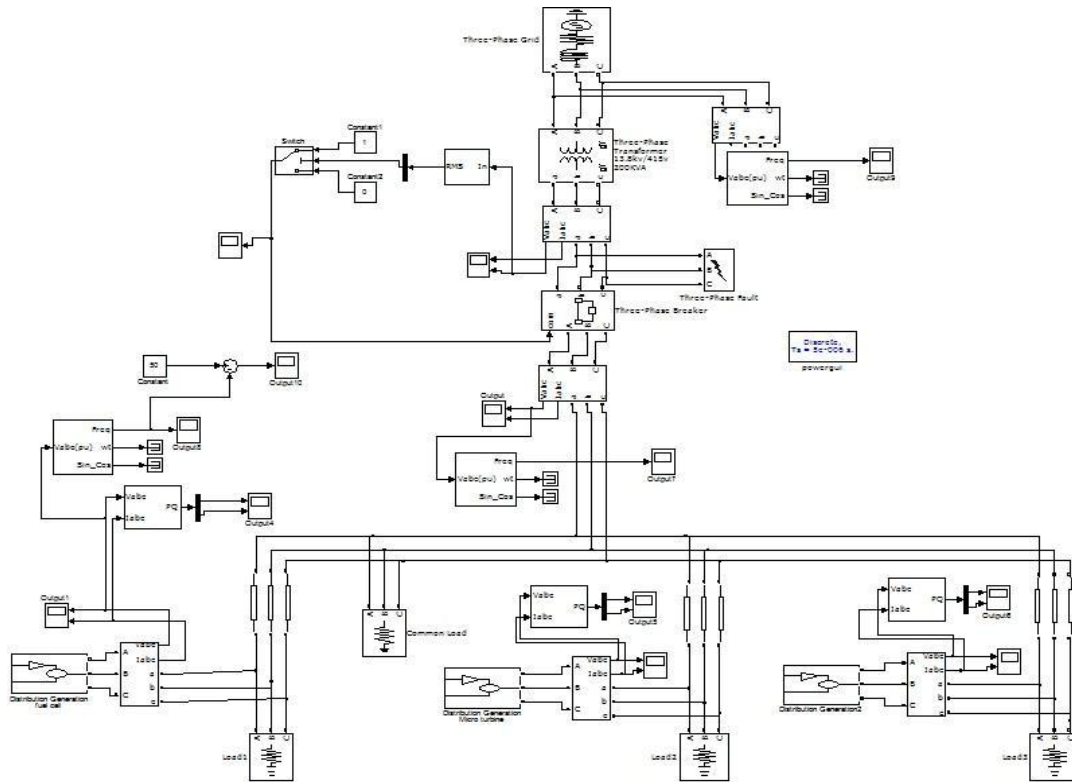


Fig 7 Simulink model of microgrid with 3DGs

The above figure represents the Simulink model of a microgrid consisting of three DGs. Simulations are carried out in MATLAB/SIMULINK environment to study the effectiveness of the proposed control topology. The scenarios involve DG startup and grid synchronization, transition to islanding mode and grid reconnection. Without loss of generality, DG units are considered as dispatchable ones with enough power and inertia-less dc link. The simulated system, depicted in Fig, has three DG units connected in parallel to the main grid through connecting cables and static switch. Each DG unit has a local load and the microgrid supplies one common load connected at PCC.
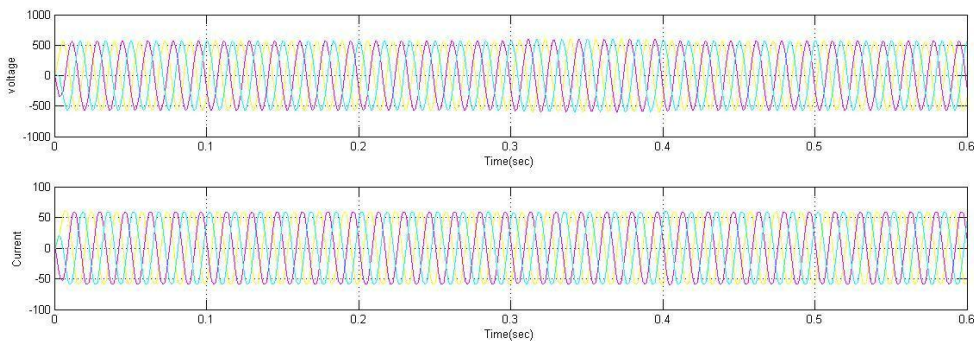


Fig 8 Voltage and current profile

The above figure shows the voltage and current profile of the microgrid system. The grid connected mode will be during the starting of simulation at time 0.3sec the system experiences a voltage sag and the islanding operation will be performed during simulation between 0.3 to 0.4 sec.In the islanding mode the load will be suddenly diconnected in 0.3 to 0.4 sec simulation time
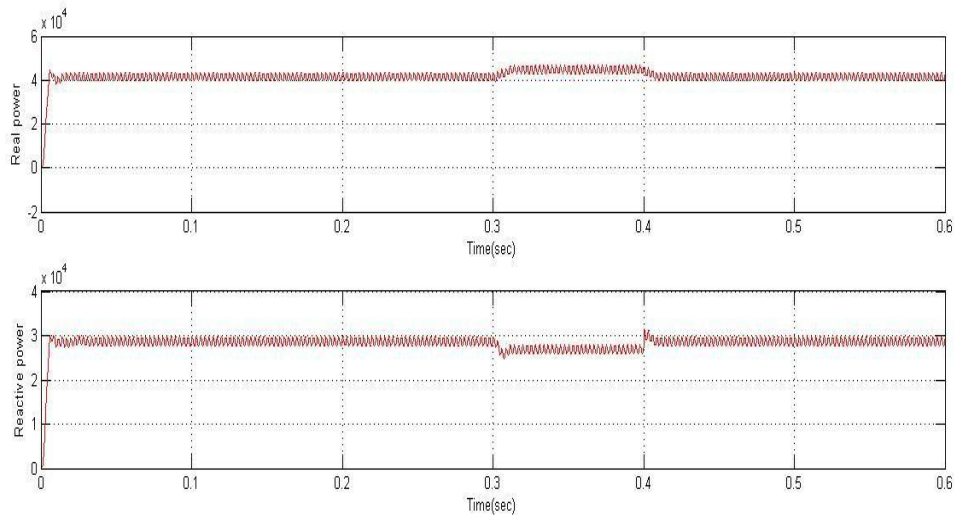
Fig 9 Real and reactive power of DG

The above figure shows the real and reactive power, the real power increases slightly during islanding and after restoration of the grid the power flow is normal . The reactive power decreases during islanding mode.
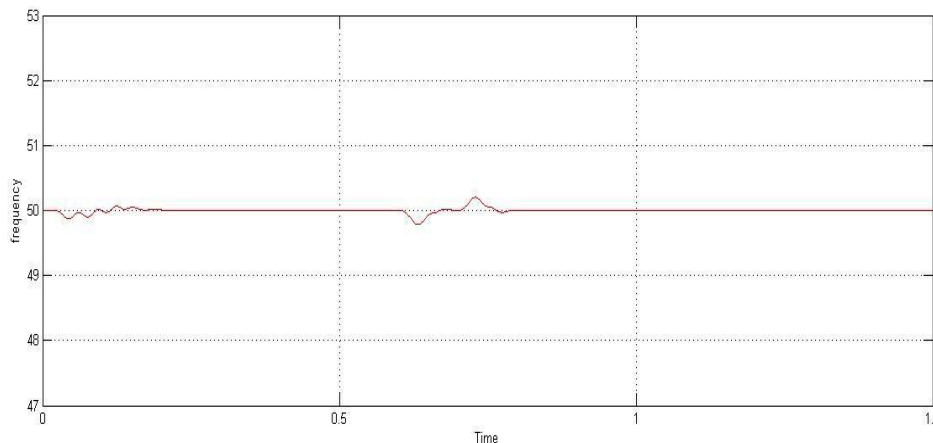


Fig 10 Frequency profile

The frequency response is shown above. The figure shows that even during grid disturbance the frequency profile is maintained and an error difference of 0.25Hz is observed.

## V.    CONCLUSION

A flexible control method for islanded and grid connected MGs with enhanced stability has been presented in this paper. The control structure does not require reconfiguration upon islanding detection. Further, it involves a nonlinear MG stabilizer that guarantees large-signal stability of the MG system. The nonlinear MG stabilizer adds a supplementary signal to the voltage loop of the VSC so that the augmented system stability is guaranteed. The controller uses only local information where the need for communication is eliminated, and better reliability is yielded. The controller works in the angle, frequency, and power domain instead of the conventional current-voltage controllers. It has been shown that using the proposed control scheme, the system is stable over a wide range of operation with minimum transients. A self-synchronized synchronverter has been implemented, so that there is no need to incorporate a dedicated synchronization unit for synchronization purposes. This leads to much improved performance, simplified controller, reduced demand for computational power, reduced development cost and e ort, and improved software reliability. It is able to synchronize itself with the grid before connection and to track the grid frequency automatically after connection. Moreover, it is able to operate in different modes as the original synchronverter but without the need of a dedicated synchronization unit to provide the grid frequency as the reference frequency.

# REFERENCES

[1]     A. Molderink,"Management and control of domestic smart grid technol-ogy,"IEEE Trans. Smart Grid,vol. 1, no. 2, pp. 109118, Sep.2010.

[2]     Seyed Mahdi Ashabani and Yasser Abdel-Rady I. Mohamed, A Flexi-ble Control Strategy for Grid-Connected and Islanded Microgrids With Enhanced Stability Using Nonlinear Microgrid Stabilizer, IEEE TRANS-ACTIONS ON SMART GRID, VOL. 3, NO. 3, SEPTEMBER 2012.

[3]     E. Santacana, G. Rackli e, L. Tang, and X. Feng,"Getting smart,IEEE Power Energy Mag., vol. 8, no. 2, pp. 4148, Mar./Apr. 2010.

[4]     J. Guerrero et al., Distributed generation,IEEE Ind. Electron. Mag., pp. 5264, Mar. 2010

[5]     J. A. P. Lopez, C. L. Moreira, andC.Marnay, De ning control strategies for microgrids islanded operation, IEEE Trans. Power Syst,vol.21, no. 2, pp. 916924, May 2006.

[6]     A. A. Salam, A. Mohamed and M. A. Hannan. "TECHNICAL CHAL-LENGES ON MICROGRIDS" ,IEEE Trans. Power syst., December 2008.

[7]     Nikkhajoei, H.; Lasseter, R.H.; , "Distributed Generation Interface to the CERTS Microgrid," IEEE Trans. Power Delivery., vol.24, no.3, pp.1598 1608, July 2009 . P. Tenti, H. K. M. Paredes, and P. Matavvelli, Conservative power the-ory, a framework to approach control and accountability issues in smart microgrids,IEEE Trans. Power Electron., vol. 26, no. 3, pp. 664673, Mar. 2011

# Compensation for Inverter Nonlinearity Using Trapezoidal Voltage

Maria Joseph M[1], Siby C Arjun[2]

*1,2 Electrical and Electronics Department, ASIET Kalady, India*

**Abstract:** *The nonlinearity of an inverter can be considered as the voltage differences between the voltage references and actual outputs of the voltage source inverter (VSI). In this paper, trapezoidal voltages were utilized to compensate for the inverter nonlinearity. The harmonic distortions in the output currents caused by the inverter nonlinearity can be controlled through the trapezoidal angle. Simulation results are given to demonstrate the validity and features of this method.*

**Keywords:** *Inverter nonlinearity, dead time compensation, trapezoidal voltage, harmonic analysis, Induction machine.*

## I. INTRODUCTION

Inverter fed ac drives are normally used in industrial application which reduces the cost for motors and its maintenance and providing maximum power savings. Behavior of the inverter influences the performance of ac machines. The nonlinear characteristics of switching devices such as dead time, switch turn on/off time delay, and voltage drop across the switches and diodes in inverters produce voltage distortion. The most significant nonlinearity is represented by the dead time to avoid short circuit of inverter legs. Voltage drop and turn on/off time inevitably exist in practical devices. However, dead time causes voltage error in the voltage source pulse width modulation (PWM) inverter by producing unwanted harmonics. In case of sensor less drives, this distortion usually causes a non optimal motor exploitation at low speed operation due to an error in the estimated position of the adopted reference frame used by the motor control scheme. In addition, the motor currents will be distorted, resulting in unnecessary torque ripple.

Various solutions have already been suggested to avoid the nonlinear characteristics of the inverter. [1], [2]. In most cases, compensation techniques are based on an average value theory and the lost volt seconds are added vectorially to the voltage reference. In a pulse-based compensation method the compensation is realized for each pulse width modulation (PWM) pulse. Meanwhile, other attempts have been carried out using the disturbance observer [3]. In these methods, the inverter nonlinearity is regarded as the disturbances to be mitigated. To estimate the disturbance voltages, the observer, used which is expected to be effective for a wide operating range. However, electrical parameters may vary depending on the circumstances, are used to design the observer. That is, the performance of the observer would be limited by the operating conditions.

In this paper, a novel method was proposed to compensate for the low-order harmonics from the inverter nonlinearity. The proposed method is similar to the observer-based method, in that the nonlinearity is regarded as voltage distortions. However, the proposed compensation method can adapt to varying operating conditions without the aid of any observers.

## II. ANALYSIS OF DEAD TIME EFFECTS

Due to definite turn-off and turn-on times of the switching devices in PWM inverters, it is necessary to insert a time delay between the switching OFF of a device and the switching ON of the other device on the same inverter leg. Fig 1 shows one phase of a PWM inverter.
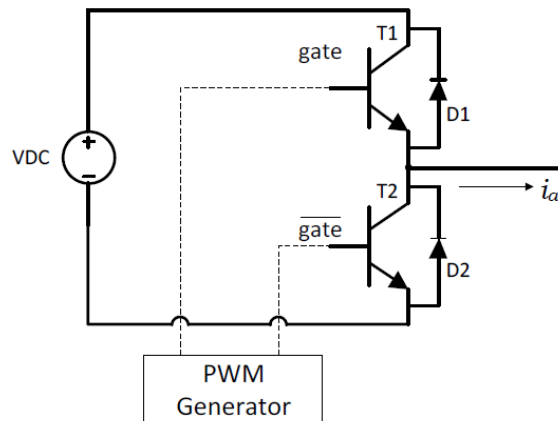
Fig 1.Single phase configuration of PWM inverter

Fig 2 shows the time delay ($t_{dead}$) between the switches T1 and T2. TON is the time for which the switch T1 is ON. $T_{SW}$ is the switching period. At time t1, T2 transitions from ON to OFF. The turning ON of T1 is delayed by time $t_{dead}$. This prevents the short circuit across both the switches of the inverter leg and the input dc voltage source. The introduction of the time delay between switching leads to reduced and distorted voltage at the output of the inverter.

To examine the effect of dead-time on the output voltage, switching waveforms on one leg of the inverter are examined. The current $i_a$ is positive in the direction of the load. The IGBTs T1 and T2 conduct when they are ON. During the dead-time period, when both T1 and T2 are OFF,

Either the reverse recovery diode D1 or D2 will conduct depending on the direction of ia.
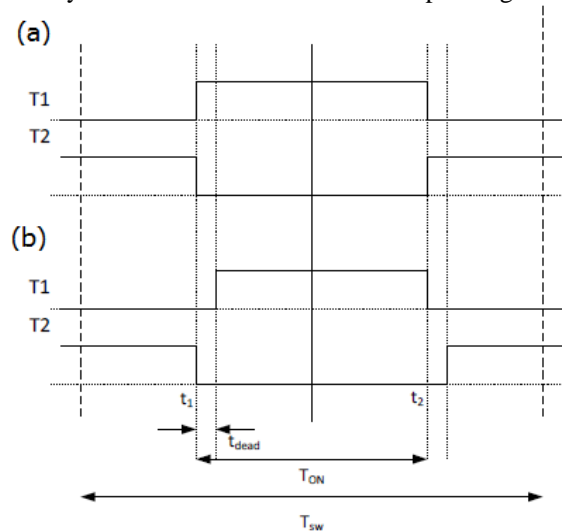


Fig 2. Time delay between turn OFF and turn ON of two switches on the same inverter leg (a)Ideal switching (b) Switching with dead time

Depending up on the direction of the switching transition and the sign of the current in phase 'a' $i_a$, four conditions are possible.

• The current $i_a$ is positive, T1 transitions from ON to OFF, T2 transitions from OFF to ON: During the dead-time period, D2 conducts and D1 blocks the flow of current. Thus, this condition results in the correct voltage being applied to the load terminals.

• The current $i_a$ is negative, T1 transitions from ON to OFF, T2 transitions from OFF to ON: During the dead-time period, D1 continues to conduct and D2 blocks the flow of current. And the condition results a gain in the voltage which being applied to the load terminals.

• The current $i_a$ is positive, T1 transitions from OFF to ON, T2 transitions from ON to OFF: During the dead-time period, D2 continues to conduct and D1 blocks the flow of current. And the condition results in a loss of voltage being applied to the load terminals.

• The current $i_a$ is negative, T1 transitions from OFF to ON, T2 transitions from ON to OFF: During the dead-time period, D1 continues to conduct and D2 blocks the flow of current. And the condition results in the correct voltage being applied to the load terminals.

In each switching cycle, T1 transitions from OFF to ON (T2 from ON to OFF) once and from ON to OFF (T2 from OFF to ON) once. Due to the distortions, the output voltage of the inverter is not equal to the desired reference voltage. In order to overcome the effect of dead time the proposed method has been suggested.

## III. PROPOSED METHOD

In proposed method, voltages in a trapezoidal form were utilized to compensate for the inverter nonlinearity. This method can adapt to varying operating conditions and physical parameters are not necessary for the adaption. [4]. An averaged model of the inverter was taken and averaged for one sampling period, to consider the temporal distortions. Then the inverter nonlinearity is entirely separated as the nonlinear loads whih is D ($i_{as}$), D ($i_{bs}$), and D ($i_{cs}$).
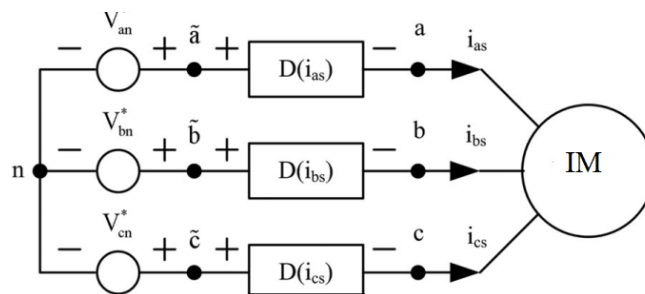


Fig 3. Modeling of an inverter: averaged inverter model per one sampling period

The compensation principle is clarified with Fig 3

$$V_{xx} = -D (i_{xs}) + V_{inv}^x = 0 \qquad (1)$$

Where the phase "x" can be a, b, or c and D ($i_{xs}$) is the distorted voltages and $V_{inv}^x$ is the compensation voltage which is added to the reference. To find the magnitude of compensation voltage, IM runs at stationary condition and plot the d-axis voltage with respect to d-axis current. Select the voltage which is more saturated as ($V_A$). This $V_A$ would be useful for compensation of the inverter non-linearity.

The compensation voltage height was determined from $V_A$. The trapezoidal angle Ɵt can be adjusted for the suitable compensation. To modulate the trapezoidal angle a dedicated modulator used. The selection of trapezoidal angle can be based on frequency analysis.
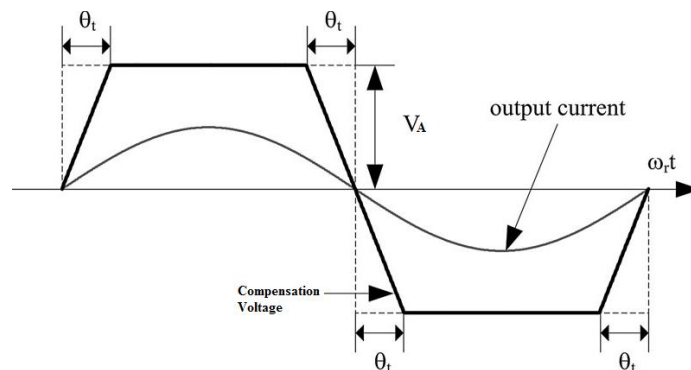


Fig 4. Shape of the compensation voltage (trapezoidal voltage).

Fig 4 showing the shape of compensation voltage and $V_{sat}$ , Ɵt represent the magnitude and angle of trapezoidal voltage.

## IV. MATLAB/SIMULINK ANALYSIS OF PROPOSED METHOD

### A. Simulink Model Of Trapezoidal Voltage Compensation
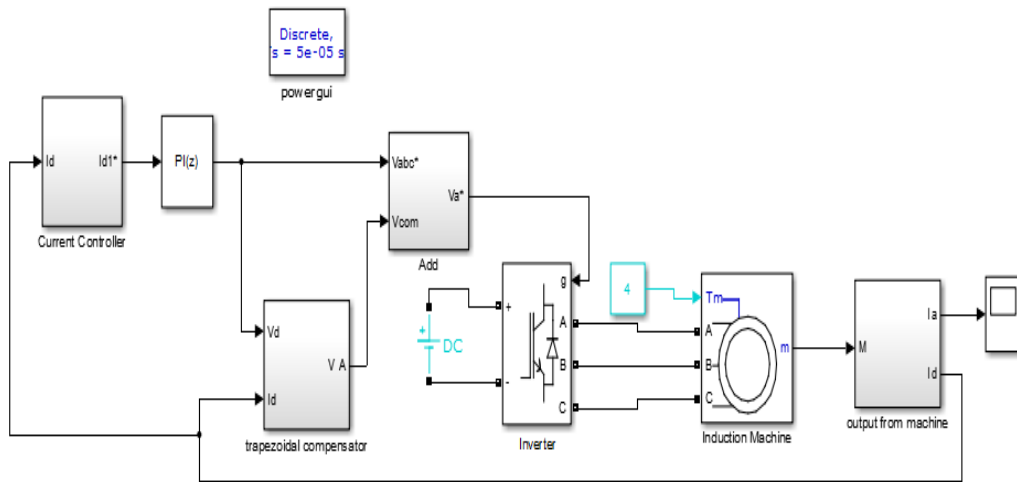


Fig 5.Simulink model for trapezoidal voltage compensation

Fig 5 shows a three-phase motor rated 10HP, 460 V; 1500 rpm is fed by a PWM inverter. The PWM inverter is built entirely with standard Simulink blocks. Its output goes through Controlled Voltage Source blocks before being applied to the IM block's stator windings. The load torque applied to the machine's shaft is originally set to its nominal value (4 Nm). The current control loop regulates the motor's stator currents. A compensation voltage generated from trapezoidal compensator block is added with the output from controller. Switching pulses for the inverter is generated by using PWM block. Hysteresis controller is used for current control. In addition, the preset dead time was 5 $\mu$s.

### B. Result Analysis
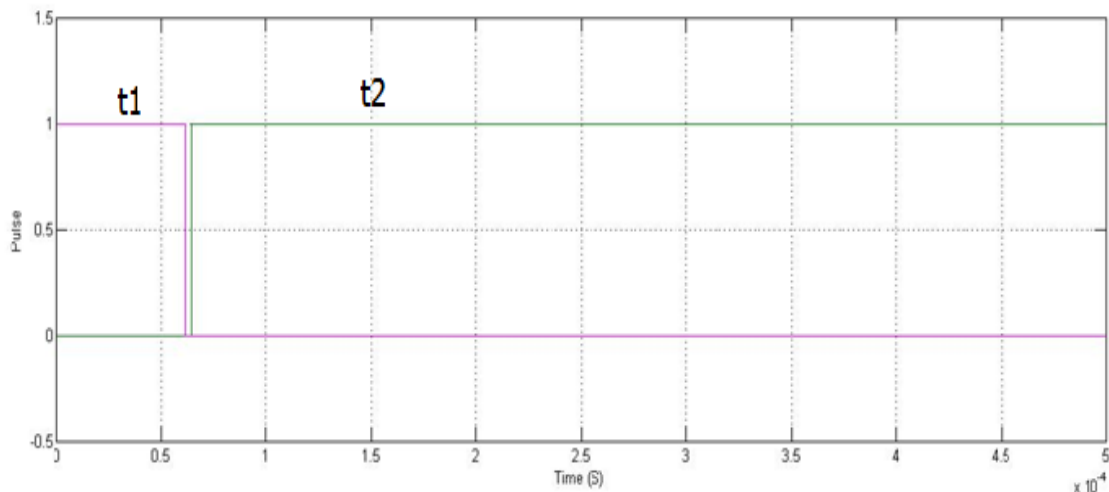


Fig 6 .Switching signal for the same leg switches with dead time

Figure showing switching pulses for switch T1 and T2 of the first inverter leg. A dead time of 5 micro second is there before T2 ON. For the compensation of inverter nonlinearity trapezoidal voltage obtained from compensation block is added to the reference having magnitude of 11V and 16.9 $^0$ angle. The angle can be varied so that at different operating condition the method is adaptable. The stator current output of IM after the compensation is shown in fig 7.
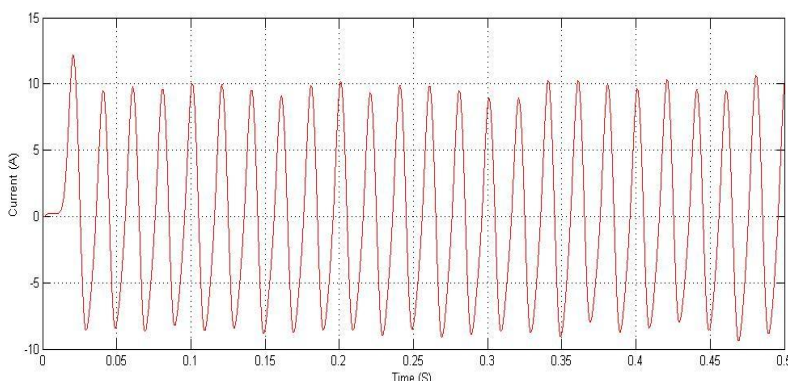
Fig 7. Stator current output ($I_a$) of IM

The result shows that with trapezoidal voltage compensation, the waveform distortions are getting reduced. While doing the harmonic analysis, the ratio to the fundamental (%) is varying between 20.19-16.97 .Result showing that at $16.9^0$, harmonic value is minimum and at $9^0$ harmonics is maximum.

Table 1. Comparison of FFT results for the output current without and with compensation.

| Ratio to the fundamental [%] | | |
|---|---|---|
| Order of harmonics | Without compensation | With trapezoidal voltage compensation |
| 5th | 1.88 | 0.14 |
| 7th | 2.23 | 0.08 |
| 11th | 0.75 | 0 |
| 13th | 0.42 | 0.01 |

The $5^{th}$ ,$7^{th}$,$11^{th}$,$13^{th}$ order harmonics are reduced by 1.74% ,2.15%,0.75%,0.41% respectively.

## V. CONCLUSION

To avoid shoot-through in voltage source inverters (VSI), a dead-time is introduced. However, such a blanking time can cause problems such as output waveform distortion and fundamental voltage loss in VSIs. To overcome dead-time effect trapezoidal voltage can be used which reduce harmonics by large amount. And it can adapt to varying operating conditions. Simulink analyze has done to validate the proposed method. Results shows that lower order harmonics and waveform distortions are decreased with proposed method .The unnecessary torque ripple with ac machine is also reduced.

## REFERENCES

**Journal Papers:**
[1]     L. Chen and F. Z. Peng, Dead-time elimination for voltage source inverters, IEEE Trans. Power Electron., vol. 23, no. 2, pp. 574-580, Mar2008.
[2]     G. Pellegrino, R. I. Bojoi, P. Guglielmi, and F. Cupertino, Accurate inverter error compensation and related self-commissioning scheme in sensorless induction motor drives,IEEE Trans. Ind. Appl., vol. 46, no. 5, pp. 1970-1978, Sep./Oct. 2010.
[3]     H.-S. Kim, H.-T. Moon, and M.-J. Youn,On-line dead-time compensation method using disturbance observer, IEEE Trans. Power Electron.,vol. 18, no. 6, pp. 1336-1345, Nov. 2003.
[4]     Yongsoon Park, Seung-Ki Sul, A Novel Method Utilizing Trapezoidal    Voltage to Compensate for Inverter Nonlinearity. , IEEE Trans. Power Electron. vol. 27, no. 12, December 2012.
[5]     J.-W. Choi and S.-K. Sul, Inverter output voltage synthesis using novel dead time compensation. ", IEEE Trans. Power Electron., vol. 11, no. 2, Mar 1996.
[6]     A. R.Munoz and T. A. Lipo, On-line dead-time compensation technique for open-loop PWM-VSI drives,IEEE Trans. Power Electron., vol. 14, no. 4, pp. 683-689, Jul. 1999.
[7]     D. Leggate , R. J. Kerkman,Pulse-based dead-time compensator for PWM voltage inverters, IEEE Trans. Power Electron., vol. 44, no. 2,pp. 191-197, Apr. 1997.

# Power Flow Control In A Transmission Line Using Unified Power Flow Controller

Liya Sebastian[1], Sajith RP[2]

[1]*Student, Department of Electrical and Electronics, ASIET / MG University, Kerala, India*
[2] *Assistant Professor, Department of Electrical And Electronics, ASIET, MG University, Kerala, India*

**Abstract:** *This paper concentrates on FACT device UPFC which is used for powerflow control in the transmission side. With the growing demand of electricity, it is not possible to erect new lines to face the situation. Flexible AC Transmission System (FACTS) makes use of the thyristor controlled devices and optimally utilizes the existing transmission network. One of such device is Unified Power Flow Controller (UPFC) on which the emphasis is given in this present work. Real, reactive power, and voltage balance of the unified power-flow control (UPFC) system is analyzed. A novel coordination controller is proposed for the UPFC. The basic control method is such that the shunt converter controls the transmission line reactive power flow and the dc-link voltage. The series converter controls the real power flow in the transmission line and the UPFC bus voltages. Experimental works have been conducted to verify the effectiveness of the UPFC in power flow control in the transmission line. The simulation model was done in MATLAB/SIMULINK platform.*

**Keywords:** *FACTS, IGBT, Reactive power balance, Real power balance, Series converter, Shunt converter, Unified Power-Flow Controller (UPFC), Voltage balance.*

## I. Introduction

The power transmitted over an ac transmission line is a function of the line impedance, the magnitude of sending-end and receiving-end voltages, and the phase angle between these voltages. Traditional techniques of reactive line compensation and step-like voltage adjustment are generally used to alter these parameters to achieve power transmission control. Fixed and mechanically shunt and series reactive compensation are employed to modify the natural impedance characteristics of transmission lines in order to establish the desired effective impedance between the sending and receiving-ends to meet power transmission requirements. Voltage regulating and phase shifting transformers with mechanical tap-changing gears are used to minimize voltage variation and control power flow. These conventional method provide adequate control under steady-state and slowly changing system conditions, but are largely ineffective in handling dynamic disturbances.

The traditional approach to contain dynamic problems is to establish generous stability margins enabling the system to recover from faults, line and generator outages, and equipment failures. This approach, although reliable, generally results in a significant under utilization of the transmission system. As a result of recent environmental legislation, rights-of-way issues, construction cost increases, and deregulation policies, there is an increasing recognition of the necessity to utilize existing transmission system assets to the maximum extent possible. To this end, electronically controlled, extremely fast reactive compensators and power flow controllers have been developed within the overall framework of the FACTS initiative. These compensators and controllers either use conventional reactive components and tap-changing transformer arrangements with thyristor valves and control electronics or employ switching power converters, as synchronous voltage sources, which can internally generate reactive power for, and also exchange real power with, the ac system.

The Unified Power Flow Controller (UPFC) is a member of this latter family of compensators and power flow controllers which utilize the synchronous voltage source(SVS) concept for providing a uniquely comprehensive capability for transmission system control. Within the framework of traditional power transmission system concepts, the UPFC is able to control, simultaneously or selectively, all the parameters affecting power flow in the transmission line. Alternatively, it can provide the unique functional capability of independently controlling both the real and reactive power flow in the line. These basic capabilities make the Unified Power Flow Controller the most powerful device presently available for transmission system control.

Unified power flow controller (UPFC) is a member of FACTS family. It is a combination of Static synchronous compensator (STATCOM) and Static synchronous series compensator (SSSC) coupled via a common dc-link, to allow bi-directional flow of real power between the series output terminals of the SSSC and the shunt output terminals of the STATCOM. The UPFC, by means of angularly unconstrained series voltage injection, is able to control the transmission line voltage, impedance and angle or the real and reactive power flow in the line.

Also the problem of low-frequency power swings is a matter of concern for power systems engineers. As it is becoming increasingly important to fully utilize the existing transmission system assets, proper attention should be given to the enhancement of utilizing the transmission capacity by damping of the power swings. Flexible AC transmission system (FACTS) devices are found to be very effective for this purpose. A FACTS device should have an adequate margin of variable compensation for effective damping of power swings. Therefore, while planning for FACTS controllers, the damping effect per MVar and the control cost should be taken into consideration. The damping provided by FACTS devices offers the means to reduce the inhibiting effects of the oscillations or swings. But the outputs of these FACTS devices should be restricted by the limits within their working conditions. Notwithstanding, low frequency oscillations are detrimental to the goals of maximum power transfer and optimal power system security.

## II.  System Overview
The first FACTS installation was at the C. J. Slatt Substation in Northern Oregon. This is a 500kV, 3-phase 60 Hz substation, and was developed by EPRI, the Bonneville P.

**Series compensation**

In series compensation, the FACTS is connected in series with the power system. It works as a controllable voltage source. Series inductance exists in all AC transmission lines. On long lines, when a large current ows, this causes a large voltage drop. To compensate, series capacitors are connected, decreasing the effect of the inductance.

**Shunt compensation**

In shunt compensation, power system is connected in shunt (parallel) with the FACTS. It works as a controllable current source. Shunt compensation is of two types:

- **Shunt capacitive compensation:**

This method is used to improve the power factor. Whenever an inductive load is connected to the transmission line, power factor lags because of lagging load current. To compensate, a shunt capacitor is connected which draws current leading the source voltage. The net result is improvement in power factor. This method is used to improve the power factor. Whenever an inductive load is connected to the transmission line, power factor lags because of lagging load current. To compensate, a shunt capacitor is connected which draws current leading the source voltage. The net result is improvement in power factor.

- **Inductive compensation:**

This method is used either when charging the transmission line or, when there is very low load at the receiving end. Due to very low, or no load very low current ows through the transmission line. Shunt capacitance in the transmission line causes voltage amplification(Ferranti Effect). The receiving end voltage may become double the sending end voltage (generally in case of very long transmission lines). To compensate, shunt inductors are connected across the transmission line. The power transfer capability is thereby increased depending upon the power equation.

The concept of Flexible AC transmission system has been proposed in 1995, which is called FACTs. The basic idea of FACTs is installing the power electronic devices at the high-voltage side of the power grid to make the whole system electronically controllable. The advances achieved in the high power semiconductor devices and control technology makes the foundation of the development of FACTs. The FACTs devices are able to provide active and reactive power to the grid rapidly. The power compensation achieved by FACTs devices could adjust the voltage of the whole system and the power flow could be satisfactorily controlled. Many works are carried out, related to the real and reactive power control in transmission line and the direct power control. The dynamic behaviour of two different flexible ac transmission system devices; the interline power-flow controller (IPFC) and the unified power-flow controller (UPFC) in a benchmark system. The small-signal model of the interline power-flow controller is developed and validated using detailed electromagnetic transients simulation.

**2.1 The Unified Power Flow Controller (UPFC)**

The basic conception of the UPFC was proposed by Nabavi-Niaki and Iravani in 1996[4].The Unified Power Flow Controller(UPFC) was devised for the real-time control and dynamic compensation of ac transmission systtem, providing multi-functional exibility required to solve many of the problems facing the power delivery industry.

The UPFC is made up of two voltage source controllers sharing the same capacitor at their dc voltage controlled side. One voltage source controller is in parallel with one side of a transmission line and the other voltage source controller in the UPFC is in series connect to the other side of the same transmission line. The basic structure of the UPFC is shown in the Figure 1. The UPFC can simultaneously control the active and reactive power flow and voltage magnitude. However it has little effect on voltage angle.
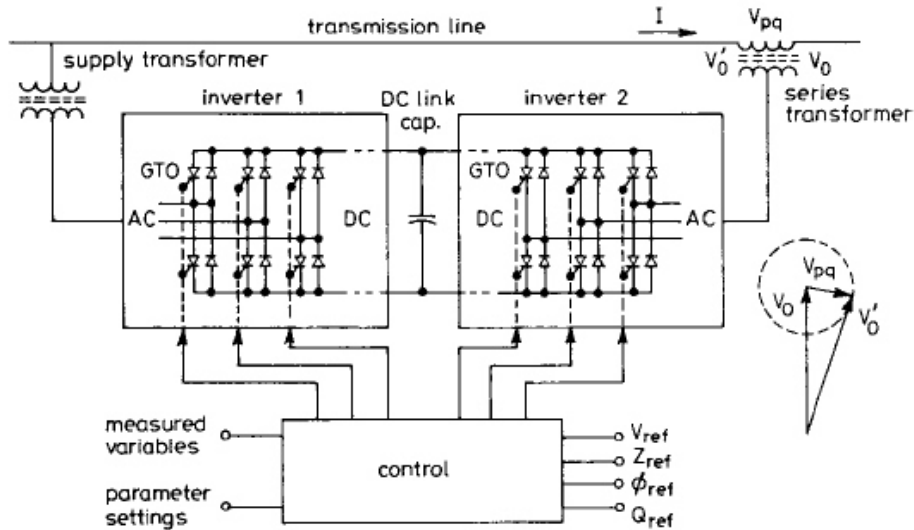


Fig. no:1 Implementation of the UPFC by two back-to-back voltage-sourced converters

AC transmission lines form the backbone of the electricity grid in most countries and continents. The power flow will follow the path of least impedance and is uncontrollable, unless active grid elements are used. To enhance the functionality of the ac transmission grid, flexible ac transmission systems (FACTS) support the transmission grid with power electronics. These devices offer a level of control to the transmission system operator. A unified power-flow controller (UPFC) is the most versatile of these FACTS devices. A transmission line equipped with a UPFC can control the balance of the transmitted power between parallel lines and, as such, can optimize the use of the transmission grid for all parallel power flows. A one-wire schematic of a transmission-line system equipped with a UPFC is given in Fig.2
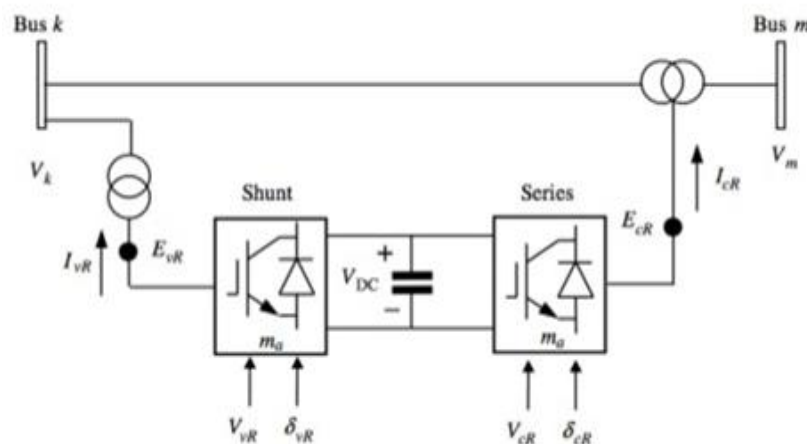


Fig. no:2 Basic structure of UPFC

A UPFC is connected to the transmission line by coupling transformers, both with a shunt and with a series connection. The UPFC consists of two ac/dc converters, the ac sides connected to the shunt and series connection with the transmission line, and the dc sides connected back to back. UPFCs are typically built with voltage-sourced converters, having a capacitor as (limited) dc energy storage.

The control scheme and comprehensive analysis for a unified power flow controller (UPFC) on the basis of theory, computer simulation, and experiment. This developed theoretical analysis reveals that a conventional power feedback control scheme makes the UPFC induce power fluctuation in transient states. The conventional control scheme cannot attenuate the power fluctuation, and so the time constant of damping is independent of active and reactive-power feedback gains integrated in its control circuit. An advanced control scheme which has the function of successfully damping out the power fluctuation. A UPFC rated at 10 kVA is designed and constructed, which is a combination of a series device consisting of three single-phase pulse width modulation (PWM) converters and a shunt device consisting of a three phase diode rectifier.

### 2.2 Power-Flow Control

The real, reactive power, and voltage balance of the unified power-flow control (UPFC) system is analyzed. Two important results related to UPFC control are shown in this paper. First, the shunt converter provides all of the required reactive power during the power-flow changes if the UPFC bus voltage is constant. Second, the UPFC bus voltage can be controlled both from the sending side and from the receiving side. Based on the analysis, a novel coordination controller is proposed for the UPFC. The basic control strategy is such that the shunt converter controls the transmission-line reactive power flow and the dc-link voltage. The series converter controls the transmission line real power flow and the UPFC bus voltage. The real/reactive power coordination controllers in the UPFC control system can obtain good performance both during transient and stable conditions. Inclusion of the real power coordination controller in the UPFC control system avoids excessive dc-link voltage excursions and improves its recovery during transient conditions. Experiments have been conducted to verify the effectiveness of the proposed control strategy.

Besides transformers, the general structure of UPFC contains also a "back to back" AC to DC voltage source converters operated from a common DC-link capacitor. First converter is connected in shunt and the second one in series with the line. The shunt converter is pri- marily used to provide active power demand of the series converter through a common DC link. Converter1 can also generate or absorb reactive power, if it is desired, and thereby provide independent shunt reactive compensation for the line. Converter 2 provides the main function of the UPFC by inject- ing a voltage with controllable magnitude and phase angle in series with the line via an voltage source. The reactance xs describes a reactance seen from terminals of the series transformer and is equal to (in p.u. base on system voltage and base power).

The real and reactive power equations are :

$$P = \frac{V_1 V_2}{x} \sin(\delta 1 - \delta 2) \qquad (1)$$
$$Q = \frac{V_2}{x}(V_1 - V_2) \qquad (2)$$
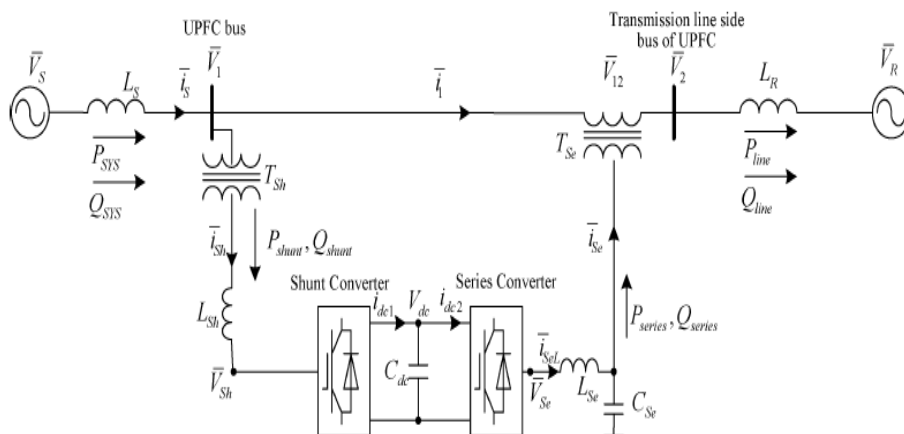


Fig. No: 3 Configuration of a UPFC based on two back-to-back three-phase converters.

**2.3 Analysis of UPFC**
**2.3.1 Voltage Balance of the UPFC System**
   The UPFC is inserted into the transmission line through a series transformer. According to Fig3, the voltage balance can be established as

$$V_S = V_1 + jwL_S i_S \qquad\qquad (3)$$
$$V_1 = V_{12} + jwL_R i_1 + V_R \qquad\qquad (4)$$

W = 314rad/s  power system angular velocity
$L_S$ = sending-end transmission-line inductance
$L_R$ = Receiving-end transmission-line inductance

**2.3.2 Real Power Balance Analysis**
   The power balance of the UPFC system is investigated as below.
For real power balance :-

$$P_{SYS} - P_{Shunt} + P_{Series} = P_{Line} \qquad\qquad (5)$$

$P_{SYS}$ = Sending-end output real power
$P_{Shunt}$  = Real power absorbed by the shunt converter
$P_{Series}$  = Real power output by the series converter
$P_{Line}$  = Real power flow from the UPFC to the receiving end

**2.3.3 Reactive Power Balance Analysis**
   According to Fig.3, The reactive power balance can be written as,

$$Q_{SYS} - Q_{Xs} - Q_{Shunt} + Q_{Series} = Q_{Line} \qquad\qquad (6)$$

$Q_{SYS}$ = Sending-end output reactive power
$Q_{Xs}$ = Reactive power consumed by the sending transmission line
$Q_{Shunt}$  = Reactive power absorbed by the shunt part of the UPFC
$Q_{Series}$  = Reactive power output by the series part of the UPFC
$Q_{Line}$ = Reactive power flow from the UPFC to the receiving end.

# III. Proposed Plan

**3.1 Problem Identification**
   The first generation of the FACTs devices. In this period, the typical devices are including tap changing and phase changing transformer, synchronous generator and series capacitors. Except the series capacitors, which could also be called capacitor bank, others are dynamic devices. These devices are mainly controlled at the generation sideof the power grid and the cost is typically expensive. When talk about the series capacitors, the drawback of this device could hardly be omitted. Since the device is made up of many fixed-capacitance capacitors, it could hardly be controlled to give the real not-fixed capacitance to the grid. The second generation of the FACTs devices. It could be classified into two categories: thyristor-based devices and fully-controlled devices based compensator. The thyristor is called half controlled device, because it can only be controlled to switch on but notto cut-off. Static Var Compensator (SVC) and Thyristor-Controlled Series Capacitor (TCSC) are included in this category. The fully controlled devices mainly involve GTO etc. The Static Compensator (STATCOM), Solid State Series Compensator (SSSC), Unified Power Flow Controller (UPFC) and HVDC- Voltage Source Converter (HVDC-VSC) are included in this group.

**3.2 Problem solution**
   AC transmission lines form the backbone of the electricity grid in most countries and continents. The power flow will follow the path of least impedance and is uncontrollable, unless active grid elements are used. To enhance the functionality of the ac transmission grid, flexible ac transmission systems (FACTS) support the transmission grid with power electronics. These devices offer a level of control to the transmission system operator. A unified power-flow controller (UPFC) is the most versatile of these FACTS devices. A transmission line equipped with a UPFC can control the balance of the transmitted power between parallel lines and, as such, can optimize the use of the transmission grid for all parallel power flows.

**3.3 Proposed controller**
**3.3.1 Series and Shunt controllers**

The shunt converter of the UPFC controls the reactive power flow in the transmission line and dc-link voltage. The control diagram for the shunt part of the UPFC is shown in Fig 4. The control scheme is composed of two loops the outer loop and the inner loop. The outer loop generates the current reference with coordination control, while the inner current loop makes the shunt converter output the necessary currents. The control system is based on the synchronous rotating frame as mentioned before. The -axis current is controlled to manage the dc-link voltage and balance the real power of the UPFC. The -axis current is controlled to manage the transmission-line reactive power flow. The decoupled control system has been employed to achieve simultaneous control of the shunt converter input current. Coordination control schemes are applied in both transmission-line reactive power flow and dc-link voltage control to obtain better dynamic performance. In the axis coordination control scheme, the transmission-line reactive power-flow variation reference is added to the reactive power-flow PI regulator output with a gain 2/3V1d. So the shunt converter can generate an appropriate amount of reactive power to compensate the reactive power-flow change with a quick response. Further, the inner control system loops are fast-acting PI controllers and ensure fast supply of both the series converter real power demand and the reactive power needed for reactive power-flow control by the shunt converter.
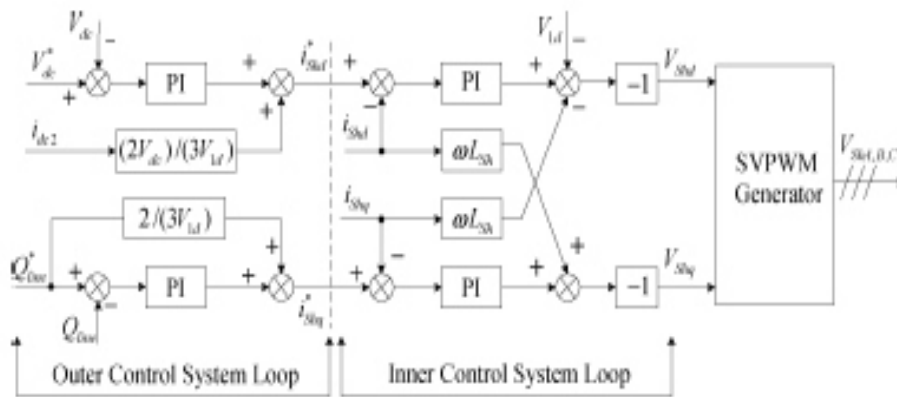


Fig. no: 4 Shunt Controller

The series converter of the UPFC provides simultaneous control of the UPFC bus voltage and real power flow in the transmission line. To do so, the series converter injected voltage is decomposed into two components. The transformation is the same as that used in shunt converter control. The axis injected component controls the UPFC bus voltage. The axis injected component controls the transmission-line real power flow. The detail of this control scheme is shown in Fig 5. The whole control system is composed of two loops as it is in the shunt converter. The outer loop generates the reference voltage signals for the inner loop with coordination control. A current feed forward is added to the -axis outer loop to compensate the voltage changes across the line impedance when there is a power flow change. The inner control loop is a typical voltage current double-loop control scheme for inverters. The same decoupled control strategy as mentioned in is applied here. With this method, the UPFC bus can be controlled directly and good performance is expected.
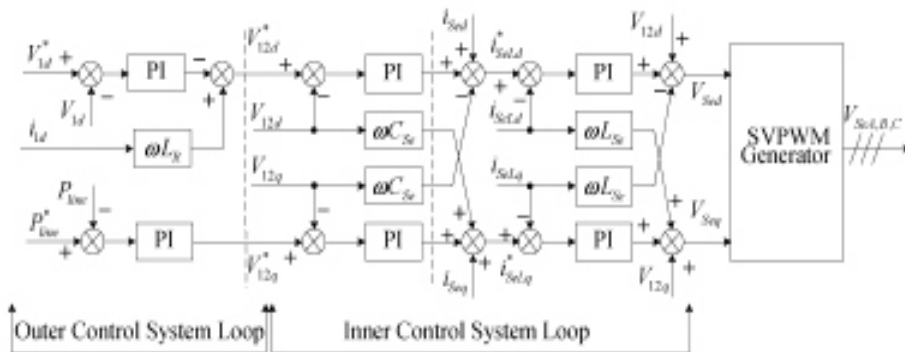


Fig. no : 5 Series Controller

## IV.   Simulations And Results

An experimental UPFC system has been built to test the power control in transmission line. Recent advances in high-voltage IGBT technology allow for higher switching frequency with lower loss, and this allows for practical implementation of PWM control for high-power converters. So in the experiment, both the shunt converter and the series converter have been built as a three-phase PWM converter with IGBT as the power device. The UPFC device is inserted into a transmission line, and with the help of the UPFC, the power flow in the transmission line can be controlled effectively while maintaining the UPFC bus voltage constant. The parameters of the whole systems are given below:-
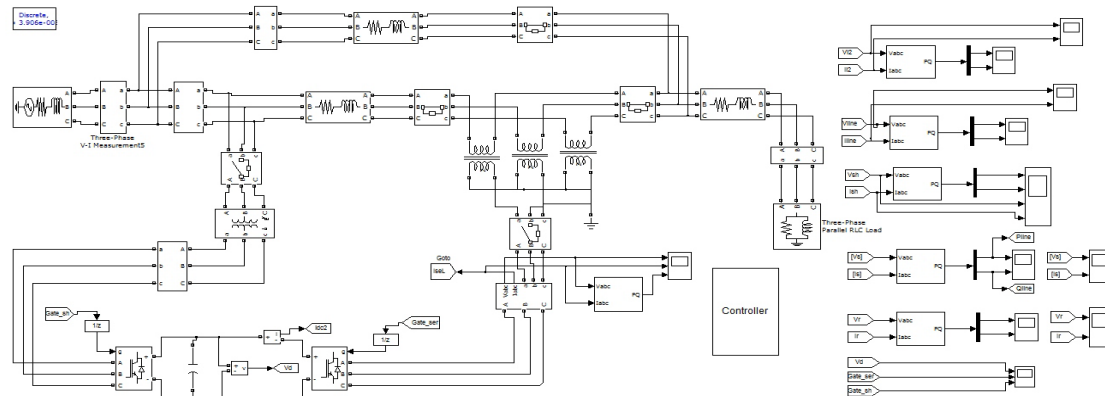


Fig. no: 6 Implementing UPFC in a transmission line

Design Specifications:-

| | |
|---|---|
| Sending end voltage Vs | - 380V (line-line) |
| Receiving end voltage Vr | - 380V (line-line) |
| The transmission angle r | - 30 degree |
| Shunt transformer turns ratio Tsh | - 2.5:1 (Y-D) |
| Series transformer turns ratio Tse | - 6:8 (Y-D) |
| Sending end line inductane LS | - 18mH |
| Transmission line inductance LR | - 60mH |
| Shunt converter output filtering inductance Lsh | - 6mH |
| Series converter output filtering inductance Lse | - 1mH |
| Series converter output filtering capacitance Cse | - 10μF |
| DC-link capacitor Cdc | - 9400μF |
| DC-link voltage Vdc | - 400V |

The UPFC under study is connected to the transmission system. In order to evaluate the operation, the UPFC power control system model has been developed and simulated in Matlab/Simulink. The components of the simulation model are built with standard electrical component blocks from the SimPower Systems block in Matlab/Simulink library.

Power control in transmission line:- With and without compensation
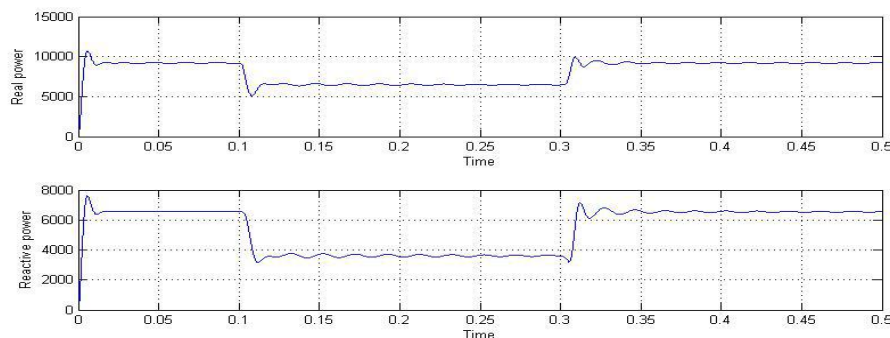


Fig. no:7 The real and reactive power in line 2.
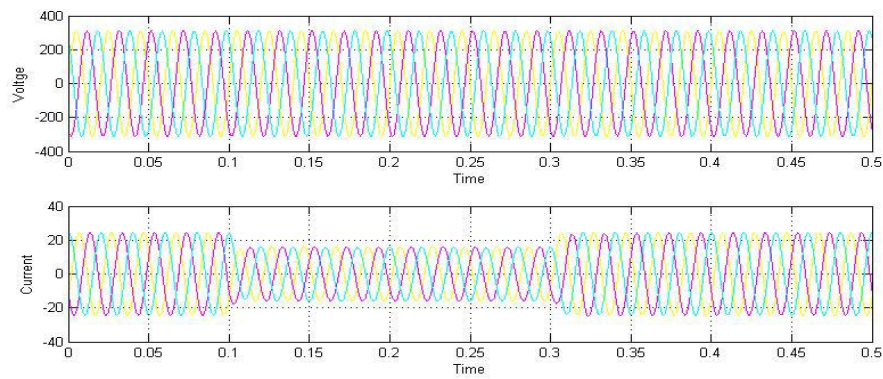
Fig. no:8 The voltage and current in line 2.
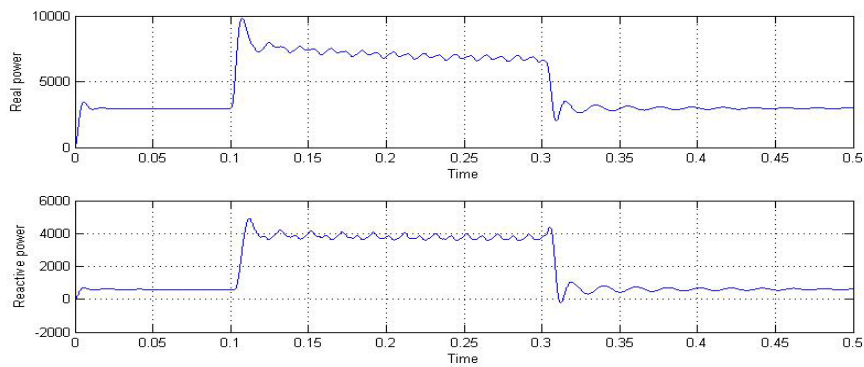


Fig. no:9 The real and reactive power in line 1.
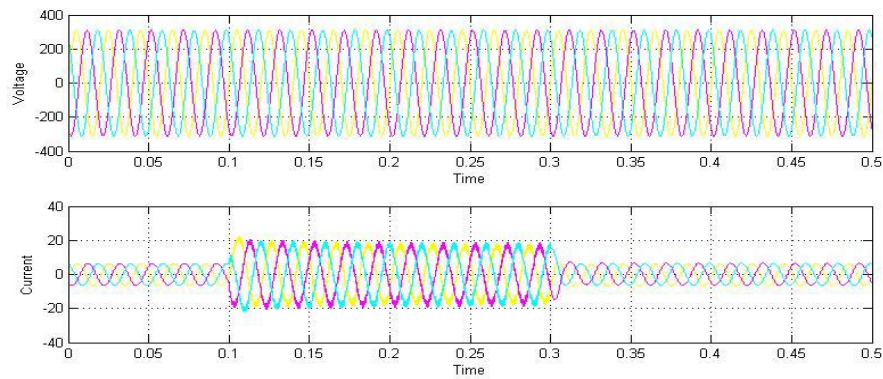


Fig. no:10 The voltage and current in line 2.
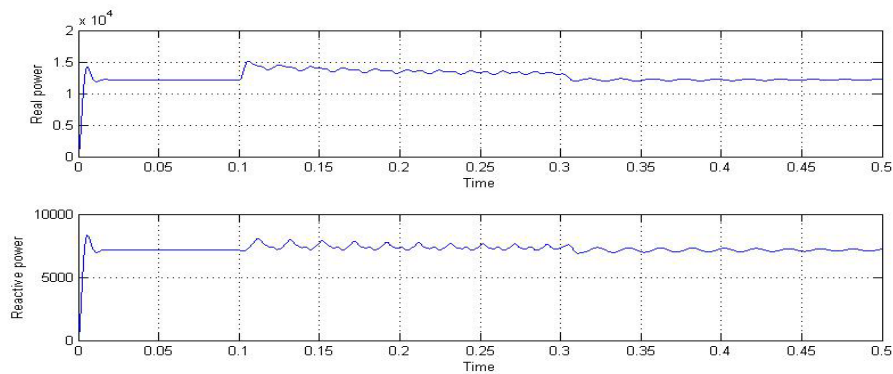


Fig. no:11 The real and reactive power in sending end side.
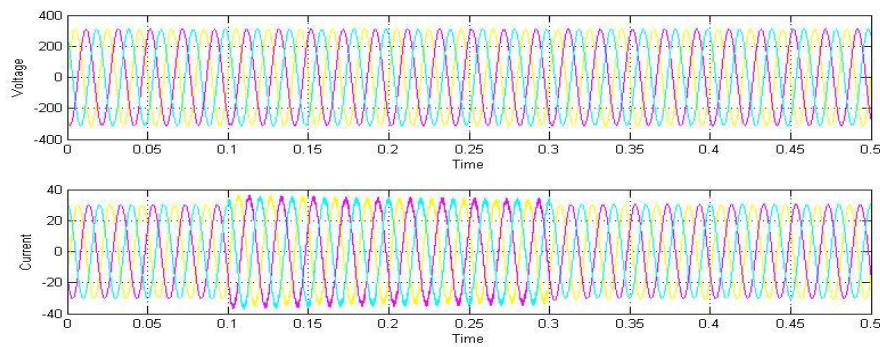
Fig. no:12 The voltage and current in the sending end side
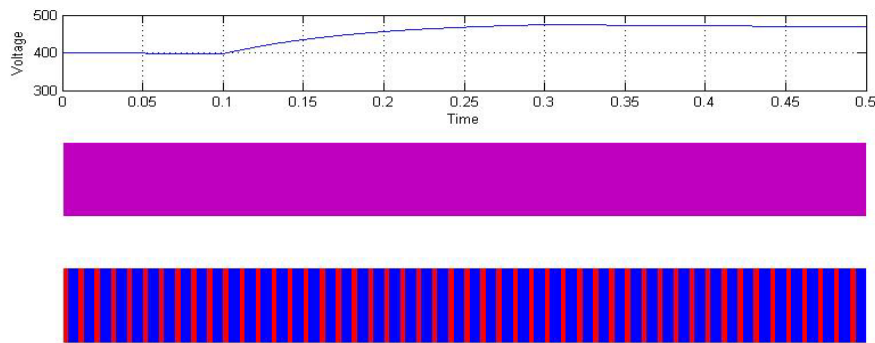


Fig. no:13 a) Capacitor voltage. b) Gate pulses to shunt converter. c)Gate pulses to series converter.

## V.    Conclusion

Real, reactive power, and voltage balance of the UPFC system are analyzed. The basic control strategy is such that the shunt converter of the UPFC controls the transmission-line reactive power and the dc-link voltage. The series converter controls the transmission- line real power flow and the UPFC bus voltage. The shunt converter provides all of the required reactive power during the power flow changes if the UPFC bus voltage is constant. The UPFC bus voltage can be controlled both from the sending side and from the receiving-end side.

## REFERENCES

[1]     L. Gyugyi,"Direct power control of series converter of unified power-flow controller with three-level neutral point clamped converter",IEEE Trans. Power system., vol. 27, no. 12, December 2012.
[2]     L. Gyugyi, C. Schauder, S.Williams, T. Rietman, D. Torgerson, and A. Edris,"The          unified power flow controller: A new approach to power transmission control",IEEE Trans. Power system,vol. 11, no. 2, pp. 221☐227, Mar. 1996.
[3]     A. R.Munoz and T. A. Lipo, "Control and analysis of a unified power flow controller" ,IEEE Trans. Power Electron., vol. 14, no. 4, pp. 683☐689, Jul.1999.
[4]     G. Pellegrino, R. I. Bojoi, P. Guglielmi, and F. Cupertino, "An improved upfc control for oscillation damping", IEEE Trans. Ind. Appl., vol. 46, no.5, pp. 1970☐1978, Sep./Oct. 2010.
[5]     T. Hoshino and J.-I. Itoh, "Output voltage correction for a voltage source type inverter of an induction motor drive", IEEE Trans. Power Electron., vol. 25, no. 9, pp. 2440☐2449, Sep. 2010.
[6]     L. Chen and F. Z. Peng, "Power-flow control performance analysis of a unified power-flow controller in a novel control scheme" IEEE Trans. Power system., vol. 23, no. 2, pp. 574☐580, Mar. 2008.
**[7]**     Mariusz Jankowski and Grzegorz Jabonski,"Effects of unified power flow controllers on transient stability", INTL JOURNAL OF POWER SYSTEM, 2012.

# Wear In Hydrodynamic Journal Bearings: A Review

Harbansh Singh[1], Dr. S. S. Sen[2]

[1]*M. Tech Scholar (ME), Green Hills Engineering College Kumarhatti, Solan, India*
[2]*Professor in ME Department, Green Hills Engineering College Kumarhatti, Solan, India*

***Abstract:*** *The importance of friction and wear control cannot be overemphasized for economic reasons and long-term reliability. This paper presents the reviews of different works in the area of wear and friction in hydrodynamic journal bearings and tries to find out latest developments and trends available in industries and other fields in order to minimize the total equipment cost, minimize damages and maximize the safety of machines, structures and materials. This paper helps us to find out the parameters on which a hydrodynamic journal bearing is selected for different conditions i.e. dry as well as lubricated conditions.*
***Keywords:*** *Friction, Hydrodynamic Journal bearing, Machine, Materials, Wear.*

## I. INTRODUCTION

Despite their presence in our everyday life, friction, wear and tribology are not phenomena that most peoples are considering on daily basis. Nevertheless, they are responsible for many problems and large cost in modern civilization and engineers and designers are always must take these factors into account when constructing technical equipment. Usually wear is undesirable, because it makes necessary frequent inspection and replacements of parts and also it will lead to deterioration of accuracy of machine parts. It can induce vibrations, fatigue and consequently failure of the parts [1]. For the particular practical application the kind of wear loading can be different, and therefore the structure of the composite material used for these applications can also be different in order to fulfill the particular requirements.

**(A) Wear**
**(i) Introduction: -**
Wear is progressive loss or removal of material from one or both the surfaces in contact as the result of relative motion between them [2].Wear is the single most influencing factor which shortens the effective life of machine or its components.
**(ii) Types of Wear: -**
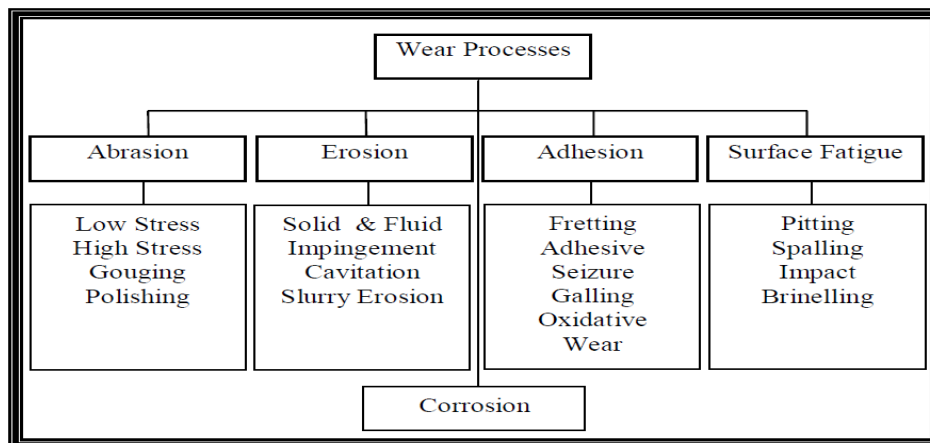


Fig. 1 Types of Wear

**Abrasive Wear:-**
Abrasive wear occurs when material is removed from one surface by another harder Material, leaving hard particles of debris between the two surfaces. It can also be called scratching, gouging or scoring depending on the severity of wear. Abrasive wear occurs under two conditions:
1. Two body abrasion: In this condition, one surface is harder than the other rubbing surface. Examples in mechanical operations are grinding, cutting, and machining.

2. Three body abrasion: In this case a third body, generally a small particle of grit or abrasive, lodges between the two softer rubbing surfaces, abrades one or both of these surfaces.
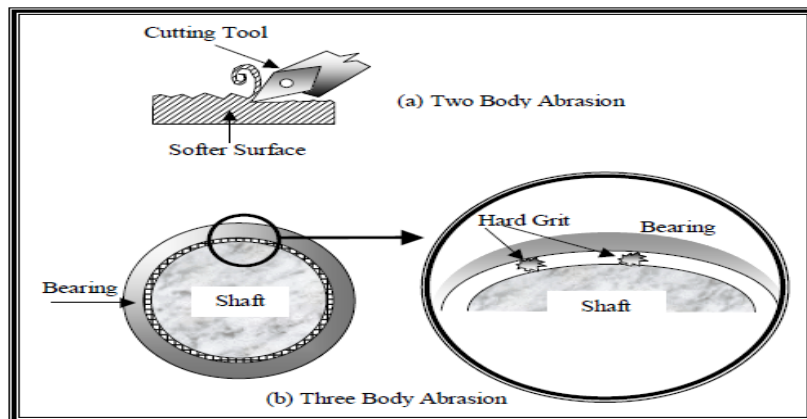


Fig 2 Abrasive Wear

**Erosive Wear:-**

The impingement of solid particles, or small drops of liquid or gas often cause what is known as erosion of materials and components. Solid particle impact erosion has been receiving increasing attention especially in the aerospace industry. Examples include the ingestion of sand and erosion of jet engines and of helicopter blades. As shown in figure the erosion mechanism is simple. Solid particle erosion is a result of the impact of a solid particle A, with the solid surface B, resulting in part of the surface B been removed. The impinging particle may vary in composition as well as in form. Cavitation erosion occurs when a solid and a fluid are in relative motion, due to the fluid becoming unstable and bubbling up and imploding against the surface of the solid, as shown in figure 4. Cavitation damage generally occurs in such fluid-handling machines as marine propellers, hydrofoils, dam slipways, gates, and all other hydraulic turbines, according to Bhushan and Gupta (1991) [4]. Cavitation erosion roughens a surface much like an etchant would.
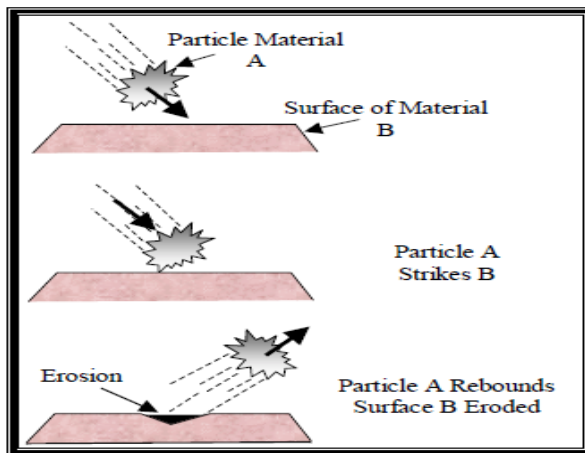


Fig 3 Abrasive Wear due to solid erosion
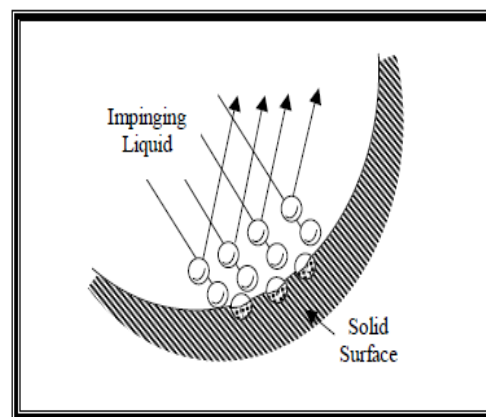


Fig 4 Abrasive Wear due to liquid erosion

**Adhesive Wear:-**

Adhesive wear is often called galling or scuffing, where interfacial adhesive junctions lock together as two surfaces slide across each other under pressure, according to Bhushan and Gupta (1991) [4]. As normal pressure is applied, local pressure at the asperities become extremely high. Often the yield stress is exceeded, and the asperities deform plastically until the real area of contact has increased sufficiently to support the applied load, as shown in figure. In the absence of lubricants, asperities cold-weld together or else junctions shear and form new junctions. This wear mechanism not only destroys the sliding surfaces, but the generation of wear particles which cause cavitation and can lead to the failure of the component.
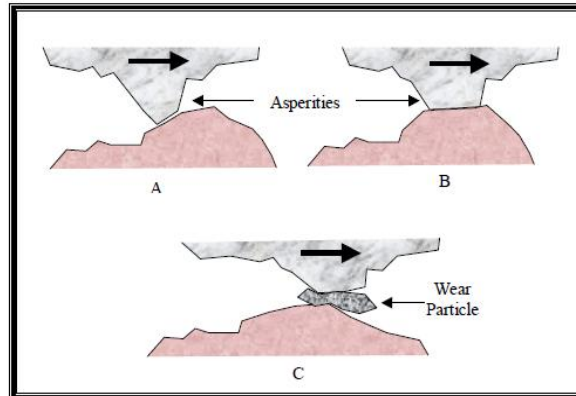
Schematic of generation of a wear particle as a result of
adhesive wear process.

Fig 5 Adhesive Wear

**Surface Fatigue:-**

When mechanical machinery move in periodical motion, stresses to the metal surfaces occur, often leading to the fatigue of a material. All repeating stresses in a rolling or sliding contact can give rise to fatigue failure. These effects are mainly based on the action of stresses in or below the surfaces, without the need of direct physical contact of the surfaces under consideration. When two surfaces slide across each other, the maximum shear stress lies some distance below the surface, causing microcracks, which lead to failure of the component. These cracks initiate from the point where the shear stress is maximum, and propagate to the surface as shown in figure. Materials are rarely perfect, hence the exact position of ultimate failure is influenced by inclusions, porosity, microcracks and other factors. Fatigue failure requires a given number of stress cycles and often predominates after a component has been in service for a long period of time.
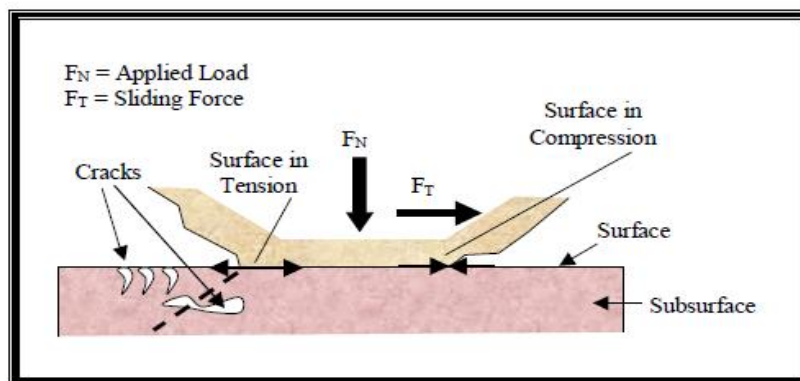


Schematic of fatigue wear, due to the formation of surface and
subsurface cracks.

Fig 6 Surface Fatigue

**Corrosive Wear:-**

In corrosive wear, the dynamic interaction between the environment and mating material surfaces play a significant role, whereas the wear due to abrasion, adhesion and fatigue can be explained in terms of stress interactions and deformation properties of the mating surfaces. In corrosive wear firstly the connecting surfaces react with the environment and reaction products are formed on the surface asperities. Attrition of the reaction products then occurs as a result of crack formation, and/or abrasion, in the contact interactions of the materials. This process results in increased reactivity of the asperities due to increased temperature and changes in the asperity mechanical properties.

**(B) Hydrodynamic Journal Bearing**

In hydrodynamic lubrication, the load supporting high pressure fluid-film is created due to shape and relative motion between the two surfaces [3]. The moving surface pulls the lubricant into a wedge shaped zone,

at a velocity sufficiently high to create the high pressure film necessary to separate the two surface against the load.
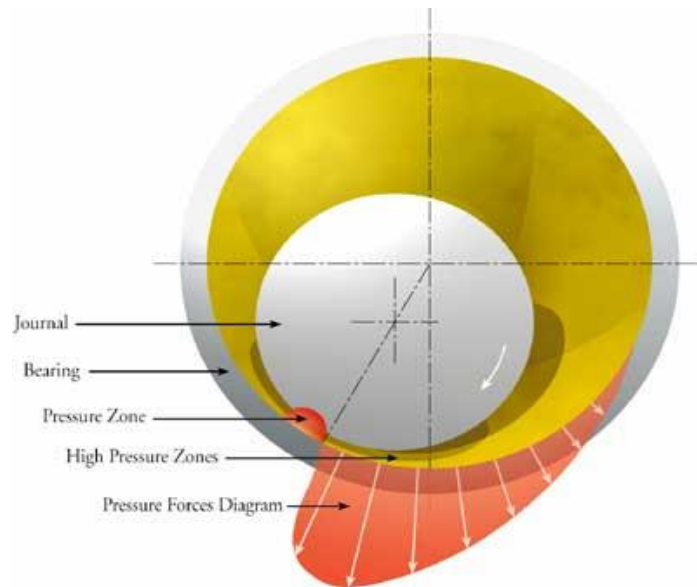


Fig.7 Hydrodynamic journal bearing

Figure shows the principle of working of hydrodynamic journal bearing. Initially when the journal is at rest, it makes contact with the bearing at its lowest point A, due to load 'W'. When the journal starts rotating in anticlockwise direction, it will climb the bearing surface and contact is made at point B. As the speed of the journal is further increased, the lubricant is pulled into the wedge-shaped region and forces the journal to the other side. The converging wedge-shaped film between points C and D supports the journal. Thus in hydrodynamic bearings, it is not necessary to supply the lubricant under pressure. The only requirement is to ensure sufficient and continuous supply of the lubricant.

## II. OBJECTIVES

- To find out the behavior of the material from wear & friction point of view and the effect of various sliding speeds and loads.
- To study the phenomenon of failure of transfer film by making use of SEM or optical microscope.
- To suggest the best suitable material for the journal bearing applications from the tested materials.
- To find out the mode of selection of material for hydrodynamic journal bearings.

## III. LITERATURE SURVEY

Journal bearings in automotive engines and other machinery are designed to operate in the hydrodynamic lubrication regime, with a film of lubricant separating the two surfaces. Despite this supposed absence of solid/solid contact during operation, however, many bearings suffer significant wear during their operating lives [5]. It is shown in this paper that wear occurs in three different locations in journal bearings, with each of the locations showing a different predominant wear mechanism. Study of the wear problem requires a different model experiment for each of the three different wear modes, and each wear mode also requires a different remedy to achieve wear reduction.

G. H. Jang et al [6]investigates the dynamic characteristics of a herringbone grooved journal bearing with plain sleeve (GJPS) and a plain journal bearing with herringbone grooved sleeve (PJGS) under static and dynamic load. FEM is used to solve the Reynolds equation in order to calculate the pressure distribution in a fluid film. Reaction forces and friction torque are obtained by integrating the pressure and shear stress along the fluid film, respectively. Dynamic behaviors of a journal, such as orbit or rotational speed, are determined by solving its nonlinear equations of motion with the Runge-Kutta method.

In the present work, a permanent magnetic–hydrodynamic hybrid journal bearing is developed [7]. The force of the journal bearing comes from the hydrodynamic film and the permanent magnetic field. When a hydrodynamic film does not form, such as during starting and stopping a machine, the journal bearing relies on the magnetic force to support the rotor system. This paper studies a model of the permanent magnetic force and develops an experimental rig of the journal bearing. Experiments show that the hydrodynamic film force

uncouples with the magnetic force in the journal bearing. Predictions from the model are compared with experimental data.

Wenyi Yan et al [ 8]  has explored that, A computational approach is proposed to predict the sliding wear caused by a loaded spherical pin contacting a rotating disc, a condition typical of the so-called pin-on-disc test widely used in tribological studies. The proposed framework relies on the understanding that, when the pin contacts and slides on the disc, a predominantly plane strain region exists at the centre of the disc wear track. The wear rate in this plane strain region can therefore be determined from a two dimensional idealization of the contact problem, reducing the need for computationally expensive three dimensional contact analyses.

S. Das et al [9] deals with the micropolar lubrication theory to the problem of the steady-state characteristics of hydrodynamic journal bearings considering two types of misalignment, e.g. axial (vertical displacement) and twisting (horizontal displacement). With the help of the steady-state film pressures, the steady-state performance characteristics in terms of load-carrying capacity, misalignment moment and friction parameter of a journal bearing are obtained at various values of eccentricity ratio, degree of misalignment and micropolar fluid characteristic parameters viz. coupling number and non-dimensional characteristic length.

The combined effects of couple stresses and surface roughness on the performance characteristics of hydrodynamic lubrication of slider bearings with various film shapes, such as plane slider, exponential, secant and hyperbolic, are studied. A stochastic random variable with non-zero mean, variance and skewness is used to mathematically model the surface roughness of the slider bearings. It is observed that, for all the lubricant film shapes under consideration, the negatively skewed surface roughness increases the load carrying capacity, frictional force and temperature rise, while it reduces the coefficient of friction10]. On the contrary, the reverse trend is observed for positively skewed surface roughness. Further, these effects are more pronounced for the couple stress fluids.

HasanBaş et al [11] studied the frictional behavior of thin-walled journal bearings produced from Zn–Al–Cu–Si alloys using a purpose-built journal bearing test rig. The alloys were produced by permanent mould casting. Mechanical properties such as ultimate tensile strength, elongation, hardness and microstructure of these alloys were determined. The friction properties of the bearings produced from these alloys were also investigated. In this investigation, the effects of surface roughness and bearing pressure on the frictional properties of the journal bearings were taken into account.

Hydrodynamic lubrication characteristics of a journal bearing, taking in to consideration the misalignment caused by shaft deformation, are analyzed. Film thickness expression of the misaligned journal bearing is inferred[12]. Film pressure, load-carrying capacity, attitude angle, end leakage flow-rate, frictional coefficient, and misalignment moment of a journal bearing are calculated for different values of misalignment degree and eccentricity ratio. The results show that there are obvious changes in film pressure distribution, the highest film pressure, film thickness distribution, the least film thickness, and the misalignment moment when misalignment takes place.

Hydrodynamic journal bearings are widely used in industry because of their simplicity, efficiency and low cost. They support rotating shafts over a number of years and are often subjected to many stops and start[13]. During these transient periods, friction is high and the bushes become progressively worn, thus inducing certain disabilities. This paper seeks to present the thermohydrodynamic performance of a worn plain journal bearing.

The dynamic characteristics of hydrodynamic journal bearings lubricated with micropolar fluids are presented [14]. The modified Reynolds equation is obtained using the micropolar lubrication theory. Applying the first order perturbation of the film thickness and steady state film pressure, the dynamic characteristics in terms of the components of stiffness and damping coefficients, critical mass parameter and whirl ratio are obtained with respect to the micropolar property for varying eccentricity ratios and slenderness ratios. The results show that micropolar fluid exhibits better stability in comparison with Newtonian fluid.

Klaus Friedrich et al [15]have observed during the wear test  that , if the particle sizes of the filler material  used in  PTFE  are diminishing down to Nano-scale, significant improvements of the wear resistance of polymers were achieved at very low Nano-filler content (1–3 vol.%). A combinative effect of nanoparticles with short carbon fibers exhibited a clear improvement of the wear resistance of both thermosetting and thermoplastic composites. In addition, this concept allowed the use of these materials under more extreme wear conditions, i.e., higher normal pressures and higher sliding velocities.

Paulo Flores et al [16] use the analytical mobility method to analyze journal bearings subjected to dynamic loads, with the intent to include it in a general computational program that has been developed for the dynamic analysis of general mechanical systems. A simple journal bearing subjected to a dynamic load is

chosen as a demonstrative example, in order to provide the necessary results for a comprehensive discussion of the methodology presented.

Gwidon W. Stachowiak et al [17] describes the fundamental wear mechanisms operating in non-metallic materials together with some prognoses concerning the future developments of these materials. Two classes of materials with entirely different characteristics—polymers and ceramics—are discussed. Polymers can provide low friction and low wear coefficients but their use is limited to lower temperatures and consequently low speeds and loads. Ceramics are resistant to high temperatures and often have a good wear resistance but their applications are limited by poor friction coefficients, especially in unlubricated applications. Ceramics and polymers are surprisingly vulnerable to accelerated wear in the presence of corrosive reagents and care should be taken in the selection of materials that are appropriate for particular operating conditions.

H. Unal et al [18] has studied and explored the influence of test speed and load values on the friction and wear behavior of pure Polytetrafluoroethylene (PTFE), glass fiber reinforced (GFR) and bronze and carbon (C) filled PTFE polymers. Friction and wear experiments were run under ambient conditions in a pin-on-disc arrangement. Tests were carried out at sliding speed of 0.32 m/s, 0.64 m/s, 0.96 m/s and 1.28 m/s and under a nominal load of 5 N, 10 N, 20 N and 30 N. From this study the have observed that, PTFE + 17% GFR exhibited best wear performance and is a very good tribo-material between materials used in this study. The friction coefficient of pure PTFE and its composites decreases when applied load increases.

N.B. Naduvinamani et al [19] presents the theoretical study of the effect of surface roughness on the hydrodynamic lubrication of porous step-slider bearings. A more general form of surface roughness is mathematically modeled by a stochastic random variable with non-zero mean, variance and skewness. The numerical computations of the results show that the negatively skewed surface roughness pattern increases the load carrying capacity and decreases the coefficient of friction whereas the adverse effects were found for the positively skewed surface roughness pattern.

It is well known that in journal bearings, friction occurs in all lubrication regimes. However, shaft misalignment in rotating systems is one of the most common causes of wear. In this work, the bearing is assumed to operate in the hydrodynamic region, at high eccentricities, wear depths, and angular misalignment [20]. The Reynolds equation is solved numerically; the friction force is calculated in the equilibrium position. The friction coefficient is presented versus the misalignment angles and wear depths for different Somerfield numbers, thus creating friction functions dependent on misalignment and wear of the bearing. The variation in power loss of the rotor bearing system is also investigated and presented as a function of wear depth and misalignment angles.

According to J. D. Bressana et al [21]the disc wear was more severe as difference in hardness between pin and disc is increased. It can be observed that decrease in pin hardness yields to lower pin wear resistance distance the trends of pin wear rate curves with sliding distance is approximately constant and linear. However, the final stage, some pins are presented the tendency to decrease the wear rate. This is due to the decrease in real contact pressure with increase in the pin contact area and/or increase in hardness of disc track.

A steady-state thermo hydrodynamic analysis of an axial groove journal bearings in which oil is supplied at constant pressure is performed theoretically [22]. Thermo hydrodynamic analysis requires simultaneous solution of Reynolds equation, energy equation and heat conduction equations in the bush and the shaft. From parametric study it is found that the temperature of the fluid film raises due to frictional heat thereby viscosity, load capacity decreases. Increased shaft speed resulted in increased load carrying capacity, bush temperature, flow rate and friction variable. It is difficult to obtain the solution due to numerical instability when the bearing is operated at high eccentricity ratios.

Steady state thermo-hydrodynamic analysis and its comparison at five different feeding locations of an axial grooved oil journal bearing is obtained theoretically [23]. Reynolds equation is solved simultaneously along with the energy equation and heat conduction equation in bush and shaft. From parametric study it is found that 12° feeding groove position is better in comparison to other feeding locations. Feeding from the bottom is very less preferable since the load capacity is lesser and temperature development is more. It is very difficult to obtain the solution due to numeric instability when the bearing operates at higher eccentricity ratio.

Detecting mechanical faults of rotating machines particularly in hydrodynamic bearings has been recognized as important for preventing sudden shut downs [24]. This technical note presents an experimental investigation that is aimed at understanding the influence of operational variables (speed, load, etc.) on generation of acoustic emission in a hydrodynamic bearing. It is concluded that the power losses of the bearing are directly correlated with acoustic emission levels.

Journal bearings are widely applied in different rotating machineries [25]. These bearings allow for transmission of large loads at mean speed of rotation. These bearings are susceptible to large amplitude lateral vibration due to self-exited instability which is known as oil whirl or Synchronous whirl. This paper presents a method to determine the Synchronous whirl i.e. Stability of hydrodynamic Journal bearings by using dynamic characteristics such as stiffness coefficients.

From time-to-time, experts endeavor to estimate the amount of energy lost due to friction and wear[26]. According to one such estimate, over $4.22 \times 10^{18}$ J of energy were lost in the United States in 1978 alone – enough to supply New York city for the entire year. A major factor in limiting our energy efficiency is energy loss through friction in tribo -elements are. In recognition of this, there have been significant efforts made during the past decades towards increasing the efficiency of bearing operations. The major influencing aspects of hydrodynamic lubrication are the structure of the lubricant film, the properties of the bearing surfaces, and the properties of the lubricant. Major past approaches for seeking efficiency improvement focused on the latter two of these aspects and concerned surface modification techniques and modification of lubricant properties. The CFB construction appears to be particularly suitable to power generating equipment. The journal bearings of these large rotating apparatus dissipate considerable energy; the CFB has the potential to cut these losses.

Fatu Aurelian et al [27] demonstrate that like surface texturing, well-chosen slip/no-slip surface patterning can considerably improve the performance of fluid bearings. Firstly, a finite element analysis is proposed in order to study the influence of wall slip over the load carrying capacity and power loss in hydrodynamic fluid bearings. A systematic comparison is made with textured bearing conditions. Secondly, the study is extended to the influence of wall slip in highly loaded compliant bearings, for steady-state and dynamical load conditions. The predictions show that well-chosen slip/no-slip surface pattern can considerably improve the bearing behavior and largely justify future numerical and experimental works.

Textured surfaces can significantly improve the performance of hydrodynamic bearings. However, there is no generally accepted method for their accurate and automated 3D characterization [28]. A promising solution to this problem is partition iterated function system (PIFS) model, which encapsulates information about 3D topography of textured surfaces. However, some loss in surface details can occur.

For some hydrodynamic bearing applications polymer-lined bearings are chosen over traditional metal alloy bearings due to their better wear and friction properties when operating at very thin films, e.g. in the mixed lubrication region [29]. The introduction of a compliant layer also affects the dynamic behavior of the bearing. The influence of the liner stiffness on the dynamic response of a highly dynamically loaded journal bearing is evaluated by varying the stiffness and comparing the response. The primary findings are that the maximum pressures are reduced significantly and this comes at the expense of slightly higher eccentricity ratios during operation.

Kim Thomsen et al [30] gives a numerical simulation presented for the thermo-hydrodynamic self-lubrication aspect analysis of porous circular journal bearing of finite length with sealed ends. It consists in analyzing the thermal effects on the behavior of circular porous journal bearings. The effects of dimensionless permeability parameter and eccentricity ratio on performance parameters are presented and discussed. The results showed that the temperature influence on the journal bearings performance is important in some operating cases, and that a progressive reduction in the pressure distribution, in the load capacity and attitude angle is a consequence of the increasing permeability.

A growing interest is given to the textured hydrodynamic lubricated contacts. The present study examines the texture location influence on the hydrodynamic journal bearing performance [31]. A numerical modelling is used to analyze the cylindrical texture shape effect on the characteristics of a hydrodynamic journal bearing. The theoretical results show that the most important characteristics can be improved through an appropriate arrangement of the textured area on the contact surface.

M. Fillon et al [32] deal with the friction coefficient during running, given a constant rotational speed. In order to understand the mechanisms occurring during the transition between mixed lubrication and hydrodynamic lubrication, several studies have been conducted over the past three years. The aim of this paper is to provide an overview of the results of these studies and also to draw several general conclusions on the behavior of a plain journal bearing during start-up. The main focus of this work is then to provide useful experimental data for bearing users and designers.

A growing interest is given to the textured hydrodynamic lubricated contacts. The use of textured surfaces with different shapes of microcavities (textures) and at different locations of the texture zone can be an effective approach to improve the performance of bearings [33]. The present study examines the texture location influence on the hydrodynamic journal bearing performance. A numerical modeling is used to analyze

the cylindrical texture shape effect on the characteristics of a hydrodynamic journal bearing. The theoretical results show that the most important characteristics can be improved through an appropriate arrangement of the textured area on the contact surface.

E.N. Santos et al [34] deal with analysis of hydrodynamic lubrication of radial journal bearings. The Reynolds equation was treated in order to obtain a hybrid numerical–analytical solution through the Generalized Integral Transform Technique (GITT) for the problem. Comparisons with results presented in the literature were also performed in order to verify the present results, as well as to demonstrate the consistency of the final results and the capacity of the GITT approach in handling journal bearing problems.

Priyanka Tiwari et al [35] presents a survey of important papers pertaining to analysis of various types of methods, equations and theories used for the determination of load carrying capacity, minimum oil film thickness, friction loss, and temperature distribution of hydrodynamic journal bearing. Predictions of these parameters are the very important aspects in the design of hydrodynamic journal bearings. The present study mainly focuses on various types of factors which tremendously affect the performance of hydrodynamic journal bearing

The magneto-hydrodynamic (MHD) dynamic characteristics of a wide power-law film-profile slider bearing lubricated with an electrically conducting fluid under the application of transverse magnetic fields has been proposed [36]. A closed-form solution is obtained for the MHD power-law film-shape slider bearings, in which special bearing characteristics of the inclined-plane shape and the parabolic-film profile can also be included. Comparing with the non-conducting-fluid power-law film-shape bearing, the MHD bearing provides an increase in the load capacity, and the stiffness and damping coefficients.

An analytic model is developed to predict static characteristics of a new hydrodynamic–rolling hybrid bearing (HRHB). Experiments are carried out to measure the equilibrium positions, the load sharing, and the rotational speeds of the rolling bearing cage [37]. The results show that the working states of HRHB are divided into two distinct phases by a transition speed at which the hydrodynamics and contact models are decoupled. The cage speeds can be used to determine transition speed. The theoretical results agree with the experimental results, and it can be employed to design the bearing parameters according to the expected performance.

In this work, performance degradation in scratched journal bearings is evaluated by means of numerical simulations. A hydrodynamic numerical model with global thermal effects is employed (lubricant temperature and viscosity are assumed to be uniform) [38]. A very fine mesh is used, which allows a deterministic representation of a large number of circumferential scratches of various sizes and rectangular cross-shape. The severity of the scratches is quantified using four parameters: their depth, the extent of the scratched region, the density of the scratches and the position of the scratched region with respect to the bearing mid-plane. Lastly, charts are presented showing the evolution of the different bearing operating parameters as a function of the scratch severity, allowing the identification of critical scratch configurations that can lead to bearing damage.

The effect of couple stress fluid on the elasto-hydrodynamically lubricated finite line contact is studied [39]. Modified Reynolds equation is derived from Stokes micro continuum theory and solved numerically using finite difference method. Owing to the finite contact analysis, the effect of couple stress fluid at the edges of the roller is examined. The study reveals that overall film thickness increases significantly with couple stress parameter.

The hydrodynamic journal bearing system has found wide spread application in high speed rotating machine such as compressors, gas turbines, water turbines, steam turbines, alternators etc. [40]. As rotor generally operates at high speed, the lubricant flow in the clearance space of journal bearing does not remain laminar and for accelerated/decelerated journals the threshold speed of instability is crossed from both sides. In this paper the numerical method has been used to compute the static and dynamic performance parameter.

Ana M. Balasoiu et al [41] present 3D, isothermal numerical analysis of a cylindrical porous journal bearing characterized by a self-circulating lubricating system that eliminates the necessity of an external circulating pump. The system includes a stationary porous bushing whose inner diameter faces the bearing clearance while the outer diameter faces a wrapped-around reservoir. The loaded, eccentric shaft is generating a high pressure zone in the convergent region followed by a low pressure zone in the divergent region causing the fluid to circulate naturally between the bearing clearance and the reservoir, as it passes through the porous bushing. The fundamental physics of the circulating mechanism are described, and its operation is numerically simulated. The study uses the complete 3D Navier–Stokes Equations (NSE) for the fluid motion in the bearing clearance and the adjacent reservoir. The results which include the flow patterns, pressure maps and attitude angles, are presented on a parametric basis, and confirm the functionality of the proposed self-circulating

system. It was found that the load capacity decreases and the attitude angle increase as permeability increases, and depending on permeability ranges, the increase in the reservoir depth may result in a reduction of the load capacity.

The concept of dynamic pressure ratio (γ) is put forward in this paper to measure the hydrodynamic effect on bearing land [42]. The Reynolds equation and flow continuity equation have been solved using finite difference method, over relaxation method and under relaxation method. Taking the four-pocket capillary compensated hydrostatic journal bearing as an example, variations of dynamic pressure ratio(γ) with eccentricity ratio (ε)and rotating speed(N) are studied.

Emiliano Mucchi et al [43] propose an experimental methodology for the analysis of the lubrication regime and wear that occur between vanes and pressure ring in variable displacement vane pumps. The knowledge of the lubrication regime is essential for the improvement of the performance of high pressure vane pumps by reducing wear, increasing the volumetric efficiency and decreasing maintenance costs. Tests using pressure rings of different materials were carried out in order to identify the best material in terms of wear and friction.

Kazuyuki Yagi et al [44] found that a small elastic deformation of less than 100 nm plays an important role in load capacity in thin film hydrodynamic lubrication. As the film thickness decreases, a flat film shape appears from the leading side of the contact area. The expansion of the flat film thickness over the contact area leads to considerably lower load capacity.

Tribological performances of non-grooved and micro-grooved journal bearings were studied under dynamic loading. Numerous experiments were performed using purpose-built test rig and then simulated using various numerical methods [45]. Friction force, friction coefficient, shaft center orbit, and film thickness were determined experimentally and numerically. The experimental and numerical results were in good agreement and the friction forces progressively increased on plain and circumferential, herringbone, and transversally micro-grooved bearing. The results show that it is necessary to complete detailed investigation about the tribological properties of the micro-grooved journal bearing by taking their shape, depth and operating condition into account.

Vijay Kumar Dwivedi et al [46] describe a theoretical study concerning static performance of four pocket rectangular recess hybrid journal bearing. Effect of recess length and width variation, number of recess variation on the load bearing capacity and oil flow parameter for rectangular recess has been carried out. The Reynolds equation for non-rotating recessed hybrid bearing was solved on a high speed computer satisfying appropriate boundary conditions and using finite difference method. Various results for different recess axial length to bearing axial length, different recess circumferential length to circumferential length of bearing, various L/D ratios and number of recesses are presented.

Gengyuan Gao et al [47] aims to provide references for designing water-lubricated plain journal bearings. Considering the differences between the physical properties of the water and of the oil, the effects of eccentricity ratio on pressure distribution of water film are analyzed by computational fluid dynamics (CFD). Then numerical analysis of journal bearings with different dimensions is undertaken under different rotational speeds. Based on the analysis, a reference is produced for selecting the initial diameter dimension which is used to design an efficient water-lubricated plain bearing under the given load and rotational speed.

## IV. SUMMARY OF LITERATURE SURVEY

The summery researches done by experts in the area of wear and friction in hydrodynamic journal bearings have been presented in Table1 which Carries the Author name, year and investigated problem types.

Table 1: Summary of the developments in wear and friction in journal bearings on literature survey

| Sr. no. | Author Name (Year) | *Investigated Problem Type* |
|---------|--------------------|----------------------------|
| 5 | F.E. Kennedy et al. (2001) | Wear of hydrodynamic journal bearings |
| 6 | G. H. Jang et al (2002) | Nonlinear Dynamic Analysis of a Hydrodynamic Journal Bearing Considering the Effect of a Rotating or Stationary Herringbone Groove. |
| 7 | Wei Li et al (2002) | Investigations on a permanent magnetic– hydrodynamic hybrid journal bearing. |
| 8 | Wenyi Yan et al (2002) | Numerical study of sliding wear caused by a loaded pin on a rotating disc |
| 9 | S. Das et al (2002) | On the steady-state performance of misaligned hydrodynamic journal |

| | | |
|---|---|---|
| | | bearings lubricated with micropolar fluids |
| 10 | N.B. Naduvinamani et al (2003) | Hydrodynamic lubrication of rough slider bearings with couple stress fluids |
| 11 | HasanBaş et al (2004) | Investigation of the tribological properties of silicon containing zinc–aluminum based journal bearings |
| 12 | Jun Sun et al (2004) | Hydrodynamic lubrication analysis of journal bearing considering misalignment caused by shaft deformation |
| 13 | M. Fillon et al (2004) | Thermo hydrodynamic analysis of a worn plain journal bearing |
| 14 | S. Das, S.K. Guha et al (2005) | Linear stability analysis of hydrodynamic journal bearings under micropolar lubrication |
| 15 | Klaus Friedrich et al (2005) | Effects of various fillers on the sliding wear of polymer composites |
| 16 | Paulo Flores et al (2006) | Journal bearings subjected to dynamic loads: theanalytical mobility method |
| 17 | Gwidon W. Stachowiak et al (2006) | Wear of Non-Metallic Materials |
| 18 | H. Unal et al (2006) | an approach to friction and wear properties of polytetraflouroethylene composite |
| 19 | N.B. Naduvinamani et al (2007) | Effect of surface roughness on the hydrodynamic lubrication of porous step-slider bearings with couple stress fluids |
| 20 | G. Padelis et al (2008) | A study of friction in worn misaligned journal bearings under severe hydrodynamic lubrication |
| 21 | J. D. Bressana et al (2008) | Influence of hardness on the wear resistance of 17-4 PH stainless steel evaluated by the pin-on-disc testing |
| 22 | U. Singh et al (2008) | Steady-state thermo-hydrodynamic analysis of cylindrical fluid film journal bearing with an axial groove |
| 23 | L. Roy et al (2009) | Thermo-hydrodynamic performance of grooved oil journal bearing |
| 24 | S.A. Mirhadizadeh et al (2010) | Influence of operational variables in a hydrodynamic bearing on the generation of acoustic emission |
| 25 | Ravindra R. Navthar et al (2010) | Stability Analysis of Hydrodynamic Journal Bearing using Stiffness Coefficients |
| 26 | Andras Z. Szeri et al (2010) | Composite-film hydrodynamic bearings |
| 27 | Fatu Aurelian et al (2011) | Wall slip effects in (elasto) hydrodynamic journal bearings |
| 28 | M. Wolski et al (2011) | Effects of information loss in texture details due to the PIFS encoding on load and friction in hydrodynamic bearings |
| 29 | Kim Thomsen et al (2011) | A study on compliant layers and its influence on dynamic response of a hydrodynamic journal bearing |
| 30 | S. Boubendir et al (2011) | Numerical study of the thermo-hydrodynamic lubrication phenomena in porous journal bearings |
| 31 | Michel Fillon et al (2011) | Effect of textured area on the performances of a hydrodynamic journal bearing |
| 32 | M. Fillon et al (2011) | Experimental measurement of the friction torque on hydrodynamic plain journal bearings during start-up |
| 33 | NacerTala-Ighil et al (2011) | Effect of textured area on the performances of a hydrodynamic journal bearing |
| 34 | E.N. Santos et al (2012) | Integral transform solutions for the analysis of hydrodynamic lubrication of journal bearings |
| 35 | Priyanka Tiwari et al (2012) | Analysis of Hydrodynamic Journal Bearing: A Review |
| 36 | Jaw-Ren Lin (2012) | Dynamic characteristics for wide magneto-hydrodynamic slider bearings with a power-law film profile |
| 37 | Dun Lu et al (2012) | Static characteristics of a new hydrodynamic–rolling hybrid bearing |
| 38 | M.B. Dobrica et al (2012) | Performance degradation in scratched journal bearings |

| 39 | S.P. Chippa et al (2013) | Elastohydrodynamically lubricated finite line contact with couple stress fluids |
|---|---|---|
| 40 | Satish Chand et al (2013) | Effect of Different Flow Regime on the Static and Dynamic Performance Parameter of Hydrodynamic Bearing |
| 41 | Ana M. Balasoiu et al (2013) | A parametric study of a porous self-circulating hydrodynamic bearing |
| 42 | Peng Liang et al (2013) | A method for measuring the hydrodynamic effect on the bearing land |
| 43 | Emiliano Mucchi et al (2013) | On the wear and lubrication regime in variable displacement vane pumps |
| 44 | Kazuyuki Yagi et al (2013) | Elastic deformation in thin film hydrodynamic lubrication |
| 45 | Hakan Adatepe et al (2013) | An investigation of tribological behaviors of dynamically loaded non-grooved and micro-grooved journal bearings |
| 46 | Vijay Kumar Dwivedi et al (2013) | Effect of Number and Size of Recess on the Performance of Hybrid (Hydrostatic/Hydrodynamic) Journal Bearing |
| 47 | Gengyuan Gao et al (2014) | Numerical analysis of plain journal bearing under hydrodynamic lubrication by water |

## V. DISCUSSION

- Journal bearings in automotive engines and other machinery are designed to operate in the hydrodynamic lubrication regime, with a film of lubricant separating the two surfaces
- When a hydrodynamic film does not form, such as during starting and stopping a machine, the journal bearing relies on the magnetic force to support the rotor system.
- Friction factor decreased with increasing bearing pressure especially in the mixed and full-film lubrication zones.
- Polymers can provide low friction and low wear coefficients but their use is limited to lower temperatures and consequently low speeds and loads.
- Ceramics are resistant to high temperatures and often have a good wear resistance but their applications are limited by poor friction coefficients, especially in unlubricated applications.
- Decrease in pin hardness yields to lower pin wear resistance distance the trends of pin wear rate curves with sliding distance is approximately constant and linear.
- The configurations with different liner stiffnesses are evaluated on the parameters that are traditionally used to evaluate hydrodynamic bearing designs: dynamic response, maximum pressure, minimum film thickness, wear, Power loss and temperature response.
- The coefficient of friction, which is of greater importance in lubrication, also decreases with increase in the couple-stress parameter.
- As rotor generally operates at high speed, the lubricant flow in the clearance space of journal bearing does not remain laminar and for accelerated/decelerated journals the threshold speed of instability is crossed from both sides.
- The knowledge of the lubrication regime is essential for the improvement of the performance of high pressure vane pumps by reducing wear, increasing the volumetric efficiency and decreasing maintenance costs.
- As the film thickness decreases, a flat film shape appears from the leading side of the contact area. The expansion of the flat film thickness over the contact area leads to considerably lower load capacity.
- It is necessary to complete detailed investigation about the tribological properties of the micro-grooved journal bearing by taking their shape, depth and operating condition into account.
- Based on the analysis, a reference is produced for selecting the initial diameter dimension which is used to design an efficient water-lubricated plain bearing under the given load and rotational speed.

## VI. CONCLUSION

Based on the literature review, it is concluded that wear is very important criteria for the selection of material of journal bearings. Selection of material is done by selecting the parameters like rate of wear, coefficient of friction, duration of use and conditions in which journal bearing is used. Wear can be observed in dry and lubricated conditions which are affected by speed, load, and temperature and working time. Wear rate analysis can be done on the different materials and in the different conditions. The main conditions are dry and lubricated condition in which some of lubricants can be used.

# REFERENCES

[1]     H.P. Jost, Tribology - origin and future, Wear 136, 1989.
[2]     I.M. Hutchings, Tribology - friction and wear of engineering materials, Edward Arnold, 1992.
[3]     Bharat Bhushan; Introduction to Tribology; John Wiley, 2001.
[4]     Bharat Bhushan, Balkishan K. Gupta; Technology & Engineering;McGraw-Hill, 1991.
[5]     L. Rozeanu, F.E. Kennedy; Wear of hydrodynamic journal bearings; Tribology Series, Volume 39, Pages 161-166, 2001.
[6]     G. H. Jang, J. W. Yoon; Nonlinear Dynamic Analysis of a Hydrodynamic Journal Bearing Considering the Effect of a Rotating or Stationary Herringbone Groove; ASME, Vol. 124/297, April 2002.
[7]     Qingchang Tan, Wei Li, Bo Liu; Investigations on a permanent magnetic–hydrodynamic hybrid journal bearing; Tribology International, Volume 35, Issue 7, Pages 443-448, July 2002.
[8]     Wenyi Yan, Noel P. O'Dowd, Esteban P. Busso, "Numerical study of sliding wear caused by a loaded pin on a rotating disc" Journal of the Mechanics and Physics of Solids, Vol. 50, pp. 449 – 470, 2002.
[9]     S. Das, S.K. Guha, A.K. Chattopadhyay; On the steady-state performance of misaligned hydrodynamic journal bearings lubricated with micropolar fluids; Tribology International, Volume 35, Issue 4, Pages 201-210, April 2002.
[10]    N.B. Naduvinamani, Syeda Tasneem Fathima, P.S. Hiremath; Hydrodynamic lubrication of rough slider bearings with couple stress fluids; Tribology International, Volume 36, Issue 12, Pages 949-959, December 2003.
[11]    Hamdullah Çuvalcı, Hasan Baş; Investigation of the tribological properties of silicon containing zinc–aluminum based journal bearings; Tribology International, Volume 37, Issue 6, Pages 433-440, June 2004.
[12]    Jun Sun, GuiChanglin; Hydrodynamic lubrication analysis of journal bearing considering misalignment caused by shaft deformation; Tribology International, Volume 37, Issue 10, Pages 841-848, October 2004.
[13]    M. Fillon, J. Bouyer; Thermohydrodynamic analysis of a worn plain journal bearing; Tribology International, Volume 37, Issue 2, Pages 129-136, February 2004.
[14]    S. Das, S.K. Guha, A.K. Chattopadhyay; Linear stability analysis of hydrodynamic journal bearings under micropolar lubrication; Tribology International, Volume 38, Issue 5, Pages 500-507, May 2005.
[15]    Klaus Friedrich, Zhong Zhang, Alois K. Schlarb, Effects of various fillers on the sliding wear of polymer composites, Composites Science and Technology, Vol. 65, pp. 2329–2343, (2005).
[16]    Paulo Flores, JC Pimenta Claro1, Jorge Ambrósio; Journal bearings subjected to dynamic loads: theanalytical mobility method; Mecânica Experimental, Vol. 13, Pg. 115-127, 2006
[17]    Gwidon W. Stachowiak, Andrew W. Batchelor; Wear of Non-Metallic Materials; Engineering Tribology (Third Edition), Pages 651-704, 2006.
[18]    H. Unal, U.sen, A Mimaroglu, 2006, "an approach to friction and wear properties of polytetraflouroethylene composite", Materials and Design, Vol. 27, pp. 694–699, 2006.
[19]    N.B. Naduvinamani, A. Siddangouda; Effect of surface roughness on the hydrodynamic lubrication of porous step-slider bearings with couple stress fluids; Tribology International, Volume 40, Issue 5, Pages 780-793, May 2007.
[20]    Padelis G. Nikolakopoulos, Chris A. Papadopoulos; A study of friction in worn misaligned journal bearings under severe hydrodynamic lubrication; Tribology International, Volume 41, Issue 6, Pages 461-472, June 2008.
[21]    J. D. Bressana, D. P. Darosa, A. Sokolowskib, R. A. Mesquitac, C. A. Barbosad, Influence of hardness on the wear resistance of 17-4 PH stainless steel evaluated by the pin-on-disc testing, journal of material processing technology, Vol. 2, pp 353-359, 2008.
[22]    U. Singh, L. Roy, M. Sahu; Steady-state thermo-hydrodynamic analysis of cylindrical fluid film journal bearing with an axial groove; Tribology International, Volume 41, Issue 12, December 2008, Pages 1135-1144
[23]    L. Roy; Thermo-hydrodynamic performance of grooved oil journal bearing; Tribology International, Volume 42, Issue 8, Pages 1187-1198, August 2009.
[24]    S.A. Mirhadizadeh, E.P. Moncholi, D. Mba; Influence of operational variables in a hydrodynamic bearing on the generation of acoustic emission; Tribology International, Volume 43, Issue 9, Pages 1760-1767, September 2010.
[25]    Ravindra R. Navthar, Dr. N.V. Halegowda; Stability Analysis of Hydrodynamic Journal Bearing using Stiffness Coefficients; International Journal of Engineering Science and Technology Vol. 2, pp. 87-93 2010.
[26]    Andras Z. Szeri; Composite-film hydrodynamic bearings; International Journal of Engineering Science, Volume 48, Issue 11, Pages 1622-1632, November 2010.
[27]    Fatu Aurelian, Maspeyrot Patrick, Hajjam Mohamed; Wall slip effects in (elasto) hydrodynamic journal bearings; Tribology International, Volume 44, Issues 7–8, Pages 868-877, July 2011.
[28]    M. Wolski, P. Podsiadlo, G.W. Stachowiak; Effects of information loss in texture details due to the PIFS encoding on load and friction in hydrodynamic bearings; Tribology International, Volume 44, Issue 12, Pages 2002-2012, November 2011.
[29]    Kim Thomsen, Peder Klit; A study on compliant layers and its influence on dynamic response of a hydrodynamic journal bearing; Tribology International, Volume 44, Issue 12, Pages 1872-1877, November 2011.
[30]    S. Boubendir, S. Larbi, R. Bennacer; Numerical study of the thermo-hydrodynamic lubrication phenomena in porous journal bearings; Tribology International, Volume 44, Issue 1, Pages 1-8, January 2011.

[31] Nacer Tala-Ighil, Michel Fillon, Patrick Maspeyrot; Effect of textured area on the performances of a hydrodynamic journal bearing; Tribology International, Volume 44, Issue 3, Pages 211-219, March 2011.

[32] J. Bouyer, M. Fillon; Experimental measurement of the friction torque on hydrodynamic plain journal bearings during start-up; Tribology International, Volume 44, Issues 7–8, Pages 772-781, July 2011.

[33] Nacer Tala-Ighil, Michel Fillon, Patrick Maspeyrot; Effect of textured area on the performances of a hydrodynamic journal bearing; Tribology International, Volume 44, Issue 3, Pages 211-219, March 2011.

[34] E.N. Santos, C.J.C. Blanco, E.N. Macêdo, C.E.A. Maneschy, J.N.N. Quaresma; Integral transform solutions for the analysis of hydrodynamic lubrication of journal bearings; Tribology International, Volume 52, Pages 161-169, August 2012.

[35] Priyanka Tiwari and Veerendra Kumar, Analysis of Hydrodynamic Journal Bearing: A Review, International Journal of Engineering Research & Technology (IJERT) Vol. 1, Issue 7, ISSN: 2278-018 September 2012.

[36] Jaw-Ren Lin; Dynamic characteristics for wide magneto-hydrodynamic slider bearings with a power-law film profile; Applied Mathematical Modelling, Volume 36, Issue 9, Pages 4521-4528, September 2012,

[37] Dun Lu, Wanhua Zhao, Bingheng Lu, Jun Zhang;Static characteristics of a new hydrodynamic–rolling hybrid bearing; Tribology International, Volume 48, Pages 87-92, April 2012.

[38] M.B. Dobrica, M. Fillon; Performance degradation in scratched journal bearings; Tribology International, Volume 51, Pages 1-10, July 2012.

[39] S.P. Chippa, M. Sarangi; Elastohydrodynamically lubricated finite line contact with couple stress fluids; Tribology International, Volume 67, Pages 11-20, November 2013.

[40] Vijay Kumar Dwivedi, Satish Chand, K.N. Pandey; Effect of Different Flow Regime on the Static and Dynamic Performance Parameter of Hydrodynamic Bearing; Procedia Engineering, Vol. 51, Pages 520-528, 2013.

[41] Ana M. Balasoiu, Minel J. Braun, Stefan I. Moldovan; A parametric study of a porous self-circulating hydrodynamic bearing; Tribology International, Volume 61, Pages 176-193, May 2013.

[42] Peng Liang, Changhou Lu, Jie Ding, Shujiang Chen; A method for measuring the hydrodynamic effect on the bearing land; Tribology International, Volume 67, Pages 146-153, November 2013.

[43] Emiliano Mucchi, Alessandro Agazzi, Gianluca D'Elia, Giorgio Dalpiaz; On the wear and lubrication regime in variable displacement vane pumps; Wear, Volume 306, Issues 1–2, Pages 36-46, 30 August 2013.

[44] Kazuyuki Yagi, Joichi Sugimura; Elastic deformation in thin film hydrodynamic lubrication; Tribology International, Volume 59, Pages 170-180, March 2013.

[45] Hakan Adatepe, Aydın Bıyıklıoglu, Hasan Sofuoglu; An investigation of tribological behaviors of dynamically loaded non-grooved and micro-grooved journal bearings; Tribology International, Volume 58, Pages 12-19, February 2013.

[46] Vijay Kumar Dwivedi, Satish Chand, K.N. Pandey; Effect of Number and Size of Recess on the Performance of Hybrid (Hydrostatic/Hydrodynamic) Journal Bearing; Procedia Engineering, Volume 51, Pages 810-817, 2013.

[47] Gengyuan Gao, Zhongwei Yin, Dan Jiang, Xiuli Zhang; Numerical analysis of plain journal bearing under hydrodynamic lubrication by water; Tribology International, Volume 75, Pages 31-38, July 2014.

# Exact Solutions for MHD Flow of a Viscoelastic Fluid with the Fractional Burgers' Model in an Annular Pipe

Ghada H. Ibraheem[1], Ahmed M. Abdulhadi[2]

[1] *Department of Mathematics, University of Baghdad, College of Education, Pure Science, Ibn A-Haitham*
[2] *Department of Mathematics, University of Baghdad, College of Science*

***Abstract:*** *This paper presents an analytical study for the magnetohydrodynamic (MHD) flow of a generalized Burgers' fluid in an annular pipe. Closed from solutions for velocity is obtained by using finite Hankel transform and discrete Laplace transform of the sequential fractional derivatives. Finally, the figures are plotted to show the effects of different parameters on the velocity profile.*
***Keywords:*** *Generalized Burgers' fluid, finite Hankel transform, discrete Laplace transform.*

## I.  Introduction

Fluid non-Newtonian does not show a linear relationship between stress and strain rate and received a lot of attention due to the increasing applications of industrial and technological field, such as polymer solutions, paints, blood and heavy oils. No model alone that can describe the behavior of all fluids non-Newtonian because of complex behavior.

Thus, it was suggested many of the foundational equations of non-Newtonian fluid models. The Burgers' fluid is one of them which cannot be described a typical relation between shear stress and the rate of strain, for this reason many models of constitutive equations have been proposed for these fluids[7,8,11]. Many applications of this type of fluid can be found in [1,2,15,18]. Many of the developments in the theory of viscoelastic flows have been mainly restricted to the formulations of the basics equation and constitutive models [12,16], and many applications of fractional calculus can be found in turbulence and fluid dynamics, stochastic dynamical system and nonlinear control theory [3,14,19].

Recently, Tong and Liu [6] studied the unsteady rotating flows of a non- Newtonian fluid in an annular pipe with Oldroyd- B fluid model. Tong … etc [5] discussed the flow of Oldroyd- B fluid with fractional derivative in an annular pipe. Hyder … etc [17] discussed the flow of a viscoelastic fluid with fractional Burgers' model in an annular pipe. Tong … etc [4] discussed the flow of generalized Burgers' fluid in an annular pipe. Khan [13] investigated the (MHD) flow of generalized Oldroyd- B fluid in a circular pipe. Later on [10] investigated the slip effects on MHD flow of a generalized Oldroyd- B fluid with fractional derivative.

In this paper, our aim is to steady the effects of MHD on the unsteady flow of a viscoelastic fluid with fractional generalized Burgers' fluid model in an annular pipe. The exact solution for velocity distribution is established by using the finite Hankel transform and discrete Laplace transform of the sequential fractional derivatives.

## II.  Governing Equations

The constitutive equations for an incompressible fractional Burger's fluid given by

$$\mathbf{T} = -p\mathbf{I} + \mathbf{S}, \qquad (1 + \lambda_1^\alpha \tilde{D}_t^\alpha + \lambda_2^\alpha \tilde{D}_t^{2\alpha})\mathbf{S} = \mu(1 + \lambda_3^\beta \tilde{D}_t^\beta)\mathbf{A} \tag{1}$$

where $\mathbf{T}$ denoted the cauchy stress, $-p\mathbf{I}$ is the indeterminate spherical stress, $\mathbf{S}$ is the extra stress tensor, $\mathbf{A} = \mathbf{L} + \mathbf{L}^T$ is the first Rivlin- Ericksen tensor with the velocity gradient where $\mathbf{L} = \text{grad}\,\mathbf{V}$, $\mu$ is the dynamic viscosity of the fluid, $\lambda_1$ and $\lambda_3$ $(<\lambda_1)$ are the relaxation and retardation times, respectively, $\lambda_2$ is the new material parameter of Burger's fluid, $\alpha$ and $\beta$ the fractional calculus parameters such that $0 \le \alpha \le \beta \le 1$ and $\tilde{D}_t^p$ the upper convected fractional derivative define by

$$\tilde{D}_t^\alpha \mathbf{S} = D_t^\alpha \mathbf{S} + (\mathbf{V}.\nabla)\mathbf{S} - \mathbf{LS} - \mathbf{SL}^T \tag{2}$$

$$\tilde{D}_t^\beta \mathbf{A} = D_t^\beta \mathbf{A} + (\mathbf{V}.\nabla)\mathbf{A} - \mathbf{LA} - \mathbf{AL}^T \tag{3}$$

in which $D_t^\alpha$ and $D_t^\beta$ are the fractional differentiation operators of order $\alpha$ and $\beta$ based on the Riemann-Liouville definition, defined as

$$D_t^p[f(t)] = \frac{1}{\Gamma(1-p)} \frac{d}{dt} \int_0^t \frac{f(\tau)}{(t-\tau)^p} d\tau \qquad ,0 \le p \le 1 \tag{4}$$

here $\Gamma(.)$ denotes the Gamma function and

$$D_t^{2p}\mathbf{S} = D_t^p(D_t^p\mathbf{S}) \tag{5}$$

The model reduced to the generalized Oldroyd- B model when $\lambda_2 = 0$ and if, in addition to that, $\alpha = \beta = 1$ the ordinary Oldroyd- B model will be obtained.

We consider the MHD flow of an incompressible generalized Burger's fluid due to an infinite accelerating plate. For unidirectional flow, we assume that the velocity field and shear stress of the form

$$\mathbf{V} = w(r,t)e_z \quad ,\mathbf{S} = \mathbf{S}(r,t) \tag{6}$$

where $e_z$ is the unit vector along z - direction .Substituting equation (6) into (1) and taking account of the initial condition

$$\mathbf{S}(r,0) = 0 \tag{7}$$

we obtain

$$(1 + \lambda_1^\alpha D_t^\alpha + \lambda_2^\alpha D_t^{2\alpha})S_{rz} = \mu(1 + \lambda_3^\beta D_t^\beta)\partial_r w(r,t) \tag{8}$$

$$(1 + \lambda_1^\alpha D_t^\alpha + \lambda_2^\alpha D_t^{2\alpha})S_{zz} - 2S_{rz}(\lambda_1^\alpha + \lambda_2^\alpha D_t^\alpha)\partial_r w(r,t) = -2\mu\lambda_3^\beta(\partial_r w(r,t))^2 \tag{9}$$

where $S_{rr} = S_{\theta z} = S_{r\theta} = S_{\theta\theta} = 0$. Furthermore, it assumes that the conducting fluid is permeated by an imposed magnetic field $\mathbf{H} = [0, \mathbf{H}_0, 0]$ which acts in the positive $\theta$ - direction. In the low- magnetic Reynolds number approximation, the magnetic body force is represented as $\sigma \mathbf{H}_0^2 w$, where $\sigma$ is the electrical conductivity of the fluid. Then in the presence of a pressure gradient in the z- direction, the equation of motion yields the following scalar equation:

$$\rho \frac{dw}{dt} = -\frac{\partial p}{\partial z} + \frac{1}{r}\frac{\partial}{\partial r}(r S_{rz}) - \sigma \mathbf{H}_0^2 w \tag{10}$$

where $\rho$ is the constant density of the fluid. Eliminating $S_{rz}$ between Eqs. (8) and (10), we obtain the following fractional differential equation

$$(1 + \lambda_1^\alpha D_t^\alpha + \lambda_2^\alpha D_t^{2\alpha})\frac{\partial w}{\partial t} = -\frac{1}{\rho}(1 + \lambda_1^\alpha D_t^\alpha + \lambda_2^\alpha D_t^{2\alpha})\frac{dp}{dz} +$$

$$+ v(1 + \lambda_3^\beta D_t^\beta)(\frac{\partial^2}{\partial r^2} + \frac{1}{r}\frac{\partial}{\partial r})w - \mathbf{M}(1 + \lambda_1^\alpha D_t^\alpha + \lambda_2^\alpha D_t^{2\alpha})w \tag{11}$$

where $v = \frac{\mu}{\rho}$ is the kinematic viscosity and $\mathbf{M} = \frac{\sigma \mathbf{H}_0^2}{\rho}$ is the magnetic dimensionless number.

### III. Plane Poiseuille Flow

Consider that the flow problem of an incompressible generalized Burgers' fluid is initially at rest between two infinitely long coaxial cylinders of radii $R_0$ and $R_1$ $(> R_0)$. At time $t = 0^+$ the fluid is generated due to a constant pressure gradient that acts on the liquid in the z- direction . Referring to Eq. (11), the corresponding fractional partial differential equation that describe such flow takes the form

$$(1 + \lambda_1^\alpha D_t^\alpha + \lambda_2^\alpha D_t^{2\alpha})\frac{\partial w}{\partial t} = -\mathbf{A}\left(1 + \lambda_1^\alpha \frac{t^{-\alpha}}{\Gamma(1-\alpha)} + \lambda_2^\alpha \frac{t^{-2\alpha}}{\Gamma(1-2\alpha)}\right) +$$

$$+ v(1 + \lambda_3^\beta D_t^\beta)(\frac{\partial^2}{\partial r^2} + \frac{1}{r}\frac{\partial}{\partial r})w - \mathbf{M}(1 + \lambda_1^\alpha D_t^\alpha + \lambda_2^\alpha D_t^{2\alpha})w \tag{12}$$

where $\mathbf{A} = \frac{1}{\rho}\frac{dp}{dx}$ is the constant pressure gradient

The associated initial and boundary conditions are as follows

$$w(r,0) = \frac{\partial}{\partial t}w(r,0) = \frac{\partial^2}{\partial t^2}w(r,0) = 0 \qquad ,R_0 \le r \le R_1 \tag{13}$$

$$w(R_0,t) = w(R_1,t) = 0 \qquad ,t > 0 \tag{14}$$

To obtain the exact analytical solution of the above problem (12)- (14), we first apply Laplace transform principle [9] with respect to t, we get

$$\text{s}\,(1+\lambda_1^\alpha s^\alpha + \lambda_2^\alpha s^{2\alpha})\overline{w} = -\frac{A}{s}(1+\lambda_1^\alpha s^\alpha + \lambda_2^\alpha s^{2\alpha}) +$$

$$+ v(1+\lambda_3^\beta s^\beta)(\frac{\partial^2}{\partial r^2} + \frac{1}{r}\frac{\partial}{\partial r})\overline{w} - \text{M}(1+\lambda_1^\alpha s^\alpha + \lambda_2^\alpha s^{2\alpha})\overline{w} \tag{15}$$

$$\overline{w}(r,0) = 0$$
$$\overline{w}(R_0, s) = \overline{w}(R_1, s) = 0 \qquad\qquad , t > 0 \tag{16}$$

where $\overline{w}(r,s)$ is the image function of $w(r,t)$ and $s$ is a transform parameter.

We use the finite Hankel transform [9], defined as follows

$$\overline{w}_H = \int_{R_0}^{R_1} r\,\overline{w}\,B_0(rk_i)dr \qquad , i = 1,2,3,\ldots \tag{17}$$

and its inverse is

$$\overline{w} = \frac{\pi^2}{2}\sum_{i=1}^\infty \frac{k_i^2 \overline{w}_H\, B_0(rk_i)J_0^2(R_1 k_i)}{J_0^2(R_0 k_i) - J_0^2(R_1 k_i)} \tag{18}$$

where $k_i$ are the positive roots of equation $B_0(R_1 k_i) = 0$ and $B_0(rk_i) = J_0(rk_i)Y_0(R_0 k_i) - Y_0(rk_i)J_0(R_0 k_i)$

where $J_0(.)$ and $Y_0(.)$ are the Bessel functions of the first and second kinds of order zero.

Now applying finite Hankel transform to Eqs. (15)-(16) with respect to r, we get

$$\overline{w}_H = -\frac{A}{s}\frac{(1+\lambda_1^\alpha s^\alpha + \lambda_2^\alpha s^{2\alpha})}{(s+\text{M})(1+\lambda_1^\alpha s^\alpha + \lambda_2^\alpha s^{2\alpha}) + v\,k_i^2(1+\lambda_3^\beta s^\beta)} \tag{19}$$

Now, writing Eq. (19) in series form as

$$\overline{w}_H = -A(1+\lambda_1^\alpha s^\alpha + \lambda_2^\alpha s^{2\alpha})\sum_{k=0}^\infty (-1)^k \sum_{a+b+c+d+n=k}^{a,b,c,d,n\geq 0} k!M^{c+d}(v\,k_i^2)^n(\lambda_1^\alpha)^{-k-1+d}$$

$$(\lambda_2^\alpha)^{b+c}(\lambda_3^\beta)^n\,\frac{s^\delta}{a!b!c!d!n!\left(s^{\alpha+1} + \dfrac{v\,k_i^2}{\lambda_1^\alpha} + \dfrac{M}{\lambda_1^\alpha}\right)^{k+1}} \tag{20}$$

where $\delta = k-1+2\alpha(b+c) - (c+d+n) - \alpha(d+n) + \beta n - \alpha n$. And its discrete inverse Laplace transform [20] will take the form

$$w_H = -A\sum_{k=0}^\infty (-1)^k \sum_{a+b+c+d+n=k}^{a,b,c,d,n\geq 0} \frac{M^{c+d}(v\,k_i^2)^n(\lambda_1^\alpha)^{-k-1+d}(\lambda_2^\alpha)^{b+c}(\lambda_3^\beta)^n}{a!b!c!d!n!}t^{(\alpha+1)k+(\alpha+1-\delta)-1}$$

$$\left\{E_{\alpha+1,\alpha+1-\delta}^k\left(-\frac{1}{\lambda_1^\alpha}(vk_i^2+M)t^{\alpha+1}\right) + \frac{\lambda_1^\alpha}{t^\alpha}E_{\alpha+1,\alpha+1-\delta}^k\left(-\frac{1}{\lambda_1^\alpha}(vk_i^2+M)t^{\alpha+1}\right) + \frac{\lambda_2^\alpha}{t^{2\alpha}}E_{\alpha+1,\alpha+1-\delta}^k\left(-\frac{1}{\lambda_1^\alpha}(vk_i^2+M)t^{\alpha+1}\right)\right\}$$

(21)

where $E_{\alpha,\beta}^m(z) = \sum_{j=0}^\infty \frac{(j+m)!z!}{j!\Gamma(\alpha j + \alpha m + \beta)}$ is the generalized Mittag- Leffler function [9] and to obtain Eq. (21), the

following property of inverse Laplace transform is used [20]

$$L^{-1}\left\{\frac{m!s^{\lambda-\mu}}{(s^\lambda \mp c)}\right\} = t^{\lambda m + \mu - 1}E_{\lambda,\mu}^m(\pm ct^\lambda) \qquad , \left(\text{Re}(s) > |c|^{\frac{1}{\lambda}}\right) \tag{22}$$

Finally, the inverse finite Hankel transform gives the analytic solution of velocity distribution

$$w(r,t) = -\frac{A\pi^2}{2}\sum_{i=1}^\infty \frac{k_i^2\,B_0(rk_i)J_0^2(R_1 k_i)}{J_0^2(R_0 k_i) - J_0^2(R_1 k_i)}\left[\sum_{k=0}^\infty (-1)^k \sum_{a+b+c+d+n=k}^{a,b,c,d,n\geq 0} \frac{M^{c+d}(v\,k_i^2)^n(\lambda_1^\alpha)^{-k-1+d}(\lambda_2^\alpha)^{b+c}(\lambda_3^\beta)^n}{a!b!c!d!n!}t^{(\alpha+1)k+(\alpha+1-\delta)-1}\right.$$

$$\left.\left\{E_{\alpha+1,\alpha+1-\delta}^k\left(-\frac{1}{\lambda_1^\alpha}(vk_i^2+M)t^{\alpha+1}\right) + \frac{\lambda_1^\alpha}{t^\alpha}E_{\alpha+1,\alpha+1-\delta}^k\left(-\frac{1}{\lambda_1^\alpha}(vk_i^2+M)t^{\alpha+1}\right) + \frac{\lambda_2^\alpha}{t^{2\alpha}}E_{\alpha+1,\alpha+1-\delta}^k\left(-\frac{1}{\lambda_1^\alpha}(vk_i^2+M)t^{\alpha+1}\right)\right\}\right]$$

(23)

---

**3.1 The limiting cases**

**1-** Making the limit of Eq.(23) when $\alpha \neq 0$ and $M \to 0$ (c=d=0), we can get similar solution velocity distribution for unsteady flows of a viscelastic fluid with the fractional Burgers' model, as obtained in Ref[17]. Thus the velocity field reduces to

$$w(r,t) = -\frac{A\pi^2}{2} \sum_{i=1}^{\infty} \frac{k_i^2 \, B_0(rk_i) J_0^2(R_1 k_i)}{J_0^2(R_0 k_i) - J_0^2(R_1 k_i)} \left[ \sum_{k=0}^{\infty} (-1)^k \sum_{a+b+n=k}^{a,b,n\geq 0} \frac{(\nu k_i^2)^n (\lambda_1^\alpha)^{-k-1} (\lambda_2^\alpha)^{b-n} (\lambda_3^\beta)^n}{a!\,b!\,n!} t^{(\alpha+1)k+(\alpha+1-\delta)-1} \right.$$

$$\left. \left\{ E_{\alpha+1,\alpha+1-\delta}^k \left( -\frac{1}{\lambda_1^\alpha}(\nu k_i^2) t^{\alpha+1} \right) + \frac{\lambda_1^\alpha}{t^\alpha} E_{\alpha+1,\alpha+1-\delta}^k \left( -\frac{1}{\lambda_1^\alpha}(\nu k_i^2) t^{\alpha+1} \right) + \frac{\lambda_2^\alpha}{t^{2\alpha}} E_{\alpha+1,\alpha+1-\delta}^k \left( -\frac{1}{\lambda_1^\alpha}(\nu k_i^2) t^{\alpha+1} \right) \right\} \right]$$

(24)

where $\delta = k - 1 + 2\alpha b - n - 2\alpha n + \beta n$.

**2-** Making the limit of Eq.(23) when $\alpha \neq 0$, $\lambda_2 \to 0$ (b=0) and $M \to 0$ (c=d=0), we can get the velocity distribution for a generalized Oldroyd- B fluid. Thus the velocity field reduces to

$$w(r,t) = -\frac{A\pi^2}{2} \sum_{i=1}^{\infty} \frac{k_i^2 \, B_0(rk_i) J_0^2(R_1 k_i)}{J_0^2(R_0 k_i) - J_0^2(R_1 k_i)} \left[ \sum_{k=0}^{\infty} (-1)^k \sum_{a+n=k}^{a,n\geq 0} \frac{(\nu k_i^2)^n (\lambda_1^\alpha)^{-k-1} (\lambda_3^\beta)^n}{a!\, n!} t^{(\alpha+1)k+(\alpha+1-\delta)-1} \right.$$

$$\left. \left\{ E_{\alpha+1,\alpha+1-\delta}^k \left( -\frac{1}{\lambda_1^\alpha}(\nu k_i^2) t^{\alpha+1} \right) + \frac{\lambda_1^\alpha}{t^\alpha} E_{\alpha+1,\alpha+1-\delta}^k \left( -\frac{1}{\lambda_1^\alpha}(\nu k_i^2) t^{\alpha+1} \right) \right\} \right]$$

(25)

where $\delta = k - 1 - n + \beta n$.

## IV. Numerical Results And Discussion:

In this work, we have discussed the MHD flow of generalized Burger's fluid in an annular pipe. The exact solution for the velocity field $u$ is obtained by using the discrete Laplace and finite Hankel transforms. Moreover, some figures are plotted to show the behavior of various parameters involved in the expressions of velocity $u$.

A comparison between the magnetic parameter effect M (Panel a) and no magnetic parameter effect (M=0) (Panel b) is also made graphically in Figs 1-5.

Figs. 1 and 2 provide the graphically illustrations for the effects of the non- integer fractional parameter $\alpha$ and $\beta$ on the velocity fields. The velocity is increasing with the increased the $\alpha$ and $\beta$ for both cases ($M = 0 \, \& \, M \neq 0$).

Fig. 3 provides the graphical illustration for the effect of relaxation parameter $\lambda_1$ on the velocity fields. The velocity is decreased with the increase of $\lambda_1$ for both cases ($M = 0 \, \& \, M \neq 0$).

Figs. 4 and 5 are prepared to show the effect of the material parameter $\lambda_2$ and the retardation parameter $\lambda_3$ on the velocity field. The velocity is increasing with the increase of $\lambda_2$ and $\lambda_3$ for the both cases ($M = 0 \, \& \, M \neq 0$).

Fig. 6 is established to show the behavior of the magnetic parameter M for small as well as for long time. It is observed in (Panel a) that for short time $t = 0.1$ the increase in magnetic field M will decrease the velocity profile, while quite the opposite effect is observed for long time $t = 0.5$ in (Panel b) i.e., the increase in magnetic field M will increase the velocity profile.

Comparison shows that the velocity profile with magnetic field effect is larger when compared with the velocity profile without magnetic field effect. The effect is explained on the long time.
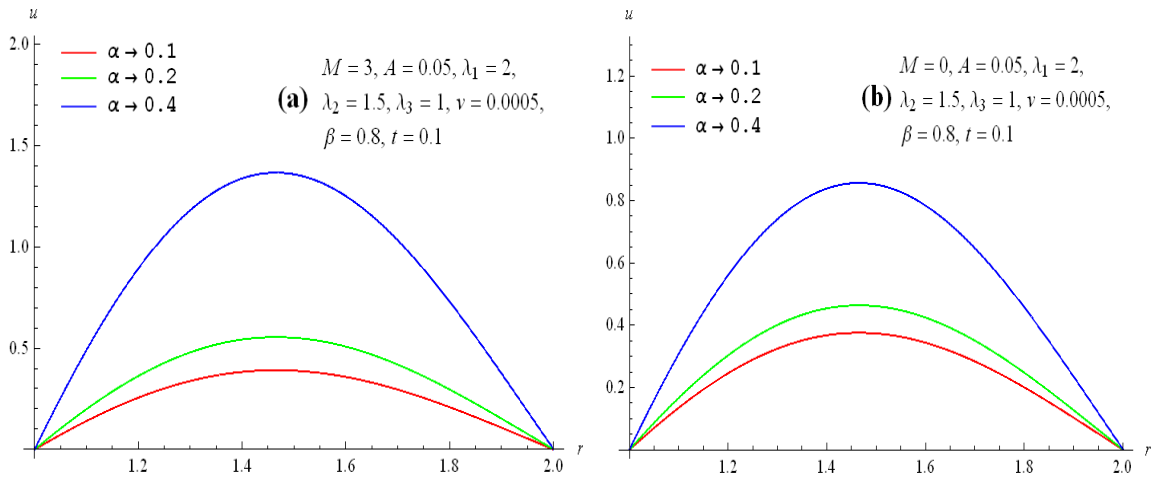
**Fig. 1.** The velocity for different value of $\alpha$ when keeping other parameters fixed a) $M = 3$ b) $M = 0$
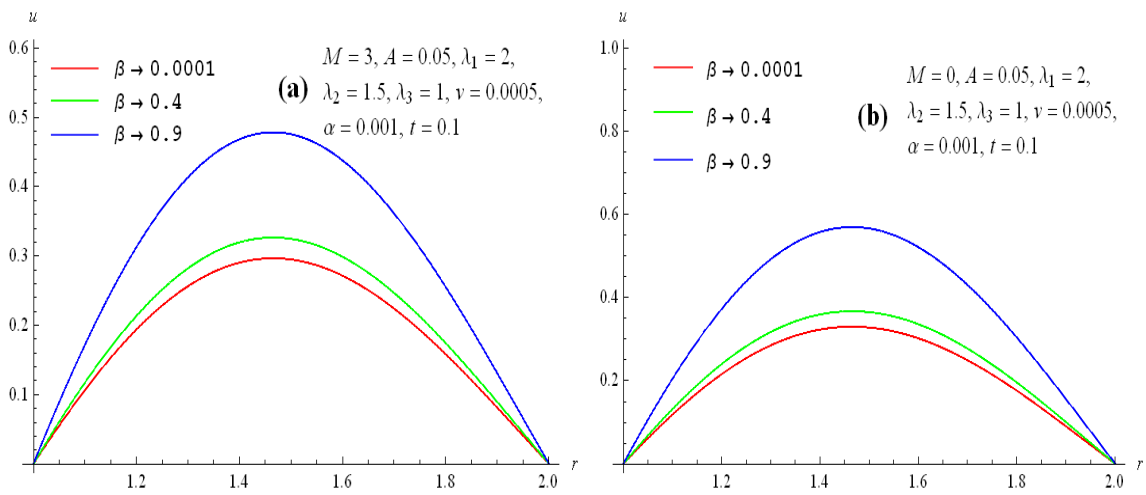


**Fig. 2.** The velocity for different value of $\beta$ when keeping other parameters fixed a) $M = 3$ b) $M = 0$
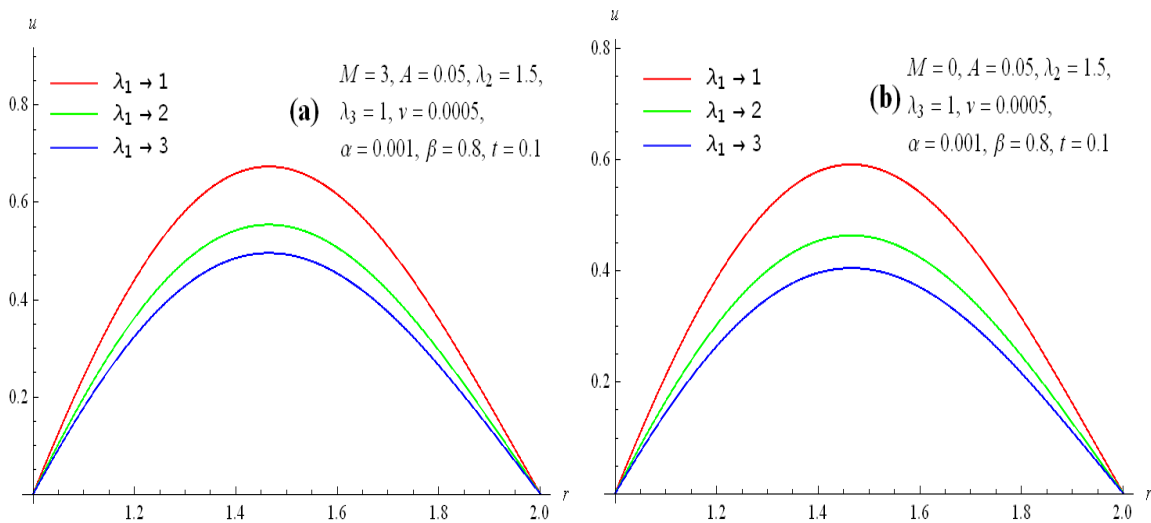


**Fig. 3.** The velocity for different value of $\lambda_1$ when keeping other parameters fixed a) $M = 3$ b) $M = 0$
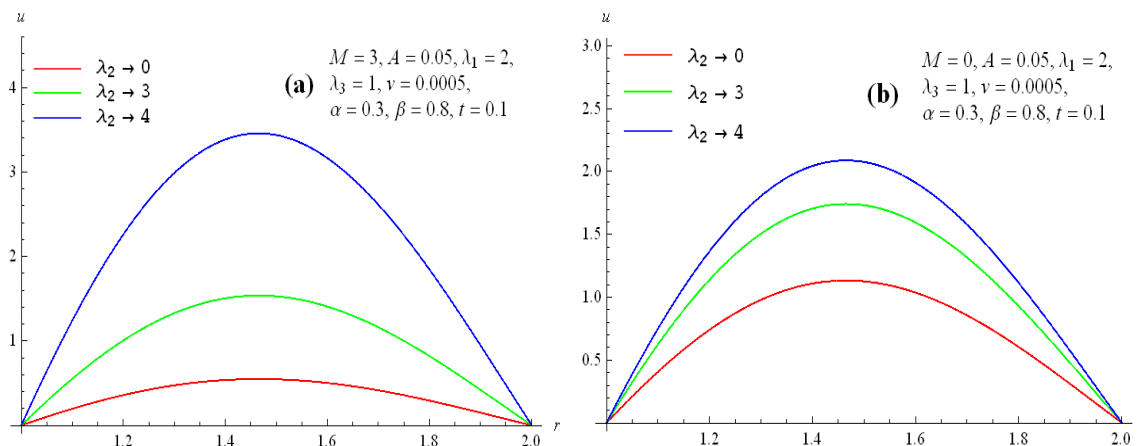
**Fig. 4.** The velocity for different value of $\lambda_2$ when keeping other parameters fixed a) $M = 3$ b) $M = 0$
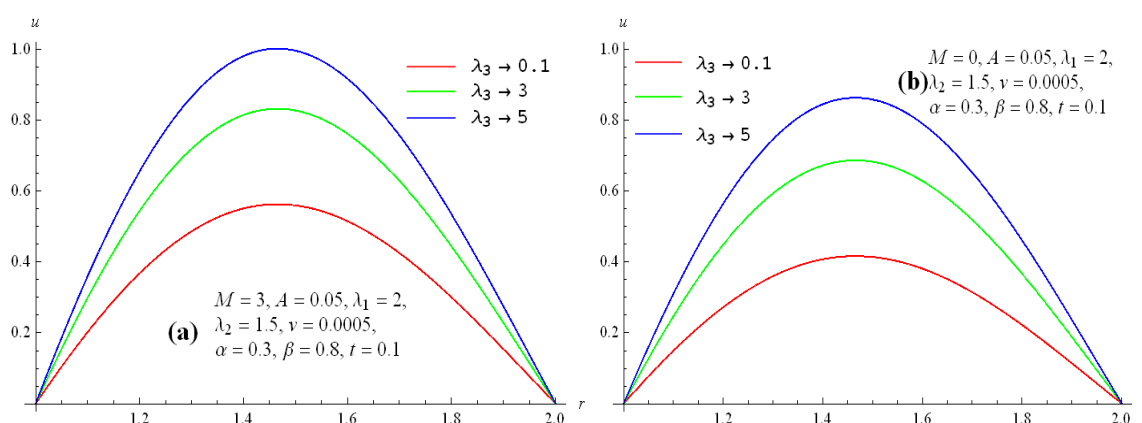


**Fig. 5.** The velocity for different value of $\lambda_3$ when keeping other parameters fixed a) $M = 3$ b) $M = 0$
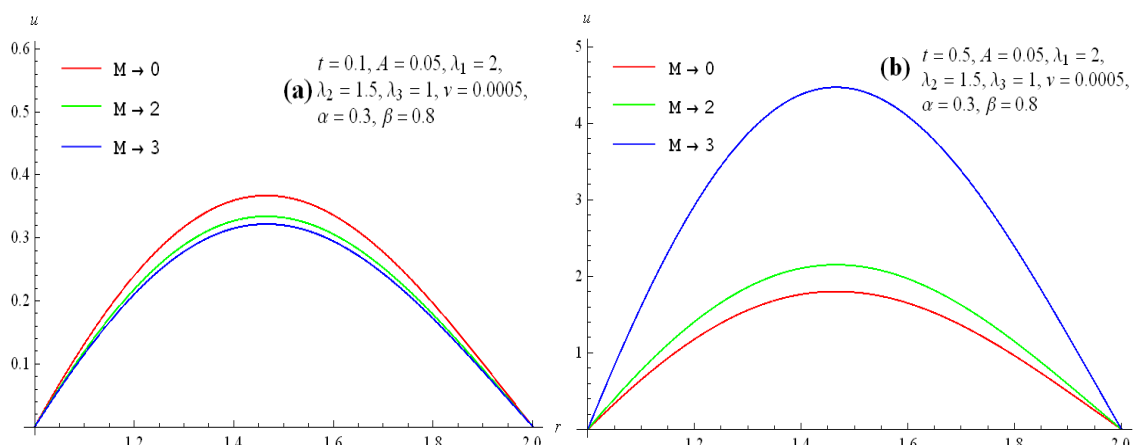


**Fig. 6.** The velocity for different value of $M$ when keeping other parameters fixed a) $t = 0.1$ b) $t = 0.5$

## REFERENCES

[1] B. H. Tan, I. Jackson and J. D. F. Gerald; " High- Temperature Viscoelasiticity of Fine- Grained Polycystalline Olivine", Phys. Chem. Miner. 28 (2001) 641.

[2] C. Fetecau, T. Hayat and Corina Fetecau; " Steady- State Solutions for Simple Flows of Generalized Burgers' Fluid", Int. J. Non- linear Mech. 41 (2006) 880.

[3] D. Baleanu and J. J. Trujillo; "On Exact Solutions of Class of Fractional Euler-Lagrange Equations", Newtonian Dynam. 52 (2008) 331-335.

[4] D. Tong and L. Shan; "Exact Solutions for Generalized Burgers' Fluid in an Annular Pipe", Meccanica 44 (2009) 427-431.

[5]     D. K. Tong, R. H. Wang and H. S. Yang; "Exact Solutions for the Flow of non- Newtonian Fluid with Fractional Derivative in an Annular Pipe", Sci. China Ser. G 48 (2005) 485-495.

[6]     D. K. Tong and Y. S. Liu; "Exact Solutions for the Unsteady Rotational Flow of non- Newtonian Fluid in an Annular Pipe", Int. J. Eng. Sci. 43 (2005) 281-289.

[7]     F. Shen, W. Tan, Y. Zhao and T. Masuoka; "The Rayleigh- Stokes Problem for a Heated Generalized Second Grade Fluid with Fractional Derivetive Model", Nonlinear Anal RWA 7 (2006)1072-1080.

[8]     H. T. Qi and M. Y. Xu; "Stokes first Problem for a Viscoelastic Fluid with the Generalized Oldroyd-B Model", Acta. Mech. Sin. 23 (2007) 463-469.

[9]     I. Podlubny;"Fractional Differentional Equations" Academic Press, San Diego, 1999.

[10]    L. Zheng, Y. Liu and X. Zheng; " Slip effect on MHD Flow of a Generalized Oldroyd- B Fluid with Fractional Derivative", Nonlinear Anal. RWA 13 (2012) 513- 523.

[11]    M. Khan; "The Rayleigh- Stokes Problem for an Edge in a Viscoelastic Fluid with a Fractional Derivative Model", Nonlinear Anal. RWA 10 (2009) 3190-3195.

[12]    M. Khan, S. Hyder Ali and H. Qi; "On Accelerated Flows of a Viscoelastic Fluid with the Fractional Burgurs' Model", Nonlinear Anal. RWA 10 (2009) 2286-2296.

[13]    M. Khan, T. Hayder and S. Asghar; "Exact Solution for MHD Flow of Generalized Oldroyd- B Fluid with Modified Darcy's", Law. Int. J. Eng. Sci. 44 (2006) 333-339.

[14]    O.P. Agrawal; "Formulation of Euler-Lagrange Equations for Fractional Variational Problems", J. Math. Anal. Appl. 272 (2002) 368-379.

[15]    P. Ravindran, J. M. Krishnan and K. R. Rajagopal; " Anote on the Flow of Burgers' Fluid in an Orthogonal Rheometer, Internat. J. Engrg. Sci. 42 (2004) 1973.

[16]    S. Hyder Ali; "Unsteady Flows of a Viscoelastic Fluid with the Fractional Burgers' Model", Nonlinear Anal. RWA 11 (2010) 1714-1721.

[17]    S. Hyder Ali and H. Qi; "Starting Solutions for a Viscoelastic Fluid with Fractional Burgers' Model in an Annular Pipe", Nonlinear Anal. RWA 11 (2010) 547-554.

[18]    T. Hayat, C. Fetecau and S. Asghar; " Some Simple Flows of Burgers' Fluid", Internat. J. Engrg. Sci. 44 (2006) 1423.

[19]    V. E. Tarasov; "Fractional Vector Calculus and Fractional Maxwells Equations", Ann. Phys. 323 (2008) 2756-2778.

# Application of Human Factor Engineering in the Design and Development of Products

Gurbhej singh[1], Hitesh vasudev[2]
[1]*Assistant Professor, Mechanical Engineering Department, GPC, BHIKHIWIND*
[2]*Assistant Professor, Mechanical Engineering Department, PIT, HOHIARPUR*

***Abstract:*** *Several studies have shown that there is a need of ergonomically fit sewing machine workstation so that sewing machine operators can perform their faddy tasks comfortably. The present study was initiated where worker's perceptions were measured by preparing questionnaire to find out difficulties during sewing machine work. Questionnaireswere filled up by 100 sewing machine operators from different parts of the region. Questionnaire included the different modules which are Perceived posture, localized postural discomfort andestimatedendurance time. Worker's perceptions were analyzed by finding their critical values.Based on the criticality index, recommended parameters were performed on selected operators.Nine sewing machine operators performed experiments at twelve different combinations of table height, desk slope and pedal position. ANOVA technique was used to analyze the data obtained from nine selected sewing machine operators after performing experiments and the dimensional adjustment of sewing machine workstation was made, in relation to desk height, desk slope and pedal position. The recommendations were formulated in order to minimize the load on the musculoskeletal system during operation in terms of anthropometric dimensions with respect to sewing desk height, desk slope and pedal position.*

***Keywords:*** *Sewing machine, Worker's perception, Worker station, Posture, ANOVA.*

## I. Introduction

The introduction of the sewing machine in the workplace has led to numerous reports of health distress from its use. A typical workstation includes work surfaces, space for all activities and components of the task, seating for operator, pedal for operating foot. It has been found that a well-designed convenient sewing area large or small saves time and energy. Knowledge of the determinants that lead workers to adopt a particular working posture increases the feasibility of posture prediction. It is required to improve the working posture and reduce the number of complaints; quantitative recommendations for the adjustment of the workstation are needed, which take these postural constraints into account and founds that employees encounter several risk factors at sewing workstation, such as awkward arm, neck, trunk, and leg postures. These postures are influenced by the size of the worker and the design of the workstation [1]. Repetitive motion caused by the foot petal can lead to CTDs (commutative trauma disorders) in the foot. Excessive noise and poor lighting can also lead to hearing and vision problems [2].It has been that studied musculoskeletal disorders of the neck and shoulders in female sewing operators [3].It has been found that a well-designed, convenient sewing area large or small saves time and energy [4].Improved design modifications based on ergonomic principles of chute and a height difference of platform and a chute can reduce the possibility of injuries among thresher operators [5].Sewing machine operators can perform their faddy tasks comfortably by using this ergo-work seat [6].Ergonomic intervention improves working conditions for sewing machine operators [7].

## II. Methodology

Questionnaires were prepared to record the perceptions of sewing machine operators. This method of data collection is quite popular, particularly in case of big enquiries. A questionnaire was consisted of number of questions printed in a definite order on a set of forms. The questionnaires were directly filled up by the sewing machine operators. Questionnaire was structured based i.e. there were definite, concrete and predetermined questions and questions were presented with exactly the same wording and in same order to all the sewing machine operators and these questionnaires were filled up by sewing operators directly by approaching to them. Questionnaires were filled up by 100 sewing machine operators from different parts of the region. Workers' perceptions were recorded by a questionnaire, containing four questionnaire modules. Critically Index was calculated in each of the module of the questionnaire, in order to find out the critical areas. Critically Index was calculated as:- Multiply point scale of that module of the questionnaire with their individual score of concerned

part and add then divide the obtained result with total of the point scale of that module of the questionnaire. Critical areas were found related to perceived posture, localized postural discomfort, estimated endurance time, Judgment on whole workstation adjustment modules of questionnaire. Based upon these critical areas, recommended Parameters related to sewing machine workstation, were decided. Experiments were performed on various recommended parameters on selected sewing machine operators. ANOVA technique was used to analyse the data obtained from selected sewing machine operators after performing experiments and recommendations were drawn for sewing machine workstation.

## 2.1 Perceived posture

The operator was asked to rate his perception of the posture of the neck, back, left shoulder, right shoulder, left upper arm, right upper arm, left lower leg, right lower leg, left foot, and right foot.

Table 1 Response of sewing machine operator related to perceived posture

| Parameter* | Posture of neck (A) | Posture of back (B) | Posture of left shoulder (C) | Posture of right shoulder (D) | Posture of left upper arm(E) | Posture of right Upperarm (F) | Posture of left lowerleg (G) | Posture of right Lowerleg (H) | Posture of left foot (I) | Posture of right foot (J) |
|---|---|---|---|---|---|---|---|---|---|---|
| 1 | 32 | 23 | 47 | 46 | 49 | 49 | 40 | 40 | 50 | 50 |
| 2 | 06 | 08 | 05 | 05 | 06 | 06 | 06 | 06 | 02 | 02 |
| 3 | 54 | 46 | 46 | 47 | 43 | 43 | 41 | 41 | 39 | 39 |
| 4 | 02 | 05 | 02 | 02 | 02 | 02 | 04 | 05 | 02 | 03 |
| 5 | 05 | 16 | 00 | 00 | 00 | 00 | 09 | 08 | 05 | 05 |
| 6 | 00 | 01 | 00 | 00 | 00 | 00 | 00 | 00 | 02 | 01 |
| 7 | 01 | 01 | 00 | 00 | 00 | 00 | 00 | 00 | 00 | 00 |
| Criticality index | 8.78 | 10.35 | 7.25 | 7.32 | 7.07 | 7.07 | 8.42 | 8.39 | 7.71 | 7.64 |

## 2.2 Localized postural discomfort

The operator was asked to rate his postural discomfort in 30 regions shown on diagram of the rear view of a human body using a scale ranging from 0 to 5.

Table 2 Response of sewing machine operators related to localized posture discomfort.

| PARAMETERS | No of operators rated their perception | | | | | | | | | |
|---|---|---|---|---|---|---|---|---|---|---|
| | A | B | C | D | E | F | G | H | I | J |
| No discomfort | 91 | 94 | 58 | 86 | 90 | 99 | 97 | 81 | 81 | 40 |
| Some discomfort | 07 | 03 | 25 | 07 | 05 | 00 | 02 | 13 | 14 | 42 |
| Minordiscomfort | 01 | 01 | 14 | 03 | 03 | 01 | 01 | 03 | 03 | 15 |
| Majordiscomfort | 01 | 02 | 03 | 04 | 02 | 00 | 00 | 02 | 02 | 02 |
| Severe discomfort | 00 | 00 | 00 | 00 | 00 | 00 | 00 | 01 | 00 | 01 |
| Verysevere discomfort | 00 | 00 | 00 | 00 | 00 | 00 | 00 | 00 | 00 | 00 |
| **Criticality Index** | 0.8 | 0.73 | 4.13 | 1.66 | 1.13 | 0.13 | 0.26 | 1.93 | 1.73 | 5.46 |

## 2.3 Estimated endurance time:

The operator was asked to estimate. On the basis of his perceptions, how long he could operate at the experimental workstation adjustment without difficulty during a regular, working day.

Table 3 Response of sewing machine operators related to estimated endurance time.

| Estimated endurance time | |
|---|---|
| Five point scale | No. of operations rated their perception |
| 1 (> 8 hours) | 39 |
| 2( 6-8 hours) | 42 |
| 3 ( 4-6 hours) | 14 |
| 4 ( 2-4 hours) | 05 |
| 5(<2 hours) | 00 |

**2.4 Desk height**

Height of person varies from person to person. That is why desk height was tested related to individual elbow height of sewing machine operator taken as:+ 5 cms  above elbow height, + 10 cms  above elbow height & + 15 cms  above elbow height.

**2.5 Desk slope**

Desk slope taken as:0° based on desk slope at shop of sewing machine operator (normal desk)and 10° slope towards sewing machine operator.

**2.6Pedal position**

Pedal position was taken as: 4 cms.to the operator's side of the needle tip and 6 cms.to the opposite side of the needle tip. These two readings were taken on the behalf of sewing machine builder's perceptions. Experimentation phase was consisted of 12 sets of experimental conditions.

Total SEC (set of experimental conditions) = 12

On the behalf of these 12 sets of experimental conditions, which are represented by different combinations of desk height, desk slope and pedal position are shown in table 3.8, response of 9 treadle sewing machine operators were considered. Response of 9 treadle sewing machine operators was considered by performing experiments with different combinations of desk height, desk slope and pedal position.

## III. Results And Discussion

In experimentation stage, 12 sets of experimental conditions were tested for different combinations of desk height, desk slope and pedal position. The existing parameters of the sewing machine operators were measured when they were asked to work for 40 minutes and the following were the findings.

Result we obtained by testing 12 sets of experimental conditions for different combinations of desk height, desk slope and pedal position. Analysis of data collected from 9 treadle sewing machine operators was done by ANOVA technique. Thus result obtained from analysis of data is shown that there is significant relation between desk height, desk lope and pedal position. So sewing machine workstation design is said to be best fitted only if it will have following combination as given in table 4.5 and shown as under:

Table 4 Dimensional adjustment of sewing machine workstation

| | |
|---|---|
| Desk height (above elbow height) | +10 cms. |
| Desk slope | 10° |
| Pedal position (i.e. pedal axis behind the needle) | - 4 cms |

## IV. Conclusions

- This was further extended to recommend the dimensional parameter of sewing machine workstation to be used by an Indian male, with the desk slope as10°, pedal position as -4 cms. The following table recommends the desk height of sewing machine for Indian male.
- From the questionnaire part, the conclusions related to four modules of questionnaires, were drawn with the criticality index on order to find the most critical areas and given as under:
- **Perceived posture:** The critical areas in perceived posture discomfort reveals that the most critical posture of left lower leg, posture of right lower leg.
- **Localized postural discomfort:**    Localized postural discomfort reveals that the most critical areas is discomfort of whole body and the others discomfort of back, discomfort of left leg, discomfort of right leg, discomfort of upper neck/back.
- **Judgment on workstation adjustment:** Judgment on workstation adjustment reveals that judgment by operator for desk slope, desk height, pedal position and judgment of operator for whole workstation have an average effect on sewing machine operator.

So from questionnaire part, it was concluded that there was a need of ergonomically for sewing machine workstation, which the researcher has proved.

## REFERENCES

[1]. A. Kumar, N. Ishii, Development of grain threshers based on ergonomics design, International journal of industrial ergonomics,33,2002,503-507.
[2]. J.F. Buneo, Flanders , Moving effortlessly in three dimensions arm movements, The journal of neuroscience,15,1995, 6271-6280.
[3]. G. Verma, Cutting And Tailoring Theory(Asian Publishers.2005).
[4]. N.J. Dellmen, Working posture-prediction and evaluation, doctoral diss., TNO, the Netherlands, Ph.D., 1999.
[5]. S.N. Shan, Work Study & Ergonomics (Dhanpat Rai & Sons, 1999).
[6]. McCormick, Human factors in engineering and design (Tata McGraw-Hill Publishing company, 1976).
[7]. Genaway, C. David, ERGONOMICS: Environment: Energy: A brief primer for site preparation,Technicalities,9,1989, 10-12.

# UPFC in order to Enhance the Power System Reliability

Vikash Anand[1], Dr. M. M. Chaudhary[2]

[1] *Research Scholar, Electrical Engineering, N.I.T (Patna), India*
[2] *Professor, Electrical Engineering, N.I.T (Patna), India*

**Abstract:** *The maintenance and reliability of the power system has become a major aspect of study. The solution is the use of FACTS devices especially the use of UPFC. Unified Power Flow Controller (UPFC) is the most widely used FACTS device to control the power flow and to optimize the system stability in the transmission line. It is used to control the power flow in the transmission systems by controlling the impedance, voltage magnitude and phase angle. This controller offers advantages in terms of static and dynamic operation of the power system. The UPFC with its various modes of operation is understood. Second, the operation of control system used in its converters is also studied. Finally by help of modeling of a power system in SIMULINK / MATLAB SIMPOWERSYSTEM and by installing single phase UPFC in transmission link, its use as power flow controller and voltage injection and constructing a lab scale model of UPFC is discussed also.*

**Keywords:** *MATLAB, Measuring Devices, Single Phase Supply, Series Converter, STATCOM*

## I. INTRODUCTION

Power system is the interconnection of generating unit, substation, and distributing unit. Generation part is the main source that supply to the load. In this area the value of voltage is about 132 kV and above. While the substation make a function like medium channel. It is use in transmitting the power from the generating station to the load. In this area the value of voltage that is used about 11kV and 66 kV. The distribution part of the power system is the load. The voltage flow at the distribution unit is 240V for single phase and 415V for three phases. In the recent year the power demand by consumer is greater than the power flow through the transmission line system. In order to provide the power demanded by the consumer, the new generation technology must be build. Because of economic and environmental reason rebuild the new generation and transmission system become more difficult.

To overcome these problem new technologies were developing to replace the mechanical control. Flexible AC Transmission System (FACTS) which was introduced by Hingorani is applying to the transmission system to increase the controllability. It optimizes the utilization for existing power system capability by replacing mechanical controller with the reliable and high speed power electronic devices.

The latest generation of FACTS controllers is based on the concept of the solid state synchronous voltages source (SVS) introduced by L.Gyugyi in the late 1980.The SVS behave as an ideal synchronous machine because it can generate fundamental three phase balanced sinusoidal voltage of controllable amplitude and phase angle. It can generate the reactive power and with the approximate storage device, it can also exchange the real power with the AC system. The SVS can be implemented by the use of voltage sourced converter (SVC).The SVS can be used as a shunt or series compensator. If it is operated as shunt compensator, it is called as static condenser (STATCOM) and if as series compensator, it is called static synchronous series compensator (SSSC). But the most versatile controller in the FACTS family is unified power flow controller (UPFC) because it can operate as a shunt and series compensator.

## II. FACTS DEVICES

In the power system FACT controllers are used for the control of voltage, impedance and phase angle. In the past, traditional controllers are employed whereas nowadays these traditional controllers are replaced by thyristor valves. FACTS controllers are basically categories in two types such as-Thyristor based FACT controllers and Voltage source converter based controllers. The power transfer ability of transmission system depends on many factors such as steady state stability limit, transient stability limit and thermal limit. Due to the fault in the system, there is increase in the system loss and decrease in the system reliability. Therefore with increase in the demand and supply, it becomes necessary to installed FACTS controllers in the power system. By utilizing FACTS controllers we can improve system stability, voltage and security. In any substation, there is a number of transmission lines hence it is difficult to compensate all the transmission lines

together. To solve this problem Inter Line Power Flow Controller is developed. This is the second generation of FACTS controller. It provides the capability of direct transfer of real power between the compensated lines. By this there is balance of real and reactive power flow between the lines. If there is not proper coordination between various FACTS controllers or they are not installed in proper location then there is a cause of voltage instability. Hence it becomes necessary that FACTS controllers are installed at proper location and there is proper coordination between them. Unified Power Flow Controller is the most versatile power flow controller among all the facts controllers. A lot of researches have been done to improve the performance of UPFC controller. The recently proposed Hoo learning method is used for updating the parameter radial basic function neural network controllers as the UPFC Controller.

FACTS controllers may be based on thyristor devices with no gate turn-off, or with power devices with gate turn-off capability. FACTS controllers are used for the dynamic control of voltage, impedance and phase angle of high voltage AC transmission lines.
FACTS controllers can be divided into four categories:
 i.   Series controllers
 ii.  Shunt controllers
 iii. Combined series-series controllers
 iv.  Combined series-shunt controllers

**1. Series Controllers**

The series controller could be variable impedance, such as capacitor, reactor, etc., or a power electronic based variable source of main frequency, sub synchronous and harmonic frequencies to serve the desired need. They inject voltage in series with the line. As long as the voltage is in phase quadrature with the line current, the series controller only supplies or consumes variable reactive power. Any other phase relationship will involve handling of real power as well. Static Synchronous Series Compensator (SSSC) is one such series controller.
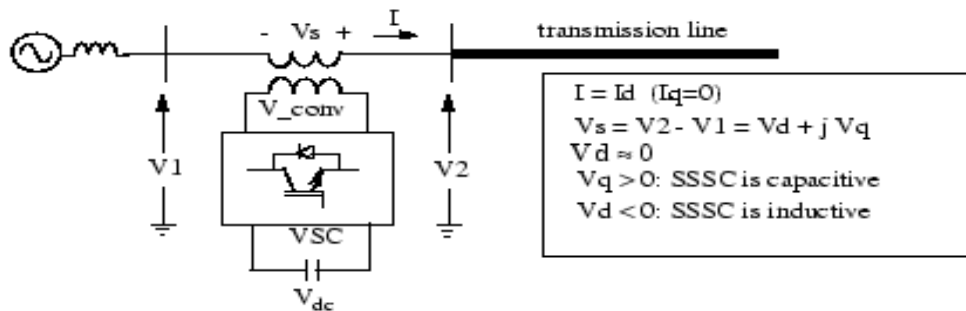


Fig.1 Series Controller

**2. Shunt Controllers**

Shunt controllers is also variable impedance, variable source, or a combination of these. All shunt controllers inject current into the system at the point of connection. As long as the injected current is in phase quadrature with the line voltage, the shunt controller only supplies or consumes variable reactive power. Any other phase relationship will involve handling of real power as well. Static Synchronous Compensator (STATCOM) is one such controller.
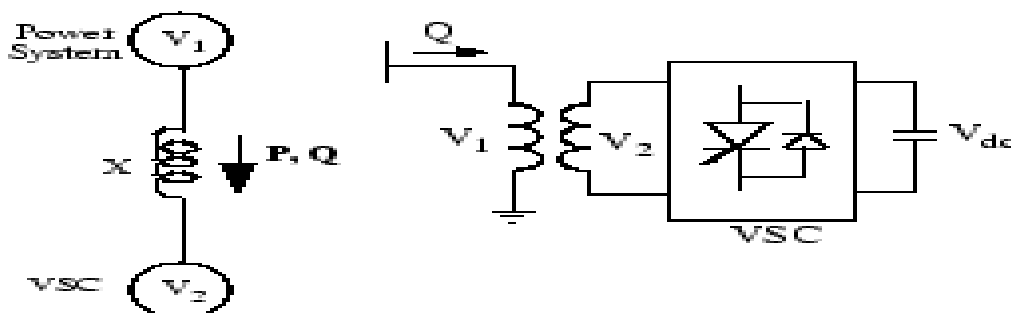


Fig.2 Shunt Controller

## 3. Combined Series-Series Controllers

This could be a series combination of separate series controllers, which are controlled in a coordinated manner, in a multilane transmission system. Interline Power Flow Controller comes in this category.

## 4. Combined Series-Shunt Controllers

This could be a combination of separate shunt and series controllers, which are controlled in a coordinated manner, or a unified power flow controller with series and shunt elements. In principle, combined shunt and series controllers inject current into the system with shunt part of the controller, voltage in series in the line with the series part of the controller. However, when the shunt and series controllers are unified, there can be a real power exchange between the series and shunt controllers via the power link.

## III.   UNIFIED POWER FLOW CONTROLLER (UPFC)

### 1. Static Representation of UPFC

The Unified Power Flow Controller (UPFC) consists of a combination of Static Synchronous Compensator (STATCOM) and a Static Synchronous Series Compensator (SSSC). Both the compensators are coupled via a DC link, which allows bidirectional flow of real power between the series output terminals of the SSSC and the shunt output terminal of the STATCOM.
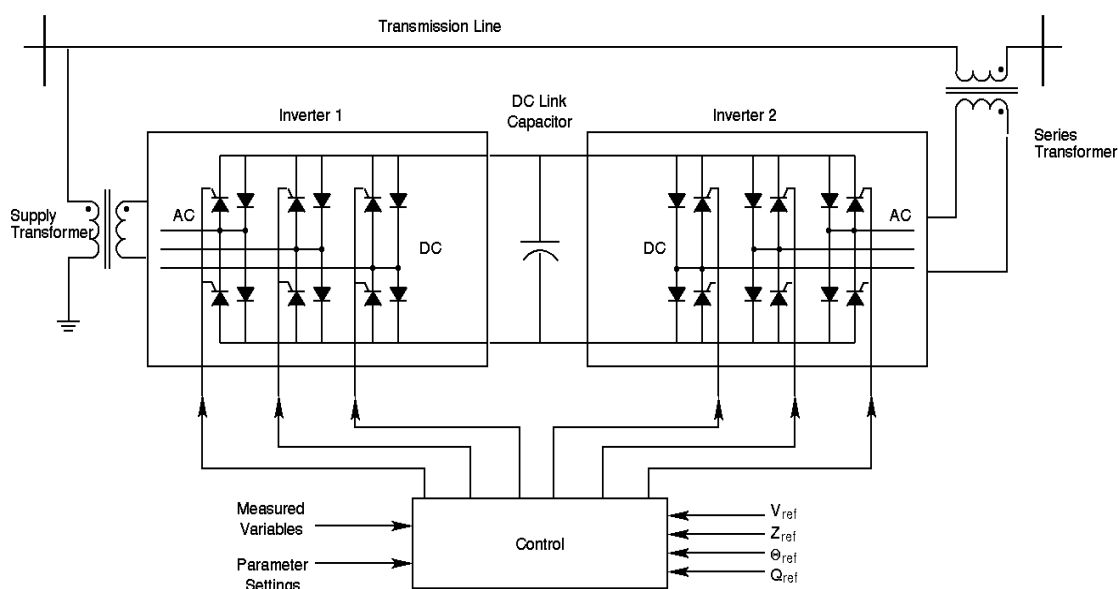


Fig.3 A Simple Model of UPFC

In the circuit we can see that there are two transformers that is shunt & series transformer & both the transformers are connected by two Gate-Turn-Off (GTO) converters and a DC circuit having a capacitor. Common DC link between both the converter works as a channel for the flow of power. The shunt converter is primarily used to provide the real power demand of the series converter via a common DC link terminal from the AC power system. Shunt converter can also generate and absorb reactive power at its AC terminal. Therefore with proper control it can also act as an independent advanced static VAR compensator providing reactive power compensation for the line and thus executing indirect voltage regulation at the input terminal of the UPFC. A series converter is used to generate voltage source at fundamental frequency with variable amplitude and phase angle, which are added to the AC transmission line by series connected boosting transformer. The converter output voltage, injected in series with the line, can be used for direct voltage control, series compensation, phase shifter and their combinations. This voltage source can internally generate or absorb all the reactive power required by different type of controls applied and transfers active power at its DC terminal.

### 2. Characteristics and Operation Modes of UPFC

In the power system there are many major issues where the capability & utilization of FACTS are noticed. These issues are power system stability loss, Line outage, cascading, line tripping, and congestion.

Representative of the last generation of FACTS devices is the Unified Power Flow Controller (UPFC). The UPFC can control simultaneously all three parameters of line power flow -line impedance, voltage and phase angle. Such "new" FACTS device combines the features of two "old" FACTS devices: the Static Synchronous Compensator (STATCOM) and the Static Synchronous Series Compensator (SSSC). These two devices are two Voltage Source Inverters (VSI's) connected respectively in shunt with the transmission line through a shunt transformer and in series with the transmission line through a series transformer. Both the converters are connected to each other by a common dc link including a storage capacitor. Shunt inverter is used to balance the real power flow exchanged between the series inverter and the transmission line and for voltage regulation at the point of connection injecting an appropriate reactive power flow into the line. Series inverter is used to control the real and reactive line power flow inserting an appropriate voltage with controllable magnitude and phase in series with the transmission line. Thus, UPFC accomplishes the functions of active and reactive series compensation, reactive shunt compensation, and phase shifting. Instead of these functions, UPFC allows a secondary but important function such as stability control to suppress power system oscillations for improving the transient stability of power system. Because of changes in the future electricity market scenario, there is a need for flexible and fast power flow controllers, such as the UPFC. To investigate the impact of UPFC on the performance of the power system, there is a corresponding need for reliable and realistic models of these controllers.

Control of power flow is achieved by adding the series voltage, $V_s$ with certain amplitude, $\Box V_s \Box$ and phase shift, $\Box$ to $V_1$. This will gives a new line voltage $V_2$ with different magnitude and phase shift. As the angle $\Box$ varies, the phase shift $\Box$between $V_2$ and $V_2$ also varies.



$$P = \frac{V_2 \times V_3 \times \sin\delta}{X}$$

$$Q = \frac{V_2(V_2 - V_3\cos\delta)}{X}$$
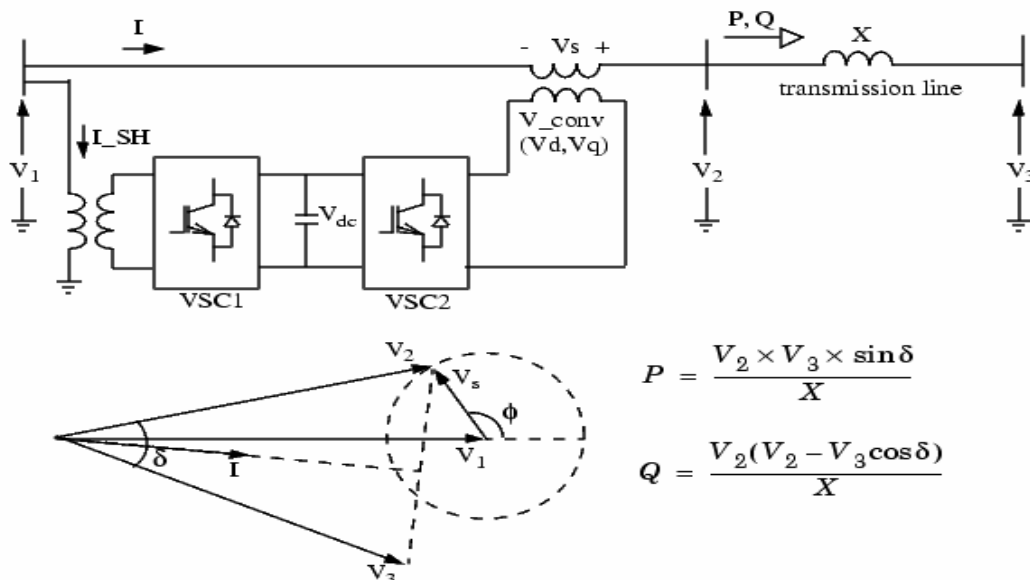
Fig.4 Single line diagram of UPFC and Phasor diagram voltage and current

With the presence of the two converters, UPFC not only can supply reactive power but also active power. The equation for the Active and Reactive power is given as follows.

$$P_{12} = \frac{V_1 V_2}{X_{12}} \sin\delta$$

$$Q_{12} = \frac{V_1 V_2}{X_{12}} (1 + \cos\delta)$$

### 3. Functional Control of Shunt Inverter

The shunt inverter is used to inject a controllable current Ic into the transmission line. This current consists of two components with respect to the line voltage.

1. The real or direct component $i_d$
2. Reactive or quadrature component $i_q$

The direct component is automatically determined by the requirement to balance the real power of the series inverter where as quadrature component can be independently set to any desired reference level (inductive or capacitive) within the capability of the inverter, to absorb or generate respectively reactive power from the line.

So, two control modes are possible:

1. VAR control mode: The reference input is an inductive or capacitive VAR request.
2. Automatic Voltage Control mode: The goal is to maintain the transmission line voltage at the connection point to a reference value.

## 4. Functional Control of Series Inverter

The series inverter injects a voltage, Vse which is controllable in amplitude and phase angle in series with the transmission line. This series voltage can be determined in different ways:

**i) Direct Voltage Injection mode**

The reference inputs are directly the magnitude and phase angle of the series voltage.

**ii) Phase Angle Shifter Emulation mode**

The reference input is phase displacement between the sending end voltage and the receiving end voltage.

**iii) Line Impedance Emulation mode**

The reference input is an impedance value to insert in series with the line impedance.

**iv) Automatic Power flow Control mode**

The reference inputs are values of P and Q to maintain on the transmission line despite system changes.

## 5. Benefits of UPFC in the Power System

UPFC is a versatile and multifunction power flow controller. It has the capabilities of terminal voltage regulation, series line compensation and phase angle regulation. It has also some additional features such as optimal power flow, reliability etc. If we perform the steady state analysis with UPFC, it gives the basic criteria for conducting dynamic stability studies with UPFC. Dynamic stability studies include frequency domain and time domain analysis that include the study of transient stability. Because of unwanted disturbances among the synchronous generator, there is a loss of synchronism. Therefore it is necessary to use a suitable control strategy. The transient stability of power system can be improved with the help of most flexible FACTS devices that is UPFC. By utilizing UPFC in the transmission line, the maximum loading point in the line is increased a compare to other FACTS devices. In order to find such advantages, it is important to locate the UPFC in the appropriate location. Various factors are considered for the optimal location of UPFC such as active power loss, transmission capacity, stability, blackout prevention. Thyristor Controlled Series Capacitor (TCSC) & Static Synchronous Series Compensator (SSSC) is also important FACT device. Series compensator in transmission line decreases unsymmetrical components, reducing net power loss, providing voltage support, limiting short-circuit currents. But the TCSC can work only in inductive and capacitive zone.

## 6. Location of UPFC Controller

Most of the FACTS devices are generally installed in substations for convenient operation and maintenance. UPFC must be located at or within the middle of the transmission line.

- The branches having transformers have not been considered for the UPFC placement.
- The branches having generators at both the end buses have not been considered for the UPFC placement.
- The line having the highest absolute load curtailment sensitivity factor with respect to UPFC angle is considered the best location for UPFC, followed by other lines having less values of sensitivity factor
  .
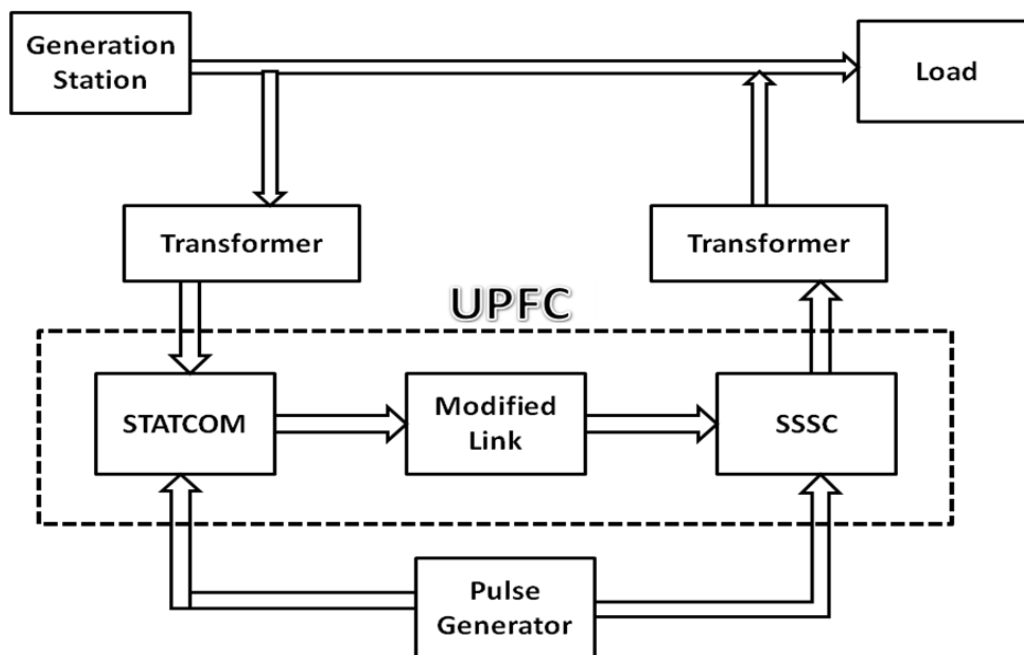
Fig.5 Block Diagram of Modified Location of UPFC

**7. Lab Scale Model of UPFC**

Programmable Interface Controller (PIC) is being programmed to generate PWM signals to the gate drive that will send the signals to trigger the IGBTs. The comparator provides a reference signal to the PIC controller board to generate triggering signals in synchronization with the supply voltage.

A lab scale model is constructed using H- bridge voltage source inverter to act as SSSC.
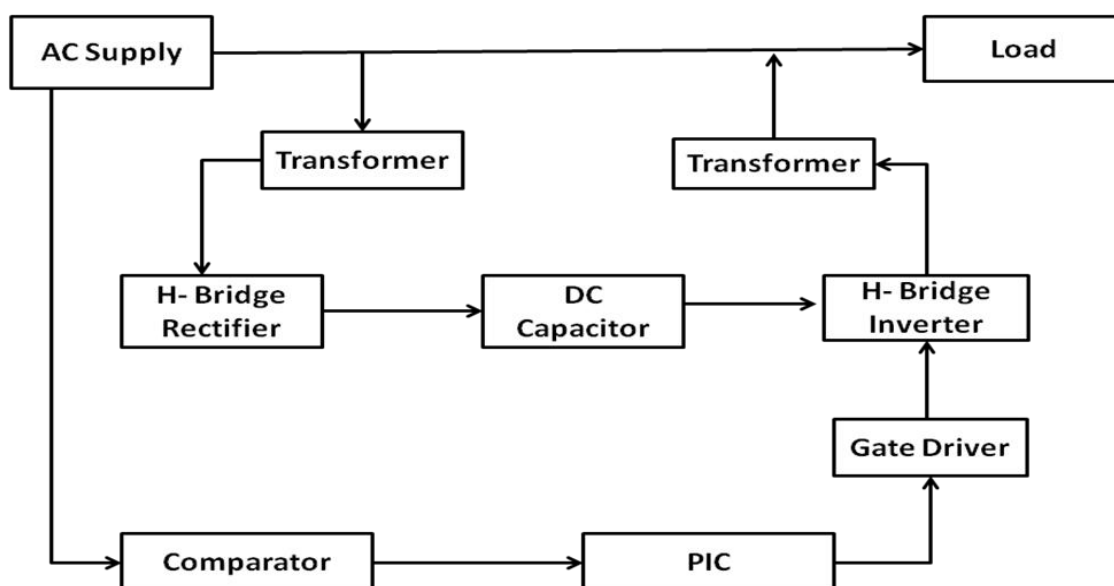


Fig.6 Block Diagram of Lab Scale of UPFC

**IV. MODELING AND ANALYSIS OF UPFC**

**1. SIMULINK Model of Single Phase UPFC**

Using the concept of control system, a power system is taken to implement the use of UPFC. The two modes i.e the power flow control and the voltage injection mode are simulated in MATLAB / SIMPOWERSYSTEM to see the effect of UPFC on a power system. Study is carried out to verify the utility of FACTS devices.
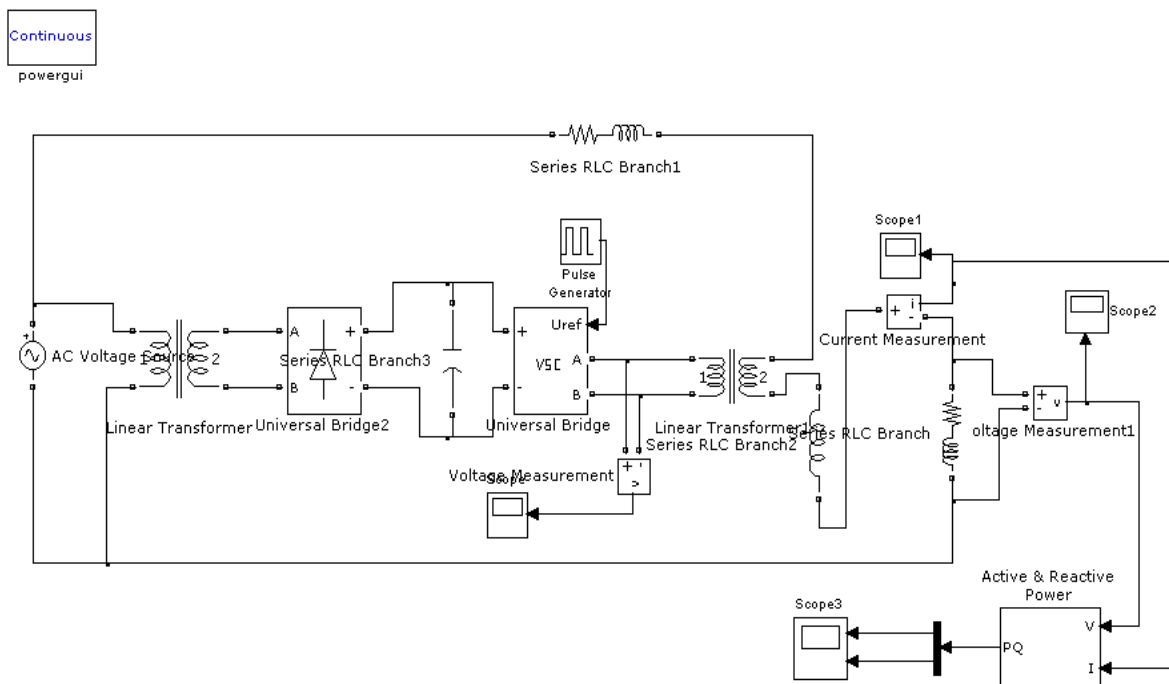
Fig.7 SIMULINK model of Single line UPFC

The capacitor connected in the model is used to balance instantaneous difference in fundamental power ($V_1 I_1 \cos \emptyset_1$) and power at different frequency ($V_n I_n \cos \emptyset_n$). The UPFC is assumed to be installed in the single phase power system with voltage source at sending end and single phase load at receiving end.

The single phase model is shown in fig.7, the value of capacitance is taken as infinity for simplicity in the single phase model. The transmission line parameters will be same, only have to do is to add another transmission line running parallel to existing line. The basic idea of this project is to attempt to transmit power or exchange power between the series and parallel part of UPFC.
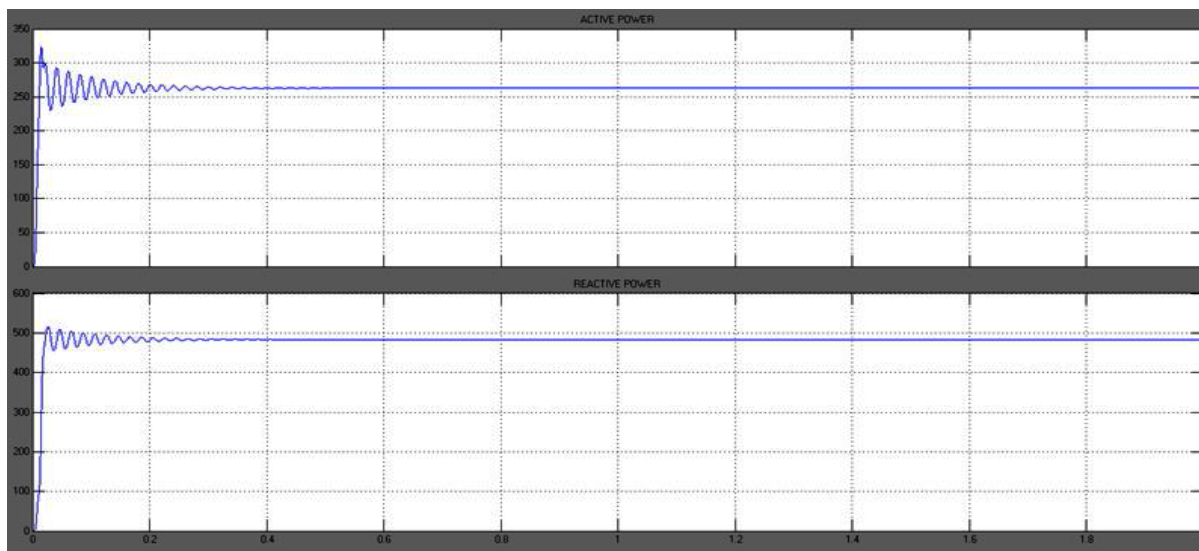


Fig.8 Output Waveform for Active and Reactive Power

## V. CONCLUSION

It represents a single phase UPFC concept of transmitting power with DC link capacitor. This gives more flexibility of UPFC installation. The active power exchange between shunt and series is transmitted through a single DC link transmission line. Therefore, to control the power from one end to another end, this concept of power flow control and voltage injection is highly acceptable.

- Power flow control is achieved and congestion is less
- Transient stability is improved
- Faster steady state achievement
- Improved voltage profile

## REFERENCES

[1]   L.Gyugyi, R. Rietman, A. Edris, C.D. Schayder, D.R.Torgerson and S.L.Williams, "TheUnified Power Flow Controller: A new Approach to Power Transmission Control", IEEE Trans. Power Delivery, vol. 10, no.2, pp. 1085-1097, Apr 1995

[2]   Enrique, A., C.R. Fuerte-Esquivel, H. Ambriz-Perez andC. Angeles-Camacho, 2004. FACTS Modelling and Simulation in Power Networks. West Sussex,England: John Wiley & Sons Ltd., pp: 200-307.

[3]   Noroozian, M., L. Angquist, M. Ghandhari andG. Andersson, 1997. Use of UPFC for  optimal poweflow control. IEEE Trans. Power Delivery, 12:1629-1634.

[4]   Narain, G.H. and G. Laszlo, 2000. Understanding FACTS: Concepts and technology of  flexible AC transmission systems. NewYork, NY: The Institute of Electrical and Electronics Engineers, pp: 297.

[5]   Nabavi-Niaki and M. R. Iravani, "Steady-state and dynamic models of unified power flow controller (UPFC) for power system studies,"*IEEE Trans. Power Syst.*, vol. 11, Nov. 1996, pp. 1937–1943.

[6]   I. Papic, P. Zunko, D. Povh and W. Weinhold, "Basic control of unified power flow controller", IEEE Trans. on PS, Vol. 12, No. 4, pp 1734-1739,1997.

[7]   Bésanger Y., Passelergue J.C., Hadj-Said N., "Improvement of power system performance by inserting FACTS devices", in Proc. IEE AC and DC Power Transmission Conf., London, UK: 263-268, 1996.

## Contents :

# Fuzzy logic Technique Based Speed Control of a Permanent Magnet Brushless DC Motor Drive

Shantanu Kumar Lakhanwal[1], Amandeep Gill[2]

[1]*Department of Electrical Engg.,SKIT Jaipur, INDIA)*
[2] *Department of Electrical Engg.,JECREC University, India*

***Abstract:*** *This paper presents an analysis by which the dynamic performances of a permanent magnet brushless dc (PMBLDC) motor drive with different speed controllers can be successfully predicted. The control structure of the proposed drive system is described. The dynamics of the drive system with a classical proportional-integral-derivative (PID) and Fuzzy-Logic (FL) speed controllers are presented. The simulation results for different parameters and operation modes of the drive system are investigated and compared. The results with FL speed controller show improvement in transient response of the PMBLDC drive over conventional PID controller. Moreover, useful conclusions stemmed from such a study which is thought of good use and valuable for users of these controllers*
***Keywords:*** *Brushless motor, derivative controller, fuzzy logic controller, integral controller,proportional controller.*

## I. INTRODUCTION

Brushless dc motors (BLDCM) provide high efficiency, reliability, ruggedness and high precision of control when compared to conventional motors. It has the best torque vs. weight or efficiency characteristics. They are used in military, grinding, aircraft, automotive applications, communications equipment etc. Brushless dc motors (BLDCM) have been desired for small horsepower control motors such as: heating, ventilation, and air conditioning systems to achieve great energy saving effects for partial loads by lowering motor speeds. In addition, BLDCM have been used as variable speed drives in wide array of applications due to their high efficiency, silent operation, compact form, reliability, and low maintenance [1]. BLDCM drives were widely employed in industry due to their intrinsic robustness and high torque-to-weight ratio. The availability of cheap embedded processing power in recent years paved the way for the widespread use of sensor less control techniques; the removal of speed and position sensors leads to substantial increase of robustness and cost savings [2]. Due to the high torque to volume ratio of BLDCM, it dominates for High Performance Drives (HPD) applications, such as robotics, guided manipulation and dynamic actuation, the precise rotor movement over a period of time must be achieved. A multi-robot system performing a complementing function must have the end effectors move about the space of operation according to a pre- selected time tagged trajectory. Also, the Brushless dc motor, as the name implies, has no brushes. This is an essential requirement for several industrial applications such as airplane actuation, food and chemical industries. This must be achieved even when the system loads, inertia and parameters are varying. To do this, the speed control strategy must be adaptive, robust, accurate, and simple to implement [3].Conventional feedback controllers, such as the PID or the linear quadratic, need accurate mathematical models describing the dynamics of the system under control. This can be a major limiting factor for systems with unknown varying dynamics. Even if a model can be obtained for the system under control, unknown conditions such as saturation, disturbances, parameter drifts, and noise may be impossible to model with acceptable accuracy. For most of the basic electric drives applications, these unknown conditions in addition to the system nonlinearities can be ignored, but it may lead to unacceptable tracking performance. High accuracy is not usually imperative [4]. Some adaptive control techniques, such as the variable structure and the self-tuning, do not need a model for system dynamics. The dynamic model is, rather, developed based on the on-line input/output response of the system under control [5].The F L C (Fuzzy Logic Controller) has several key features like its robustness, fault tolerant, noise free and capability of generating a nonlinear mapping between the inputs and outputs of an electric drive system without the need for a predetermined model makes it suitable for speed control of BLDC motors under varying load torque.

## II.    Analysis Of P MBLDC Drive

The flux distribution in PM brushless dc motor is trapezoidal; therefore, the d-q rotor reference frames model developed for the PM synchronous motor is not applicable. Given the non sinusoidal flux distribution, it is prudent to derive a model of the PMBDCM in phase variables. The derivation of this model is based on the assumptions the induced current in the rotor due to stator harmonics fields are neglected and iron and stray losses are also neglected .Damper winding are not usually a part of the PMBDCM[4].Damping is provided by the inverter control. The motor is considered to have three phase, even thought the derivation procedure is valid for any number of phases.

The coupled circuit equation of the stator winding in terms of motor electrical constant are

$$\begin{bmatrix} v_{as} \\ v_{bs} \\ v_{cs} \end{bmatrix} = \begin{bmatrix} R_s & 0 & 0 \\ 0 & R_s & 0 \\ 0 & 0 & R_s \end{bmatrix} \begin{bmatrix} i_{as} \\ i_{bs} \\ i_{cs} \end{bmatrix} + p \begin{bmatrix} L_{aa} & L_{ab} & L_{ac} \\ L_{ba} & L_{bb} & L_{bc} \\ L_{ca} & L_{cb} & L_{cc} \end{bmatrix} \begin{bmatrix} i_a \\ i_b \\ i_c \end{bmatrix} + \begin{bmatrix} e_{as} \\ e_{bs} \\ e_{cs} \end{bmatrix} \qquad (1)$$

Where $R_s$ is the stator resistance per phase, acquired to be equal for all three phases. The induced emf $e_{as}, e_{bs}$ and $e_{cs}$ are all assumed to be in geometric shape of trapezoidal, as shown in fig.
Where $E_p$ is the peak value, derived as

$$E_p = (B*l*v) N=n (B1r\omega_m) =N\phi_a \omega_m = \lambda_p \ \omega_m \qquad (2)$$

The instantaneous induced emfs can be written from equation (2.2)

$$e_{as} = f_{as} (\theta_r) \lambda_p \ \omega_m \qquad (3)$$
$$e_{bs} = f_{bs}(\theta_r) \lambda_p \ \omega_m \qquad (4)$$
$$e_{cs} = f_{cs} (\theta_r) \lambda_p \ \omega_m \qquad (5)$$

Where the functions $f_{as}(\theta_r)$, $f_{bs}(\theta_r)$ and $f_{cs}(\theta_r)$ have the same shape as $e_{as}, e_{bs}$ and $e_{cs}$
With a maximum magnitude of ±1.The induced emfs do not have sharp edged corners, as is shown in trapezoidal functions, but rounded edges. The emfs the result of the flux-linkages derivatives and the flux linkage are continuous functions. Fringing also makes flux density functions smooth with no abrupt edges. The electromagnetic torque then is

$$T_e = \lambda_p [f_{as}(\theta_r) i_{as} + (\theta_r) i_{bs} + f_{cs}(\theta_r) i_{cs}](N.m) \qquad (6)$$

the same signs as the stator phase current in the motoring mode ,but opposite sign in the regeneration mode .The result of such sigh relationship is simplification of torque command as,

$$T_e^* = 2\lambda_p \ i_p^* \qquad (7)$$

The individual stator-phase current commands are generated from the current magnitude command and absolute rotor position. These commands are amplifier through the inverter by comparing them with their respective current in the stator phases. Only two phase current are necessary in the balanced three-phase system to obtain the third phase current, since the sum of the three-phase current is zero

## III.    Speed Control

This section explores the controller schemes applied to a PMBLDC motor with a trapezoidal back emf for providing a satisfactory speed control performance. It will examine the PMBLDC motor with PID and FL controllers.

### 3.1 PID Controller

The PID controller calculation algorithm involves three separate constant parameters, and is accordingly sometimes called three-term control: the proportional, the integral and derivative values are denoted by P, I, and D. By putting these values can be interpreted in terms of time: P depends on the present error, I on the collection of past errors, and D is a anticipation of future errors, grounded on current rate of change [7]. The weighted down sum of these three actions is used to adjust the process via a control element such as the position of a control assess, a damper, or the power furnished to a heating element. The response of the controller can be described in terms of the responsiveness of the controller to an error, the stage to which the controller overshoots the set point, and the stage of system oscillation. Some applications may

involve using only one or two actions to provide the appropriate system control. This is accomplished by setting the other parameters to zero. PID controller will be called by PI, PD, P or I controller in the absence of the various control actions [16]. PI controllers are reasonably common, since derivative action is sore to measurement noise, whereas the absence of an integral term may prevent the system from reaching its target value due to the control action.

The PID controller is calculated using the transfer function

$$G_c \ s = k_p (1 + \frac{1}{T_{i\ s}} + T_d s)$$

(8)
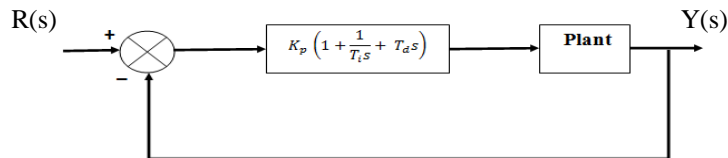


Fig.1 Schematic Block Diagram of Speed Controller

**3.2. Fuzzy Logic Controller Theory**

Fuzzy logic is a mathematical environment, based on fuzzy set theory, which admits for degrees of truth or falsehood". As opposition to "binary logic" which gives a confirmation that must be either true or false. 'Fuzzy logic' conciliates the possibility that the logic can be exactly false. The degree of truth or falsehood in the affirmation can be both qualitatively and quantitatively explained. As given above fuzzy logic deals with dubiety, ambiguity and imprecision, which exists in difficult real world troubles specifically in engineering [22]. Fuzzy logic is multi-valued logic basically dealing with uncertainty and approximate reasoning.
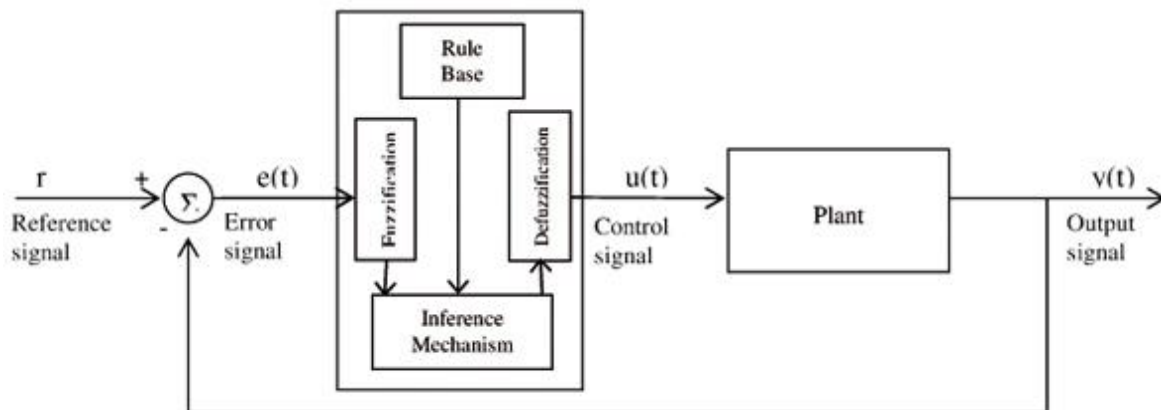


Fig.2 Block diagram of fuzzy logic controller

The fuzzy membership function for the input variable and output variable are described as follows: Positive: PB, Negative Big: NB Positive Medium: PM, Negative Medium: NM Positive Small: PS, Negative Small: NS and Zero: ZE

The triangular shaped functions are picked out as the membership functions due to the output best control performance and simplicity The membership function for the speed error and the change in speed error and the change in torque reference current are shown in Fig. 4.5 .For all variables seven levels of fuzzy membership function are used. TABLE 1 shows the 7×7 rule base table that is used in the system.

The processing stage is based on a collection of logic rule in the form of IF-THEN statements. In practice, the fuzzy rule sets usually have several antecedents that are combined using fuzzy operators, such as AND, OR, and NOT. For example: IF e = ZE AND delta = ZE THEN output = ZE. The results of all the rules that have fired are "defuzzified" to a crisp value by one of several methods. There are dozens in theory, each with various advantages and drawbacks.

The "centroid method" is very popular, in which the "center of mass" of the result provides the crisp value. Another approach is the "height" method, which takes the value of the biggest contributor. The centroid method favors the rule with the output of greatest area, while the height method obviously favors the rule with the greatest output value.

Table 1

| E/ΔE | NB | NM | NS | ZE | PS | PM | PB |
|------|----|----|----|----|----|----|----|
| NB | NB | NB | NB | NB | NM | NS | ZE |
| NM | NB | NB | NB | NM | NS | ZE | PS |
| NS | NB | NB | NM | NS | ZE | PS | PM |
| ZE | NB | NM | NS | ZE | PS | PM | PB |
| PS | NS | NS | ZE | PS | PM | PB | PB |
| PM | NS | ZE | PS | PM | PB | PB | PB |
| PB | ZE | PS | PM | PB | PB | PB | PB |

## IV.   Simulation And Results

Several results were simulated to evaluate the performance of the proposed FLC-based PMBLDC drive system. The effectiveness of the proposed FL controller is investigated and compared to the conventional PI controller through the following results. The speed, stator current, and torque responses are observed under different operating conditions such as change in command speed, step change in load, etc.

The motor speed, current, and torque responses of the PMBLDC drive with PI and FL controllers are shown in Fig. The results show the starting performance as well as the response with a step change in reference speed. The drive system was unloaded with a speed reference set at 3000 rpm. Consequently, the reference speed is increased to 8000 rpm motor speed with FL controller converges to the reference value within 0.2 s without any overshoot/undershoot and with zero steady- state error. Fig.3-12 shows the speed, current, and torque responses of the PMBLDC drive under loading conditions with PI and FL controllers. It is shown that the proposed drive with FL controller is also capable of following the reference speed very quickly with zero steady-state error and almost without any overshoot/undershoot when the motor is loaded. From these results it is concluded that the FL controller ensures better damping of speed, current, and torque.
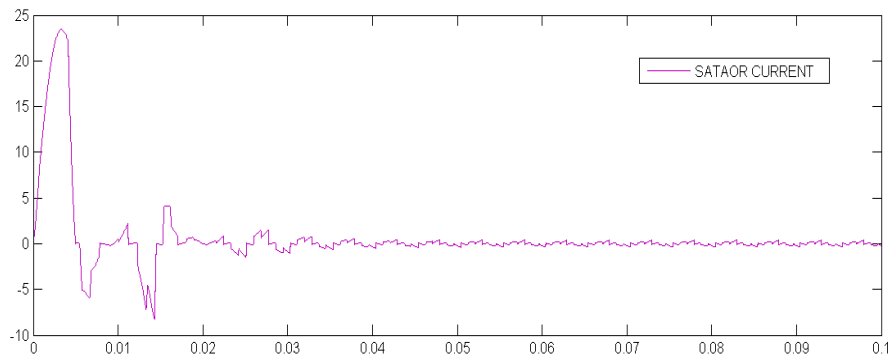


Fig. 3 Waveform of the stator current (phase a) of BLDCM
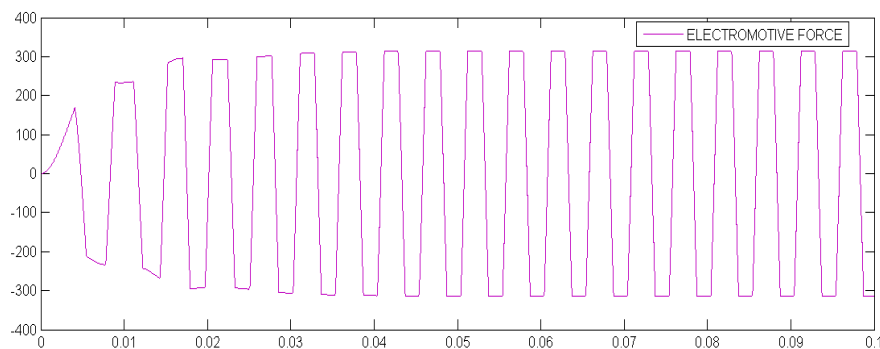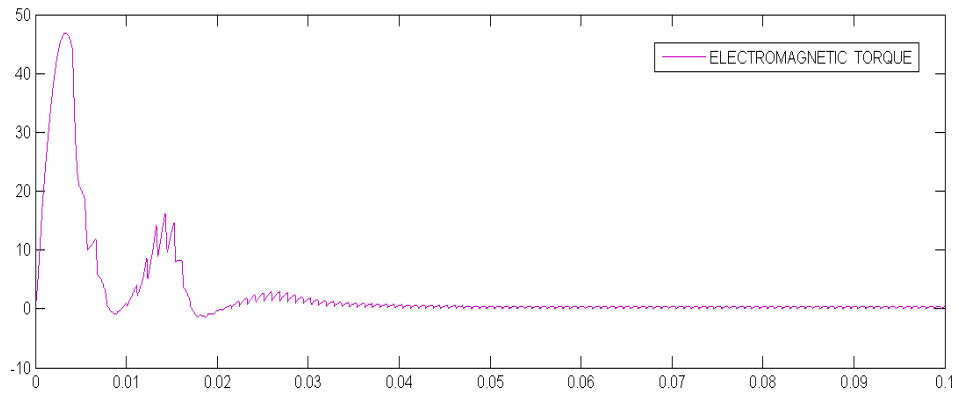


Fig.4  Waveform of Stator back EMF

Fig.5 Waveform of the Electromagnetic Torque Te (Nm) of BLDCM
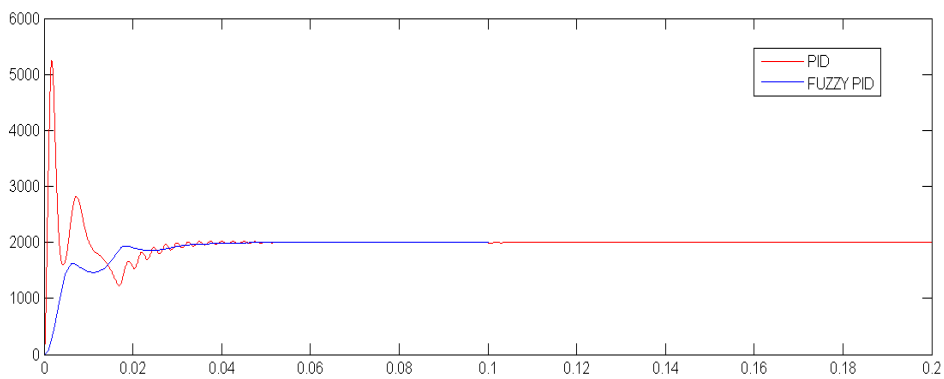


Fig. 6  Waveform of the BLDCM at  2000 rpm
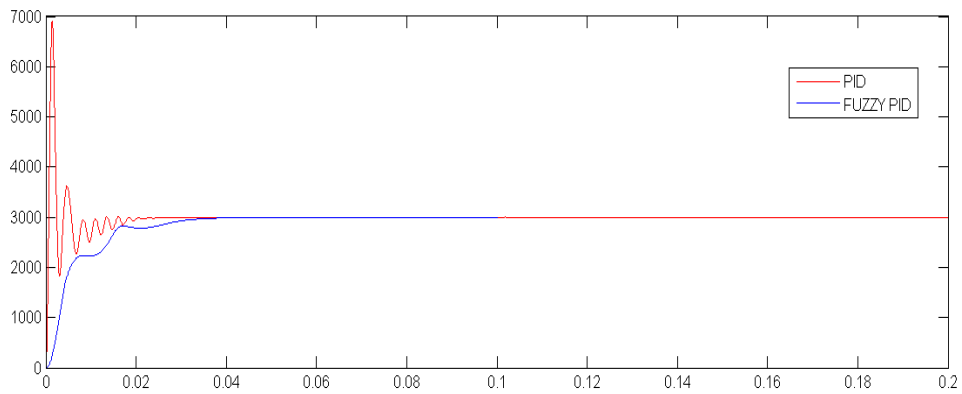


Fig.7 Waveform of the BLDCM at  3000 rpm
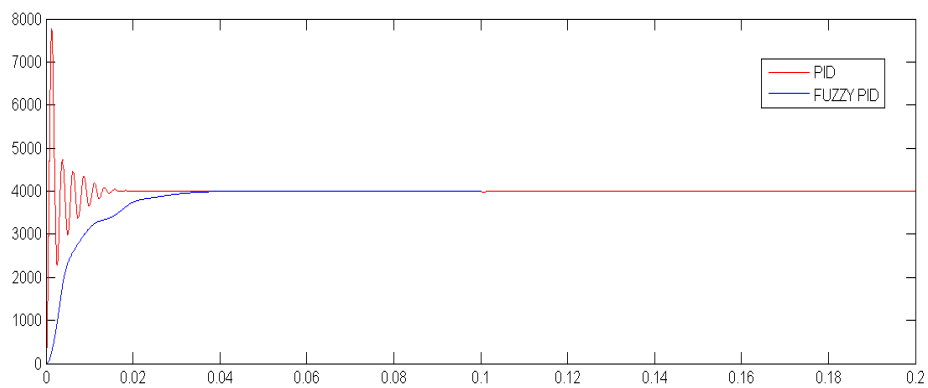


Fig. 8 Waveform of the BLDCM at 4000 rpm
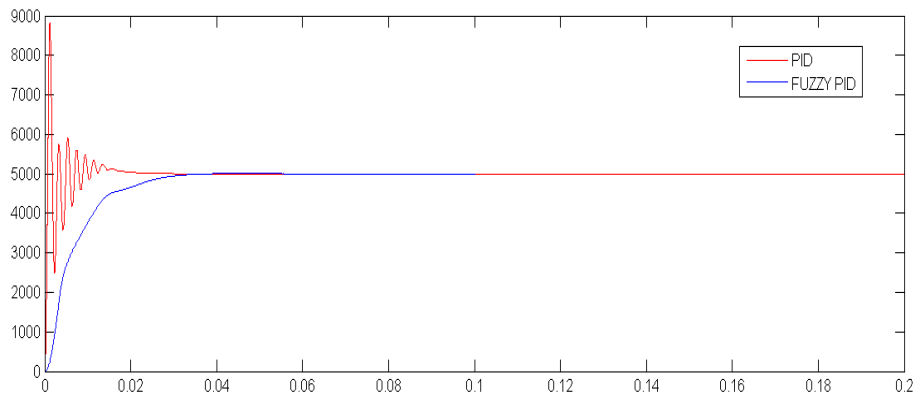
Fig.9 Waveform of the BLDCM at 5000 rpm
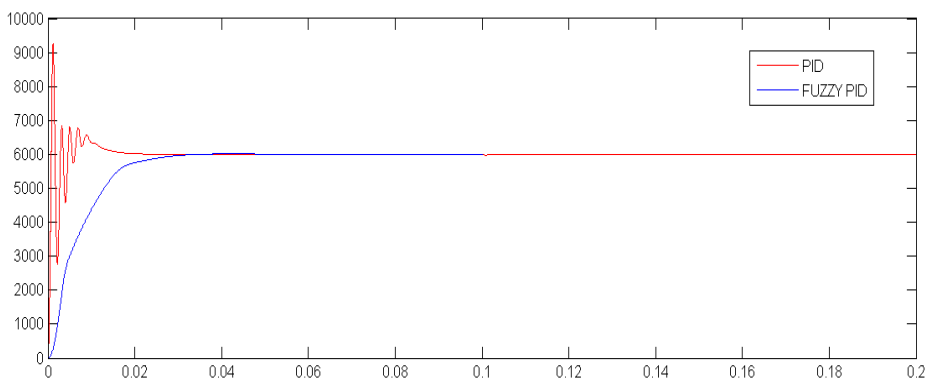

Fig. 10 Waveform of the BLDCM at  6000 rpm
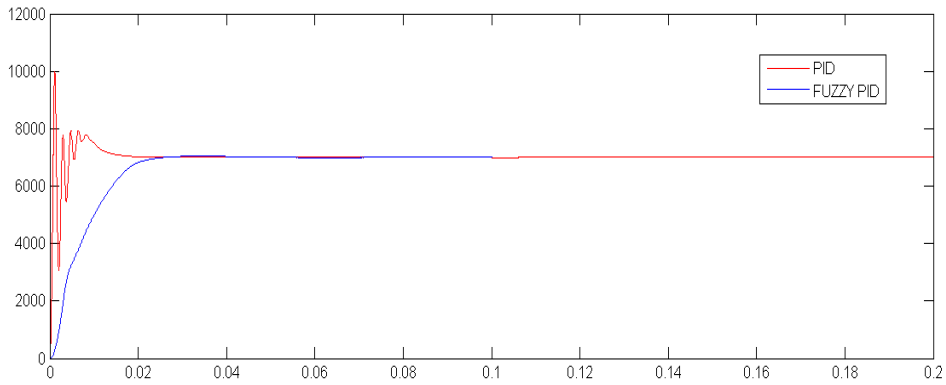

Fig. 11Waveform of the BLDCM at 7000 rpm
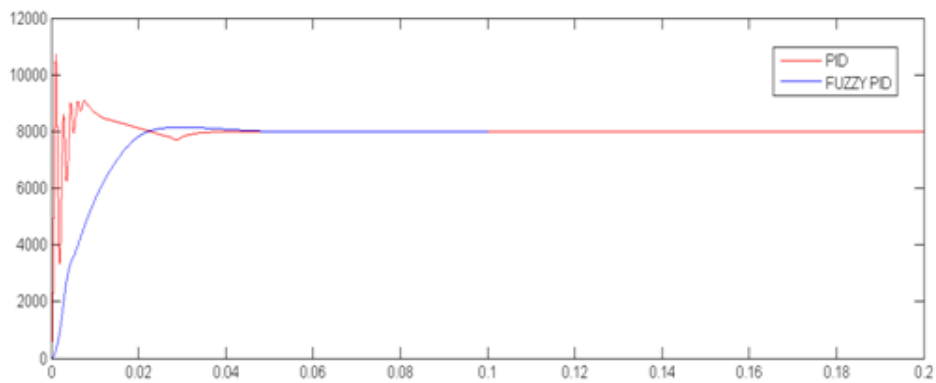

Fig. 12 waveform of the BLDCM at 8000 rpm

Oscillations over the whole speed range. This feature is valid for various operating conditions of the drive system, for speed reference changes as well as for load torque changes. It confirms that the FL controller is more robust to changes of operating condition of the drive system.

## V. CONCLUSION

A fuzzy logic controller (FLC) has been used for the speed control of PMBLDC motor drive and outcome of a fuzzy controller is presented. The modeling and simulation of the complete drive system is explained in this paper. Effectiveness of the model is established by performance prediction over a wide range of operating conditions. A performance comparison between the fuzzy logic controller and the conventional PID controller has been analyzed out by simulation runs confirming the validity and superiority of the fuzzy logic controller. For implementing the fuzzy logic controller, tuning of gains to be adjusted such that manual tuning time of the classical controller is significantly reduced. The performance of the PMBLDCM drive with reference to PI controller and FLC controller have been experimentally verified with conventional PID controller using DSP processor. Fuzzy logic speed controller improves the performance of PMBLDC Drive.

## REFERENCES

**Journal Papers:**

[1] Tolliver.C.L, Shieh.L.S, Ali.W.H, Zhang.Y,and, Akujuobi.C.M ,"Load disturbance resistance speed controller design for permanent magnet synchronous motor(BLDC)," IEEE Transition. Ind. Electron., vol. 53, no. 4, pp. 1198– 1207, August. 2006.

[3] Rahman.M.A,"Special section on Permanent magnet motor drives; Guest editorial," IEEE, Trans. on Ind. Electronics, vol. 43, no. 2, pp. 245,1996.

[5] Wang.X.Y, Chau.K.T Jiang.J.Z. Chen.G.H, and Chan.C.C, "A novel poly phase multi pole square wave permanent magnet motor drive for electric vehicles", IEEE, Transactions on Industry App., vol. 30, no. 5, pp.1258-1266, 1994.

[8] Pillay. P and Krishnan. R, "Application Characteristics of Permanent Magnet Synchronous and Brushless dc Motors BLDCM for Servo Drives," IEEE Trans. Industrial. Application., vol. 27, no.5, pp. 986-996 September./October. 1991.

[9] Chan. C. and Cheng. M, "Design and analysis of a new doubly salient permanent magnet motor," IEEE Trans. Magazine., vol. 37, pp. 3012–3020, July 2001.

**Proceedings Papers:**

[2] Concari.C, Torni.F ,"Sensor less control of BLDC motor at Lower Speed based on differential back emf measurement ",IEEE, Conference on energy conversion congress & exposition, pp. 1772-1777, sept.2010.

[4] Hwang.R.C, Yu.G.R, "Optimal PID Speed control of BLDC motor Iqr approach", IEEE, Conference on system, man & cybernetics, vol.1, pp. 473-478, Oct.2004.

[6] Bakly.A.E,Fouda.A and Sabry.W. , "A Proposed DC Motor Sliding Mode Position Controller Design using Fuzzy Logic and PID Techniques," ASAT, 13th International Conf. on Aerospace Sciences & Aviation Technology, pp 13-14May 2009.

[7] Baek.S and Kuc.T., " An Adaptive PID Learning Control of DC Motors" IEEE, Conference on System, Man, and Cybernetics, vol. 3,pp 2877 – 2882, Oct 1997.

[10] Fallahi.M and Azadi.S.," Fuzzy PID Sliding Mode Controller Design for the position control of a DC Motor",IEEE, International Conf. on Education Technology and Computer, pp 73-77, April 2009.

## I. FIGURES AND TABLES
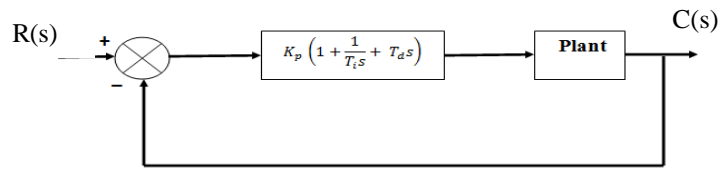


Fig.1 Schematic Block Diagram of Speed Controller
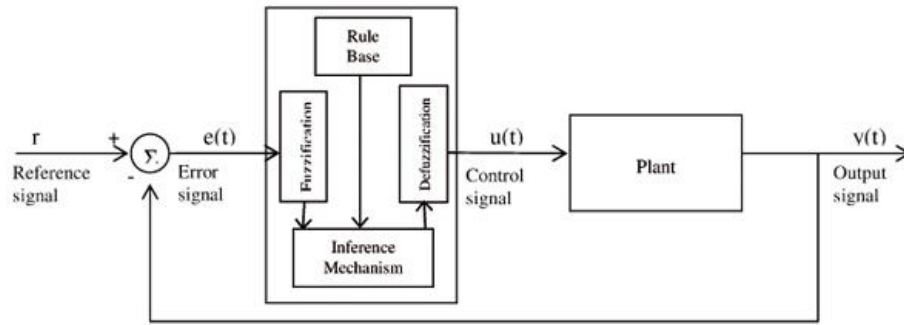


Fig.2 Block diagram of fuzzy logic controller
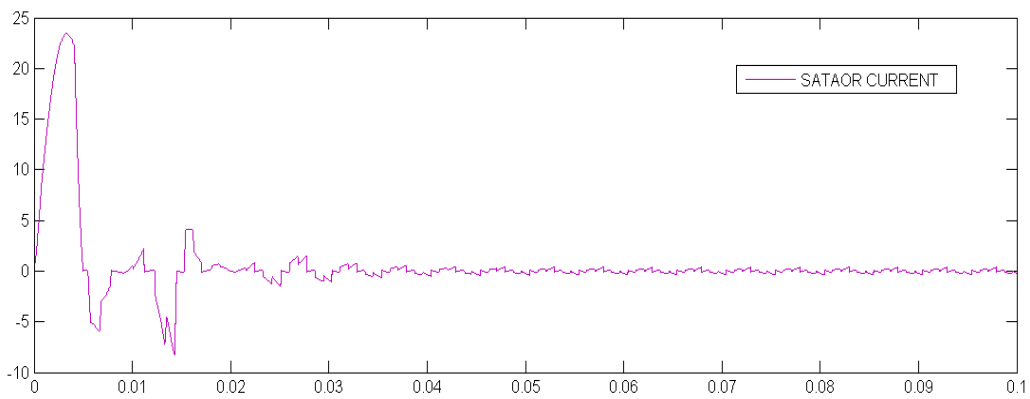


Fig. 3 Waveform of the stator current (phase a) of BLDCM
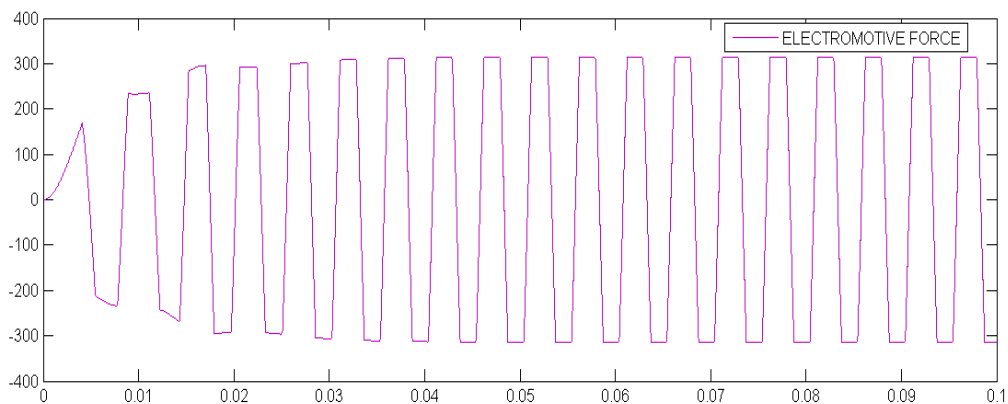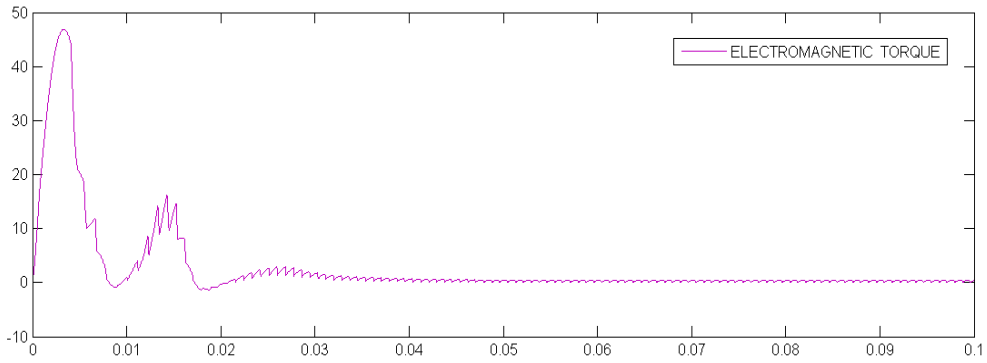


Fig.4  Waveform of Stator back EMF

Fig.5 Waveform of the Electromagnetic Torque Te (Nm) of BLDCM
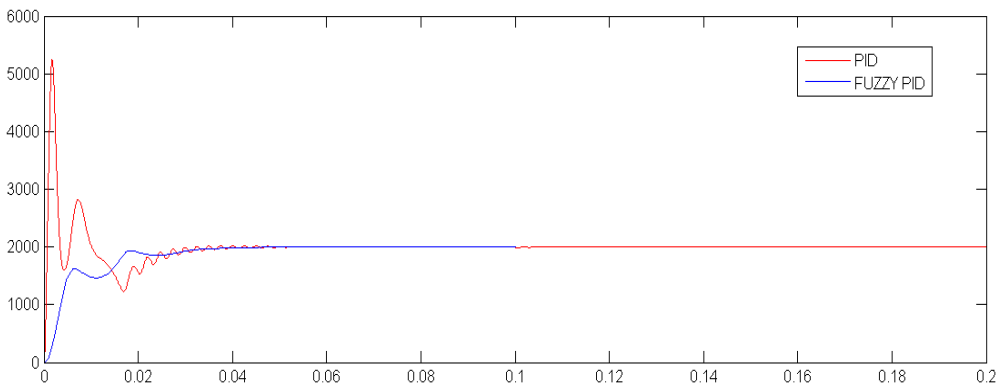


Fig. 6  Waveform of the BLDCM at  2000 rpm
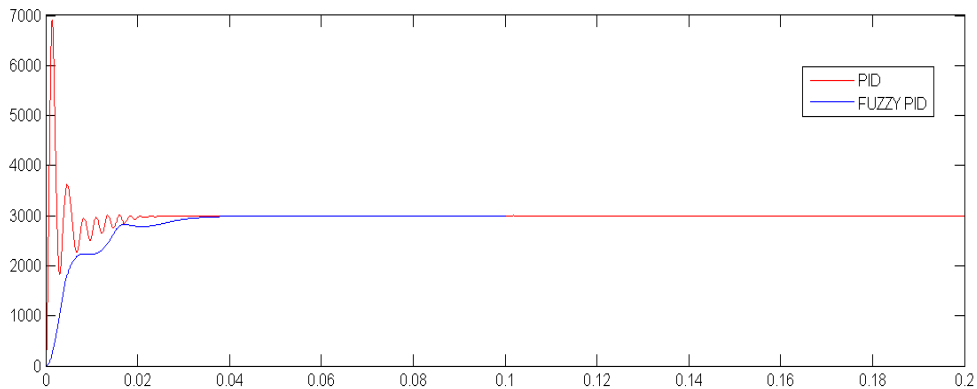


Fig.7 Waveform of the BLDCM at  3000 rpm
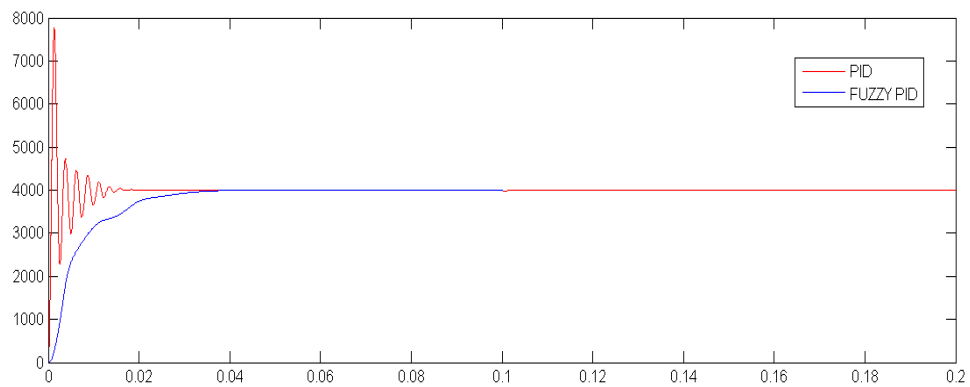


Fig. 8 Waveform of the BLDCM at 4000 rpm
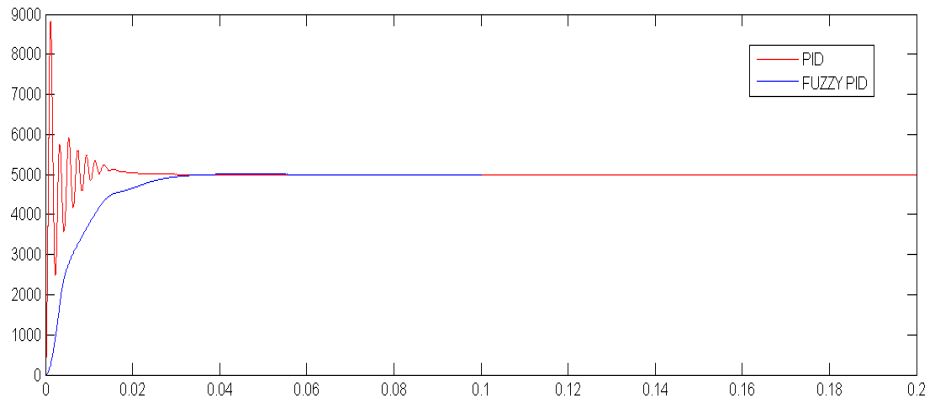
Fig.9 Waveform of the BLDCM at 5000 rpm
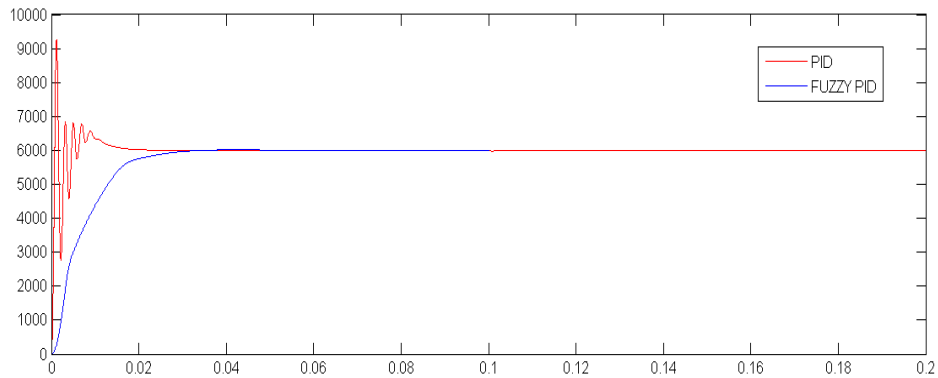

Fig. 10 Waveform of the BLDCM at 6000 rpm
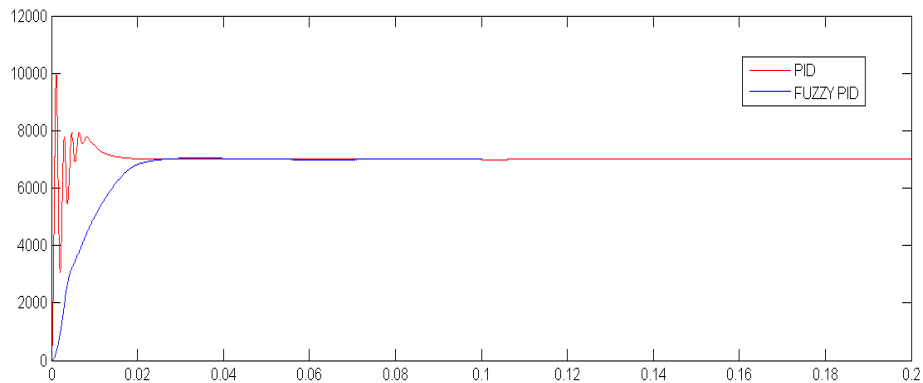

Fig. 11Waveform of the BLDCM at 7000 rpm
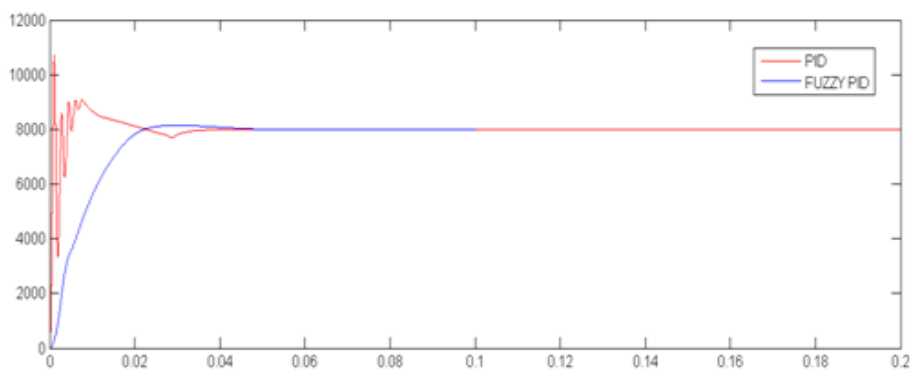

Fig. 12 waveform of the BLDCM at 8000 rpm
Table 1

7×7 Rule base table for Fuzzy Logic Controller

| E/CE | NB | NM | NS | ZE | P | P | PL |
|------|----|----|----|----|-----|-----|-----|
| NB | NB | NM | NS | NS | NS | NS | ZE |
| NM | NM | NM | NS | NS | NS | ZE | ZE |
| NS | NS | NS | NS | NS | ZE | NS | PM |
| ZE | NS | NS | NS | ZE | PS | PM | PM |
| PS | NS | NS | ZE | PS | PS | PS | PS |
| PM | NS | ZE | NS | PM | PS | PL | PL |
| PL | ZE | PS | PM | PL | PL | PL | PL |

Table 2
Comparison between Rise time and maximum peak overshoot of FLC and PID controller

| controllers | Speed (rpm) | Rise Time (sec) | rcentage ershoot |
|-------------|-------------|-----------------|-------------------|
| gler- Nicholus based PID Controller | 2000 | 4.03e-4 | 162.50 |
| | 3000 | 4.05e-4 | 130.49 |
| | 4000 | 4.44e-4 | 94.03 |
| | 5000 | 4.35e-4 | 76.40 |
| | 6000 | 4.70e-4 | 56.85 |
| | 7000 | 4.90e-4 | 42.85 |
| | 8000 | 4.90e-4 | 33.75 |
| tuned Fuzzy logic PID controller | 2000 | .01484 | 0.00556 |
| | 3000 | .01365 | .02366 |
| | 4000 | .01628 | 0.05862 |
| | 5000 | .01373 | 0.1736 |
| | 6000 | .01366 | 0.2720 |
| | 7000 | .01403 | 0.6165 |
| | 8000 | .01431 | 1.7975 |

Table 3
Ziegler & Nichols tuning parameters

| Type of Controller | $k_p$ | $T_i$ | $T_d$ |
|--------------------|-------|-------|-------|
| P | T/L | □ | 0 |
| PI | 0.9 T/L | L/0.3 | 0 |
| PID | 1.2 T/L | 2L | 0.L |

Table 4
Brushless DC motor Parameters

| | |
|---|---|
| Power input | 1 KW |
| No. of Poles | 4 |
| No. of Phases | 3 |
| Type of connection | star -delta |
| Supply voltage ($V_{dc}$) | 500volt |
| Rated speed | 3000 RPM |
| Stator phase resistance | 2 .8750ohm |
| Stator phase Inductance | $8.5 \times 10^{-3}$Henry |
| Flux linkage established by magnet | 250V.s |
| Inertia | $.8 \times 10^{-3}$(Kg.m^2) |
| Friction factor | 0.3(N.m.s) |

Table 5
FLC(Fuzzy Logic Controller) Parameters

| FLC Type | Mamdani |
|---|---|
| Number of Inputs | 2 |
| Number of outputs | 3 |
| Number of Rules | 49 |
| AND Method | Min. |
| OR Method | Max. |
| Defuzzification Method | Height Defuzzification |

**INDENTATIONS AND EQUATIONS**

$$\begin{bmatrix} v_{as} \\ v_{bs} \\ v_{cs} \end{bmatrix} = \begin{bmatrix} R_s & 0 & 0 \\ 0 & R_s & 0 \\ 0 & 0 & R_s \end{bmatrix} \begin{bmatrix} i_{as} \\ i_{bs} \\ i_{cs} \end{bmatrix} + p \begin{bmatrix} L_{aa} & L_{ab} & L_{ac} \\ L_{ba} & L_{bb} & L_{bc} \\ L_{ca} & L_{cb} & L_{cc} \end{bmatrix} \begin{matrix} i_a \\ i_b \\ i_c \end{matrix} + \begin{bmatrix} e_{as} \\ e_{bs} \\ e_{cs} \end{bmatrix}$$
(1)

$$E_p = (B*l*v) \ N=n \ (B1r\omega_m) = N\phi_a \ \omega_m = \lambda_p \ \omega_m \tag{2}$$

$$e_{as} = f_{as}(\theta_r) \ \lambda_p \ \omega_m \tag{3}$$

$$e_{bs} = f_{bs}(\theta_r) \ \lambda_p \ \omega_m \tag{4}$$

$$e_{cs} = f_{cs}(\theta_r) \ \lambda_p \ \omega_m \tag{5}$$

$$T_e = \lambda_p[f_{as}(\theta_r)i_{as} + (\theta_r)i_{bs} + f_{cs}(\theta_r)i_{cs}] \ (N.m) \tag{6}$$

$$T_e^* = 2\lambda_p \ i_p^* \tag{7}$$

$$G_c \ s = k_p(1 + \frac{1}{T_i \ s} + T_d s)$$

(8)

# Power Quality Improvement Using FACT Devices

Aparna .A[1], Athira. M[2]

[1]*Student, Department Of Electrical &Electronics Engineering, ASIET, MG University, India*
[2]*Assistant Professor, Department of Electrical &Electronics Engineering, ASIET, MG University, India*

***Abstract:*** *Improvement of power quality has to be treated as a matter of at most importance in the open market economy due to the increased use of non linear loads. Several devices have been used to mitigate the power quality problems. Now a days researchers are concentrating on the use of FACT devices to overcome power quality issues. Unified Power Quality Conditioner is one among such FACT devices upon which this paper has concentrated for mitigating the Power Quality problems. Here a 3 phase 3 wire UPQC is realised using MATLAB/SIMULINK to mitigate voltage sag and swell as well as to maintain sinusoidal voltage and current at PCC irrespective of load dynamics.*

***Keywords****: UPQC, Fact devices, Power Quality, Non-linear load, PCC.*

## I. INTRODUCTION

The Power Quality is a factor of great concern in day today life. The increased use of electronic devices may cause pollution in the supply. The industrial loads are also very much sensitive to the voltage variations[1]. This may result in unsatisfactory performance of the system. Also there are necessities in medical field where the quality of supply matters. The variations in supply voltage may not be acceptable to a small extent, due to the high risk of rescuing a life. Another major area where the quality of supply matters is in research labs. For obtaining accurate output the quality of power has to be maintained at the supply side.

Several devices assure to mitigate power quality issues. Some of such devices includes passive filters, active filters and hybrid filters. But these devices have their own limitation[2]-[3]. Hence the use of CUSTOM power devices came prominent to mitigate power quality issues. Among them no devices can assure to mitigate more than two power quality problem at a time. Under such a circumstance, Unified Power Quality Conditioner (UPQC), which is a combination of DVR and STATCOM emerged by promising to maintain the quality of power at PCC, eliminates voltage distortions, current distortions, improvement of power factor and reduction in harmonics.

This paper includes the simulation of a three phase three wire UPQC. The simulation output reveals the effective performance of the system against voltage sag and swell. Also the system performance against the effect of load dynamics was satisfactorily evaluated.

## II. SYSTEM OVERVIEW

The Unified Power Quality Conditioner (UPQC) is a multifunction conditioner. It comes under second generation of FACT devices. It mainly concentrates on improving the power quality at the utility grid. The UPQC consists of a series inverter and a shunt inverter which are linked by a dc link capacitor[4]-[6]. It also consists of series transformers and low pass filters. The role of LP filters is to attenuate the high frequency signals at the output of series converter that are generated by high frequency switching. The basic configuration of UPQC is given below in figure 1.
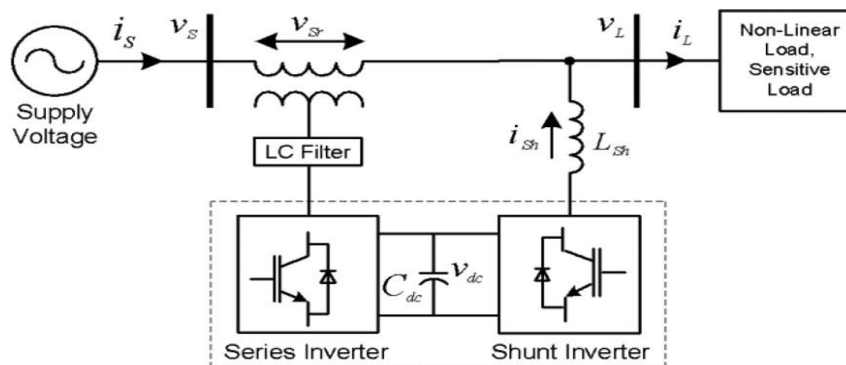


Figure:1 Block diagram of Unified Power Quality Conditioner

Where,   i$_s$=   Source current
v$_s$ =  Source voltage
v$_{sr}$= Voltage across series inverter
v$_l$ =  Load voltage
i$_l$ =   Load current
i$_{sh}$ =  Current injected by shunt inverter
C$_{dc}$ =  DC link capacitor
v$_{dc}$ = DC link voltage.

**Source:** The AC loads or equipments on the power system is supplied by single or three phase source of power. Power quality related problems are similar for both these supply systems except an additional voltage unbalance compensation is needed in case of three phase systems. Here a three phase supply of 415V and frequency 50 Hz is used for carrying out the simulations.

**Load :**  The use of non linear loads are increasing extensively now a day. They are responsible for introducing harmonics in the system which have their own adverse effects including power factor reduction. A 3 phase diode rectifier is used as the load in this paper to carry out the simulations. Also, later a linear load is being introduced into the system in order to validate the system performance against load dynamics.

**Series inverter:** Series inverter is connected in series with the supply and usually mitigates voltage distortions. It is also capable of handling supply voltage flickers and load voltage imbalance in the system. It is responsible for mitigating voltage sag in the system. The series inverter in generally is a DVR(Dynamic Voltage Restorer) which is connected in series with the system. The gating signals for triggering of series inverter are developed by comparing the reference signal with the load voltage. The reference signal is generated by comparing the voltages at the load and the source.

**Shunt inverter:** Shunt inverter is connected in shunt with the AC line. It usually deals with current distortions, improvement of power factor and reactive power compensation. It is also responsible for DC voltage regulation whereby we can achieve reduced DC capacitor rating. Inorder to provide electrical isolation of UPQC converters high pass filters are installed at the output of shunt inverter for quenching the current ripples.

In this paper, a three phase three wire UPQC is realised and the effect of load dynamics is studied. For this purpose a linear and a non-linear load is supposed to be injected to the system. Also the system response in mitigating the voltage sag as well as swell with a non linear load  is also simulated.

### III.   Design Of Controllers
The major criteria in UPQC designing includes the designing of series inverter control, dc link voltage control and designing of shunt inverter control[7]-[8].

**A. Control of Series Inverter**
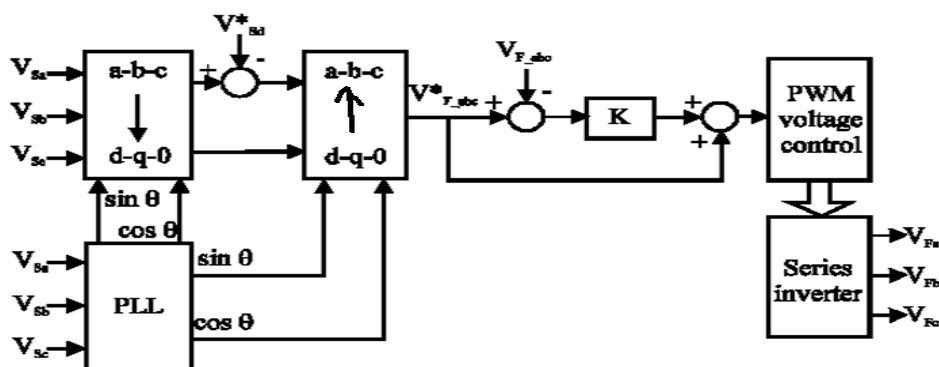


Figure 2. Series inverter control

The compensation of the entire voltage distortion is obtained by the proper controlling of the series inverter. The controlling of the series inverter also ensures a 3 phase balanced sinusoidal voltage.

The synchronous reference frame theory is applied in the controller by which the desired value of load phase voltage in d-q axis is compared with the load voltage for generating the reference signal. The response of the series inverter is optimized with the help of SPWM method. Figure 2 ,above shows the controller block of series inverter.

**B. Control of Shunt Active Filter**

Figure 3 shows the control diagram of the shunt inverter.The sine and cosine functions are extracted from the supply voltage using PLL. The measured load currents are transferred to dqo frame by the dqo conversion block. $I_d$ is considered to be the active part and $I_q$ is taken as the reactive part of the current. The role of PI controller is to track the difference which is taken as the error between the measured value and desired value of capacitance voltages. Thus generated reference current is converted back into abc frame with the help of dqo to abc transformation block. This is now compared with the shunt inverter output current and required pulses for switching the inverter gates are produced.

.
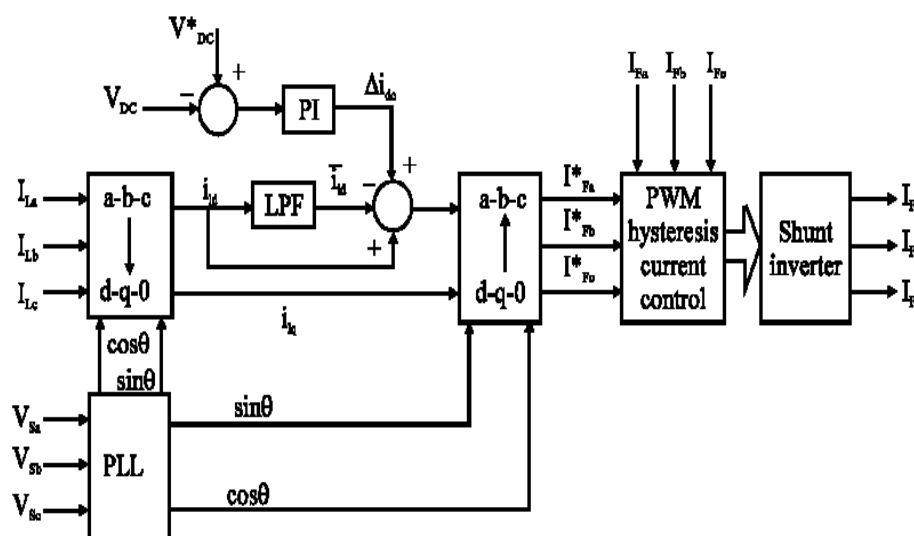


Figure 3. Control diagram of shunt inverter.

**C. Control of DC link voltage**

The DC link voltage is controlled by tracking the error that exists between the measured and desired value of the capacitance voltage. The control block of DC capacitance is given below in figure 4.
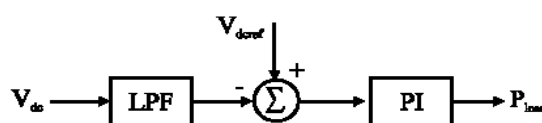


Figure 4. Single phase nine level inverter

It plays important role in control system DC voltage response is taken by the proper tuning of the PI controller. Increase in proportional gain leads to the instability of control system where as its reduction may cause decrease in the response speed of the control. In a similar way since the integral gain is responsible for correcting the steady state voltage error, its increase may results in correction of error at a faster rate. But it should be noted that too much of increase in integral gain ends in overshoot in the system response

## IV.  Simulation Results

Simulations have been performed in MATLAB/SIMULINK based on the Figure 1. The system parameters are chosen as given in table 1. Here the results are concentrated to the response of voltage and current waveforms at the point of common coupling. In the basic system simulink model due to the affect of nonlinear load applied the voltages and currents at PCC were found to be distorted. The system simulink model and their corresponding waveforms are given are given in figure 5 and figure 6 respectively[9]-[13].
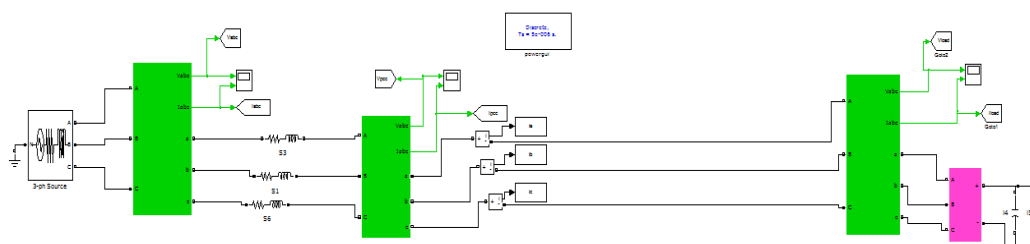
Figure 5. Simulink diagram of basic system
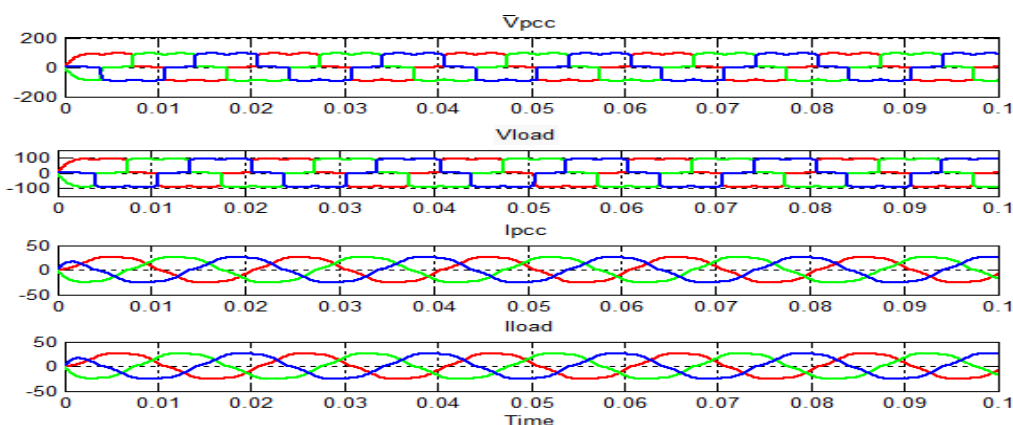


Figure 6. Wave forms of the basic system

The aim of UPQC is to maintain a sinusoidal volage and current at PCC inspite of any unbalance,or distortions at the load side. Hence a three phase three wire UPQC system was simulated inorder to justify its performance against voltage sag, swell and load distortions. Figure7 shows the simulink model of UPQC system.

A voltage sag of 50% the peak voltage system of the was introduced for the simulation time of 0.02 to 0.08s. The voltage and current waveforms at PCC and load side shows a reduction in value of current and voltage. Then the effect of UPQC in mitigating sag was tested by connecting it to the system. The waveforms shows that this system can effectively mitigate the voltage sag which occurred for a time duration from 0.02 to 0.08 s. The series inverter played its role in mitigating the sag. It injected the required amount of voltage for sag compensation. The waveforms of the uncompensated and compensated system are given in figure 8 and figure 9 respectively.

TABLE.1
SYSTEM PARAMETERS

| System voltages | 415V, 50 Hz |
|---|---|
| Non linear load | 3 phase full bridge rectifier load of 1μF and 3.6Ω |
| Series interfacing transformer | 1:1, 100V, 1000VA |
| Shunt VSI parameters | $L_{sh}$=2mH, $C_{sh}$=0.1μF |
| Series VSI parameters | $L_s$=13.5mH, $C_s$=0.004μF |
| PI controller gains | $K_p$=1, Ki=5 |
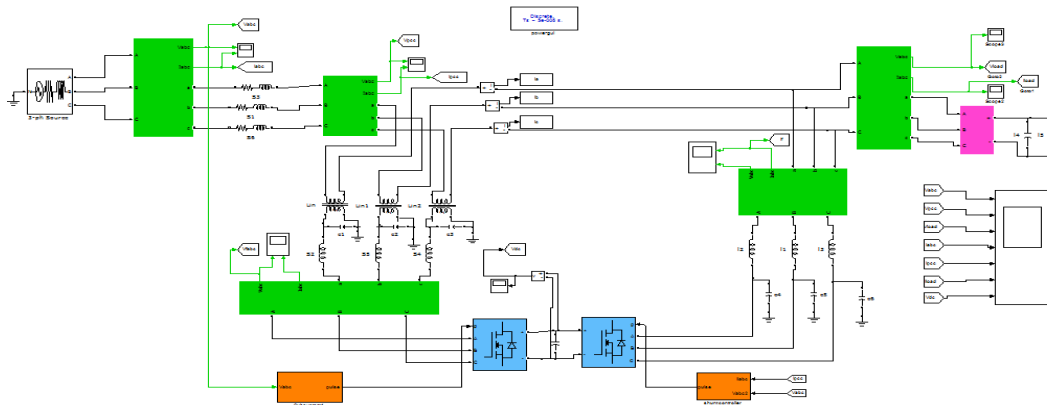
Figure 7. Simulink diagram of UPQC system

Next the system performance in mitigating voltage swell was analysed by introducing a swell in the system voltage from a period 0.2 to 0.6 using capacitor banks. The waveforms of voltages and currents at PCC and load end are as shown in figure 10. Here we can see a small increase in the value of voltages and currents due to the occurrence of swell. Now the system is connected with UPQC for validating its performance. It is seen that the UPQC eliminates voltage swell which occurred due to the capacitor bank switching. The waveforms of swell compensated system is given in figure 11.
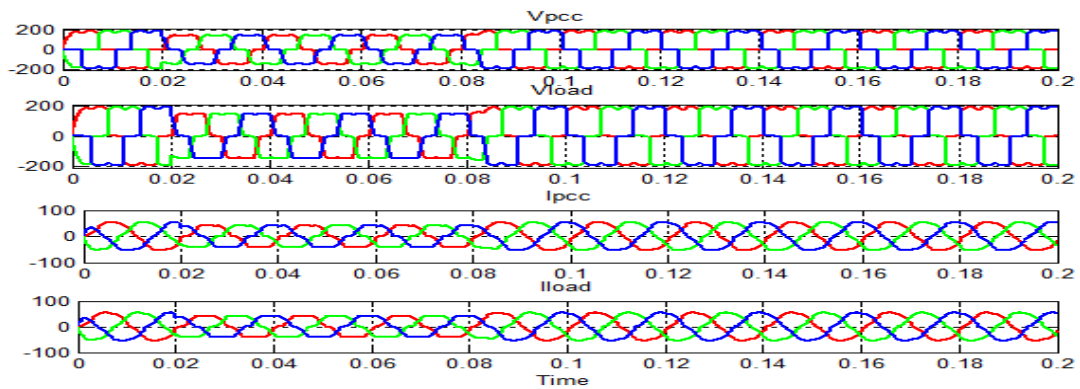


Figure 8. Wave forms of the uncompensated system during sag

The effect of load dynamics in the system with UPQC is studied by applying a three phase linear load together with the nonlinear load to the system. The effect of UPQC in the system shows that in spite of load variations it can maintain the voltage and current waveforms at PCC sinusoidal and to a desired value. This is shown in figure 12
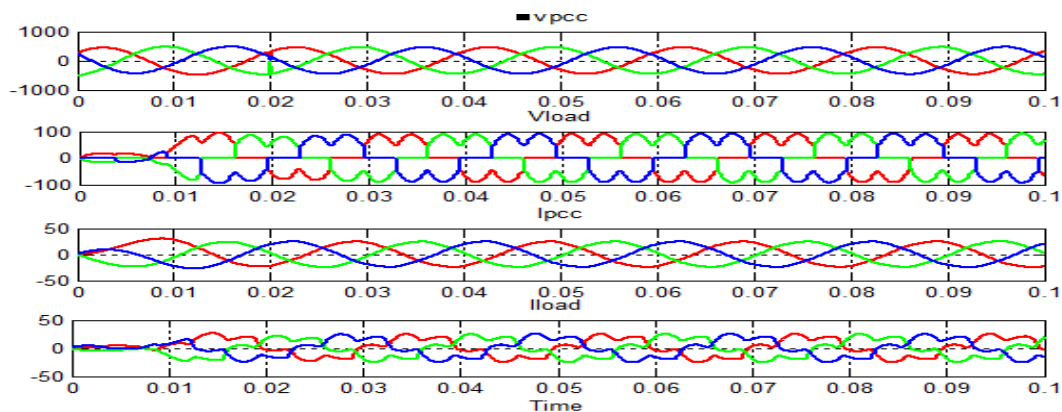


Figure 9. Wave forms of the sag compensated system
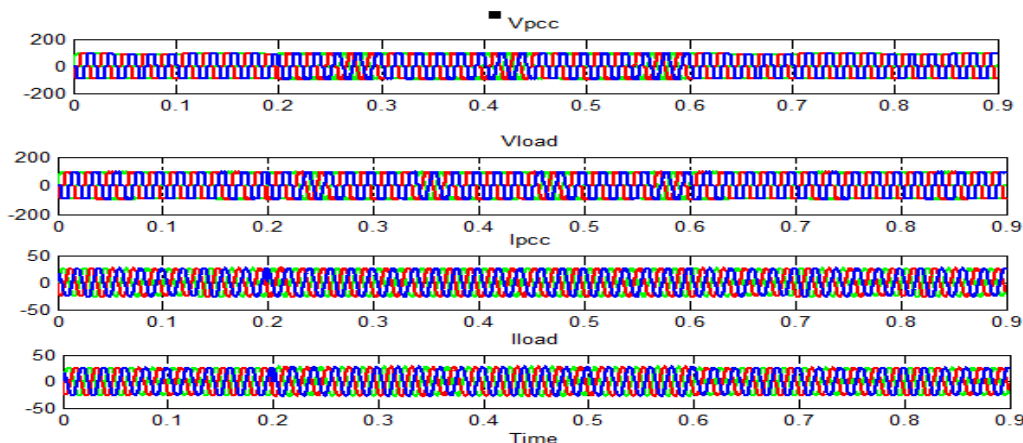
Figure 10. Wave forms of the uncompensated system during swell
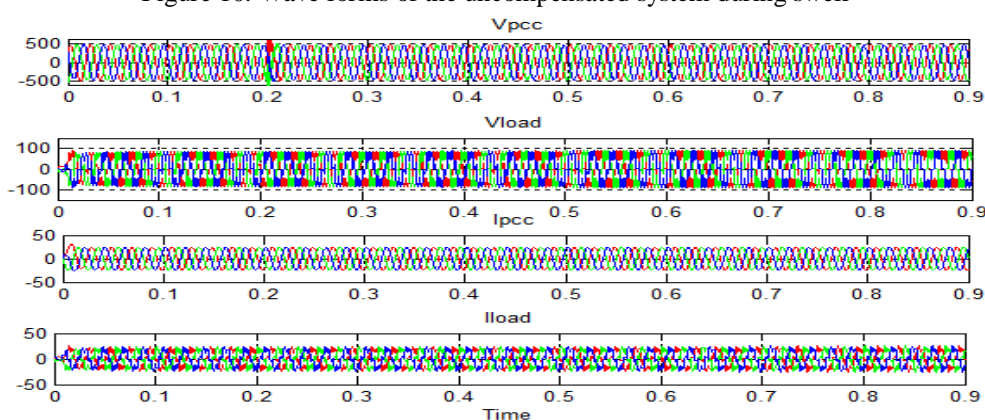


Figure 11. Wave forms of the swell compensated system

Also UPQC plays an important role in harmonic reduction. Table II compares the harmonics in a uncompensated and a compensated system during the occurrence of fault. This clearly reveals that the application of UPQC reduces the fifth and seventh order harmonics in the system.

TABLE.2
Before and after compensation

| Harmonics | $I_a$ (%) | $I_a$ (%) | $I_c$ (%) | $I_a$ (%) | $I_a$ (%) | $I_c$ (%) |
|---|---|---|---|---|---|---|
| 5th order | 7.65 | 5.46 | 8.23 | 3.60 | 0.78 | 4.11 |
| 7th order | 3.75 | 3.05 | 4.95 | 2.41 | 0.58 | 2.15 |
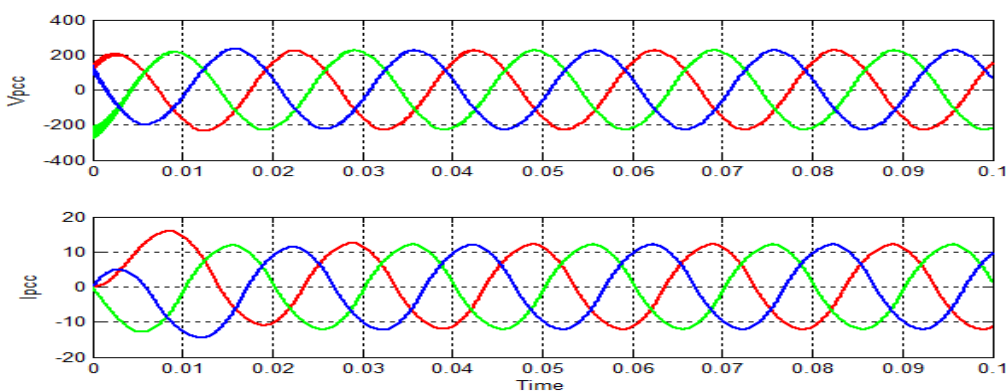


Figure 12. Waveforms at PCC showing the compensating nature of UPQC on applying load dynamics

# V. Conclusion

The FACT devices are emerging as an important tool for reducing the power quality issues. Among them UPQC is seen to be more affective since it eliminates voltage distortions,current distortions, reduces harmonics, improves power factor etc. The simulation in this paper shows that UPQC ensures voltage stability, Harmonic reduction and desired accurate frequency.

# REFERENCE

[1]     E. W. Gunther and H. Mehta, A survey of distribution system power quality ,IEEE Trans. Power Del., vol. 10, no. 1, pp. 322329, Jan.1995.

[2]     M. Aredes, K. Heuman and E. Watanabe, An Universal Active Power Line Conditioner, in IEEE Trans. on Power Delivery, vol. 13, no 2, pp. 545-551,   April   1998.

[3]     G. Joos, L. Morn, Principles of Active Power Filters, Tutorial Course Note. of IEEE Ind. Appl. Society Annual Meeting, Oct. 1998.

[4]     Math H.J. Bollen, Understanding power quality problems: Voltage sags and interruptions in IEEE Press, 2000, New York.

[5]     Hideaki Fujita and Hirofumi Akagi, The Unified Power Quality Conditioner: The Integration of Series- and Shunt-Active Filters, IEEE Transactions on   Power Electronics, vol. 13, no. 2, March 1998.

[6]     H. Fujita and H. Akagi, The unified power quality conditioner: The integration of series active filter and shunt active filters, in Proc. IEEE/ Power Eng. Soc. Power Electronics Specialist Conf., Jun. 1996, pp.

[7]     S. Bhattacharya and D. Divan, Synchronous frame based controller implementation for a hybrid series active filter system , in Proc. 30th Ind.Appl. Soc. Annu. Meet. Ind. Appl. Conf., Oct. 812, 1995, pp. 25312540

[8]     Metin Kesler and Engin Ozdemir, Senior Member, IEEE, Synchronous-Reference-Frame-Based Control Method for UPQC Under Unbalanced and Distorted Load Conditions IEEE transactions on industrial electronics, vol. 58, no. 9, September 2011 3967

[9]     B. Gopal, Pannala Krishna Murthy and G.N. Sreenivas, A Review on UPQC for Power Quality Improvement in Year 2013 Distribution System, Global Journal of Researches in Engineering Electrical and Electronics Engineering, Volume 13 Issue 7 Version 1.0 .

[10]    M. A. Hannan and Azah Mohamed, PSCAD/EMTDC Simulation of Unified Series-Shunt Compensator for Power Quality Improvement, Reviewed for the journal of IEEE Transaction on Power Delivery, manuscript number is: TPWRD-00462-2003 R1, 2004.

[11]    Arindam Ghosh, Compensation of Distribution System Voltage Using DVR, in IEEE Trans. Power Del., vol. 17, no. 4, pp 1030 1036, October 2002.

[12]    H. Fujita and H. Akagi, The unified power quality conditioner: The integration of series and shunt-active filters, in IEEE Trans. Power Electron., vol. 13, no. 2, pp. 315322 Mar. 1998.

[13]    C.H. Ram Jethmalani1, V. Karthikeyan2, and Narayanappa3, Implementation of UPQC for Voltage Sag Mitigation, International Journal of Computer Communication and Information System ( IJCCIS)– Vol2. No1. ISSN: 0976–1349 July – Dec 2010

# A method for solving quadratic programming problems having linearly factorized objective function

M. Jayalakshmi[1], P. Pandian[2]

[1] *Department of Mathematics, School of Advanced Sciences, VIT University, Vellore-14, India.*

**Abstract:** *A new method namely, objective separable method based on simplex method is proposed for finding an optimal solution to a quadratic programming problem in which the objective function can be factorized into two linear functions. The solution procedure of the proposed method is illustrated with the numerical example.*

**Keywords:** *Quadratic programming problem, Linear programming problem, Objective separable*

## I. Introduction

Non-linear programming problem is an optimization problem in which either the objective function is non-linear, or one or more constraints have non-linear relationship or both. A quadratic programming (QP) problem is the simplest non-linear programming problem in which the objective function is quadratic and the constraints are linear. Because of its usefulness in Management Science, Health Science and Engineering, QP is viewed as a discipline in Operational Research and it has become a fertile area in the field of research in recent years. A large number of algorithms for solving QP problems have been developed. Some of them are extensions of the simplex method and others are based on different principles. In the literature, a great number of methods (Wolfe [1], Beale [2], Frank and Wolfe [3], Shetty [4], Lemke [5], Best and Ritter [6], Theil and van de Panne [7], Boot [8], Fletcher [9], Swarup[10], Gupta and Sharma[11], Moraru [12,13], Jensen and King[14], Bazaraa et al.[15]) are available to solve QP problems. Among them, Wolf's method [1], Swarup's simplex method [10] and Gupta and Sharma's method [11] are more popular than the other methods.

Quazzafi Rabbani and Yusuf Adhami [16] used modified Fourier elimination method for solving QP problems after applying the K-T conditions. Babul Hasan [17] has developed a computer oriented solution method for solving special type of QP problems in which the objective function is a quasi-concave in the feasible region and it can be factorized into two linear functions such that both linear factors are positive in the feasible region. Jan Busa [18] proposed a regularization method for solving the QP problem with linear constraints containing absolute values of variables.

In this paper, we propose a new method namely, objective separable method for finding an optimal solution to a QP problem in which the objective function can be factorized into two linear functions. In this proposed method, we construct two linear programming problems both of maximization type from the given QP problem and then, we obtain an optimal solution to the given QP problem from the solutions of the two constructed linear programming problems. The objective separable method is based only on the simplex method which differs from the existing methods (Wolfe's method [1], Beale's algorithm [2], Swarup's simplex method [10] and Babul Hasan method [17]). Numerical example is given for better understanding the solution procedure of the proposed method.

## II. Preliminaries

We need the following definition and the result which can be found in Ezio Marchi [19].

**DEFINITION 2.1.** Let $f_1(x)$ and $f_2(x)$ be two differentiable functions defined on $X \subset R^n$, an n-dimensional Euclidean space. The functions $f_1(x)$ and $f_2(x)$ are said to have the Gonzi property in $X \subset R^n$ if $(f_1(x) - f_1(u))(f_2(x) - f_2(u)) \le 0$, for all $x, u \in X$.

**THEOREM 2.1** The product $f_1(x)f_2(x)$ of two linear functions $f_1(x)$ and $f_2(x)$ is concave if and only if the functions $f_1(x)$ and $f_2(x)$ have the Gonzi property.

## III. Quadratic Programming Problems

Consider the following general form of a QP problem:

$$\text{Maximize} \quad f(X)$$
$$\text{subject to} \quad AX \le B, \; X \ge 0$$

where $f : R^n \to R$ is a quadratic function on $R^n$, X is an *n*-dimensional column vector X, A is an ($m \times n$) matrix and B is an *m*-dimensional column vector.

In this paper, we consider a special type of QP problem in which the objective function can be factorized into two linear functions. Such QP problem can be represented as follows:

(P)     $\text{Maximize} \quad Z(X) = \left(C^T X + \alpha\right)\left(D^T X + \beta\right)$

$\text{subject to} \quad AX \le B, \; X \ge 0$

where A is an ($m \times n$) matrix, B is an *m*-dimensional column vector, X, C, D are *n*-dimensional column vectors and $\alpha, \beta$ are real numbers.

Now, we assume that the two functions $\left(C^T X + \alpha\right)$ and $\left(D^T X + \beta\right)$ have the Gonzi property in the feasible set and the set of all feasible solutions to the problem (P) are non-empty and bounded. Thus, by the Theorem 2.1., it is concluded that the problem (P) is a concave non-linear programming problem with linear constraints. This implies that the optimal solution of the problem (P) exists and it occurs at an extreme point of the feasible region.

Now, from the problem (P), two single objective linear programming problems are constructed as follows:

$\left(P_1\right)$     $\text{Maximize} \quad Z_1(X) = C^T X + \alpha$

$\text{subject to} \quad AX \le b, \; X \ge 0$

and

$\left(P_2\right)$     $\text{Maximize} \quad Z_2(X) = D^T X + \beta$

$\text{subject to} \quad AX \le b, \; X \ge 0.$

**REMARK 3.1**: From the above theorem, we can easily conclude that if both $\left(P_1\right)$ and $\left(P_2\right)$ are solvable, then (P) is solvable.

Now, we prove the following theorem connecting the optimal solutions of the problem (P), the problem $\left(P_1\right)$ and the problem $\left(P_2\right)$ which is used in the proposed method.

**THEOREM 3.1:** Let $X_0$ be an optimal solution to the problem $\left(P_1\right)$. If $\{X_n\}$ is a sequence of basic feasible solutions to the problem $\left(P_2\right)$ by simplex method considering the solution $X_0$ as an initial feasible solution such that $Z(X_k) \le Z(X_{k+1})$ for all $k = 0,1,2,...,n$ and either $X_{n+1}$ is an optimal solution to the problem $\left(P_2\right)$ or $Z(X_{n+1}) \ge Z(X_{n+2})$, then $X_{n+1}$ is an optimal solution to the problem (P).

**PROOF:** It is obvious that $X_{n+1}$ is a feasible solution to the problem (P)

Let V be a feasible solution to the problem (P).

Now, since $X_{n+1}$ is an optimal solution to the problem $\left(P_2\right)$, we have

$Z_2(V) \le Z_2(X_{n+1})$.

**Case(i):** Now, since $Z(X_k) \le Z(X_{k+1})$, for all $k = 0,1,2,...,n$ and $X_{n+1}$ is an optimal solution to the problem $\left(P_2\right)$, we can conclude that $Z(X_{n+1}) \ge Z(V)$. Therefore, $X_{n+1}$ is an optimal solution to the problem (P).

**Case(ii):** Now, since $Z(X_k) \le Z(X_{k+1})$ for all $k = 0,1,2,...,n$ and $Z(X_{n+1}) \ge Z(X_{n+2})$, we can conclude that $Z(X_{n+1}) \ge Z(V)$. Therefore, $X_{n+1}$ is an optimal solution to the problem (P).

Hence the theorem is proved.

## IV. Objective Separable Method

Now, we proposed a new method namely, objective separable method for finding an optimal solution to the QP problem.

The proposed method proceeds as follows:

**Step 1:** Construct two single objective linear programming problems namely, the problem $(P_1)$ and the problem $(P_2)$ from the given problem (P).

**Step 2:** Compute the optimal solution to the problem $(P_1)$ using the simplex method. Let the optimal solution to the problem $(P_1)$ be $X_\circ$ and the maximum value of $Z_1(X) = Z_1(X_\circ)$.

**Step 3:** Use the optimal table of the problem $(P_1)$ as an initial simplex table for the problem $(P_2)$, and obtain a sequence of basic feasible solutions to the problem $(P_2)$ by the simplex method.

**Step 4:** Let $\{X_n\}$ be a sequence of basic feasible solutions to the problem $(P_2)$ obtained by the Step 3. If $Z(X_k) \leq Z(X_{k+1})$ for all $k = 0,1,2,...,n$ and $X_{n+1}$ is an optimal solution to the problem $(P_2)$ for some n, stop the computation process and then, go to the Step 5 or Step 6.

**Step 5:** If $Z(X_k) \leq Z(X_{k+1})$ for all $k = 0,1,2,...,n$ and $Z(X_{n+1}) \geq Z(X_{n+2})$, then stop the computation process and then, go to the Step 6.

**Step 6:** $X_{n+1}$ is an optimal solution to the problem (P) and the maximum value of $Z(X) = Z(X_{n+1})$ by the Theorem 3.1.

**REMARK 4.1:** The maximum value for (n +1) is less than or equal to the number of the iterations to obtain the optimal solution to the problem $(P_2)$ by the simplex method.

The proposed method for solving the QP problem is illustrated by the following examples.

**EXAMPLE 4.1:** Consider the following QP problem.

(P) Maximize $Z = (2x_1 + 4x_2 + x_3 + 1)(x_1 - x_2 + 2x_3 + 2)$

subject to $x_1 + 3x_2 \leq 4$; $2x_1 + x_2 \leq 3$; $x_2 + 4x_3 \leq 3$; $x_1, x_2, x_3 \geq 0$.

The following two LP problems can be obtained from the given problem:

$(P_1)$ Maximize $Z_1(X) = (2x_1 + 4x_2 + x_3 + 1)$

subject to $x_1 + 3x_2 \leq 4$; $2x_1 + x_2 \leq 3$; $x_2 + 4x_3 \leq 3$; $x_1, x_2, x_3 \geq 0$.

and

$(P_2)$ Maximize $Z_2(X) = (x_1 - x_2 + 2x_3 + 2)$

subject to $x_1 + 3x_2 \leq 4$; $2x_1 + x_2 \leq 3$; $x_2 + 4x_3 \leq 3$; $x_1, x_2, x_3 \geq 0$.

Now, by simplex method, the optimal solution to the problem $(P_1)$ is $x_1 = 1$, $x_2 = 1$, $x_3 = \dfrac{1}{2}$, Max.

$Z_1 = \dfrac{15}{2}$ and the value of $Z = \dfrac{45}{2}$.

Now, by the Step 3 of the proposed method, the solution to the problem $(P_2)$ by simplex method is given below:

| Iteration | Solution $(x_1, x_2, x_3, s_1, s_2, s_3)$ | Value of $Z_1$ | Value of $Z_2$ | Value of $Z = Z_1 Z_2$ |
|-----------|------------------------------------------|----------------|----------------|------------------------|
| 0 | $X_0 = (1, 1, \frac{1}{2}, 0, 0, 0)$ | $\frac{15}{2}$ | 3 | $\frac{45}{2}$ |
| 1 | $X_1 = (\frac{3}{2}, 0, \frac{3}{4}, \frac{5}{2}, 0, 0)$ | $\frac{19}{4}$ | 5 | $\frac{95}{4}$ |

Since the 1st iteration table is optimal and by the Step 4 of the proposed method, the optimal solution to the given quadratic programming problem is $x_1 = \frac{3}{2}$, $x_2 = 0$, $x_3 = \frac{3}{4}$ and Maximum value of $Z = \frac{95}{4}$.

**EXAMPLE 4.2:** Consider the following QP problem.

(P) Maximize $Z = (-x_1 + x_2 + 4)(x_1 - x_2 + 2)$

subject to $-x_1 + 2x_2 \le 2$; $x_1 + x_2 \le 4$; $x_1, x_2 \ge 0$.

The following two LP problems can be obtained from the given problem:

$(P_1)$ Maximize $Z_1 = -x_1 + x_2 + 4$

subject to $-x_1 + 2x_2 \le 2$; $x_1 + x_2 \le 4$; $x_1, x_2 \ge 0$.

and

$(P_2)$ Maximize $Z_2 = x_1 - x_2 + 2$

subject to $-x_1 + 2x_2 \le 2$; $x_1 + x_2 \le 4$; $x_1, x_2 \ge 0$.

Now, by simplex method, the optimal solution to the problem $(P_1)$ is $x_1 = 0$, $x_2 = 1$, Max. $Z_1 = 5$ and the value of $Z = 5$.

Now, by the Step 3 of the proposed method, the solution to the problem $(P_2)$ by simplex method is given below:

| Iteration | Solution $(x_1, x_2, s_1, s_2)$ | Value of $Z_1$ | Value of $Z_2$ | Value of $Z = Z_1 Z_2$ |
|-----------|--------------------------------|----------------|----------------|------------------------|
| 0 | $X_0 = (0, 1, 0, 3)$ | 5 | 1 | 5 |
| 1 | $X_1 = (2, 2, 0, 0)$ | 4 | 2 | 8 |
| 2 | $X_2 = (4, 0, 6, 0)$ | 0 | 6 | 0 |

Since the 2nd iteration table is optimal and by the Step 4 of the proposed method, the optimal solution to the given linear quadratic programming problem is $x_1 = 0$, $x_2 = 0$ and the Maximum value of $Z = 8$.

## V. Conclusion

The objective separable method is proposed to solve QP problems in which the objective function can be factorized into two linear functions. Since the proposed method is based on simplex method, without using KKT conditions and complementarity constraints [2]. Also, we can solve such QP problems using the existing LP solvers. Further, the present work can be extended to integer QP problems and fully fuzzy QP problems.

## REFERENCES

[1] P. Wolfe, The simplex method for quadratic programming, Econometrica, 27, 1959, 382-398.
[2] E.M.L. Beale, On quadratic programming, Naval Research Logistics Quarterly, 6, 1959, 227-243.
[3] M. Frank, P. Wolfe, An algorithm for quadratic programming, Naval Research Logistics Quarterly, 3, 1956, 95–110.
[4] C.M. Shetty, A simplified procedure for quadratic programming, Operations Research, 11, 1963, 248–260.
[5] C.E. Lemke, Bi-matrix equilibrium points and mathematical programming, Management Science 11, 1965, 681–689.
[6] M.J. Best, K. Ritter K, A quadratic programming algorithm, Zeitschrift for Operations Research, 32, 1988, 271–297.
[7] H. Theil, C. Van de Panne, 1961. Quadratic programming as an extension of conventional quadratic maximization, Management Science 7, 1961, 1–20.

[8]     J.C.G., Boot, Notes on quadratic programming: The Kuhn-Tucker and Theil-van de Panne conditions, degeneracy and equality constraints, Management Science, 8, 1961, 85–98.

[9]     R. Fletcher, A general quadratic programming algorithm, J. Inst., Maths. Applics 7, 1971, 76–91.

[10]    K. Swarup, Quadratic Programming, CCERO (Belgium) 8, 1966, 132-136.

[11].   A.K. Gupta, J.K. Sharma, A generalized simplex technique for solving quadratic programming problem, Indian Journal of Technology, 21, 1983, 198-201.

[12]    V. Moraru, An algorithm for solving quadratic programming problems, Computer Science Journal of Moldova 5, 1997, 223-235.

[13]    V. Moraru, Primal-dual method for solving convex quadratic programming problems, Computer Science Journal of Moldova, 8, 2000, 209-220.

[14]    D.L. Jensen, A.J. King, A decomposition method for quadratic  programming, IBM Systems Journal 31, 1992, 39–48.

[15]    M. Bazaraa, H. Sherali, C.M. Shetty, Nonlinear programming: Theory and Algorithms (John Wiley, New York, 2006).

[16]    Quazzafi Rabbani, A. Yusuf Adhami, Modified Fourier's method for solving  quadratic programming problems, International Journal of Mathematical Archive, 2, 2011, 2005-2012.

[17]    M. Babul Hasan,   A technique for solving special type quadratic programming problems, Dhaka University Journal of Sciences, 60, 2012, 209-215.

[18]    Jan Busa, Solving quadratic programming problem with linear constraints containing absolute values, Acta Electrotechnica et Informatica, 12, 2012, 11–18.

[19]    Ezio Marchi, When is the product of two concave functions concave?, IMA Preprint Series # 2204, Institute for Mathematics and its Applications, University of Minnesota, 2008, 1-8.

# Heat Transfer Analysis of Refrigerant Flow in an Evaporator Tube

C. Rajasekhar[1], S. Suresh[2], R. T. Sarathbabu[3]

[1,2]*Department of Mechanical Engineering, SIETK College, Puttur, Chittoor Dist, Andhra Pradesh, INDIA*
[3]*Department of Mechanical Engineering, Trumalai Engineering College, Kiambi, Kanchipuram Dist, Tamil Nadu, INDIA*

**Abstract:** *the paper aim is to presenting the heat transfer analysis of refrigerant flow in an evaporator tube is done. The main objective of this paper is to find the length of the evaporator tube for a pre-defined refrigerant inlet state such that the refrigerant at the tube outlet is superheated. The problem involves refrigerant flowing inside a straight, horizontal copper tube over which water is in cross flow. Inlet condition of the both fluids and evaporator tube detail except its length are specified. here pressure and enthalpy at discrete points along the tube are calculated by using two-phase frictional pressure drop model. Predicted values were compared using another different pressure drop model. A computer-code using Turbo C has been developed for performing the entire calculation.*
**Keywords:** heat transfer, refrigerant flow, evaporator tube, pressure drop model, copper tube, Turbo C

## I.   Introduction

Two phase flow of gases and liquids or vapors and liquids in pipes, channels, equipment, etc. is frequently encountered in industry and has been studied intensively for many years. Exact prediction of pressure gradients an d boiling heat transfer phenomenon during the flow of two phase mixtures is an essential step in the design of a great variety of industrial equipment in the power and process industries. Knowledge of boiling heat transfer phenomenon, flow patterns and heat transfer correlations can reduce the cost and avoid the drastic results due to over design and under design of evaporators, boilers and other two-phase process equipments.

### 1.1  Flow boiling

In the literature, two types of boiling of a saturated fluid are described, pool boiling and flow boiling. In pool boiling, heat is transferred to a stagnant fluid, a pool. During flow boiling, heat is transferred to a fluid having a velocity relative to the surface from where the heat is supplied. In saturated flow boiling heat is transferred by two different mechanisms, nucleate boiling and convective evaporation. Convective evaporation resembles ordinary convective heat transfer in single phase heat transfer; i.e. the main resistance to heat transfer is at the heated wall. This part of the heat transfer is often modeled using heat transfer correlations similar to single phase heat transfer correlations. In nucleate boiling, heat is mainly transferred into the bulk of the gas/liquid by means of bubbles nucleating on the surface, growing and finally detaching from the surface. This part of the heat transfer is similar to pool boiling and is often modeled as pool boiling. The total heat transfer coefficient is then calculated accounting (by weighing) for both mechanisms.

The weighing is carried out differently, as may be found in the literature. In the most cases, a correction factor is introduced into the pure convective and nucleate parts. The convective part is often said to be enhanced due to the presence of bubbles. In a similar way, the nucleate part is often said to be suppressed due to the fact that the flow of the liquid may suppress bubble nucleation. The combined effect of these two mechanisms is not yet well understood and several different approaches may be found in the literature.

### 1.1.1. Flow boiling heat transfer correlations

Numerous flow boiling correlations exist in the literature. In this section, some of the better known correlations are listed.

### 1.1.1.1. Chen (1966) correlation

Chen (1966) published his classical paper on flow boiling, where the evaporating heat transfer coefficient was a sum of macro and micro mechanisms.

$$\alpha = \alpha_{mic} + \alpha_{mac} \tag{1.1}$$

The micro evaporation, nucleate boiling, was calculated as

$$\alpha_{mic} = 0.00122 \left[ \frac{k_l^{0.79} \, c_{pl}^{0.45} \, \rho_l^{0.49} \, g^{0.25}}{\sigma^{0.5} \, \mu_l^{0.29} \, h_{fg}^{0.24} \, \rho_g^{0.24}} \right] \Delta t^{0.24} \, \Delta p^{0.75} \, S \qquad (1.2)$$

**1.1.1.2 Kandlikar (1990, 2003) correlation**

The correlation is $\dfrac{\alpha_{TP}}{\alpha_l} = C_1 \, Co^{C_2} \left(25 \, Fr_{lo}\right)^{C_5} + C_3 \, Bo^{C_4} \, F_{fl}$

The correlation is calculated twice using each set of constants and the greater of the two values is used as the heat transfer coefficient. The Froude number is calculated with the entire flow as liquid.

$$Fr_{lo} = \frac{G^2}{\rho_l^2 \, g \, d}$$

**1.1.1.3 Pressure drop correlations**

There are numerous correlations on pressure drop in two-phase flows in the literature. The purpose of the present thesis is not to cover them all; merely the most important contributions will briefly be discussed. A good introduction of adiabatic two-phase flow pressure drop may be found in Chisholm (1983) and in Collier and Thome (1996).

Lockhart and Martenelli (1949) presented their classical paper where they introduced a new parameter, later denoted the Lockhart- Martenelli parameter, defined as

$$X^2 = \frac{\left(\Delta p_l \middle/ \Delta l\right)}{\left(\Delta p_g \middle/ \Delta l\right)} \qquad (1.26)$$

They graphically correlated the two phase multiplier with the Lockhart- Martenelli parameter. The two-phase multiplier was defined as

$$\phi_l^2 = \frac{\left(\Delta p_{TP} \middle/ \Delta l\right)}{\left(\dfrac{\Delta p_l}{\Delta l}\right)} \qquad (1.27)$$

Baker (1954) presented a paper investigating pressure drop of simultaneous flow of oil and gas. The data does not correlate well with the Lockhart- Martenelli correlation. He observed a distinct change in slope when plotting the data in the Lockhart- Martenelli chart. He concludes that something radical changed the flow. He suggests different correlations for different flow regimes and stresses the importance of taking into account the actual flow pattern when correlating the pressure drop.

Chisholm and Laird (1958) revisited the work by Lockhart and Martenelli (1949) and suggested that the two-phase frictional data could be correlated with reasonable accuracy as

$$\frac{\Delta p_{TP}}{\Delta p_l} = 1 + C / \hat{X}^m \qquad (1.28)$$

For rough tubes. The value of C and m depends on the tube surface and liquid flow rate. The variable $\hat{X}^m$ differs from the definition by Lockhart and Martenelli.

Later, Chisholm (1967) conducted a more refined analysis. However, at the end of the paper he states that the derived equations are too complicated for practical calculations and suggests

$$\phi_l^2 = 1 + C / X + C / X^2 \qquad (1.29)$$

Where he now used the definition of X according to Lockhart- Martenelli. He also included the classical values for the Chisholm parameter, C.

## II. Problem Description

**2.1. Problem**

The problem involves refrigerant flowing through a straight, horizontal copper tube over which water is in cross flow. Inlet conditions of both the fluids and evaporator tube detail except its length are specified. The

main objective is to find the length of the evaporator tube for a pre defined inlet refrigerant state such that the refrigerant at the tube outlet is super heated.
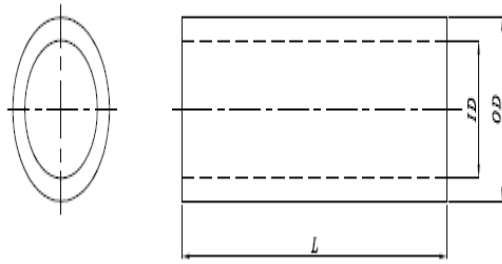


Fig.2.1. Geometry of evaporator tube        Fig.2.2. Problem Visualization
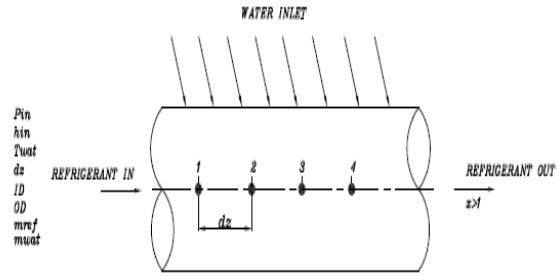
### 2.2. Input parameters to be specified
1. Refrigerant inlet pressure
2. Refrigerant inlet enthalpy
3. Name of the refrigerant
4. Mass flow rate of the refrigerant
5. Water velocity
6. Water temperature
7. Inner diameter of the tube
8. Outer diameter of the tube
9. Space between two nodes

### 2.3. Solution approach
We require two properties to fix the state of the refrigerant i.e., pressure and enthalpy. In this analysis pressure and enthalpy can be found at discrete points along the length of the tube. For calculating enthalpy one ordinary differential equation is required. This can be obtained by balancing energy, which flows through an elementary strip as shown below. Energy balance can be defined as "The amount of energy entering into the strip is equal to the energy leaving from that strip".
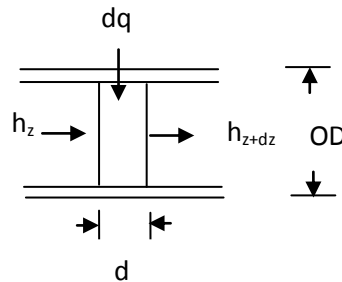


Fig.2.3. Energy balance through strip of length dz

Energy balance for a strip of length dz
Energy input = Energy output

$$m_f h_z + dq = m_f h_{z+dz} \tag{2.1}$$

where $m_f$ is the mass flow rate of the refrigerant.

After simplification equation 2.1 becomes

$$(2.2)$$

$$h_{z+dz} - h_z = \frac{2\pi \left( T_{wat} - T_{ref} \right) dz}{m_f \left( \dfrac{1}{\alpha_i r_i} + \dfrac{\ln\left(\dfrac{r_o}{r_i}\right)}{k} + \dfrac{1}{\alpha_o r_o} \right)}$$

In equation (2.2) $\alpha_i$ and $\alpha_o$ are inside and outside heat transfer coefficients. The inside heat transfer coefficients can be found from boiling heat transfer correlations by Klimenko and outside heat transfer coefficient is calculated from the correlations of flow over bodies. Then enthalpy at next node can be found by using equation

For calculating the pressure we require another differential equation is required which gives the pressure drop between two nodes. Pressure drop includes both frictional pressure drop as well as acceleration pressure drop. Frictional pressure drop can be obtained from Chisholm's model. Acceleration pressure drop can be obtained from momentum equation along axial direction.

By using pressure and enthalpy state of the refrigerant can be fixed at next node. Length of the tube can be found by marching from one node to another until the state of the refrigerant is super heated.

## III. Boiling Heat Transfer

Boiling process occurs when the temperature of a liquid at a specified pressure is raised to saturated temperature at that pressure. It is considered to be one form of convection heat transfer as it involves fluid motion (such as rise of bubbles to the top). It differs from other forms of convection in that it depend on latent heat of vaporization of the fluid and surface tension at the liquid-vapor interface, in addition to properties of the fluid in each phase. The heat transfer coefficients associated with boiling are typically much higher than those encountered in other forms of convection processes that involve single phase.

### 3.1. Introduction

Many familiar engineering applications involve boiling and condensation heat transfer. In the household refrigerator, for example, the refrigerant absorbs heat from the refrigerated space by boiling in the evaporator section and rejects heat to air by condensing in the condenser section. Some electronic components are cooled by boiling by immersing them in a fluid with an appropriate boiling temperature. Boiling is a liquid-to-vapor change process just like evaporation, but there significant differences between the two.

### 3.2. Types of boiling

Based on the presence of bulk fluid motion boiling is classified into two types. They are
I.   Pool boiling
II.  Flow boiling

Boiling is called pool boiling in the absence of bulk fluid motion and flow boiling or forced convection boiling in presence of it. In pool boiling, fluid is stationary, and any motion of fluid is due to natural convection currents and motion of bubbles under the influence of buoyancy. In flow boiling the fluid is forced to move in a heated pipe or over a surface by external means such as pump. Pool and flow boiling are further classified into two types depending on the bulk liquid temperature. They are
*   Sub cooled boiling
*   Saturated boiling

## IV. Pressure Drop

### 4.1. Introduction

During two phase flow in a non horizontal channel, the pressure drop is made up of contributions due to geodetic changes in position, acceleration and friction. Because of very complicated phenomena occurring in two phase flow empirical or semi empirical relationships or physical models are used for calculating pressure drop. These physical models are correlated with the experimental results. They are broadly classified into three categories
*   Homogeneous flow model
*   Heterogeneous flow model
*   Hybrid flow model

Out of all, homogeneous model is the simplest. This assumes that the liquid and the gas or vapor are uniformly distributed over the flow cross section and in the flow direction, so that the mixture can be regarded as a single phase flow with suitably defined mean values of the thermodynamic and hydrodynamic properties of the two phases. It is frequently used as a reference model because of its ease of manipulation.

In the heterogeneous model or slip model it is assumed that the gas or vapor and the liquid flow separately as continuous phases with distinct mean velocities within different parts of the flow cross section or flow channel.

Generally, the actual flow behavior of a two phase mixture lies between these two limiting cases. Only at very small mass fractions of vapor does the condition occur in which the velocities of the two phases are the same. As a result, a series of mixed or hybrid models have been developed such as variable density model, drift-velocity model.

Total pressure drop constitutes
   1. Pressure drop due to change in level
   2. Acceleration pressure drop
   3. Frictional pressure drop

The first two components describe a reversible change of pressure, since a part of the energy or momentum of the flow only appears in another form and can be converted back again without loss. On the other hand, the frictional pressure drop is an irreversible change of pressure resulting from the energy dissipated in the flow by friction, eddying, etc.

In the flow of a two phase mixture through a pipe with a constant flow cross section, there is always an increase in the volumetric flow due to the reduction in pressure caused by friction, and in a single-component mixture also due to flash evaporation. This results in an increase in the velocity of both phases. The resulting momentum changes make themselves felt as a pressure drop due to acceleration. When vaporizing mixtures are heated, there is an increase of the vapor fraction resulting in further increase in the volumetric flow and an additional pressure drop due to acceleration.

In general, frictional pressure drop contributes most significantly to the total pressure drop. However, even today its calculation is still quite imprecise. Experimental results show that under comparable conditions, frictional pressure drop in two phase flow may be considerably larger than in single flow. The ratio of two pressure drops indicates how many times larger the frictional pressure drop in two phase flow is than in single phase flow. It is usually referred to as the two phase friction multiplier. The determination of frictional pressure drop or friction multiplier is not possible by theoretical means alone, since the individual phenomena occurring such as in momentum transfer between two phases, wall friction or shear at the phase interface , can still not be specified quantitatively. In practice, using of relationships based on different frictional pressure drop models, which are corrected or correlated by measurements

### 4.1.1. Pressure drop due to change in level
The pressure drop as a result of changes in geodetic position is given by the relationship

$$\left(\frac{dp}{dz}\right)_h = \left[\varepsilon\, \rho_g + (1-\varepsilon)\, \rho_f\right] g\,(\sin\phi)$$

(4.2)

Where $\phi$ denotes the angle between the pipe axis and the horizontal. The pressure drop disappears for a horizontal pipe since $\sin\phi = 0$. At small mean void fractions of gas or vapor and large density ratios this component may form the largest contribution to the overall pressure drop in a non horizontal flow. In the more usual case, in which the geodetic pressure drop is very small, calculations with the homogeneous flow model are sufficient, i.e., with the volumetric flow quality instead of with the mean void fraction.

### 4.1.2. Acceleration pressure drop
An exact calculation of the pressure drop due to acceleration in two phase flow is not possible, since this requires a knowledge of local phase velocities or mass flow rates, which can be only incompletely approximated by the mean phase velocities. If homogeneous flow of the two phases is assumed, the pressure drop due to acceleration can be calculated from

$$(dp)_{acc} = G^2 \int_1^2 \frac{d}{dz}\left(\frac{x^*}{\rho_g} + \left(\frac{1-x^*}{\rho_l}\right)\right) dz$$

(4.3)

Compared to the equation for the pressure drop due to acceleration when heterogeneous flow is assumed:

$$(dp)_{acc} = G^2 \int_1^2 \frac{d}{dz}\left(\frac{x^{*2}}{\rho_g\,\varepsilon} + \left(\frac{(1-x^*)^2}{\rho_l\,(1-\varepsilon)}\right)\right) dz$$

(4.4)

The first equation leads in most cases to a more accurate conservative form. The assumption of a homogeneous flow is valid for only for special flow conditions. Acceleration pressure drop can be calculated by solving momentum equation. In unheated two phase flows the pressure drop due to acceleration can often be

neglected. A simple rule for estimating the pressure drop in flows of refrigerants consists of comparing the frictional pressure drop with saturation pressure.

### 4.1.3. Frictional pressure drop

In general, frictional pressure drop contributes most significantly to the total pressure drop. However, even today its calculation is still quite imprecise. Experimental results show that under comparable conditions, frictional pressure drop in two phase flow may be considerably larger than in single flow. As a rule the frictional pressure drop in two- phase is referred to that of pure liquid flow at the same total mass flow rate.

$$\phi^2 = \frac{\left(\dfrac{dp}{dz}\right)_{2,ph}}{\left(\dfrac{dp}{dz}\right)_{1,ph,o}}$$

The ratio of two pressure drops indicates how many times larger the frictional pressure drop in two phase flow is than in single phase flow. It is usually referred to as the two phase friction multiplier. The determination of frictional pressure drop or friction multiplier is not possible by theoretical means alone, since the individual phenomena occurring such as in momentum transfer between two phases, wall friction or shear at the phase interface , can still not be specified quantitatively.

In practice, using of relationships based on different frictional pressure drop models, which are corrected or correlated by measurements.

### 4.1.3.1. Frictional pressure drop models

The frictional pressure drop models given below come under heterogeneous model category. They are classified as

1. Chisholm model
2. Friedel model

## V. Pressure Drop Models

### 5.0.1. Chisholm model

$$\phi^2 = 1 + \left(\tau^2 - 1\right)\left[\left(B\, x^{0.875}\,(1-x)^{0.875}\right) + x^{1.75}\right] \tag{5.1}$$

$$\left(\frac{dp}{dz}\right)_{go} = \frac{2\, f_{go}\, G^2}{D\, \rho_g} \tag{5.2}$$

$$f_{go} = 0.079\,(\mathrm{Re}_{go})^{-0.25} \tag{5.3}$$

$$\mathrm{Re}_{go} = \frac{G\, D}{\mu_g} \tag{5.4}$$

$$\tau^2 = \frac{\left(\dfrac{dp}{dz}\right)_{go}}{\left(\dfrac{dp}{dz}\right)_{lo}} \tag{5.5}$$

$$f_{lo} = 0.079\,(\mathrm{Re}_{lo})^{-0.25} \tag{5.6}$$

$$\mathrm{Re}_{lo} = \frac{G\, D}{\mu_l} \tag{5.7}$$

$$\left(\frac{dp}{dz}\right)_{fric} = -\phi^2 \left(\frac{dp}{dz}\right)_{lo} \qquad (5.8)$$

$$\left(\frac{dp}{dz}\right)_{lo} = \frac{2 f_{lo} G^2}{D \rho_l} \qquad (5.9)$$

**5.0.2. Friedel model**

$$\psi_{lo} = E + \frac{3.24 \, F \, H}{Fr^{0.045} \, We^{0.035}} \qquad (5.10)$$

$$E = (1-x)^2 + x^2 \frac{\rho_l \, f_{go}}{\rho_g \, f_{lo}} \qquad (5.11)$$

$$F = x^{0.78} (1-x)^{0.24} \qquad (5.12)$$

$$H = \left(\frac{\rho_l}{\rho_g}\right)^{0.91} \left(\frac{\mu_g}{\mu_l}\right)^{0.19} \left(1 - \frac{\mu_g}{\mu_l}\right)^{0.7} \qquad (5.13)$$

$$Fr = \frac{G^2}{g \, d \, \rho_H^2} \qquad (5.14)$$

$$We = \frac{G^2 \, d}{\sigma \, \rho_H} \qquad (5.15)$$

$$\frac{1}{\rho_H} = \frac{1-x}{\rho_l} + \frac{x}{\rho_g} \qquad (5.16)$$

## VI. Procedure

Step 1: Specify the inlet refrigerant conditions.
Step 2: Calculation of pressure at node 2
       a) Frictional pressure drop
       b) Acceleration pressure drop
   Frictional pressure drop is calculated by using Chisholm model. Acceleration pressure drop is calculated by using the following equation.

$$dp_{acc} = \left(\frac{G^2}{\rho_1} - \frac{G^2}{\rho_2}\right) \qquad (6.1)$$

But for that equation we require the density of refrigerant at state 2. For that one we assume pressure at node 2 as the calculated pressure by considering frictional pressure drop only.

Step 2.1: Calculation of enthalpy at node 2(Est.)
   Enthalpy is calculated by using the following equation

$$h_2 - h_1 = \frac{2\pi(T_{wat} - T_{ref})dz}{m_f \left(\dfrac{1}{\alpha_i r_i} + \dfrac{\ln\left(\dfrac{r_o}{r_i}\right)}{k} + \dfrac{1}{\alpha_o r_o}\right)} \qquad (6.2)$$

Step 2.1.1. Calculation of alpho ($\alpha_o$) is calculated by using the following equation.

$$Nu = C * \operatorname{Re}_D{}^m * \operatorname{Pr}^{0.333} \qquad (6.3)$$

All the relevant properties are calculated at mean film temperature by assuming $T_{wo}=T_{ref.}$
Step 2.1.2. Calculation of alphi ($\alpha_i$) is calculated by using the boiling heat transfer equations.

$T_{wi}$ is calculated by using the following equation.

$$\frac{T_{wi} - T_{ref}}{\left(\dfrac{1}{\alpha_i A_i}\right)} = \frac{T_{wat} - T_{ref}}{\left(\dfrac{1}{\alpha_i A_i} + \dfrac{\ln\left(r_o/r_i\right)}{2\pi k_c L} + \dfrac{1}{\alpha_o A_o}\right)} \tag{6.4}$$

By using the iterative procedure we will refine the alphi and $T_{wi}$ values until the error (%) should be less than or equal to 0.0001.By using the value of ($\alpha_o$) outside wall temperature ($T_{wo}$) is calculated from the following equation.

$$\frac{T_{wo} - T_{wi}}{\left(\dfrac{\ln\left(r_o/r_i\right)}{2\pi k_c L}\right)} = \frac{T_{wi} - T_{ref}}{\left(\dfrac{1}{\alpha_i A_i}\right)} \tag{6.5}$$

Step.2.1.3. $\alpha_o$ is refined from the outside wall temperature ($T_{wo}$) by the equation
Step.2.1.4. At the end of step 2.1.3., we will get all refined values of $\alpha_i$ and $\alpha_o$. We can fix the estimated state of the refrigerant at next node.
Step2.2:  Calculate the acceleration pressure drop using the equation 6.1.
Step2.3:  Find the pressure at node 2 considering both frictional and acceleration pressure drops
Step 3:  Calculation of enthalpy at node 2 by repeating the step.2.1.
Step 4:  At the end of step2 we will get pressure at node 2 and at the end of step 3 we will get enthalpy at node 2.
         By using these two values we can fix the exact state of refrigerant at node 2.
Step5:  Repeat the steps from 1 to 4 until the condition of the refrigerant reaches superheated   condition
Step6:   Finally check for law of conservation of energy.

## VII.   Results and Discussion
        Length of the evaporator tube was determined for a pre-defined refrigerant inlet state and finally checked for law of conservation of Energy. Energy is conserved for all refrigerant inlet states and for all combination of pressure drop, boiling heat transfer models. This chapter is divided into two sections. In the first section, variation of parameters along the length for same mass flow rate of 60 kg/hr and different combination of pressure drop and boiling heat transfer correlations are discussed. In the second section, comparison of length of the evaporator tube at different mass flow rates and two different combinations of models is compared. Variation of different parameters along length of the tube for different mass flow rates, for different initial states of the refrigerant for the two different combinations were observed. Those investigations are not producing here.
        As shown in Fig.7.1. For the same mass flow rate of 60 kg/hr of R-22, pressure drop for Klimenko-Chisholm combination is high for a given length. Pressure drop depends on the state of the refrigerant. Two-phase flow multiplier is large for Chisholm's model when compared to Friedel's model. Therefore frictional pressure drop is large, in Chisholm's model. Slope of the Klimenko-Chisholm curve is larger than Dembi-Friedel curve, so pressure drop is large for Klimenko-Chisholm curve.
        As shown in Fig.7.2. Enthalpy variation is more or less constant through out length of the tube for the same mass flow rate of R-22 and for both combinations. Both curves merge one over other as. Strictly speaking enthalpy difference is a little bit high for Dembi- Friedel curve.
        As shown in Fig.7.3. Saturated temperature variation is large in Klimenko- Chisholm combination, since the saturated pressure difference is large for that combination. Slope of the curve is larger for that combination. As shown in Fig.7.4. For the same mass flow rate dryness fraction varies linearly for both types of combinations and both the curves overlap one over other. And their slopes are more or less constant.
        As shown in Fig.7.5. Inside heat transfer coefficient increases along the length of the tube for both types of combination. But their range is different. In Klimenko's model single phase forced convection heat transfer is incorporated and convective boiling number is used to distinguish between nucleate boiling and forced convection boiling. As the flow progresses single phase forced convection heat transfer coefficient

decreases and nucleate boiling heat transfer increases in Klimenko's model. But in Dembi's model forced convection heat transfer increases much faster than nucleate boiling. The contribution of forced convection in Dembi's correlation is large when compared to single phase forced convection in Klimenko's correlation. So heat transfer coefficient is high in Dembi's model.

As shown in Fig.7.6. Outside heat transfer coefficient decreases along the length of the tube and both the curves are parallel to each other .The variation of outside heat transfer coefficient is very less in these two models, as it depends on outside wall temperature.

In the second section length of evaporator tube for different mass flow rates and different combinations are compared and finally checked for energy conservation. Energy is conserved for all sets of input data as shown in Table.7.1.It was observed that if the mass flow rate increases, length of the tube was increasing due to larger pressure drop and less increment in enthalpy.

| S.No | Mass flow rate(kg/hr) | combination | Heat lost by water(W) | Heat gained by refrigerant(W) | Length(m) |
|---|---|---|---|---|---|
| 1 | 60 | Dembi- Friedel | 3583.51 | 3583.58 | 3.13 |
| | | Klimenko-Chisholm | 3581.72 | 3581.73 | 3.19 |
| 2 | 50 | Dembi- Friedel | 2991.12 | 2991.12 | 2.63 |
| | | Klimenko-Chisholm | 2986.95 | 2986.96 | 2.67 |
| 3 | 40 | Dembi- Friedel | 2392.55 | 2392.55 | 2.12 |
| | | Klimenko-Chisholm | 2393.29 | 2393.29 | 2.14 |

Table.7.1. Comparison of energy balance and Length of evaporator tube for different mass flow rates and different combination
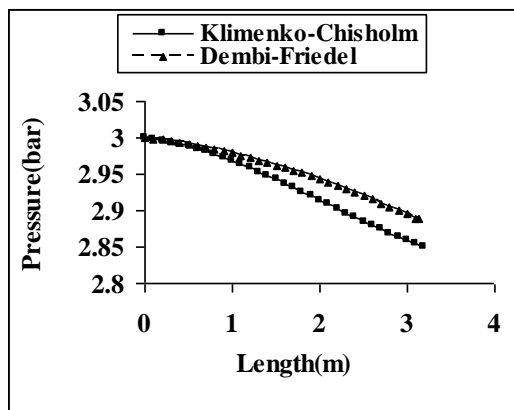


Fig.7.1. Pressure along length of tube for same mass flow rate and for different combinations
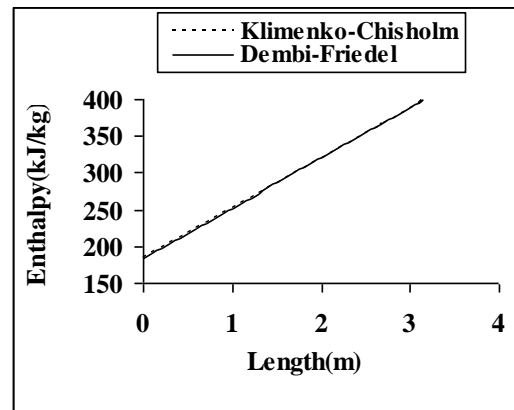


Fig.7.2. Enthalpy variation along length of tube for same mass flow rate and for different combinations
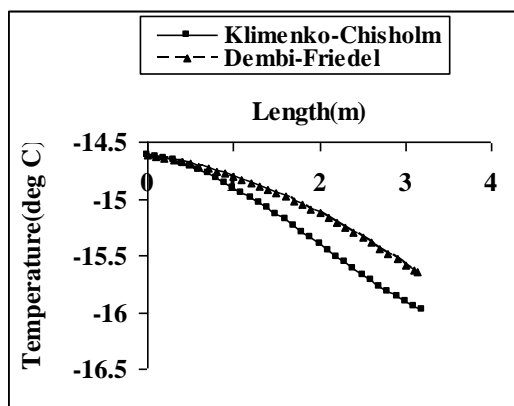


Fig.7.3. Temperature along length of tube for same mass flow rate and for different combinations
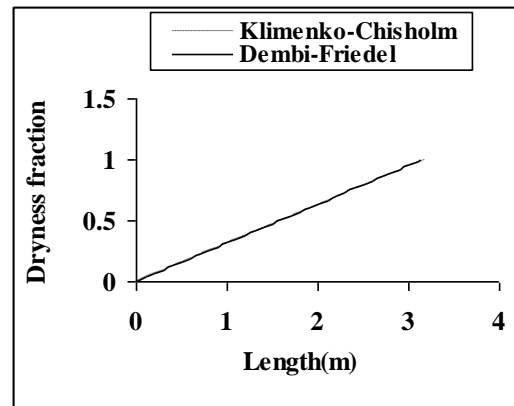


Fig.7.4.Dryness fraction along length of tube for same mass flow rate and for different combinations
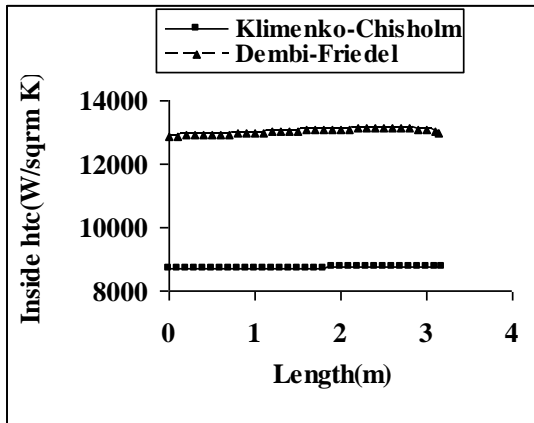
Fig.7.5. Inside heat transfer coefficient along length of tube for same mass flow rate and for different combinations
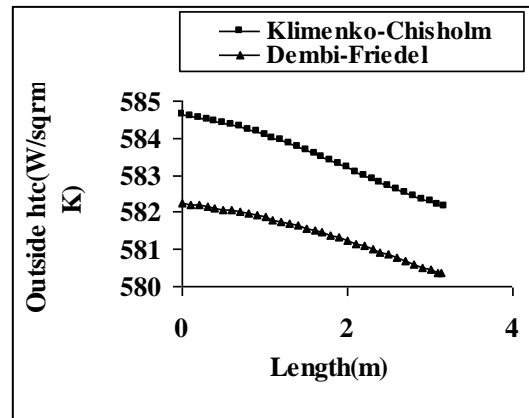


Fig.7.6.Outside heat transfer coefficient along length of tube for same mass flow rate and for different combinations

## VIII.  Conclusion

The obtained results were satisfactory and energy was conserved for all refrigerant inlet states. There is good agreement between the two combinations of models when they compared and yield results with minimum deviation.

## REFERENCES

**Journal Papers:**
[1].    "A generalized correlation for two-phase forced flow heat transfer" - V.V.Klimenko, Int.J.Heat and Mass Transfer. Vol.31, pp.541-552, 1988.
[2].    "A general correlation for flow boiling in tubes and annuli" – K.E.Gungor and R.H.S.Winterton, Int.J.Heat and Mass Transfer. Vol.29, No.3, pp.351-358, 1986.
[3].    "Pressure gradients due to friction during the flow of evaporating two-phase mixtures in smooth tubes and channels" – D.Chisholm, Int.J.Heat and Mass Transfer. Vol.16, pp.347-358, 1973.
[4].    "Pressure drop during gas or vapor-liquid flow in pipes" – L.Friedel, Int.J.Chemical Engineering. Vol 20, No.3, pp.352-367, 1980.

# Voltage Stability Improvement by Reactive Power Rescheduling Incorporating PSO Algorithm

Rajalakshmy S[1], Jasmy paul[2]

[1]*Student, Department of Electrical &Electronics Engineering, ASIET, MG University, India*
[2]*Assistant Professor, Department of Electrical &Electronics Engineering, ASIET, MG University, India*

***Abstract:*** *In this paper, reactive power rescheduling is done to keep the voltage stable. Due to system disturbances the active as well as reactive power flows changes. Generators being always connected to the system reactive power rescheduling of generators can be effectively done. Therefore it is selected as the suitable method for voltage control. The voltage and reactive power management is studied from the generator's point of view to minimize generator reactive power loss. To reduce the reactive losses optimization procedure is used. The simulations are done using MATLAB.*

***Keyword****s: Voltage stability, Reactive power rescheduling, Particle Swarm Optimization (PSO).*

## I. INTRODUCTION

The operation of any electric power system shows that the frequency and the voltage are the main indicators of proper system operation. Disturbance in the system operation causes variation in these two parameters separately or jointly. In case of severe disturbances, the frequency or voltage variations may be abnormally high indicating the loss of system stability. Frequency variation is caused by the real power mismatch, while voltage is the indicator of the reactive power mismatch [1,2,3].

For the system reliability, both active and reactive power consumptions are to be controlled properly. As there is a direct link between the voltage and the reactive power, it is possible to control the voltage to desired values by the control of the reactive power [3]. During normal operation state, the reactive power balance is kept in such a way that the voltages are within the accepted limits. If there is no change between reactive power generation and consumption ,then the voltage will be maintained within the prescribed limits. If there is a mismatch in reactive power generation and consumption level in the system, it will result in an inappropriate voltage profile [4]. Reactive power generation and consumption have to be very close to each other to avoid excessive reactive power transmission. It is due to this fact that reactive power transmission is a highly localized service. The various voltage control methods which are commonly used are under load tap changers, load shedding and installation of new generating units, synchronous condensers, FACTS devices, capacitor banks and reactive power rescheduling [1].

Voltage instability and power system security should be analyzed at various decision stages from planning to real-time implementation. T. Van Cutsem in [5] discussed the methods which can be used for analysis are classified in four categories: contingency analysis, loadability limit determination[6-8], determination of security limits, and preventive and corrective control.

Contingency analysis finds the system response on a particular operating point to credible contingencies that may cause or lead to voltage instability or even ultimately give way to voltage collapse. The system should be operated in such a way that it is enabled to survive the credible contingencies by providing proper pre- and post-contingency controls[9-11]. These can be accomplished by a) static methods based on load flow, modified load flow, multi-time scale simulation, and b) time-domain methods. In this paper contingency analysis is carried along with optimization technique to keep the voltage stable.

Generator reactive power is used to control voltage .The amount of reactive power injection keeps the voltage stable. It also depends on the capacity of the generator. Keeping in mind the above mentioned two facts, optimization techniques will give the best results. Among the different optimization techniques, evolutionary computation techniques give rapid solutions[12]. These optimization algorithms are widely used due to their high precision for modelling engineering problems and simple programming in computers. Particle Swarm Optimization is an effective tool for analysis as it gives better results with few parameters to adjust.

## II. REACTIVE POWER RESCHEDULING

The generators are the primary and main source of reactive power. Generator supplied reactive power is especially an effective resource due to a) its superior performance at low voltage in comparison to static reactive devices, b) fast response of excitation system to changes, and c) having a large reactive power supply

range. Therefore we can select reactive power rescheduling from the generator side which provides an effective way to the control of voltage at the load buses[1].

## III. Problem Formulation

From the discussions above we concentrate on reactive power rescheduling. The reactive power losses reduce the amount of reactive power availability in the circuit. By optimizing the losses we can find the condition with less reactive loss and the voltage remaining stable during contingencies. Therefore the problem is formulated for normal operating condition as given below.

$$\textbf{\textit{Minimize}} \, \boldsymbol{f_x} = \sum_{i=1}^{N_b} \boldsymbol{Q_{loss}} \tag{3.1}$$

$N_b$    No of branches
$Q_{loss}$    Reactive power loss

With power flow constraints

$$\boldsymbol{P_g - P_d - P_{loss} = 0} \tag{3.2}$$
$$\boldsymbol{Q_g - Q_d - Q_{loss} = 0} \tag{3.3}$$

$\boldsymbol{P_g}$- Active power generation
$\boldsymbol{P_d}$ - Active power demand
$\boldsymbol{P_{loss}}$ - Line losses (active power)
$\boldsymbol{Q_g}$- Reactive power generation
$\boldsymbol{Q_d}$- Reactive power demand
$\boldsymbol{Q_{loss}}$- Line losses(reactive power)

And active and reactive power and voltage constraints

$$\boldsymbol{P_{gmin} \le P_g \le P_{gmax}} \tag{3.4}$$
$$\boldsymbol{Q_{gmin} \le Q_g \le Q_{gmax}} \tag{3.5}$$
$$\boldsymbol{V_{imin} \le V_i \le V_{imax}} \tag{3.6}$$

$\boldsymbol{P_{gmin}}$- Minimum active power generation
$\boldsymbol{P_g}$- Active power generation at the particular instant
$\boldsymbol{P_{gmax}}$- Maximum reactive power generation
$\boldsymbol{Q_{gmin}}$ − Minimum reactive power generation
$\boldsymbol{Q_g}$    - Reactive power generation at the particular instant
$\boldsymbol{Q_{gmax}}$- Maximum reactive power generation
$\boldsymbol{V_{imin}}$ - Minimum reactive power generation
$\boldsymbol{V_i}$    - Voltage at *i* th bus at the particular instant
$\boldsymbol{V_{imax}}$ - Maximum reactive power generation

### PARTICLE SWARM OPTIMIZATION

It is a population based search procedure used for solving optimization problems. This procedure is based on the behaviour of flocking birds. The birds in a swarm fly towards the position of food in a random manner. In a similar way the candidate solutions (individuals) called particles change their position with time and updating themselves in each iteration find the solution of the problem from a solution space.

Similar to seeking food, the solution to an optimization problem is found out from a solution space[13,14,15]. The accuracy and rate of convergence of this algorithm depends on the appropriate choice of particle size, maximum velocity of particles and discrete time index. There are no specific guidelines available to select the particle size. It may vary from problem to problem.

### ALGORITHM FOR MINIMIZATION OF REACTIVE POWER LOSSES

The formulated problem is optimized using the PSO algorithm. The steps involved in this procedure is given below. The flow chart is shown in Fig.1.

Step 1: Input the parameters and specify the limits of each parameters. Initialize the population with a set of random solution.

Step 2: Newton-Raphson power flow algorithm is applied to calculate line flows and transmission loss.

Step 3: Parameters in the objective function are calculated and find the value of objective function for each particle. Compare this value with that value of the best solution in the population (pBest). The best solution among the pBest is taken as the best solution among all the particles inthe population (gBest).The pBest and gBest values are updated.

Step 4:The velocity and position of each particle is updated using equations 3.7 and 3.8. If any of the particle is outside limit set its position within the proper limit.

$$V_i\,(k+1) = V_i(k) + \gamma_{1i}\big(p_i - X_i(k)\big) + \gamma_{2i}\big(G - X_{i(k)}\big) \qquad\qquad (3.7)$$
$$X_i(k+1) = X_i(k)\ + V_i\,(k) \qquad\qquad (3.8)$$

i      particle index
k      discrete time index
V      velocity of i th particle
X      position of i th particle
p      best position of i th particle (personal best)
G      best position found by swarm (global best),
$\gamma_{(1,2)}$ random numbers on the interval [0,1] given to i th particle.
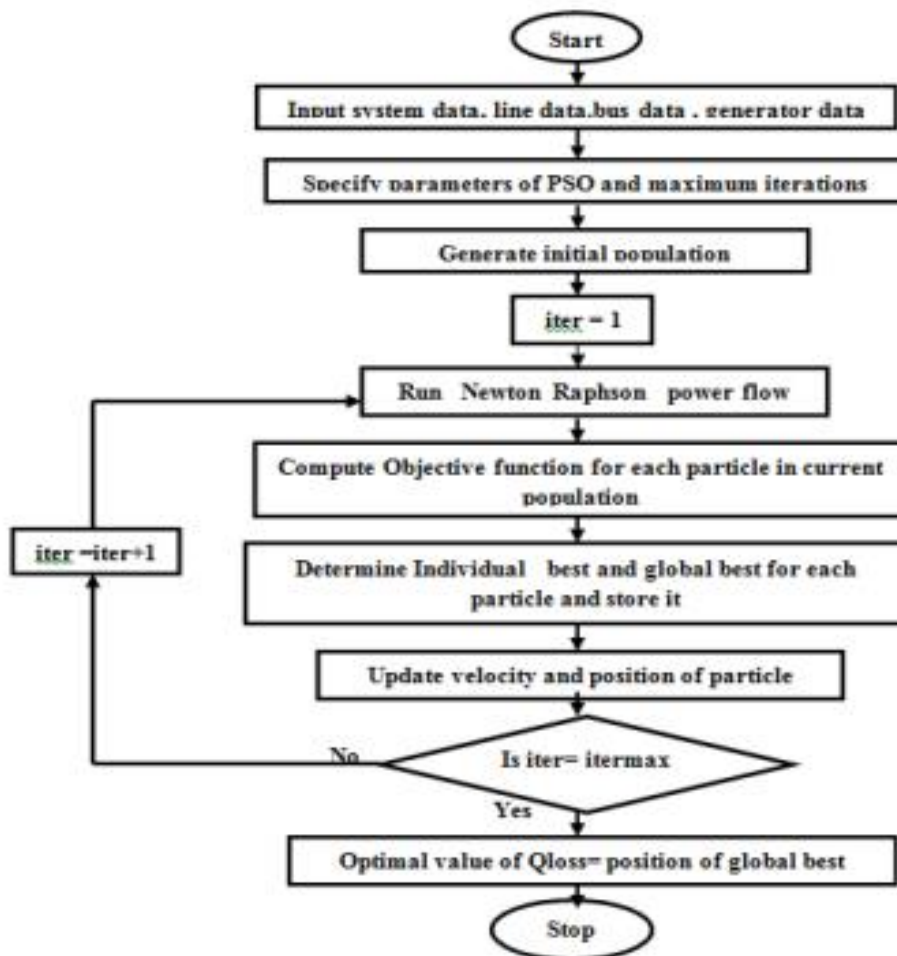


Fig 1. Flow chart of PSO algorithm

Step 5: If any one of the stopping criteria

- If the number of iterations after the last change of the solution is greater than a pre specified number.
- If he number of iterations reaches the maximum allowable number. is satisfied, then go to step 6.Otherwise repeat the steps 2,3 and 4.

Step 6: The particle that produces the latest gBest is the optimal value.

Table 1 PSO parameters

| Parameters | Optimal value |
|---|---|
| Number of particles | 50 |
| Number of iterations | 50 |
| $\gamma_1$ | 2 |
| $\gamma_2$ | 2 |
| Initial inertia weight | 0.9 |
| Final inertia weight | 0.4 |

## IV. Simulation Results
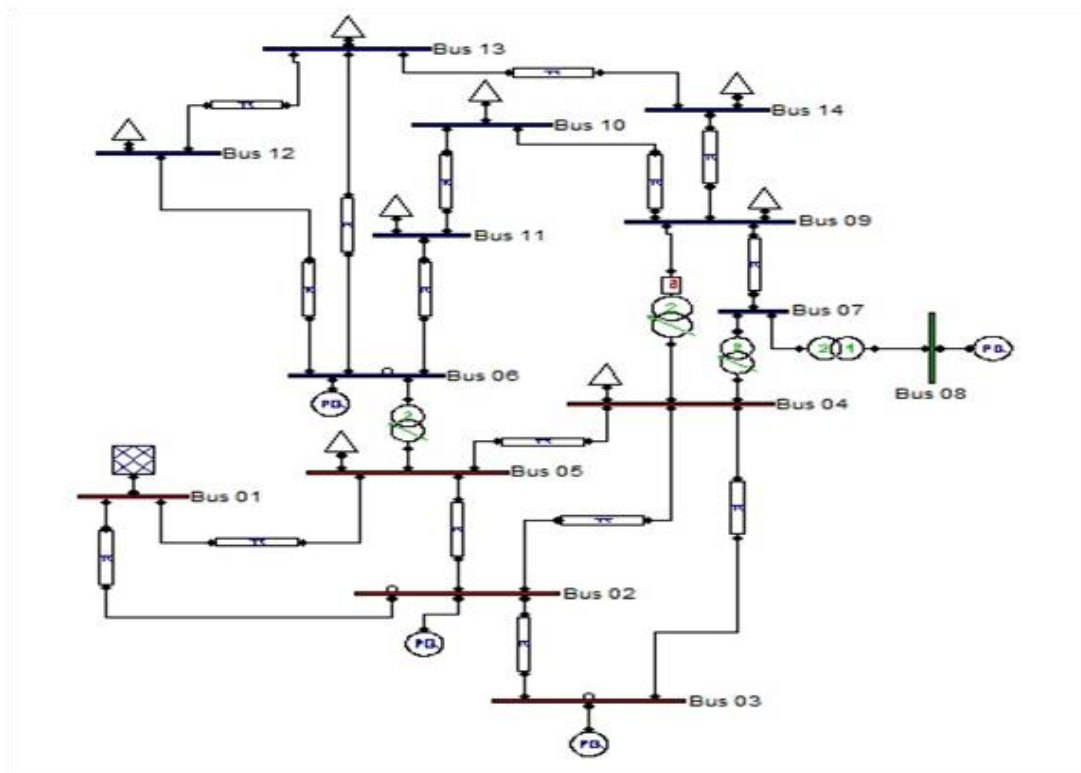


Fig 2.PSAT Simulink model of IEEE 14 Bus system

In order to find out the effectiveness of proposed approach, it was tested on IEEE 14 bus system. IEEE 14 bus system consists of 5 generators, 14 buses,16 lines,4 transformers and 11 loads as shown in Fig 2 .The system has generators located at buses 2, 3, 6 and 8 and 10 and four transformers with off-nominal tap ratio in line 4-7,4–9,5- 6 and 8-9. The lower voltage magnitude limits at all buses are 0.9 p.u. and the upper limit 1.1 p.u. Generator reactive power is optimized by calculating the minimum reactive power loss . Solution is found

by using Newton Raphson Power flow method (PSAT model)[15] and the program was coded in MATLAB software.

Power flow analysis was conducted and the voltage profile for normal condition was observed.
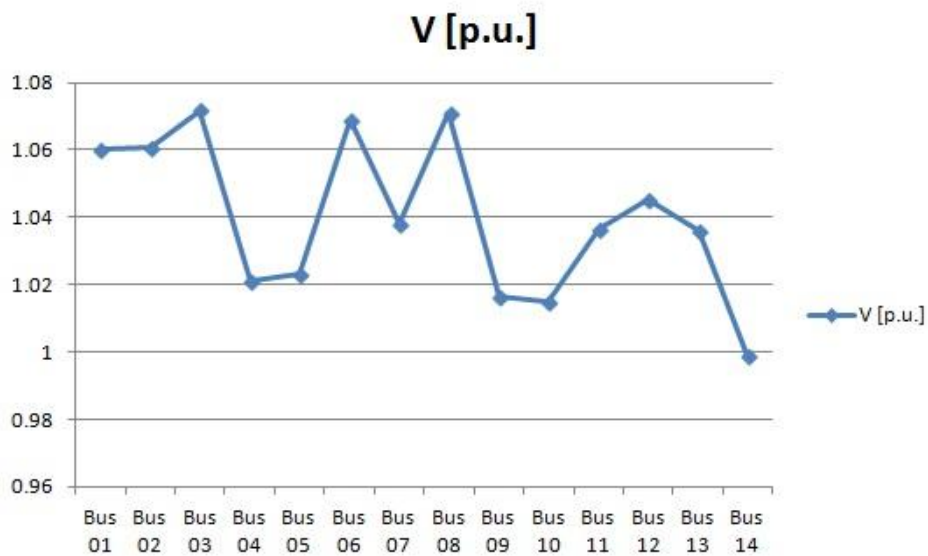


Fig 3. Voltage profile during normal condition

Fig 3. shows that the voltage is within permissible limits.(ie between 0.9 and 1.1 p,u).

A contingency (Increase in reactive load such as starting of induction motor or arc furnace) was simulated.
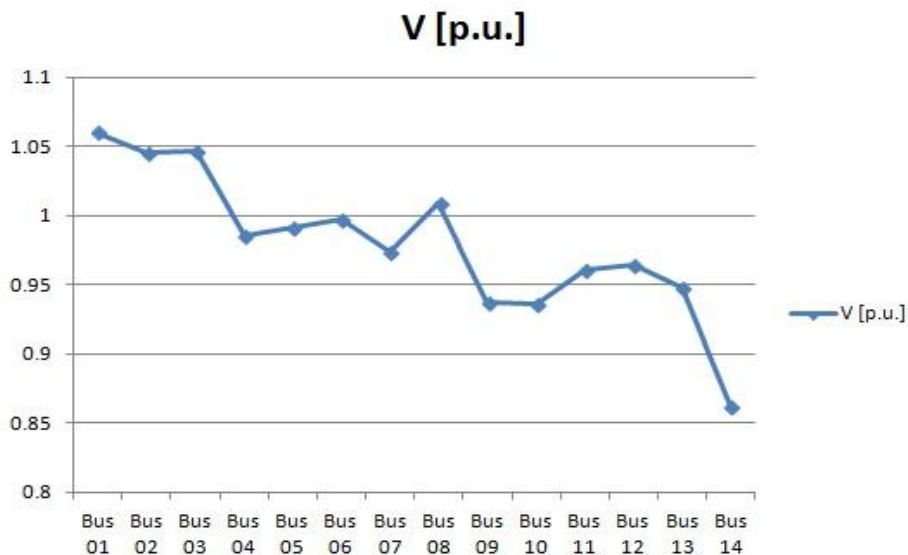


Fig 4.Voltage profile during contingency

The power flow analysis was again conducted and it was found that the voltage at bus no.14 has reduced below 0,9 p.u.(0.86216 p.u). There is an increase in reactive and active losses as found from the power flow results.

The above mentioned algorithm is used to find the optimum value of Qloss as well as the value of needed reactive power generations in the generators to keep the voltage stable. The convergence of Qloss after optimization is shown in Fig 5. Starting from a random value it reaches a minimum point which gives the optimal value.
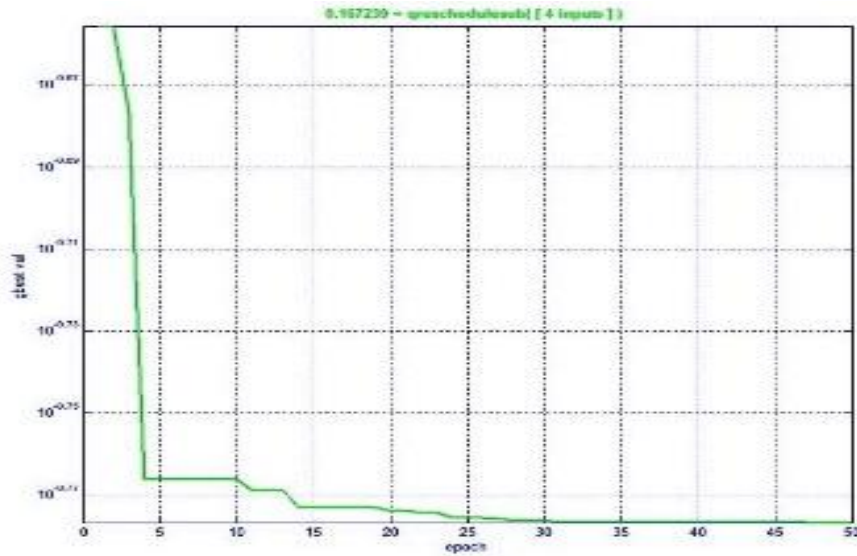
Fig 5. Convergence property of proposed algorithm

Fig 6. compares the voltage during normal condition, contingency condition and voltage after power flow using the values of reactive power to be injected to the generator buses. It indicates that with the optimization technique the voltage has improved during contingency.
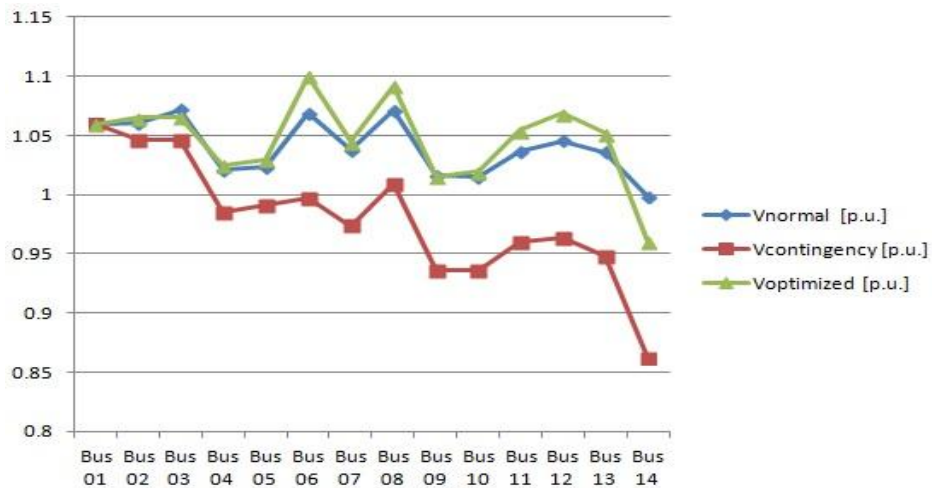


Fig 6.Comparison of voltages

| Condition | Voltage at bus no 14 (p.u) | Reactive power at generator 2,3,4,8 (p.u) | Reactive losses (p.u) | Active Losses (p.u) |
|---|---|---|---|---|
| Normal | 0.99868 | 0.3 0.3 0.2 0.2 | 0.12518 | 0.09046 |
| Contingency | 0.86216 | 0.3 0.3 0.2 0.2 | 0.25509 | 0.11696 |
| After optimization | 0.95996 | 0.4154 0.1783 0.5412 0.2907 | 0.16723 | 0.10738 |

Table 1.Result Analysis

The result analysis shown in the Table 1 . Indicates that with the optimization technique the voltage is within the limits ie.0.95996 p.u. with a contingency in the system. This is achieved by rescheduling generator reactive power with the help of Particle swarm optimization algorithm. The reactive power at generators 2,3,6,8 are set to the value of reactive power obtained after optimization. The power flow results indicate that the voltage has improved.

The value of reactive losses during contingency has increased to 0.25509 p.u and after optimization it has reduced to 0.16723 p.u. thus our objective of voltage stability along with reactive loss reduction is achieved.

The reactive power loss during contingency is 25.509 MVAR. The loss after optimization has decreased to 16.723 MVAR. Percentage reduction in losses is about 34.44%.This will give a cost reduction if we account it in terms of economic considerations. We can observe that the active power loss also get reduced which is an added advantage.

## V.   Conclusion

Reactive power rescheduling was applied in this paper and it was found that by using the   Particle Swarm Optimization technique the reactive losses can be reduced along with the voltage stability achievement. The use of this technique proves to give an added advantage of reduction of active power losses.

## REFERENCES

[1]   O. Alizadeh Mousavi, R. Cherkaoui, "Literature survey on fundamental issues of voltage and reactive power control", October 2011.
[2]   C. W. Taylor," Power System Voltage Stability.": McGraw-Hill, 1994.
[3]   Voltage and reactive power support services,NPTEL
[4]   Venkataramana Ajjarapu, Ping Lin Lau, Srinivasu Battula,"An optimal reactive power planning strategy against voltage collapse",IEEE Trans. Power Syst., 9 (2), pp 906-917,1994.
[5]   T. Van Cutsem, "Voltage Instability: Phenomena, Counermeasures, and Analysis Methods," Proceedings of the IEEE, vol. 88, no. 2, pp. 208-227, February 2000.
[6]   P. Kundur, "Power System Stability and Control.": McGraw-Hilll, 1994
[7]   T. Van Cutsem and C. Vournas," Voltage Stability of Electric Power Systems".: Kluwer Academic Publisher, 1998.
[8]   Carolina M. Affonso, Luiz C. P. da Silva, Flávio G. M. Lima, and Secundino Soares ,"MW and MVar Management on Supply and Demand Side for Meeting Voltage Stability Margin Criteria",IEEE Transactions on Power Systems, Vol. 19, No. 3, August 2004.
[9]   D. Feng, B.H. Chowdhury, M.L. Crow, L. Acar," Improving voltage stability by reactive power reserve management", IEEE Transactions on Power Systems 20 (1) (2005) 338–345.
[10]   B. Lee, Y.H. Moon, H. Song, "Reactive optimal power flow incorporating margin enhancement constraints with nonlinear interior point method", IEE Proceedings Generation, Transmission & Distribution 152 (6) (2005) 961–968.
[11]   Y. Phulpin, M. Begovic, M. Petit, J.B. Heyberger, D. Ernst, "Evaluation of networkequivalents for voltage optimization in multi-area power systems," IEEETransactions on Power Systems 24 (2) (2009) 729–743.
[12]   G. M. Huang and N. C. Nair, "Voltage Stability Constrained Load Curtailment Procedure to Evaluate Power System Reliability Measures," 2002, pp. 761-765.
[13]   B.Lavanya, I.Satish Kumar,"Optimal Placement of Distributed Generation Using PSO/OPF",  IJEAR Vol. 4, Issue Spl-1, Jan - June 2014
[14]   J. Kennedy, R. Eberhart, "Particle swarm optimization in," Proceedings of the IEEE International Conference on Neural Networks, pp. 1942- 1948 1995.
[15]   M.Padma lalithaV.C, Veera reddy, V.Usha ,"Optimal dg placement for minimum real power Loss in radial distribution systems using pso", Journal of Theoretical and Applied Information Technology,2010.
[16]   F. Milano, "An Open Source Power System Analysis Toolbox," IEEE Transactions on Power Systems, vol. 20, no.3, pp. 1199-1206, Aug. 2005.

# "Influence of Initial Preform Aspect Ratios on the Densification Mechanism of Sintered Preforms of Iron and AISI 3115 P/M Steel during Hot Upset Forging"

Rajesh Reddy Koppula[1], K. S. Pandey[2]

[1]*Ex. M. Tech Student and* [2]*Former Professor, Department of Metallurgical and Materials Engineering, National Institute of Technology Tiruchirappalli-620015, Tamil Nadu, India*

**Abstract:** *Hot upset forging experiments were carried out on sintered Iron and AISI 3115 Powder Metallurgy (P/M) steel preforms at $1120°\pm10°C$ which were sintered at the same temperature for a period of sixty minutes. Present investigation, therefore, pertains to evaluate the effect of initial preform geometry on how the densification mechanism/s operate/s during hot upsetting mode. Preforms of initial aspect ratios of 0.6, 0.85 and 1.05 respectively were prepared on a 1.0 MN capacity Universal Testing Machine from Iron as well as from AISI 3115 composition powder blend using suitable die punch and bottom insert assembly in the pressure ranges of $537\pm10M$ Pa; $557\pm10M$ Pa; and $578\pm10MPa$ respectively. With the control of pressure and powder weights, the initial compact densities were maintained in the range of $0.91\pm0.01$ of theoretical density. All compacts were coated with a thin film by using indigenously developed ceramic coating twice and at each time they were dried for a period of twelve hours under an ambient conditions. Ceramic coated compacts were sintered in an electric muffle furnace for a period of sixty minutes at $1120°\pm10°C$. All sintered compacts except one from each aspect ratios were hot upset forged to different height strains and suitable plots were drawn between fractional theoretical density and the true height strains, true diameter strain and the true height strains, Poisson's ratio and the fractional theoretical density, the fractional theoretical density and the bulging ratio to establish empirical relations in the above said parameters. Analysis of the experimental and the calculated parameters along with the various plots have yielded several empirical relationships of practical as well as of theoretical importance.*

**Keywords:** *Aspect Ratio, Sintered Preforms, AISI 3115, Upset Forged, Densification, Poisson's Ratio, Bulging.*

## I. Introduction

Worldwide popularity of powder metallurgy (P/M) lies in the ability of this technique to produce complex metal shapes to exact dimensions, at high rates at extremely economical prices and providing much higher levels of technical achievements in quality [1]. P/M is at times the only manufacturing method that can be used for producing some materials such as porous materials, refractory metals and specially designed high duty alloys [2]. P/M processes possess the ability to produce net shape or near net shape high precision components with highest level of material utilization [3]. Therefore, the P/M processes compete with other methods on the basis of cost which can be lower for high volume production of complicated and intricate shaped components [3]. Further the sintered materials inherently possess high flexibility in their alloying design to increase their heat resistance and wear resistance in comparison with that of the conventionally produced wrought steels and cost alloys [2, 4]. The manufacturing processes for conventional P/M parts consist of powder production, blending (if the same is designed for the production of an alloy), compaction and finally sintering [5]. However, the sintered materials do contain inherent porosities whose presence have both beneficial as well as detrimental roles on the part performance [6]. Conventional P/M components are used in applications requiring low mechanical property levels [5]. In order to produce/prepare sound metallurgical structure, voids are to be eliminated or completely closed down. It is reported [6] that an increase in density would increase the strength, the fracture toughness and the resistance to crack growth. This can be achieved by secondary operations like forging, rolling, extrusion and extrusion forging etc. [7, 8]. Hot forging is generally employed to produce highly dense products by the P/M route. Powder preform forging involves the fabrication of preforms by the usual press and sinter processes followed by forging of the porous preforms into the final shapes [9]. Powder preform forging (PPF) has the advantages like optimum utilization, uniformity in properties, single blow finishing operation, improved weight control and savings in secondary machining operations [10]. The

basic process parameters such as forging temperature, initial preform density, alloying elements and the flow stresses do affect the density of the component/s after the forging operation is completed [10-13]. Therefore, a perfect combination of the above parameters for enhanced density is a must. Keeping this in mind Torre [14] considered porous metal as a metal containing a void for investigation of densification, i.e., a thick-walled sphere. According to him, the pressure required for the plastic deformation of a sphere containing a hole is given by:

$$P = 2\sigma_o \ln (r_o/r_i)\ldots\ldots\ldots\ (1)$$

Where, $\sigma_o$ = Flow stress of the material,
$r_o$ = Outside radius of the sphere,
$r_i$= Hole radius (equal to the void radius), and,
$P$ = Pressure required to close down the pore.

Now, if the void radius is high, the pressure required to deform the sphere is substantially low. However, when the void radius approaches to zero, the pressure required to deform the sphere, i.e., then in this event in order to densifying the material becomes infinitely large. Therefore, it is, obvious that under the application of hydrostatic mode of loading, the void shape does not change, instead the size is reduced. The pore can be closed by applying the compression pressure (upsetting) which allows the material to flow freely in lateral direction, and, hence, the void becomes extremely flattened and elongated and the voids fragment into smaller voids. Since the shearing occurs along the interface of the opposite sides of the collapsed void, and, therefore, this would result in an increase in final density. It is reported [9] that the dynamic properties like fatigue and impact resistance depend not only on the residual porosity, but, also do depend, upon the characteristics of the metal flow during the densification mode. Hence, it is absolutely necessary to investigate the mechanism of material flow during metal preform hot upsetting.

In the present investigation, an attempt has been made to establish the densification mechanism/s and further to assess the influence of initial aspect ratios on the densification phenomenon during hot upset forging in a comprehensive manner. The materials used for the present study were Iron powder and AISI 3115 blend prepared from the elemental powders with the initial aspect ratios of 0.60, 0.85 and 1.05 respectively.

## II.  Experimental Details

### 2.1 Materials Required and Their Procurements
Iron powder of -180µm has been procured from M/s. The Sundaram Fasteners Limited, Hyderabad, Andhra Pradesh, India. The basic characteristic features of the Iron powder and the blend corresponding to AISI 3115 steel composition prepared from the elemental powders are given in Tables 1, 2,and 3 respectively. Suitable die set assembly was selected for compaction and the same one was made of High Carbon and High Chromium die steel. The assembly includes the mother die, the punch, the bottom insert, and the top and the bottom plates. These die parts have been machined from a suitable blanks of High Carbon and High Chromium steel, soaked in the temperature range of 950º±10ºC for one hour to four hours depending upon the part keeping in mind that every 25mm diameter part was heated and soaked for one hour at the above temperature and quenched in oil. The hardness values were in the range of 59-61Rc. These parts were tempered to hardness values of 54-56Rc. Powder compaction was carried out on a 1.0MN capacity Universal Testing Machine. However, electric muffle furnace was used for sintering the compacts, which was kept near the Friction Screw Press of 1.0MN capacity to be used for forging operation. The material selected for the flat top and the bottom blocks of the forging hot dies was Molybdenum die steel and the each one of them having the dimensions of 240mmx150mmx100mm. The main alloying powders such as silicon, manganese, chromium, and nickel were procured from M/s. Grishma Enterprises, Mumbai, India. However, the graphite powder of 2 to 5µm was supplied by Ashbury Inc. New Jersey, USA exclusively for research purposes.

**Table1 Selected Composition of AISI 3115 P/M Steel (Wt. %)**

| System | C | Si | Mn | Cr | Ni | Fe |
|---|---|---|---|---|---|---|
| AISI 3115 | 0.16 | 0.28 | 0.5 | 0.65 | 1.25 | 97.16 |

**Table 2 Basic Characteristic of Iron Powder and AISI 3115 Powder Blend**

| Property | Iron | AISI 3115 |
|---|---|---|
| Apparent Density, g/cc | 2.877 | 3.349 |
| Flow Rate( By Hall Flow meter), S/100g | 57.520 | 56.37 |
| Compressibility, g/cc at a Pressure of 480±10 MPa | 6.751 | 6.757 |

**Table 3 Sieve Size Analysis of Iron Powder**

| Sieve size (μm) | -180 +150 | -150 +125 | -125 +106 | -106 +90 | -90 +75 | -75 +63 | -63 +53 | -53 +45 | -45 +38 | -38 |
|---|---|---|---|---|---|---|---|---|---|---|
| Wt.% Ret. | 0.019 | 0.115 | 0.046 | 0.048 | 0.184 | 3.505 | 26.090 | 25.24 | 2.249 | 42.469 |
| Cum. Wt.% Ret. | 0.019 | 0.134 | 0.180 | 0.228 | 0.412 | 3.917 | 30.007 | 55.247 | 57.496 | 99.965 |

**2.2 Blending of Required Elemental Powders**
Preparation of the powder blend of the AISI 3115 steel composition was carried out by taking accurately weighed elemental powders which can correspond to AISI 3115 composition as is given in Table 1 after sintering operation is completed. Elemental powders of the above requirements were taken and mixed in the stainless steel pot of the pot mill with a powder weight to ball weight ratio as 1.2:1. The lid of the pot was securely tightened and the pot was fixed on the pot mill and the mill was switched on. Immediately after the completion of every one hour of blending, nearly 100g of powder mix was taken and the flow rates and the apparent densities were measured. Once the above measurements were successfully completed, the tested powder mix was returned back to the pot and the pot's lid was securely tightened and the pot was re-fixed on the pot mill and the mill was switched on again. The above process was repeated thirty times or till the last three consecutive readings were consistently the same. Thus, the blending time arrived at was 30 hours, and, then the blending operation was discontinued. Now the powder blend was ready for compaction.

**2.3 Compaction of Iron Powder and Blend of AISI 3115 P/M Steel Composition**
Iron powder and the above prepared powder blend corresponding to AISI 3115 composition were accurately weighed and taken for the preparations of compacts with three initial aspect ratios, namely, 0.60, 0.85 and 1.05 respectively. Compacts of above initial aspect ratios were prepared on Universal Testing Machine of 1.0 MN capacity while using suitable die set assembly. In all, a total of 36 compacts were prepared. The compact densities were maintained in the range of 91±1 per cent of theoretical by applying the pressure in the range of 535±10 MPa for 0.60, 555±10MPa for 0.85 and 575±10MPa for 1.05 aspect ratios respectively. The diameter of the compaction die was $24.84^{+0.01}$ mm. Graphite powder with acetone as a paste was employed as a lubricant during compaction. The schematic diagram for powder compaction assembly is shown in fig.1.
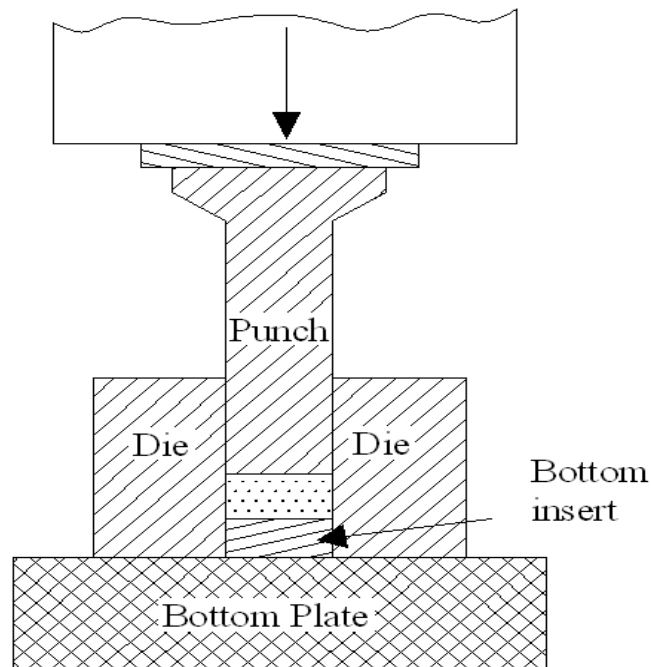


**Figure 1 Schematic Diagram of Powder Compaction Assembly.**

**2.4 Application of Indigenously Developed Ceramic Coating**
A thin film of indigenously developed ceramic coating [16] was applied on the entire surfaces of all the compacts to protect them against oxidation during sintering in the temperature range of $1120°±10°C$ for a period of sixty minutes in an electric muffle furnaceand subsequently transferring them to the bottom platen of the friction screw press for hot upset forging.

The ceramic coated compacts were recoated perpendicular to the previous coating and then both the coatings were allowed to dry under an ambient conditions for a period of twelve hours independently, i.e., one followed by the other after the completion of each coatings.

### 2.5 Sintering the Ceramic Coated Compacts of Iron Powder and AISI 3115 Powder Blend
Once the drying operation was completed, the ceramic coated compacts were kept in a ceramic tray and the tray was charged inside the uniform temperature zone of the electric muffle furnace. The furnace was switched on and the temperature was raised to 700º±10ºC and retained at this temperature for a period of 45 minutes in order to allow the volatile ingredients to be expelled out. Immediately after the completion of the pre-heating schedule, the furnace temperature was raised to 1120º±10ºC, and, this temperature was retained for a period of sixty minutes. This completes the sintering schedule, and now the compacts are sintered and are ready for hot upset forging.

### 2.6 Hot Upset Forging
All sintered compacts except one of each aspect ratios, namely, 0.60, 0.85 and1.05 and of each of the systems respectively were hot upset forged to different height strains on a 1.0MN capacity friction screw press on a Molybdenum hot flat steel dies. Immediately after hot upset forging of the sintered preforms were completed, the forged discs were quenched in linseed oil bath so as to retain the forged structures. Compacts of the each of the systems were separately sintered and separately forged in order to avoid the intermingling's of the forged discs of each of the systems.

### 2.7 Removal of Residual Ceramic Coatings from the Forged P/M Discs
Residual ceramic coatings if any was removed by mild machining/grinding or by mild filing or by using abrasive papers ensuring that no metal is abraded out. This procedure was employed to all the forged discs of both the systems and for all the three aspect ratios mentioned above. This adoption of removal of residual ceramic coating would bring uniformity as well as the accuracy in density measurements along with their actual forged dimensions.

### 2.8 Dimensional Measurements of Forged Discs and Sintered Preforms
Dimensions such as forged height ($H_f$), contact diameters [(top ($D_{ct}$), & bottom ($D_{cb}$)] and the bulged diameter ($D_b$) were accurately measured using digital Vernier calipers. A minimum of five readings were taken for each of the above parameters and then averaged out independently. Apart from the measurements of these parameters, initial height ($H_o$) and the initial diameter ($D_o$) of the sintered, but, thoroughly cleaned preforms were also measured by using the digital Vernier calipers. Now using these parameters, true height strain ln ($H_o/H_f$); true diameter strain ln ($D_c/D_o$); bulging ratio (Br = {$D_b/Do$}) and log ($D_b/Do$) were calculated and subsequently used to draw series of plots. Where, $D_c$ = {($D_{ct}$ + $D_{cb}$)/2}.

### 2.9 Density Measurements of Sintered and Forged Preforms
Density measurements of all the forged and sintered, but, cleaned compacts were found out by employing Archimedean principle [15]. Whereas, the density of sintered compacts were found out by calculating the volume geometrically and the mass in air using Adair-180 electronic balance with a sensitivity of 0.0001g. Prior to measuring the weights of the forged discs, a very fine film of a repellant oil [17] was applied on all the forged discs in order to avoid the penetration of water into the pores, thus, affecting true volume of the forged discs. The standard formula used to measure the density of the forged discs is given beneath:
**Density of the forged discs,$\rho_f$ g/cc = {$M_{air}$ / ($M_{air}$ − $M_{water}$)} x $\rho_{water}$----------- (2)**

Where, **$M_{air}$** = Mass in air, g; **$W_{water}$**= Mass in water, g, and, **$\rho_{water}$** = water density in g/cc.

Density correction was introduced depending upon the room temperature by using standard chart for density variations of water with respect to varying room temperature/s.

## III.  Results and Discussions

### 3.1 Deformation and Densification
Fig. 2 (a) has been drawn between fractional theoretical density ($\rho_f/\rho_{th}$) and the true height strain {ln ($H_o/H_f$)} obtained during hot forging of sintered iron powder preforms of different aspect ratios. This fig. veryexplicitly indicates that the lower aspect ratio (0.60 and 0.85) preforms densified comparatively at a much faster pace in contrast to the largest aspect ratio (1.05) preforms. However, the curve corresponding to initial performs.
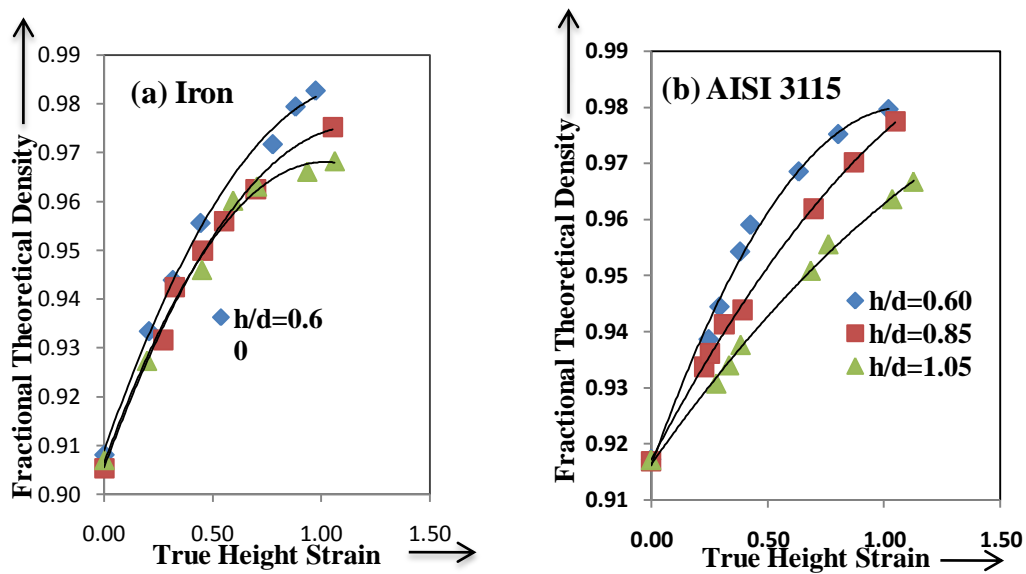
**Figure 2 Relationship between the Fractional Theoretical Density and the True Height Strains during Hot Upset Forging of Sintered (a) Iron and (b) AISI 3115 P/M Steel Preforms**

of aspect ratio of 0.85 positioned itself in between the curves corresponding to the lowest and largest aspect ratio preforms. In the initial stages of deformation, both the preforms, i.e., the largest and the medium sized densified with almost at the same pace up to the true height strains of 0.84 and there onwards the middle aspect ratio preforms densified at a faster rate compared to the largest aspect ratio preforms. This establishes that the largest aspect ratio preforms would always densify poorly compared to the lowest and the middle aspect ratio preforms which have shown much improved densification rates. Fig. 2 (b) has been drawn between fractional theoretical density attained and true height-strains during hot upset forging of sintered preforms of AISI 3115 P/M steel. This fig. very clearly shows that the densification rate shown by the lowest aspect ratio preforms have been maximum whereas the largest aspect ratio preforms exhibited the least rate of densification. This goes to establish that this AISI 3115 P/M steel is highly affected by the initial preform geometry during hot deformation and densification at $1120°\pm10°$C. The characteristic nature of curves shown in each of these figs. i.e., 2(a) and 2(b) are similar to each other, and, therefore, it is anticipated that all these densification curves would conform to a similar mathematical expression. Hence, the curve fitting techniques have been employed which resulted in yielding a second order polynomial to which all these curves conformed to. Thus, the densification curves shown through figs. 2(a) and 2(b) conformed to a second order polynomial of the form:

$$(\rho_f/\rho_{th}) = A_0 + A_1 \ln (H_0/H_f) + A_2 [\ln (H_0/H_f)]^2 ……………… (3)$$

Where, '$A_0$', '$A_1$' and '$A_2$' are empirically determined constants found to depend upon the composition and the preform geometries. These constants are tabulated in Table-4. Observing these constants carefully it is found that the constant '$A_0$' is in very much close proximity to the initial preform density, and, therefore, did not contribute to densification. The values of the constant '$A_1$' is found to be positive and linearly multiplied to the true height strain, and, therefore, assisting to densification linearly. However, the values of the constant '$A_2$' is almost always negative and the same is multiplied to the square of the true height strain giving rise to a small negative value which can affect the density curves only in the final stages of deformation in such a manner so as to flatten the curves in last stages of deformation and densification. The observation that the lowest aspect ratio preforms densified at an enhanced pace compared to other larger aspect ratio preforms is justified because during the deformation, though percentage porosity content in the lowest and highest aspect ratio preforms are same, but, their effective depth of the pore bed in the lower aspect ratio preform is low, and, therefore, the load transfer along the direction of loading is quite quick and uniform. But, in larger aspect ratio preforms, the pore bed depth is comparatively higher, and, therefore, damping is on the higher side. Hence, the effective load transfer in the direction of loading is of lower magnitude in the larger aspect ratio preforms, and, therefore, results in poor densification in larger aspect ratio preforms. Further observing the Table-4, it is, found that the regression co-efficient, i.e., '$R^2$' values are in close proximity to unity indicating that the curve fittings have been carried out excellently well and accurate. Therefore, the above logistic discussion and the proposed densification equation of the second order polynomial stand the test of trial and are valid within the framework of the investigation.

**Table 4 The Coefficients of the Second Order Polynomial of the Form ($\rho$f/$\rho$th) =$A_{0}$ + $A_1$ ln ($H_o/H_f$) + $A_2$ [ln ($H_o/H_f$)] $^2$ for Iron and AISI 3115 Steel during Hot Deformation.**

| System | Aspect Ratio | $A_0$ | $A_1$ | $A_2$ | $R^2$ |
|---|---|---|---|---|---|
| **Iron** | 0.6 | 0.906 | 0.122 | -0.061 | 0.992 |
| | 0.85 | 0.904 | 0.138 | -0.069 | 0.994 |
| | 1.05 | 0.906 | 0.138 | -0.067 | 0.991 |
| **AISI 3115** | 0.6 | 0.915 | 0.12 | -0.055 | 0.991 |
| | 0.85 | 0.916 | 0.086 | -0.027 | 0.995 |
| | 1.05 | 0.916 | 0.06 | -0.013 | 0.995 |

### 3.1 Relationship between True Diameter and True Height Strains

Figs. 3(a) and 3(b) have been drawn between the true diameter strains and true height strains for sintered Iron powder and AISI 3115 powder blend preforms during hot upset forging at 1120º±10ºC respectively. Observing these two figs. 3(a) and 3(b) respectively, it is evident that all the data points remained below the theoretical line irrespective of the initial aspect ratios of the preforms and the compositions establishing very clearly that the values of the Poisson's ratio would always remain less than 0.5. Further, it is observed that the data points corresponding to the lowest aspect ratio preforms always remained closer to the theoretical line except.
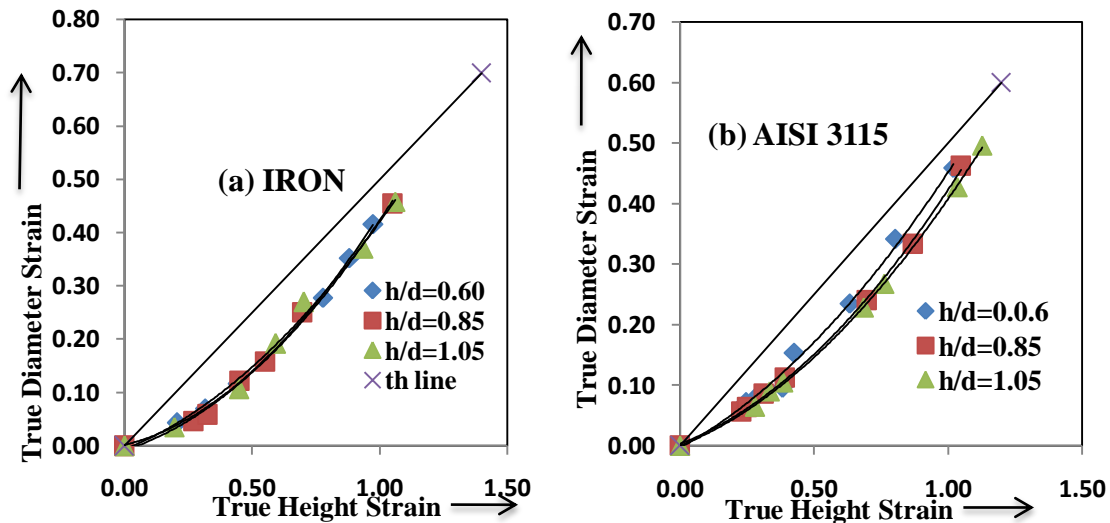


**Figure 3 Relationship Between True Diameter Strain and True Height Strain During Hot Upset Forging of Sintered (a) IRON and (b) AISI 3115 Preforms.**

In the case of iron powder preforms of all the aspect ratios, the data points lied in a very narrow band. It is further observed that the data points for largest aspect ratio preforms remained farthest away from the theoretical line. But, the data point corresponding to the middle aspect ratio (0.85) remained in between the lowest and largest aspect ratio preforms. The curves drawn in figs. 3(a) and 3(b) are found to be quite similar to each other irrespective of the initial preform geometries and the systems compositions. Further it is established that the values of the Poisson's ratios always remained less than one half. However, the critical analysis of these curves revealed that the curves conformed to a second order polynomial of the form:

$$Ln\ (D_f/D_o) = B_0 + B_1\ ln\ (H_o/H_f) + B_2\ [ln\ (H_o/H_f)]^2 \ldots\ldots\ldots\ldots\ldots\ldots..(4)$$

Where, 'B$_0$', 'B$_1$' and 'B$_2$' are found to be empirically determined constants and are dependent upon the initial aspect ratios and alloy compositions. These constants along with the values of the regression coefficients are given in Table 5. Observing this table carefully, it is, found that the constant 'B$_0$' is virtually negligible and small, and, therefore, can be taken to be practically zero and can be taken off from the above polynomial because at no deformation, there is no diameter strain with respect to height strain. The constant 'B$_1$' is generally positive and contributes to linear increase in the diameter strain with respect to height strain, but, 'B$_2$' being always positive and multiplied by the square of the height strain giving rise to a parabolic increase, but, in

the final stages, the curves tended to be almost parallel to the theoretical line conforming to a positive fact that in the final stages of

**Table 5 The Coefficients of the Second Order Polynomial of the Form: [ln (D$_f$/D$_o$)] = B$_0$ + B$_1$ ln (Ho/H$_f$) +B$_2$ {ln (H$_o$/H$_f$)}$^2$ for Iron and AISI 3115 Steel During Hot Deformation.**

| System | Aspect Ratio | B$_0$ | B$_1$ | B$_2$ | R$^2$ |
|---|---|---|---|---|---|
| Iron | 0.6 | -0.002 | 0.12 | 0.312 | 0.999 |
| | 0.85 | -0.007 | 0.158 | 0.278 | 0.995 |
| | 1.05 | -0.006 | 0.192 | 0.233 | 0.993 |
| AISI 3115 | 0.6 | -0.008 | 0.193 | 0.273 | 0.994 |
| | 0.85 | -0.004 | 0.109 | 0.322 | 0.998 |
| | 1.05 | -0.021 | 0.098 | 0.309 | 0.998 |

Upsetting mode of deformation, the flow of the material and the pores became almost simultaneous. Now analyzing the regression coefficients whose values are found to be extremely close to unity indicating that the empirical equation arrived at, is justified and is valid under the boundary conditions of deformations, i.e., presuming that absolutely, too, little or absolutely, too, high strains are not induced. In, too, little deformations, the effect of true diameter strain and the true height strain is neglected and also inducing, too, high strains would be leading to circumferential crack formations which would result in a deceptive outcome. Therefore, in the nutshell, the equation relating the true diameter strain and the true height strain is given as underneath:

$$Ln (D_{fc}/D_o) = B_1 \ln (Ho/H_f) + B_2 [\ln (H_o/H_f)]^2 \quad \ldots\ldots\ldots\ldots\ldots\ldots..(5)$$

### 3.2 Deformation, Densification and Poisson's Ratio

Figs. 4 (a) and 4 (b) show the variation between Poisson's ratio ($v_p$) and the percentage theoretical density {% ($\rho_f/\rho_{th}$)} during hot upset forging of sintered preforms of Iron and AISI 3115 P/M steel respectively. General observations of these curves shown in these figs. 4 (a) and 4 (b) are found to be very much similar to each other. There is a very clear distinction that the curves corresponding to the largest aspect ratio preforms is on the top of all the curves and the curves representing the minimum aspect ratio preforms positioned themselves at the bottom of all other aspect ratio curves. However, the curves representing to the middle aspect ratio preforms remained in the middle of above two curves. It is, also observed from these curves starting from around 92% density till around 98% density, the Poisson's ratio has gone up quite slowlywith an increased level of densification, and, thereafter
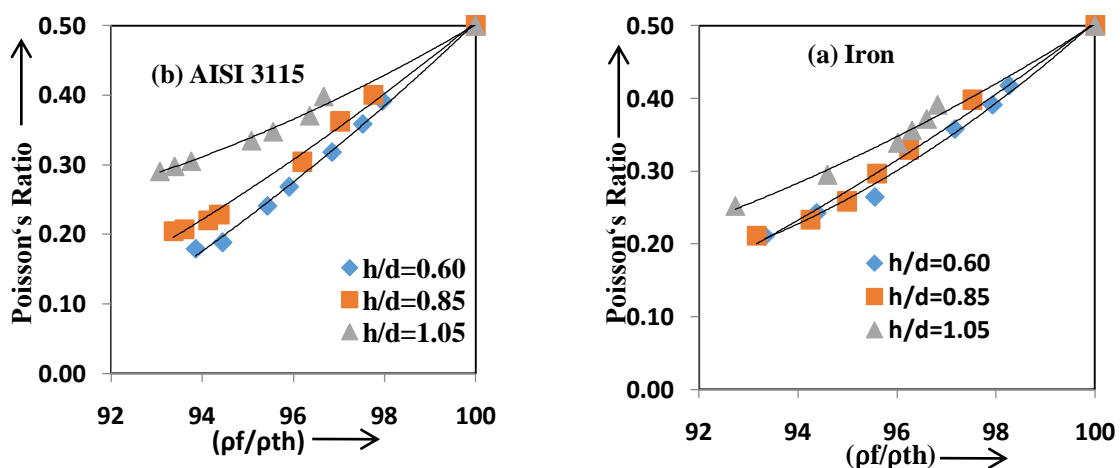


**Figure 4 Relationship between Poisson's Ratio and Percentage Theoretical Density during Hot Upset Forging of Sintered (a) Iron Preforms and (b) AISI 3115 P/M Steel Preforms**

The rate of densification has been low with high rise in the values of the Poisson's ratio. It is further noted that in the near vicinity of the theoretical density, the value of the Poisson's ratio tended to approach to a theoretically feasible value of Poisson's ratio, i.e., 0.5. This ably supports the argument that in upset forging a cent per cent dense product cannot be achieved and, hence, the limiting value of Poisson's ratio of 0.5 is not approached. The curves drawn in figs. 4 (a) and 4 (b) on analysis have revealed that an empirical relationship

between Poisson's ratio and the percentage theoretical density conformed to a second order polynomial of the form as is given below:

$$\nu_p = C_0 + C_1 \{\%(\rho f/\rho th)\} + C_2 \{\%(\rho f/\rho th)\}^2 \quad \ldots\ldots\ldots\ldots\ldots\ldots \quad (6)$$

Where, the coefficients of the second order polynomial given in equation 6 are 'C$_0$', 'C$_1$' and 'C$_2$' respectively and they are found to depend upon the compositions of the systems and the preform geometriesof the preforms. The values of these constants 'C$_0$', 'C$_1$' and 'C$_2$' for both the systems along with the values of regression coefficient 'R$^2$'are given in Table-6. The values of 'R$^2$' are found to be in close vicinity of unity. It is, therefore, clearly established that the relationship empirically arrived at stands ably justified

**Table 6 The Coefficients of the Second Order Polynomial of the Form: Poisson's Ratio ($\nu_p$) = C$_0$ + C$_1$ {(%($\rho f/\rho th$)} + C$_2$ {%($\rho f/\rho th$)}$^2$ for Sintered Iron and AISI 3115 P/M Steel Preforms during Hot Upset Deformation.**

| System | Aspect Ratio | C$_0$ | C$_1$ | C$_2$ | R$^2$ |
|--------|--------------|-------|-------|-------|-------|
| | 0.6 | 15.7 | -0.366 | 0.002 | 0.995 |
| Iron | 0.85 | -9.13 | 0.145 | 0.001 | 0.989 |
| | 1.05 | -2.379 | 0.017 | 0.001 | 0.99 |
| | 0.6 | -43.18 | 0.836 | 0.004 | 0.992 |
| AISI 3115 | 0.85 | -19.22 | 0.357 | 0.001 | 0.997 |
| | 1.05 | -28.66 | 0.565 | 0.002 | 0.99 |

### 3.3 Deformation, Densification and Bulging

Figs. 5 (a) and 5 (b) have been drawn between percent theoretical density attained and the bulging ratio for both the systems investigated in the present work. The characteristic nature of the curves drawn in these two figs. 5(a) and 5(b) stand quite similar to each other and when analytically analyzed were found to be in close conformitywith a second order polynomial of the form as stated below:

$$\{\%(\rho f/\rho th)\} = E_0 + E_1 (D_b/D_o) + E_2 (D_b/D_o)^2 \quad \ldots\ldots\ldots\ldots\ldots\ldots \quad (7)$$
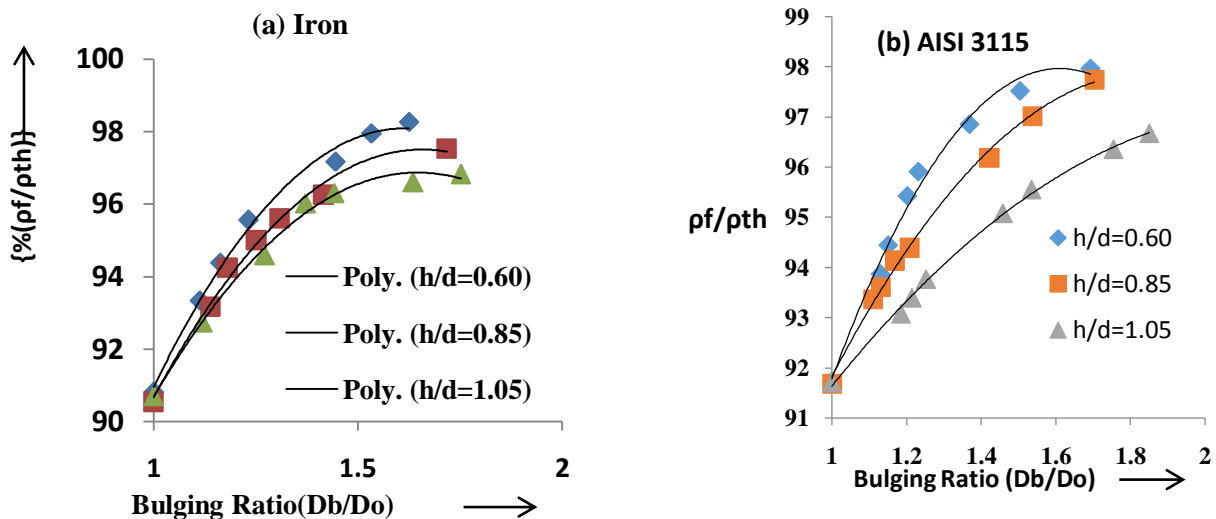


**Figure 5 Relationship between percent Fractional Theoretical Density and Bulging Ratio during Hot Upset Forging of Sintered AISI 3115 Preforms.**

Where, 'E$_0$', 'E$_1$' and 'E$_2$' are empirically determined constants and are found to depend upon the preform geometries and the systems compositions. The values of these coefficients. i.e., 'E$_0$', 'E$_1$' and 'E$_2$' along with the values of the regression coefficient 'R$^2$'are listed in Table-7. Observing the values of the regression coefficient 'R$^2$', it is found that they are in close proximity to unity and hence the expression {%( $\rho_f/\rho_{th}$)} = E$_0$+ E$_1$ (D$_b$/D$_o$) + E$_2$ (D$_b$/D$_o$)$^2$ empirically arrived at stands technically validated.

**Table 7 The Coefficients of the Second Order Polynomial of the Form (% $\rho_f/\rho_{th}$) = $E_0$+ $E_1$ ($D_b/D_o$) + $E_2$ ($D_b/D_o$) $^2$ for Iron and AISI 3115 Steel during Hot Deformation.**

| System | Aspect Ratio | $E_0$ | $E_1$ | $E_2$ | $R^2$ |
|---|---|---|---|---|---|
| Iron | 0.6 | 43.64 | 69.79 | -22.34 | 0.989 |
| | 0.85 | 45.06 | 66.72 | -21.22 | 0.991 |
| | 1.05 | 56.31 | 49.5 | -15.1 | 0.993 |
| AISI 3115 | 0.6 | 53.14 | 55.94 | -17.43 | 0.99 |
| | 0.85 | 66.37 | 35.46 | -10.03 | 0.995 |
| | 1.05 | 78.13 | 17.58 | -4.093 | 0.996 |

**3.4 Deformation, Densification and Power Law Relationship**

Figs. 6 (a) and 6 (b) have been drawn between logarithm of per cent theoretical density and the logarithm of bulging ratio for both the systems that were investigated in the present study. It has been found that straight lines continuous or in two segments were found to be well represented by the calculated parameters such as percent theoretical density and the bulging ratio. These plots show that a relationship of the form given below:

$$\text{Log } \{\% \ (\rho f/\rho\rho_{th})\} = m \log (D_b/D_o) + Q \ldots\ldots\ldots\ldots. \ (8)$$

The above expression when simplified represents a power law equation of the form as given underneath:

$$(\rho_f/\rho_{th}) = Q_0 (D_b/D_o)^m \ \ldots\ldots\ldots\ldots\ldots\ldots\ldots \ (9)$$

Where, the constants 'Q' and 'm' are found to be empirically determined constants depending upon the values of initial preform geometries and the composition. However, one interesting aspect which can be observed from Table 8 where the constants 'Q' and 'm' are listed is that for a given aspect ratio in a given segment the values of 'm' keeps decreasing while the values of 'Q' remaining more or less constant. The values of the regression coefficient '$R^2$' is found to be very much in close vicinity of unity and, therefore, the expression proposed in the equation (7) is justified and the values of the constants including the values of '$R^2$' are listed in Table 8 which determine the rapidity to an increase in per cent theoretical density on deformation and the resultant increase in bulging.
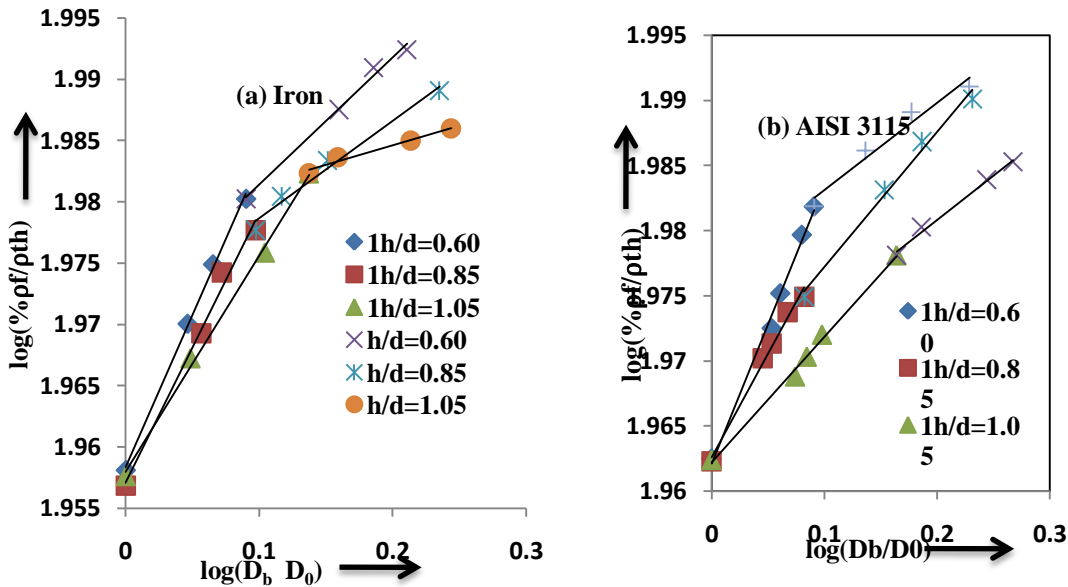


**Figure 6 Relationship between Log (% Fractional Theoretical Density) and log (Bulging Ratio) during Hot Upset Forging of Sintered Preforms of (a) Iron and (b) AISI 3115 P/M Steel Preforms.**

**Table 8 The Slope and Intercepts of the of the Form Log {%($\rho_f/\rho_{th}$)} = mLog (%$D_b/D_o$) + Q for Iron and AISI 3115 Steel During Hot Deformation.**

| System | Aspect Ratio | m | Q | $R^2$ |
|---|---|---|---|---|
| Fe | 0.6 | 0.247 | 1.958 | 0.998 |
| | 0.85 | 0.22 | 1.957 | 0.99 |
| | 1.05 | 0.176 | 1.958 | 0.997 |
| | 0.6 | 0.104 | 1.971 | 0.992 |
| | 0.85 | 0.079 | 1.97 | 0.991 |
| | 1.05 | 0.032 | 1.97 | 0.993 |
| AISI 3115 | 0.6 | 0.223 | 1.961 | 0.99 |
| | 0.85 | 0.158 | 1.962 | 0.989 |
| | 1.05 | 0.096 | 1.962 | 0.996 |
| | 0.6 | 0.058 | 1.977 | 0.99 |
| | 0.85 | 0.103 | 1.966 | 0.989 |
| | 1.05 | 0.067 | 1.967 | 0.993 |

## IV.  Conclusions

Based on the experimental data and calculated parameters and their analysis critically carried out has yielded the major findings of the present investigation are given as underneath:

1.  Rate of densification has been established as a function of preform geometries and the compositions of the systems investigated. Lower aspect ratio preforms have been found to densify at a much faster rates compared to the larger aspect ratio preforms due to rapid and uniform load transfer across the axial direction which is caused due to lower pore bed depth. The relationship between fractional theoretical density($\rho_f/\rho_{th}$) and the true height strains is given as beneath:

$$(\rho_f/\rho_{th}) = A_0 + A_1 \ln (Ho/H_f) + A_2 [\ln (H_o/H_f)]^2$$

Where, ($\rho_f/\rho_{th}$) is the fractional theoretical density, ln ($H_o/Hf$) is representing the true height strain, and, '$A_0$', '$A'_1$' and '$A'_2$' are empirically determined constants. The constant '$A_1$' played a major role in enhancing the densification rate especially in the lower range of height strains. The constant '$A_0$'did not contribute to densification as the same has been constant and equal to the initial preform densities, but, the constant '$A_2$' contributed mainly towards flattening the  curves in the final stages of deformation and densification as all its values for each aspect ratios were negative, but, of low magnitude,

2.  All data points corresponding to plots representing the true diameter strain and the true  height strains have been found to lie below the theoretical line with a slope of 0.5 conforming that the values of  the Poisson' ratio would tend to approach to a value of 0.5, but, would never reach it. This is true irrespective of the preform geometry and the alloying compositions considered in the present investigation. The curves corresponding to the above strains have well conformed to a second order polynomial of the form:

$$Ln (D_f/D_o) = B_0 + B_1 \ln (Ho/H_f) + B_2 [\ln (H_o/H_f)]^2$$

Where, ln ($D_f/D_0$) is true diameter strain and ln ($H_o/Hf$) is true height strain.

3.  The relationship between the Poisson's ratio and the per cent fractional theoretical density was established to conform to a second order polynomial of the form as given underneath:

$$v_p = C_0 + C_1 \{\% (\rho_f/\rho_{th})\} + C_2 \{\% (\rho_f/\rho_{th})\}^2$$

Where, $v_p$ is the Poisson's ratio, {%($\rho_f/\rho_{th}$)} is percentage fractional theoretical density attained at a given deformation and '$C_0$', '$C_1$' and '$C_2$' are empirically determined constants depending upon initial preform geometry and the composition. There are two modes of densification which is clearly observed and one of them is a region of slow rise of Poisson's ratio with maximum densification and the other one is the steep rise in the values of Poisson's ratio with lesser degree of densification corresponded to a situation where pore and material flow became almost simultaneous meaning thereby that the pores have thermodynamically got stabilized. Hence, the above relationship is ably justified

4.  Definite relationships between fractional theoretical density ($\rho f/\rho th$) and the bulging ratio have been found and the same conformed to a second order polynomial of the form given below:

$$(\rho_f/\rho_{th}) = E_0 + E_1 (D_b/D_o) + E_2 (D_b/D_o)^2$$

Where, '$E_0$', '$E_1$' and '$E2$' are empirically determined constants and established to depend upon the initial preform geometries and the compositions of the systems investigated.

5.  A power Law relationship between per cent fractional theoretical density and the  and the bulging ratio have been established which covered the two different density zones  of fractional theoretical densities and the two different regions of the Poisson's ratio and the same is given as under:

$$(\% \rho_f/\rho_{th}) = Q_0 (D_b/D_o)^m$$

Where, 'Q_0' and 'm' are empirically determined constants which were found to depend upon the initial preform geometries and the compositions of the systems investigated.

## REFERENCES

[1]. Anil Kumar Sinha, "Powder Metallurgy", Dhanpat Rai Publications (P) Ltd. 1987.
[2]. Syed Ummer M. Thangal, K. S. Pandey, C. Natarajan and S. Shanmugam, "Ring Fracture strength and Hardness in Sintered Hot Deformed High Carbon Steel Preforms", International Journal of Materials Science, Vol. 3, No. 1, pp. 75-88, 2008.
[3]. Ryuichro Goto, "Powder Metallurgy Growth in Automotive Market', In: Business Briefing: Global Automotive Manufacturing and Technology, Materials, London, UK, pp. 44-45, 2007.
[4]. Rober. J. Causton and Christophere. Schade, "Machinability: Material Property or Process Response", Hoeganaes Corporation, Cimanamission, NS08077, Presented at PMTEL, Las Vegas, 2003.
[5]. Rajesh Kannan, K. S. Pandey, S. Shanmugam and R. Narayanasamy, "Sintered Fe-0.8%C-1.0%Si-0.4%Cu P/M steel Preform Behaviours During Cold Upsetting", Journal of Iron and Steel Research, International, Vol. 15 (5), pp. 81-87, 2008.
[6]. Dhanasekaren and R. Ganamoorthy, "Microstructure Strength and Tribological Behaviour of Fe-C-Cu-Ni Sintered Steel Prepared with MoS$_2$ Addition', Journal Materials Science, Vol. 42, pp. 4659-4666, 2007.
[7]. K.S.Pandey and R. Vijayaraghavan, " Extrusion Forging of Indigenously Developed Iron- 0.25% Phosphorous Alloy Powder Preforms in Different Die Cavities", Quarterly International Journal of Powder Metallurgy Science and Technology, Vol.6 ,No.4, pp. 8-18, 1995.
[8]. T. Kimura and H. Hamamoto, "Strengthening of Iron Compacts by Infiltration", Modern Developments in Powder Metallurgy, Vol. 8, pp.135-147, 1974.
[9]. R. Chandramouli, T. K. Kandavel, D. Shanmugasundaram and T. Ashok Kumar, "Deformation, Densification and Corrosion Studies of sintered Power Metallurgy Plain carbon Steel Preforms", Materials and Design, Vol. 28, pp. 2260-2264, 2008.
[10]. H. A. Kuhn and A. Lawley, "Powder Metallurgy Processing New Techniques", Acadamic Press, New York, pp. 99-138, 1978.
[11]. J. Wisker and P.K. Jones, "The Economics of Powder Forging Relative to Competing: Process Present and Future", Modern Developments in Powder Metallurgy, Vol. 7, pp. 33-49, 1974.
[12]. K. S. Pandey. "Salient Characteristics of High Temperature Forging of Ferrous Preforms", Key Engineering Materials, Switzerland: Trans. Tech. Publications, pp. 465-486, 1989.
[13]. Halter. R.F, "Recent Advances in the Hot Forming of P/M Preforms", Modern Developments in Powder Metallurgy, Edited by; Hausner, H.H, Smith W.E, Vol.7, pp.137-152, 1974.
[14]. Torre's Model ( C. Huttenmannische Montsh, Vol. 93, pp. 62, 1948) as Quoted by K.S.Pandey in his Ph.D. Thesis entitled "Densification Behaviour of Iron and Iron Based Alloy Powder Preforms During Hot Forging" at University of Roorkee (now IIT Roorkee) August 1982.
[15]. Olle Grinder, Caoyoung Jia and Lyla Nisson, "Hot Upsetting and Hot Repressing of Sintered Steel Preform", Modern Developments in Powder Metallurgy, Vol. 15, pp. 33-49, 1982.
[16]. K.S. Pandey, "Modified Indigenous High Temperature Coating", REC Trichy, 1986.
[17]. Moyer K.H, "Measuring Density of P/M Materials with Improved Precision", International Journal of Powder Metallurgy and Powder Technology, Vol. 15, pp. 33-42, 1979.

# Results from set-operations on Fuzzy soft sets

## D. R Jain[1], Bhu Dev Sharma[2]

[1]*Department of Mathematics, Jaypee Institute of Information Technology, Noida, UP, India*
[2]*Formerly at the Department of Mathematics, Jaypee Institute of Information Technology, Noida, UP, India*

**Abstract:** *In this paper considering a class of Fuzzy-Soft Sets, seven set operations are defined and several relations arising from these set-operations are established using matrix representation of fuzzy soft sets.*
**Key words:** *Fuzzy Soft Sets, equality, operations, Fuzzy Soft matrix.*

## I. Introduction

Recent advances present phenomena, in many areas including engineering, social and medical sciences that are neither deterministic nor stochastic in nature. These cannot be characterized in terms of classical set theory. As such fundamental extensions and generalizations of sets in mathematics have been proposed.

Zadeh [1], in 1965, introduced the theory of fuzzy sets for dealing with imprecise phenomena. These were further generalized by Atanassov [2,3], to what has come to be known as 'Intuitionistic fuzzy sets', to characterize a broader class of vague phenomena. Molodstov [4], in 1999, on the other hand, introduced the concept of 'Soft set' associating characteristics or parameters in considering subsets of a set.

Maji, et. al [5], inducing the concept of fuzzyness on soft-sets, introduced the concept of Fuzzy Soft Sets. The hybrid 'Fuzzy Soft Set theory' has attracted the attention of researchers for its further study and applications. Yong Yang and Chenli Ji [6], using matrix representation of Fuzzy Soft Sets considered applications. The notion of Fuzzy Soft matrices has been further extended in [7] and applied in certain decision making problems.

While set-operations, refer Verma & Sharma [8], on intitutionistic fuzzy sets have been studied, for mathematical viability and usefulness, there is a need to examine and to study these over fuzzy-soft-sets. In this paper we define seven operations analogous to [8] on fuzzy soft sets in terms of their matrices and prove various different relations amongst these operations.

## II. Preliminaries

In this section we give definitions and notions, refer [7], used in following work.

**Definition 1: Fuzzy Soft Set -** Let X be an initial universal set and E be a set of parameters. Let $\tilde{P}$ (x) denotes the power set of all Fuzzy Subsets Sets of X. Let A $\subseteq$ E. A pair (F, A) is called Fuzzy Soft Set over X. where F is a mapping given by F : A $\rightarrow \tilde{P}(X)$.

**Definition 2: - Fuzzy Soft Class -** The pair (X, E) denotes the collection of all Fuzzy Soft Sets on X with attributes from E and is called Fuzzy Soft Class.

**Definition 3: Fuzzy Soft Matrices**

Let X = {$x_1$, $x_2$, ...... $x_m$} be the universal set and E = {$e_1$, $e_2$, ......$e_n$} be the set of parameters. Let A $\subseteq$ E and (F, A) be a Fuzzy Soft Set in the Fuzzy Soft Class (X, E). Then we represent the Fuzzy Soft Set (F, A) in the matrix form as:

$$A_{mn} = \left[a_{ij}\right]_{mxn} \text{ or simply by } A = \left[a_{ij}\right]$$

where

$$a_{ij} = \begin{cases} \mu_j(x_i) & if \;\; e_j \in A \\ 0 & if \;\; e_j \notin A \end{cases}.$$

Here $\mu_j(x_i)$ represent the membership of $x_i$ in the Fuzzy Set F($e_j$). We would identify a Fuzzy Soft Set with its Fuzzy Soft matrix and vice versa. The set of all mxn Fuzzy Soft Matrices will be denoted by FSM$_{mxn}$ over X.

**Definition 4: Set of Operations on FSM$_{mxn}$**

Let A = $\left[a_{ij}\right]_{mxn}$ and B = $\left[b_{ij}\right]_{mxn}$ be two Fuzzy Soft matrices over the universal set X.

Some operations on FSM$_{mxn}$ are defined as follows:

(1) $A \cup B = C = \left[c_{ij}\right]_{mxn}$      where    $c_{ij} = \max\left(a_{ij}, b_{ij}\right)$ , for all i and j

(2) $A \cap B = C = \left[c_{ij}\right]_{mxn}$      where    $c_{ij} = \min\left(a_{ij}, b_{ij}\right)$, for all i and j

(3) $A \lozenge B = C = \left[c_{ij}\right]_{mxn}$      where    $c_{ij} = a_{ij} + b_{ij} - a_{ij} b_{ij}$ , for all i and j

(4) $A . B = C = \left[c_{ij}\right]_{mxn}$      where    $c_{ij} = a_{ij} b_{ij}$ , for all i and j

(5) $A @ B = C = \left[c_{ij}\right]_{mxn}$      where    $c_{ij} = \dfrac{1}{2}\left(a_{ij} + b_{ij}\right)$ , for all i and j

(6) $A \$ B = C = \left[c_{ij}\right]_{mxn}$      where    $c_{ij} = \sqrt{a_{ij} b_{ij}}$ , for all i and j

(7) $A \# B = C = \left[c_{ij}\right]_{mxn}$      where    $c_{ij} = \dfrac{2 a_{ij} b_{ij}}{a_{ij} + b_{ij}}$ , for all i and j,

for which we will accept that if $a_{ij} = b_{ij} = 0$ then $\dfrac{a_{ij} b_{ij}}{a_{ij} + b_{ij}} = 0$ .

### III. Main Results
Before starting discussion of the main results we prove some rather simple inequalities to be used in the subsequent work.

$$a_{ij} + b_{ij} \geq 2\sqrt{a_{ij} b_{ij}} \geq 2 a_{ij} b_{ij} \qquad (2.1)$$

$$\Rightarrow \quad a_{ij} + b_{ij} - a_{ij} b_{ij} \geq a_{ij} b_{ij} \qquad (2.2)$$

$$\Rightarrow \quad a_{ij} + b_{ij} - 2 a_{ij} b_{ij} \geq 0$$

$$\Rightarrow \quad 2\left(a_{ij} + b_{ij} - a_{ij} b_{ij}\right) \geq a_{ij} + b_{ij}$$

$$\Rightarrow \quad \left(a_{ij} + b_{ij} - a_{ij} b_{ij}\right) \geq \frac{1}{2}(a_{ij} + b_{ij}) \qquad (2.3)$$

Next

$$a_{ij} + b_{ij} - a_{ij} b_{ij} - \sqrt{a_{ij} b_{ij}}$$

$$\geq 2\sqrt{a_{ij} b_{ij}} - a_{ij} b_{ij} - \sqrt{a_{ij} b_{ij}} \qquad \text{(on using 2.1)}$$

$$= \sqrt{a_{ij} b_{ij}} - a_{ij} b_{ij} \geq 0$$

$$\Rightarrow \quad a_{ij} + b_{ij} - a_{ij} b_{ij} \geq \sqrt{a_{ij} b_{ij}}) \qquad (2.4)$$

Also

$$a_{ij} + b_{ij} - a_{ij} b_{ij} - \frac{2 a_{ij} b_{ij}}{a_{ij} + b_{ij}}$$

$$= \frac{(a_{ij})^2 (1 - b_{ij}) + (b_{ij})^2 (1 - a_{ij})}{a_{ij} + b_{ij}} \geq 0$$

$$\Rightarrow \quad a_{ij} + b_{ij} - a_{ij} b_{ij} \geq \frac{2 a_{ij} b_{ij}}{a_{ij} + b_{ij}} . \qquad (2.5)$$

Further

$$\frac{2 a_{ij} b_{ij}}{a_{ij} + b_{ij}} - a_{ij} b_{ij} = \frac{a_{ij} b_{ij} (2 - a_{ij} - b_{ij})}{a_{ij} + b_{ij}} \geq 0 .$$

Thus

$$\frac{2a_{ij}\ b_{ij}}{a_{ij} + b_{ij}} \quad \geq \quad a_{ij}\ b_{ij}.$$  (2.6)

**<u>Theorem</u>** If A = $\lfloor a_{ij} \rfloor$ and B = $\lfloor b_{ij} \rfloor$ are any two FSM$_{\text{mxn}}$, then

(1) (A @ B) \$ (A # B) = A \$ B

(2) (A ◊ B) ∩ (A . B) = A . B ,           (A ◊ B) ∪ (A . B) = A ◊ B

(3) (A ◊ B) ∩ (A @ B) = A @ B ,   (A ◊ B) ∪ (A @ B) = A ◊ B

(4) (A . B) ∩ (A @ B) = A . B ,           (A . B) ∪ (A @ B) = A @ B

(5) (A ◊ B) ∩ (A \$ B) = A \$ B,           (A ◊ B) ∪ (A \$ B) = (A ◊ B)

(6) (A . B) ∩ (A \$ B) = A . B ,           (A . B) ∪ (A \$ B) = A \$ B

(7) (A ◊ B) ∩ (A # B) = A # B ,           (A ◊ B) ∪ (A # B) = (A ◊ B)

(8) (A . B) ∩ (A # B) = A . B ,   (A . B) ∪ (A # B) = (A # B)

**Proof of the Theorem:** Using definitions, we have:

(1)    (A @ B) \$ (A # B)    =    $\left[ \dfrac{a_{ij} + b_{ij}}{2} \right] \$ \left[ \dfrac{2a_{ij}\ b_{ij}}{a_{ij} + b_{ij}} \right]$

                              =    $\left[ \sqrt{\dfrac{a_{ij} + b_{ij}}{2} \cdot \dfrac{2a_{ij}\ b_{ij}}{a_{ij} + b_{ij}}} \right]$

                              =    $\left\lfloor \sqrt{a_{ij}\ b_{ij}} \right\rfloor$ $_=$ A \$ B

(2)    (A ◊ B) ∩ (A . B)    =    $\lfloor a_{ij} + b_{ij} - a_{ij}\ b_{ij} \rfloor \cap \lfloor a_{ij}\ b_{ij} \rfloor$

                              =    $\lfloor \min\left( a_{ij} + b_{ij} - a_{ij}\ b_{ij}, a_{ij}\ b_{ij} \right) \rfloor$

                              =    $\lfloor a_{ij}\ b_{ij} \rfloor$           (on using 2.2)

                              =    A . B

and

        (A ◊ B) ∪ (A . B)    =    $\lfloor \max\left( a_{ij} + b_{ij} - a_{ij}\ b_{ij}, a_{ij}\ b_{ij} \right) \rfloor$

                              =    $\lfloor a_{ij} + b_{ij} - a_{ij}\ b_{ij} \rfloor$

                              =    A ◊ B

(3)    (A ◊ B) ∩ (A @ B)    =    $\lfloor a_{ij} + b_{ij} - a_{ij}\ b_{ij} \rfloor \cap \left[ \dfrac{a_{ij} + b_{ij}}{2} \right]$

                              =    $\left[ \min\left( a_{ij} + b_{ij} - a_{ij}\ b_{ij}, \dfrac{a_{ij} + b_{ij}}{2} \right) \right]$

                              =    $\left[ \dfrac{a_{ij} + b_{ij}}{2} \right]$           on using (2.3)

                              =    A @ B

and

        (A ◊ B) ∪ (A @ B)    =    $\left[ \max\left( a_{ij} + b_{ij} - a_{ij}\ b_{ij}, \dfrac{a_{ij} + b_{ij}}{2} \right) \right]$

                              =    $\lfloor a_{ij} + b_{ij} - a_{ij}\ b_{ij} \rfloor$           on using (2.3)

                              =    (A ◊ B)

(4)    (A . B) ∩ (A @ B)    =    $\left[ a_{ij}\ b_{ij} \right] \cap \left[ \dfrac{a_{ij} + b_{ij}}{2} \right]$

$$= \left[\min\left(a_{ij}\,b_{ij},\ \frac{a_{ij}+b_{ij}}{2}\right)\right]$$

$$= \left[a_{ij}\,b_{ij}\right] \qquad \text{on using (2.1)}$$

$$= \text{A . B}$$

and

$$(\text{A . B})\ \cup (\text{A @ B}) = \left[\max\left(a_{ij}\,b_{ij},\ \frac{a_{ij}+b_{ij}}{2}\right)\right]$$

$$= \left[\frac{a_{ij}+b_{ij}}{2}\right] \qquad \text{on using (2.1)}$$

$$= \text{A @ B}$$

(5) $\quad (\text{A} \lozenge \text{B})\ \cap (\text{A \$ B}) = \left[a_{ij}+b_{ij}-a_{ij}\,b_{ij}\right] \cap \left\lfloor\sqrt{a_{ij}\,b_{ij}}\right\rfloor$

$$= \left\lfloor\min\left(a_{ij}+b_{ij}-a_{ij}\,b_{ij},\ \sqrt{a_{ij}\,b_{ij}}\right)\right\rfloor$$

$$= \left\lfloor\sqrt{a_{ij}\,b_{ij}}\right\rfloor \qquad \text{on using (2.4)}$$

$$= \text{A \$ B}$$

and

$$(\text{A} \lozenge \text{B})\ \cup (\text{A \$ B}) = \left\lfloor\max\left(a_{ij}+b_{ij}-a_{ij}\,b_{ij},\ \sqrt{a_{ij}\,b_{ij}}\right)\right\rfloor$$

$$= \left\lfloor a_{ij}+b_{ij}-a_{ij}\,b_{ij}\right\rfloor \qquad \text{on using (2.4)}$$

$$= \text{A} \lozenge \text{B}$$

(6) $\quad (\text{A . B}) \cap (\text{A \$ B}) = \left[a_{ij}\,b_{ij}\right] \cap \left[\sqrt{a_{ij}\,b_{ij}}\right]$

$$= \left\lfloor\min\left(a_{ij}\,b_{ij},\ \sqrt{a_{ij}\,b_{ij}}\right)\right\rfloor$$

$$= \left\lfloor a_{ij}\,b_{ij}\right\rfloor \qquad = \qquad \text{A . B}$$

and

$$(\text{A . B}) \cup (\text{A \$ B}) = \left\lfloor\max\left(a_{ij}\,b_{ij},\ \sqrt{a_{ij}\,b_{ij}}\right)\right\rfloor$$

$$= \left\lfloor\sqrt{a_{ij}\,b_{ij}}\right\rfloor = A \$ B$$

(7) $\quad (\text{A} \lozenge \text{B})\ \cap (\text{A \# B}) = \left[a_{ij}+b_{ij}-a_{ij}\,b_{ij}\right] \cap \left[\frac{2a_{ij}\,b_{ij}}{a_{ij}+b_{ij}}\right]$

$$= \left[\min\left(a_{ij}+b_{ij}-a_{ij}\,b_{ij},\ \frac{2a_{ij}\,b_{ij}}{a_{ij}+b_{ij}}\right)\right]$$

$$= \left[\frac{2a_{ij}\,b_{ij}}{a_{ij}+b_{ij}}\right] \qquad \text{on using (2.5)}$$

$$= \text{A \# B}$$

and

$$(\text{A} \lozenge \text{B})\ \cup (\text{A \# B}) = \left[\max\left(a_{ij}+b_{ij}-a_{ij}\,b_{ij},\ \frac{2a_{ij}\,b_{ij}}{a_{ij}+b_{ij}}\right)\right]$$

$$= \left\lfloor a_{ij}+b_{ij}-a_{ij}\,b_{ij}\right\rfloor \qquad \text{on using (2.5)}$$

$$= \text{A} \lozenge \text{B}$$

(8)  $(A \cdot B) \cap (A \# B)$  $=$  $\left[a_{ij} \; b_{ij}\right] \cap \left[\dfrac{2a_{ij} \; b_{ij}}{a_{ij} + b_{ij}}\right]$

$=$  $\left[\min\left(a_{ij} \; b_{ij} \, , \; \dfrac{2a_{ij} \; b_{ij}}{a_{ij} + b_{ij}}\right)\right]$

$=$  $\left[a_{ij} \; b_{ij}\right]$  on using (2.6)

$=$  $A \cdot B$

and

$(A \cdot B) \cup (A \# B)$  $=$  $\left[\max\left(a_{ij} \; b_{ij} \, , \; \dfrac{2a_{ij} \; b_{ij}}{a_{ij} + b_{ij}}\right)\right]$

$=$  $\left[\dfrac{2a_{ij} \; b_{ij}}{a_{ij} + b_{ij}}\right]$  on using (2.6)

$=$  $A \# B$

## IV. Concluding Remarks

The results obtained in terms of various operations must go a long way in applications of Fuzzy Soft Sets.

## REFERERENCES

[1]  L.A. Zadeh, Fuzzy Sets, Information and Control,8, 1965, 338-353.
[2]  K.T. Atanassov, Intuitionistic fuzzy sets, Fuzzy sets and  systems 20(1) 1986 ,87-96.
[3]  K.T. Atanassov, Intuitionistic fuzzy sets, Springer Physica-Verlag, Heidelberg,1999.
[4]  D. Molodstov, Soft Set Theory-first Results, Computers Math with Applications, 37, 1999, 19-31.
[5]  P.K. Maji, R. Biswas and A.R. Roy, Fuzzy Soft Sets, J. Fuzzy Math, 9(3), 2001,   589-602.
[6]  Yong Yang and Chenli Ji, Fuzzy Soft Matrices and their Applications, AICI 2011, Part I, LNAI 7002, 2011, 618-627.
[7]  Manash Jyoti Borah, Tridiv Jyoti Neog, Dusmanta Kumar Sut, Fuzzy Soft Matrix Theory and its Decision Making, International Journal of Modern Engineering Research  (IJMER) Vol. 2 Issue 2, 2012, 121-127.
[8]  Rajkumar Verma, Bhu Dev Sharma, some new equalities connected with Intuitionistic  fuzzy sets, Notes on Intuitionistic fuzzy sets Vol. 19 ,2,2013, 25-30.

# Solar Water Heater with Rotating Reflectors and Light Dependent Resistor (LDR)

Harshil Sinha[1], Deepesh Yadav[2]

[1,2] *B. tech, Mechanical & Automation , Amity University Haryana ,India*

***Abstract:*** *Solar energy is a type of renewable energy and it is expected to play a very important role in the future world. The purpose of this project is to increase the efficiency of solar water heating system by using moving reflectors, which tracks the sun's rotation using light dependent diodes. In today's world solar energy applications are enhanced. Like solar water heating systems.it can be used as an alternative to replace the electrical water heating system. Solar energy helps in reducing the consumption of limited resources, such as petroleum resources. Solar energy is used in many applications like in solar water heater which is used in domestic (provides hot water) as well as in industrial (generates electricity).Heating water by using sun energy is not a new idea. In the past century many countries used black painted water tanks as simple solar water heaters. Solar energy applications have improved greatly in the last 3-4 decades.*

***Keywords:*** *Efficiency Renewable Energy Sources , Solar Energy , Solar Water Heater.*

## I. INTRODUCTION

Solar water heater absorbs the sun energy (solar radiation) falling on the reflector and converts this energy into heat and transfer this heat to water flowing through the heater.

### 1.1 Types of solar water heating systems:

In Asia specially in India, where the countries energy imports account for more than 65% of total exports, fossil fuels are often scarce, making solar thermal energy one of the few low cost options available. Generally solar water heater can be classified in two categories:

(i) Direct absorption of solar radiation where the sun's rays incident on the absorber material after passing through a transparent material.

(ii) Indirect solar water heater where the water is fast heated in a solar collector and then stored in a storage tank.

### 1.2 Passive and Active solar water heating system:

In passive solar water heating system, the absorber pipe is coated with a material that absorbs the solar radiation falling on it. Surface is coated with the  black paint which can absorb maximum solar radiation(more than others). The absorbed solar radiation is converted into heat. Some of this absorbed heat is conducted through the pipe to the riser tubes and then through the riser tubes walls to the water. This will increase the water temperature. Some of the heat is lost to the surroundings. The passive solar water heating systems are cheap and have very low or no maintenance, but the efficiency of a passive system is generally lower than the active solar water heater system .The heat loss should be keep as low as possible.

### 1.3 Methods of reducing heat loss:

- By putting the absorber pipe in an insulating box.
- By placing extra insulation behind the absorber pipe to reduce heat loss from the back of the pipe.
- By placing a transparent cover over the box for two reasons
    - (a) It prevents the wind from blowing over the hot absorber pipe and cooling it.
    - (b) It transmits solar energy but prevents heat radiated from the absorber pipe.

Active solar water heating systems use one or more pumps to circulate water  in the system.Acive system have more efficiency than the passive system.

**1.4 Solar power in India:**

India has high solar insolation, ideal for using solar power in India .In the solar energy sector, some large projects have been proposed, and a 35,000 km$^2$ (14,000sq mi) area of the Thar Desert has been set aside for solar power projects, sufficient to generate 700 to 2,100 GW. Solar Energy in India is one of the most exciting growing industries in the world right now. Solar Energy in India is poised to take off in a exponential manner because of a unique confluence of favorable Supply and Demand factors. In India the rates of electricity are going up rapidly each year due to various factors like higher costs of fossil fuels, increasing capital expenditure by utilities and privatization of power .And the cost of solar energy is very low comparatively .So the solar water heating system is a very good alternate in India to replace the electrical water heating system.
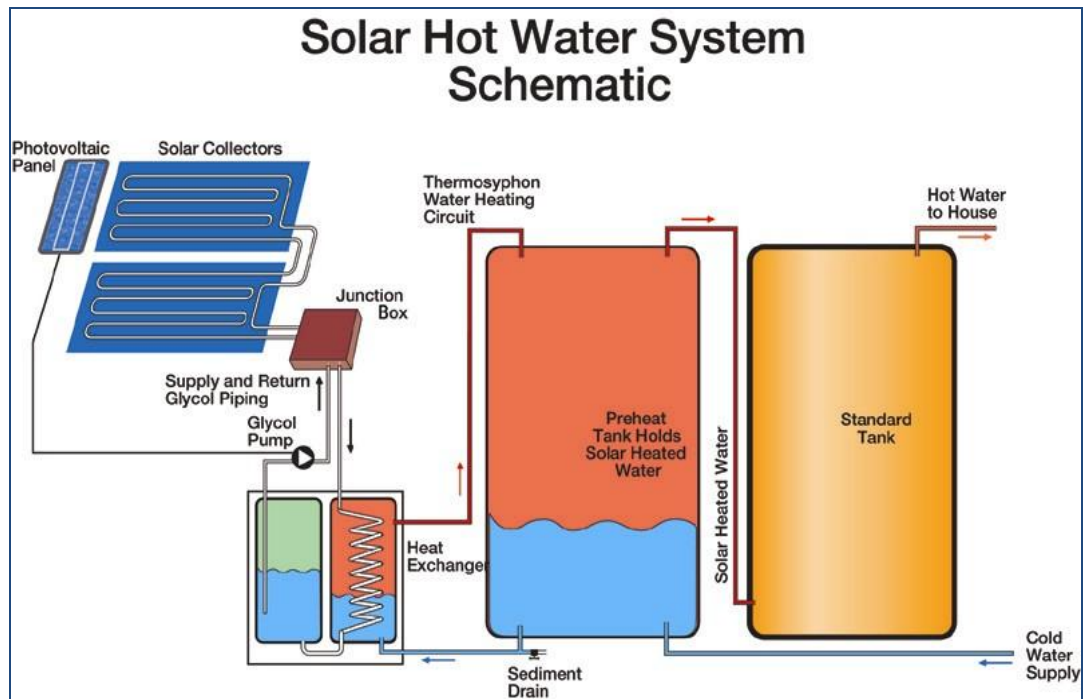


Fig-1 SWH Schematic Diagram

## II.  Design

**2.1 Specifications**

- ➢ Cardboard base of dimension **18*12 inches**
- ➢ Aluminum sheet of dimension **21*15 inches**
- ➢ Wooden frame of dimension 18*12*1.3 inches with inside border of  0.78 inch
- ➢ Copper pipe of length 96 inch &  mean diameter of 0.27 inch with outlet tap, inlet pipebeing connected to plastic pipe
- ➢ Acrylic sheet of dimension 18*12 inches

**2.2 Fabrication Methods**

A wooden frame of above dimension is fixed to the cardboard base initially with the help of the nails .The holes are drilled in the wooden frame on left bottom and top right side for inlet & outlet flow of water through copper pipes.

Aluminum sheet is placed over an entire frame combination and fixed to wooden frame. Copper pipe is bent in shape of 'U' to provide large exposure of solar energy to flowing water. Finally, An acrylic sheet  secured firmly to wooden frame for completion of FPC

Fig-3 Flat Plate Collector

- Step Down Transformer is used that convert 220v AC supply to 12v AC supply.
- Dual Power Supply that works as a rectifier which convert 12v AC supply to 12v DC supply and works as dual +ve as well as –ve voltage regulator between 24v to 12v.
- 2 LDR circuits. are attached to the battery as per the connections shown in Fig-4.
- Relay which act as circuit breaker in either operating condition of one of the LDR connected to the motor,
- LDR which are light dependent resistors whose resistance vary with the intensity of solar light intercepted .These are used in pairs on both side of FPC to reverse it automatically according to the sun's rotation
- 4-3v each solar cells get attached to FPC generates electricity to power up the battery whose efficiency also improved by facing always towards sun
- 12v motor is attached to shaft which is fixed to FPC to provide desired angular rotation w.r.t. sun
- 6v Battery which gets charged from dual power source , one being solar cells and other is dynamo attached to shaft producing electricity through simple EMI principle.
- 6w Tube light is also joined just to demonstrate the use of solar cells which can be used to heat water in absence of electricity and sun using immersion rod connecting it to rechargeable battery.

CIRCUIT DIAGRAM FOR ROTATING REFLECTOR
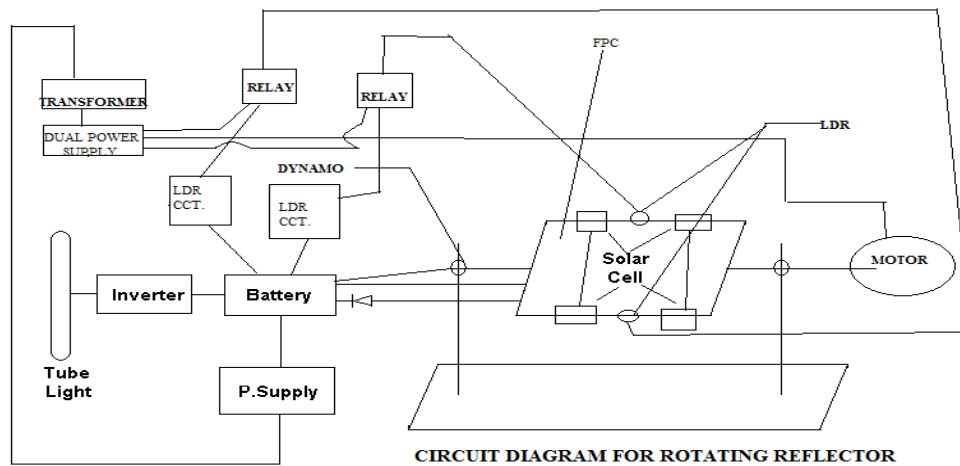
Fig-4

### 2.3 Storage Tank

A insulated (to reduce heat losses) plastic bucket of 40 litre capacity is used for hot water storage along with cover. A separate hole is made on cover for the easy movement of outlet plastic pipe along with rotation of FPC. Another hole of small size is made to accommodate the digital thermometer to measure hot water temperature.



Fig 5

## III. Theoretical Analysis

Length of Acrylic sheet = 18 inch
Breadth of Acrylic sheet = 12 inch
Area of Acrylic sheet = 0.140 m$^2$

Length of Copper pipe = 240 cm
Diameter of Copper pipe = 0.7 cm
Area of copper pipe($A_c$) = $\pi DL$ = 527.8 cm$^2$
                = 0.053 m$^2$
Average daily solar intensity falling on India ($I_T$) = 5000 w/m$^2$
Transmittance value of Acrylic sheet (T) = 0.92
Solar energy trapped by Acrylic sheet = T . $I_T$ = 0.92*5000
                   = 4600 w/m$^2$
Absorptivity value of copper pipe($\alpha$) = 0.6
Heat energy gained by copper pipe($H_c$) = $\alpha$.4600.$A_c$
                  = 0.6*4600*0.053
                  = 146.28 w

# IV. Experimental Results

**4.1 Table I**

| Initial level of water in Bucket (l) | Measured level of water at Reading (l) | Time taken (seconds) |
|---|---|---|
| 13 | 12 | 1020 |
| 12 | 11 | 1020 |
| 11 | 10 | 1020 |
| 9 | 8 | 1020 |

Discharge through outlet pipe = 0.98ml/s
Mass flow rate = 0.98gm/s
Assuming no pipe loss through plastic pipe
Heat energy absorbed by water = $m*c*\Delta t$
Taking $T_{mean}$ = 38˙c
Ambient temperature = 29˙c
$\Delta t$ = 9˙c
Specific heat of water (c) = 4.186 J/gm˙c
Heat energy absorbed by water($H_W$) = 0.98*4.186*9
$\qquad\qquad$ =36.9 w
Mean efficiency ($\eta_{mean}$) = Heat energy absorbed by water/Amount of energy
$\qquad\qquad\qquad$ absorbed by copper pipe
$\quad\eta_{mean}$ = 36.9/146.28
$\qquad$ = 25%

**4.2 FPC-ROTATING (Weather Condition :Sunny)**

**(Date 06.05.14)**
**Weather condition – Sunny**
**FPC – Rotating**

| Day Time | Inlet water temp. (°C) | Outlet water Temp. (°C) | Temperature Difference (°C) | $E_W$ (w) | $E_C$ (w) | Efficiency % |
|---|---|---|---|---|---|---|
| 10.30 a.m. | 27.8 | 31.9 | 4.1 | 16.41 | | 11.2 |
| 11.00 a.m. | 27.9 | 33.6 | 5.7 | 22.56 | | 15.42 |
| 11.30 a.m. | 28 | 35.8 | 7.8 | 32.81 | | 22.43 |
| 12.00 p.m. | 28.6 | 39.4 | 10.8 | 43.48 | | 29.72 |
| 12.30 p.m. | 29 | 43 | 14 | 56.6 | 146.28 | 38.7 |
| 1.00 p.m. | 29.5 | 44 | 14.9 | 60.2 | | 41.2 |
| 1.30 p.m. | 29.9 | 44.9 | 14.7 | 59.9 | | 41 |
| 2.00 p.m. | 30 | 44.8 | 14.8 | 60.7 | | 41.5 |
| 2.30 p.m. | 30 | 44.7 | 14.7 | 60.4 | | 41.2 |
| 3.00 p.m. | 29.7 | 44.5 | 14.8 | 59.9 | | 40.9 |
| 3.30 p.m. | 29.7 | 43.3 | 13.4 | 55.1 | | 37.58 |
| 4.00 p.m. | 29.6 | 41.3 | 11.7 | 47.99 | | 32.81 |
| 4.30 p.m. | 29.6 | 40.5 | 11 | 10.9 | | 30.84 |
| 5.00 p.m. | 29.4 | 40 | 10.6 | 43.37 | | 29.7 |

Table 2
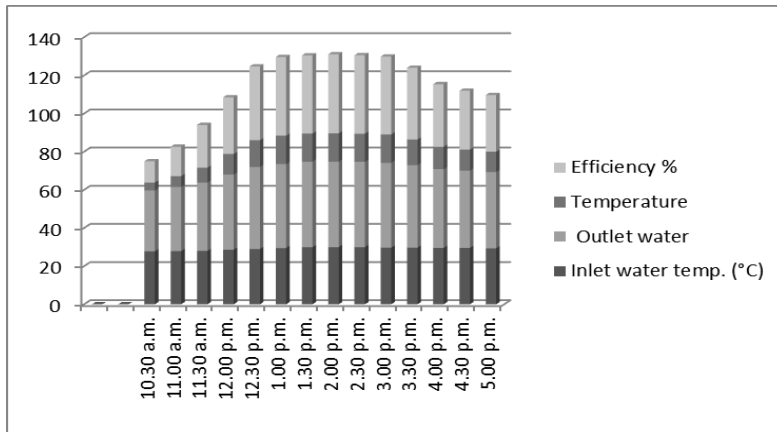


Fig 6
Graph Based On Table 2
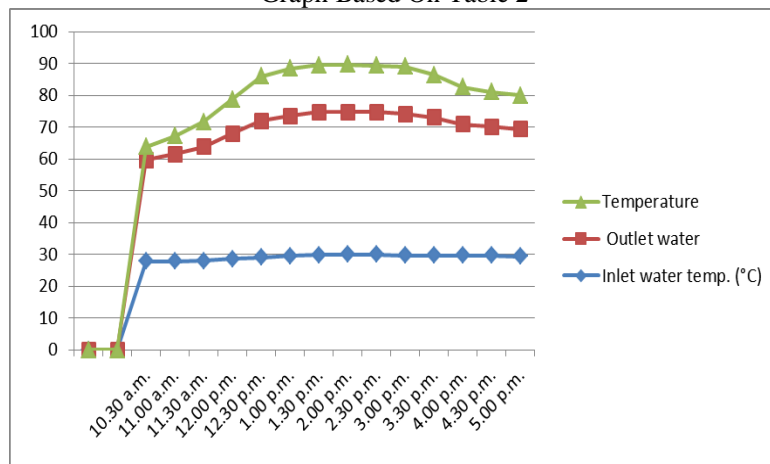


**4.3 FPC-ROTATING (Weather Conditions: Partly Cloudy)**
**(Date 08.05.14)**
**Weather condition – Partly cloudy**
**FPC - Rotating**

**For mass flow rate $\overset{\circ}{m}$ = 59gm/min**

| Day Time | Inlet water temp. (°C) | Outlet water temp. (°C) | Temperature difference | $E_{W\,(w)}$ | $E_C$ | Efficiency % |
|---|---|---|---|---|---|---|
| 10.30 a.m. | 29 | 33 | 5 | 16.41 | | 11.2 |
| 11.00 a.m. | 29 | 34.5 | 5.5 | 22.56 | | 15.42 |
| 11.30 a.m. | 29 | 36.8 | 7.8 | 31.99 | 146.28 | 21.87 |
| 12.00 p.m. | 29.7 | 39.6 | 9.9 | 40.6 | | 27.76 |
| 12.30 p.m. | 29.7 | 40.9 | 11.2 | 45.94 | | 31.41 |
| 1.00 p.m. | 29.3 | 39.5 | 10.2 | 41.8 | | 28.6 |

| 1.30 p.m. | 29.2 | 39.3 | 10.1 | 41.43 | | 28.3 |
| 2.00 p.m. | 29.2 | 39.3 | 10.1 | 41.43 | | 28.3 |
| 2.30 p.m. | 29.2 | 39.2 | 10 | 41.02 | | 28.04 |
| 3.00 p.m. | 29.2 | 39.3 | 10.1 | 41.43 | | 28.3 |
| 3.30 p.m. | 29.1 | 39.4 | 10.2 | 41.84 | | 28.6 |
| 4.00 p.m. | 29 | 38.6 | 9.8 | 40.2 | | 27.48 |
| 4.30 p.m. | 29 | 38.6 | 9.6 | 39.38 | | 26.9 |
| 5.00 p.m. | 28.8 | 38.2 | 9.4 | 38.56 | | 26.36 |

**Table 3**
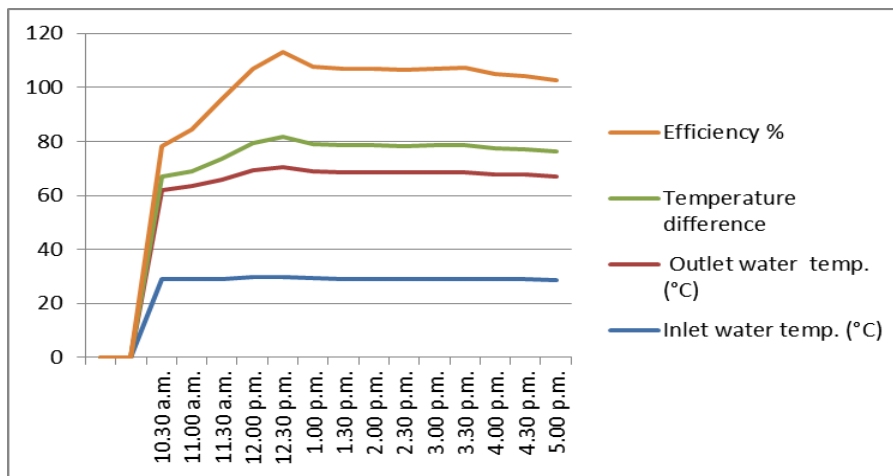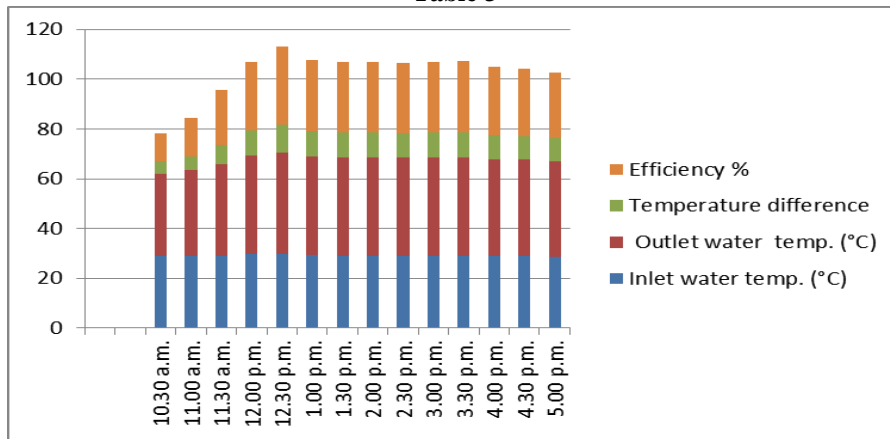




Fig 8 Graphs Based On Table 2

**4.4 FPC-STATIONARY & FACING TOWARDS SOUTH**
**(Weather Conditions: Sunny)**
**(Date 06.05.14)**
**Weather condition – Sunny**
**FPC -  Stationary & facing towards South**

| Day Time | Inlet water temp. (°C) | Outlet water temp. (°C) | Temperature difference | $E_{W (w)}$ | $E_C$ | Efficiency % |
|---|---|---|---|---|---|---|
| 10.30 a.m. | 29 | 32.3 | 3.3 | 13.53 | 146.28 | 9.2 |

| 11.00 a.m. | 29 | 32.7 | 3.7 | 15.17 | | 10.3 |
|---|---|---|---|---|---|---|
| 11.30 a.m. | 29 | 33.2 | 4.2 | 17.23 | | 11.77 |
| 12.00 p.m. | 29.5 | 34.5 | 5 | 20.51 | | 14.2 |
| 12.30 p.m. | 30 | 35.5 | 6.1 | 25 | | 17.1 |
| 1.00 p.m. | 30.3 | 36.4 | 6.1 | 25 | | 17.1 |
| 1.30 p.m. | 30.7 | 37.4 | 7 | 28.71 | | 19.6 |
| 2.00 p.m. | 31 | 38.5 | 7.5 | 30.77 | | 21.03 |
| 2.30 p.m. | 31 | 39 | 8 | 32.8 | | 22.42 |
| 3.00 p.m. | 30.8 | 39.1 | 8.3 | 34.05 | | 23.3 |
| 3.30 p.m. | 30.8 | 38.9 | 8.1 | 33.23 | | 22.7 |
| 4.00 p.m. | 30.6 | 38.5 | 7.9 | 32.41 | | 22.16 |
| 4.30 p.m. | 30.6 | 38.1 | 7.5 | 30.76 | | 21.03 |
| 5.00 p.m. | 30.3 | 37.4 | 7.1 | 29.13 | | 19.9 |

**Table 4**
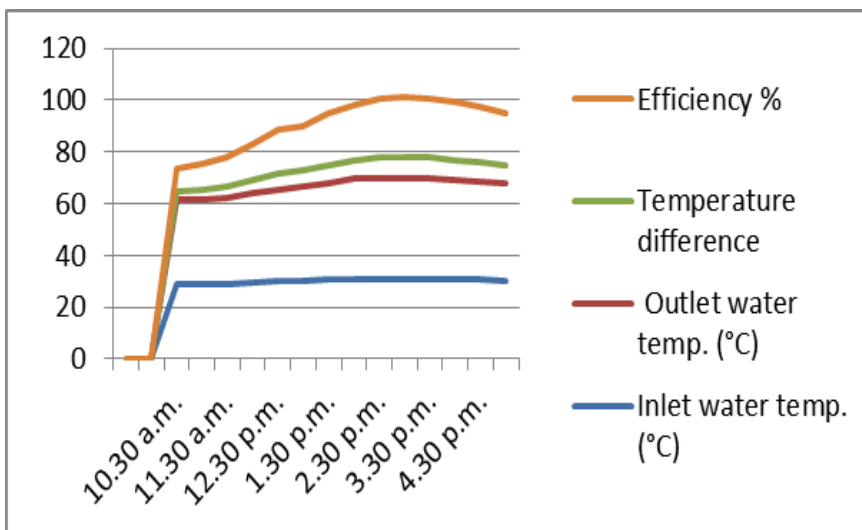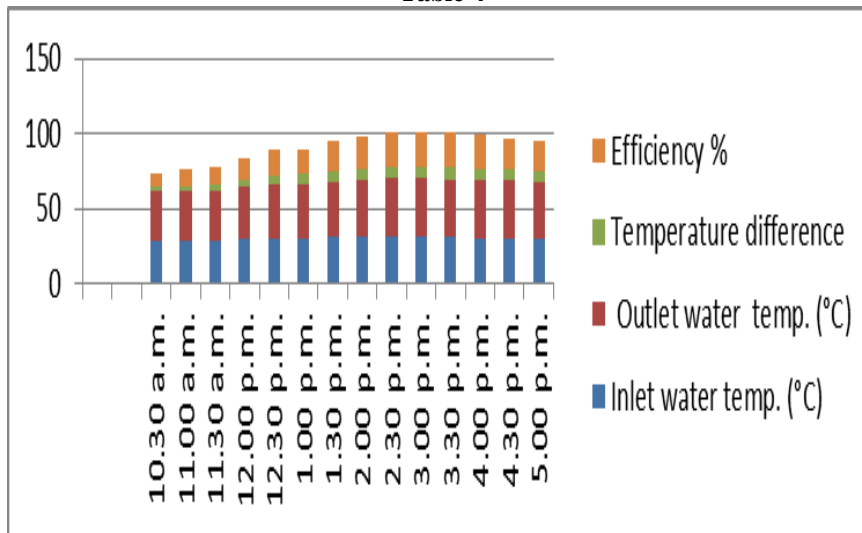




Fig 9 Graphs Based On Table 4

## V. Conclusion

The efficiency of the solar water heater depends on the heat intensity. The more the intense heat on absorber pipe the more the water heater is efficient.

The intensity of solar energy varies according to the sun position. Thus the intensity is depending at different time in a day.

The solar cell was used to measure the intensity of solar radiation. When the sky was cloudy the intensity of solar radiation was less. It was found from the experimental data that the efficiency was high at noon, it increases from 9.00 am to 12.30 pm and decreases after 1.00 pm.

The project work was started with the four main objectives and those were design, fabrication and performance test of a solar water heater and all the objectives have been fulfilled. The main point of view was to make a simple design and to minimize the cost and to use the local available materials properly. The design of the heater was made carefully and the materials required for fabrication were selected, which were inexpensive comparison with the other materials. The highest efficiency was found at noon. Due to discontinuity of flow rate and variation of intensity the efficiency was not found accurately. The efficiency was found different at different water flow rate.

The main consideration is to improve stationary FPC efficiency by rotating with sunlight which however increases SWH efficiency. But the use of external power supply limits its effectiveness that reduces its overall performance, this can be compensated by the use of solar cell combination that drive LDR cct. and tubelight.

Hence , future scope of this project is to remove dependency of SWH on external power to rotate as tracking solar rays.

## REFERENCES

[1]    Book on 'Solar Energy' by H.P. Garg
[2]    http://energy.gov/energysaver/articles/small-solar-electric-systems
[3]    http://energy.gov/energysaver/articles/estimating-cost-and-energy-efficiency-solar-water-heater
[5]    S. Rao Peddada, October 2012 "National Solar Mission & Solar Technology Deployment in India" Surya Power,.
[6]    Solar Water Heating: A Comprehensive Guide to Solar Water and Space Heating Systems by Bob Ramlow
[7]    http://www.theindianrepublic.com/tbp/future-solar-energy-india-scope-jnnsm-needs-broadened-100042088.html

# Design Consideration and Construction of a Biplane

Harshil Sinha[1], Deepesh Yadav[2]

[1,2] *B. Tech, Mechanical & Automation , Amity University Haryana ,India*

***Abstract****: A biplane is a type of an aircraft where two fixed wings are placed one over another providing lift. In the early aviation era, the first plane to overcome gravity was a biplane. The first prototypes of aircrafts were monoplanes which ceased to provide the required uplift due to technological barriers of the bygone era i.e; weak and underpowered engines coupled with non-refined, weak construction materials and wings Biplanes, were designed to overcome the shortcomings of monoplanes and generates a 20% more lift than a monoplane. This paper provides the design considerations to build symmetrical wings of a biplane and the fuselage to mount the wing. And then provide mechanical installations to make the biplane airworthy. The design work for the fuselage and the wings are done using catia and the analyses of the same are done using solid works. The material used and the fabrication process is enclosed the article*

***Keywords:*** *Biplane, Catia & Solid works, Fuselage, Lift, Symmetrical Wings.,*

## I. INTRODUCTION

### 1.1 Fuselage

The main body of the aircraft that holds and supports the passengers or the cargo is the fuselage. In the Single Engine Aeroplanes, the fuselage contains the engine. It provides the position control and stabilization surfaces In respect to the lifting surfaces important for the overall stability and maneuvering abilities.



Fig-1 Biplane

### 1.2 Wing

A wing can be defined as a fin which provides a surface for flight by generating aerodynamic force through a medium I.e; gas or liquid .The word 'wing' has been derived from an old Norse vængr and is referred to the foremost limb of a bird. But with the advent of technology it has come about to include lift producing airfoils of insects boomerangs bats fishes and animals which use fins to propel themselves .The expression of aerodynamic quality of a wing is given by its lift to drag ratio.

**1.3 Propulsion Systems**

'Propulsion ' is derived from 2 latin words : pro meaning before or forwards and pellere meaning to drive propulsion is the generating of force directed towards motion. A propulsion system includes some type of motor or muscles which provides a raw mechanical power. This is coupled  with devices (propellers, axles nozzles, etc)  which converts the power to generate force.

**1.4 Control surfaces**

The flight control surfaces   provides the pilot the means of maneuvering and controlling the airplane's flight altitude. The flight control devices of the modern era  are more or less self-sufficient and capable of handling flight sequences of increasing complexities .The fixed wing aircraft designs were capable of generating lift, sufficient enough to get them off the ground but were harder to maintain control of once airborne .Effective flight controls developments in the later stages allowed stable flight sequences .

## II.   Design Considerations And Fabrication

**2.1 Design Aspects:**
**2.1.1 Wing support:**

The wing is affixed on the fuselage with cantilever support. The upper and lower wing are further supported by strut at both end of the wing. Hence, the wing support is of **cantilevered strut braced type**

**2.1.2 Airfoil:**

Airfoil is symmetrical type.ie the profile is **symmetrical** below and above the camber line. Camber is usually designed into an aero foil to increase the maximum lift coefficient. This minimizes the stalling speed of aircraft using the aero foil. Aircraft with wings based on cambered aero foils usually have lower stalling speeds than similar aircraft with wings based on symmetric aero foils.

**2.1.3Angle of incidence:**

Angle of incidence meaning the angle between the chord of an aero foil and some fixed datum in the aero plane. The angle of incidence in the model used is greater than zero as wing shape is symmetrical.





Figures-2,3,4  Bi plane model

### 2.2 Fabrication:

Tools used:

- Cutter
- Hammer
- Sand paper
- Glue
- Epoxy
- Iron
- Nails

### 2.3 Fabrication Technique:

Balsa wood is very soft so most of the parts were handcrafted using cutter. Sand papers were used to smoothen the surface. Glue and epoxy were used to fix the wooden parts with each other. Nails were hammered for fixing the plywood. Iron was used to cure the lotto cot paper over the surface.

### 2.4 Specifications:

- Wing length: 1390 mm
- Chord length : 255 mm
- Aspect ratio: 5.4
- Fuselage length: 1135 mm

### 2.5 Material used:

- Balsa Wood(2,4,6,15,12)mm
- Plywood(2 mm)
- Lotto cot paper
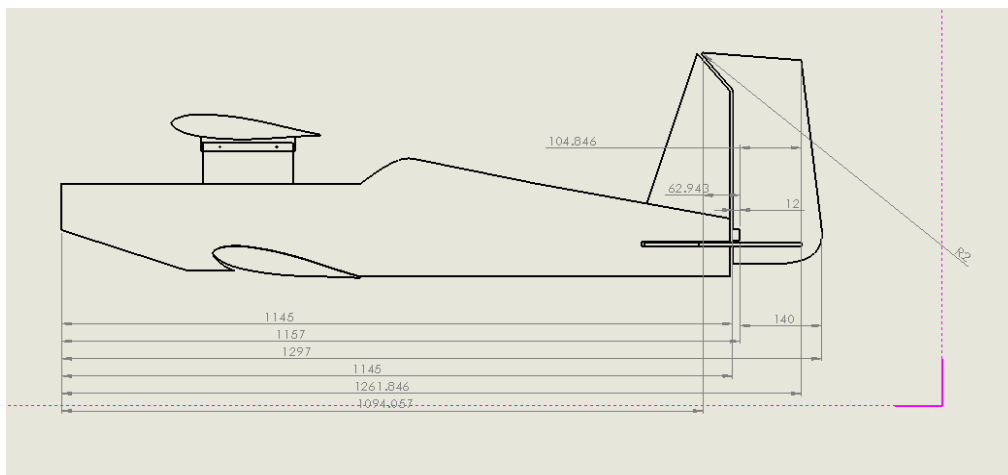


Fig-5 Side view



Fig 6 Top view

Fig-7 Front view

### III. CAD Models And Analysis Report (Generated By CAD Software):

Catia was used for the Design purpose and Solid works for Analysis.
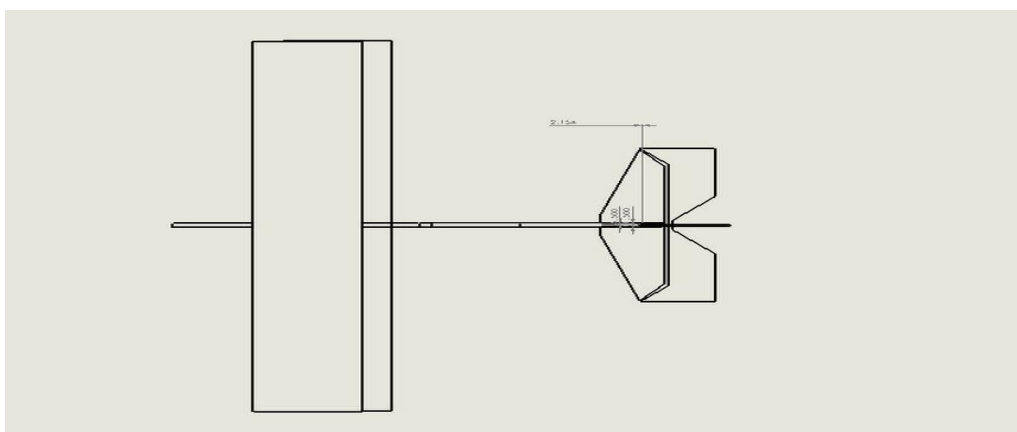


Fig 8 CAD models
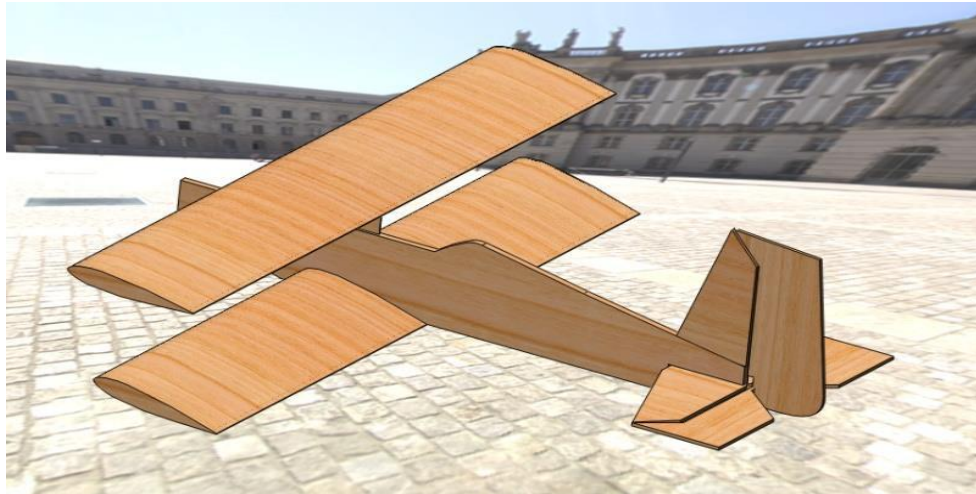


Fig 9 CAD models

Fig-10 CAD models

## IV. Full Report

### 4.1 System Info

| Product | Flow Simulation 2013 SP0.0. Build: 2177 |
|---|---|
| Computer name | REDDY-XPS |
| User name | SRAVAN SINGIREDDY |
| Processors | Intel(R) Core(TM) i3-2310M CPU @ 2.10GHz |
| Memory | 3990 MB / 8388607 MB |
| Operating system | (Build 9200) |
| CAD version | SolidWorks 2013 SP0.0 |
| CPU speed | 2100 MHz |

### 4.2 General Info

| Model | R:\Extra feature\Google Drive\Solid works\FUSELAGE\Assem1.SLDASM |
|---|---|
| Project name | Default |
| Project path | R:\Extra feature\Google Drive\Solid works\FUSELAGE\1 |
| Units system | SI (m-kg-s) |
| Analysis type | External (exclude internal spaces) |
| Exclude cavities without flow conditions | Off |
| Coordinate system | Global coordinate system |
| Reference axis | X |

### 4.3 INPUT DATA
#### 4.3.1 Initial Mesh Settings
Automatic initial mesh: On
Result resolution level: 5
Advanced narrow channel refinement: Off
Refinement in solid region: Off

### 4.4 GEOMETRY RESOLUTION
Evaluation of minimum gap size: Automatic
Evaluation of minimum wall thickness: Automatic

**4.5 LOCAL MESH SETTINGS**
**Local Initial Mesh 1**

| Components | Face <3WING2-4@Boss-Extrude1> |
|---|---|
| | Face <1WING-3@Boss-Extrude1> |
| | Face <4WING2-4@Boss-Extrude1> |
| | Face <2WING-3@Boss-Extrude1> |
| Solid/fluid interface | Small solid features refinement level: 1 |
| | Curvature refinement level: 0 |
| | Curvature refinement criterion: 0.318 rad |
| | Tolerance refinement level: 0 |
| | Tolerance refinement criterion: 0.102 m |
| Refining cells | Refine fluid cells: Off |
| | Refine solid cells: Off |
| | Refine partial cells: Off |
| Narrow channels | Advanced narrow channel refinement: Off |

**4.6 COMPUTATIONAL DOMAINS**
**Size**

| X min | -0.978 m |
|---|---|
| X max | 1.027 m |
| Y min | -0.173 m |
| Y max | 0.382 m |
| Z min | -0.686 m |
| Z max | 0.776 m |

**4.7 BOUNDARY CONDITIONS**

| 2D plane flow | XY - plane flow |
|---|---|
| At X min | Default |
| At X max | Default |
| At Y min | Default |
| At Y max | Default |
| At Z min | Symmetry |
| At Z max | Symmetry |

**4.8 PHYSICAL FEATURES**
Heat conduction in solids:
Off
Time dependent: Off
Gravitational effects: On
Flow type: Laminar and
turbulent
 High Mach number flow: Off
Humidity: Off
Default roughness: 0
micrometer

**4.9 GRAVITATIONAL SETTINGS**

| X component | 0 m/s^2 |
|---|---|
| Y component | -9.81 m/s^2 |
| Z component | 0 m/s^2 |

Default wall conditions: Adiabatic wall

## 4.10 AMBIENT CONDITIONS

| Thermodynamic parameters | Static Pressure: 101325.00 Pa<br>Temperature: 293.20 K |
|---|---|
| Velocity parameters | Velocity vector<br>Velocity in X direction: 20.000 m/s Velocity in Y direction: 0 m/s Velocity in Z direction: 0 m/s |
| Turbulence parameters | Turbulence intensity and length<br>Intensity: 0.10 % Length: 0.004 m |

## 4.11 MATERIAL SETTINGS
### *4.11.1 Fluids*
Air
## 4.12 Goals
*Surface Goals*
### 4.12.1 SG Av Velocity (X) 1

| Type | Surface Goal |
|---|---|
| Goal type | Velocity (X) |
| Calculate | Average value |
| Faces | Face<3>@WING2-4 |
| | Face<2>@WING2-4 |
| Coordinate system | Global coordinate system |
| Use in convergence | On |

### 4.12.2 SG Av Velocity (Y) 1

| Type | Surface Goal |
|---|---|
| Goal type | Velocity (Y) |
| Calculate | Average value |
| Faces | Face<3>@WING2-4 |
| | Face<2>@WING2-4 |
| | Face<1>@WING-3 |
| | Face<4>@WING-3 |
| Coordinate system | Global coordinate system |
| Use in convergence | On |

### 4.12.3 SG Force (X) 1

| Type | Surface Goal |
|---|---|
| Goal type | Force (X) |
| Faces | Face<3>@WING2-4 |
| | Face<2>@WING2-4 |
| | Face<1>@WING-3 |
| | Face<4>@WING-3 |
| Coordinate system | Global coordinate system |
| Use in convergence | On |

### 4.12.4 SG Force (Y) 1

| Type | Surface Goal |
|---|---|
| Goal type | Force (Y) |
| Faces | Face<3>@WING2-4 |
| | Face<2>@WING2-4 |
| | Face<1>@WING-3 |
| | Face<4>@WING-3 |
| Coordinate system | Global coordinate system |
| Use in convergence | On |

### 4.13 Calculation Control Options
**Finish Conditions**

| Finish conditions | If one is satisfied |
|---|---|
| Maximum calculation time | 360 s |
| Maximum travels | 2 |
| Goals convergence | Analysis interval: 5e-001 |

**Solver Refinement**

Refinement: Disabled

### 4.14 Results Saving

| Save before refinement | On |
|---|---|
| Periodic saving | Units: Iterations<br>Period: 10 |

### 4.15 Advanced Control Options
**Flow Freezing**

| Flow freezing strategy | Disable |
|---|---|

## V. Problems And Proposed Solutions

### 5.1 PROBLEMS

We lacked the expertise of simulating the forces that the wing would encounter in flight. Besides, the attempt to analyze the prepared model in Solid Works resulted no concrete findings as the software generated millions meshing points. As a result the memory in the system could not process such large number of meshing points.

There was lack of wind tunnel of required size. So the real time data of the forces experienced by wing was therefore unavailable. Servo mechanism to link the control surfaces basically ailerons of both the upper and lower wings was difficult.

### 5.2 PROPOSED SOLUTIONS

- The model could be further reduced in scale to eliminate the meshing problem in the existing software and system.
- Also high power computing could be done to process the data in the existing scale.
- Wind tunnel testing of the wing and other structures for real time forces

## VI. CONCLUSION

Symmetrical wing for a bi plane was constructed using balsa wood. The support structure for the wing i.e., fuselage was also made and incorporated with other control surface, elevator and rudder.

Further improvement in the existing model can be made by installing mechatronic system to make it airworthy. The system would include the servo mechanisms to link the various control surfaces, radio equipment, receiver and transmitter, to remotely control the flight of the bi plane.

The symmetrical wing is used in aerobatic aircrafts as the particular wing profile supports inverted flying and other aerobatic stunts

## REFERENCES

[1]. Allen R Miller and Emanuel Vegh (1993). "Exact Result for the Grazing Angle of Specular Reflection from a Sphere.

[2]. Anderson, John, D (2007). Fundamentals of Aerodynamics. McGraw-Hill.

[3]. Kermode, A.C. (1972); Mechanics of Flight, Chapter 3 (Eighth (metric) edition). Sir Isaac Pitman and Sons Ltd, London.

[4]. Airplane Aerodynamics, Dommasch and Lomb

[5]. Chatterjee S, Templin RJ 'Biplane wing planform and flight performance of the feathered dinosaur Microraptor gui'

[6]. White, Lynn. "Eilmer of Malmesbury, an Eleventh Century Aviator: A Case Study of Technological Innovation, Its Context and Tradition .

# Multilevel Inverter for Grid-Connected PV System Employing Digital PI Controller with an Improved PWM Scheme

Polasa Praveen Kumar[1], Subhash rathod[2], Chowhan mothilal[3]

[1]*M .Tech Student, Department of Electrical Electronics Engineering,VREC,Nizamabad, Telangana, India*
[2]*Assistant professor, Department of Electrical and Electronics Engineering, VREC,Nizamabad, Telangana, India*
[3]*Assistant professor, Department of Electrical and Electronics Engineering, VCEW,, Nizamabad, Telangana, India*

***Abstract:*** *A single-phase MULTI-level Photovoltaic (PV) inverter topology for grid-connected PV systems with a novel Pulse Width-Modulated (PWM) control scheme. The inverter offers much less Total Harmonic Distortion (THD) and can operate at near-unity power factor. The proposed system is verified through simulation results are compared with that with the conventional single-phase three-level grid-connected PWM inverter. The circuit topology, modulation law, and operational principle of the proposed inverter were explained in detail. The performances of the inverter and Simulation results indicate that the THD of the five-level inverter is much lesser than that of the conventional three-level inverter. Furthermore, both the output voltage and the output current are in phase at near-unity power factor.*
***Keywords***: *Grid-connected, multilevel inverter, photovoltaic (PV), pulse width modulated (PWM), inverter, proportional-integral (PI) current.*

## I. Introduction

**R**enewable Energy Sources, particularly solar and wind energy, have become very popular and demanding as the world is concerned with fossil-fuel exhaustion and environmental problems caused by conventional power generation. PV sources have the advantage of being maintenance and pollution free. Due to decreasing costs and prices, Solar-electric- energy demand has grown consistency by20%-25% per annum over the past 20 years. This decline has been driven by Mainly three factors: 1) an increasing efficiency of solar cells; 2) improvements in manufacturing- technology; 3) economics of scale. An inverter, which is an important element in the system, is used to convert dc power from the sources into ac power to be fed into grid.

This paper presents a multisource five-level inverter. In this, a PV panel, an AC source and a DC source are interfaced with their own dc-dc converter to a common dc-ac inverter. This is beneficial compared with the centralized system, because every source can be controlled individually. Further enlargements are easily achieved because a new source with a dc-dc converter can be added into the existing system. A High efficiency is thereby achieved with a flexible design. A five level inverter have great advantages such as improved output waveforms, smaller filter size and lower electromagnetic interference.

In this paper, a single phase multisource five level inverter is presented. It consists of a PV panel, an AC source and a DC source connected to their own dc-dc boost converter. A modified PWM control scheme is presented to generate PWM switching signals for the switches and to produce five output-voltage levels. In this, two reference signals are used instead of one to generate PWM signals for the switches. $V_{ref1}$ and $V_{ref2}$ are the two reference signals and are identical.
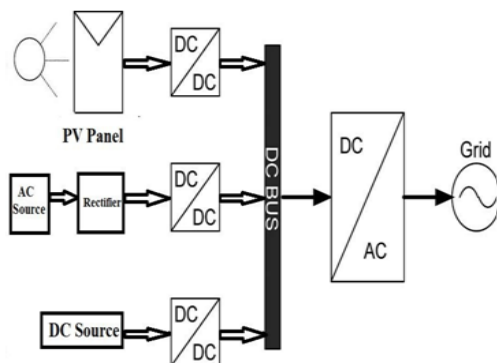


**Fig.1**. Configuration of multisource inverters.
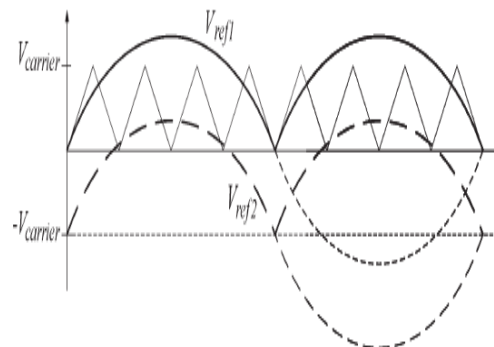


**Fig.2**. Carrier and reference signals

A Proportional-Integral Current Control Scheme is employed since the inverter is used in PV system in order to keep the output current sinusoidal and to have high dynamic performance under Simulation and experimental results are presented to validate the proposed configuration.

## II. Multisource Five-Level Inverter Topology

The single phase multisource five- level inverter topology is shown in fig. 3. It consists of a PV panel, an AC source and a DC source connected to a common.
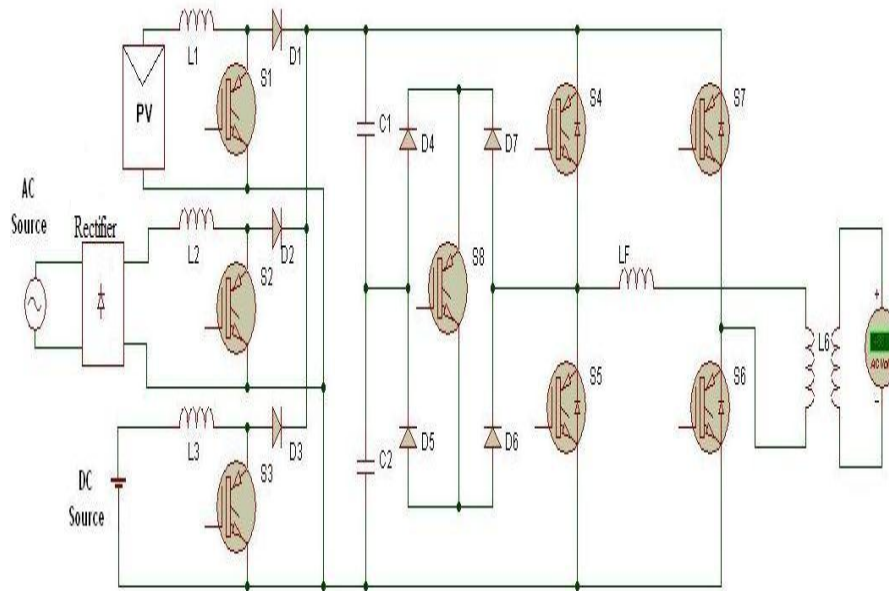


**Fig.3**. Single-phase multisource five-level inverter topology

dc bus, an auxiliary circuit and a full bridge inverter configuration. Input sources, PV panel, AC source and DC source are connected to the inverter via the dc-dc boost converters. The utility grid is used instead of a load since the inverter is used in a grid-connected system. To track the Maximum Power Point [MPP] independently and to step up inverter output voltage, the dc-dc boost converters are used. A Step-up transformer with a ratio of 1:2 is used.

DC-DC converter can perform MPP tracking [MPPT] for the PV panel. An advantage of using Multisource approach in parallel configuration is that the mixing of different sources becomes possible, i.e., existing PV sources can be extended by adding new higher output sources without comprising the overall system reliability or performance. It also have the advantage of greater safety during installation and maintenance. Each converter module may be able to isolate its connected power source so that wiring of series or parallel connection of these sources can be performed safely depending on the design. Asafelow voltage connection is used for power- source-converter connection To avoid high dc-dc voltage, the dc- dc boost converters are connected in parallel which will eventually increase the size of capacitors and the inverter's cost. Therefore, as the dc bus, only two capacitors with equal capacitance rating are used and the other dc-dc boost converters are connected to this dc bus as shown in fig. 3.

To filter the current injected into the grid, a filtering inductance is used. The current injected into the grid must be sinusoidal with low harmonic distortion. In order to generate sinusoidal current, a sinusoidal PWM is used because it is one of the most effective methods. A sinusoidal PWM is obtained by comparing a high frequency carrier signal with a low- frequency sinusoid signal, which is the modulating or reference signal. The carrier has a constant period; therefore, the switches have constant switching frequency. The switching instant is determined from the crossing of the carrier and the modulating signal.

### III. Operating Principles of Multisource Five-Level Inverter

Combinations of PV panel, AC source and DC source are used as the input voltage sources. Voltages across the input sources are boosted by dc-dc converters to exceed grid voltage. The proposed inverter produces five output voltage levels. An auxiliary circuit is used which consists of four diodes and a switch connected between the dc-bus capacitors and the full bridge inverter. A five level of input supply voltage is generated by the proper switching control of the auxiliary circuit.

$V_{ref1}$ and $V_{ref2}$ are the two reference signals which will take turns to be compared with the carrier signal at a time.
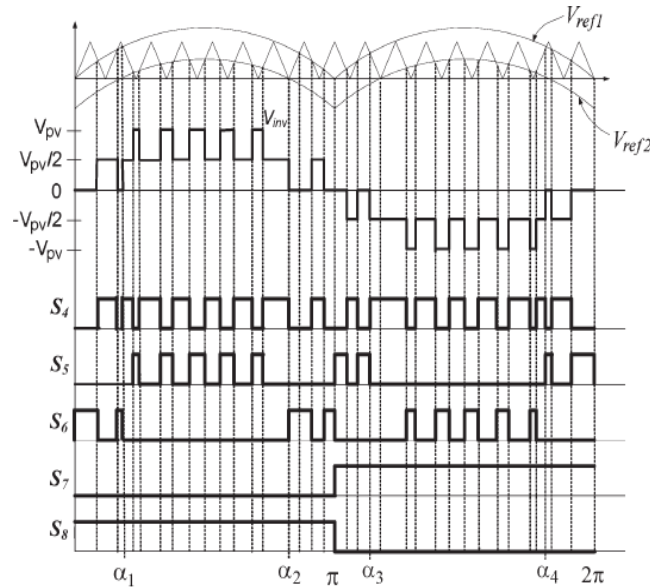


Fig.1 Inverter Output Voltage ($V_{inv}$) and switching pattern for the single-phase five-level inverter.

TABLE 1
Inverter Output Voltage During S4-S8 Switch On And Off

| $S_4$ | $S_5$ | $S_6$ | $S_7$ | $S_8$ | $V_{inv}$ |
|-------|-------|-------|-------|-------|-----------|
| ON | OFF | OFF | OFF | ON | $+V_{pv}/2$ |
| OFF | ON | OFF | OFF | ON | $+V_{pv}$ |
| OFF | ON or OFF | OFF or ON | ON or OFF | OFF or ON | 0 |
| ON | OFF | OFF | ON | OFF | $-V_{pv}/2$ |
| OFF | OFF | ON | ON | OFF | $-V_{pv}$ |

$V_{ref2}$ will be compared with the carrier signal until it reaches zero when $V_{ref1}$ exceeds the peak amplitude of carrier signal $V_{carrier}$. A switching pattern shown in fig.4 is obtained. Switches S4-S6 will be switching at the rate of the carrier signal frequency whereas Switches S7 and S8 will operate at fundamental frequency. Table 1 shows inverter output voltage level $V_{inv}$ during S4-S8 switch on and off.

Since dc-dc boost converters are connected in parallel, if one of the sources is disconnected from the dc bus, the operation of the other dc-dc boost converters will not be affected. Expansion of sources is possible by adding a dc-dc boost converter.

### IV. Control System Algorithm

The main problem in PV generation systems is that the amount of electric power generated by the solar arrays is always changing with weather conditions, i.e., the intensity of solar radiation. An MPPT method or algorithm has quick response characteristics and is able to make good use of the electric power generated in any weather. This method is needed to solve the aforementioned problem.

The perturb-and-observe algorithm is used in this paper to extract the maximum power from the PV arrays and deliver it to the inverter. PI algorithm is used as controller for the feedback controller.

The grid current $I_g$, which is the current injected into the grid is sensed and fed back to the comparator, which compares it with the reference current $I_{ref}$.

The instantaneous current error is fed to a PI controller. The integral term in the PI controller improves the tracking by reducing the instantaneous error between the reference and the actual current. The resulting error signal is used to control the pulse-width modulation for the switches. Below the minimum power condition or above the maximum power condition, the inverter should not operate to ensure the safety of the PV panel.
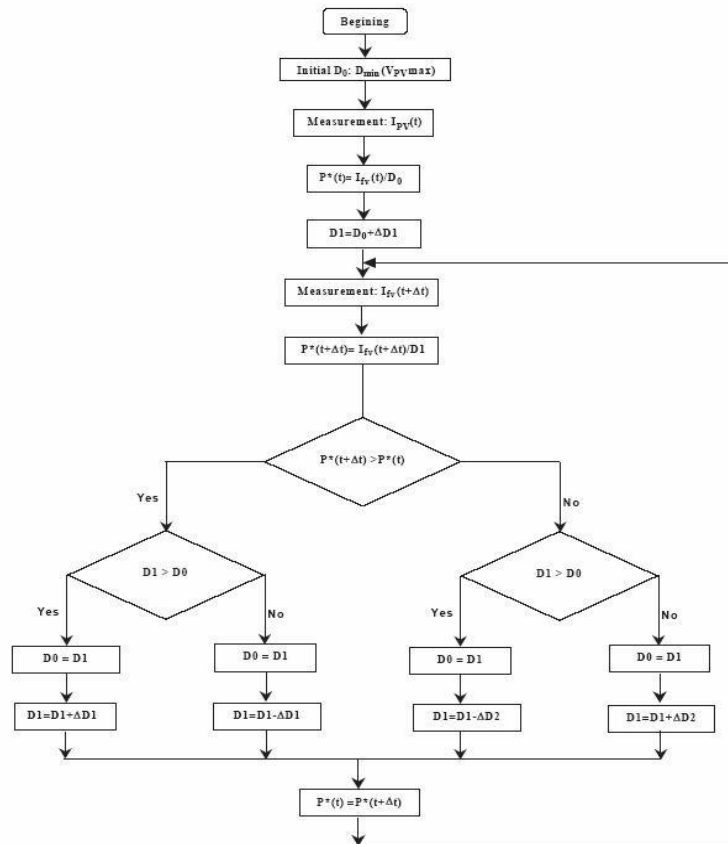


Fig.4 MPPT Flow Chart

## V. Simulation Result
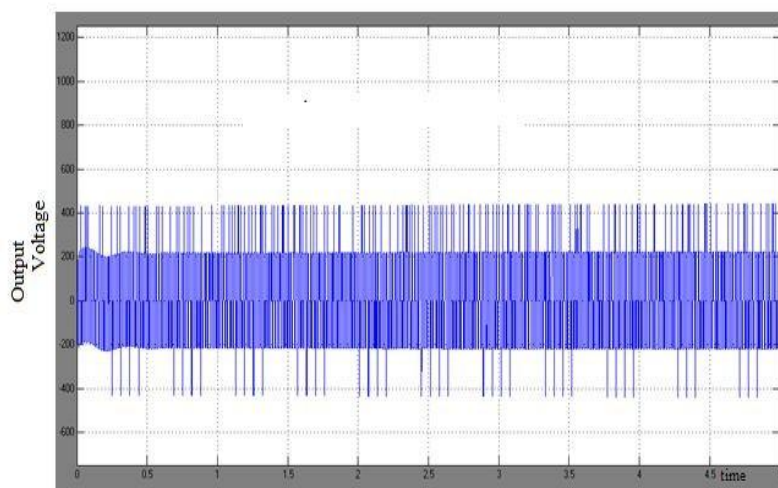


***Fig.5*** Output Voltage of Multisource Five- Level Inverter.

## V. Conclusion

This paper presented a single-phase multilevel inverter forPV application. It utilizes two reference signals and a carrier signal to generate PWM switching signals. The circuit topology, modulation law, and operational principle of the proposed inverter were analyzed in detail. A digital PI current control algorithm is implemented in DSP TMS320F2812 tooptimizethe performance of the inverter. Experimental results indicate that the THD of the five-level inverter is much lesser than that of the conventional three-level inverter. Furthermore, both the grid voltage and the grid current are in phase at near-unity power factor.

## REFERENCES

[1]   J. M. Carrasco, L. G. Tranquillo, J. T. Bialasiewicz, E. Galvan,R. C. PortilloGuisado, M. A. M. Prats, J. I. Leon, andN.MorenoAlfonso,"Power-electronic systems for the griintegration of renewable energysources: A survey," IEEE Trans. Ind. Electron., vol. 53, no. 4, pp. 1002–1016, Aug. 2006.
[2]   V. G. Agelidis, D. M. Baker, W. B.Lawrance, and C. V. Nayar, "Amultilevel PWMinverter topology for photovoltaic applications," in Proc.IEEE ISIE, Guimarães, Portugal, 1997, pp. 589–594.
[3]   S. Kouro, J. Rebolledo, and J. Rodriguez, "Reduced switching-frequency modulation algorithm for high-power multilevel inverters," IEEE Trans.Ind. Electron., vol. 54, no. 5, pp. 2894–2901, Oct. 2007.
[4]   S. J. Park, F. S. Kang, M. H. Lee, and C. U. Kim, "A new single-phase fivelevelPWM inverter employing a deadbeat control scheme," IEEE Trans. Power Electron., vol. 18, no. 18, pp. 831–843, May 2003.
[5]   L. M. Tolbert and T. G. Habetler, "Novel multilevel inverter carrier-based PWM method," IEEE Trans. Ind. Appl., vol. 35, no. 5, pp. 1098–1107,Sep./Oct. 1999.
[6]   M. Calais, L. J. Borle, and V. G. Agelidis, "Analysis of multicarrier PWM methods for a single-phase five-level inverter," in Proc. 32nd Annu. IEEEPESC, Jun. 17–21, 2001, vol. 3, pp. 1173–1178.
[7]   N. S. Choi, J. G. Cho, and G. H. Cho, "A general circuit topology ofmultilevel inverter," in Proc. 22nd Annu. IEEE PESC, Jun. 24–27, 1991,pp. 96–103.
[8]   G. Carrara, S. Gardella, M. Marchesoni, R. Salutari, and G. Sciutto, "Anew multilevel PWMmethod: A theoretical analysis," IEEE Trans. PowerElectron., vol. 7, no. 3, pp. 497–505, Jul. 1992.

## BIOGRAPHIES

**Polasa Praveen Kumar**
My Self Polasa Praveen Kumar, pursuing my M.Tech from VREC, Nizamabad,Telangana state. And I am having hands on experience in teaching with of two years have been attend ICTIEE(International conference on transformation in engineering education), hubli, Karnataka. Mail id: praveen.polasa@gmail.com

**Subhash Rathod**
Subhash Rathod, working as assistant professor at Vijay rural engineering college, Nizamabad Telangana state.  with having 7 years of teaching experience. And he has done his M.Tech form NIT, Warnagal. Mail id: rathodmt@gmail.com

**Chowhan Mothilal**
Chowhan Mothilal, he has completed his  M.Tech in 2012 and working as assistant professor in Vijay College of engineering for women's, Nizamabad ,Telangana state., having 6years of teaching experience. Mail id: chouhan_bunty@yahoo.com

# Position Determination of an Aircraft Using Acoustics Signal Processing

D. Lakshmanan[1], P Anand[2], P. Manmathakrishnan[3]

[1,2,3]*Department of Aeronautical Engineering, Bannari Amman institute of technology, Sathyamangalam, India*

**Abstract:** *This paper deals with the determination of an aircraft position using the acoustic source emitted from it. As per the experimental setup, sound energy emitted from the aircraft is captured with the help of microphones and processed further using MATLAB toolbox and LABVIEW software. Localization algorithm is sub divided into two categories, in which the first method involves time delay estimation of acoustic source through simulation process and the second method is analyzing the Doppler frequency shift from the aircraft sound. Using the above methods the navigation parameters such as velocity, Height, Mach number, RPM of the propeller, Elevation angle and slant range will be determined.*

**Keywords:** *frequency shift, time delay, Acoustic signal processing simulation, Aircraft velocity and Altitude.*

## I. Introduction

### 1.1 Acoustic Source and Sensor

The ground sensors are mostly used in remote areas for surveillance and early instruction about the target for identification purposes. The maximum amount of acoustic energy emitted by the engine systems of aircraft or vehicles will be taken for position determination. It can be possible to detect the aircraft sound source using highly sensitive acoustic sensors mounted closed to the ground. The presence of an acoustic source can be detected automatically when the aircraft is nearing to fixed position with different distance. Data from acoustic sensors can also be processed for source classification, localization, and tracking. When an aircraft travels at constant velocity and constant altitude, the path is completely specified by a set of flight parameters. The retardation effect, which arises when the speed of the source is comparable with the speed of sound propagation in the medium, enables the estimation of some or all of the aircraft flight parameters using passive acoustic methods.

### 1.2 Acoustic Technology Overview

As the acoustic wave propagates through the surface of the material, any changes to the characteristics of the propagation path affect the velocity and/or amplitude of the wave. Changes in velocity can be monitored by measuring the frequency or phase characteristics of the sensor and can then be correlated to the corresponding physical quantity being measured.

Hardware section of an all acoustic wave devices and sensors use a piezoelectric material to generate the acoustic wave. Piezoelectricity refers to the production of electrical charges by the imposition of mechanical stress. When the certain amount of electrical field is applied to a piezoelectric material, it creates a mechanical stress. Piezoelectric acoustic wave sensors will generate an oscillating electric field to create a mechanical wave, which propagates through the substrate and is then converted back to an electric field for measurement.

### 1.3 Techniques Involved

The Doppler Effect is used when the aircraft is moving with respect to the fixed sensors on the ground. This can be described as the effect produced by a moving source of waves in which there is an apparent upward shift in frequency at sensors towards whom the source is approaching and an apparent downward shift in frequency at sensors from whom the source is receding.

## II. Microphone Specifications (Sensor)

### 2.1 A Typical 4190 ½" Inch Free Field Microphone

| | |
|---|---|
| Capacitance | 16 Pf |
| Diameter | 1/2 inch |
| Range | 15 - 147 dB |
| Freq. Range | 3.15 - 20000 Hz |

| | |
|---|---|
| Polarization Voltage | 200 V |
| Pressure Coefficient | – 0.01 dB/kPa |
| Sensitivity | 50 mV/Pa |
| Temperature Coefficient | -0.012 dB/ºC |
| Temperature Range | - 30 - 150 ºC |

## III.  Field Works That Were Carried Out

A field experiment is conducted near to Chennai airport in which three microphones are located above the ground level. Data are collected for varies time period. After the initial setup has been made, free field microphone is switched on. When the aircraft is moving away or towards the sensor is noted and the corresponding frequency is captured for the initial time t. After a particular time period again the sensor is switched on, at which the aircraft is flying exactly over the sensor and frequency is captured for the corresponding time $t_c$. The output of the sensor is sampled at 1 kHz through MATLAB simulation process.
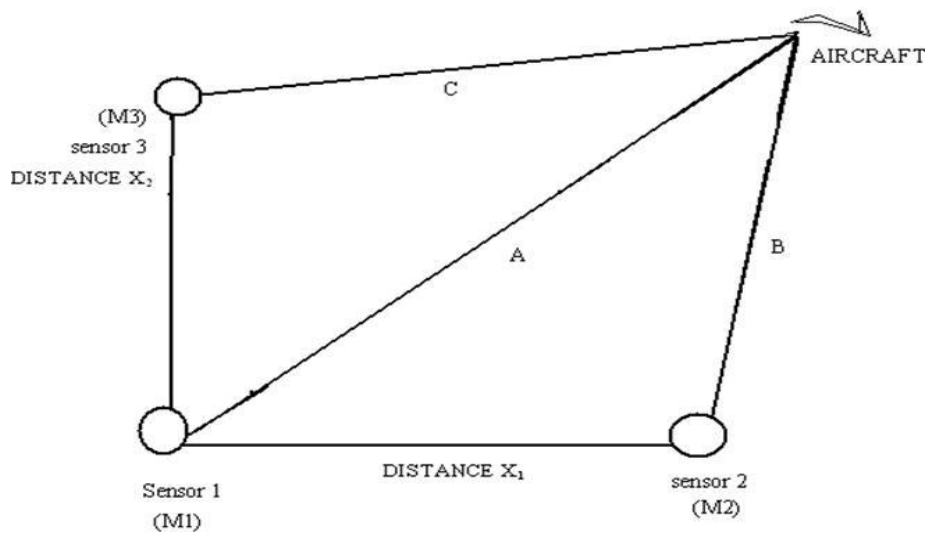


**Fig 1: Sensors arrangements with equally separated Distance**

## IV.  Matlab Simulation Process With Acoustic Source Input

*4.1 Aircraft Acoustic Simulation*

Simulation blocks which shows that how input wave signal is given to blocks and further signal processing is done through it. Recorded aircraft sound file is given to the block through wave file simulation setup and it is connected with cross correlation block and time vector scope. Time delay between the sensors can be analyzed by simulation setup and the results will be displayed.
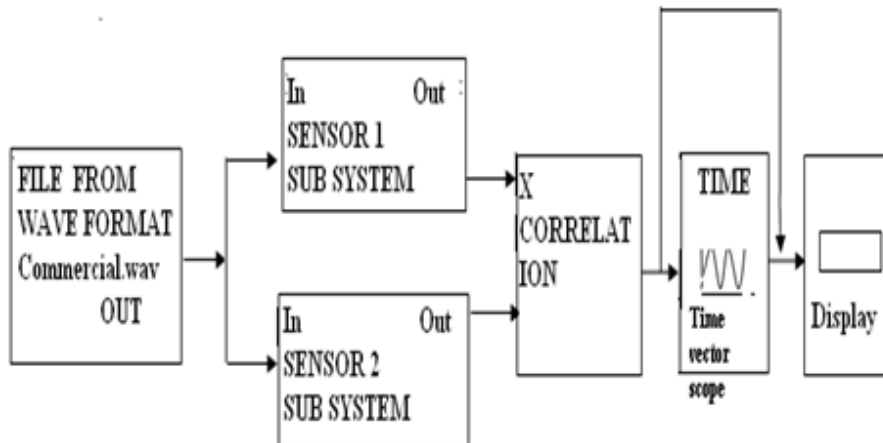


**Fig 2: Simulation blocks contain aircraft sound source**

Fig 2 shows that the wave file form of converted aircraft sound from three different microphones are given to the MATLAB blockset for cross correlation signal processing in which time delay between each sensor is measured. Time delay values are subjected to least square mathematical algorithm to estimate the final results.

### 4.1 Time - Frequency Estimation

When the aircraft is moving along a constant path at a constant speed at time at a separation distance or slant range of $R_c$. The aircraft emits an acoustic tone of constant frequency $f_o$ and the speed of sound in air is *c*. The frequency of the signal, as received by the sensor, changes with time due to the acoustical Doppler Effect. The acoustic signal received by the sensor at time t is given by

$$X(t) = a + b\, B(t, t_c, s) \qquad ...(1)$$

$t_c$   the time at which aircraft moving near to sensors
B  is constant parameter
a,b are relative parameters to source frequency and velocity
$f_o$ – constant frequency (KHZ)
 s – Acoustic lines from software simulation from MATLAB
 $a = f_o\, c^2 / c^2 - v^2$
 $b = -f_o\, c\, v / c^2 - v^2$
 $c = R_c\, (c^2 - v^2)^{1/2} / (v\, c)$
 v  is the velocity of aircraft km/hr

## V.   Mathematical Approach

Calculation of the initial estimate of T(initial) ($\tau_c = t_c$) time at which when the aircraft is moving near to sensors
$T = \arg \text{Min} \{ f(t_k) - \tfrac{1}{2}\{ f(t_1) + f(t_k) \} \}$  sec      ...(2)
$f(t_1)$, $f(t_k)$ are the initial and final estimate of time varying frequencies observed by the sensors and estimated in MATLAB simulation.

Estimates the source velocity $V_0$ is given by
$V = c * \{ f(t_1) - f(t_k) / f(t_1) + f(t_k) \}$ km/hr          ...(3)
C is the velocity of sound (330 m/sec)

Estimates the source range at ground mounted sensors R is given by
$R = f_0\, (c\, v_0)^2 / \{[(c^2 - v_0^2)]^{3/2} * g_{max}\}$ m          ...(4)
Here $V = v_0$
$G_{max}$ = Maximum magnitude obtained from signal processing graph.

Elevation angle (θ)
$\theta = \tan^{-1}(h / t - t_0)$ Deg                    ...(5)

RPM of the propeller(s)                    ...(6)
$S = (f_0 * 60) / 2$
h is the height of the aircraft from the microphones
$f_0$ is estimated constant source frequency of an aircraft.

## VI.   Power Spectrum Analysis

The acoustic source emitted from the aircraft is captured and it is further processed through LABVIEW and MATLAB software to estimate the source properties accurately.

**Fig 3: Spectrum lines of Aircraft sound**

The Fig(3) depicts the simulation results of an aircraft sound source for frequency versus decibel properties. At 2000 to 2800 Hz, the frequencies are received little bit uniformly with small variation in decibels.
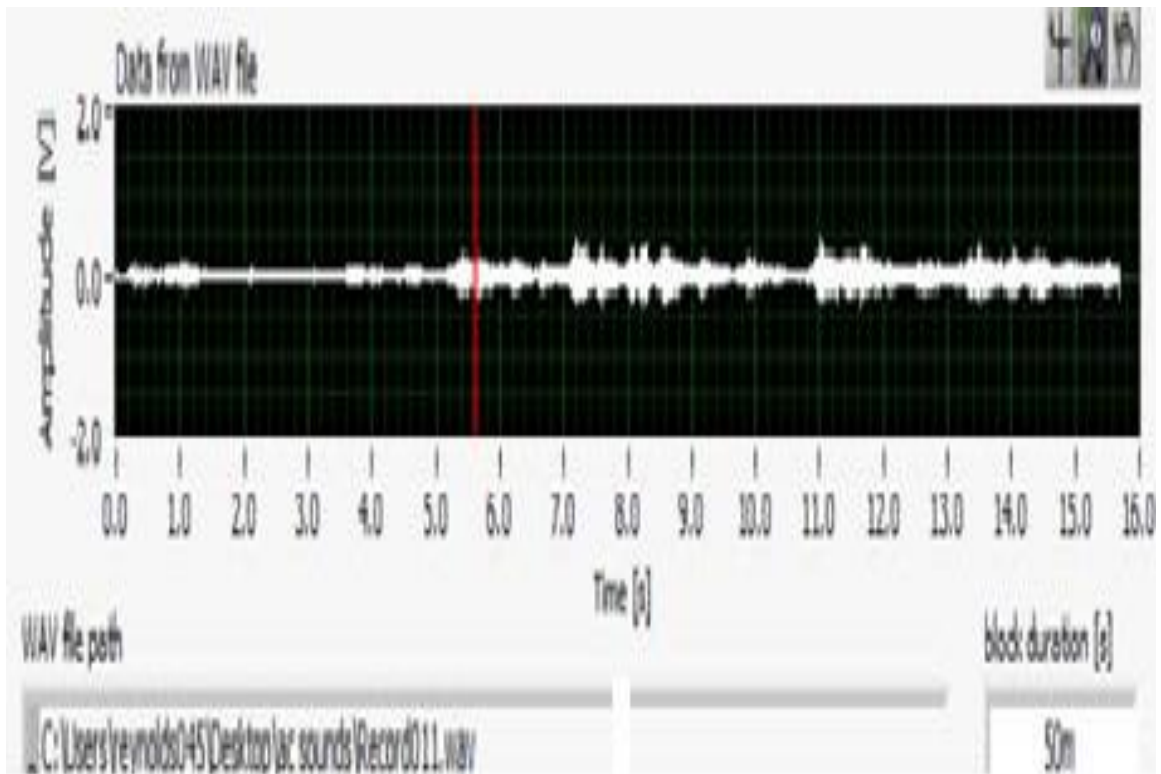


**Fig 4: Aircraft sound source from first Microphone**
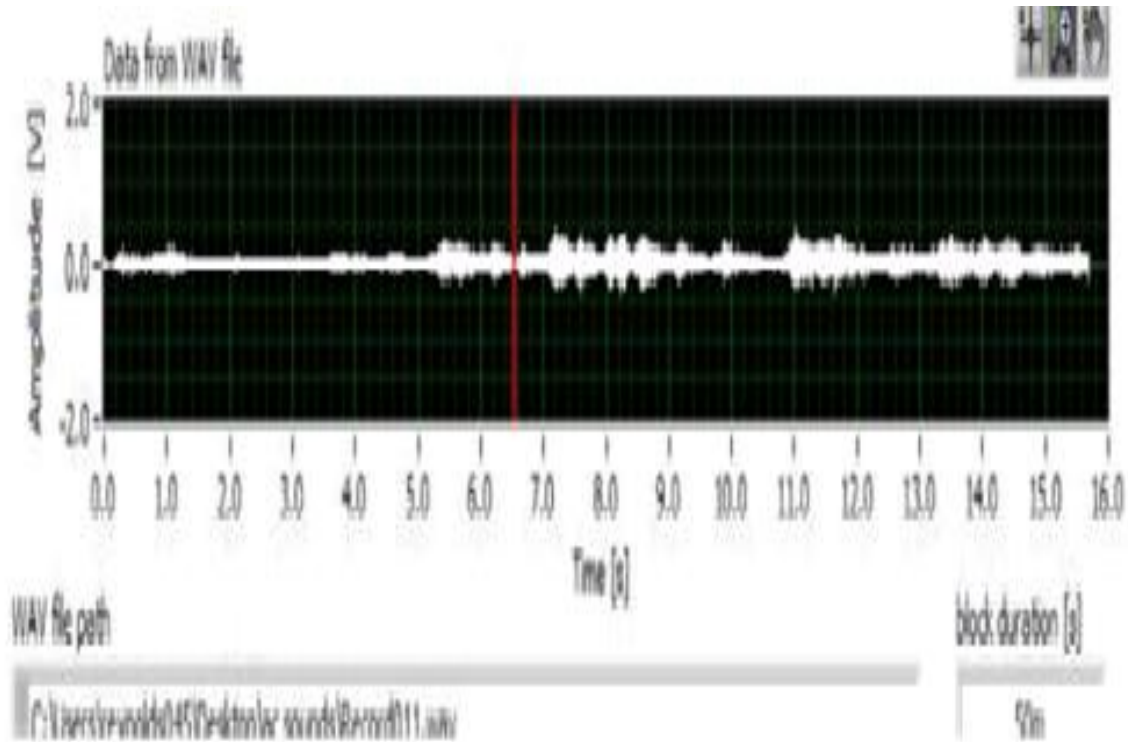
**Fig 5: Aircraft sound source from second Microphone**
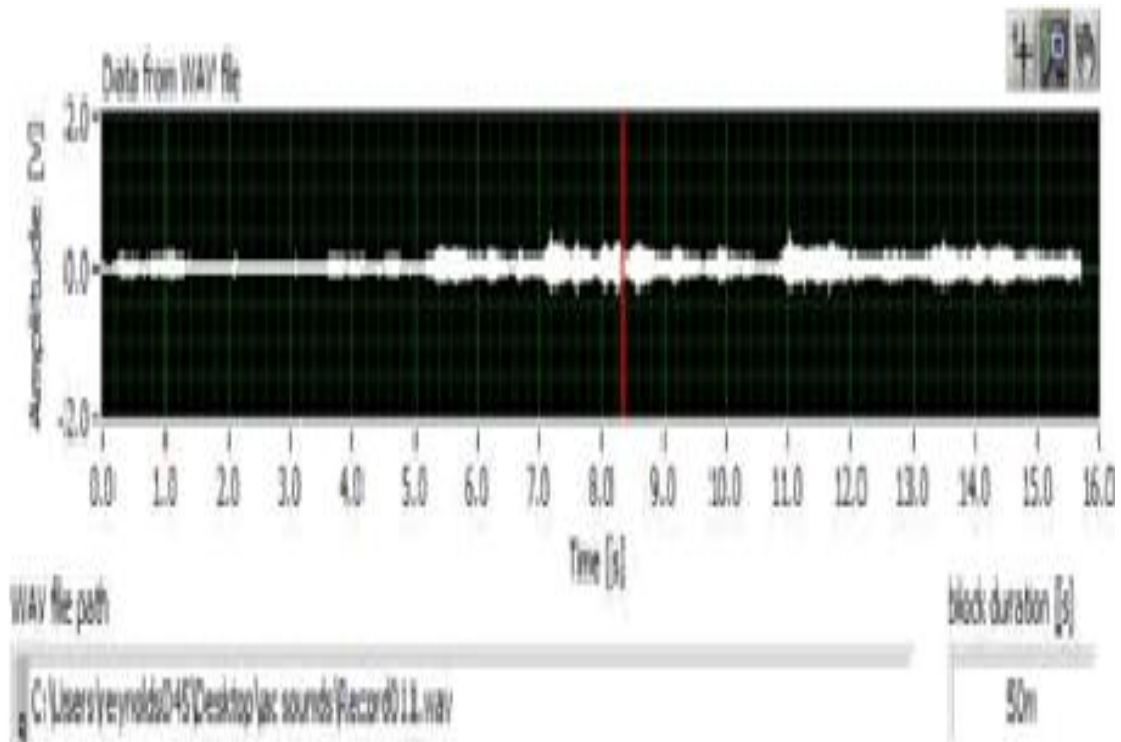


**Fig 6: Aircraft sound source from Third Microphone**

Fig. 4, 5 and 6 depicts the simulation results of time delay with respect to amplitude of sound source recorded by each sensor mounted over the ground. By simulation data, clearly it shows that the time delays between the sensors are like as 0.5sec, 1sec and 1.8 sec. The amplitude of the signal, which also changes due to the variation in distance between the aircraft and microphones.
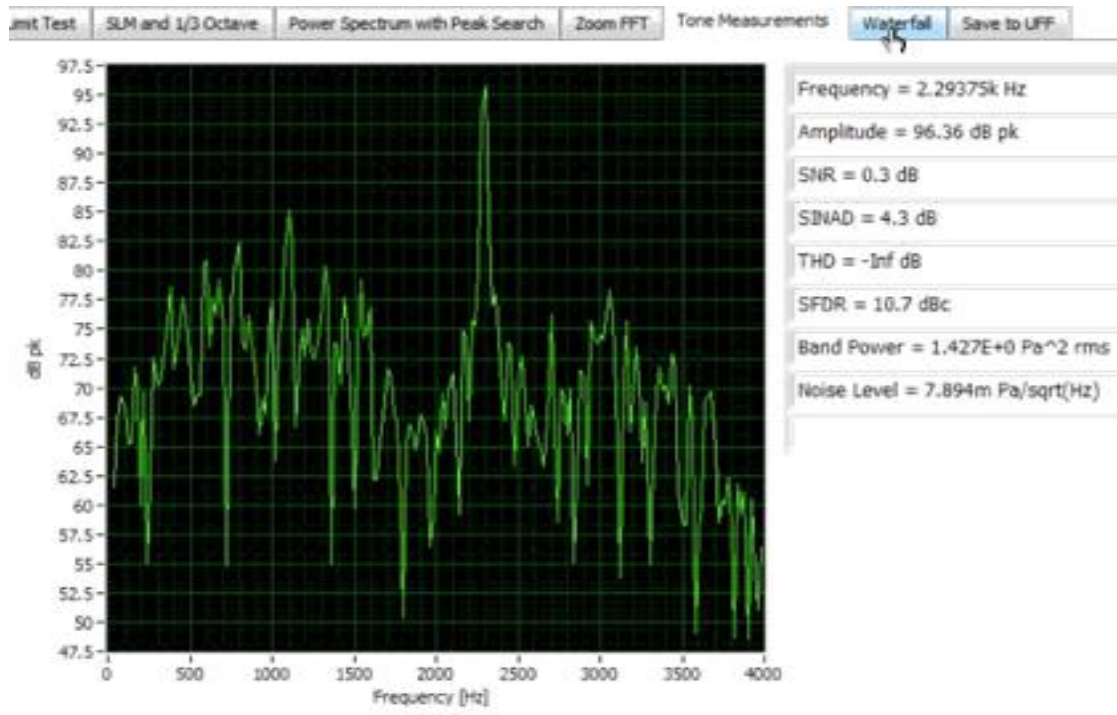
**Fig 7: Tone measurements through LABVIEW**

The Fig (7) depicts the simulation results to determine the exact initial frequency. Initial frequency is shown at the right of the graph with other tone properties. Accurately, Initial frequency is 2.93 KHz, Signal to Noise ratio also determined as 0.3 db.
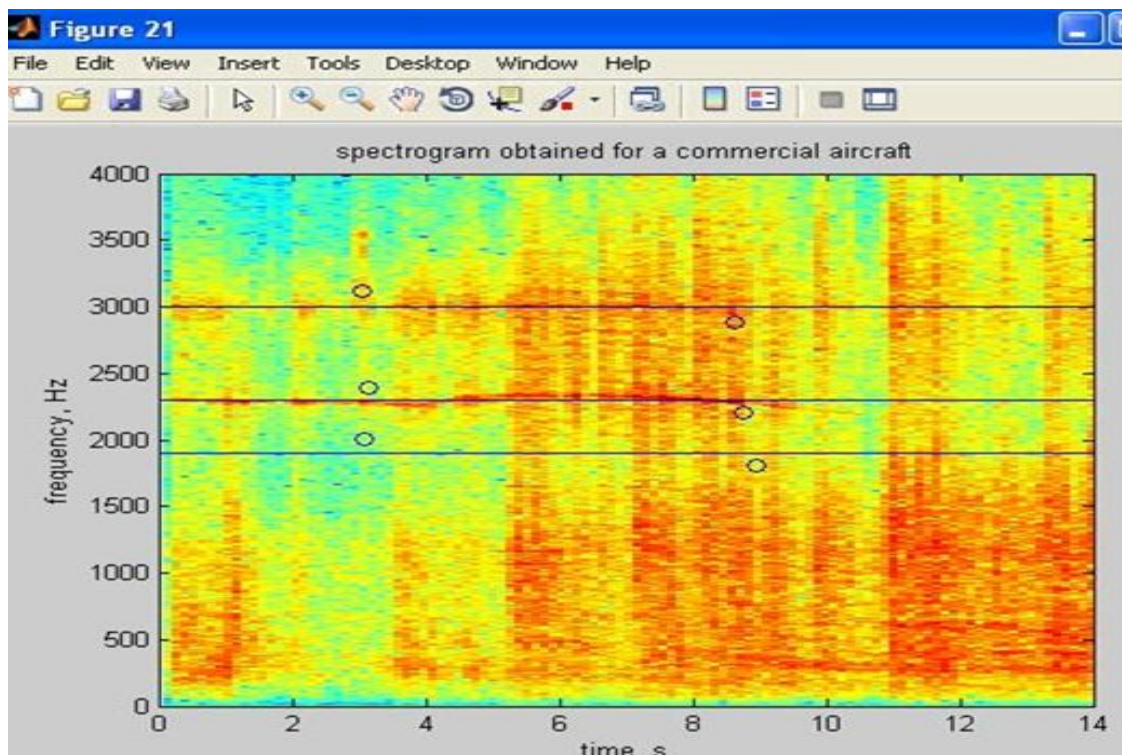


**Fig 8: Spectrogram process for Aircraft Sound**

Fig 8 is observed that the constant tone of Doppler frequency $f_0$ is lies between the range of 2000 Hz to 3000 Hz. The above three horizontal lines which are exactly gives the values of $f(t_1)$ and $f(t_2)$ to calculate the navigational parameters such as velocity and Range from the microphones.

## VII. Results

Observed datas from the simulation process are analysed mathematically with least square approach. From the analysis of Doppler shifting frequency, the initial and final time varying Frequencies are taken as $f(t_1)$ = 2 KHz, $f(t_2)$ = 3.5 KHz.

Velocity of the aircraft V = 1224 * (3.5 - 2) / 5.5 = 333.81 km/ hr

Constant frequency source emitted from the aircraft $F_0$ = 2.5428 kHz

Slant Range of an aircraft near the ground mounted sensors R = 267 m

RPM of the propeller = 75000/m

Elevation angle = 0.8753*10^-3 Deg

Height from the microphone = 325.27 m

Mach number = 0.2721(subsonic)

## VIII. Conclusion

The process of aircraft position determination method provides reliable estimates of the aircraft speed during takeoff, height from the microphones, slant range distance between the aircraft to the microphone, elevation angle, RPM of the propeller and Mach number of a transiting aircraft. In this work sound of a commercial aircraft is recorded by free field microphones which are fixed on the ground. From the recorded sound, spectrogram and tone properties are obtained using MATLAB and LABVIEW toolbox.

## REFERENCE

[1]. Barry D Bullard," Pulse Doppler signature of Rotary wing aircraft," Georgia tech research institute Atlanta
[2]. B.G. Quinn, 1996, "Application of short time Fourier transform and Winger – Ville to the acoustic localization of Aircraft," Journal of Acoustic society of America.
[3]. Kam W.Lo and Brain G. Ferguson,1996,"Passive emission of aircraft motive parameters using destructive interference between direct and ground reflected sound waves," Journal of Acoustic society of America.
[4]. Severino, A. Zaccaron and R. Ardoino, 2002, "Performances of Doppler based direct passive localization techniques," University of California.
[5]. Giovanni and Gaetano Scarano, 2000, "Discrete time techniques for time delay estimation," IEEE transactions on digital signal processing.
[6]. Debadeepta Dey, Christopher geyer, Sanjiv singh, Matt digioia, 2009, "Passive, long range detection of aircraft: Towards a field deployable sense and avoid systems," In.proc field & service robotics.
[7]. B.Friendlander, 1987,"Passive localization algorithm and its accuracy analysis,"IEEE Journal of Ocean Engineering.